Late Quaternary hydrological change from fluvial archives in southwestern Africa and the palaeoclimate implications

Ella Victoria Walsh
Supervisors: Professor D.S.G. Thomas & Dr S.L. Burrough
Hertford College

Thesis submitted for the degree of
Doctor of Philosophy



University of Oxford
Hilary Term 2022

Abstract

Fluvial sedimentary sequences provide important archives of late Quaternary palaeoenvironmental change. In drylands, these stores of information in fluvial landforms can be found in regions that are commonly scarce in long-term palaeoproxy records due to low levels of precipitation and poor organic preservation. In southwestern Africa, proposed drivers of Quaternary climate change carry with them a suite of hypotheses with respect to patterns of precipitation variability, yet poor coverage of palaeoclimate archives has to date made it challenging to assess model-based predictions. Here, fluvial archives offer the potential to provide the spatial and temporal coverage of palaeorecords that is required. Whilst it is well-established that dryland fluvial systems respond to hydroclimate changes on Quaternary timescales, deciphering the palaeoenvironmental histories they preserve is often complex. To date, the utility of records from fluvial archives in southwestern Africa has been hindered by low-resolution chronologies, limited use of robust methods to interrogate the context of sediment deposition, and a focus on individual studies with limited consideration of regional controls.

This thesis addresses these challenges through: i) the production of a new fluvial record from the Huab River using a detailed assessment of stratigraphic, compositional, and sedimentological changes and a high-resolution luminescence chronology; ii) the construction of a chronological database to compile and analyse quality-assessed fluvial histories from southwestern Africa; and iii) an empirical-model data comparison to interrogate these fluvial records in the context of other palaeorecords and palaeoclimate model simulations to test hypotheses of the spatial patterning of late Quaternary precipitation. The new Huab River record spans the entirety of the Holocene, recording evidence of distinct flow regimes at 12 to 9 ka, 7 to 5 ka, 4 to 1 ka, and 1 ka to present. The database collates a scattered fluvial literature and has enabled an assessment of controls on fluvial archive preservation and interpretation. The timing and nature of phases of river flow are consistent between the Huab and nearby records, and patterns of fluvial activity across southwestern Africa map onto patterns of precipitation anomalies inferred from other palaeorecords and those simulated by a suite of climate models. These data indicate spatial differences in rainfall response between coastal and inland southwestern Africa, supporting hypotheses of a difference in the dynamics of the tropical rainbelt over the ocean and land, the role of ocean-atmosphere feedbacks, and the role of westerly-derived rainfall. Together, these findings demonstrate the utility of robust fluvial archives for reconstructing palaeoenvironmental change and have allowed for recommendations to be made for priorities for future research on fluvial archives, both in southwestern Africa and beyond.

Acknowledgements

Firstly, a huge thank you goes to my supervisors Professor David Thomas and Dr Sallie Burrough. Their guidance, support, and encouragement over the last four years has made this thesis possible. I am very grateful for the time they have spent, from fieldwork in the Huab River, to guidance on preparation of samples in the lab, and many hours reading my writing. It has been great working with them and I have gained so much from their knowledge and enthusiasm for understanding the palaeoclimates of southern Africa.

Thank you also to Sam, Kaja, Lillian, Julie, and Maike for their advice and discussions in the lab, and for the fun times both in and out of the office. I am grateful to Szilvi for guiding me through luminescence dating sample preparation and to Mona and Hong for making the lab work possible. Thank you to colleagues at the University of Erlangen-Nuremberg, particularly to Domenico and Luca, for inviting me to Erlangen, helping with the sedimentology analysis, and for teaching me how to identify minerals under the microscope. Thank you also to Baoli for joining us in the field.

I would like to thank NERC Environmental Research Doctoral Training Partnership (DTP) for funding this research and thank Hertford College for the Mortimer May Scholarship and travel grants that made fieldwork possible. Fieldwork was also funded by grants from the British Society for Geomorphology, the School of Geography and the Environment, and the Quaternary Research Association.

I also want to say the biggest of thanks to my friends. The DPhil would have been a completely different experience without them. Thank you in particular to Hamish, Becca, Oscar, and Louis for making Oxford a great place to live, and to many others both in and beyond Oxford who made the last four years so much fun. Finally, thank you to my wonderful family. They have given me so much love and support, and have encouraged me the whole way through.

Contents

Abstract i
Acknowledgements iii
List of Figures ix
List of Tables xiii
List of Equations xiv
Units xiv
Abbreviations xiv
Chapter 1: Introduction 1
1.1. Background 2
1.2. Research aim and objectives 4
1.3. Thesis structure 5
Chapter 2: Context 9
2.1. Introduction 10
2.2. Drylands 10
2.3. Dryland Rivers 12
2.4. Fluvial sediments as palaeoenvironmental archives 14
2.4.1. Environmental signal propagation 15
2.4.2. Types of fluvial archive in drylands 15
2.4.3. Complexity in interpretation of fluvial geomorphological archives 16
2.4.4. Approaches to studying fluvial records in drylands 20
2.5. Southern Africa: climate, geological, and fluvial setting 21
2.5.1. Southern African climate 21
2.5.2. Southern Africa's structure and geology 26
2.5.3. Southern African rivers 27
2.6. Southern African palaeoclimate change 32
2.6.1. Insolation forcing 33
2.6.2. Complexity in southern Africa's palaeoclimate response 34
2.6.3. Availability of records 35
2.7. The Huab 37
Chapter 3: Methods 41
3.1. Introduction 42
3.2. Fieldwork 42
3.2.1. Ground Penetrating Radar 45
3.2.2. Sample site selection 49

3.3. Luminescence dating 50
3.3.1. Principles of OSL 51
3.3.2. Laboratory preparation and measurement protocol 53
3.3.3. Preheat and dose recovery tests 55
3.3.4. Environmental dose rate 57
3.3.5. Age estimation 60
3.4. Sedimentological approaches 61
3.4.1. Grain size analysis 61
3.4.2. Lithofacies analysis 62
3.4.3. Initial characterisation of samples: XRD, Geochemistry, LOI 63
3.4.4. Compositional analysis: heavy minerals and petrography 67
3.5. Construction of a chronological fluvial database 72
3.5.1. Selection criteria 72
3.5.2. Database structure 73
3.5.3. Data quality assessment 76
3.6. Palaeoclimate model-data comparison 79
3.6.1. Palaeoclimate model data 79
3.6.2. Palaeodata filtering 82
Chapter 4: Holocene fluvial depositional regimes of the Huab River, Skeleton Coast, Namibia 84
Abstract 84
4.1. Introduction 85
4.1.1. Regional setting 88
4.2. Methods 92
4.2.1. Site selection 92
4.2.2. Optically Stimulated Luminescence (OSL) dating 93
4.2.3. Lithostratigraphic and grain size analysis 95
4.2.4. Raman heavy mineral and petrographic analysis 96
4.3. Results 97
4.3.1. Chronology 97
4.3.2. Sedimentary characteristics of the Huab valley fill 102
4.4. Interpretation 116
4.4.1. Provenance: compositions and drainage lithologies 116
4.4.2. Stratigraphy: fluvial processes 118
4.4.3. Combining provenance and process interpretation 120
4.5. Discussion 124
4.6. Conclusions 127

Chapter 5: A chronological database assessing the palaeoenvironmental record from fluvial sediments in southwestern Africa 130
Abstract 130
5.1. Introduction 131
5.1.1. Dryland rivers and fluvial palaeoenvironmental archives 135
5.1.2. Regional setting 137
5.2. The Database 139
5.2.1. Data selection 139
5.2.2. Database structure and content 139
5.2.3. Data quality 145
5.3. Current status of the database 149
5.4. Discussion 157
5.4.1. River typology 157
5.4.2. Controls on the preserved fluvial record 158
5.4.3. Sources of evidence 164
5.4.4. The Quaternary fluvial record 171
5.5. Conclusion 178
Chapter 6: Model-archive comparison of mid Holocene and Last Glacial Maximum climates in central southwestern Africa 182
Abstract 182
6.1. Introduction 183
6.1.1. Background 185
6.2. Methods 192
6.2.1. Palaeoclimate models 193
6.2.2. Palaeorecords 196
6.3. Results 202
6.3.1. Mid Holocene (MH) 207
6.3.2. Last Glacial Maximum (LGM) 214
6.4. Discussion 219
6.4.1. Spatial pattern of precipitation response 219
6.4.2. Differing controls on the tropical rainbelt over ocean and land 221
6.4.3. Role of ocean-atmosphere feedbacks 224
6.4.4. Extension of the latitudinal reach of westerly frontal rainfall 225
6.4.5. Assessing data contributions 227
6.4.6. Recommendations 231
6.5. Conclusions 232

Chapter 7: Conclusions 235
7.1. Introduction 236
7.2. Depositional regimes of the Huab River 236
7.2.1. Timing of sediment deposition 237
7.2.2. Nature of sediment deposition 239
7.3. Fluvial sediments as palaeoenvironmental records in southwestern Africa 240
7.3.1. Status of fluvial research in southwestern Africa 241
7.3.2. Controls on records obtained 241
7.3.3. Quaternary history recorded 243
7.4. Model-data comparison of southwestern African Quaternary climate 245
7.4.1. Which hypotheses are supported by the available evidence? 245
7.4.2. Utility of fluvial archives 247
7.5. Future research 248
7.5.1. Fluvial records from the Skeleton Coast, Namibia 248
7.5.2. Fluvial records from southwestern Africa 250
7.5.3. Database of fluvial archives in other dryland regions 253
References 255
Appendices 307
Appendix A – Author contributions 308
Appendix B – Initial study of the Huns River valley fill, southern Namibia 309
Appendix C – Supplementary material for Chapter 3 (Methods) 321
Appendix D – Supplementary material for Chapter 4 (Paper 1) 338
Appendix E – Supplementary data for Chapter 5 (Paper 2): part 1 345
Appendix F – Supplementary data for Chapter 5 (Paper 2): part 2 The Database 354

List of Figures

Figure 2.1. World dryland areas demarcated by contemporary global aridity index (Trabucco and Zomer, 2022). 11

Figure 2.2. Linear flow occupancy scale detailing the diversity in hydrology of dryland rivers from Tooth and Nanson (2011). 13

Figure 2.3. Schematic of filtering processes within sedimentary records (Bailey and Thomas, 2014). 17

Figure 2.4. Annual contemporary precipitation (mm) across southern Africa and main climate systems responsible for rainfall. 22

Figure 2.5. Contemporary precipitation (mm month^{-1}) per season across southern Africa using the WorldClim 2.0 dataset (Fick and Hijmans, 2017). 23

Figure 2.6. Map of key geological units in southern Africa map from Garzanti *et al*. (2018) and Garzanti *et al.* (2022) adapted from Schulter (2008). 27

Figure 2.7. Distribution of probability of flow intermittence for southern Africa using the dataset on global prevalence of non-perennial rivers and steams from Messager *et al*. (2021). 28

Figure 2.8. Examples of river systems in southwestern Africa. 29

Figure 2.9. Map of Namibian and ephemeral rivers with river gauge station locations. 31

Figure 2.10. The Huab River catchment, Namibia. 38

Figure 2.11. Rainfall data from two rainfall stations within the Huab Basin (from Gil-Romera *et al*., 2006, showing data from Namibian Meteorological Service). 38

Figure 3.1. A) Location of valley fill studied within the Skeleton Coast National Park, Huab River. B) Location of sampling sections along the natural exposure in the valley fill. 43

Figure 3.2. Google earth images of meander change over 15 years. 45

Figure 3.3. Location of GPR transects across the surface of the valley fill and in the modern ephemeral channel. 46

Figure 3.4. Radargrams from ground penetrating radar (GPR) analysis. 47

Figure 3.5. Photos of fieldwork in the Huab River. 48

Figure 3.6. Example of sections of the natural exposure within the Skeleton Coast valley fill chosen for sampling. 50

Figure 3.7. Examples of signals and dose response curves. 55

Figure 3.8. Examples of preheat plateau tests. 56

Figure 3.9. Dose recovery results using a preheat of 200˚C and cut heat of 180˚C. 57

Figure 3.10. Comparison of the radionuclide concentrations and dose rates obtained through ICP-MS analysis and gamma spectroscopy. 59
Figure 3.11. D_e distribution of sample NAM18/1/5. 61
Figure 3.12. Stratigraphic log of individual lithofacies for site NAM18/2. 63
Figure 3.13. Results of XRD analysis of six key samples. 64
Figure 3.14. Location of samples collected from the Huab River catchment (Dansie *et al*., 2018) for geochemical analysis in the context of the underlying geology. 65
Figure 3.15. Geochemistry biplot of valley fill (black) and catchment (coloured) samples to interrogate the relationship between geochemistry and geology. 66
Figure 3.16. A) Polished slide for HM analysis. B) and C) inserts of the polished slide, crosses indicate the Raman laser position, D) Examples of distinctive spectra obtained from HM slides. 70
Figure 3.17. Digital scan of thin section of NAM18/1/12 with a 1 mm grid to guide Raman laser position and locate grains for optical microscopic assessment. 71
Figure 3.18. Content of the chronological fluvial database. 73
Figure 3.19. Examples of river catchment analysis performed in ArcGIS on rivers that contain sites in the database. 76
Figure 3.20. Simulated LGM and preindustrial precipitation values for two models within PMIP3 and calculated anomalies between the two. 81

Figure 4.1. A) Map of drainage basins and main fluvial systems in Namibia. B) Location of the Huab Skeleton Coast valley fill (20km upstream of the river mouth) within the Huab catchment. 86
Figure 4.2. Map of geological groups of northern Namibia (Mendelsohn *et al.*, 2002). 90
Figure 4.3. Location of sample sites in the Huab Skeleton Coast valley fill. 93
Figure 4.4. A) Dose recovery test results. Dotted line indicates unity, where the laboratory administered dose and recovered dose are equal. B) Example of an OSL signal: natural signal (OSL counts per 0.05 s) against time, for sample NAM18/2/10. 98
Figure 4.5. Sedimentary logs and luminescence ages from sections NAM18/1, NAM18/2, NAM18/7, NAM18/4. 106
Figure 4.6. Lithofacies examples from sites NAM18/1, NAM18/2, NAM18/7. 107
Figure 4.7. Grain size distributions by volume coloured by grain size cluster. 109
Figure 4.8. Petrographic (A) and heavy mineral (B) assemblages. 111
Figure 4.9. Petrography of Huab sands under cross-polarised light. 112

Figure 4.10. Ternary diagrams for Huab petrographic and heavy mineral datasets. A) QFL: quartz, feldspar, lithic fragments (Dickinson, 1985; Garzanti, 2018), B) QFRf: quartz, feldspar, rock fragments (Pettijohn *et al*., 1987), C) LmLvLs: low-grade metamorphic, volcanic and sedimentary lithic fragments, D) PxEpAmp: pyroxene, epidote, amphibole. 113

Figure 4.11. Compositional biplots of petrographic and heavy mineral assemblages. A) Petrographic compositional biplot following Dickinson. B) Heavy mineral compositional biplot. 121

Figure 4.12. Box and Whisker plots of A) modal grain size (μm) by age group, and B) sorting (σ μm) by age group. 123

Figure 5.1. All sites in the fluvial chronological database coloured by sedimentary context. 135

Figure 5.2. Content of the Quaternary chronological fluvial database. 140

Figure 5.3. Spatial distribution of fluvial sites in the database. 141

Figure 5.4. Histograms of number of ages by publication year for all data within the database. 152

Figure 5.5. Temporal distribution of ages, sedimentary context, chronology type, data quality, and analysis approaches from southwestern Africa's fluvial deposits. 153

Figure 5.6. Relationship between sedimentary context fluvial (flow occupancy (A) and magnitude (B)) and climate interpretations (C). 161

Figure 5.7. Maximum age at each site by region and by river setting. 162

Figure 5.8. Framework for considering the data required for interpretation of dryland fluvial sedimentary records. 168

Figure 5.9. Southwestern Africa's late Quaternary fluvial and climate conditions inferred from the fluvial records. 172

Figure 6.1. Seasonal variability in contemporary synoptic circulation patterns over southern Africa. 187

Figure 6.2. PMIP simulations of the annual cycle of precipitation (mm month^{-1}) averaged over central southwestern Africa (defined by box in Figure 6.1) for: A) the pre-industrial period (PI), B) the mid Holocene (MH) and C) the Last Glacial Maximum (LGM). 195

Figure 6.3. Location of archive sites used for model-data comparison within central southwestern Africa. 197

Figure 6.4. Terrestrial records of palaeoclimate and environmental change arranged by proxy type and by latitude. 203

Figure 6.5. A) Sedimentary archive depositional ages from fluvial sites in central southwestern Africa organised by river and by latitude. 205

Figure 6.6. Marine records of Benguela current upwelling and terrestrial change. 206

Figure 6.7. Mid Holocene PMIP annual precipitation anomalies (mm $year^{-1}$) over Africa relative to the pre-industrial period. 209

Figure 6.8. The extent of summer (DJF) precipitation anomalies over ocean (9-15˚E, 14-27˚S) and over land (15-21˚E, 17-30˚S) for each model at each time step (circles: MH, triangles: LGM). 209

Figure 6.9. Model-data comparison for the mid Holocene (palaeodata: 5-7 ka, models: 6 ka) detailing the spatial pattern of precipitation anomalies across central southwestern Africa. 211

Figure 6.10. Last Glacial Maximum PMIP annual precipitation anomalies (mm $year^{-1}$) over Africa relative to the pre-industrial period. 214

Figure 6.11. Model-data comparison for the Last Glacial Maximum (palaeodata: 20-22 ka, models: 21 ka) detailing the spatial pattern of precipitation anomalies across central southwestern Africa. 216

Figure 6.12. Interpretation of the distribution of climate anomalies based on available palaeodata and the PMIP3 model simulations. A) Mid Holocene (6 ka), B) Last Glacial Maximum (21 ka). 221

Figure 7.1. Correspondence between chronologies established for Huab Skeleton Coast valley fill stratigraphic sections. 238

Figure 7.2. Location of sites, river courses, and river catchments within southwestern Africa, and possibilities for future foci of research. 251

List of Tables

Table 2.1. Challenges faced in the study of fluvial deposits, with reference to factors both common to river systems globally and specific to dryland settings. 18

Table 3.1. Details of sampling sites. 49

Table 3.2. Sources of data added to the database. 75

Table 3.3. Criteria used for assessment of chronological data quality. 77

Table 3.4. Orbital and trace gas parameters used for the simulation of pre-industrial (PI), mid Holocene (MH; 6 ka), and last glacial maximum (LGM; 21 ka) climates. 80

Table 3.5. Filtering criteria applied to palaeodata for model-archive comparison. 82

Table 4.1. Results of luminescence dating. 100

Table 4.2. Lithofacies table summarising sedimentary structures and interpretation of depositional environment. 102

Table 4.3. Results of grain size analysis: modal grain size, sorting, skew, and kurtosis. 110

Table 4.4. Petrographic assemblage of the Huab valley fill samples. 114

Table 4.5. Heavy mineral assemblage of the Huab valley fill samples. 116

Table 5.1. Key characteristics of the sedimentary contexts recorded in the chronological database. 142

Table 5.2. Description of categories used to classify fluvial interpretation. 144

Table 5.3. Chronological data quality criteria. 146

Table 5.4. Characteristics of southwestern Africa's rivers that have been studied as records of palaeoenvironmental change. 150

Table 5.5. Results of data quality assessment by region. 151

Table 5.6. Summary of the number of sites in the full database by sedimentary contexts and river setting. 155

Table 5.7. Summary of the sources of evidence to reconstruct palaeoenivronmental change. 156

Table 6.1. Paleoclimate Modelling Intercomparison Project (PMIP3) models used in palaeo model-data comparison. 194

Table 6.2. Palaeorecords used for model-data comparison (locations in Figure 6.3). 198

Table 6.3. Data evaluation considerations by archive type based on assessments in published syntheses. 200

Table 6.4. PMIP precipitation anomaly results averaged over central southwestern Africa. 208

List of Equations

Equation 3.1. Equation for calculating a luminescence age. 51

Units

˚C	Degrees Centigrade	**Ma**	Million years
g cm^{-3}	Grams per centimetre cubed	**mm**	Millimetre
Gy	Gray (1 Gy = 1 J kg^{-1})	**MHz**	Megahertz
Gy ka^{-1}	Grays per thousand years	**s**	Second
ka	Thousand years	**µm**	Micrometre
km	Kilometre	**yr**	Year
m	Metre		

Abbreviations

AI	Aridity Index	**DRAC**	Dose Rate and Age Calculator
CAB	Congo Air Boundary	**DRC**	Dose Response Curve
CAM	Central Age Model	**GPR**	Ground Penetrating Radar
CCA	Canonical Correspondence Analysis	**H_2O_2**	Hydrogen peroxide
CMIP	Climate Modelling Intercomparison	**H_2SiF_6**	Fluorosilicic
Project		**HCl**	Hydrochloric acid
D_e	Equivalent Dose	**HF**	Hydrofluoric acid
DJF	December to February	**HM**	Heavy mineral

HWM High-water mark

ICP-MS Inductively Coupled Plasma Mass Spectrometry

IR Infra-red

ITCZ Intertropical Convergence Zone

JAXA Japanese Space Agency

JJA June to August

KDE Kernel Density Estimation

LED Light-emitting diode

LGM Last Glacial Maximum

MH Mid Holocene

LIA Little Ice Age

L_x Natural or regenerative dose

L_x/T_x Sensitivity-corrected OSL signal

MAM Minimum Age Model

MAAD Multiple Aliquot Additive Dose

MG Multigrain

NERC Natural Environment Research Council

OSL Optically Stimulated Luminescence

PCA Principal Component Analysis

PET Potential evapotranspiration

PH Preheat

PMIP Palaeoclimate Modelling Intercomparison Project

PSI Palaeostage indicator

PT Petrography

SAA South Atlantic Anticyclone

SAR Single Aliquot Regenerative

SG Single grain

SRS Sediment Routing System

SST Sea surface temperature

SWD Slackwater deposit

TL Thermoluminescence

TTCB Tropical temperate cloud band

TTT Tropical temperate trough

Tx Test Dose

UNEP United Nations Environment Programme

Chapter 1:

Introduction

1.1. Background

Drylands are defined as hyper-arid to dry sub-humid environments and cover ~40 % of the world's land area (Mirzabaev *et al*., 2019). These regions are vulnerable to future climate change impacts (Lian *et al*., 2021; Mirzabaev *et al*., 2019; Wang *et al*., 2012), yet for regions such as southern Africa, a range of modelled futures exist (Trisos *et al*., 2021). Beyond testing global climate models against historical datasets, we can also evaluate how environments have responded to past forcing on Quaternary timescales. Key palaeoclimate and palaeoenvironmental archives record the response of southern African climate systems to insolation forcing during the late Quaternary, yet debate exists regarding the relative controls on precipitation and the nature and spatial heterogeneity of terrestrial response. Critical to understanding past climate change is the availability of palaeoproxy robust records with sufficient spatial coverage. This research focuses on deciphering the environmental history preserved in fluvial archives (i.e. a store of information contained within fluvial sediments or landforms) to test hypotheses of Quaternary climate change.

Fluvial sedimentary archives can be found in many southern African dryland contexts (Grenfell and Grenfell, 2021; Stone and Thomas, 2013; Stone, 2021; Tooth, 2016), including in areas that lack a diversity of palaeoproxy records for reconstruction of Quaternary climates (Chase and Meadows, 2007). Poor organic preservation, limited occurrence of depocenters, and extended periods of aridity have restricted the availability and temporal continuity of lacustrine, speleothem, and palynological archives. Whilst novel terrestrial proxies have been developed from hyrax middens (e.g. Chase *et al*., 2012, 2019) and marine core sedimentary archives can integrate evidence of terrestrial palaeoenvironmental change to produce long, well-dated records (e.g. Farmer *et al.* 2005), the records obtained from these archives are accompanied by respective challenges of low spatial coverage (Humphries, 2021) and large and uncertain source regions (Scott *et al*., 2004). Within this context, fluvial sedimentary deposits can attest to the response of rivers to past hydroclimatic regimes and can preserve evidence of more significant river flow (Hurkamp *et al*.,

2011; Srivastava *et al*., 2004; Tooth *et al*., 2022) in systems that are currently intermittent and ephemeral (Messager *et al*., 2021).

There is increasing recognition of the potential for geomorphological features, or 'geoproxies', to be studied as archives of landscape response to past climates in dryland regions globally (Fitzsimmons *et al*., 2013; Stone, 2021; Thomas, 2013; Woor *et al*., 2022), yet these opportunities come with appreciation of the complexities associated with filtering of climate signals through archive formation (Bailey and Thomas, 2014; Jerolmack and Paola, 2010; Macklin *et al*., 2012). In the case of fluvial geoproxies, the use of robust methods for deciphering and interpreting hydrological conditions responsible for sedimentary deposition is critical. Climate signals are preserved in sedimentary archives as changes in sediment volume, character, and composition (Tofelde *et al*., 2021). Fluvial sediments in southern Africa have commonly been investigated in terms of sedimentary texture, stratigraphic context, and palaeodischarge, yet studies linking sedimentological and compositional changes to palaeoflow dynamics in dryland settings have been more limited. With a greater understanding of the controls on dryland fluvial archive formation and the use of robust methods (e.g. Ramisch *et al*., 2017), there is potential for fluvial geoproxies to contribute robustly to the palaeoclimate literature.

In addition to the use of empirical proxy records, global climate models (GCMs) offer an opportunity to simulate palaeoclimate conditions and identify the large-scale atmospheric systems that might be responsible for changes in precipitation (e.g. Braconnot *et al*., 2011; Singarayer *et al*., 2017). Whilst interpretations of large amplitude palaeoenvironmental changes have been linked to orbital drivers, the southern African climate response to insolation appears to have been spatially complex. From model simulations, it has been suggested that differences in the response of the tropical rainbelt over the ocean compared to land resulted in a divergence between environmental conditions in inland and coastal regions (Singarayer and Burrough, 2015; Singarayer *et al*., 2017).

To date, however, a focus on a limited suite of high-resolution terrestrial archives, and marine cores that encompass wide source areas, has meant that the spatial extent of changes simulated by models in the western portion of southern Africa has been difficult to verify. A growing dataset from investigated fluvial sites, with a good spatial coverage in southwestern Africa, has the potential to help resolve challenges of understanding spatial complexity in past climate conditions that have driven environmental responses.

1.2. Research aim and objectives

The overall aim of this thesis is to ***assess the hydroclimatic history preserved in the depositional record of southwestern Africa's dryland rivers to address how the palaeoclimate responded to past forcing.*** This thesis incorporates field sampling and laboratory analysis to produce a new fluvial record, constructs and analyses a chronological database, and undertakes a comparison between empirical palaeoclimate and palaeoenvironmental archives and palaeoclimate models.

A valley fill archive in the Huab River, northern Namibia, was chosen as the principal study site for the new record produced in this thesis. In the Skeleton Coast, upstream of a topographic constriction, a rich history of stratified fluvial deposition spans the valley. Exposed sediments allow for a combined assessment of detailed stratigraphy and compositional analysis, and the extensive deposit enables a wider analysis of palaeoflow changes than has been possible in other systems to date. A period of fieldwork was also undertaken in the Huns River, southern Namibia. Initial samples were collected, analysis began, and it was intended to conduct a second field season to collect further samples. Due to COVID-19, it was not possible to return to the site, so this element of research has not been included in the reshaped work that led to this thesis. The aim and objectives therefore reflect the form of the thesis after the impacts of COVID-19, in which opportunities arose for a more detailed investigation of samples from the Huab River and

interrogation of the wider climate implications of this work through analysis of climate model outputs.

Together, the approaches used in this thesis address the overarching research aim through three primary research objectives:

1. To establish the timing and nature of depositional regimes of the Huab River valley fill archive, Skeleton Coast, Namibia, using a high-resolution luminescence chronology and a systematic assessment of stratigraphic, compositional, and sedimentological changes;
2. To construct a database of chronologies established from dryland fluvial contexts to critically evaluate how sediments have been used as palaeoenvironmental archives in southwestern Africa;
3. To test hypotheses of the spatial patterning of late Quaternary precipitation change using quality-assessed data from empirical palaeoarchives and palaeoclimate model simulations.

1.3. Thesis structure

The structure of this thesis follows the paper route guidelines of the School of Geography and the Environment, University of Oxford. The main results of this thesis are detailed in three papers submitted to journals. These papers are presented here as chapters, where the section numbering and organisation is adapted to fit the flow of the thesis. Co-author contributions are described in Appendix A.

Chapter 1 provides an overview of the background to this thesis, the overarching research aim, and the three primary research objectives. **Chapter 2** presents a review of literature on dryland regions, dryland rivers, and considerations for studying and interpreting fluvial records. Southern Africa's climate and geological setting and key drivers of palaeoclimate change are also explored.

Chapter 3 focuses on the methodological approaches used in this thesis to address the primary research objectives. The focus of this chapter is to identify the range of methods used throughout the study, to detail methods which do not appear in detail elsewhere in the thesis, and to summarise methods that are dealt with in greater detail in the three papers (in chapters that represent published or submitted papers, where it is required to include methods to generate self-contained publications). Methods include: i) site selection, sampling strategy, ground penetrating radar, luminescence dating, and sedimentology for the production of a new fluvial record; ii) creation of a chronological fluvial database and development of filtering criteria to assess data quality; and iii) analysis of palaeoclimate model outputs and the approach for model-archive comparison.

Chapter 4 (Paper 1) reconstructs the timing and nature of fluvial deposition of the Huab River valley fill through integrated petrographic, heavy mineral, lithostratigraphic, and particle-size analysis, and a chronology established through 42 luminescence ages. This study identifies the important source drainage lithologies, assesses changes in the type of river flow over time, and infers links between sedimentary response and Holocene precipitation changes in the Huab catchment.

Chapter 5 (Paper 2) presents a new chronological database of late Quaternary fluvial records from the western, driest portion of southern Africa. This analysis identifies the nature of documented deposits and the river systems they are located in. It then assesses the sources of evidence and approaches used to reconstruct fluvial histories and presents the Quaternary fluvial record from a quality-assessed dataset. This paper examines the contribution of fluvial systems to understanding the amplitude and nature of late Quaternary hydrological change and assesses the status of fluvial records from this complex region.

Chapter 6 (Paper 3) addresses questions of how southwestern Africa's climate responded to forcing at key timesteps within the late Quaternary. This empirical-model data comparison analyses the magnitude and seasonality of precipitation anomalies at the Last Glacial Maximum and in the mid Holocene. Using a compilation of robust palaeoclimate and palaeoenvironmental archives (including the quality-assessed fluvial data from Chapters 4 and 5) and a multi-model ensemble of palaeoclimate model simulations, this study evaluates whether hypotheses of past precipitation changes in southwestern Africa are supported by the current dataset.

Chapter 7 summarises the findings from each of these papers to detail how the overarching research aim and the three specific research objectives have been addressed. This chapter concludes with an assessment of the implications of this research and recommendations for future research in this field. Finally, the **Appendices** provide the supporting data for this thesis, including a study of chronology and sedimentology on the Huns River, southern Namibia (Appendix B), additional detail on the methods used in this thesis (Appendix C), and the Supplementary Material for papers 1 and 2 (Appendices D, E, and F).

Chapter 2: Context

2.1. Introduction

This chapter presents a summary of the background literature on two key aspects of this thesis: river systems within drylands and the use of fluvial archives to understand southern African palaeoclimate change. This chapter begins with a discussion of dryland regions and the characteristics of rivers located within them. It then considers how sedimentary deposits in fluvial systems can be used as palaeoenvironmental archives and the challenges that are faced in interpreting climate signals from geomorphological responses. The importance of fluvial archives is then explored in relation to southern African palaeoclimate change specifically. The climatic and geological contexts of southern Africa and the key drivers of climate change on Quaternary timescales are discussed. Given the complexity of southern African palaeoclimate change, and the potential importance of fluvial archives in determining the spatial extent of precipitation patterns, the climate and geological context of the Huab River, southwestern Africa, as a site of study in this thesis, is described.

2.2. Drylands

Drylands are defined as hyper-arid to dry sub-humid environments. Following the UNEP (1992) definition, these are regions with an aridity index (ratio between mean annual precipitation and mean annual evapotranspiration) of <0.65 (Figure 2.1; Trabucco and Zomer, 2022). Drylands cover >40 % of the world's land area (Koutroulis, 2019; Middleton and Thomas, 1997; Mirzabaev *et al*., 2019), support >50 % of the world's livestock (Millennium Ecosystem Assessment, 2005), and have a population of ~3 billion people (Mirzabaev *et al*., 2019; van der Esch, *et al*., 2017). Whilst the drivers of aridity are complex, the spatial distribution of drylands globally is influenced by the role of atmospheric stability, continentality, topography, and cold ocean currents (D'Odorico *et al*., 2013; Thomas, 2011).

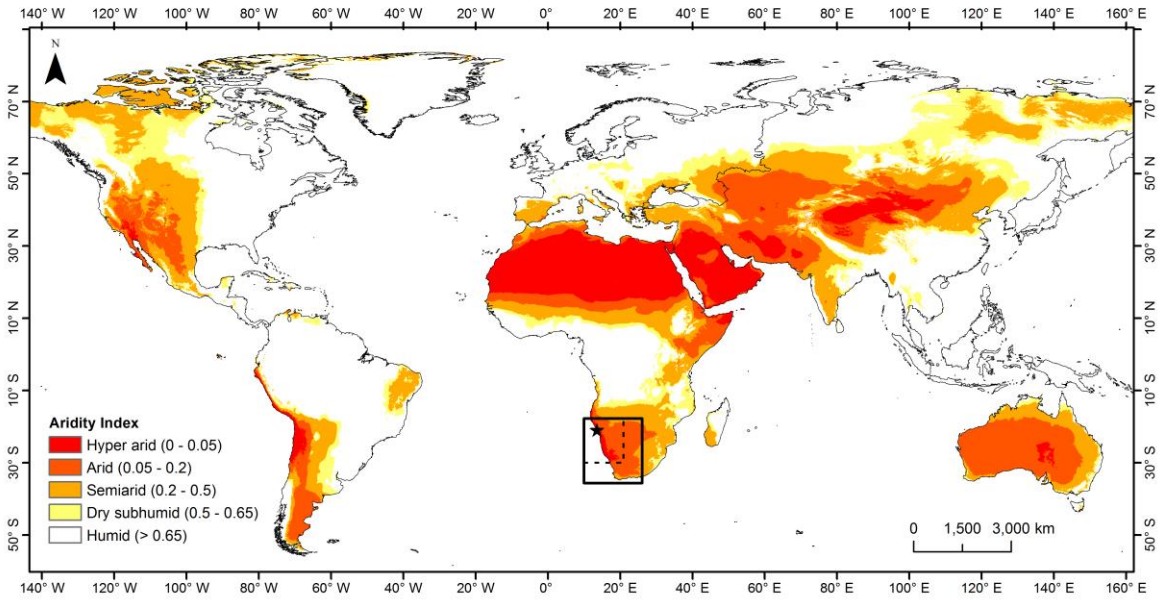

Figure 2.1. World dryland areas demarcated by contemporary global aridity index (Trabucco and Zomer, 2022). Aridity Index (AI) defined as mean annual precipitation over mean annual evapotranspiration (P/PET) (UNEP, 1992). Hyper-arid: <0.05, arid: 0.05-0.2, semi-arid: 0.2-0.5, dry sub-humid: 0.5-0.65. The study areas of this thesis are defined by: black star (Huab River, Chapter 4); solid black box (fluvial database, Chapter 5); dotted black box (model-data comparison, Chapter 6). Justification of these are specific sites of study are described in further detail in Chapters 4-6.

Dryland regions are considered to be highly vulnerable to future climate change impacts (Koutroulis, 2019; Lian *et al*., 2021; IPCC, 2021; Wang *et al*., 2012), with projections of increased aridity across many drylands globally (Cook *et al*., 2014; Rodell *et al*., 2018; Schewe *et al*., 2014). Given the complex interplay between climate and environmental response and projections of decreased runoff within hydrological systems (Jiménez Cisneros *et al*., 2014; Milly and Dunne, 2020; Ukkola *et al*., 2016), concerns over water availability are particularly acute in dryland regions (De Wit and Stankiewicz, 2006). Across the African continent, >60 % of the population is dependent on limited and irregular water resources (Niang *et al.* 2014; Vörösmarty *et al*., 2005). Surface waters are sporadic and unequally distributed (Lange, 2005) and alluvial aquifers provide a critical source of water via boreholes to wildlife, livestock and human populations (Dahan *et al*., 2008; Morin *et al*., 2009; Jacobson *et al*., 1995). Extreme floods have the potential to replenish aquifers (Lange,

2005; Morin *et al*., 2009), but ephemeral dryland rivers are rarely well-gauged or monitored (Jacobson *et al*., 1995; Kundzewicz *et al*., 2014; Milly *et al*., 2002; Zimmer *et al*., 2020) and data on the frequency and magnitude of these extremes is particularly scarce (Benito *et al*., 2010). On timescales beyond that of instrumental records, fluvial palaeoenvironmental records have the potential to improve our understanding of the relationship between river flow and climate that is critical for future planning in these regions and critical for model-data assessments.

2.3. Dryland Rivers

River flow in drylands occurs on a suite of temporal and spatial scales, with flow occupancy ranging from ephemeral to perennial (Figure 2.2). Whilst dryland regions can support extensive exogenic perennial river flow (e.g. the Orange River in South Africa and the Nile in Egypt), a global assessment of flow intermittence shows that where aridity is high, rivers are particularly dominated by intermittent and ephemeral flow (Messager *et al*., 2021). In hot and dry to extremely hot and arid environments (following biomes of Metzger *et al.* 2013), 62 to 98 % of the length of rivers periodically cease to flow (Messager *et al*., 2021).

Intermittent and ephemeral flow, however is not unique to drylands (Datry *et al*., 2017), where ~60 % of global rivers by length, across all biomes and continents, cease to flow for at least one day a year (Messager *et al*., 2021). The continuum of hydrological conditions demonstrated in Figure 2.2 means that commonalities can exist between the characteristics of river flow regimes in dryland and temperate regions (Knighton and Nanson, 1997; Tooth and Nanson, 2011). Drylands host a diversity of river types, in part linked to their climate setting (Larkin *et al*., 2020; Tooth and Nanson, 2011), yet dryland rivers have been relatively understudied in comparison to their temperate counterparts. Several dryland river characteristics exist outside those typically found in temperate regions (Bull and Kirkby, 2002), where mechanisms inferred from temperate systems do not do not

always explain the changes recorded elsewhere. Dryland fluvial systems therefore merit further study.

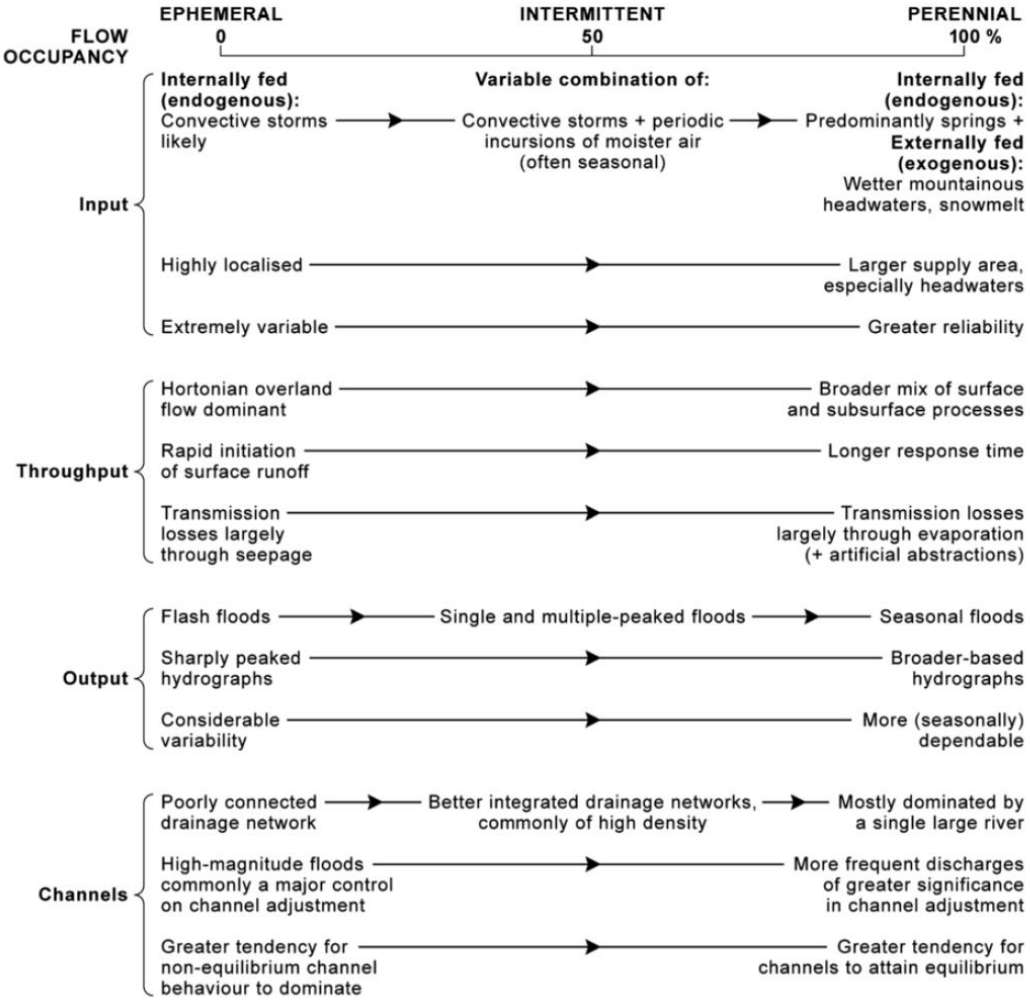

Figure 2.2. Linear flow occupancy scale detailing the diversity in hydrology of dryland rivers, from Tooth and Nanson (2011) (following Knighton and Nanson, 1997, and Nanson *et al*., 2002).

In the context of regions dominated by intermittent and ephemeral river flow, rainfall in dryland regions can support extensive, yet spatially variable, hydrological activity (Nanson *et al*., 2002; Tooth, 2000a, 2013; Tooth and Nanson, 2011). High intensity precipitation events are associated with spatially-discrete convective cells (typically ~10-14 km diameter; Diskin and Lane, 1972; Reid and Frostick, 2011; Sharon, 1974) which produce significant runoff in systems where extended periods of relative channel stability prevail (Tooth and Nanson, 2011). This contrasts with temperate regions, in which the impact of individual extreme events can be muted by the perennial

flow of rivers (Bull and Kirkby, 2002). In ephemeral systems, flashy discharge can occur with steep rising hydrographs (Reid and Frostick, 1987) where surface infiltration capacities can rapidly be overwhelmed by high rainfall intensities (Liu *et al*., 2004). As a result, three types of flow can occur: Hortonian overland flow, exfiltration, and formation of subsurface pipes (Wainwright and Bracken, 2011). Where transmission losses are high (Lange, 2005; Mujere *et al*., 2021) and surface vegetation cover across the catchment is particularly variable (Reid and Frostick, 2011), ephemeral river flow rarely occurs throughout the full length of the main channel (Bull and Kirkby, 2002). Where groundwater is high, or rainfall events are less sporadic, intermittent river flow can occur through multi-peak floods (Busch *et al*., 2020; Messager *et al*., 2021) as more sustained, yet still highly variable, river flow.

The interaction between dryland surface conditions and the nature of ephemeral and intermittent flow mean that water is a powerful erosive agent in these systems (Wainwright and Bracken, 2011) and runoff can result in high rates of sediment mobilisation (Alnedeij and Diplas, 2005; Jacobson *et al*., 2000; Reid and Frostick, 1987). Fluvial systems can therefore play an important role in the geomorphological evolution of landscapes (Reid and Frostick, 1997; Thomas, 2011; Tooth, 2013).

2.4. Fluvial sediments as palaeoenvironmental archives

Sedimentary archives in fluvial systems provide evidence of past river flow and offer the potential to reconstruct environmental responses of rivers to hydroclimatic regimes on historical to Quaternary timescales (Bridgland and Westaway, 2014; Burt and Allison, 2010; Macklin *et al*., 2012; Mather *et al*., 2017; Reid, 1994, 2009; Woodward *et al*., 2010). Sedimentary units can be used to reconstruct fluvial change on scales of individual *events*, multi-year *episodes*, and multi-decadal to centennial-scale *phases* (Toonen *et al*., 2017). These sediments have the potential to preserve evidence e.g. of increased flood frequency (e.g. Benito *et al*., 2020) and changes in the nature of flow as evidence of variations in moisture availability (e.g. Tooth *et al*., 2022). Fluvial systems in

dryland regions have been relatively unaffected by glacial reworking on Quaternary timescales (Hall, 2004; Merifield, 1987; Tooth, 2000a), so have the potential to preserve important evidence of past environmental changes.

2.4.1. Environmental signal propagation

Fluvial systems constitute an important part of sediment routing systems (SRS; Allen, 2008, 2017). Transport pathways take place from erosional zones of sediment production (source), through transfer zones, to final zones of deposition and sediment accumulation (sink) (Romans *et al*., 2016; Schumm, 1977). Climatic, tectonic, and anthropogenic changes can produce environmental signals that are transferred within SRSs (Tofelde *et al*., 2021). Environmental signals constitute changes in the amount of sediment that is produced, transported, and deposited (Romans *et al*., 2016). These changes can be measured in sedimentary archives (Allen, 2017; Caracciolo, 2020; Romans *et al*., 2016; Tofelde *et al*., 2021) as changes in sediment volume (e.g. Benito *et al*., 2020; Stokes *et al*., 2017), character (e.g. textural, Stone *et al.*, 2010; architectural facies elements, Miall, 2006; Srivastava *et al*., 2006), and composition (e.g. provenance, Ramisch *et al*., 2017). Fluvial systems respond to climate perturbations through changes in stream flow and sediment availability, resulting in geomorphological change (Macklin *et al*., 2012). Sedimentary archives in fluvial systems therefore typically detail evidence of both past and current environmental conditions (Tooth, 2016).

2.4.2. Types of fluvial archive in drylands

Across drylands globally, environmental signals are preserved in a range of fluvial sedimentary archives. This can include rapid sediment accumulation from flash floods and gradually accreting sections as evidence of past significant flow of rivers within currently inactive landscapes (e.g. Shaw *et al.* 1992). Alluvial successions and valley fill archives have been studied widely across drylands globally (e.g. in southern Africa, Damm and Hagedorn, 2010, Lyons *et al*., 2014; and India, Williams

et al., 2006). These sedimentary units can be altered by both incision and aggradation that typically indicate contrasting conditions of river flow and sediment supply: incision can occur as a result of increased river discharge and decreased sediment availability, whereas aggradation can occur when river discharge is low and sediment availability is high (Tooth, 2016). Deposition can be preserved within channels (e.g. Srivastava *et al*., 2004) and overbank floodplain settings (e.g. Damm and Hagedorn, 2010; Srivastava *et al*., 2006). In environments where palaeoflow was more substantial or occurred in a different position than today, palaeochannels that are currently inactive can be preserved (e.g. Murrumbridgee, Australia, Forbes *et al*., 2020, Mueller *et al*., 2018; Ghaggar-Hakra, India, Durcan *et al*., 2019; Okavango Delta, Botswana, Tooth *et al*., 2022).

Evidence of flash flood regimes is commonly preserved as slackwater deposits (SWD) and high-water marks (HWM). These constitute unconsolidated sands, silts, and organic material such as driftwood that accumulate from suspension. These deposits reflect the peak stage of major flood events (Baker, 1987; Cloete *et al*., 2018; Frances, 2004; Jarrett and England, 2002; Kochel and Baker, 1982) and can be used to estimate fluvial discharge of palaeoflood events (Baker, 2008; Benito *et al*., 2020). Other deposit types in dryland river settings can include the endoreic sediments of 'river end deposits' in settings upstream of contemporary river terminations (e.g. Hoanib, Namibia, Eitel *et al*., 2001; Eitel *et al*., 2005), and fluvial interdune deposits where fluvial termination in a sand sea results in deposition from still-water ponding (e.g. (e.g. Namib Desert, Namibia, Brook *et al*., 2006, Stone *et al*., 2010; and Wahiba Sands, Oman, Kocurek *et al*., 2020).

2.4.3. Complexity in interpretation of fluvial geomorphological archives

Ascribing palaeoenvironmental interpretations to evidence of change in fluvial deposits has been a topic of debate over several decades, yet is critical for reaching a robust record of past environments and interpretation of climate drivers. A number of challenges are common to the study of geomorphological archives in general, where environmental signals are not always

translated along the full length of the SRS (Tofelde *et al*., 2021). Following a change in climate dynamics, information is progressively modified as it passes through a set of filters (Figure 2.3; Bailey and Thomas, 2014). These filtering steps include factors that are both intrinsic to archive formation (steps 1-3; Figure 2.3) and the blurring of information through sampling, dating, and interpretation (steps 4-6; Figure 2.3).

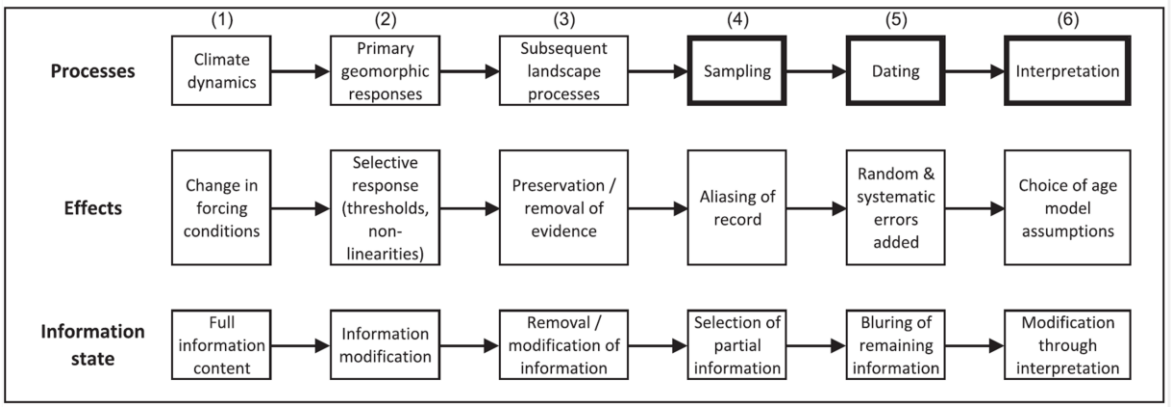

Figure 2.3. Schematic of filtering processes within sedimentary records (Bailey and Thomas, 2014). Information relating to climate signals are progressively removed through each filtering step. These steps incorporate a role of geomorphological processes and factors related to sampling and data analysis. Boxes in bold are steps that can, in-part, be controlled.

Using the framework discussed in Bailey and Thomas (2014), Table 2.1 details challenges faced in the study of dryland fluvial geomorphological archives. These factors are in part due to the nature of dryland rivers, but also relate more broadly to the formation of geoproxies. Whilst these factors complicate interpretation of fluvial archives, appreciation of these challenges means that appropriate methods can be chosen and the limits to what is possible to find out can be acknowledged.

Table 2.1. Challenges faced in the study of fluvial deposits, with reference to factors both common to river systems globally and specific to dryland settings. Following Bailey and Thomas (2014), these challenges are grouped into i) geomorphological response, ii) landscape processes, iii) sampling, iv) dating, and v) interpretation.

	Factor	Detail
Geomorphological response to climate signals	Spatial flow variability within catchments	• Small-scale convective storms wet some tributaries while others remain dry (Bull *et al*., 1999; Hooke and Mant, 2000; Tucker *et al*., 2006). • Transmission losses are high and variable across catchments (Costa *et al*., 2012; Mujere *et al*., 2021; Tooth, 2000b). • Runoff events limited to short reaches of rivers. Ephemeral river flow rarely occurs throughout the full length of the channel (Enzel and Wells, 1997; Jacobson *et al*., 1995; Knighton and Nanson, 1994). • River discharge and sediment availability are influenced by topography (Daniels, 2003; Milan *et al*., 2020) and vegetation cover (Dean and Topping, 2019).
	Non-linear response and thresholds	• Range in the nature of river response, e.g. flood frequency, flow magnitude, flow occupancy, and changes in channel pattern (Macklin *et al*., 2012). • Response can be non-linear (Coulthard *et al*., 2005; 2008) and linear relationships incorporate a high degree of scatter (Macklin *et al*., 2012). • Thresholds for sediment entrainment (e.g. channel bed armour needs to be penetrated before sediments are entrained) and thresholds for sedimentation (e.g. SWDs along the Kuiseb River, Namibia, record floods above 400m^3s^{-1}, Grodek *et al*., 2013).
	Autogenic processes	• Intrinsic self-organising capabilities (Phillips, 1995; 2009). • Climate signals (allogenic change) are autogenically processed by fluvial systems (e.g. meander cut-offs, avulsions; Macklin *et al*., 2012; Trampush *et al*., 2017). • Channel dimensions can change through sediment accumulation, incision, and avulsion, and can influence the response of rivers to future climate drivers (Tooth, 2000a).
	Non-climatic drivers	• Tectonic processes, e.g. uplift (Hartley *et al*., 2010), seismic activity (Xie *et al*., 2022), sea level rise (Das *et al*., 2017), and human activity (Damm and Hagedorn, 2010; Draut, 2012) can influence sediment availability, sedimentation, and rates of incision (Macklin *et al*., 2012; Tooth, 2016). • Fluvial-aeolian interactions are common (Liu and Coulthard, 2015, 2017) and aeolian derived sediment can be interbedded in fluvial deposits.

Landscape processes	Remove of material/ modification of the signal	• Catastrophic floods can remove previous flood deposits (e.g. in the main channel of the Kuiseb River deposits persist for <200 yrs, Grodek *et al*., 2013). Channel migration and cut-and-fill sequences can result in partial preservation and fragmentary depositional sequences (Lewin and Macklin 2003; Macklin *et al*., 2012; Tooth *et al.* 2013). • Removal of material by aeolian processes (e.g. valley fills in ephemeral rivers are important sources of dust; Dansie *et al*., 2017; Thomas *et al*., 2017). • Information decreases further back in time as reworking of older material biases towards younger deposits (Bailey and Thomas, 2014).
Sampling	Accessibility of sites	• Difficulty of access where dryland fluvial sites are remote. Bias towards more accessible sites. • Ephemeral flow, remoteness of sites, and unstable river channels limits the availability of long term river gauge stations (Jacobson *et al*., 1995; Zimmer *et al*., 2020). This is particularly important for records of historical floods where SWD records overlap with instrumental.
	Selection of partial information	• Sampling resolution can distort the information obtained e.g. aliasing, where signals become indistinguishable from one another. Low sampling resolutions have the risk of missing depositional events, yet oversampling can artificially place weight on certain units/events if the data are not used correctly. • Natural exposures enable systematic sampling approaches to be undertaken, but are not always present and commonly limited by depth. • A near surface bias, producing a younger distribution of ages as only the most recent deposits are sampled. • Sampling for chronometric techniques, such as luminescence dating, focuses on units of silt to sand sized particles (Murray *et al*., 2021). Potential to miss extreme fluvial events where depositional layers consist predominantly of coarse gravel or boulders.
Dating	Limitations of luminescence and radiocarbon dating	• Luminescence dating relies on the removal of trapped charge within a sand grain prior to burial, but partial bleaching can occur in in dryland fluvial systems where river flow often occurs in short duration highly sediment laden flows (Jain *et al*., 2004; Olley *et al*., 2004). • Heterogeneity in environmental dose rates (Nathan *et al*., 2003) and post depositional mixing (e.g. through flood reworking or biological activity) (Bateman *et al*., 2003) can reduce the extent to which a luminescence age reflects the true burial age. • Radiocarbon dating is performed on organic material, such as charcoal, wood, organic sediment, but the timing of death of these materials might not directly reflect the fluvial event itself. • Reworking of older carbon from previous flood deposits or introduction of younger carbon (e.g. through root penetration) is possible.
	Limits to precision	• Errors increase as the age of deposit increases. The ability to distinguish between distinct events decreases further back in time (Bailey and Thomas, 2014; Macklin *et al*., 2012) as uncertainties represent a larger time-frame.
Interpretation	Availability of other data to inform interpretation	• Given the complex nature of fluvial response and the divergent patterns, fluvial sediments can represent a range of past fluvial conditions. Fluvial deposits therefore require independent proxies for interpretation of palaeoconditions in addition to chronologies of sediment deposition. • Many studies are restricted in the use of specific proxies and data, e.g. the availability and preservation of pollen within fluvial sediments is poor (Nash *et al*., 2006) and instrumental records for calibration of palaeohydrological estimates are scarce (Benito *et al*., 2010).

2.4.4. Approaches to studying fluvial records in drylands

Despite the complexities associated with interpreting fluvial change from sedimentary records, a number of sophisticated approaches are providing opportunities for robust reconstruction of fluvial system responses to late Quaternary climate change (e.g. Hesse *et al*., 2018; Macklin *et al*., 2012; Tooth *et al*., 2022; Woodward *et al*., 2015). Advances in radiometric techniques to establish chronological control have been made in recent decades and several studies have focused specifically on improvements to dating fluvial sediments (e.g. Colarossi *et al*., 2020; Guyez *et al*., 2022; Smedley and Skirrow, 2019). As the controls on the formation of landforms by fluvial sediment transport in drylands are also better understood through the use of model simulations and process-based assessments (e.g. Larkin *et al*., 2020; Liu and Coulthard, 2017), the contribution of fluvial geoproxies to assessing the amplitude and nature of hydrological change in drylands has increased. When taken together, multiple fluvial records can be collated to establish fluvial responses across several sites (e.g. Macklin and Lewin, 2003). This approach can account for some of the site-specific complexities and can present a combined fluvial record for comparison with other palaeoclimate records (Macklin *et al*., 2012).

Tofelde *et al*. (2021) detail how environmental signals are recorded in measurable changes in sediment volume, character, and composition (see Section 1.1 for examples). In the study of dryland fluvial archives, important approaches have been developed in analyses relating to each of these aspects. Palaeohydrological assessments of SWDs and palaeochannels across drylands globally are enabling estimations of both the frequency and magnitude of individual flood events (Benito *et al*., 2020) and discharge of late Quaternary river channels using established relationships between discharge, channel meander parameters, and hydraulic geometry relationships (e.g. Hesse *et al*., 2018; Tooth *et al*., 2022). Through analysis of exposed sections, identification of diagnostic lithofacies has enabled links to be made between stratigraphic changes and the nature of dryland river flow (e.g. Miall 2006; Srivastava *et al*., 2006). Where available, pollen analyses detail

vegetation dynamics at the point of sediment deposition (Nash *et al*., 2006) and analysis of geochemical changes in sediment can detail prevailing climates (Lyons *et al*., 2014). Finally, through analysis of mineralogy and sediment composition, such as in the form of bulk petrography and heavy mineral analysis, potential source regions can be identified and provenance of sedimentary units can be established (Ramisch *et al*., 2017).

2.5. Southern Africa: climate, geological, and fluvial setting

This research focuses on fluvial archives within the western driest part of southern Africa. Southern Africa, taken here as the landmass south of approximately 17˚S (Humphries, 2021; Knight and Fitchett, 2021; Stone, 2021; Thomas, 2019), hosts a suite of river systems with differing landscape and climatic contexts, with an emerging palaeoenvironmental record from the sedimentary archives located along them. Given examples of the complexities detailed in Table 2.1, the climatic and geological setting of the region needs to be understood as a basis for considering the controls on the palaeoenvironmental records preserved.

2.5.1. Southern African climate

Southern Africa is located at the confluence between tropical and temperate climate systems and the interaction between these systems results in a seasonally and spatially variable distribution of rainfall across the subcontinent (Figures 2.4 and 2.5). Palaeoclimate interpretations have often greatly oversimplified these atmospheric components, and in doing so may have underestimated the level of spatial complexity of precipitation that occurred in the past (Nicholson *et al*., 2012).

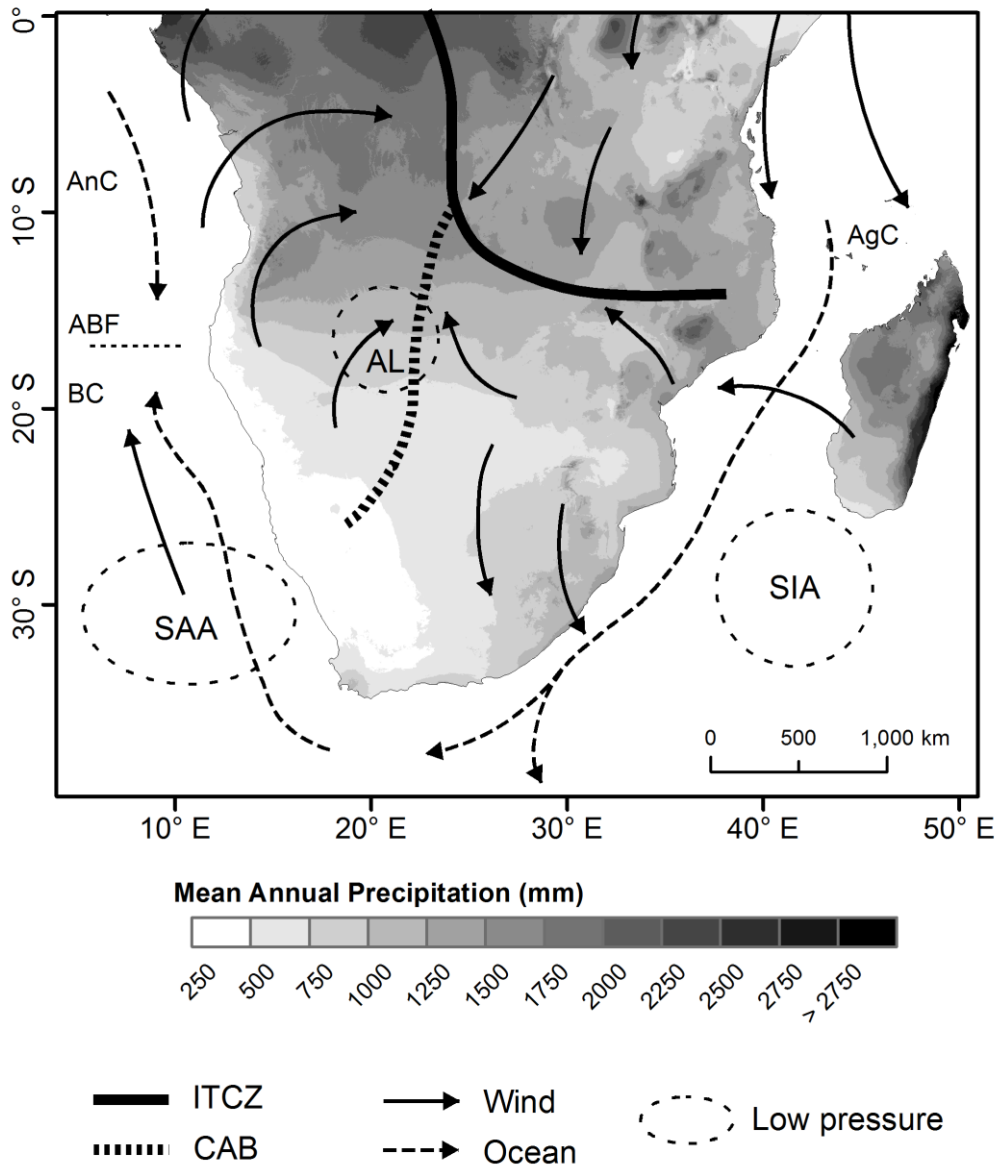

Figure 2.4. Annual contemporary precipitation (mm) across southern Africa and main climate systems responsible for rainfall (positions relative to summer rainfall). Data sourced from WorldClim 2.0 (Fick and Hijmans, 2017). positions of the Intertropical Convergence Zone (ITCZ) and Congo Air Boundary (CAB) are marked by the solid black and dotted lines. Ocean currents of the Agulhas (AgC), Angola (AnC), and Benguela (BC) are detailed as dotted lines. SAA: South Atlantic Anticyclone, SIA: South Indian Anticyclone

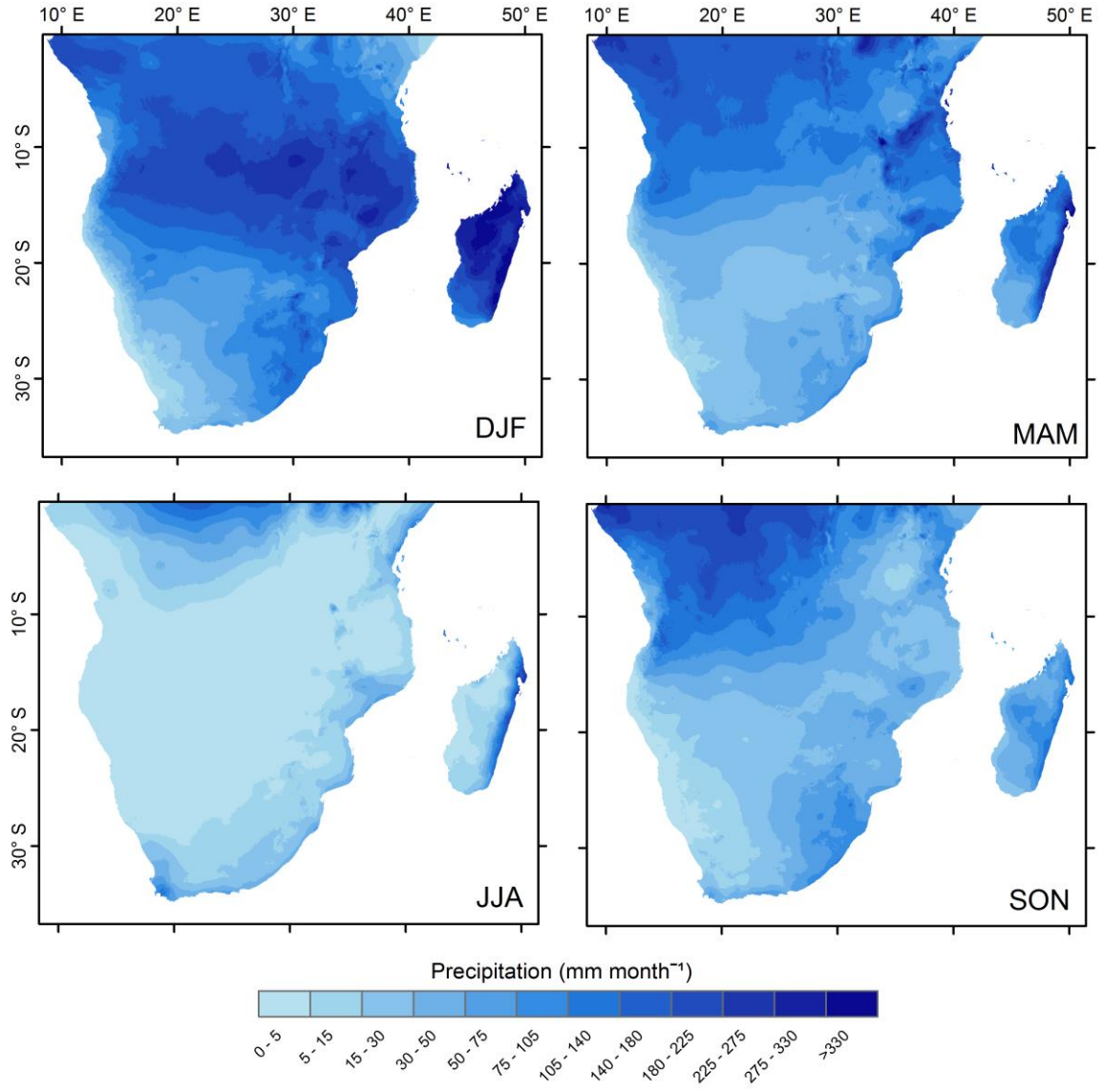

Figure 2.5. Contemporary precipitation (mm month^{-1}) by season across southern Africa using the WorldClim 2.0 dataset (Fick and Hijmans, 2017). Seasons are defined as DJF (December, January, February), MAM (March, April, May), JJA (June, July, August), and SON (September, October, November).

Contemporary southern African precipitation is sourced from, or influenced by, a suite of climate systems:

1. **Tropical rainbelt:** Across the majority of southern Africa, the seasonal cycle of rainfall maxima mirrors the latitudinal displacement of the tropical rainbelt. Following insolation, the interhemispheric temperature gradient influences the position and strength of the

rainbelt in a generally antiphase manner between the hemispheres. The rainfall maximum in southern Africa therefore occurs during austral summer months (DJF). Whilst the location of the tropical rainbelt is often thought to be linked to the location of the Intertropical Convergence Zone (ITCZ; the zone of greatest surface convergence), there is increasing recognition that the two are not synonymous and that the term ITCZ and its perception as a distinct convergence and rainfall belt may over-simplify conditions over land (Nicholson, 2009, 2018).

2. **Southeasterly trade winds from the Indian Ocean:** Atmospheric high pressure over southern Africa is split into anticyclonic cells over the Indian and South Atlantic oceans. To the east of the subcontinent, moisture is advected from the Indian Ocean as part of the South African monsoon region (Wang and Ding, 2008). The warm Agulhas Current enhances humidity and the orography of the southern African escarpment enhances rainfall in this region (Rouault *et al*., 2002). Continentality reduces the extent of Indian Ocean derived rainfall, with Indian Ocean derived rainfall diminishing from east to west with distance travelled by the SE trade winds. The amount of rainfall received by the western portion of the subcontinent is further decreased by an orographic effect of the Namibian Great Escarpment.

3. **Congo Air Boundary (CAB):** At the southern edge of the tropical rainbelt, southern African rainfall is governed by the Congo Air Boundary (CAB) (Howard and Washington, 2019). Rainfall occurs at the confluence of the moist low level westerlies from the Atlantic Ocean with dry air of the southeasterlies from the Indian Ocean (Taljaard, 1972; Torrance, 1979). The position of this confluence is driven by the relative strength of these two systems (Reason *et al*., 2006; Tyson and Preston-Whyte, 2000).

4. **Angola Low:** Located to the east of the Angolan and Namibian highlands at ~17˚S, the Angola Low is a region of cyclonic low-pressure. Strengthening of the Angola Low enhances the pressure gradient between the Atlantic and Indian Oceans. During austral summer, this increases moisture transport from the Atlantic Ocean (Hart *et al*., 2010) and increases convection over southern Africa (Cook *et al*., 2004; Hermes and Reason, 2009; Rouault *et al*., 2003).

5. **South Atlantic Anticyclone (SAA):** To the west of the subcontinent, upwelling of the cold Benguela Current is strengthened by intensification of southeasterly trade winds associated with the South Atlantic Anticyclone. This upwelling produces a temperature inversion which limits the potential for convection (Nicholson, 2000, Nicholson *et al*., 2012; Tyson and Preston-Whyte, 2000). High pressure associated with the SAA blocks the incursion of moisture bearing systems within tropical flow and therefore results in aridity in the western portion of the subcontinent (Reason, 2017).

6. **Circumpolar westerlies and Tropical Temperate Troughs (TTTs):** Precipitation in the southern-most portion of South Africa is principally driven by rainfall associated with the mid-latitude circumpolar westerlies. Linked to strengthening of the SAA, storm tracks associated with the westerlies bring incursions of low pressure. Whilst the direct influence is limited to the south, the interaction between westerly transient eddies and a strong Angola Low can form tropical temperate troughs (TTTs) or cloud bands (TTCBs) (Hart *et al*., 2010; Macron *et al*., 2014). These TTTs bring rainfall to a wider region of southern Africa (Harrison, 1984; Todd and Washington, 1998).

2.5.2. Southern Africa's structure and geology

Southern Africa's geology primarily comprises the Damara, Kaoko, and Mozambique Belts, linking the Congo, Kaapvaal and Zimbabwe Cratons (Figure 2.6). The initial formation of this geological setting dates back to the Archean period (4,000-2,500 Ma; Hanson, 2003). Trending along the coast of Namibia and South Africa, the Great Escarpment demarcates the central elevated interior of the continent from the low relief regions at the coast. Glaciation during the Permo-Carboniferous (300 Ma) formed valleys spanning from the Escarpment towards the coast in Namibia (Jacobson *et al*., 1995; Martin, 1953). Propagation of the East African Rift has accentuated the central depression that the Okavango Delta drains into (Kinabo *et al*., 2007; McCarthy and Ellery, 1998; Modisi *et al*., 2000; Vainer *et al*., 2021).

Following the breakup of the Gondwana continent, during the Upper Carboniferous to Lower Jurassic, Karoo Supergroup sediments covered a large proportion of the continent. At around 183 Ma, this sedimentation was interrupted by eruptions of basalt (Greber *et al*., 2020; Svensen *et al*., 2012). By ~138 Ma the Paraná-Etendeka large igneous province formed across Namibia and Uruguay (Peate, 1997; Renne *et al*., 1996; Garzanti *et al.*, 2021). In the interior of southern Africa, Kalahari group sediments filled the central basin during the Late Cretaceous (100-66 Ma; Garzanti *et al*., 2022; Haddon and McCarthy, 2005; Schulter, 2008). In the context of extensive provenance analyses in Namibia and across the wider Kalahari (Garzanti *et al*., 2012, 2014, 2022) detail on this geological setting enables consideration of sourcing of sediment within fluvial systems.

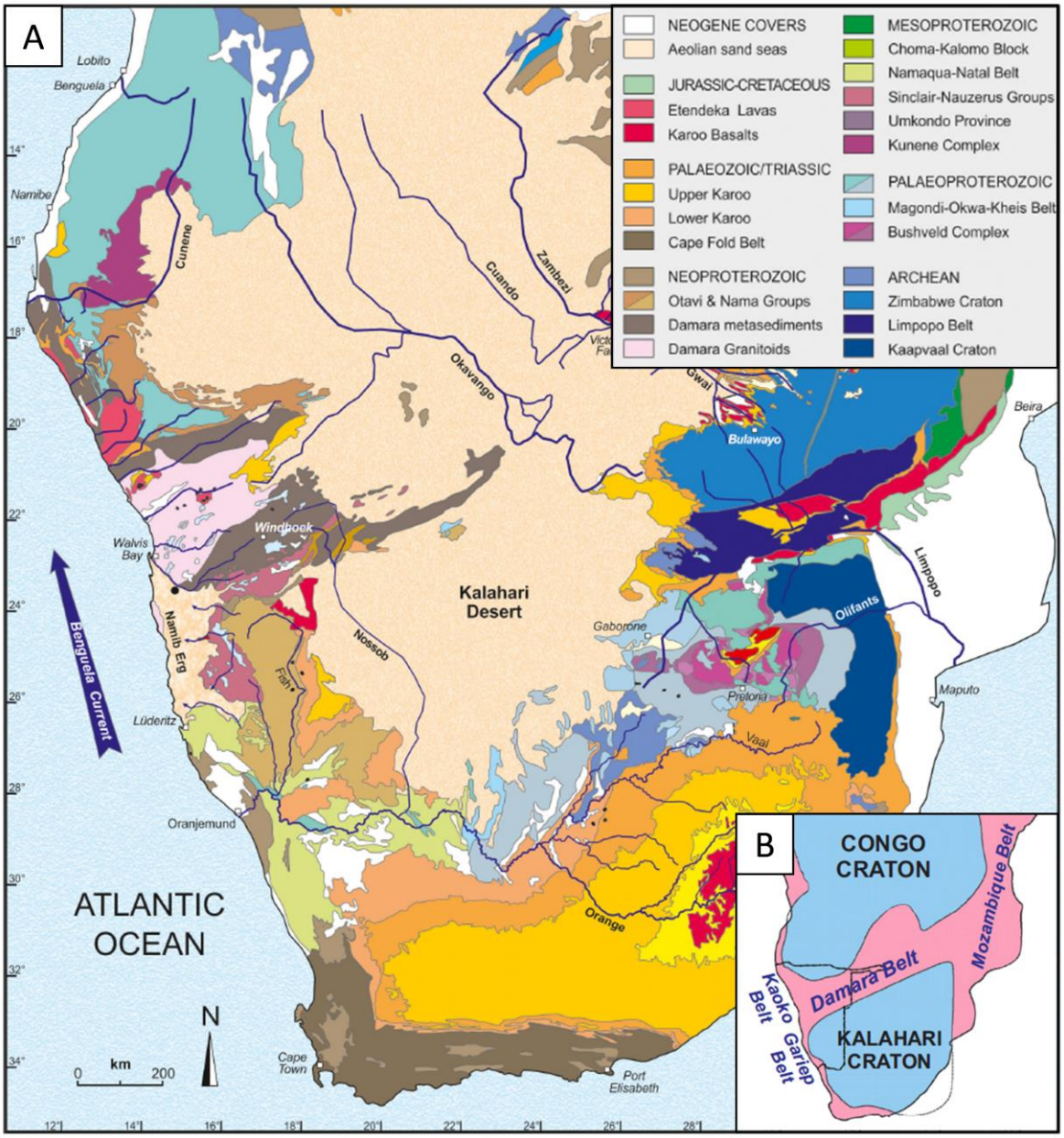

Figure 2.6. Map of key geological units in southern Africa map from Garzanti *et al*. (2018) and Garzanti *et al.* (2022) adapted from Schulter (2008).

2.5.3. Southern African rivers

Today, southern Africa's climate supports exogenous perennial systems and endogenous intermittent to ephemeral river systems (Figure 2.7; De Wit and Stankiewicz, 2006; Jacobson *et al*., 1995; Messager *et al*., 2021). Since the break-up of Gondwana, uplift and river incision resulted in widespread removal of overlying sediments reaching more resistant rocks beneath, forming

numerous bedrock-confined fluvial systems (Tooth, 2016; Tooth and Nanson, 2011; e.g. Figure 2.8A). Since the Cenozoic, a long term drying trend has influenced the extent of drainage systems in southern Africa (Tankard and Rogers, 1978), and wet-dry transitions during the Quaternary have resulted in a range of sedimentary deposits along these systems (Grenfell and Grenfell, 2021; Stone and Thomas, 2013; Stone, 2021; Tooth, 2016).

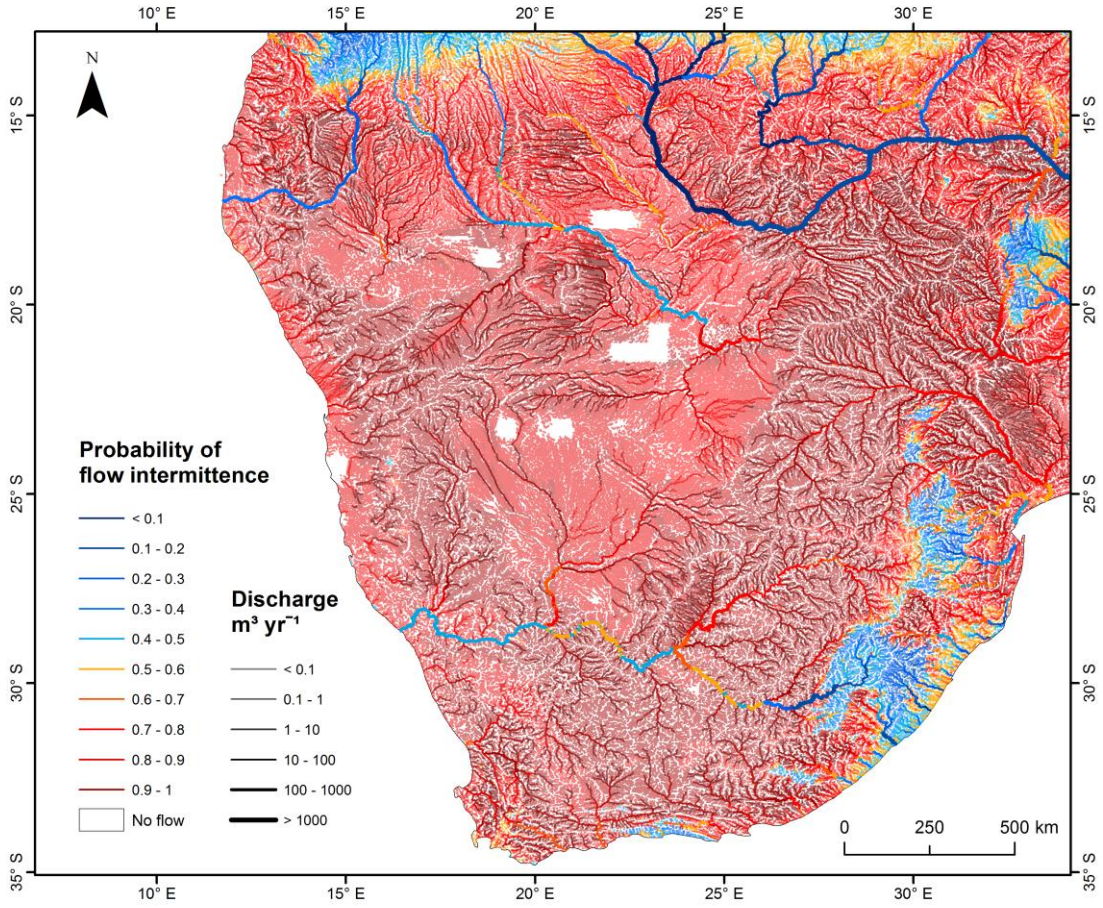

Figure 2.7. Distribution of the probability of flow intermittence for southern Africa using the dataset on global prevalence of non-perennial rivers and streams from Messager *et al*. (2021). Dark blue perennial (probability of intermittence: 0), to red non-perennial (probability of intermittence: 1). The width and opacity of lines reflect the mean annual discharge.

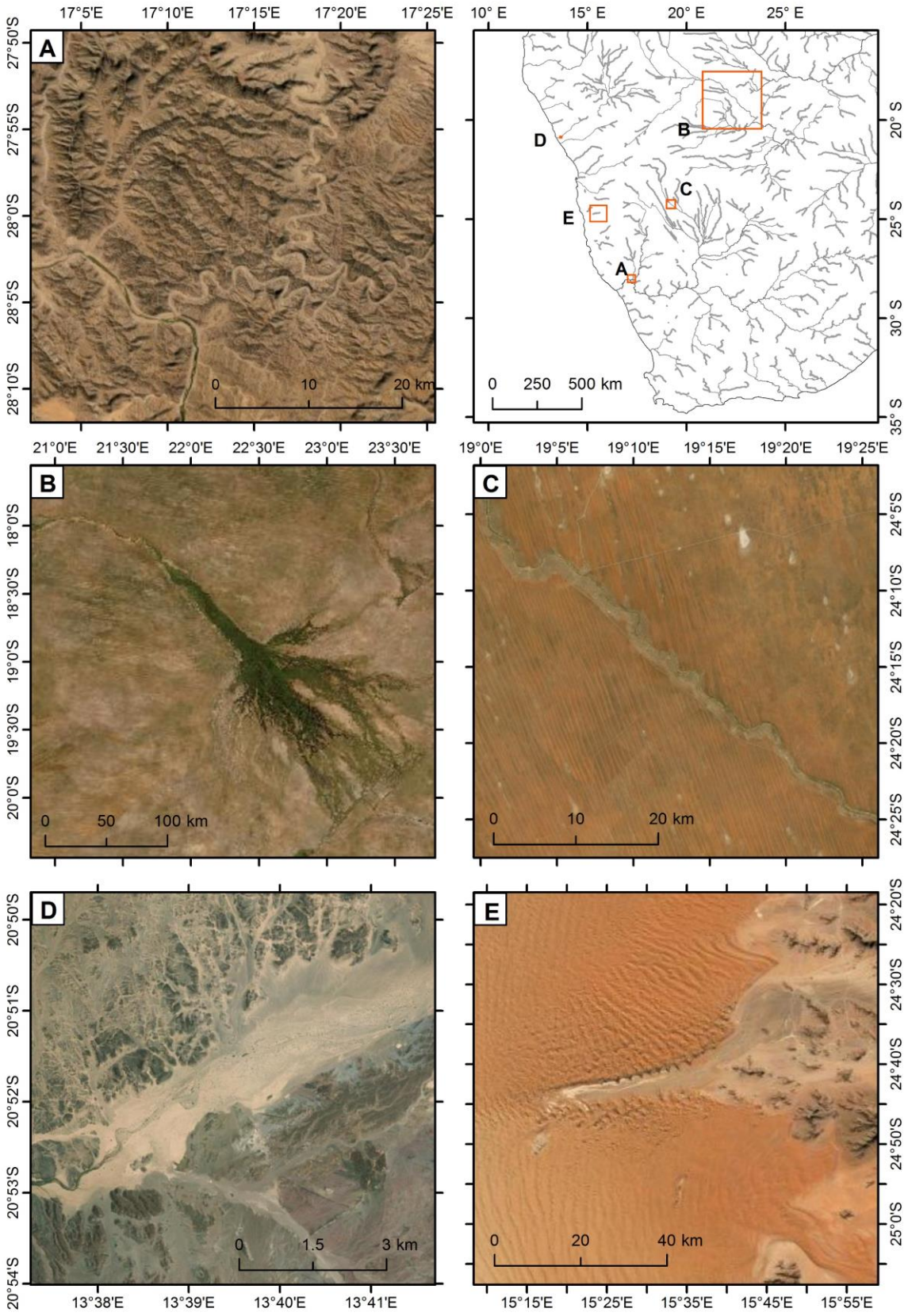

Figure 2.8. Examples of river systems in southwestern Africa. **A)** Bedrock confined canyon of the Fish River, Namibia. **B)** Alluvial fan setting of the Okavango Delta, Botswana, at the termination of

the perennial Okavango River, with active channels and palaeochannels. **C)** Auob River flowing through the southwestern Kalahari dune field. **D)** Alluvial fill of the Huab River channel, Skeleton Coast, Namibia. **E)** Termination of the Tsauchab River in the Namib Desert, Namibia.

Perennial rivers

In southern Africa, perennial river flow is recorded in the main channels of the Orange, Okavango, Kunene, Limpopo, Vaal, and Zambezi rivers, and in rivers flowing towards the south-eastern coast of South Africa (Figure 2.7; Messager *et al*., 2021). These systems are either fed by headwaters in regions of higher precipitation e.g. the Orange is sourced from the highlands of Lesotho, or are located in more humid climates, e.g. in Lesotho and Kwazulu Natal, South Africa. Several fluvial styles occur along these systems, e.g. meanders (McCarthy and Tooth, 2004) and an inland alluvial fan (Figure 2.8B; McCarthy *et al*., 1991, 1992).

Intermittent and Ephemeral rivers

The rivers across southern Africa are characterised predominantly as having intermittent or ephemeral flow (Figure 2.7; Messager *et al*., 2021). In the west of the subcontinent, moderate gradient river channels originate from the Great Escarpment and extend towards the Atlantic Coast. Flow in these rivers is currently typically activated by the passage of convective thunderstorms, initiating hydrological activity typically for only a few hours or days (Jacobson *et al*., 1995). River flow is highly sporadic throughout the year, but principally occurs during the austral summer (Figure 2.9). River styles within this region range from bedrock-confined reaches (Figure 2.8A), alluvial fills with meander migration of channels (Figure 2.8D) and rivers that terminate within sand seas (e.g. Tsondab River, Figure 2.8E).

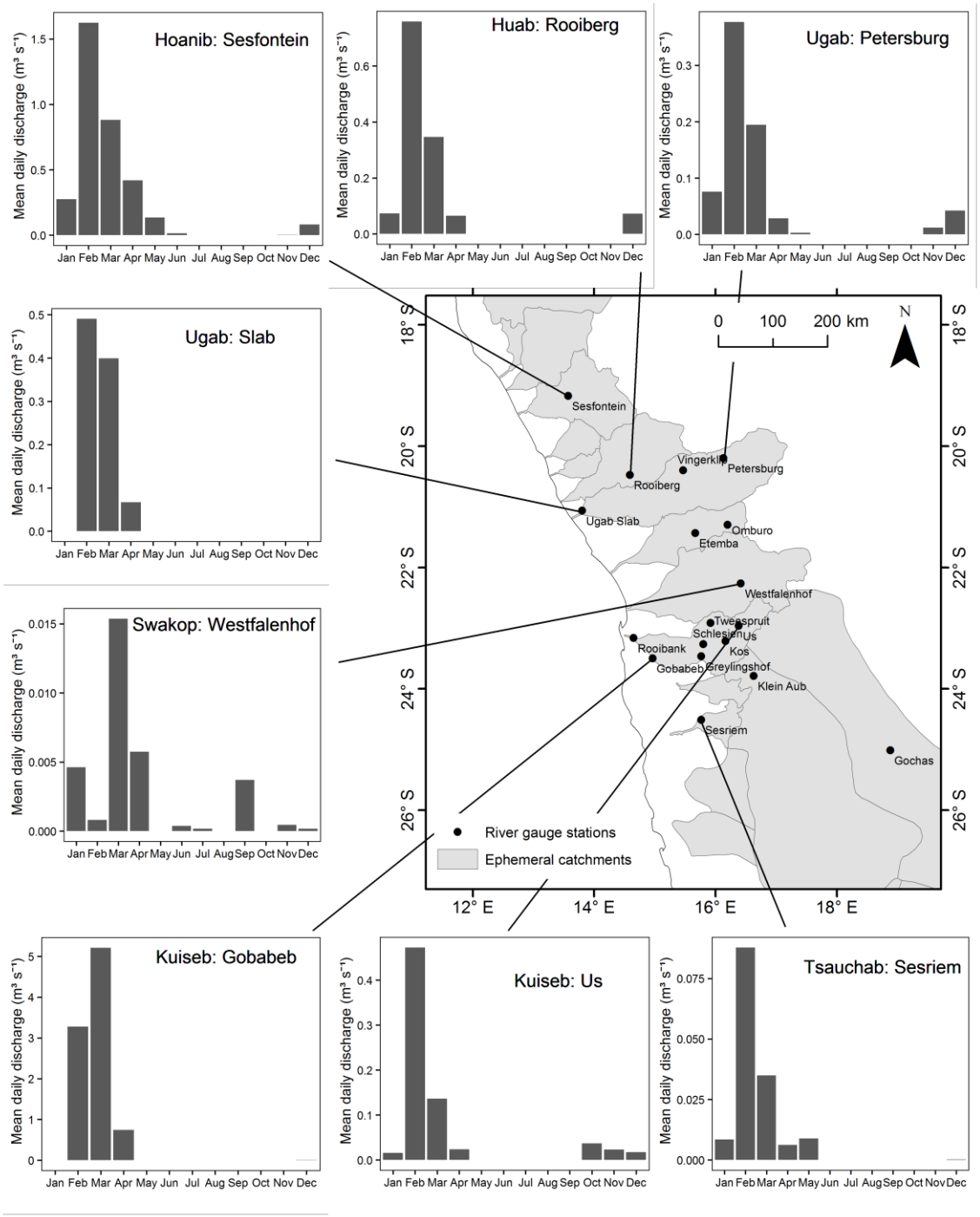

Figure 2.9. Map of Namibian ephemeral rivers with river gauge station locations. Time series of mean daily discharge by month for a selection of Namibian river gauge stations, averaged over a 10-year time period (2007 - 2017). Variability is noted both spatially (e.g. the two records from each of the Kuiseb and Ugab considered here show differences), and temporally (where some years have no flow).

Within the Kalahari, ephemeral and intermittent rivers flow both endoreically towards the Okavango Delta (e.g. Xaudum River) and exoreically as straight single thread (e.g. Auob River, Figure 2.8C) and meandering bedrock confined rivers (e.g. the Molopo River) to the south as part of the Molopo Basin. Within the Kalahari, many of the rivers exist in the form of channels that have not flowed in historical records and remain persistently dry, and are locally called mekgacha 'fossil' valleys (e.g. Okwa River, Shaw *et al*., 1992). Across the wider southern African subcontinent, flow intermittence is recorded in the rivers that drain towards the southwest coast of South Africa and across the wider catchments of the perennial rivers described above. In these perennial systems, the probability of intermittence increases with distance from the main channel (Messager *et al*., 2021).

River gauge stations are particularly limited in southwestern Africa's drylands (Jacobson *et al.* 1995). Despite this, river gauges from Namibia detail a strong seasonal trend in occurrence of river flow and show that river flow is variable amongst sites within individual catchments. For example, over a 10-year period, average river flow by seasons shows differences between the headwaters and lower reaches of the Ugab and Kuiseb (Figure 2.9).

2.6. Southern African palaeoclimate change

On Quaternary timescales, changes in the intensity and relative importance of climate systems discussed in Section 2.5.1 are thought to have occurred in response to both high and low latitude forcing. Several hypotheses have been proposed, but debate remains surrounding the timing and magnitude of precipitation changes. In recent decades, the ability to both resolve evidence of climate change and to explain the mechanisms behind the changes has advanced. For example, important patterns of past rainfall change were noted from long-term marine core records (e.g. Collins *et al*., 2011), yet the observations could not be extrapolated across the terrestrial region or indeed be explained by clear mechanisms of change. Following the simulation of past climates using

global climate models (e.g. Singarayer and Burrough, 2015; Singarayer *et al*., 2017), greater detail on both the spatial patterns and potential mechanisms could be determined. The terrestrial spatial coverage of proxy records to support or refute model-based predictions, however, was limited. The following section discusses the roles of high and low latitude forcing on palaeoclimates, the spatial complexity noted in southern Africa's palaeoclimates, and the availability of records to test model outcomes.

2.6.1. Insolation forcing

On orbital timescales, changes in the earth's orbital parameters of eccentricity, precession, and obliquity alter the amount and distribution of insolation received by Earth. The ~100 ka eccentricity cycle, paces the development of large ice sheets at the poles during glacial periods and contraction during interglacials, which is a key high latitude forcing (Chase, 2021). Glacial-interglacial transitions, and abrupt northern hemisphere changes such as Heinrich events, influence global temperatures, ocean circulations and SSTs. These high latitude signals are transmitted to lower latitudes of southern Africa through teleconnections in the ocean and atmosphere (Chase *et al*., 2015; Chevalier and Chase, 2015). Contemporary transport of moisture from the Indian Ocean to the southern African subcontinent is intricately linked with Indian Ocean SSTs (Hermes and Reason, 2005), and is thought to have been a key driver in late Quaternary changes. These high latitude changes influenced the thermal contrast between the poles and the equator, which is thought to have driven changes in the tropical rainbelt (Braconnot *et al.*, 2007; Broccoli *et al.*, 2006), the northerly extent of the westerlies and associated storms tracks (Chase and Meadows, 2007; Heine, 1982; van Zinderen Bakker, 1976), and sea level change (DiNezio and Tierney 2013).

Southern African climate systems also respond directly to low-latitude insolation changes, principally in response to the ~20 ka precessional cycle. In contrast to high latitude forcing where ice extent changes occur in both hemispheres, low-latitude drivers are thought to result in an

asymmetric response between hemispheres. This is due to the antiphase pattern of insolation change: when northern hemisphere summer insolation is high, southern hemisphere summer insolation is low. Changes in precession influence the intensity of seasons and therefore modify the amount of precipitation received. When perihelion occurs in the southern hemisphere summer, southern hemisphere summers are intensified and northern hemisphere summers are muted (Woillez *et al*., 2014). This mechanism is supported by the seminal paper by Partridge *et al*. (1997) which presents a sediment record from Tswaing Crater, South Africa, that details an antiphased response of southern African climate compared to north Africa as a result of direct insolation forcing. The role of high- and low-latitude forcing can be difficult to disentangle, however, especially at times when low-latitude forcing is modulated by high-latitude forcing. Eccentricity modulates precession, e.g. where the development of substantial ice cover at the poles dominates over a local precessional signal when eccentricity is low (Chase, 2021).

2.6.2. Complexity in southern Africa's palaeoclimate response

Whilst low-latitude forcing is thought to result in asymmetry between the hemispheres, marine and terrestrial evidence of palaeoenvironmental change show spatial complexity, with some suggesting that southern Africa's climate responded in phase with north Africa on precessional timescales (Chase *et al*., 2010; Collins *et al*., 2011; Stager *et al*., 2011). The response of the tropical rainbelt on millennial timescales to insolation changes is well documented in marine, lacustrine, and fluvial archives in North Africa (e.g. deMenocal *et al*., 2000; Lézine *et al*., 2011; Kröpelin *et al*., 2008), yet is less-established for southern Africa (Burrough and Thomas, 2013). This is in part thought to be a result of the greater oceanic influence in southern Africa (less landmass) leading to increased influence of other forcing factors (Singarayer and Burrough, 2015). Model simulations indicate that spatial complexity could result from a differing response of the tropical rainbelt to insolation over the ocean and terrestrial regions (Singarayer *et al*., 2017). Advection of this oceanic signal over land would result in differences in response between the coastal and inland regions.

This hypothesis is supported and developed by a compilation of hyrax middens from the Namib Desert (Chase *et al*., 2019), yet the terrestrial extent of this signal is uncertain.

Whilst high latitude forcing has been used to propose an increase in the areal extent of the Winter Rainfall Zone (Chase and Meadows, 2007) to explain precipitation changes in records across southern Africa during glacial periods, there is increasing recognition that the climate systems are more complex than a differentiation between winter and summer rainfall zones. Research on the interactions between temperate and tropical systems (TTTs) suggest that TTTs are important drivers of rainfall in contemporary southern Africa (Hart *et al*., 2010), and on Quaternary timescales (Chase *et al*., 2017). It is therefore important to re-assess long-debated hypotheses in the context of literature on contemporary climate dynamics, and in the context of emerging sets of palaeoproxy data.

2.6.3. Availability of records

To pick apart the complexity of terrestrial environmental responses to past climates on Quaternary timescales, a suite of robust records with sufficient spatial coverage are required. The climate and topographic setting of southern Africa, however, has limited the formation and accumulation of geochemical and botanical proxies (Chase and Meadows, 2007; Thomas and Burrough, 2012). Limited occurrence of closed sites and poor preservation of organic material have restricted the availability of palaeoecological and geochemical proxy sources in archives such as speleothems and lacustrine settings. Where available, resulting terrestrial records from the western dryland regions in southern Africa are often spatially and temporally discontinuous (e.g. Brook *et al*., 1999; Heine, 1992; Scott *et al.* 2004).

Several studies have focused on sedimentary, leaf wax, and pollen assemblages preserved in marine environments (e.g. Collins *et al*., 2011; Shi *et al*., 1998) as these contexts provide the

opportunity for well-dated, continuous, long-term records. As a result, data from marine settings have typically been focused on in syntheses of palaeoclimate and model-data comparisons. However, extrapolating marine records to terrestrial systems can be problematic in cases. The terrestrial component in marine records can provide a palaeoenvironmental signal relating to large terrestrial regions, integrating palaeoenvironmental change and masking regional differences that may reflect the influence of a number of synoptic-scale climate systems (Scott *et al.* 2004). This is particularly a problem for marine pollen records, where clarity of source regions are difficult to establish (Scott *et al*., 2004, 2012, 2018). A reliance on a small group of well-dated, long term records has resulted in an oversimplification of climate dynamics on Quaternary timescales (Chase, 2021). Where coverage of sites is poor, the ability to resolve spatial complexity or to verify model outputs has been limited.

Several high-resolution terrestrial records have been developed in the last decades, e.g. from hyrax middens (Chase *et al*., 2019), speleothems (e.g. Railsback *et al*., 2016; Sletten *et al*., 2013) and pan sediments (Belz *et al*., 2020; Schüller *et al*., 2018), yet the spatial coverage of these sites is limited. Southern Africa does, however, host numerous records of geomorphological change (Grenfell and Grenfell, 2021; Humphries, 2021; Stone, 2021; Thomas, 2013; Thomas and Burrough, 2012). Whilst geoproxies are complicated to interpret (Bailey and Thomas, 2014), studies on the controls of archive formation, and interrogation of the information that can be gained from a suite of records in conjunction, is increasing the potential of these archives. The spatial coverage of fluvial sites in southern Africa is now substantial (Stone and Thomas, 2013; Stone, 2021; Tooth, 2016), extending across important longitudinal and latitudinal gradients, and together providing the potential to consider spatial patterns of late Quaternary change that is critical for model-data comparison. Following principles presented by Thomas (2013) for the study of geoproxies, fluvial records must: i) be well dated; ii) incorporate methods that robustly interrogate the nature of river flow; iii) be

interpreted in the scale of catchment specific contexts; and iv) taken together with multiple individual records across a region.

2.7. The Huab

Given debate on palaeoenvironmental conditions in the western portion of southern Africa, and the importance of fluvial archives to reconstruct these changes, this thesis produces a new fluvial record from the Huab River, northern Namibia. The Huab River is one of twelve major ephemeral river systems in Namibia (Figure 2.9). From its headwaters in the Great Escarpment, the river course extends westward for 300 km towards the Atlantic Coast (Jacobson *et al*., 1995). To date, the Huab has been the focus of three palaeoenvironmental studies: in the headwaters (Eitel and Zoller, 1996; Eitel *et al*., 2001) and in the Skeleton Coast (Thomas *et al*., 2017). These records detail evidence of past flow conditions, yet a detailed reconstruction of palaeohydrological change has not been undertaken. The choice of sample site location and sampling strategy in the Huab River for the study in this thesis are described in the Methods chapter (Section 3.2).

The majority of the Huab catchment (87 %) receives precipitation of <300 mm yr^{-1}, decreasing westward to <50 mm yr^{-1} at the coast (Figure 2.10A). As rainfall decreases to the west, its variability increases (Jacobson *et al*., 1995). Aridity in this region occurs as a result of the combined influence of limited Indian Ocean derived rainfall, the role of orography, and the influence of the cold upwelling current and SAA in blocking incursions of rainfall. Convective systems bring rainfall to the region predominantly in the austral summer (Figure 2.11). At present, the Huab has a similar distribution in the timing of river flow to the other ephemeral systems in Namibia (Figure 2.9), where the channel remains dry for most of the year but can experience significant floods associated with short intense episodes of rainfall (Jacobson *et al*., 1995; Morin *et al*., 2009). A river gauging station on the Aba-Huab tributary records on average only 14 days of river flow a year (2007-2017),

but with variable timing and extent (between 0 and 54 days with river flow a year over the last decade) (Ministry of Environment and Tourism Namibia).

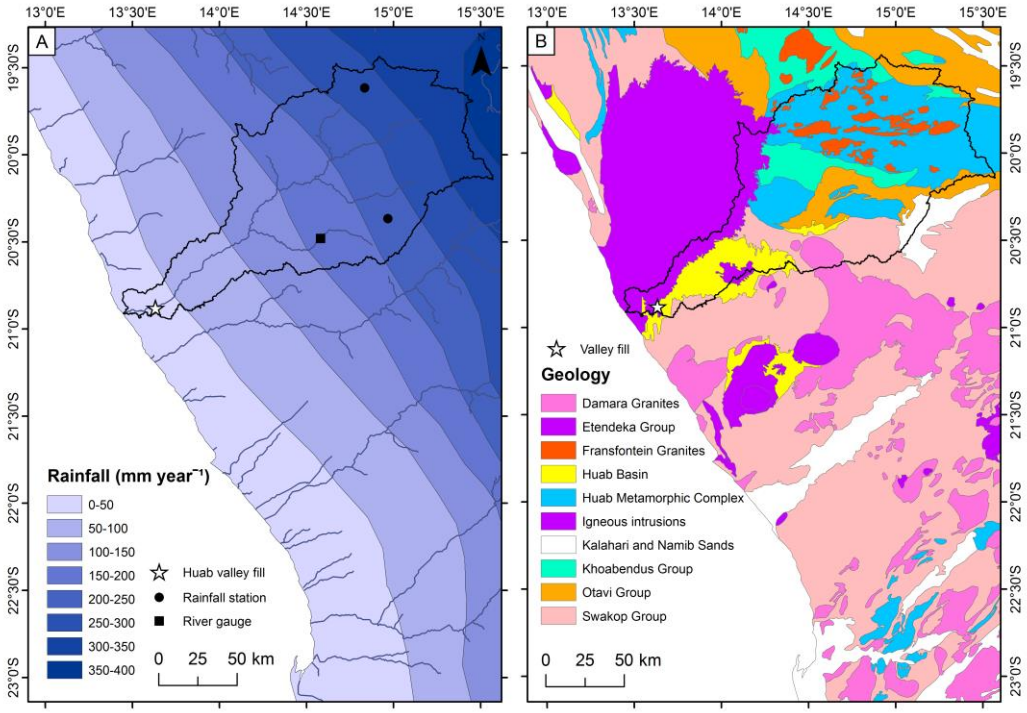

Figure 2.10. The Huab River catchment, Namibia. **A)** Contemporary annual rainfall (mm year^{-1}) (Mendelsohn *et al*., 2002) with the location of currently available rainfall and river gauge stations and the Huab Skeleton Coast valley fill. **B)** Major geological divisions by geological group. For more detail on the geological setting of the Huab, see Chapter 4. Datasets sourced from Project E1 – Atlas of Namibia (http://www.uni-koeln.de/sfb389/e/e1/download/atlas_namibia/).

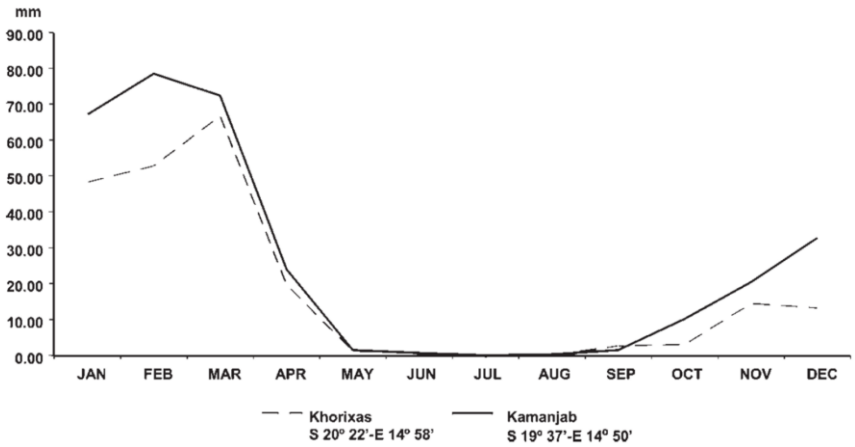

Figure 2.11. Rainfall data from two rainfall stations within the Huab catchment (from Gil-Romera *et al*., 2006, showing data from Namibian Meteorological Service). See Figure 2.10A for location of rainfall stations in the context of the Huab River catchment.

In the context of the broad geological descriptions in Section 2.5.2, the Huab River catchment spans the interface between the Damara Belt, the Kaoko Belt, and the Congo Craton. The source area comprises the Kamanjab basement within the Congo Craton, and the main river channel passes between the Etendeka Plateau (Kaoko Belt) to the north and Damara inland branch (Damara Belt) to the south (Figure 2.10B). Between 270 and 200 Ma, glacial incision during the Permo-Carboniferous formed the deep valley landscape of the Huab seen today (Jacobson *et al*., 1995; Martin, 1953). Understanding the geological setting of the Huab River is important for assessing the sourcing of sand to the Skeleton Coast valley fill to provide a context for compositional analysis. Further description of the heavy mineral and petrographic assemblages the Huab geological shed is provided in Chapter 4.

Chapter 3: Methods

3.1. Introduction

This chapter discusses the methodological approaches used to address the key research objectives of this thesis (Chapter 1). The methods map onto the three papers (Chapters 4-6) and are discussed here in three parts: i) a new fluvial palaeoenvironmental record (including fieldwork, ground penetrating radar, sample site selection, luminescence dating for chronological control, and stratigraphic and sedimentological analysis for interpretation of palaeoflow dynamics); ii) a fluvial chronological database; and iii) palaeoclimate model-data comparison. The focus of this chapter is to introduce and justify the suite of methods used in the thesis and to detail methods that guided this analysis but that do not appear elsewhere in the thesis. To maintain the integrity of chapters that are also published or submitted papers, detailed aspects of some methodology elements remain in the chapters as they appear in the original papers.

PART 1: A new fluvial record

3.2. Fieldwork

To address the first research objective of this thesis, fieldwork was conducted in the Huab River, northern Namibia. Chapter 4 (Paper 1) aims to establish the timing and nature of fluvial deposition, and infer links between the sedimentary response of the Huab River and Holocene precipitation changes. Samples were collected for luminescence dating and sedimentological analysis from a valley fill in the Skeleton Coast National Park (Figure 3.1). This fieldwork took place in September 2018 under research permit RPIV00212018 issued by the National Commission on Research, Science, and Technology.

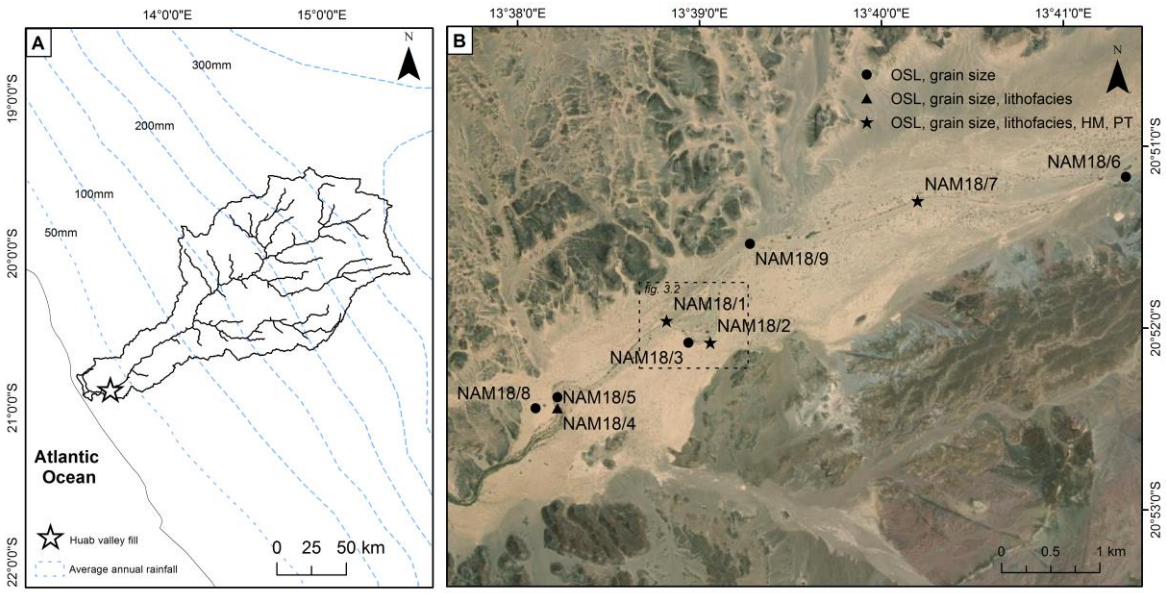

Figure 3.1. A) Location of the valley fill studied within the Skeleton Coast National Park, Huab River. **B)** Location of sampling sections along the natural exposure in the valley fill. At all sites, samples were collected for luminescence and grain size analysis. Lithofacies, heavy mineral (HM) and petrographic (PT) analyses were additionally undertaken on samples from sites NAM18/1, NAM18/2, NAM18/7, and lithofacies analysis was performed at site NAM18/4. Dashed box demarcates the extent of Figure 3.2.

Upstream of a narrow pinch-point in the bedrock configuration, in a remote area of the Skeleton Coast National Park, a thick unit of sediment accumulation exists across the 1 km-wide valley floor (Figure 3.1). This site was chosen for four main reasons. First, an existing luminescence chronology from the valley fill details fluvial deposition within the Holocene (Thomas *et al*. 2017). This record establishes that the fluvial archive covers the time period of interest and that the sediments are dateable through luminescence methods. This chronology is based on small sample set and the nature of fluvial deposition was not studied. Second, incision of the modern ephemeral channel across this extensive deposit provides exposures of sediment that allow for a combined assessment of stratigraphy and compositional analysis. Third, access to the Skeleton Coast valley fill site had previously been established through prior fieldwork to the region (sample collection for Thomas *et al*. 2017; Dansie *et al*., 2017). Sampling in other parts of the river system was restricted due to difficulty of vehicle access, so this route into the valley fill was critical. And finally, fluvial and hyrax

midden archives in the headwaters of the Huab River (Eitel and Zoller, 1996; Eitel *et al*., 2001; Gil-Romera *et al*., 2006) provide records of geomorphological and vegetation response to past climates for comparison. Ephemeral river channels in Namibia have been identified as significant sources of atmospheric dust (Eckardt and Kuring, 2005; von Holdt and Eckardt, 2018), and the Huab valley fill is a particular hot-spot because of the extensive sediment availability (Dansie *et al*., 2017, 2018). Reconstruction of the sedimentary context in this thesis can provide further information on the source of sediment to this dust source.

One of the key complexities of using sedimentary archives in dryland river systems is that discontinuous sedimentary sequences can inconsistently preserve depositional events. Variable processes of erosion and deposition can result in 'shredding' of environmental signals (Jerolmack and Paola, 2010; Kemp, 2012; Van De Wiel and Coulthard, 2010). In the case of the Huab River, Google Earth images indicate that even over a 15-year period, the modern river meander has migrated (Figure 3.2), removed units of deposition in certain settings, and created new exposures at others. The sampling strategy is one of the few processes that can be controlled in the path from climate perturbation to sedimentary interpretation (see Figure 2.3; Allen, 2017; Bailey and Thomas, 2014; Macklin *et al*., 2012). A sufficient number of sections need to be studied, and samples need to be collected from a large enough number of depths to increase the stratigraphic completeness and avoid aliasing the record through under-sampling. Within the context of what was possible to sample within the constraints of fieldwork, 42 samples were collected for OSL dating from nine sites across the fill to obtain as broad a coverage as possible from available exposures (Figure 3.1).

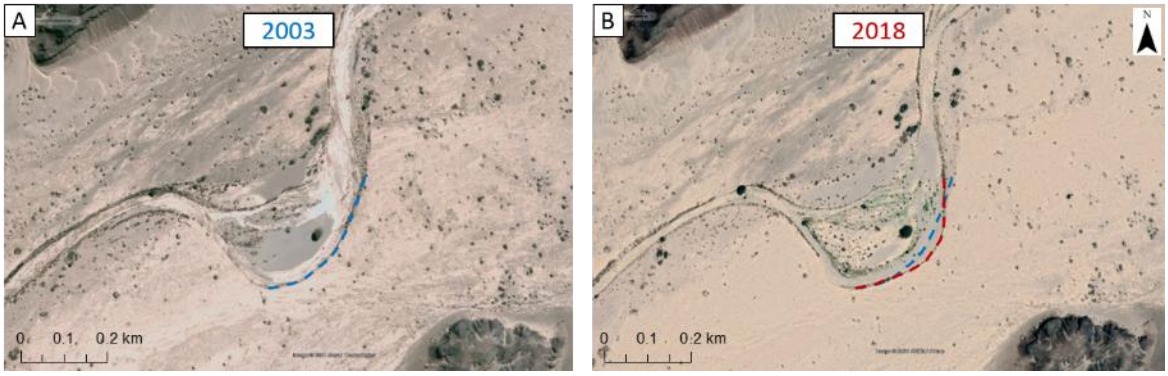

Figure 3.2. Google Earth images of meander change over 15 years. **A)** Meander position in 2003. **B)** Meander position in 2018 (red) relative to 2003 (blue). Location of meander demarcated in Figure 3.1 by dashed box.

3.2.1. Ground Penetrating Radar

To guide the sampling strategy, ground penetrating radar (GPR) was employed across a suite of test sections to interrogate the nature of subsurface structures within the valley fill. GPR is a non-destructive method based on the propagation and reflection of electromagnetic waves (Annan, 2009; Baker *et al*., 2007; Cassidy, 2009) and is commonly used to image sedimentary architecture and identify stratigraphic breaks (Bristow and Jol, 2003). In the study of Namibian geomorphological archives, GPR has been used on aeolian dune features to guide sampling for luminescence dating (e.g. Bristow *et al*., 2000; Bristow *et al*., 2005; Bristow *et al*., 2007) and in an initial investigation of the nature of ephemeral fluvial deposits (Leopold *et al*., 2006).

At seven locations, 17 GPR transects (covering a total of 350 m) were acquired using a Sensors and Software PulseEKKO PRO (Figure 3.3; Appendix C Table C1). Assessment of signals from a suite of measurement parameters found that data quality improved by increasing antenna frequency from 100 MHz to 200 MHz and using a stacking value (number of signals obtained per measurement) of 64. The GPR data were processed and imaged using ReflexW software (Sandmeier; Appendix C Figure C1).

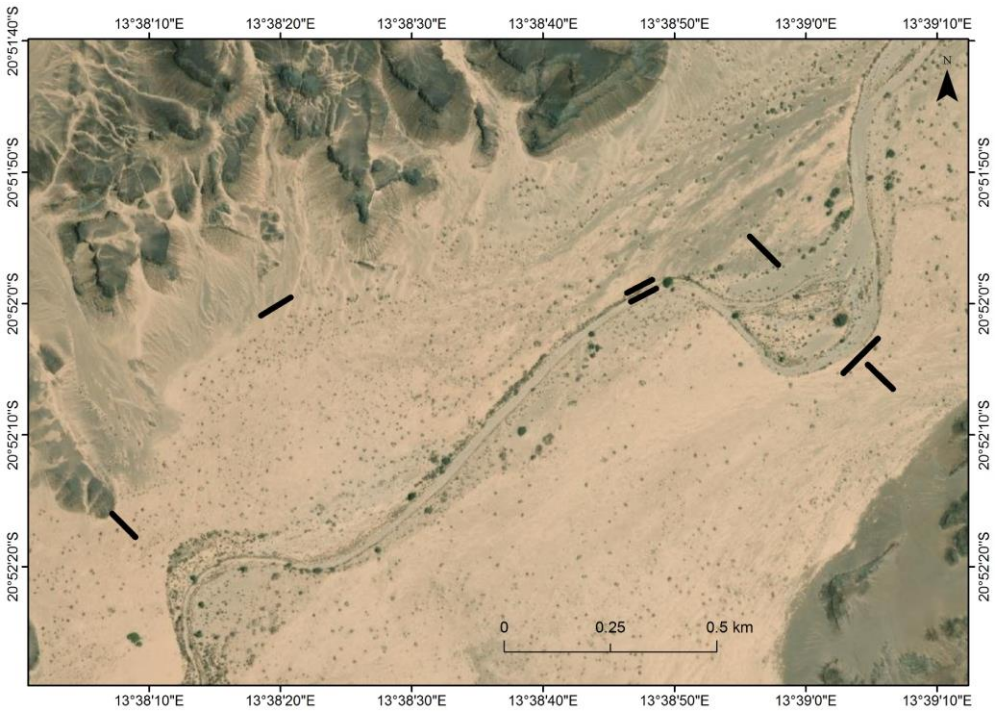

Figure 3.3. Location of GPR transects across the surface of the valley fill and in the modern ephemeral channel.

GPR data from a transect along the contemporary channel shows evidence that the valley fill is at least 3 m deeper than the extent of the natural exposure (Figure 3.4A). This suggests that by coring deeper into the sediment, a more extensive record of palaeoenvironmental change could be obtained. The GPR data also indicate that preservation of depositional units varies over space, where there is horizontal variability in the depth of reflections in a transect perpendicular to the channel exposure (Figure 3.4B). This suggests that samples should be collected from multiple sites across the fill to gain a representative record of sedimentation in the system. Whilst it was possible to image some subsurface features, meaningful reflections of structures within the fill were limited to the top 2 m, and ringing (a form of horizontal noise) obscures the signal (Figure 3.4C). The depth of penetration of GPR signals is likely influenced by the fine-grained nature of the upper sedimentary units (low resistivity leading to rapid attenuation; Bristow and Jol, 2003), and has therefore placed limitations on the extent to which GPR could be used to image subsurface structures and guide sampling at specific sites.

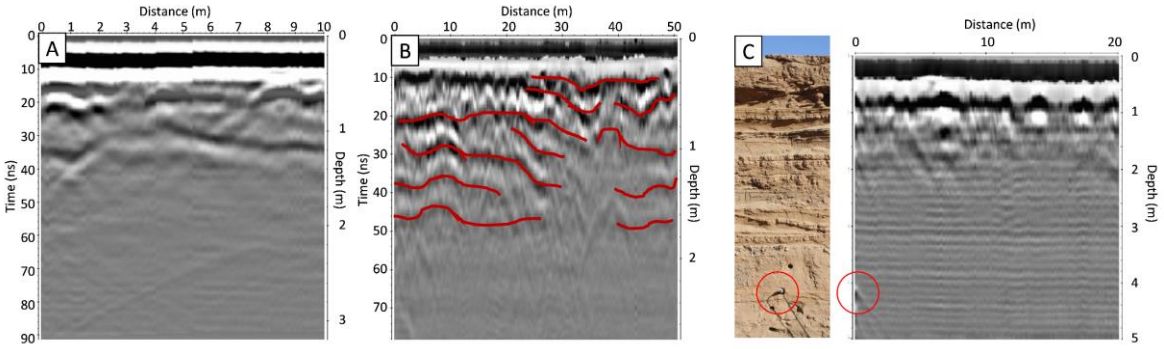

Figure 3.4. Radargrams from ground penetrating radar (GPR) analysis. **A)** Radargram from the base of the contemporary channel showing no indication of reaching bedrock for at least 3 m. **B)** Horizontal variability in signals obtained from a transect perpendicular to the channel. **C)** Assessment of signal clarity: an object inserted into the fill could be identified in the radargram at a depth of ~4 m, yet useful GPR signals are limited to the upper 2 m.

Whilst an initial aim of using GPR was to provide a detailed investigation of the stratigraphy beyond the natural exposure, this use was limited both by the ability of GPR to image these structures with sufficient detail and the challenge of accessing sub-surface sediments through coring. Access to sediment beyond the active channel was hindered by coverage of coarse scree slope deposits, rock fall, and aeolian deposits (Figure 3.5B, C, D). Where valley fill surfaces were exposed, the capacity to drill or auger was limited by the loose and dry nature of the sediment not holding a face (Figure 3.5G). The natural exposure formed by modern migration of the channel, however, provides an extensive distribution of sections to study, so a focus was placed on these sections for sampling.

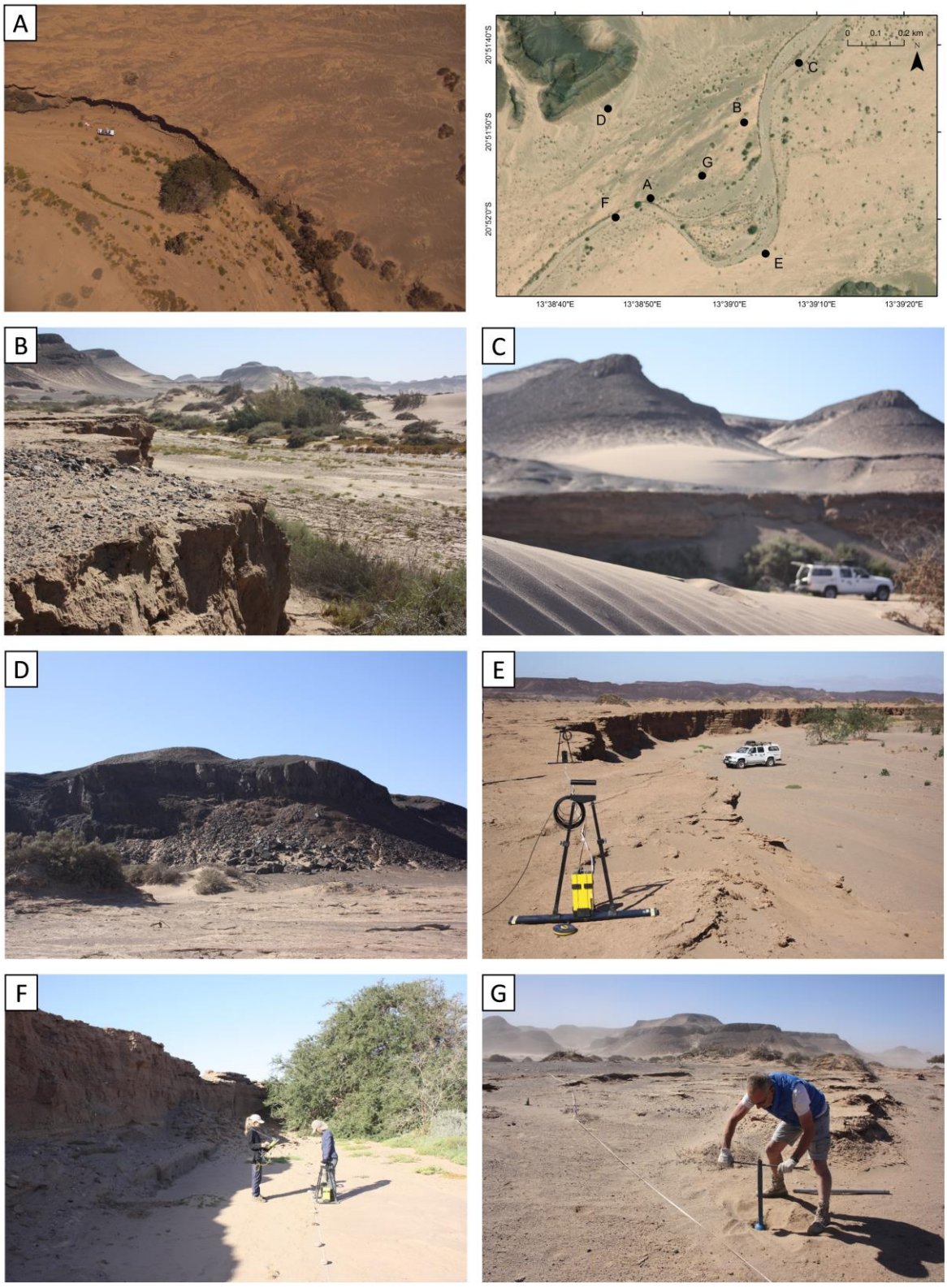

Figure 3.5. Fieldwork in the Huab River. **A)** Drone footage of the exposure within valley fill, car for scale, **B** and **C)** the natural exposure and aeolian features, **d)** scree slope deposits at the edge of the valley fill, **E)** GPR transect on the surface of the fill, **F)** GPR transect at the base of the channel, **G)** attempt to auger the valley fill beyond the natural exposure.

3.2.2. Sample site selection

Following the considerations identified through GPR analysis and after reconnaissance of sedimentary sections across the fill, exposures were sampled systematically from nine sites (Figure 3.1, Table 3.1). These sites were chosen to encompass as much of the full width and length of the fill as possible. In places, ~4 m of stratified sediment deposition was exposed and a further 1 m was uncovered through pits dug at three sites.

Table 3.1. Details of sampling sites.

Site	Location	Description
NAM18/1	20.866˚ S, 13.647˚ E	Located on the north-western bank of the valley fill, 2.6 km upstream of the constriction. 12 samples collected from 5 m exposure
NAM18/2	20.868˚ S, 13.651˚ E	Located in the southern-eastern unit of the fill, on the other side of the meander from NAM18/1. 12 samples collected from a 5 m exposure
NAM18/3	20.868˚ S, 13.649˚ E	Located between NAM18/1 and NAM18/2, where the meander has incised perpendicular to the orientation of the valley. 2 samples collected at the same depth to detail timing of lateral migration and channel infill
NAM18/4	20.874˚ S, 13.637˚ E	Closest site to the constriction (1.1 km upstream). 5 samples collected from a 2 m exposure. Evidence of bioturbation and desiccation
NAM18/5	20.873˚ S, 13.637˚ E	2 samples collected from a preserved unit higher than the rest of fill, near NAM18/4
NAM18/6	20.853˚ S, 13.689˚ E	Samples collected from the top and bottom of a site furthest away from the constriction (6.9 km upstream)
NAM18/7	20.855˚ S, 13.670˚ E	7 samples collected from a 5 m exposure 5.3 km upstream of the constriction
NAM18/8	20.873˚ S, 13.634˚ E	Nebkha dune and preservation of higher unit of valley fill that has been removed across much of the fill
NAM18/9	20.859˚ S, 13.655˚ E	1 sample from a unit below a rock layer to investigate the potential that this layer has protected a longer history of deposition below. 3.9 km upstream of constriction

Samples for luminescence dating and grain size analysis were collected from each of the nine sites, and samples for compositional analysis were collected from the three key sites (Figure 3.1). These sites were chosen because they have the most extensive stratigraphic preservation and enabled a comparison of depositional histories at different distances along the length and width of the fill. At

each site, samples were collected from distinct sedimentary units (Figure 3.6). Where possible, the sampling strategy aimed to collect samples from units of corresponding depths and features between sections to assess consistency across the fill. At additional sites, samples were taken from the top and bottom to characterise the full stratigraphic section (e.g. site NAM18/6).

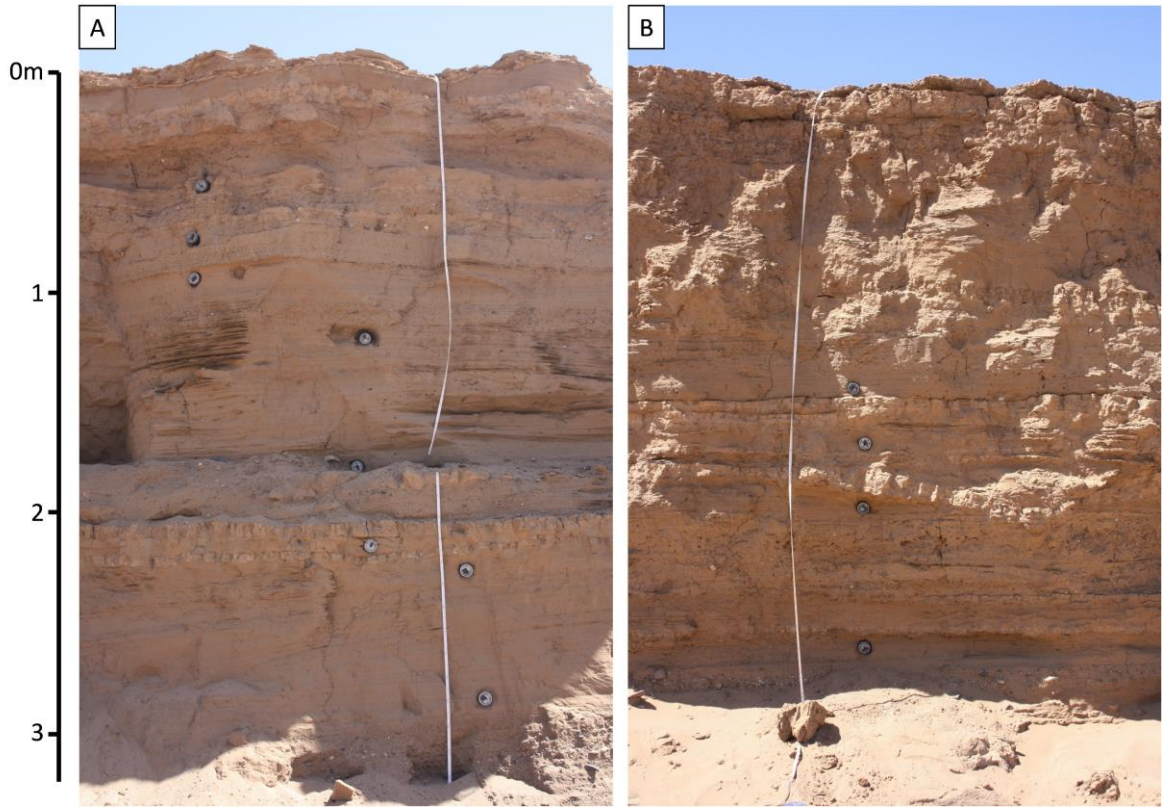

Figure 3.6. Example of sections of the natural exposure within the Skeleton Coast valley fill chosen for sampling. **A)** NAM18/1, **B)** NAM18/2. Luminescence samples were collected in opaque sampling tubes (pictured here, with additional samples collected from upper sections after the photo was taken).

3.3. Luminescence dating

The timing of sediment deposition was established through 42 optically stimulated luminescence (OSL) ages. OSL dating is a well-established method for reconstructing the timing of geomorphological events, particularly in dryland contexts where organic material is limited. This section discusses the considerations for dating fluvial sediments and introduces the laboratory

preparation and analysis approach used. Further detail on the preparation of samples and measurement protocols are described in Chapter 4.

3.3.1. Principles of OSL

OSL dating measures the amount of time elapsed since the last exposure of a mineral grain to sunlight. Minerals such as quartz accumulate charge within 'traps', or imperfections within the crystal lattice. When exposed to sunlight or heating, trapped charge (measured as an optical luminescence signal) is released. Under controlled conditions, the amount of accumulated charge can be measured to estimate the equivalent dose (a laboratory recreation of the total charge accumulated during burial; the palaeodose). Following calculation of the rate of ionising background radiation emitted from the surrounding sediment (the environmental dose rate), the amount of time elapsed since the mineral grain was last bleached can be estimated (Equation 3.1; Duller, 2004, 2008a; Murray *et al*., 2021; Preusser *et al*., 2008).

Equation 3.1. Equation for calculating a luminescence age.

$$\textit{Estimated age (ka)} = \frac{\textit{Equivalent dose (Gy)}}{\textit{Estimated dose rate (Gy/ka)}}$$

Luminescence measurements are commonly undertaken on quartz or feldspar grains, depending on the mineralogy of the deposit and the suspected time since burial. Quartz is frequently used because it's potential to trap and retain charge are understood best (Aitken, 1998; Bailey, 2001; Preusser *et al*., 2008; Preusser *et al*., 2009). Quartz is abundant in sediment sourced from the Huab Basin (Garzanti *et al*., 2014; Garzanti *et al.*, 2021) and is present in the valley fill sedimentary deposit in sufficient quantities for dating (see Section 3.4.3 for XRD analysis, and Section 3.4.4 for petrography of Huab samples). OSL dating using standard SAR (single-aliquot regenerative-dose) protocols starts to underestimate ages over c. 150 Gy in quartz (Buylaert *et al*., 2007; Lowick *et al*.,

2010), but below this, these standard procedures have a dating range sufficient for determining the depositional age of Huab sediment within the aims of this study. Maximum equivalent doses in existing research in the Huab Basin are 23.68 ± 1.14 Gy (coarse grained quartz, equating to an age of 9.79 ± 0.73 ka; Thomas *et al*., 2017) from the Skeleton Coast valley fill, and 33 ± 4 Gy (fine grained polymineral, equating to an age of 8.3 ± 1.0 ka; Eitel *et al*., 2001) from the headwaters of the Huab.

3.3.1.1. Considerations for luminescence dating of fluvial deposits

To date fluvially deposited sediments in drylands, several considerations need to be made (Cunningham and Wallinga, 2012; Rittenour, 2008; Wallinga, 2002). These particularly relate to the ability for fluvial transport to 'bleach' and reset the signal within mineral grains. In any water body there is a moderate increase in the likelihood of partial bleaching due to attenuation of both the wavelength and intensity of incident light through a water column (Berger, 1990), and potential for floods to occur at night where no bleaching occurs, but partial bleaching can be particularly problematic in some dryland contexts because of high sediment availability and occurrence of flash flooding (high intensity, short duration flows). Under these conditions: i) sunlight is further blocked by suspended sediment (Ditlefsen, 1992), which is commonly high (Jacobson *et al*., 2000), limiting the effectiveness of bleaching, and ii) dryland river flow commonly occurs over short distances in isolated floods (Tooth, 2013), resulting in shorter periods for bleaching of grains.

Despite these challenges, there is increasing recognition that mineral grains can be well bleached in some transport conditions in fluvial systems (e.g. Kale *et al*., 2000; Medialdea *et al*., 2014). Following advances in dating protocols, luminescence dating has been widely used to reconstruct the timing of past fluvial activity in drylands globally (e.g. Cohen *et al*., 2010; Das *et al*., 2020; Durcan *et al*., 2019; Tooth *et al*., 2022), and specifically in Namibian ephemeral systems with similar depositional contexts to the Huab Skeleton Coast valley fill (e.g. Greenbaum *et al*., 2014; Srivastava *et al*., 2006; Völkel *et al*., 2021). In such systems, it is likely that fluvial sediments contain a

combination of partially- and well-bleached grains, and considerations can be made to account for this. For example, a 2 mm mask in combination with sand-sized grains (180-210 µm) results in ~70 grains per measured subsample (aliquot) (Burow, 2020; Heer *et al.*, 2012), of which only 5 % typically give a signal (Duller, 2008b). Measurement at the single grain scale using a focused laser in combination with a single grain disc containing 100 x 300 µm holes enables an assessment of the trapped charge at an individual scale (Duller, 2008b; Smedley *et al*., 2019; Thomsen *et al*., 2007), allowing any variability in the residual (unbleached) dose to be identified (Stone and Bailey, 2012).

3.3.2. Laboratory preparation and measurement protocol

Light tight samples were collected by hammering 12 cm-long opaque black PVC tubes into sediment exposures. The tubes were sealed and wrapped in black plastic bags for transport from the field to the lab. All samples were prepared under subdued orange light (600 nm) in the Oxford Luminescence Dating laboratory (OLDLab). Light-exposed sediments from the ends of the tube were removed and used for dose rate calculation (Section 3.3.4), grain size analysis (Section 3.4.1), and compositional analysis (Section 3.4.4). The remaining unexposed sediment was processed using standard quartz preparation procedures to remove carbonate and organic material, to isolate the quartz fraction (2.62-2.72 g cm^{-3}) through density separation, and to remove the alpha irradiated surface using a hydrofluoric acid etch (see Section 4.2.2 in Chapter 4 for detail on this approach). Samples were sieved to either 90-125 µm or 180-210 µm based on their modal grain size distribution (Table 4.1 in Chapter 4) and multigrain discs were prepared for each sample. Single grain (SG) discs with 300 µm hole diameters were additionally prepared for 13 of these samples using the 180-210 µm grain size fraction (following Arnold *et al*., 2012). It was not possible to date all samples at this scale due to the finer grained nature of some samples (meaning there wasn't sufficient 180-210 µm fraction for dating), and a broken single grain machine meant that there was limited machine time.

Equivalent doses (D_es) were calculated using the single-aliquot regenerative-dose (SAR) protocol (Murray and Wintle, 2000; Wintle and Murray, 2006). This protocol uses a fixed test dose to correct for aliquot-specific changes in sensitivity during the measurement process and is now the most widely used protocol for equivalent dose estimation (Murray *et al*., 2021). OSL measurements were made using Risø TL/OSL luminescence readers and data was processed using Analyst v4.57 (Duller 2015) and the 'Luminescence' R package (Kreutzer *et al*., 2012; 2020). Observations on the natural signal (OSL counts) decay during the measurement time (1 s for MG and 0.05 s for SG) suggests that the signals are dominated by the fast component (Figure 3.7). Section 4.2.2 of Chapter 4 provides detail on the measurement conditions and rejection criteria used to accept D_es.

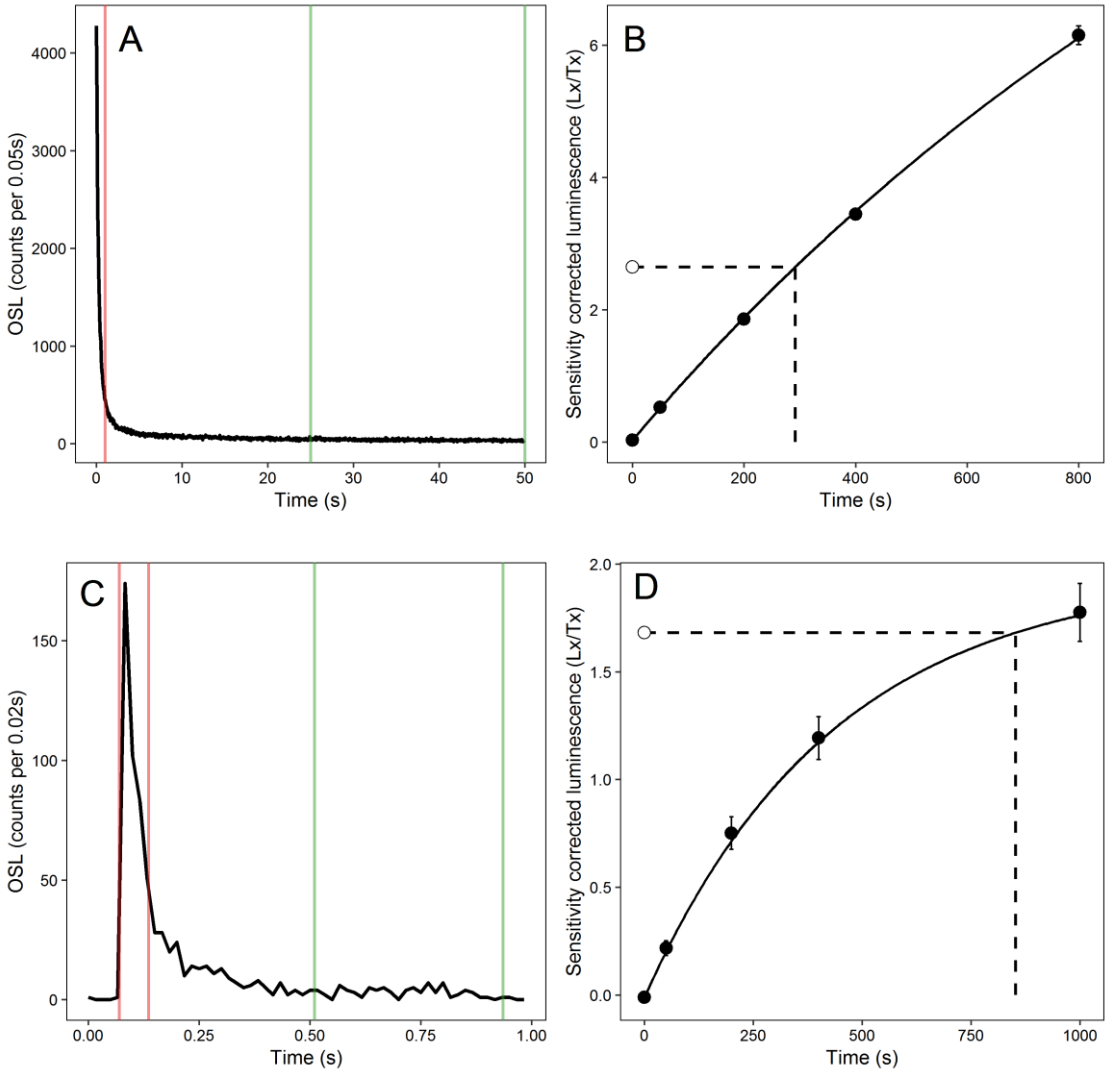

Figure 3.7. Examples of signals and dose response curves. **A)** Multigrain natural OSL signal from NAM18/2/10. **B)** Dose response curve fitted with an exponential function for signal in A, where Lx/Tx represents the OSL signal (Lx) normalised by the test dose (Tx). **C)** Single grain natural OSL signal from NAM18/1/12. **D)** Dose response curve for signal in C. D_es are calculated through subtraction of the mean background (25 s to 50 s (MG) or 0.5 s to 0.9 s (SG); green lines) from the main signal (1s (MG) or 0.05 s (SG); red lines).

3.3.3. Preheat and dose recovery tests

To test the applicability of the SAR protocol for dating Huab sediments, preheat plateau and dose recovery experiments were performed. These tests enable the selection of the optimal preheat temperature for analysis, ensure that thermal transfer is not observably problematic during the

measurement process, and assess the ability of the SAR cycle to recover a known dose (Murray, 1996; Murray *et al*., 2021; Rhodes, 2011; Roberts *et al*., 1999; Wintle and Murray, 2006). Preheat plateau tests were performed on 8 samples using 5 preheat temperatures ranging from 200˚C to 280˚C. These samples were chosen to span a range of depths from two of the main sections studied: NAM18/1 and NAM18/2. All samples recovered a dose well using a preheat of 200˚C for 10 s and a cut heat of 180˚C for 10 s (Figure 3.8, Appendix C Figure C2 for full dataset).

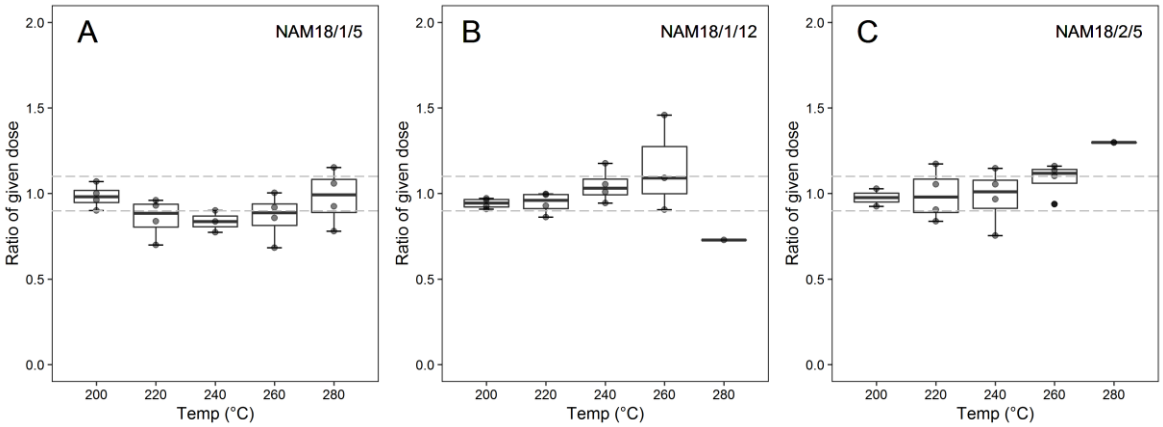

Figure 3.8. Examples of preheat plateau tests. Aliquots were bleached twice with blue LEDs for 100 s at 20˚C, followed by a 10,000 s pause to remove the trapped charge. Aliquots were irradiated with a known dose (chosen based on range finder ages for each sample to reflect natural conditions) and analysed following the SAR protocol using different preheats. Preheat temperatures were set to 200˚C, 220˚C, 240˚C, 260˚C, and 280˚C for 10 s, each with a cut heat of 180˚C for 10 s. Results here show accepted aliquots plotted as the ratio between given and recovered dose. **A)** NAM18/1/5 irradiated with 6.53 Gy; **B)** NAM18/1/12 irradiated with 20.85 Gy; **C)** NAM18/2/5 irradiated with 4.65 Gy.

The applicability of this preheat temperature to a wider set of samples was verified through recovery of a laboratory administered dose (dose recovery test) on a further 28 samples at the multigrain scale and 4 samples at the single grain scale. Results show that the SAR protocol was able to recover a given dose at a ratio of 0.97 ± 0.1 (MG) and 1.03 ± 0.1 (SG) of the given dose

respectively (Figure 3.9, Appendix C Table C2), so these preheat conditions were applied to all D_e measurements of Huab samples.

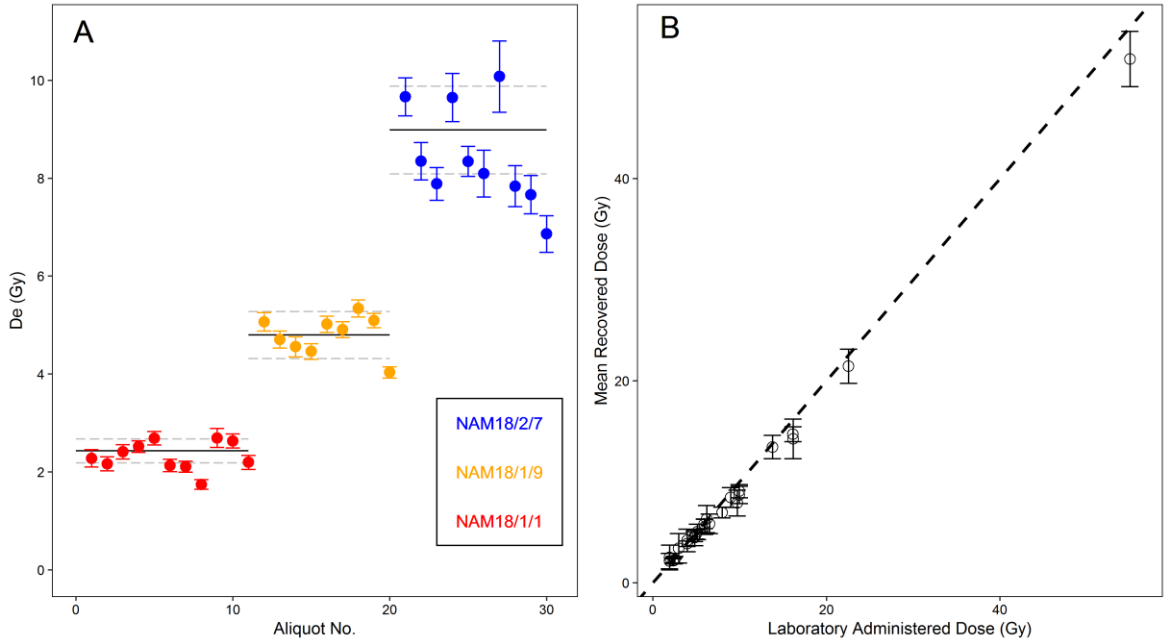

Figure 3.9. Dose recovery results using a preheat of 200˚C and cut heat of 180˚C. **A)** Recovered dose (Gy) for aliquots of multigrain samples NAM18/2/7, NAM18/1/9, and NAM18/1/1 (solid line represents the given dose, and the dotted lines represent 10 % away from unity). The administered dose was determined by initial range finder D_es to mimic natural conditions. **B)** Average recovered dose against laboratory administered dose for each multigrain sample. The dotted line indicates unity, where administered and recovered doses are equal.

3.3.4. Environmental dose rate

Using Equation 3.1, each luminescence age was calculated through division of the equivalent dose by the environmental dose rate. This dose rate represents the alpha, beta, gamma (from radioactive decay of radionuclides), and cosmic radiation (received from the sun) that is absorbed per unit of time by mineral grains in the sediment matrix (Duller, 2008a; Guérin, 2013).

3.3.4.1. Measurement

For all samples, the concentrations of Uranium (^{238}U), Thorium (^{232}Th), and Potassium (^{40}K) were measured through Inductively Coupled Plasma Mass Spectrometry (ICP-MS) analysis following silicate rock dissolution. Samples were prepared through digestion of ~25 mg of homogenised sample within a tri-acid digestion protocol. Samples were treated with concentrated HNO_3, HF, HCl, and diluted with 2 % HNO_3 and were analysed in a Perkin Elmer 2000B ICP-MS with an ESI prepFAST sample introduction system. Reference material (HISS-1; NRC-CNRC, Berman *et al*., 1997) and blanks were prepared and analysed alongside samples. Assessment of measurement variability (incorporating analytical errors, variability amongst digestion repeats and subsamples; Appendix C Table C3) show that uncertainties are within the scale recorded in inter-laboratory comparisons (Murray *et al*., 2015; Preusser and Kasper, 2001)

For 12 samples, the concentrations of radionuclides were also estimated using in-situ gamma spectroscopy in the field. Measurements were made using a hand-held Canberra digital NaI/LaBr Spectrometer (InSpector 1000™) for ~45 minutes at each site. Due to time constraints and limited battery life of the machine, a selection of representative samples were chosen across sites and depths. Calibration was conducted on the Oxford blocks (Rhodes and Schwenninger, 2007) and radionuclide concentrations were calculated from the magnitude of defined peaks in the gamma spectra (Appendix C Table C4). Comparison between the ICP-MS and gamma spectra show close correspondence between the two methods (Figure 3.10), indicating that disequilibria in the decay series of radionuclides is not an issue that needs to be considered in detail here (Preusser and Kasper, 2001). Uranium and Thorium concentrations are slightly lower in ICP-MS measurements, but the overall dose rates calculated from both ICP-MS and gamma spectroscopy are comparable. As ICP-MS data are available for all samples, these data are used for further dose rate calculation.

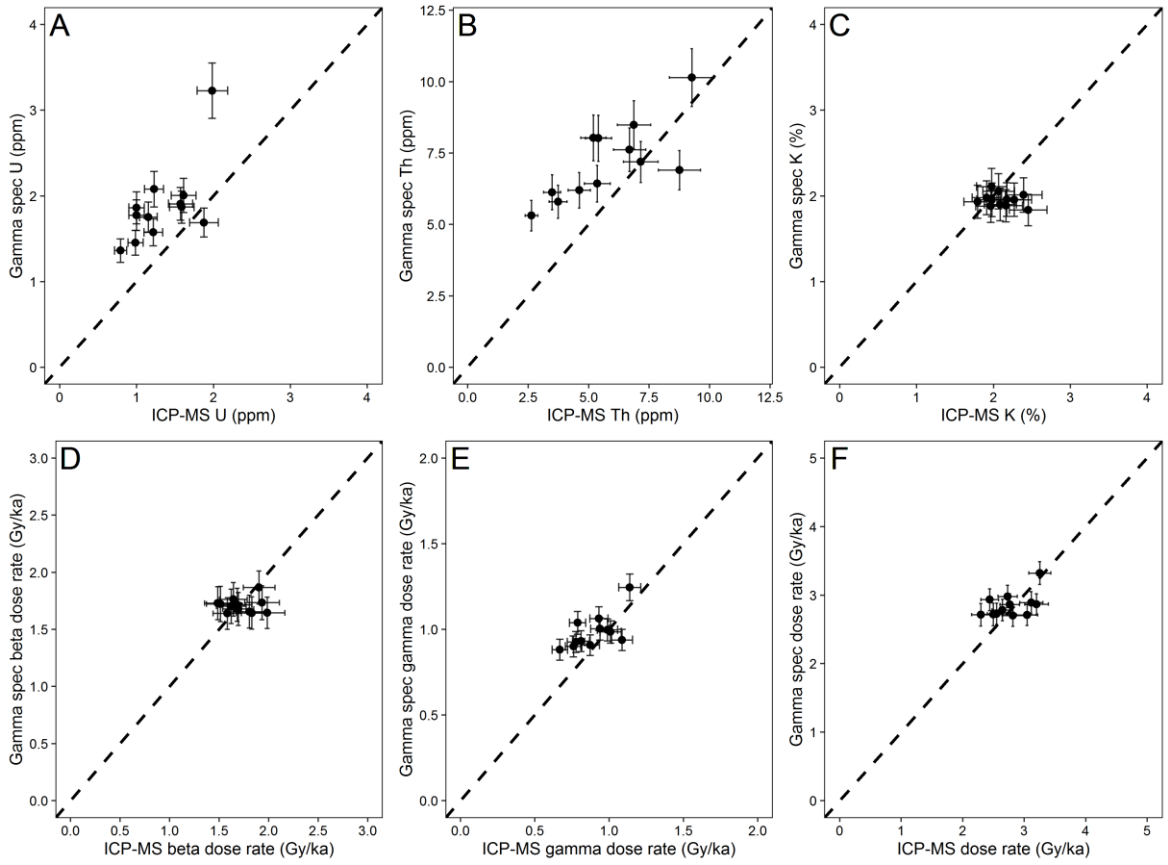

Figure 3.10. Comparison of the radionuclide concentrations and dose rates obtained through ICP-MS analysis and gamma spectroscopy. **A)** Uranium (^{238}U), **B)** Thorium (^{232}Th), and **C)** Potassium (^{40}K) concentrations. Dose rates (**D)** beta, **E)** gamma, **F)** total environmental dose rate) were calculated using U, Th, K values in DRAC (Durcan *et al.*, 2015), with a water content of 5 ± 2 %. The dotted line represents unity where ICP-MS and gamma spec results are equal.

3.3.4.2. Dose rate calculation

Radionuclide concentrations were converted to dose rates using the DRAC (v1.2) software (Dose Rate and Age Calculator for trapped charge dating; Durcan *et al*., 2015; Appendix C Figure C3). Dose rates were attenuated by water content (Aitken, 1985), grain size (Mejdahl, 1979), chemical etching (Bell, 1979), and beta attenuation (Guérin *et al*., 2011). Cosmic dose rates took into account location (longitude and latitude), altitude, and overburden depth and density. Based on the modern climate setting and estimates typically used in Namibian fluvial literature (e.g. Cloete *et al*., 2018; Srivastava *et al*., 2006; Thomas *et al*., 2017), a water content of 5 ± 2% was used for all samples. The contribution from alpha radiation to the dose rate was considered negligible as all quartz grains

were etched with HF to remove the alpha irradiated surface. Calculated environmental dose rates are presented in Table 4.1. in Chapter 4. The average contributions of each dose rate were 62.3 % beta, 31.9 % gamma, and 5.8 % cosmic. Variation in dose rate as a result of changes in overburden thickness are therefore presumed to be low, and additional detailed assessments of cosmic dose rates were not required.

3.3.5. Age estimation

The D_e distributions of the Huab samples were positively skewed (Figure 3.11), which could be indicative of partial bleaching. Given the potential challenges of bleaching of quartz grains through fluvial transport, the D_e distribution likely contains both bleached and unbleached components. For this reason, D_e determinations for age calculation were performed using the logged Minimum Age Model (MAM-3) of Galbraith *et al*. (1999). This also follows the protocol using in several other Namibian fluvial settings (e.g. Brook *et al*., 2006; Grodek *et al*., 2013; Srivastava *et al*., 2006). Within the age model calculation, dispersion results from the dose recovery tests (i.e. the amount of scatter intrinsic to sample measurement conditions) were used as the σ_b value where possible, or 0.15 (MG) or 0.2 (SG) where dose recovery data was not available (following Cunningham and Wallinga, 2012). Using DRAC (Durcan *et al*., 2015) environmental dose rates were combined with modelled equivalent doses to calculate final ages following Equation 3.1. Overdispersion values were calculated using the 'Luminescence' R package (Kreutzer *et al*., 2012; 2020).

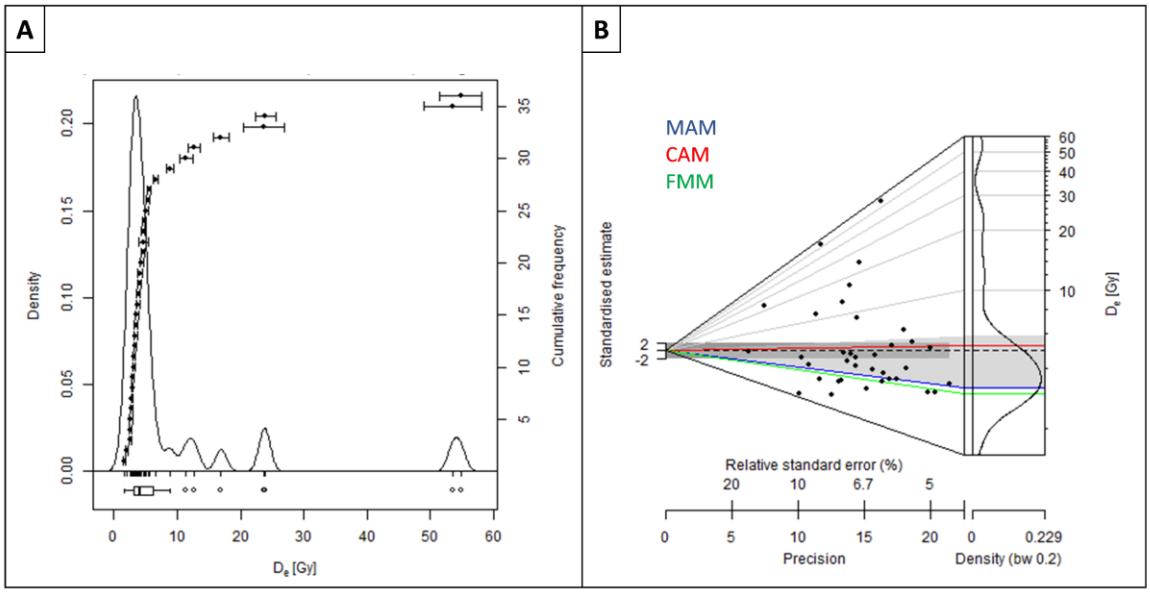

Figure 3.11. D_e distribution of sample NAM18/1/5. **A)** Kernel Density Estimate, **B)** Abanico plot with D_e estimate based on the Minimum Age Model (MAM; blue), the Central Age Model (CAM; red), and the Finite Mixture Model (FMM; green).

3.4. Sedimentological approaches

To reconstruct the nature of Huab River palaeoflow dynamics, a suite of sedimentological approaches were employed to characterise the character and composition of the valley fill sediments. This includes grain size and lithofacies analysis, initial characterisation of samples (XRD, geochemistry), and detailed compositional analysis of mineralogy (petrography and heavy minerals). In the southwestern African Quaternary fluvial literature so far, grain size and lithofacies analysis form key strands of evidence, but the use of compositional analysis to reconstruct hydrological regimes has been limited.

3.4.1. Grain size analysis

Grain size analysis is commonly used in geomorphological research to understand depositional processes (Kondolf and Piegay, 2016). In fluvial systems, the size of grains deposited can be influenced by the efficiency of particle sorting (Garzanti and Andò, 2019) and processes of sediment

transfer and storage within sedimentary systems (Allen, 2017, Caracciolo, *et al*., 2020). Grain size analysis was performed on 70 samples. These include samples analysed for OSL dating and samples collected from additional units to guide categorisation of units to specific lithofacies (Section 3.4.2). Samples were oven dried overnight and riffle split to obtain a representative fraction for analysis. Grain size measurements were performed using the wet dispersal method in the Malvern Mastersizer 2000MU with no pre-treatment (following Rowell, 2016). Statistics were calculated using Folk and Ward (1957) in Gradistat version 8.0 (Blott and Pye, 2001).

To statistically differentiate samples based on their grain size distributions, a cluster analysis was performed. Euclidean distance was used to create a dissimilarity matrix, and hierarchical clustering was undertaken through the Ward method following analysis to identify the optimal number of clusters (Appendix D Figure D1). To interrogate the potential drivers of change, such as the role of grain size distribution in driving variability in heavy mineral and petrographic datasets, canonical correspondence analyses (CCA) were performed in the 'vegan' R package (Oksanen *et al*., 2020).

3.4.2. Lithofacies analysis

Detailed sedimentological analyses were performed on four key stratigraphic sequences (NAM18/1, NAM18/2, NAM18/4, NAM18/7), to investigate the nature of sediment deposition in the Huab valley fill (e.g. Figure 3.12). Detailed interpretation of lithofacies was undertaken in collaboration with Domenico Ravidà at the GeoZentrum Nordbayern, Friedrich-Alexander-University, Erlangen-Nürnberg, using field sketches, detailed photography of features (Figure 3.12B, C) and grain size data. Individual lithofacies were identified based on grain size, bedding and associated sedimentary structures following the criteria of Miall (1985; 2006). Based on the distribution, facies were grouped into two main lithofacies associations: channelised associations (with associated floodplains) and unconfined stream associations. The characteristics of the lithofacies identified, the stratigraphic progression, and interpretation of palaeoenvironments are

discussed in detail in Chapter 4 (Table 4.2, Figures 4.5 and 4.6). This approach was possible given the nature of incision of the modern ephemeral channel deep into the valley fill.

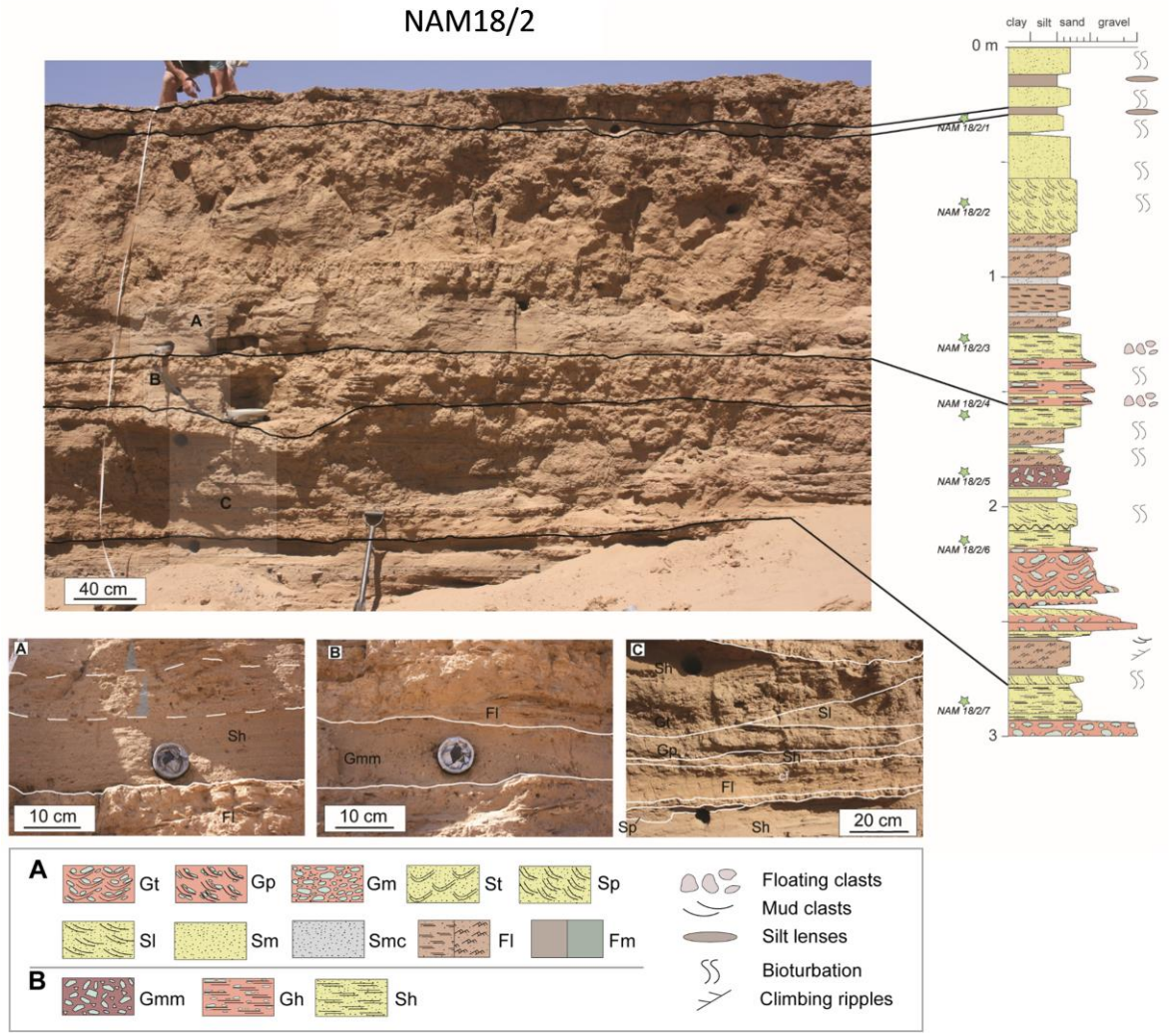

Figure 3.12. Stratigraphic log of individual lithofacies at site NAM18/2. Inserts **B)** and **C)** detail examples of the nature and distribution of lithofacies. See Appendix C Figure C4 to C7 for all stratigraphic sections.

3.4.3. Initial characterisation of samples: XRD, Geochemistry, LOI

Bulk sample methods were used to assess a subset of samples to give an indication of the minerals present. These methods helped guide further detailed investigation using heavy mineral and petrographic analysis (Section 3.4.4).

3.4.3.1. XRD

Six samples were analysed using X-ray Diffraction (XRD). XRD is a semi-quantitative method that identifies the phase of crystalline minerals through irradiation with X-rays (Pryor and Hester, 1969). XRD was performed on the bulk and clay fractions at the Department of Earth Sciences, University of Oxford. Samples were chosen from the top, middle, and bottom of two sections (NAM18/1 and NAM18/2) to detail variability in mineral composition amongst deposits of different ages. Results show that the samples comprise >50 % quartz and feldspar (K feldspar and plagioclase), ~6 % pyroxene and amphibole, and up to 40 % clay (of which samples comprise mostly muscovite and chlorite) (Figure 3.13., Appendix C Table C5). The XRD results show differences between samples and justify further detailed investigation into the mineralogy. XRD provides data on individual minerals present but does not enable an assessment of how these minerals occur in sand grains as rock fragments. This detail is important for assessing source regions and the distribution of minerals amongst mono- and poly-mineralic fragments. At this resolution, it is also possible to identify the presence of heavy minerals (e.g. amphibole and pyroxene), yet the relative abundance of other heavy minerals of lower concentration within this fraction is not possible to discern.

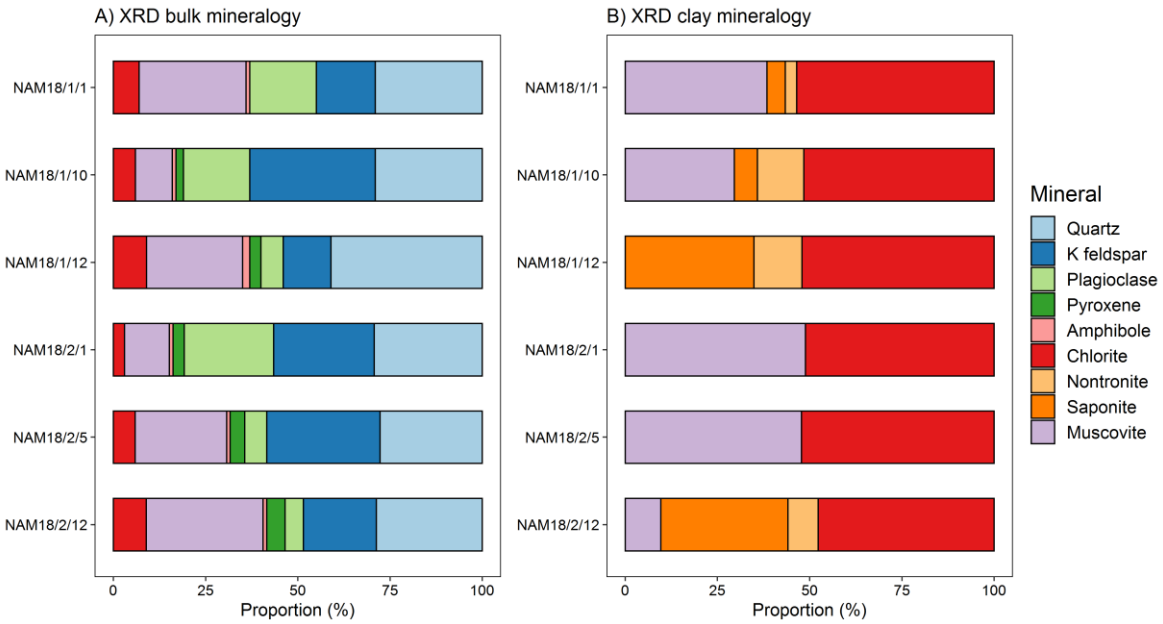

Figure 3.13. Results of XRD analysis of six key samples. **A)** bulk mineralogy, **B)** clay mineralogy.

3.4.3.2. Geochemistry

To characterise the elemental composition of Huab valley fill sediments in the context of potential source regions, geochemical analysis was undertaken using ICP-MS. 14 samples from the valley fill were analysed alongside 17 samples collected from sites across the catchment in a previous study of the Huab Basin (Dansie *et al*., 2018; Figure 3.14). This new analysis of catchment samples aimed to test whether bulk sample geochemistry of surface samples reflects the underlying geology, and therefore to characterise the geochemical signature of source regions. Samples were prepared within a tri-acid digestion protocol (HNO_3-HCl-HF). Calibration, analysis of reference material and blanks in the Perkin Elmer 2000B followed the protocol used for analysis of radionuclide concentrations for luminescence dating (Section 3.3.4). Here, a suite of 9 major and 18 trace elements were analysed.

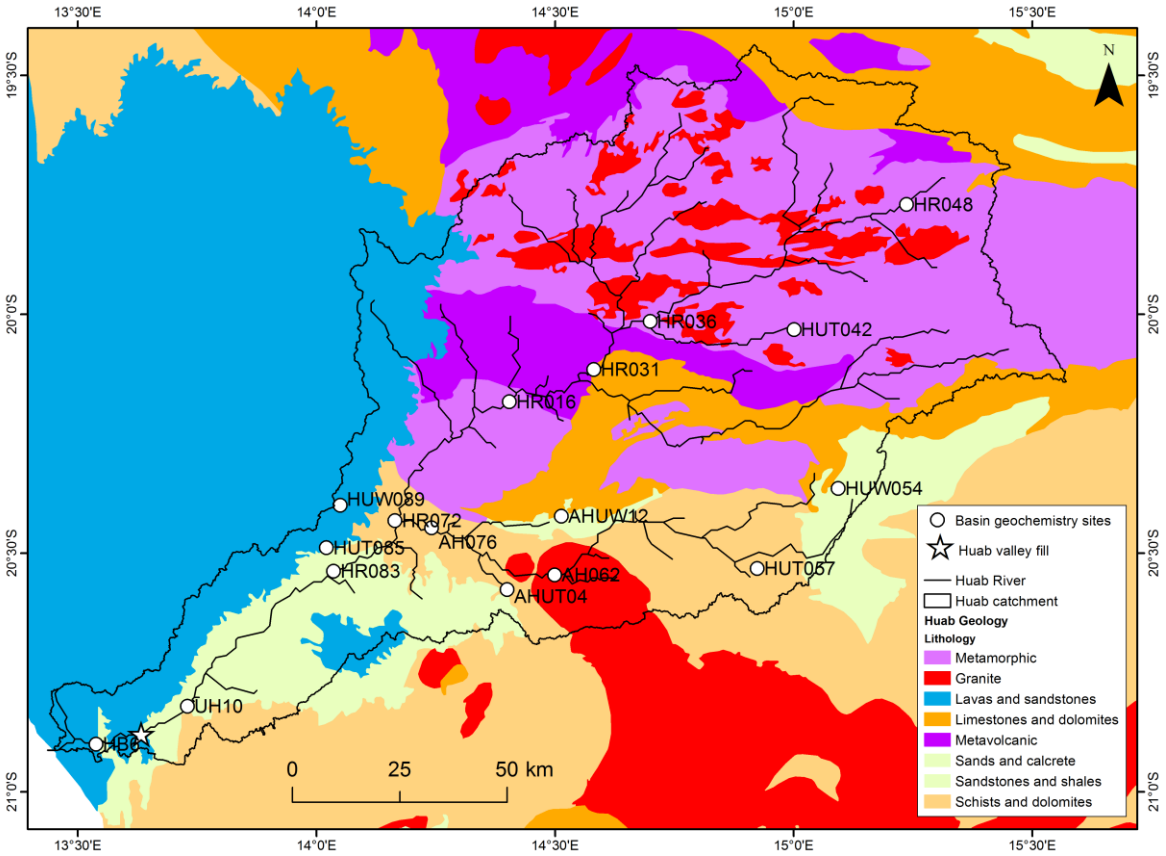

Figure 3.14. Location of samples collected from the Huab River catchment (Dansie *et al*., 2018) for geochemical analysis in the context of the underlying geology. The location of the Huab valley fill is demarcated with a star.

The relationship between geochemistry of surface samples and the geology of the underlying units is statistically significant (CCA, p <0.001, Figure 3.15). Samples sourced from the Etendeka Plateau are rich in Ti and rare earth elements. These elements are commonly associated with pyroxene and plagioclase found in basalts, the main constituent of the Etendeka large igneous province (Ewart *et al*., 2004; Garzanti *et al.*, 2021; Marsh *et al*., 2001). Samples sourced from Dolomites here, on the other hand are rich in Mg and Ca, and the samples overlying metavolcanic and granite units are particularly rich in Th. When the Huab valley fill samples are incorporated into this analysis, we see a mixed signal, indicative of sourcing from all major groups (Figure 3.15). Variability within the valley fill signatures show that further assessment of the mineralogy is important.

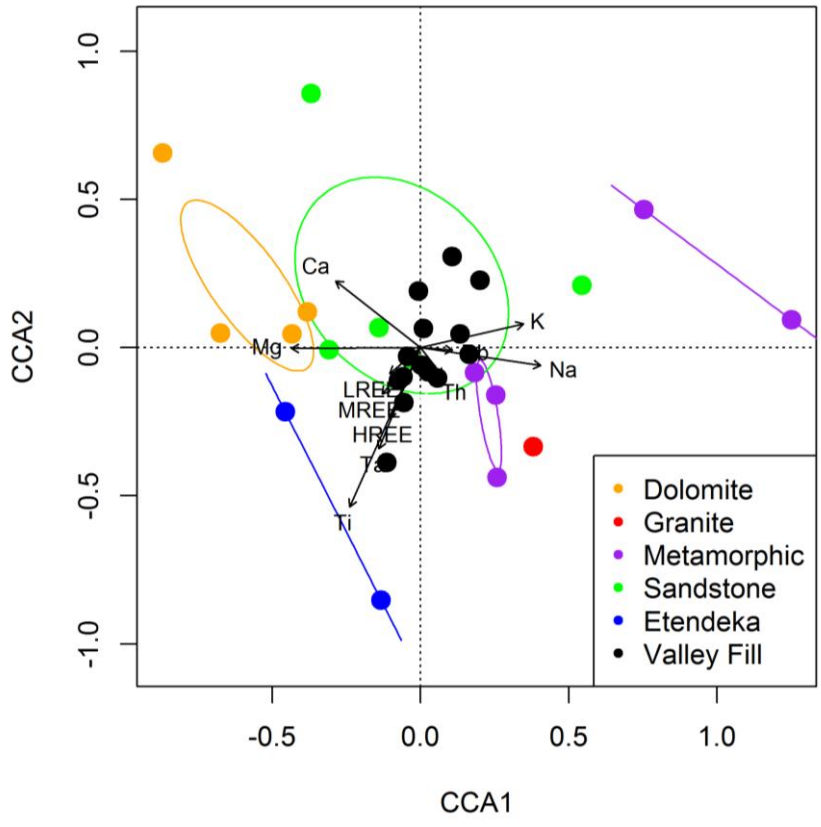

Figure 3.15. Geochemistry biplot of valley fill (black) and catchment (coloured) samples to interrogate the relationship between geochemistry and geology. Biplots enable a consideration of multivariate observations (points) and variables (rays) (Gabriel, 1971). The length of the ray is proportional to variability of the species, and the angle between rays details correlation between different species: 0˚, 90˚ and 180˚ correspond to correlation, no correlation and inverse correlation

respectively. Catchment samples are coloured by the underlying geology at sample collection site. Coloured circles indicate the spread of data by geological unit. The geochemistry dataset used here includes elements indicative of source rock composition (following Craigie, 2018). Rare earth elements were grouped into: light (LREE, e.g. La, Ce, Pr, Nd), mid (MREE, e.g. Sm, Eu, Gd), and heavy (HREE, e.g. Tb, Dy, Ho, Er, Tm, Yb, Lu, Y). Elements such as Be, W, Tl, Sn are excluded as they have very low concentrations here and uncertain affinities (Craigie, 2018). CCA shows that the underlying geology is statistically significant in explaining the variability recorded in the geochemistry ($p < 0.001$).

3.4.3.3. Loss-on-ignition

Water, organic, and carbonate contents were estimated through sequential loss on ignition at 105˚C, 550˚C and 950˚C (LOI; Heiri *et al*., 2001). Samples were heated to these temperatures for 12, 4, and 2 hours respectively. Loss on ignition is an established method for characterising sediments (Bengtsson and Enell, 1986; Dean, 1974). The results of loss on ignition analysis are presented in Appendix C Table C6.

3.4.4. Compositional analysis: heavy minerals and petrography

Following initial characterisation of the sediment, Raman laser spectroscopy was used to quantify the mineralogy of the Huab samples in greater detail. Petrographic and heavy mineral (grains with density >2.9 g cm^{-3}) assemblages in sedimentary deposits can provide important information on source regions, transport processes, and depositional regimes (Caracciolo, 2020; Garzanti and Andò, 2019; Resentini *et al*., 2017). Source lithology types shed distinctive assemblages and evidence can be preserved in the abundance of rock and lithic fragments, and the type and concentration of heavy minerals. Hydraulic sorting processes can also significantly alter the relative abundance of specific heavy minerals (Garzanti and Andò, 2019; Komar and Wang, 1984; Malusà *et al*., 2013, 2016; Rubey, 1933). Processes of selective entrainment and preferential deposition of specific types and sizes of grains can provide important palaeoenvironmental information on the nature of river flow (Garzanti and Andò, 2019).

In southern Africa, compositional analysis has been widely used to trace sand transport from the Orange River to Angola (Garzanti *et al*., 2012; 2014; 2018), and into the Kalahari Basin (Garzanti *et al*., 2022), yet heavy mineral and petrographic datasets have not yet played a major part in the literature on interpretation of hydrological regimes on Quaternary timescales. This section discusses the use of Raman laser spectroscopy and optical microscopy for mineral identification and provides an overview of the approach applied to heavy mineral and petrographic analyses. Further detail of the preparation of samples, measurement parameters, and interpretation of petrographic and heavy mineral assemblages is provided in Chapter 4.

3.4.4.1. Raman laser spectroscopy

Mineral identification was undertaken using Raman laser spectroscopy (following Ando and Garzanti, 2014; Andò, 2020), and optical microscopy for manual identification of rock fragments (see Section 3.4.4.4). Raman spectroscopy is a light-scattering method used to study the properties of materials (Frezzotti *et al*., 2012). When focused on a polished thin section slide, the laser can be centred on a mineral of interest and the back-scattered spectra recorded. Spectra are diagnostic of the composition of each mineral, and so the position of peaks in the spectra can be compared to a reference database of spectra (Ando and Garzanti, 2014). Mineral identification was undertaken using the TrueMatch software (WITec) using the RRUFF dataset (www.rruff.info), and manual verification. Raman analysis was performed at the GeoZentrum Nordbayern of the Friedrich Alexander Universitat Erlangen-Nürnberg (Germany) using a Raman WITech Alpha 300R system (see Section 4.2.4 of Chapter 4 for measurement parameters).

Identification of minerals within heavy mineral slides and thin sections for petrography is conventionally undertaken solely through optical microscopy. Raman spectroscopy, however, is increasingly being used in heavy mineral analyses as it has brought several advantages (Ando and Garzanti, 2014). First, it is a faster and more efficient tool for analysis (Lünsdorf *et al*., 2019) and

has increased the potential to analyse a larger number of grains per sample. Optical heavy mineral analyses typically analyse ~200 grains (e.g. Garzanti *et al*., 2018), yet here, we were able to analyse ~1500 grains per sample and increase the potential to pick up very uncommon minerals. Second, Raman provides data on mineral chemistry, enabling greater confidence in mineral identification and allowing for greater detail in distinguishing between mineral species (e.g. between pyroxene polymorphs of diopside and augite, and between K feldspar and plagioclase). The variety of minerals that can be confidently identified has also increased, particularly in relation to opaque and turbid grains that cannot be differentiated using an optical polarising microscope. And third, Raman enables the analysis of smaller grains than is possible using optical microscopy. Here, a grain size range to as low as 30 µm was used. Whilst the applicability has been noticed predominantly in heavy mineral research (e.g. Lünsdorf *et al*., 2019), similar opportunities for increased speed and skill in analysis are possible for the study of thin sections for point count petrographic analysis.

3.4.4.3. Heavy minerals

19 samples were selected for heavy mineral (HM) and petrographic (PT) analysis. These samples span key stratigraphic units across sites NAM18/1, NAM18/2, and NAM18/7, and samples were chosen to represent a range of ages (following Section 3.3) and depositional contexts (following Section 3.4.2). HM fractions were isolated through density separation (>2.90 g cm^{-3}) following removal of organic and carbonate material (following Andò, 2020). The HM fraction was obtained for three grain sizes (32-63 µm, 63-125 µm and 125-250 µm) and grains were mounted to slides and polished for analysis (see Section 4.2.4 in Chapter 4 for detail on this approach). Separation by grain size improved the production of polished thin sections and enabled a wider assessment of the HM assemblage through removal of bias of a limited grain size window. Raman spectra were obtained from ~500 signals per grain size of each sample and mineral identification was undertaken for each of these spectra (e.g. Figure 3.16).

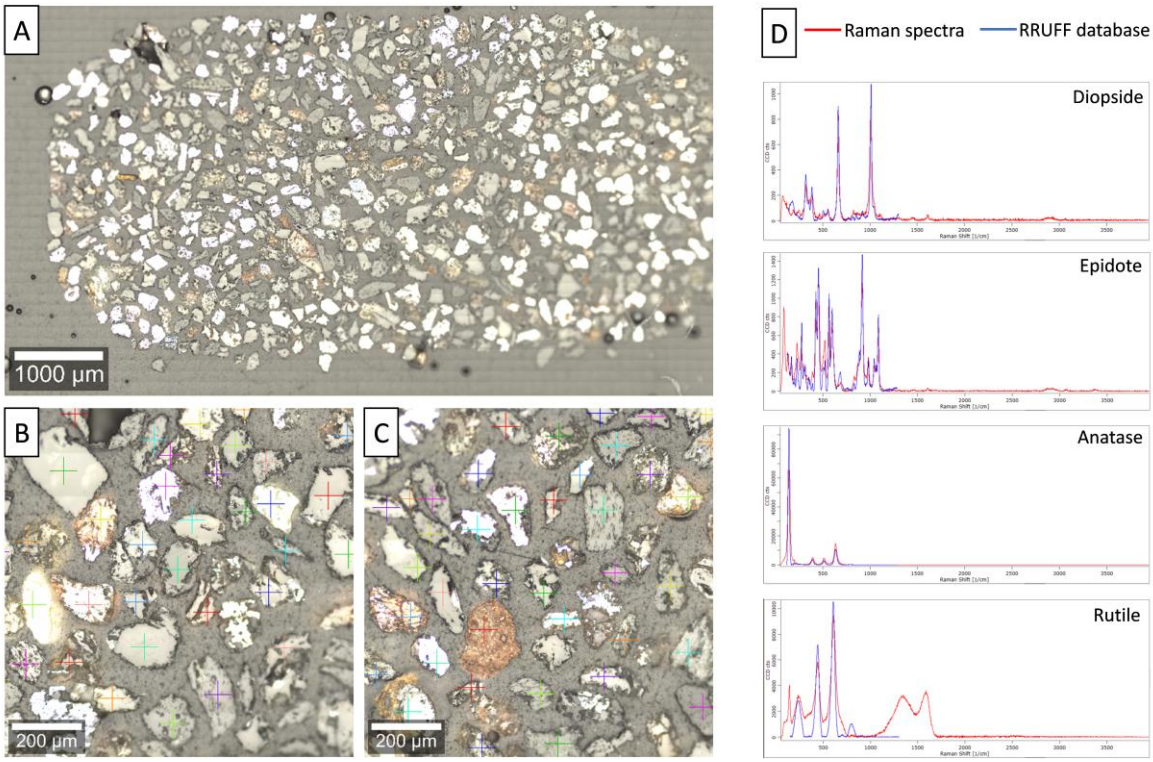

Figure 3.16. A) Polished slide for HM analysis. **B)** and **C)** inserts of the polished slide, crosses indicate the Raman laser position. **D)** Examples of distinctive spectra obtained from HM slides. Each mineral has a characteristic Raman spectra, so mineral identification was undertaken using the TrueMatch software and manual classification.

3.4.4.4. Petrography

For petrographic analysis, bulk samples were sieved to >63 µm as it is not possible to determine the textural parameters in grains below this size. Samples were impregnated with epoxy resin and prepared as standard polished thin sections by MiĘKiNiA Lab in Poland. Thin sections were digitised for semi-automated analysis (following Lünsdorf *et al.*, 2019). This included the production of a high-resolution scan (x 50) of each slide and creation of a grid to extract coordinates of grains to be identified (Figure 3.17). These coordinates were used to determine the laser position for Raman analysis. The PT composition of each sample was determined through 300 points at a regular 1 mm spacing following the Gazzi-Dickinson method (Ingersoll *et al.*, 1984; Zuffa, 1985) (Raman spectra examples in Appendix C Figure C8).

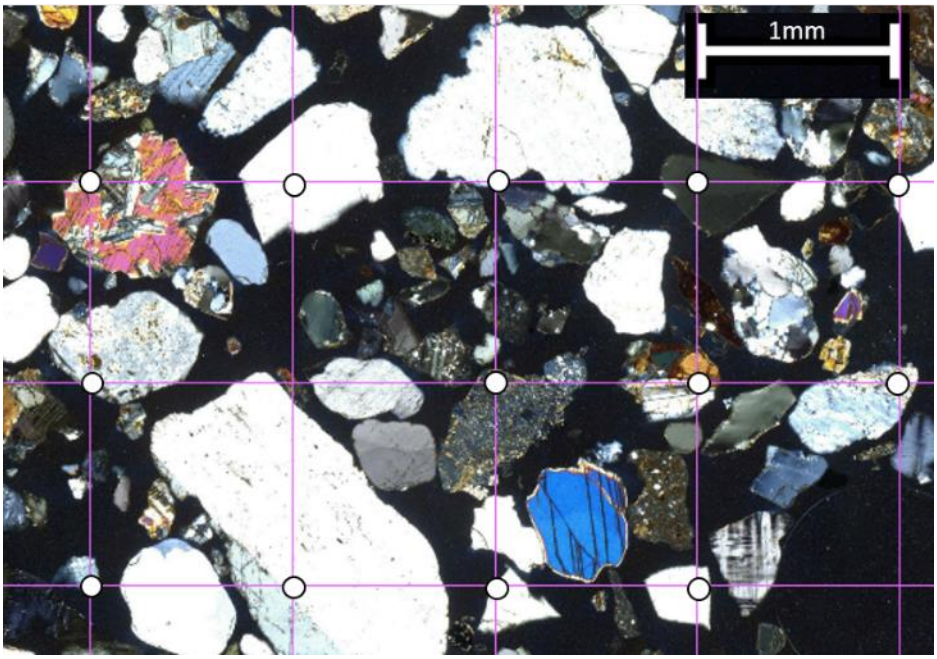

Figure 3.17. Digital scan of thin section of NAM18/1/12 with a 1 mm grid to guide Raman laser position and locate grains for optical microscopic assessment.

The coordinate system established on petrographic slides (e.g. Figure 3.17) was also used to locate grains for optical microscope assessment. In comparison to HM analysis where mineral identification was solely undertaken through Raman analysis, Raman spectra only provided an identification of the individual mineral that the laser is focused on and identification of polycrystalline grains (lithic or rock fragments) for petrographic assessments requires optical microscopy. Optical microscope assessments were undertaken at 20 x magnification in plane-polarised and cross-polarised light (see examples in Appendix C Figures C9 to C12). Section 4.2.4 in Chapter 4 provides further detail on the point count approach and framework for classification of polymineralic grains.

PART 2: Fluvial database

3.5. Construction of a chronological fluvial database

To address the second objective of this thesis, Chapter 5 (Paper 2) aims to produce a chronological database of Quaternary fluvial records from southern Africa's western dryland regions (Figure 2.1) and to use this database to reconstruct the nature of documented hydrological change during the late Quaternary. Analysis of this database then sets out to: i) classify the typologies of rivers studied; ii) investigate the role of catchment and site characteristics on the preserved fluvial record; iii) assess the proxies and approaches used. To be rigorous and systematic, this database has a clear selection criteria for inclusion of records (Section 3.5.1), a defined structure for reporting of metadata and standardisation of chronological data (Section 3.5.2), and records were filtered based on chronological data quality and the availability of supporting independent proxies for interpretation (Section 3.5.3). The database process and protocols used to select and analyse the data are explained in further detail in Chapter 5 and Appendix E, and the database is provided in Appendix F.

3.5.1. Selection criteria

A set of selection criteria were established to reduce ambiguity in determining inclusion and exclusion of records. To be included in this database, source publications had to be peer reviewed and had to present chronological data associated with fluvial processes from sites (with data available on longitude and latitude) within the region south of 17˚S and west of 26˚E (Figure 2.1; Figure 5.1). These criteria ensured quality of research (where findings could be directly related to original publications) and specified the inclusion of site-specific Quaternary archives that could be compiled to interrogate the regional fluvial record. 603 ages from 44 publications met the criteria

for inclusion in this database. The full list of sites in this database is available in Appendix E Table E1 (Supplementary Material for Paper 2).

3.5.2. Database structure

To achieve the aims of this analysis, a framework for data entry was determined to report data on the setting and geomorphological contexts of archives, the chronologies established, and the interpretations reached (Figure 3.18). The level of detail required for reporting of metadata followed considerations made in other databases (e.g. De Cort *et al*., 2021; Lancaster *et al*., 2016) and the crowd-sourced reporting standards presented by Khider *et al*. (2019). Criteria were established for reporting of sedimentary context (Table 5.1) and fluvial interpretation (Table 5.2). For more detail on the specific data reported within each category in this database, see the Supplementary Material for Paper 2 in Appendix E. The database is provided electronically as Appendix F.

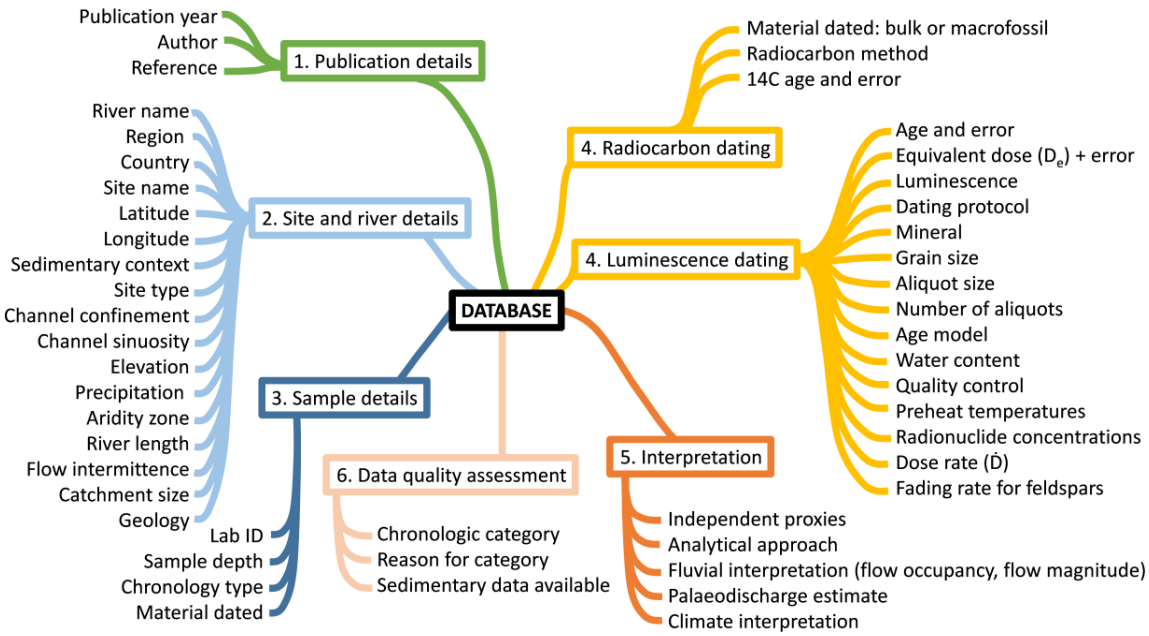

Figure 3.18. Content of the chronological fluvial database. The structure of this database follows reporting standards from Khider *et al*. (2019) (PaCTS 1.0: A Crowdsourced Reporting Standard for Paleoclimate Data). The database contains information on **1)** publication details, **2)** site and river

details, **3)** sample details, **4)** chronologies, including luminescence and radiocarbon specific reporting, **5)** interpretation, and **6)** data quality assessment.

Geochronological control of the timing of fluvial deposition within southwestern Africa is predominantly established through luminescence and radiocarbon dating methods. Chronologies are available from uranium-thorium (Selby *et al*., 1979), palaeomagnetism (e.g. Brink *et al*., 2012), and cosmogenic nuclide burial dating (e.g. Erlanger *et al*., 2012; Gibbon *et al*., 2009; Matmon *et al*., 2015), yet publications using these approaches are scarce or typically correspond to processes pre-dating the late Quaternary. For this reason, the database focuses on luminescence and radiocarbon chronologies and the data quality assessment is based on these methods. To make comparisons between datasets, consistency in reporting of chronologies and standardisation (i.e. calibration) of radiocarbon ages was important (Small *et al*., 2017). Publications within this database span ~40 years, and the calibration curves used to calculate calendar years from radiocarbon ^{14}C ages have been updated regularly throughout this period (e.g. SHCal02, Nash *et al*., 2006; INTCal09, Hurkamp *et al*., 2011; SHCal20, Völkel *et al*., 2021). To account for this, all radiocarbon ages in this database were recalibrated using SHCal20 (Hogg et al., 2020) and Bomb13SH12 (Hogg *et al*., 2020; Hua *et al*., 2013) in OxCal v 4.4.4. (Bronk Ramsey, 2021) (e.g. Appendix C Figure C13).

To interrogate the topographic and climate context of fluvial palaeoenvironmental sites and catchments, data were obtained from a suite of datasets for analysis (Table 3.2, Figure 3.19). By combining site and catchment data with chronologies and detail on the type of deposit and approaches used (Figure 3.18), this analysis aimed to interrogate the complexities and controls on fluvial archive formation and preservation.

Table 3.2. Sources of data added to the database. Analysis of channel reach sinuosity was performed in Google Earth. Analysis of mean flow intermittence, catchment size, and river length were performed in ArcGIS. See Figure 3.2 for examples of calculation in ArcGIS.

Parameter	Dataset and source
Contemporary precipitation (mm $year^{-1}$)	WoldClim 2.0 (Fick and Hijmans, 2017)
Aridity index (AI)	Global Aridity Index and Potential Evapotranspiration Climate Database v3 (Trabucco and Zomer 2022)
Channel sinuosity	Distance measured between two points along a stream divided by the straight distance between two points. Classification of river reaches as straight, sinuous, meandering
Channel confinement	Classification following Fryirs *et al.* (2016): confined, partly confined, unconfined
Probability of flow intermittence (probability that a river will cease to flow for at least one day a year)	Dataset on global prevalence of non-perennial rivers and streams (Messager et al., 2021)
Elevation (m): at sites and elevation change across catchments. Relief calculated as difference between highest and lowest point in the catchment	30 m ALOS Global Digital Surface Model; AW3D30 (JAXA, 2021)
Catchment size (km^2)	HydroSHEDS (Lehner and Grill, 2013)
River length (km): main channel length and combined total length of channels in the catchment	HydroSHEDS (Lehner and Grill, 2013)
Drainage density (km km^{-2}): length of total channels in catchment by the catchment size	HydroSHEDS (Lehner and Grill, 2013)
Gradient (km m^{-1}): elevation change from start to end of channel divided by the length of main channel	HydroSHEDS (Lehner and Grill, 2013), 30m ALOS Global Digital Surface Model (JAXA, 2021)
Geology	Geological map from Garzanti *et al.* (2022)

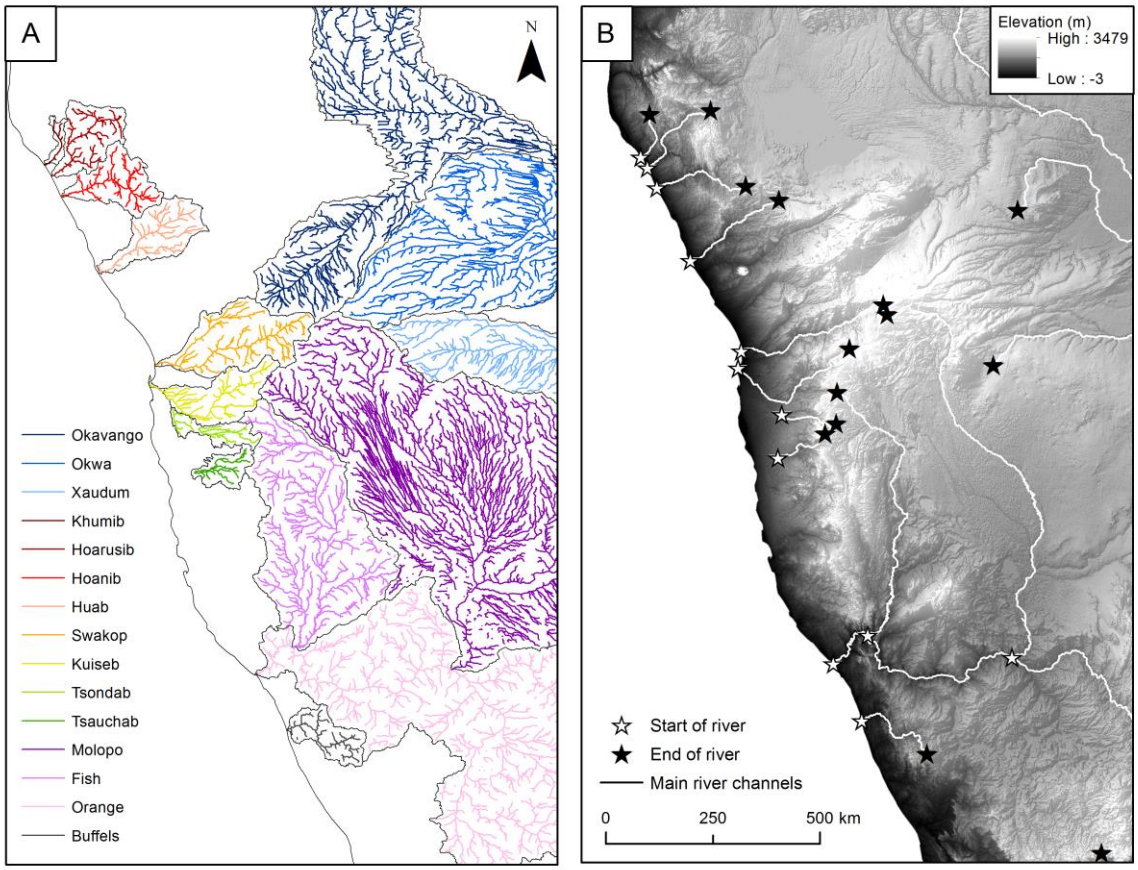

Figure 3.19. Examples of river catchment analysis performed in ArcGIS on rivers that contain sites in the database. **A)** Calculation of total channel length (km) and catchment size drawn from the global river network HydroSHEDS dataset (Lehner and Grill, 2013). **B)** Calculation of channel gradient using river channel data from HydroSHEDS and elevation data from ALOS AW3D30 (JAXA, 2021). Strahler stream order data was used to isolate the main channel. Elevation values were calculated for the start (black stars) and end points (white stars) of each river and divided by the length of the main channel.

3.5.3. Data quality assessment

Accurate reconstruction of palaeoenvironmental change from sedimentary archives is dependent on both the quality of the chronology and the independent proxies used to reach palaeoenvironmental interpretations. Through assessment of uncertainties associated with record production and chronologies, it is possible to make judgments on whether anomalies and data conflicts are related to dating error, or if they detail real palaeoenvironmental heterogeneity. Selection of quality-assured datasets here follows approaches used in other Quaternary research

settings, both in and beyond drylands, to obtain a subset of the most robust ages (Small *et al*., 2017; Woor *et al*., 2022).

To filter based on the availability of supporting information for palaeoenvironmental interpretation, a distinction was made between records that are accompanied by independent proxies alongside chronology and those that are not. Examples of these approaches include stratigraphic context and sedimentology (e.g. Srivastava *et al*., 2005), and the interpretation of geochemical parameters for direct interpretation of prevailing climate conditions (Lyons *et al*., 2014). Where only a chronology was presented, such as in several early investigations of Namibian deposits (e.g. Vogel, 1989; Vogel and Visser, 1981), we deemed information solely on the location and age of deposit to not be enough to have confidence in the interpretations reached. For the assessment of chronological data quality, there are several established uncertainties that need to be taken into account (e.g. discussed in Small *et al*., 2017), so the filtering required a more detailed set of criteria. Here, each age was classified from Category 1 (most robust ages with the highest data reporting) to Category 3 (least robust ages with the lowest data reporting). Chronological data quality criteria are discussed in Table 3.3, and the use of these criteria to classify ages into categories is detailed in Table 5.3 in Chapter 5.

Table 3.3. Criteria used for assessment of chronological data quality. These criteria draw on established uncertainties in luminescence and radiocarbon dating and are based on aspects of established filtering protocols of Small *et al*. (2017) and Lancaster *et al*. (2016).

	Criteria	**Justification**
All ages	Documentation of stratigraphic context	Stratigraphic relationships between ages cannot be assessed without reporting of sample depth.
	Stratigraphic consistency of ages from a site	Multiple corroborating geochronological methods at the same depth or stratigraphic consistency between ages at a site detail the potential for ages to give a robust assessment of the timing of deposition.

Luminescence ages	Reporting of results (e.g. D_e, $\dot{D}$), protocols (e.g. age model), and corrections (e.g. water content)	D_e and $\dot{D}$ are required for recalculation of luminescence ages. Dose rates can be variable in geomorphological environments (Nathan *et al*., 2003), so dose rates should be calculated for each sample. The choice of protocols such as age model and grain size dated can influence the age obtained (Arnold *et al*., 2009; Timar-Gabor *et al*., 2017), so must be reported.
	Use of a sensitivity normalised dating protocol (e.g. SAR; Murray and Wintle, 2000)	The single-aliquot regenerative dose protocol (SAR) makes it possible to assess sensitivity change, measure a large number of D_es per sample, and produce ages that are more precise (Duller, 2004; Hilgers *et al*., 2001; Jain *et al*., 2003; Wintle and Murray, 2006) than previous methods such as the multiple aliquot additive dose (MAAD).
	Reporting of quality control analysis (e.g. dose recovery)	Dose recovery experiments test the applicability of SAR, assessing the ability of the SAR cycle to recover a known dose and ensuring that thermal transfer is not observably problematic during the measurement process (Murray *et al*., 2021; Rhodes, 2011).
	Use of small aliquots or single grain scale of analysis if partial bleaching is identified	A key challenge in dating fluvial deposits is the potential for partial bleaching (Olley *et al*., 2004), particularly in dryland regions where suspended sediment load can be high (Jacobson *et al*., 1995). Single grain measurements enable the bleached component of the signal to be isolated (Duller, 2008b).
	Assessment of anomalous fading if dating feldspars	Luminescence signals in feldspars fade anomalously (Lamothe and Auclair, 1999; Wintle, 1973). The post-IR IRSL protocol helps to minimise this fading (Thomsen *et al*., 2008), but assessments of the fading rate are still required (Roberts, 2012).
Radiocarbon ages	Reporting of radiocarbon results (e.g. ^{14}C age and error) and protocols (e.g. material dated)	Reporting of the ^{14}C age and the associated error is required for recalibration of radiocarbon ages. Reporting of material dated is required for classification based on use of bulk or micro/macrofossils.
	Differentiation between ages obtained from bulk samples and macro/microfossil samples	Bulk samples commonly comprise organic or calcareous sediment and have a greater chance of combining multiple depositional events through incorporation of organisms or formation of a unit over a period of time, and can contain dissolved land-derived 'old carbon' (Strunk *et al*., 2020). Age estimates from macrofossils, in contrast, are commonly obtained from shell or wood. Analysis of individual organisms increases the potential of capturing discrete timings of death and individual depositional events (Rey *et al*., 2019; Strunk *et al*., 2020).
	Assessment of the potential for reservoir effects and contamination	If unaccounted for, hard water effects can result in the production of anomalously old ages (Deevey *et al*., 1954). Contamination with modern carbon or re-deposition of fossil wood has the potential to produce anomalously young or old ages.

PART 3: Palaeoclimate model-data comparison

3.6. Palaeoclimate model-data comparison

To address the third objective of this thesis, Chapter 6 (Paper 3) analyses the palaeoclimate implications of the regional quality-assessed fluvial record (Paper 2), including the new record from the Huab River (Paper 1), and a compilation of palaeoclimate and palaeoenvironmental records from southwestern Africa. To do this, empirical palaeoclimate and palaeoenvironmental archive data was compared to palaeoclimate modelling simulations from the third generation of the Palaeoclimate Modelling Intercomparison Project (PMIP) and findings were discussed in the context of prevailing hypotheses of precipitation changes (discussed in further detail in Chapter 6). This analysis focuses on the central southwestern region (Figure 2.1) defined in Chapter 6 as the land mass 10˚ and 21˚E, and between 17˚ and 30˚S (Figure 6.1). This region was chosen following the discussion in Chapter 2 of the debate on the nature of palaeoclimate change in the western portion of southern Africa, and the availability of quality assessed geomorphological archives that offer an opportunity to assess the spatial extent of change.

3.6.1. Palaeoclimate model data

As part of the Coupled Model Intercomparison Project (CMIP), model simulations have been run at timesteps during the Quaternary. The Palaeoclimate Modelling Intercomparison Project (PMIP) was developed to collate model simulations run under defined boundary conditions. This standardised protocol facilitates direct comparison of model results (Harrison *et al*., 2015; Taylor *et al*., 2012). Analysis in Chapter 6 focuses on two timesteps of PMIP simulations: the mid Holocene

(MH; 6ka) and the Last Glacial Maximum (LGM; 21 ka). The LGM and MH present end-members of modelled conditions to assess how models deal with forcing factors (Table 3.4). The MH simulation assesses the influence of changes in insolation forcing and atmospheric greenhouse gasses appropriate to 6 ka. This particularly tests the response to the seasonal distribution of heating between the hemispheres. The LGM simulation tests the influence of atmospheric greenhouse gas concentrations, sea level, and ice sheets appropriate to 21 ka, with a similar orbital configuration to present (Abe-Ouchi *et al*., 2015). Simulations are also run under pre-industrial conditions (PI) to provide a baseline for comparison. These modelled snapshots are important both in terms of the debate that exists on southern Africa's response to climate drivers (see Section 6.1.1.2 in Chapter 6) and the availability of palaeoproxy records to test the underlying mechanisms and prevailing hypotheses of past climates.

Table 3.4. Orbital and trace gas parameters used for the simulation of pre-industrial (PI), mid Holocene (MH; 6 ka), and Last Glacial Maximum (LGM; 21 ka) climates (https://wiki.lsce.ipsl.fr/pmip3/doku.php/pmip3:design:index) For further detail see Braconnot *et al*. (2012) and Taylor (2012). The LGM simulation incorporates a difference in ice extent at the poles.

	Orbital Parameters			**Trace Gases**					**Ice sheet extent**
	Eccentricity	**Obliquity**	**Perihelion -180˚**	**CO_2 (ppm)**	**CH_4 (ppb)**	**N_20 (ppb)**	**CFC**	**O_3**	
PI	0.016724	23.446	102.04	280	760	270	0	Modern-10 DU	Present day
MH	0.018682	24.105	0.87	280	650	270	0	Same as PI	Same as PI
LGM	0.018994	22.949	114.42	185	350	200	0	Same as PI	ICE5G

3.6.1.3. Palaeoclimate model data analysis

PMIP3 model data are available for all three timesteps from eight models (see Table 6.1 in Chapter 6 for details). Analyses of PMIP3 netcdf files were performed within 'ncdf4' R package (Pierce, 2019). Data on monthly climatologies of precipitation flux (pr) were downloaded from https://esgf-node.llnl.gov/projects/cmip5/. To assess how simulations of LGM and MH precipitation differ from

present, anomalies were calculated through subtraction of pre-industrial control values (Figure 3.20). The multi-model ensemble of PI simulations was found to be representative of contemporary rainfall distributions (annual timeseries; Figure 6.2 in Chapter 6). Variability exists between models in the spatial resolution of simulations (e.g. Figure 3.20), so all datasets were re-gridded to the same resolution in Python (to the highest resolution model: 320˚ x 160˚) to enable direct comparison of anomalies across longitudes and latitudes. Analyses of PMIP anomalies were undertaken annually and for both the austral summer (December, January, February; DJF) and the austral winter (June, July, August; JJA) to capture changes in seasonality. Further detail on the choice of these time periods in the context of contemporary precipitation regimes is discussed in Chapter 6.

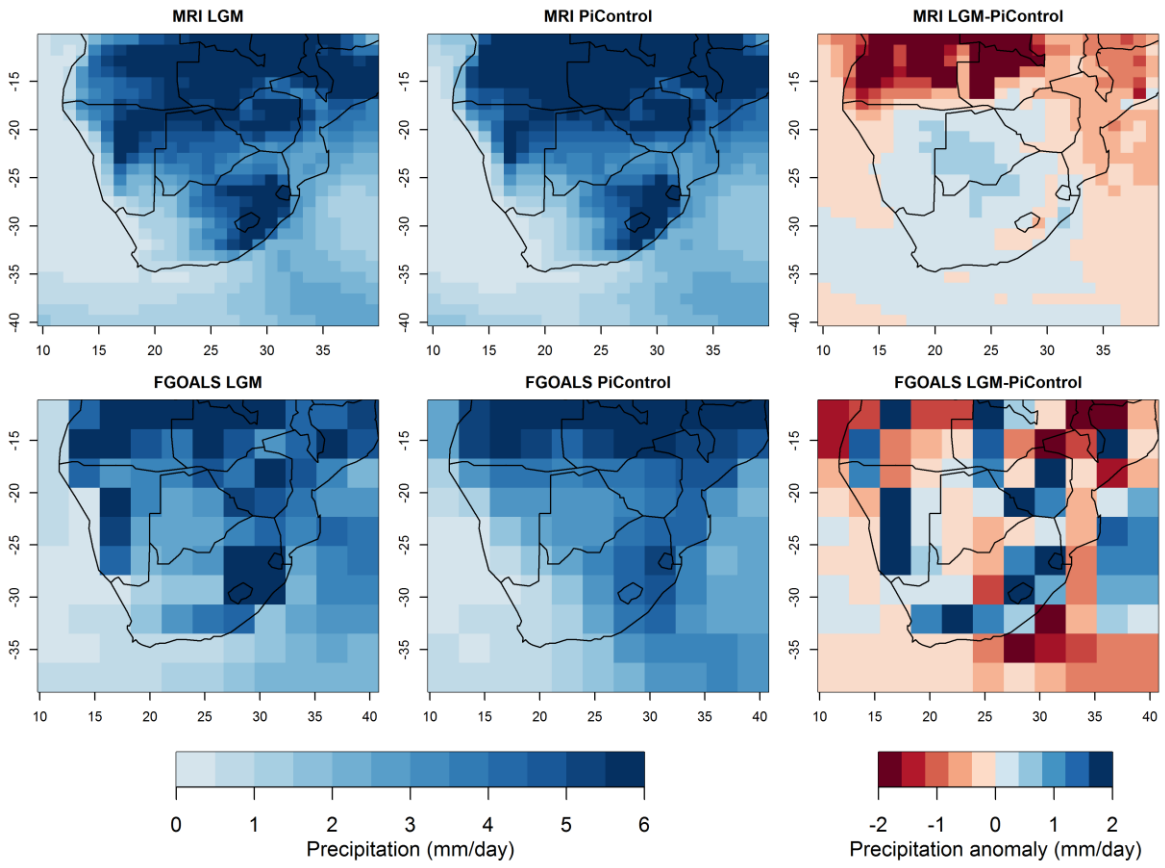

Figure 3.20. Simulated LGM and preindustrial precipitation values for two models within PMIP3 and calculated anomalies between the two. These examples show the variability in resolution, from the lowest resolution model (FGOALs) to the highest resolution model (MRI-CGCM3).

3.6.2. Palaeodata filtering

Following the analysis of palaeoclimate model simulations, palaeodata from southwestern Africa were compiled for model data comparison. The criteria used for inclusion are discussed in detail Section 6.2.2 in Chapter 6 and are briefly described here in Table 3.5. The palaeodata encompassed both palaeoclimate archives and geoproxy records of palaeoenvironmental change in response to climate. The incorporation of geoproxy datasets was possible following the data quality assessment of fluvial records described in Section 3.5, and the availability of existing analyses such as records of sediment accumulation of dunes (Thomas and Bailey, 2017) and a database of lake-status histories (De Cort *et al*., 2021). Using the approach described in Section 3.5.2 on standardisation of radiocarbon chronologies, all radiocarbon ages were recalibrated using SHCal20 (Hogg et al., 2020) in OxCal v 4.4.4. (Bronk Ramsey, 2021) where necessary. The full list of records included in analysis of model-data comparison are detailed in Table 6.2 in Chapter 6.

Table 3.5. Filtering criteria applied to palaeodata for model-archive comparison.

Criteria	Justification
Palaeoclimate change within 17-30˚S and 10-21˚E	This analysis interrogates the spatial patterning of palaeoclimate change over southwestern Africa, so records must reflect change within this region. Marine pollen records in particular were not included if the source area was large and uncertain (following discussion by Scott *et al*., 2004, 2012), as these likely incorporate change beyond the region of interest.
Data within 5-7 ka (MH) or 20-22 ka (LGM)	Time windows of ± 1 ka follows protocols used by Bartlein *et al*. (2011) and Chevalier *et al*. (2017). Several records infer changes at these key timesteps but without chronology within the period of interest, e.g. relating to a wider definition of the LGM or interpretations based on hiatuses within sedimentation. Whilst these both likely provide important palaeoclimate information, they are either not directly comparable to the model timestep, or the lack of chronology means that the timing of events cannot be confidently established.
Data satisfies archive specific quality assessments	Through assessment of these uncertainties associated with geoproxy archive formation, it is possible to reduce anomalies that are a relic of dating error and isolate key spatial and temporal trends in palaeoenvironmental change (Woor *et al*., 2022). Data quality considerations used in Chapter 6 vary by archive (e.g. following Chapter 5 for fluvial archives, Thomas and Bailey (2017) for dunes, and De Cort *et al.* (2021) for lakes), but have a common goal of incorporating robust records of change. Here, key criteria include assessments of chronological data quality, levels of data reporting, and availability of data on the context and independent proxies to interpret depositional conditions.

Chapter 4: Paper 1

Chapter 4: Holocene fluvial depositional regimes of the Huab River, Skeleton Coast, Namibia

Paper 1: Ella Walsh, Luca Caracciolo, Domenico Ravidà, Sallie Burrough, David Thomas

Published online in *Earth Surface Processes and Landforms* on 17/2/22.
https://doi.org/10.1002/esp.5349

Abstract

Dryland fluvial systems respond to hydroclimate changes on Quaternary timescales, yet deciphering the palaeoenvironmental histories they preserve is often complex. Whilst hydrological signals are preserved in sediment stores as variations in sediment volume, character and composition, studies in dryland settings such as Namibia that link sedimentological and compositional changes to palaeoflow are limited. Focusing on the Huab River, Skeleton Coast, this paper presents the first integrated study of textural, compositional, and stratigraphic features from a Namibian fluvial archive. Petrographic and heavy mineral assemblages from Raman laser spectroscopy are combined with lithostratigraphic and particle size analysis. Together, with a chronology established through 42 optically stimulated luminescence ages, we reconstruct provenance, changes in river style, and fluvial response to climate.

The Huab lithostratigraphic record details periods of flashy ephemeral flow interbedded with flow within well-defined channels. Compositional assemblages indicate that humid conditions during the early to mid Holocene resulted in activation of sediment stores across the catchment. Episodic discharge within an ephemeral river from 12 to 9 ka was followed by a more sustained river flow in a channelised system from 7 to 5 ka. During the late Holocene, enhanced hydraulic sorting, increased mechanical breakdown of polycrystalline grains, and flash flood lithofacies suggest that flow occurred within a more arid climate. This fine scaled analysis of an ephemeral fluvial system

indicates the utility of assessing compositional changes to distinguish between depositional regimes. This is an important approach for reconstructing fluvial response to climate and for obtaining palaeoenvironmental records from complex sedimentary archives in dryland river settings.

4.1. Introduction

In dryland regions, an increasing number of systematic approaches are being employed to reconstruct late Quaternary palaeoenvironmental change from ephemeral fluvial systems. For fluvial records to contribute to the growing body of palaeoenvironmental literature, a robust understanding of terrestrial environmental response to past climate conditions is important. Environmental signals of climate perturbations relate to sediment production, transport and deposition (Romans *et al*., 2016) and are recorded in sedimentary archives in terms of sediment volume, character, and composition (Caracciolo, 2020; Tofelde *et al*., 2021). Studies linking sedimentological and compositional changes to palaeoflow in dryland settings have, however, been limited.

Sedimentary archives in Namibian fluvial systems provide a record of past river flow and depositional environments (Lancaster, 2002; Stone and Thomas, 2013) that are, in part, a response to changes in precipitation dynamics throughout the late Quaternary (e.g. Eitel *et al*., 2006; Srivastava *et al*., 2006; Stone *et al*., 2010). Along ephemeral rivers that flow from the Great Escarpment towards the Atlantic Coast (Figure 4.1), fluvial sedimentary evidence is preserved within a hyper-arid region that otherwise lacks a diversity of paleo-proxy records. Low levels of precipitation and limited occurrence of depocenters (e.g. continuous sedimentation in lake basins) have generally restricted the occurrence of major Quaternary archives such as speleothems, lakes and wetlands (Chase and Meadows, 2007). Marine sediment core and hyrax midden records detail significant climate change during the late Quaternary (e.g. Chase *et al*., 2019; Collins *et al*., 2014),

yet terrestrial variability of Namibia's dryland landscape means that these records, given their respective marine and topographic contexts, might not reflect the complexity of environmental responses (Maslin and Christensen, 2007; Thomas, 2019). As the ability to radiometrically date geomorphological records has improved (e.g. Colarossi *et al*., 2020), and the controls on the formation of landforms by sediment transport are understood (e.g. Larkin *et al*., 2020; Mayaud *et al*., 2017; Paola *et al*., 2009), so has the contribution of geoproxies such as fluvial records to assessing the amplitude and nature of hydrological change (Stone and Thomas, 2013).

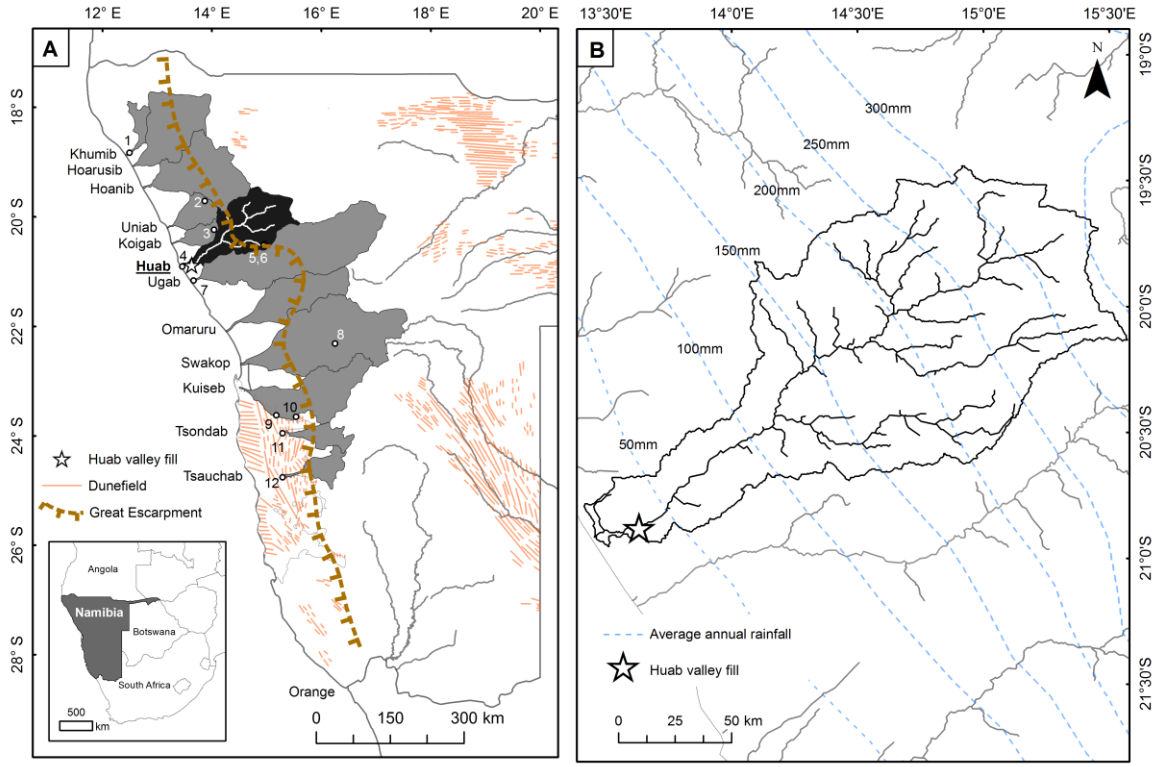

Figure 4.1. A) Map showing the drainage basins and main fluvial systems in Namibia. The Huab River catchment is highlighted in black, the catchments of the ephemeral systems detailed in grey, and location of dunefields (Kalahari and Namib) in orange. Sites discussed in the text are located by numbers (where L: lithofacies analysis, HM: heavy mineral and petrographic analysis, P: palaeohydrological analysis). 1: Khumib (L, Srivastava *et al*., 2004), 2: Axiab (HM, Garzanti *et al*., 2014); 3: Koigab (HM, Garzanti *et al*., 2014), Huab (HM, Garzanti *et al*., 2014); 5: Aba-Huab (HM, Eitel and Zoller, 1996), 6: Aba-Huab (HM, Eitel *et al*., 2001); 7: Ugab (HM, Garzanti *et al*., 2014); 8: Swakop (P, Greenbaum *et al*., 2014); 9: Kuiseb (L, Srivastava *et al*., 2006), 10: Kuiseb (P, Grodek *et*

al., 2013), 11: Tsondab (L, Stone *et al*., 2010), 12: Tsauchab (L, Brook *et al*., 2006). **B)** Location of the Huab Skeleton Coast valley fill (20 km upstream of the river mouth) within the Huab catchment. Average annual rainfall isohyets are detailed at 50 mm intervals (Mendelsohn *et al*., 2002; pg 84. Data sourced from http://www.uni-koeln.de/sfb389/e/e1/download/atlas_namibia/).

Critical to the utility of Namibia's fluvial archives, and in dryland regions more generally, is the capacity to interpret the hydrological conditions responsible for deposition. Terrestrial sedimentary archives are the culmination of geomorphic processes along sediment routing systems (Allen, 2017): from sediment production (see Caracciolo, 2020) to propagation of environmental signals (Tofelde *et al*., 2021), through discontinuous downstream sediment pulses from temporary sediment stores within the 'sediment cascade' (Burt and Allison, 2010). Climate perturbations can therefore be recorded and recognised in the sedimentary record through measurable changes in the amount, character, and composition of sediment stored, and associated weathering features (Romans *et al*., 2016). In dryland regions, reconstructing environmental signals can be challenging due to the lack of long term records and remoteness of sedimentary archives (Benito *et al*., 2011; Reid and Frostick, 1987; Tooth and Nanson, 2011). Consequently, whilst there exists a longstanding body of research in fluvial systems in Namibia, palaeohydrological interpretations have frequently been contested (e.g. Homeb Silts, Kuiseb River; Heine and Heine, 2002; Marker and Muller, 1978; Smith *et al*., 1993; Srivastava *et al*., 2006).

Compositional analysis of petrographic and heavy mineral assemblages is an established method for quantitatively reconstructing provenance, transport pathways and depositional processes in sedimentary systems (Caracciolo, 2020; Garzanti and Andò, 2019; Resentini *et al*., 2017). Abundance of rock and lithic fragments, and concentration of heavy minerals, can be used to identify source lithologies (Garzanti and Andò, 2007). Through analysis of settling equivalence, and the abundance of specific heavy minerals, the sedimentary processes and hydraulic conditions responsible for deposition can also be reconstructed (Garzanti and Andò, 2019; Komar and Wang,

1984; Malusà *et al*., 2013; 2016). In Namibia, compositional analysis has been used to trace sand transport from the Orange River as far north as southern Angola, considering the role of input from the ephemeral rivers along this course (Garzanti *et al*., 2012; 2014; 2018). In Namibian Quaternary fluvial literature, heavy minerals have been used to consider weathering of local inputs (Eitel and Zoller, 1996; Eitel *et al*., 2001, 2005, 2006), but have not yet played a major part in the interpretation of palaeoflow dynamics.

The Huab River, northern Namibia, provides an excellent location to reconstruct Holocene fluvial regimes. Upstream of a topographic constriction in the river channel in the Skeleton Coast, a rich history of fluvial deposition is recorded in a stratified sedimentary unit spanning the valley. This extensive deposit enables a consideration of river morphological dynamics, an assessment of variable preservation potential, and a wider analysis of palaeoflow changes than has been possible in other systems. An existing optically stimulated luminescence (OSL) chronology highlights a fluvial history spanning over 9,000 years (Thomas *et al*., 2017), but the context of deposition and detail on periods of fluvial activity are yet to be fully understood.

This paper systematically reconstructs the timing and nature of deposition of the Huab River valley fill through integrated petrographic, heavy mineral, lithostratigraphic, and particle-size analysis, and a chronology established through 42 new OSL ages. This study combines depositional ages with sedimentological and compositional features to: i) identify which drainage lithologies are important source areas; ii) assess changes in the type of river flow over time; and iii) infer links between sedimentary response and Holocene precipitation changes in the Huab catchment.

4.1.1. Regional setting

The Huab River is one of twelve major ephemeral river systems in Namibia (Figure 4.1). From its headwaters in the Great Escarpment (~1,600 a.m.s.l.), the river course extends westward for 300

km towards the Atlantic Coast, with a catchment area of 14800 km^2 (Jacobson *et al*., 1995). 87 % of the Huab catchment receives precipitation of <300 mm yr^{-1}, decreasing westward to <50 mm yr^{-1} at the coast. Aridity in Namibia for much of the year is associated with the persistence of dry descending air within the high pressure region of the South Atlantic Anticyclone. These conditions are reinforced by stabilisation of airmasses above the cold Benguela current. Localised convective systems bring incursions of rainfall during the austral summer as a result of intensification of the Angola Low (Hermes and Reason, 2009) and tropical-temperate troughs when coupled with mid-latitude waves (Hart *et al*., 2010; Macron *et al*., 2014). At present, the Huab River valley remains dry for most of the year but can experience significant floods associated with short intense episodes of rainfall (Jacobson *et al*., 1995; Morin *et al*., 2009).

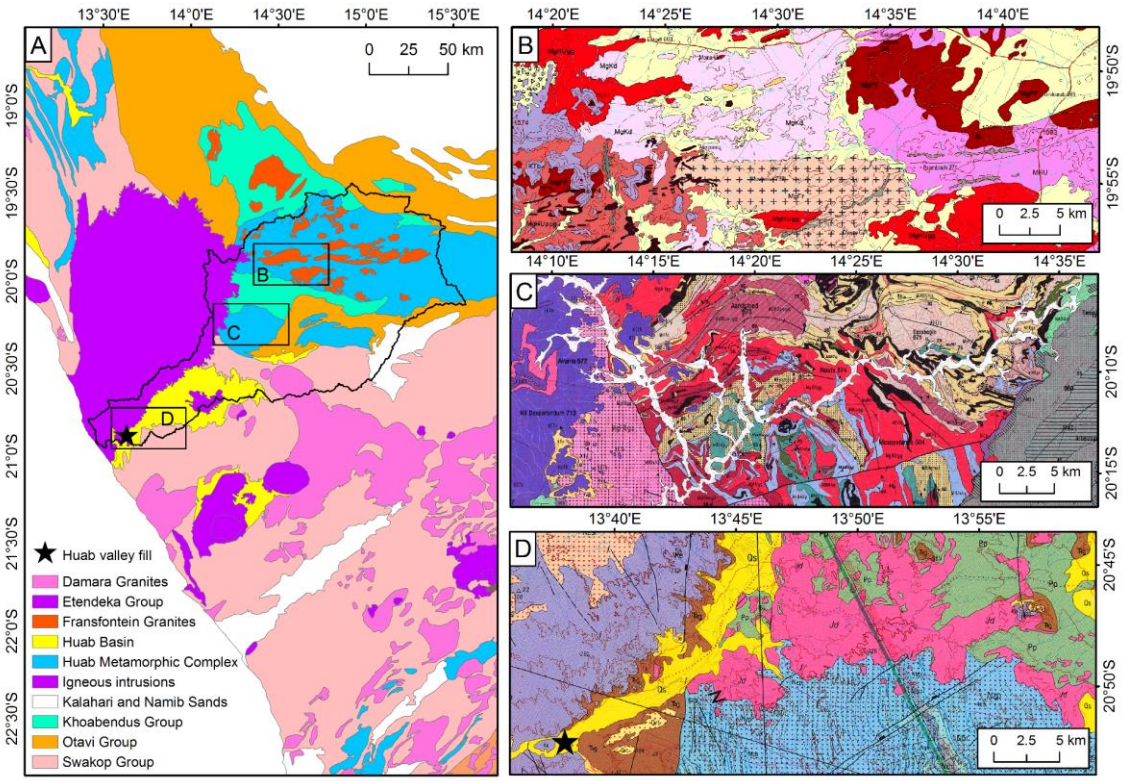

Figure 4.2. A) Map of geological groups of northern Namibia (Mendelsohn *et al*., 2002, pg. 42, data sourced from (Project E1 – Atlas of Namibia http://www.uni-koeln.de/sfb389/e/e1/download/atlas_namibia/). Huab Basin and valley fill location are highlighted. **B)** Insert from the Kamanjab (ref: 1914) geological map **C)** Insert from the Fransfontein (ref: 2014) geological map. **D)** Insert from the Cape Cross (ref: 2013) geological map. Inserts B, C, and D are 1:250,000 geological maps from the Geological Survey of Namibia, Ministry of Mines and Energy. Legend: Jd: dolerite, Kdo: dolerite, Ke: basalt, KETb: basalt, KTb: tholeiitic basalt, KTy: aeolian sandstone, MdHUpogd: granodiorite to gneiss, MgFF: Fransfontein, MgFr: coarse to megacrystic, porphyritic, biotite-bearing granodiorite, MgHUgg: orthogneiss, MgHUgp: MHU invaded by garnet-bearing granite, MgHUpog: porphyritic quartz-feldspar-biotite gneiss, MgKd: biotite-bearing granite with mafic inclusions, MHU: Huab Metamorphic Complex, MHUmgd: granodiorite gneiss; MHUq: orthoquartzite, MHUqms: quartz-mica schist, MHUsg: garnet-cordierite-silimanite-muscovite quartz schist, MHUwbg: quartz-feldspar gneiss, NABdol: dolomite, Nbb: limestone, Nzp: schist, Nbr: turbidite Pp: shale, Qrt: fluviatile cobble-pebble terrace, NCh: diamictite, NMDq: quartzite, NMDs: slate, metasandstone, schist, Qs: surficial deposits, TRg: shale and siltstone. For analysis of the lithological contribution in relation to the surface area of the catchment, see Appendix D.

Namibia's geology is primarily composed of the Namaqua and Damara Orogens linking the Kalahari and Congo Cratons (Jacobs *et al*., 2008; Miller, 2008, Schulter, 2008). The Huab's deep valley landscape was formed by glacial incision during the Permo-Carboniferous glaciation (200-270 Ma) (Jacobson *et al*., 1995; Martin, 1953). To interpret compositional changes in sedimentary units in the Huab valley fill, and to identify which drainage lithologies are important source areas, it is important to consider the potential geological contributions. Detailed geological maps are presented in Figure 4.2 and the heavy mineral and petrographic assemblages that these lithologies produce are described below.

The main branch of the Huab River, the Goantagab, sources sediment from the largely metamorphic Kamanjab Inlier (KI) (Coward, 1981; Goscombe *et al*., 2017). The Huab Metamorphic Complex (Frets, 1969; Kleinhanns *et al*., 2015) and the metavolcanoclastic Khoabendus Group (Mhopjeni, 2006; Muvangua, 2006) shed an epidote-rich heavy mineral assemblage (Eitel *et al*., 2001). Within the KI, the Fransfontein Granite Suite (FFG) contributes quartz, microcline, and plagioclase, and minor biotite and green hornblende (Burger *et al*., 1976; Clifford *et al*., 1969; Kleinhanns *et al*., 2015; Muvangua, 2006). Downstream of the Goantagab-Aba Huab confluence, the Huab is sourced from the Eastern and Northern Zones of the Damara Orogen (Gray *et al*., 2008; Jung and Mezger, 2003; Lehmann *et al*., 2016). Neoproterozoic sediments overlain by metamorphic gneisses contain amphibole-epidote-garnet-rich heavy mineral suites (Garzanti *et al*., 2012; 2014; 2018). Dolomite, limestone and schist are present within the Otavi Group (Prave, 1996), and granit crops out within the Damara Granite Intrusions (Miller, 1983; Seth *et al*., 1998).

The Etendeka large igneous province is composed of basalt, basaltic andesite, and quartz latites (Ewart *et al*., 2004; Garzanti *et al*., 2021; Marsh *et al*., 2001). Assemblages from the Koigab and Axiab rivers draining the Etendeka are dominated by mafic lathwork volcanic fragments, clinopyroxene, and plagioclase (Garzanti *et al*., 2014; 2021). Alongside Lower Cretaceous fluvial and

aeolian sandstones (Jerram *et al*., 2000; Stanistreet and Stollhofen, 1999), igneous intrusives in the form of gabbros and dolerite sills occur in the southern part of the Huab Basin (Jerram *et al*., 1999). These intrude both the Karoo glacial sedimentary sequence and underlying Damara Orogen basement (Duncan *et al*., 1989). Huab dolerite sills typically contain clinopyroxene, plagioclase, olivine, and oxides (Duncan *et al*., 1989). These formed at a similar time to the Etendeka Formation but are compositionally distinct (Duncan *et al*., 1989; Marsh *et al*., 1991).

Long distance littoral transport of sediment occurs along the west coast of Namibia. Garzanti *et al*. (2012; 2014; 2018) record a persistent signal of the Orange River throughout the multi-sink sediment routing system: river-derived sediments have been transported to the Namib Sand Sea, the Skeleton Coast, and the Kunene Erg and Angolan Moçadames Desert. The Orange signal is characterised by abundant clinopyroxene and basalt rock fragments. Inputs from the Namibian ephemeral systems are recorded in varying amounts throughout this sediment routing system.

4.2. Methods

4.2.1. Site selection

Upstream of a narrow valley pinch-point in the bedrock, thick units of sediment have accumulated across the 1 km wide valley floor within a remote area of the Skeleton Coast National Park. Incision by the modern ephemeral channel has created extensive natural exposures, in cases exposing ~5m of stratified sediment. Access to sediment beyond the active channel was not possible, as much of the surface is covered in coarse scree slope deposits, rock fall or aeolian deposits, and the capacity to drill or auger is limited in the very dry sediment. After reconnaissance of sedimentary sections, exposures were sampled systematically from nine sites, at multiple points within the river meanders and at various distances upstream of the constriction (Figure 4.3). Samples were collected from distinct sedimentary units at each site and at similar depths across sites.

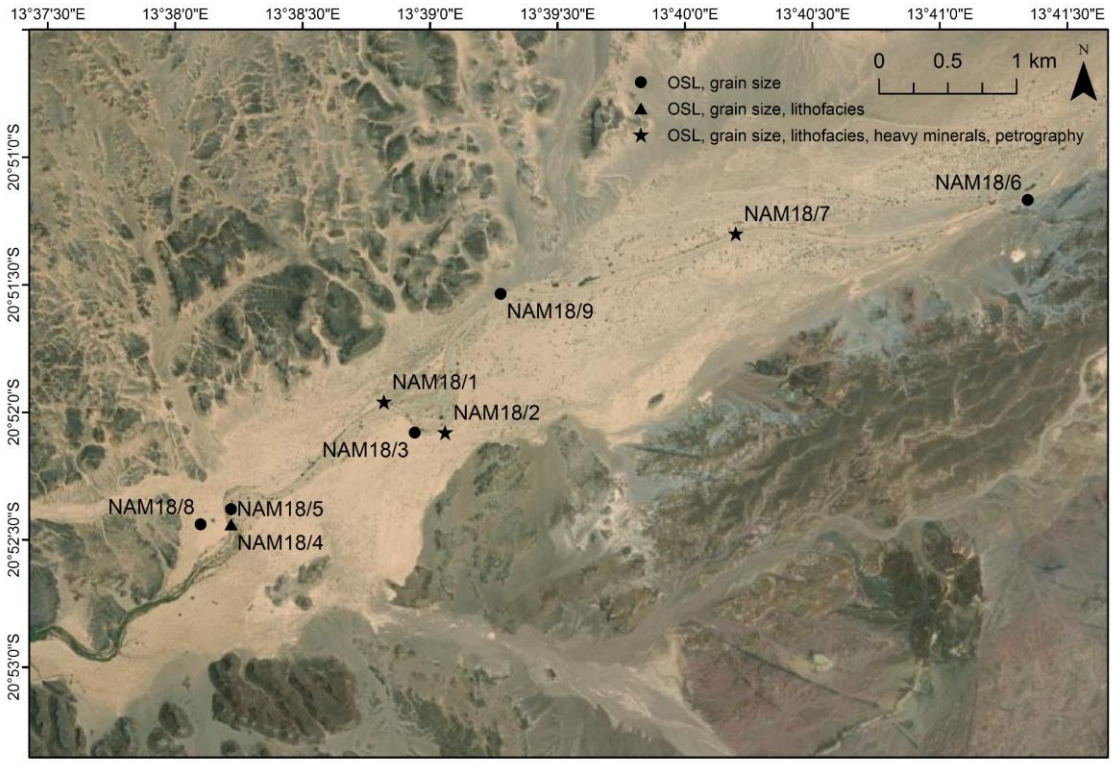

Figure 4.3. Location of sample sites. At all sites, samples were collected for luminescence and grain size analysis. Lithofacies, heavy mineral and petrographic analyses were performed at sites demarcated with a star (NAM18/1, NAM18/2, NAM18/7). Lithofacies analysis was also performed on site demarcated with a triangle (NAM18/4). Section locations: NAM18/1 (20.866˚S, 13.647˚E; 2.6 km upstream of constriction), NAM18/2 (20.868˚S, 13.651˚E; 2.8 km upstream), NAM18/3 (20.868˚S, 13.649˚E; 2.7km upstream), NAM18/4 (20.874˚S, 13.637˚E; 1.1 km upstream), NAM18/5 (20.873˚S, 13.637˚E; 1.3 km upstream), NAM18/6 (20.853˚S, 13.689˚E; 6.9km upstream), NAM18/7 (20.855˚S, 13.670˚E; 5.3km upstream), NAM18/8 (20.873˚S, 13.634˚E; 1.2 km upstream), NAM18/9 (20.859˚S, 13.655˚E; 3.9km upstream).

4.2.2. Optically Stimulated Luminescence (OSL) dating

42 light tight samples were collected using opaque tubes and prepared under subdued orange light (600 nm) in the Oxford Luminescence Dating laboratory (OLDLab). Light-exposed sediments from tube ends were removed and used for grain size analysis and dose rate calculation. Sediment was treated with 32 % hydrochloric acid (HCl) to remove carbonates, and 30 % hydrogen peroxide (H_2O_2) to remove organic matter. Samples were sieved to 90-125 µm and 180-210 µm, and choice of grain size for dating was determined by availability of quartz within each grain size fraction. The

quartz fraction was isolated using sodium polytungstate density separation at 2.62 and 2.72 g cm^{-3} and etched with hydrofluoric acid (HF) for 45 minutes to remove the alpha irradiated surface. For samples with persistent feldspar contamination (tested through the OSL IR depletion ratio; Duller, 2003), a treatment of 30 ml 35 % fluorosilicic acid (H_2SiF_6) was applied for 10 days. Quartz grains were mounted into aluminium discs using Silkospray to obtain small aliquots (2 mm) for multigrain (MG) analysis. Single grain (SG) discs with 300 µm hole diameters were additionally measured for 13 of these samples. The 180-210 µm fraction was used for single grain analysis to ensure only one grain was present in each hole.

OSL measurements were made using Risø TL/OSL luminescence readers fitted with a 10 m W green (532 nm, Nd:YVO4) focused laser (for SG measurements) or blue-light emitting diodes (470 nm) (for MG measurements). Irradiation was undertaken using a calibrated 90 Sr/90 Y beta source and OSL signals were measured using a bialkali photomultiplier tube fitted with a 7.5 mm U-340 glass filter for UV signal detection. Equivalent doses (D_es) were calculated using the single-aliquot regenerative dose (SAR) protocol (Murray and Wintle, 2000; Wintle and Murray, 2006). Following pre-heat plateau and dose recovery tests, a pre-heat of 200˚C for 10 s and a cut-heat of 180˚C were selected. OSL measurements were made at 130˚C for 50 s (MG) or 1 s (SG), with the D_e calculated through subtraction of the mean background 25 s (MG) or 0.2 s (SG), from the first 1 s (MG) or 0.05 s (SG) of stimulation. Luminescence data were processed using Analyst v4.57 (Duller 2015) and the Luminescence R package (Kreutzer *et al*., 2012, 2020). D_es were accepted if they met a standard set of rejection criteria: i) recycling ratio <10 %; ii) OSL IR depletion ratio <10 % (Duller, 2003); iii) recuperation <5 %; iv) test dose signal >3 σ above background. Uncertainties were propagated with a 1.5 % (MG) or 2.5 % (SG) measurement error and using 1000 Monte Carlo repeats. D_e determinations for age calculation were performed used the Minimum Age Model (MAM) of Galbraith *et al*. (1999).

Environmental dose rates were calculated from radio-nuclide concentrations (^{238}U, ^{232}Th, and ^{40}K) measured using inductively coupled plasma mass spectrometry (ICP-MS). These concentrations were converted to dose rates in the DRAC (v1.2) software (Durcan *et al*., 2015) using the attenuation factors of Guérin *et al*. (2011). Dose rates were attenuated by water content (5 ± 2 %), grain size, and chemical etching.

4.2.3. Lithostratigraphic and grain size analysis

Detailed sedimentological analyses were performed on four key stratigraphic sequences within the Huab valley fill. These sites were chosen because they have the most extensive stratigraphic preservation and enable a comparison of sites at different locations along the length and width of the fill (Figure 4.3). Individual lithofacies were identified based on grain size, bedding and associated sedimentary structures following the criteria proposed by Miall (2006). Based on the distribution, facies were grouped into two lithofacies associations representative of specific depositional settings.

Grain size analyses were undertaken on oven-dried samples using the wet dispersion method in a Malvern Mastersizer Hydro 2000MU. Statistics were calculated following Folk and Ward (1957) in Gradistat (Blott and Pye, 2001). Cluster analysis of grain size data was performed using Euclidean distance to create a dissimilarity matrix, and hierarchical clustering using the Ward method (for detail on analysis of the optimal number of clusters, see Appendix D Figure D1). Canonical correspondence analysis (CCA) was used to interrogate potential drivers of variability seen in the datasets, principally whether grain size is significant in explaining variability in compositional datasets.

4.2.4. Raman heavy mineral and petrographic analysis

To investigate the composition of the Huab valley fill deposits, 19 samples from three key stratigraphic sections (Figure 4.3; sections with the greatest number of ages) were selected for petrographic (PT) and heavy mineral (HM) analysis. Analysis was performed using Raman laser spectroscopy; a tool that is increasingly being applied to the study of sediment composition analysis (Ando and Garzanti, 2014). Raman spectroscopy enables confidence in identification of mineral species, enables identification of altered or turbid grains, and increases the speed of analysis compared to optical assessments (Lünsdorf *et al*., 2019).

HM fractions were obtained after crushing, removal of organic and carbonate matter using acetic acid (10 %), centrifuge separation in sodium polytungstate (2.90 g cm^{-3}) and partial freezing using liquid nitrogen (following Andò, 2020). The HM fraction was sieved to three grain-sizes including sand and silt (32-63 µm, 63-125 µm and 125-250 µm; e.g. Ando and Garzanti, 2014; Caracciolo *et al*., 2020) to reduce biases introduced by a limited grain size window (Garzanti *et al*., 2008; 2009; Garzanti and Andò, 2019) and improve the ability to polish slides. Micro-riffle-split subsets were mounted on slides, polished, and digitised for point-logging (Lünsdorf *et al*., 2019) for analysis by Raman spectroscopy (Ando and Garzanti, 2014). Raman analysis was performed at the GeoZentrum Nordbayern of the Friedrich Alexander Universität Erlangen-Nürnberg (FAU, Germany) using a Raman WITech Alpha 300R system. The Raman was fitted with a confocal microscope coupled to a 200 mm focal length spectrograph with a four-grating turret. The confocal hole and slit were set to 100 µm. Analyses were performed at 1800 gr mm^{-1} using a 50x objective (numerical aperture: 0.5) and 532 nm laser at 100 mW output power. Calibration of the spectrometer was performed on a 520.70 cm^{-1} band of Si, and the recorded spectrum was centred at 840 cm^{-1} (1800 gr mm^{-1}). Raman spectra were obtained from ~500 signals per grain size of each sample. Raman spectra were assigned a mineral identification from the RRUFF database (Lafuente *et al*., 2016) using the automated TrueMatch software (WITec) and manual verification.

For PT analysis, bulk samples were sieved to >63 µm, impregnated with epoxy resin, and prepared as standard polished thin sections. Slides were digitised for point logging and coordinates were used to determine the laser position for Raman analysis. These coordinates were then used to locate grains that required optical microscopic assessment, such as polycrystalline grains and grains where the Raman signal was poor. The PT composition of each sample was determined through 300 points at a regular 1 mm spacing following the Gazzi-Dickinson method (Ingersoll *et al*., 1984; Zuffa, 1985). This method enabled the textural discrimination between rock fragments and lithic fragments. Here, rock fragments were defined from a textural point of view as they contain polycrystalline grains with crystals >63 µm. In this case, the mineral intercepted by the ocular haircross was recorded and classified as rock fragments in accordance to its lithological affinity (e.g. plagioclase in plutonic rock fragment). Aphanitic fine grained lithic fragments have crystals <63 µm and have been classified using the genetic criteria. Volcanic lithic grains were classified according to Marsaglia and Ingersoll (1992), and metamorphic lithic grains according to Garzanti and Vezzoli (2003). QFL ternary diagrams were used to constrain sedimentary provenance (Dickinson, 1985; Garzanti, 2018; Ingersoll *et al*., 1984), and the grain-size dependent QFR diagram (Pettijohn *et al*., 1987) was used to further constrain changes in sediment texture and composition. Therefore L in the Dickinson diagram corresponds only to genetically classified fine aphanitic grains and coarse polycrystalline grains are recalculated as Q and F in the QFL ternary composition. According to Pettijohn, all polycrystalline grains are counted as rock fragments and are grouped into R.

4.3. Results

4.3.1. Chronology

Dose recovery tests show that an applied laboratory dose can be recovered well (average recovery ratio of 0.97 ± 0.1 (MG), and 1.03 ± 0.1 (SG); Figure 4.4). Average overdispersion values are 52.7 % (MG) and 74.4 % (SG), where more precise younger ages have higher overdispersion values, which

is to be expected (Thomsen *et al.*,2012). D_e distributions commonly show a high level of scatter and a leading edge in lower D_es. Given the occurrence of flashy flow in this desert environment, it is likely that heterogeneous bleaching (Olley *et al.*, 2004) has driven this positively skewed distribution. For this reason, the Minimum Age Model (Galbraith *et al.*, 1999) has been used to calculate final D_es. This follows the protocol used in several other Namibian fluvial settings (e.g. Brook *et al.*, 2006; Grodek *et al.*, 2013; Srivastava *et al.*, 2006). Where possible, depositional ages are based on single grain analysis, as it allows for the well-bleached component to be isolated (Colarossi *et al.*, 2020; Duller, 2008b). Single grain analysis shows that detectable signals derive from 2-3 % of grains, and as small aliquot 180-210 µm multigrain discs contain ~68 grains per disc (Burow, 2020; Heer *et al.*, 2012), it is likely that D_es are derived from only one to two grains. Close correspondence (within errors) between ages from single grain and small aliquot multigrain scales of analysis show that it is appropriate in this context to use minimum multigrain ages where single grain ages are not available (as also inferred by Srivastava *et al.*, 2006).

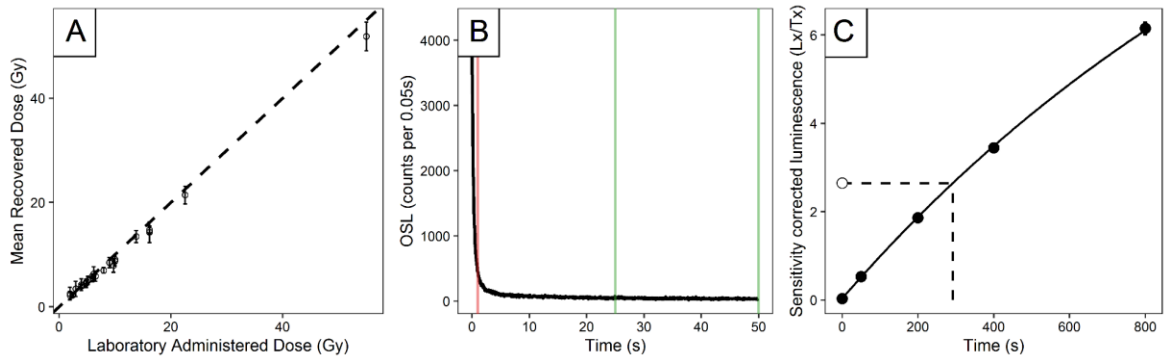

Figure 4.4. A) Dose recovery test results. Dotted line indicates unity, where the laboratory administered dose and recovered dose are equal. **B)** Example of an OSL signal: natural signal (OSL counts per 0.05 s) against time, for sample NAM18/2/10. This shows that the natural signal is dominated by the fast component. D_e is calculated through subtraction of the mean background (between green lines at 25s and 50s) from the main signal (red line at 1s). **C)** Dose response curve of one aliquot of NAM18/2/10 (MG). Lx/Tx represents the OSL signal (Lx) normalised by the test dose (Tx). This curve has been fitted with an exponential function. The sensitivity corrected signal gave a dose of 16.2 ± 0.4 Gy.

Depositional ages span almost the entire Holocene, with ages from NAM18/1 ranging from 11.85 ± 1.78 ka (NAM18/1/12) to 0.52 ± 0.13 ka (NAM18/1/1) (Table 4.1). Within-error ages in the top 3m of this site suggest that deposition was rapid between 0.99 ± 0.17 ka and 0.52 ± 0.13 ka. At NAM18/2, luminescence ages span from 7.10 ± 1.08 ka (NAM18/2/9) to 0.45 ± 0.08 ka (NAM18/2/1). Deposition between 7 ka and 5 ka at NAM18/2 corresponds to deposition at NAM18/9 (7.81 ± 0.86 ka), but is not recorded at other sites. Ages at the base of NAM18/7 correspond to NAM18/1, with samples dating to 11.58 ± 0.95 ka and 12.10 ± 1.11 ka. NAM18/4 only contains units dating to within the last 1 ka. The top of NAM18/5 dates the youngest preserved depositional units to 0.2 ± 0.05 ka. NAM18/6 contains ~2m of deposition from 1.82 ± 0.32 ka and 1.18 ± 0.15 ka. NAM18/8 details contemporaneous fluvial and aeolian deposition of a nebkha dune at 0.43 ± 0.08 years.

Table 4.1. Results of luminescence dating. Grain size dated, number of discs measured, overdispersion, equivalent doses, beta, gamma, cosmic and calculated dose rates, and OSL age. MG: multigrain, SG: single grain. Calculations were made prior to rounding to two decimal places. Ages used for interpretation are highlighted in bold (single grain ages used where available). [a]Number of accepted aliquots, [b]overdispersion from Galbraith *et al.* (1999), [c]Minimum age model used to calculate D_e.

Sample NAM18/	Depth (m)	Grain size (μm)	n^a		σ_d		D_e (Gy)[c]		Beta dose rate (Gy.ka^{-1})	Gamma dose rate (Gy.ka^{-1})	Cosmic dose rate (Gy.ka^{-1})	Environmental dose rate (Gy.ka^{-1})	Age (ka)	
			MG	SG	MG	SG	MG	SG					MG	SG
1/1	0.05	180-210	23	39	60 ± 9	91 ± 12	1.28 ± 0.17	1.32 ± 0.31	1.56 ± 0.14	0.69 ± 0.05	0.27 ± 0.03	2.52 ± 0.15	0.51 ± 0.07	**0.52 ± 0.13**
1/2	0.25	180-210	26	-	47 ± 8	-	1.86 ± 0.09	-	1.57 ± 0.14	0.84 ± 0.06	0.23 ± 0.02	2.63 ± 0.15	**0.71 ± 0.05**	
1/4	0.85	180-210	38	-	71 ± 9	-	2.02 ± 0.35	-	2.02 ± 0.19	0.95 ± 0.07	0.18 ± 0.02	3.15 ± 0.20	**0.64 ± 0.12**	
1/5	1.05	180-210	36	23	82 ± 10	124 ± 20	2.91 ± 0.42	1.75 ± 0.42	1.69 ± 0.16	0.78 ± 0.06	0.18 ± 0.02	2.65 ± 0.17	1.10 ± 0.17	**0.66 ± 0.17**
1/6	1.35	180-210	18	12	83 ± 14	106 ± 26	1.66 ± 0.15	2.11 ± 0.66	1.97 ± 0.18	1.01 ± 0.07	0.17 ± 0.02	3.15 ± 0.19	0.53 ± 0.06	**0.67 ± 0.21**
1/7	1.95	180-210	23	-	69 ± 11	-	1.98 ± 0.35	-	1.59 ± 0.15	0.69 ± 0.05	0.16 ± 0.02	2.44 ± 0.16	**0.81 ± 0.15**	-
1/8	2.3	180-210	25	-	72 ± 11	-	2.09 ± 0.32	-	1.55 ± 0.14	0.83 ± 0.06	0.15 ± 0.02	2.53 ± 0.15	**0.83 ± 0.13**	-
1/9	2.45	90-125	25	-	65 ± 9	-	3.27 ± 0.29	-	1.98 ± 0.17	1.04 ± 0.07	0.15 ± 0.02	3.17 ± 0.19	**1.03 ± 0.11**	-
1/10	3.0	180-210	23	41	80 ± 12	92 ± 12	2.04 ± 0.32	2.79 ± 0.46	1.81 ± 0.17	0.87 ± 0.06	0.14 ± 0.01	2.82 ± 0.18	0.73 ± 0.12	**0.99 ± 0.17**
1/11	4.6	180-210	21	54	30 ± 7	52 ± 8	22.38 ± 2.94	26.74 ± 4.02	1.81 ± 0.17	0.79 ± 0.06	0.12 ± 0.01	2.72 ± 0.19	8.22 ± 1.22	**9.83 ± 1.62**
1/12	5	180-210	24	66	25 ± 7	26 ± 6	20.94 ± 2.70	27.21 ± 3.66	1.52 ± 0.14	0.67 ± 0.05	0.11 ± 0.01	2.30 ± 0.15	9.13 ± 1.32	**11.85 ± 1.78**
2/1	0.3	180-210	23	66	101 ± 15	98 ± 10	1.82 ± 0.06	1.14 ± 0.21	1.54 ± 0.14	0.80 ± 0.06	0.22 ± 0.02	2.56 ± 0.15	0.71 ± 0.05	**0.45 ± 0.08**
2/2	0.7	180-210	14	-	102 ± 20	-	7.05 ± 0.69	-	2.32 ± 0.20	1.24 ± 0.08	0.19 ± 0.02	3.75 ± 0.22	**1.88 ± 0.22**	-
2/3	1.3	180-210	20	34	66 ± 11	114 ± 16	4.33 ± 0.44	2.65 ± 0.62	1.85 ± 0.17	0.90 ± 0.06	0.17 ± 0.02	2.92 ± 0.18	1.49 ± 0.18	**0.91 ± 0.22**
2/4	1.6	180-210	22	36	52 ± 9	81 ± 11	6.36 ± 0.82	5.25 ± 0.96	1.49 ± 0.13	0.79 ± 0.05	0.17 ± 0.02	2.44 ± 0.14	2.61 ± 0.37	**2.15 ± 0.42**
2/5	1.85	180-210	25	47	35 ± 6	34 ± 7	4.30 ± 0.44	3.34 ± 0.33	1.53 ± 0.14	0.78 ± 0.05	0.16 ± 0.02	2.47 ± 0.15	1.74 ± 0.21	**1.35 ± 0.16**
2/6	2.15	90-125	34	-	47 ± 7	-	10.69 ± 1.25	-	1.71 ± 0.15	0.93 ± 0.06	0.15 ± 0.02	2.80 ± 0.16	**3.83 ± 0.50**	-
2/7	2.85	180-210	21	42	30 ± 5	83 ± 11	6.49 ± 0.60	5.00 ± 0.93	1.68 ± 0.15	0.94 ± 0.06	0.14 ± 0.01	2.76 ± 0.16	2.35 ± 0.26	**1.92 ± 0.38**
2/8	3.3	180-210	22	-	19 ± 7	-	17.51 ± 2.19	-	1.76 ± 0.17	0.78 ± 0.06	0.14 ± 0.01	2.67 ± 0.18	**6.55 ± 0.93**	-
2/9	3.75	90-125	27	-	46 ± 8	-	22.15 ± 3.12	-	1.91 ± 0.16	1.09 ± 0.07	0.13 ± 0.01	3.12 ± 0.18	**7.10 ± 1.08**	-
2/10	3.9	180-210	23	27		33 ± 8	18.32 ± 2.10	16.40 ± 2.84	1.62 ± 0.15	0.77 ± 0.06	0.13 ± 0.01	2.52 ± 0.16	7.28 ± 0.96	**6.52 ± 1.21**
2/11	4.15	180-210	20	-	21 ± 7	-	19.41 ± 2.07	-	1.82 ± 0.16	0.96 ± 0.07	0.12 ± 0.01	2.91 ± 0.18	**6.68 ± 0.82**	-
2/12	4.7	180-210	27	114	19 ± 6	41 ± 5	16.16 ± 1.86	13.80 ± 1.58	1.62 ± 0.15	0.76 ± 0.06	0.12 ± 0.01	2.50 ± 0.16	6.47 ± 0.85	**5.53 ± 0.73**
3/1	1.5	180-210	31	-	63 ± 8	-	3.92 ± 0.30	-	1.70 ± 0.15	0.98 ± 0.07	0.17 ± 0.02	2.85 ± 0.16	**1.38 ± 0.13**	-

3/2	1.5	90-125	26	-	36 ± 5	-	4.85 ± 0.16	-	1.92 ± 0.16	1.16 ± 0.07	0.17 ± 0.02	3.25 ± 0.18	**1.50 ± 0.09**	-
4/1	0.4	90-125	45	-	34 ± 6	-	2.26 ± 0.12	-	1.98 ± 0.17	1.14 ± 0.07	0.21 ± 0.02	3.33 ± 0.18	**0.68 ± 0.05**	-
4/3	1.35	90-125	25	-	39 ± 6	-	2.26 ± 0.15	-	1.99 ± 0.17	1.07 ± 0.07	0.17 ± 0.02	3.23 ± 0.19	**0.70 ± 0.06**	-
4/4	1.8	180-210	18	-	88 ± 16	-	1.07 ± 0.28	-	1.91 ± 0.17	1.00 ± 0.07	0.16 ± 0.02	3.07 ± 0.18	**0.35 ± 0.09**	-
4/5	1.95	180-210	22	-	42 ± 8	-	2.66 ± 0.42	-	1.58 ± 0.14	0.81 ± 0.06	0.16 ± 0.02	2.55 ± 0.16	**1.04 ± 0.18**	-
5/1	0.25	180-210	21	-	100 ± 16	-	0.65 ± 0.16	-	1.99 ± 0.18	0.99 ± 0.07	0.23 ± 0.02	3.20 ± 0.19	**0.20 ± 0.05**	-
5/2	0.5	90-125	12	-		-	1.23 ± 0.07	-	2.24 ± 0.19	1.30 ± 0.08	0.20 ± 0.02	3.74 ± 0.21	**0.33 ± 0.03**	-
6/1	0.85	180-210	22	-	59 ± 9	-	3.67 ± 0.42	-	1.92 ± 0.17	1.01 ± 0.07	0.18 ± 0.02	3.11 ± 0.19	**1.18 ± 0.15**	-
6/2	3.15	180-210	30	-	69 ± 10	-	4.28 ± 0.70	-	1.54 ± 0.15	0.68 ± 0.05	0.14 ± 0.01	2.36 ± 0.16	**1.82 ± 0.32**	-
7/1	0.5	180-210	21	-	62 ± 10	-	0.85 ± 0.06	-	1.66 ± 0.15	0.80 ± 0.06	0.20 ± 0.02	2.66 ± 0.16	**0.32 ± 0.03**	-
7/3	1.2	90-125	25	-	46 ± 8	-	7.48 ± 0.46	-	1.77 ± 0.14	1.10 ± 0.07	0.17 ± 0.02	3.05 ± 0.16	**2.45 ± 0.20**	-
7/4	1.5	180-210	30	-	61 ± 8	-	2.63 ± 0.31	-	1.88 ± 0.17	0.91 ± 0.07	0.17 ± 0.02	2.96 ± 0.18	**0.89 ± 0.12**	-
7/5	2.45	180-210	22	-	11 ± 8	-	36.21 ± 1.94	-	1.98 ± 0.18	1.00 ± 0.07	0.15 ± 0.02	3.13 ± 0.19	**11.58 ± 0.95**	-
7/6	2.85	180-210	19	-	18 ± 7	-	21.53 ± 2.90	-	1.78 ± 0.17	0.84 ± 0.06	0.14 ± 0.01	2.77 ± 0.18	**7.78 ± 1.16**	-
7/7	3.65	90-125	36	-	33 ± 4	-	32.23 ± 2.17	-	1.72 ± 0.16	0.81 ± 0.06	0.13 ± 0.01	2.66 ± 0.17	**12.10 ± 1.11**	-
8/1	1.35	90-125	15	-	22 ± 15	-	1.40 ± 0.26	-	1.93 ± 0.16	1.15 ± 0.07	0.17 ± 0.02	3.25 ± 0.18	**0.43 ± 0.08**	-
8/2	1.65	90-125	30	-	74 ± 10	-	1.38 ± 0.15	-	1.89 ± 0.16	1.13 ± 0.07	0.16 ± 0.02	3.18 ± 0.17	**0.44 ± 0.05**	-
9/1	1.3	180-210	20	-	30 ± 7	-	24.32 ± 2.22	-	1.93 ± 0.18	1.01 ± 0.07	0.17 ± 0.02	3.11 ± 0.19	**7.81 ± 0.86**	-

4.3.2. Sedimentary characteristics of the Huab valley fill

4.3.2.1 Lithofacies associations

Twelve lithofacies were identified in the Huab sections (Table 4.2) and assigned to two main associations indicative of changes in flow regime: (i) channelised fluvial associations with floodplain elements, and (ii) unconfined stream associations.

Table 4.2. Lithofacies table summarising sedimentary structures and interpretation of depositional environment following Miall (2006).

Facies	Description	Secondary structures	Interpretation	Reference
Gmm	Matrix-supported gravels. Clast size from pebble to cobble. Matrix from silt to very fine sand.	-	Unconfined medium to high viscosity clast-rich plastic debris flows. Deposition in medial to proximal portion of alluvial fan.	Bowman (2019); Miall (2006); Stanistreet and McCarthy (1993)
Gt	Trough cross-bedded conglomerates. Clasts size from granule to cobble.	Fining upward tendency; clast imbrication; scoured base.	Middle to upper part of lower flow regime. Channel infills. Downstream migration of 3D gravel dunes.	Miall (2006); Srivastava *et al*. (2004)
Gp	Planar, high-angle (>15°) cross-bedded conglomerates. Clasts size from granule to cobble.	Fining upward tendency; clast imbrication; scoured base.	Middle to upper part of lower flow regime. Channel infills. Downstream migration of 2D gravel dunes; Channel lag elements.	Miall (2006); Srivastava *et al*. (2004)
Gm	Massive conglomerates with no evident stratification. Clast size from granule to pebble.	Fining upward tendency; scoured base.	Middle to upper part of lower flow regime. Gravel bars; channel lag element.	Miall (1978); Srivastava *et al*. (2004)
Gh	Horizontally, plane-bedded gravel deposits. Clasts size from granule to pebble.	-	Upper flow regime plane bedding. Non-channelised flashy sheetflood. Distal alluvial fan elements.	Bowman (2019); Stollhofen and Stanistreet (1994)
St	Trough, cross-bedded sand. Grain size from coarse to medium.	Fining upward tendency; scoured base; rare intraformational mud-clasts.	Upper part of lower flow regime. 3D dune-scale channel infill bedforms.	Miall (2006); Srivastava *et al*. (2004)

Sp	Planar, high-angle (>15°) cross-bedded sand. Grain size from coarse to medium.	Fining upward tendency; scoured base; intraformational mud-clasts.	Upper part of lower flow regime. 2D dune-scale channel infill bedforms.	Miall (2006); Srivastava *et al*. (2004)
Sl	Planar, low-angle (<15°) cross-bedded sand. Grain size from medium to fine.	Fining upward tendency; upward decreases in steepness.	Upper part of lower flow regime. 2D dune-scale channel infill bedforms and pointbar.	Donselaar and Overeem (2008); Miall (2006); Srivastava *et al*. (2004)
Sh	Horizontally, plane-bedded sand. Grain size from coarse to medium.	-	Upper flow regime plane bedding. Ephemeral flashy sheetfloods. Distal alluvial fan elements.	Bowman (2019); Miall (2006)
Sm (Smc)	Massive sand. Grain size from medium to fine. Sands locally display intense carbonate cementation (Smc).	Bioturbation induced by vegetation; faint lamination; root-prints; silt lenses.	Lower flow regime. Deposition in proximal overbank settings.	Srivastava *et al*., 2005
Fl	Ripple to plane laminated silt to very fine sand.	Bioturbation induced by vegetation; climbing ripples.	Lower part of flow regime. Deposition from suspension load. Abandoned channel. Waning flood deposits on the floodplain area.	Gary *et al*. (1974); Miall (2006); Srivastava *et al*. (2006)
Fm	Massive clay and silt.	Bioturbation induced by vegetation, root-prints, mud cracks.	Lower part of the flow regime. Deposition from suspension load in the floodplain area.	Miall (2006); Srivastava *et al*. (2005)

Channelised fluvial association and floodplain elements

This lithofacies association consists of cross-bedded conglomerates and sands commonly organised into fining upward successions capped by fine silt to clay beds. These units develop as >5 m long tabular or convex bodies bounded by sharp erosional surfaces. Conglomerates consist of rounded granules and pebbles typically imbricated in the downstream direction, and medium to coarse-grained sands. Lithofacies display trough (Gt, St) to high- and low-angle cross-bedding (Gp, Sp, Sl) or are massive (Gm) (0.2-1 m thick). Set boundaries are commonly highlighted by micaceous laminae. Cross-bedded deposits locally display stacked internal fining upward cycles (0.1 - 0.6 m) and basal scoured surfaces are floored by intraformational clay clasts and gravel lags. Fine to

medium sands also display massive aspect (Sm) associated with bioturbation, silt lenses, or carbonate cementation (Smc). Ripple and horizontally laminated silt to fine sand layers (Fl; 0.1-0.2 m) occur at the top of the fining upward cycles or as isolated bodies. Massive silt to clay units (Fm; <0.4 m) display bioturbation, root prints and desiccation cracks.

Interpretation

These features are indicative of fluvial sedimentary infill of channels dominated by mixed load sediment transport (Miall, 1985). Lithofacies indicate flow within a well-defined channel where deposition also occurs in the surrounding floodplain during overbank flows (Asselman and Middelkoop, 1995; Miall, 2014; Srivastava *et al*., 2004). Cross-bedded deposits result from bed-load migration of sub-aqueous dune and channel bars with downstream accretionary tendencies (Miall, 2006). Isolated gravel lenses at the bottom of the fining-upward cycles represent channel lags (Brook *et al*., 2006; Miall, 1978; Srivastava *et al*., 2004). Laminated fine-grained deposits capping these cycles result from falling stages and settling of suspended river load under low-to-stagnant flow regimes in floodplains or abandoned channels (Viseras *et al*., 2018). Similar flow conditions are interpreted for massive and bioturbated silt and clay units, and the occurrence of rootprints and desiccation cracks indicate subaerial exposure and pedogenic overprint (Galloway and Hobday, 2012; Miall, 2006).

Unconfined stream association

This lithofacies association consists of horizontally bedded sands and gravels, and local interbedded breccia. These units develop as isolated or vertically stacked tabular bodies (<4 m) bounded by sharp, non-erosional surfaces. Horizontally plane-bedded conglomerates (Gh) contain sub-angular to sub-rounded granules and pebbles (<0.3 m thick), whereas sands (Sh) vary in grain size from fine to coarse (<0.7 m thick). Breccia deposits (Gmm) contain angular pebbles and cobbles floating in a silty matrix with no visible internal organization (<0.3 m thick units).

Interpretation

These features are indicative of deposition of unconfined flash floods (Sneh, 1983; Miall, 1985; Stollhofen and Stanistreet, 1994), where sediment mobilization is associated with ephemeral flow, and rapid water and sediment influxes occur in an otherwise arid environment (Calvache *et al*., 1997; Fraser and Suttner, 1986). Tabular horizontally plane-bedded units reflect the establishment of upper plane regimes. The absence of cross-bedding and the occurrence of sharp, non-erosional boundaries indicate dominantly traction load transport and deposition of flashy sheetfloods. Matrix-supported breccias occur as a result of medium to high viscosity clast-rich debris flows (Bowman, 2019).

4.3.2.2 Stratigraphic sections

The vertical succession of facies associations and change in depositional settings throughout the investigated sequences are illustrated in Figure 4.5 and are described in detail below.

Figure 4.5. Sedimentary logs and luminescence ages from sections NAM18/1, NAM18/2, NAM18/7, NAM18/4. Channel infill association and floodplain (legend: **A** comprised of lithofacies Fl, Fm, Gm, Gp, Gt, Sl, Sm, Sp, St, Sr; and unconfined stream associations legend: **B** comprised of Gh, Gmm, Sh. Orange stars indicate samples included within heavy mineral and petrography analysis. All samples were analysed for luminescence and grain size. Period 1: 12-9 ka channel deposition at NAM18/1, floodplain deposition NAM18/7. Period 2: conglomerate deposition at NAM18/1. Period 3: 7-5 ka channel deposition at NAM18/2. Period 4: 4-1 ka channel and unconfined facies deposition at NAM18/2. Period 5: 1 ka to present: channel deposition at NAM18/1 and NAM18/7, floodplain deposition at NAM18/2 and NAM18/4. In the text, these periods are referred to as P1 to P5.

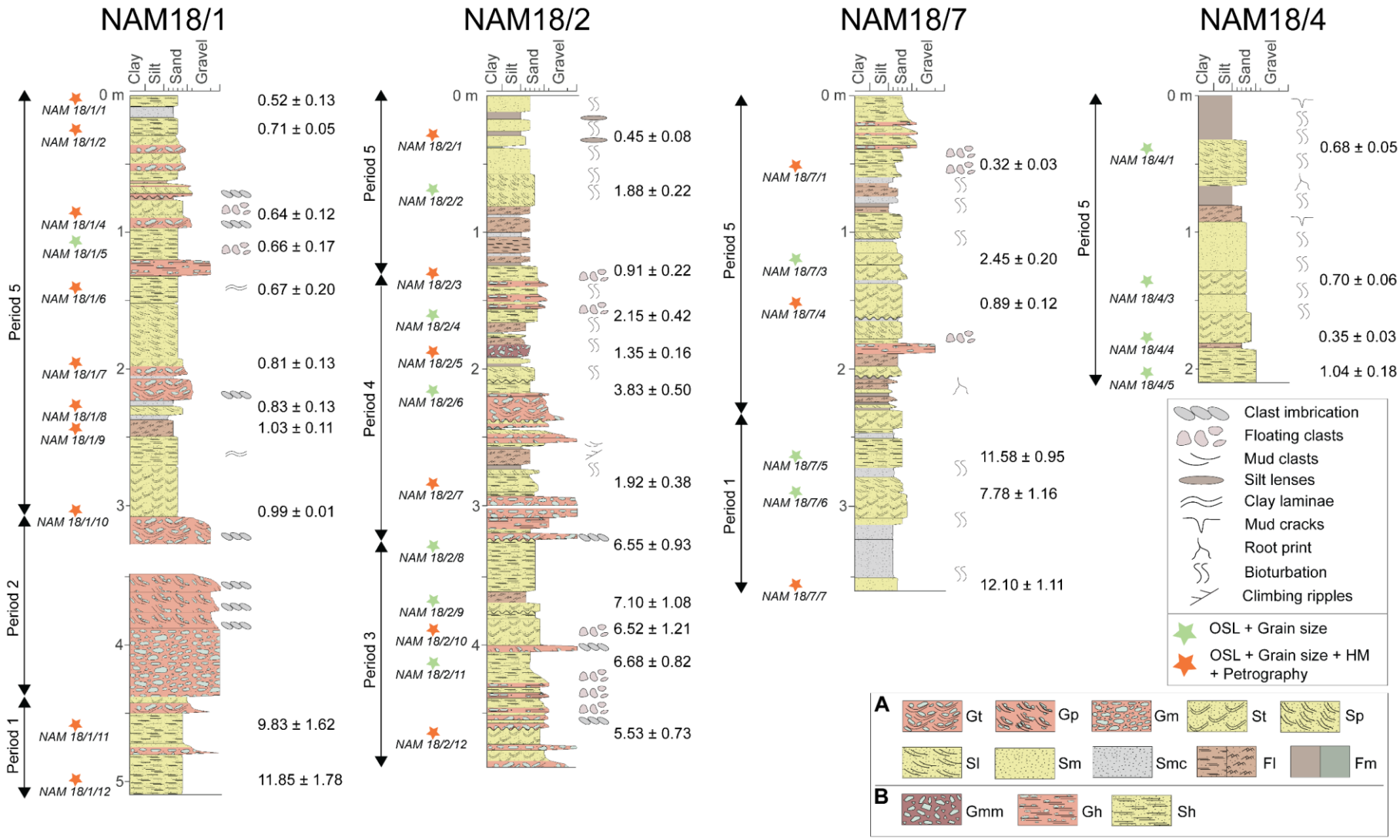
NAM18/1
NAM18/2
NAM18/7
NAM18/4
Clay
Silt
Sand
Gravel
0 m
Period 5
Period 2
Period 1
Period 4
Period 3
NAM 18/1/1
NAM 18/1/2
NAM 18/1/4
NAM 18/1/5
NAM 18/1/6
NAM 18/1/7
NAM 18/1/8
NAM 18/1/9
NAM 18/1/10
NAM 18/1/11
NAM 18/1/12
0.52 ± 0.13
0.71 ± 0.05
0.64 ± 0.12
0.66 ± 0.17
0.67 ± 0.20
0.81 ± 0.13
0.83 ± 0.13
1.03 ± 0.11
0.99 ± 0.01
9.83 ± 1.62
11.85 ± 1.78
NAM 18/2/1
NAM 18/2/2
NAM 18/2/3
NAM 18/2/4
NAM 18/2/5
NAM 18/2/6
NAM 18/2/7
NAM 18/2/8
NAM 18/2/9
NAM 18/2/10
NAM 18/2/11
NAM 18/2/12
0.45 ± 0.08
1.88 ± 0.22
0.91 ± 0.22
2.15 ± 0.42
1.35 ± 0.16
3.83 ± 0.50
1.92 ± 0.38
6.55 ± 0.93
7.10 ± 1.08
6.52 ± 1.21
6.68 ± 0.82
5.53 ± 0.73
NAM 18/7/1
NAM 18/7/3
NAM 18/7/4
NAM 18/7/5
NAM 18/7/6
NAM 18/7/7
0.32 ± 0.03
2.45 ± 0.20
0.89 ± 0.12
11.58 ± 0.95
7.78 ± 1.16
12.10 ± 1.11
NAM 18/4/1
NAM 18/4/3
NAM 18/4/4
NAM 18/4/5
0.68 ± 0.05
0.70 ± 0.06
0.35 ± 0.03
1.04 ± 0.18
Clast imbrication
Floating clasts
Mud clasts
Silt lenses
Clay laminae
Mud cracks
Root print
Bioturbation
Climbing ripples
OSL + Grain size
OSL + Grain size + HM + Petrography
A
Gt
Gp
Gm
St
Sp
Sl
Sm
Smc
Fl
Fm
B
Gmm
Gh
Sh

NAM18/1: This 5 m thick succession records a transition from unconfined to channelised streams, where basal sheetflood deposits (0.6 m thick) are overlain by cross-bedded fluvial conglomerates (1 m). The latter association persists upward as stacked sandy-dominated fluvial infill sequences displaying fining-upward cycles and floodplain caps (1.7 m; Figure 4.6C). Within the top 1.5 m, scoured channel infills are commonly interbedded with unconfined stream associations. Overlying cemented sands indicate sheetflood and proximal floodplain deposits.

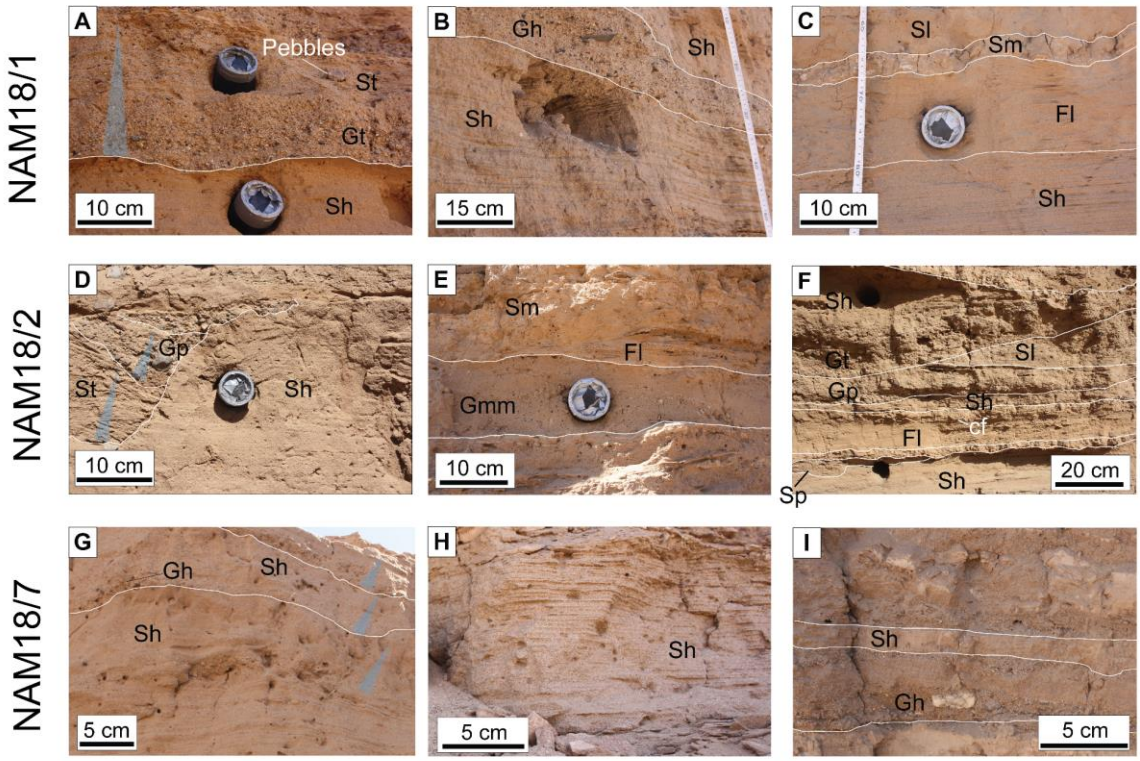

Figure 4.6. Lithofacies examples from sites NAM18/1, NAM18/2, NAM18/7. St: trough, cross-bedded sand, Gt: trough, cross-bedded conglomerates, Sh: horizontally, plane-bedded sand, Gh: horizontally, plane-bedded gravel, Sl: planar, low-angle cross-bedded sands, Sm: massive sand, Fl: ripple to plane laminated sand to silt, Gp: planar, high-angle cross-bedded conglomerates, Gmm: matrix supported gravel, cf: clay flakes.

NAM18/2: The basal portion of this succession contains stacked fining-upward cycles consisting of cross-bedded conglomerates grading into sands (0.5 m thick). This sedimentation is interrupted by horizontally-bedded sands and conglomerates associated with sheetfloods (0.5 m). Channel lag

deposits and scoured basal surfaces show evidence of the erosional nature of the channel infill associations (Figure 4.6D). Throughout the following 1.4 m, NAM18/2 records the establishment of predominantly channel-infill deposition. Abundance of floodplain beds is indicative of lateral channel migration, avulsion, and overbank flooding processes. Interbedded breccia and sheetflood deposits point to occasional progradation of alluvial fan lobes (Figure 4.6F) (Srivastava *et al*., 2006). In the upper 1.25 m of this sequence, ripple- to plain-laminated fine deposits record deposition from suspended load in floodplain settings.

NAM18/4: Sheetflood deposits comprise the basal 0.25 m of this section, and are overlain by cross-bedded to massive and bioturbated sands (1 m thick), developing fining-upward patterns linked to within-channel deposition. Ripple laminated silts cap these deposits as a result of suspended load deposition. Massive clay and silt exhibiting bioturbation and desiccation features characterise the majority of this section, and point to long-term sub-aerial exposure of the floodplain region and periods of water logging (Srivastava *et al*., 2005).

NAM18/7: The basal 1.2 m of this sequence consists of stacked massive cemented and bioturbated sands deposited in proximal overbank regions, in which channel-infill and sheetflood units are interbedded. Above, cross-bedded sands with basal scoured surfaces alternate with ripple laminated and massive muds. These features reflect lateral migration of the channel, and deposition in the surrounding floodplain region during overbank flows. Above, thin sheetfloods are interbedded with pedogenically overprinted floodplain deposits, indicating ephemeral flow conditions. Within the upper 0.5 m, at least 3 cycles grading from gravel to horizontally bedded sands likely represent a higher frequency of flash flood events (Figure 4.6G).

4.3.2.3 Grain size distributions

Sediment grain size distributions are predominantly unimodal very fine to medium sand (Figure 4.7). Samples range from very poorly sorted to moderately well sorted (Table 4.3, full detail in Appendix D Table D1), and are predominantly composed of sand-sized particles (84 % >63 µm) with modal grain sizes ranging from 60 to 600 µm. Cluster analysis details four distinct groups, distinguishable by modal grain size and sorting (Figure 4.7). Both modal grain size (µm) and sorting (σ µm) broadly increase with age, indicating that deposits dating to the early Holocene have predominantly larger grain sizes with more poorly sorted distributions. Canonical correspondence analysis (CCA) shows that grain size is statistically significant in explaining HM and PT variability ($p < 0.001$ and < 0.01 respectively).

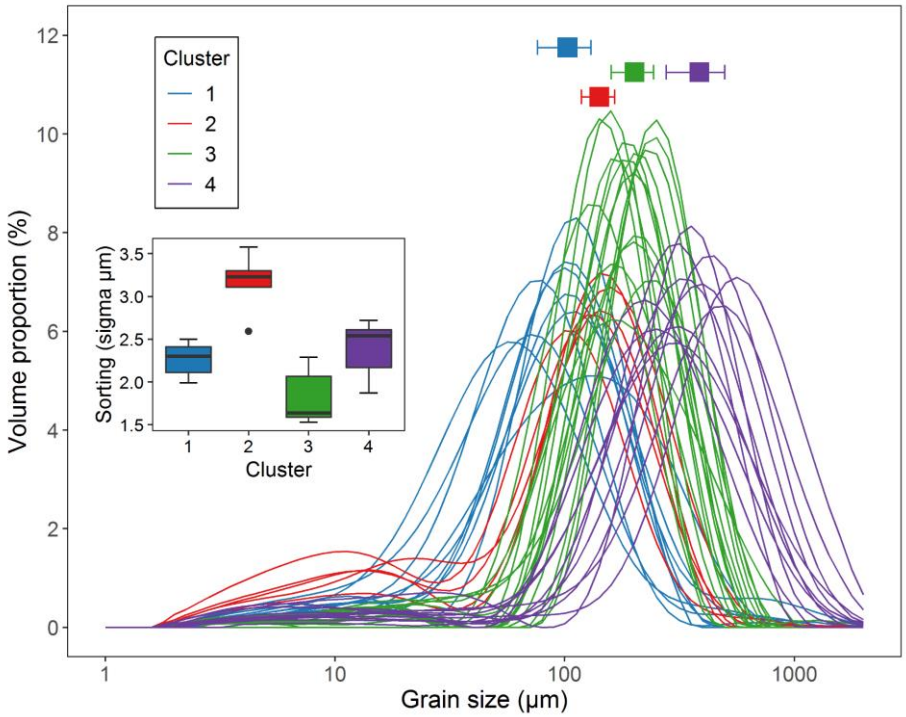

Figure 4.7. Grain size distributions by volume coloured by grain size cluster. Modal grain size is shown above the distributions (following Miall, 2014). Inset shows sorting values by grain size cluster, where higher sorting values reflect more poorly sorted distributions. Cluster analysis was performed using Euclidean distance and hierarchical clustering using Ward's method on data grouped into categories: % very coarse to medium sand (2 mm-250 µm), % fine sand (250 µm-125 µm), % very fine sand (125 µm-63 µm), % very coarse to coarse silt (63 µm-16 µm), % medium to fine silt (16 µm-4 µm), % very fine silt (4 µm-2 µm), % clay (<2 µm). Modal grain size and number of samples in each cluster: cluster 1: 103 µm (9 samples); cluster 2: 142 µm (5 samples); cluster 3: 202 µm (16 samples); cluster 4: 387 µm (11 samples).

Table 4.3. Results of grain size analysis: modal grain size, sorting, skew, and kurtosis. Grain size parameters calculated according to Folk and Ward (1957). All data quoted to 1 decimal place. * Sorting (σ μm): very poorly sorted (VPS), poorly sorted (PS), moderately sorted (MS), moderately well sorted (MWS), well sorted (WS). ** Skewness (Sk μm): symmetrical (S), finely skewed (FS), very finely skewed (VFS). *** Kurtosis (K μm): mesokurtic (M), leptokurtic (L), very leptokurtic (VL). See Figure 4.7 for graphical illustration of grain size distributions.

Sample	Depth	Modal grain size (μm)	Sorting *	Skewness **	Kurtosis ***
NAM18/1/1	0.05	212.2	2.2 (PS)	-0.3 (FS)	1.6 (VL)
NAM18/1/2	0.25	133.9	3.3 (VPS)	-0.5 VFS	1.4 (VL)
NAM18/1/4	0.85	336.3	2.0 (MS)	-0.1 (S)	1.1 (M)
NAM18/1/5	1.05	189.1	1.6 (MWS)	-0.1 (S)	1.0 (M)
NAM18/1/6	1.35	267.2	1.6 (MWS)	0.00 (S)	1.0 (M)
NAM18/1/7	1.95	475.1	1.9 (MS)	-0.1 (S)	1.0 (M)
NAM18/1/8	2.30	150.2	3.2 (VPS)	-0.5 (VFS)	1.6 (VL)
NAM18/1/9	2.45	119.3	2.1 (PS)	-0.3 (FS)	1.6 (VL)
NAM18/1/10	3.00	212.2	1.6 (MWS)	-0.1 (S)	1.0 (M)
NAM18/1/11	4.60	377.4	2.7 (PS)	-0.4 (VFS)	2.2 (VL)
NAM18/1/12	5.00	533.	2.5 (PS)	-0.3 (FS)	1.5 (L)
NAM18/2/1	0.30	150.2	2.4 (PS)	-0.1 (FS)	1.0 (L)
NAM18/2/2	0.70	133.9	1.8 (MS)	-0.1 (FS)	1. 2 (L)
NAM18/2/3	1.30	267.2	1.6 (MWS)	-0.0 (S)	1.0 (M)
NAM18/2/4	1.60	212.2	1.7 (MS)	-0.1 (S)	1.0 (M)
NAM18/2/5	1.85	168.6	2.6 (PS)	-0.3 (VFS)	1.7 (VL)
NAM18/2/6	2.15	168.6	1.6 (MWS)	-0.1 (FS)	1.1 (M)
NAM18/2/7	2.85	150.2	1.5 (MWS)	0.0 (S)	1.0 (M)
NAM18/2/8	3.30	336.3	2.6 (PS)	-0.4 (VFS)	2.1 (VL)
NAM18/2/9	3.75	106.4	3.6 VPS)	-0.5 (VFS)	1.0 (L)
NAM18/2/10	3.90	267.2	2.4 (PS)	-0.2 (FS)	1.3 (L)
NAM18/2/11	4.15	336.3	2.6 (PS)	-0.2 (FS)	1.5 (L)
NAM18/2/12	4.70	336.3	2.6 (PS)	-0.2 (FS)	1.3 (L)
NAM18/3/1	1.50	189.1	1.6 (MWS)	-0.1 (S)	1.0 (M)
NAM18/3/2	1.50	106.4	2.1 (PS)	-0.2 (FS)	1.3 (L)
NAM18/4/1	0.40	59.8	2.4 (PS)	-0.1 (S)	1.2 (L)
NAM18/4/3	1.35	75.3	2.5 (PS)	-0.3 (VFS)	1.2 (VL)
NAM18/4/4	1.80	168.6	2.00 (MS)	-0.3 (FS)	1.8 (VL)
NAM18/4/5	1.95	423.4	2.1 (PS)	-0.2 (FS)	1.2 (L)
NAM18/5/1	0.25	267.2	2.3 (PS)	-0.3 (FS)	1.4 (L)
NAM18/5/2	0.50	150.2	3.1 (VPS)	-0.5 (VFS)	1.2 (VL)
NAM18/6/1	0.85	238.1	1.6 (MWS)	-0.1 (S)	1.0 (M)
NAM18/6/2	3.15	598.1	2.3 (PS)	-0.2 (FS)	1.5 (L)
NAM18/7/1	0.50	168.6	2.2 (PS)	-0.3 (FS)	1.4 (L)
NAM18/7/3	1.20	84.5	2.1 (PS)	-0.2 (FS)	1.2 (L)
NAM18/7/4	1.50	119.3	2.3 (PS)	-0.2 (FS)	1.2 (L)
NAM18/7/5	2.45	212.2	2.0 (PS)	-0.2 (FS)	1.3 (L)
NAM18/7/6	2.85	168.6	2.1 (PS)	-0.1 (S)	1.1 (M)
NAM18/7/7	3.65	106.4	2.4 (PS)	-0.1 (S)	1.5 (L)

NAM18/8/1	1.35	106.4	2.0 (MS)	-0.2 (FS)	1.2 (L)
NAM18/8/2	1.65	94.8	2.5 (PS)	-0.2 (FS)	1.1 (M)
NAM18/9/1	1.30	238.1	2.7 (PS)	-0.3 (FS)	1.8 (VL)

4.3.2.4 Sand composition

Following the Dickinson point count classification scheme, the framework components of the PT assemblage comprise 38.1-52.9 % quartz, of which on average 67.2 % is monocrystalline (Qm), 0.9 % is in plutonic rock fragments (Rg), 3.5 % is in metamorphic fragments (Rm), and 22.9 % is composite (Qc). Samples contain 33-42.8 % feldspar, of which on average 88.9 % is monocrystalline (KF or P), 7.1 % is in Rg, 3.2 % is in Rm, and 0.6 % is in volcanic fragments (Rv). Samples comprise 3.6-13.7 % heavy minerals (HM), 0-6 % mica and 1.7-8 % lithic fragments. According to the classification of Pettijohn, the relative proportion of Rg, Rv, and Rm rock fragments (including lithic fragments) is 43.9 %, 15.3 %, and 40.8 % respectively (Figures 4.8, 4.9, 4.10, Table 4.4). The contribution of rock fragments to the PT assemblage is generally higher in coarser grained samples.

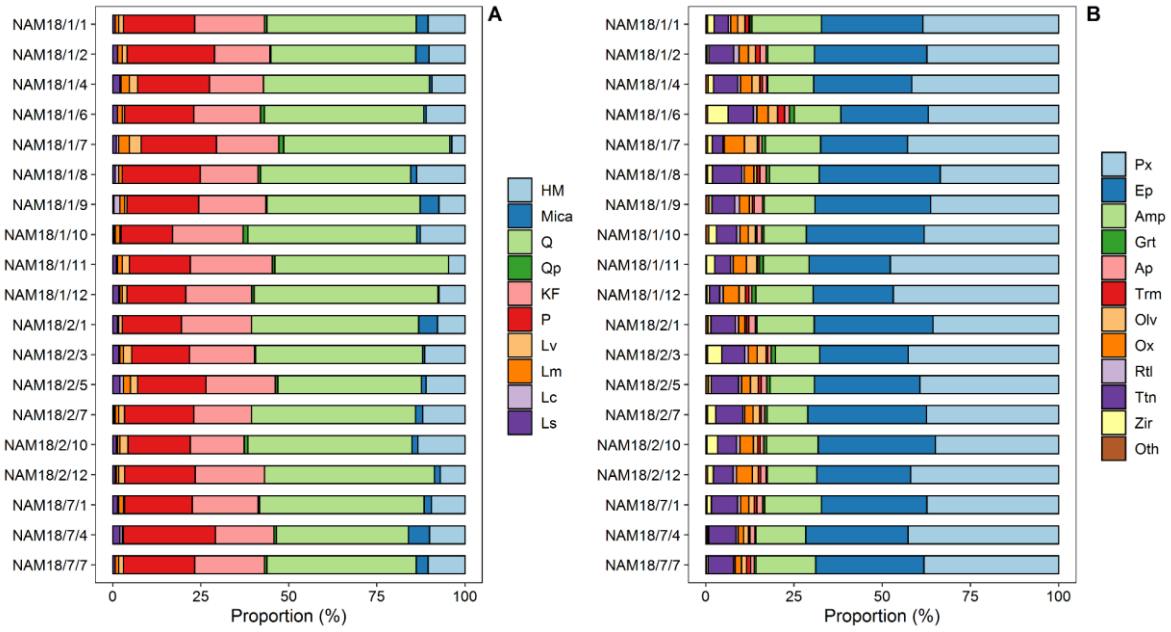

Figure 4.8. Petrographic **(A)** and heavy mineral **(B)** assemblages. **A)** Petrographic assemblage following Dickinson: heavy minerals (HM), mica, quartz (Q), polycrystalline quartz (Qp), K-felspar (KF), plagioclase (P), volcanic lithics (Lv), metamorphic lithics (Lm), carbonate lithics (Lc), sedimentary lithics (Ls). **B)** Heavy mineral assemblage: pyroxene (Px), epidote (Ep), amphibole

(Amp), garnet (Grt), apatite (Ap), tourmaline (Trm), olivine (Olv), oxides (Ox), rutile (Rtl), titanite (Ttn), zircon (Zir), other (Oth). Samples are listed in stratigraphic order by site.

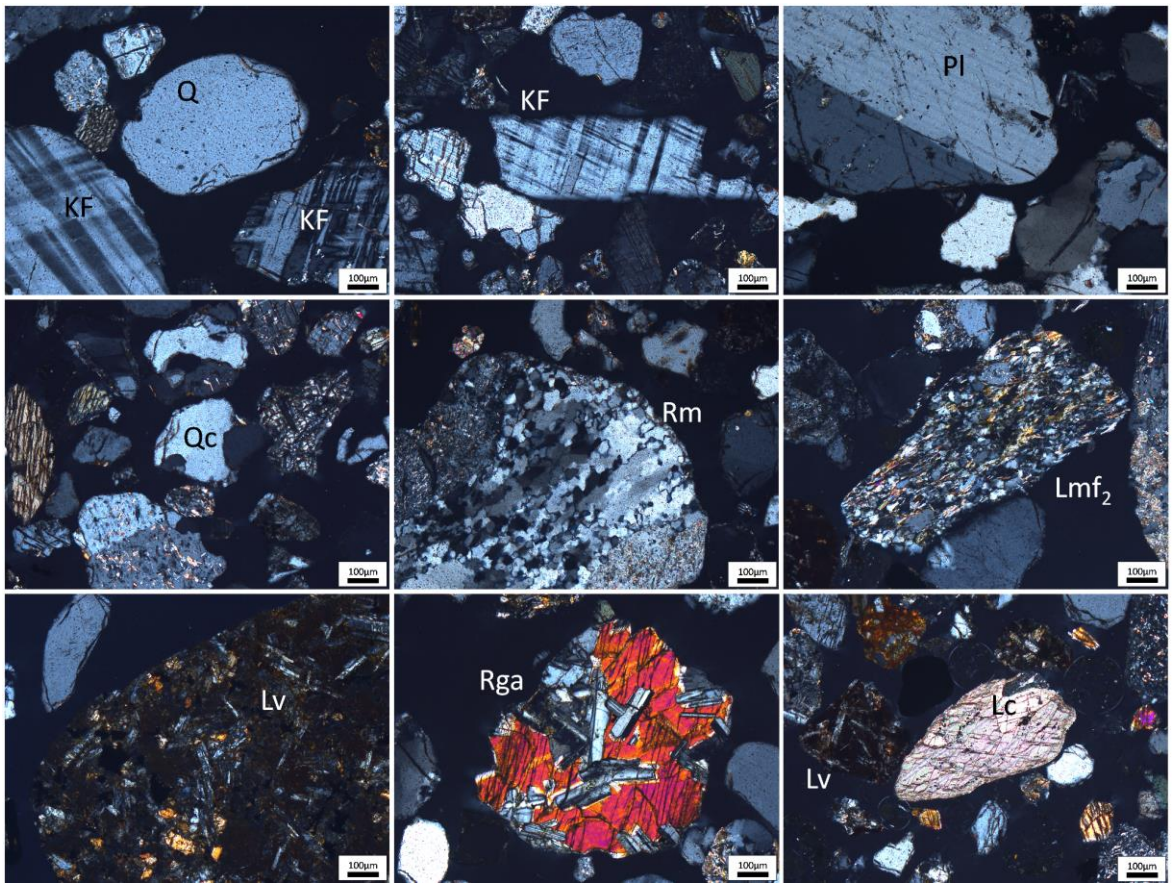

Figure 4.9. Petrography of Huab sands under cross-polarised light. Quartz (Q), K-feldspar (KF), plagioclase (P), composite quartz (Qc), metamorphic rock fragment (Rm), low grade metamorphic lithic fragment (Lmf_2; Garzanti and Vezzoli, 2003), volcanic rock fragment (Lv), plutonic rock fragment (Rga; gabbro), carbonate lithic (Lc). Scale bar = 100 µm for all images.

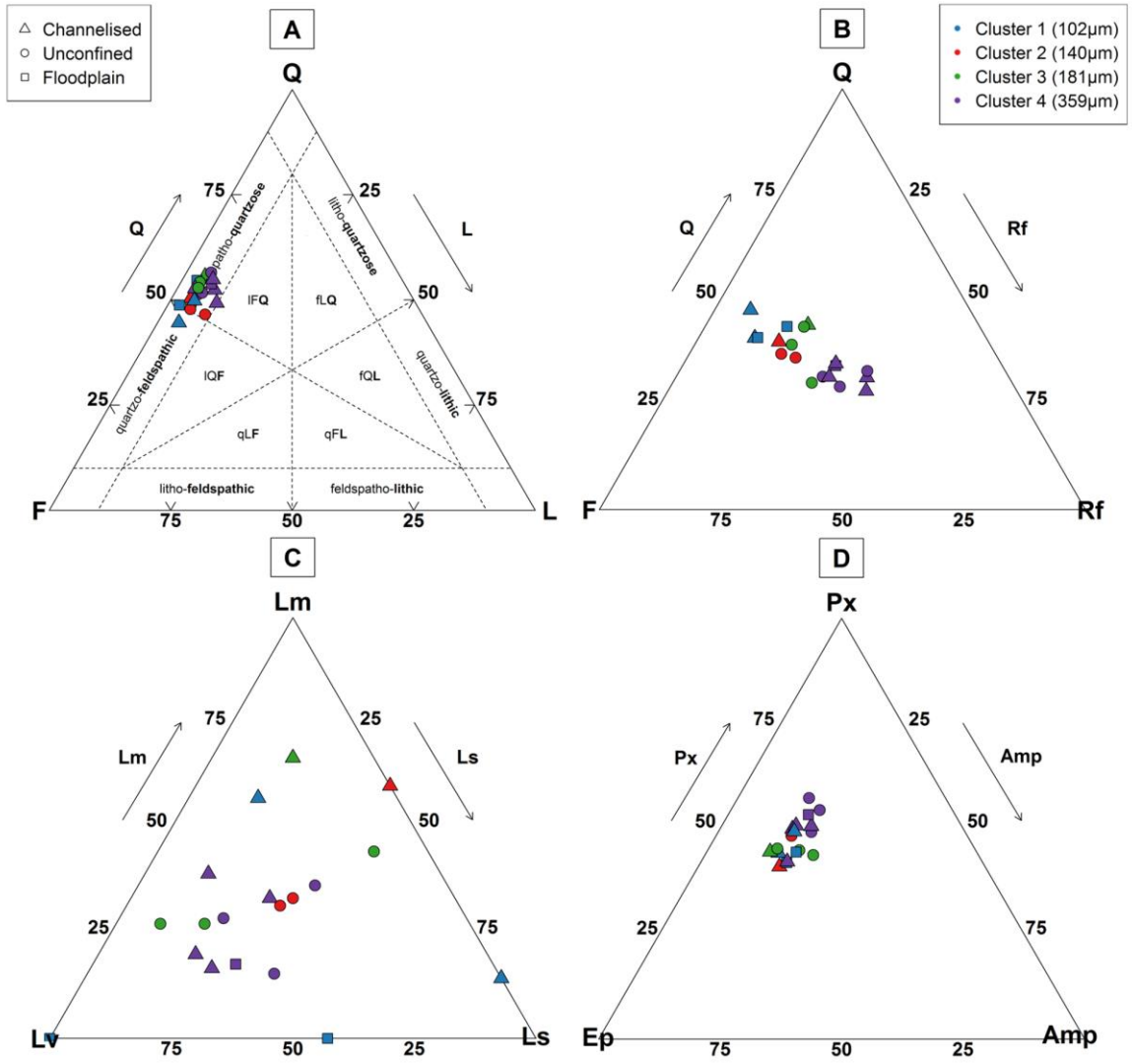

Figure 4.10. Ternary diagrams for Huab petrographic and heavy mineral datasets. Within the litofacies associations, channelised lithofacies are differentiated from floodplain deposits here. A) QFL: quartz, feldspar, lithic fragments (Dickinson, 1985; Garzanti, 2018), B) QFRf: quartz, feldspar, rock fragments (Pettijohn *et al*., 1987), C) LmLvLs: low-grade metamorphic, volcanic and sedimentary lithic fragments, D) PxEpAmp: pyroxene, epidote, amphibole. Symbols are coloured by the grain size cluster that the sample belongs to. Average modal grain sizes increase among grain size clusters. Cluster 1 (blue): 102 µm, cluster 2 (red): 140 µm, cluster 3 (green): 181 µm, cluster 4 (purple): 359 µm. See Figure 4.7 for characteristics of samples within each cluster. The shape of the symbol reflects the lithofacies association.

			Sample (NAM18/)																	
			1/1	**1/2**	**1/4**	**1/6**	**1/7**	**1/8**	**1/9**	**1/10**	**1/11**	**1/12**	**2/1**	**2/3**	**2/5**	**2/7**	**2/10**	**2/12**	**7/1**	**7/4**	**7/7**
Grain size		µm	212	134	336	267	475	150	119	212	377	533	150	267	169	150	267	336	169	119	106
Ternary Diagrams (%)	**QFL**	Q	49.2	47.8	52.4	51.3	49.3	50.4	55.6	51.7	56.5	49.8	54.7	53.8	46.6	54.3	54.9	52.7	52.9	44.6	49.0
		F	46.5	47.0	39.8	43.8	40.9	45.6	40.2	42.7	38.4	45.2	42.2	39.7	44.7	41.9	38.8	43.6	42.9	51.0	49.0
		L	4.3	5.1	7.8	4.9	9.8	4.0	4.2	5.6	5.1	5.0	3.1	6.5	8.8	3.9	6.3	3.7	4.2	4.4	2.0
	QFRf	Q	46.2	44.0	46.8	46.7	44.5	48.4	54.4	48.3	49.6	49.6	52.3	49.1	44.3	52.9	50.0	47.7	51.0	44.0	46.6
		F	41.2	44.0	29.1	38.2	30.7	42.6	35.0	35.8	28.2	44.3	39.1	34.1	40.9	36.0	33.7	36.6	40.6	47.2	46.2
		Rf	12.6	12.0	24.1	15.1	24.8	9.0	10.6	16.0	22.2	6.1	8.5	16.9	14.8	11.1	16.3	15.8	8.4	8.7	7.2
	RgRvRm	Rg	41.4	34.6	48.3	50.0	38.7	37.5	68.2	37.5	40.7	33.3	46.7	31.6	33.3	55.6	42.9	41.0	43.8	66.7	42.9
		Rv	20.7	15.4	13.3	8.8	17.7	0.0	4.5	17.5	11.1	22.2	20.0	23.7	25.9	25.9	20.0	15.4	6.3	0.0	21.4
		Rm	37.9	50.0	38.3	41.2	43.5	62.5	27.3	45.0	48.1	44.4	33.3	44.7	40.7	18.5	37.1	43.6	50.0	33.3	35.7
Framework components (% of 300 grains)		Q	26.6	32.7	29.1	28.7	27.1	33.9	38.3	28.0	31.1	40.8	37.4	30.5	31.4	37.7	30.3	29.1	34.8	34.1	33.7
		Qc	14.1	6.1	14.4	13.7	16.1	7.7	9.3	18.3	16.1	2.7	8.1	13.4	7.7	8.3	13.7	15.4	10.6	3	5.3
		Qp	0.7	0.3	0	1	1.3	0.7	1.3	0.7	0.7	0.3	0	0.3	0.7	0	1	0	0.3	0.7	0
		Q in RF	1.7	2.4	3.7	3.0	4.0	1.0	0.3	3.0	5.0	0.0	2.0	3.4	1.7	0.7	2.7	3.7	1.4	0.3	1.0
		KF	18.2	15.0	13.0	18.0	14.4	15.8	18.3	21.3	15.4	18.7	18.9	17.1	18.1	15.7	14.0	17.4	17.7	14.7	17.7
		KF in RF	1.7	0.7	2.3	1.0	3.3	0.7	1.7	2.0	3.3	0.3	1.0	1.3	1.7	0.7	1.3	2.3	1.0	2.0	0.3
		P	18.2	23.8	14.0	16.7	15.4	20.8	12.3	13.0	11.4	20.1	15.2	13.4	18.1	15.7	15.7	16.7	18.4	25.1	21.0
		P in RF	2.0	1.0	6.4	3.0	6.0	1.3	2.3	4.3	5.4	0.3	1.7	3.0	1.3	4.0	2.0	3.3	0.7	1.0	1.0
		HM	8.8	8.5	6.4	9.0	2.3	12.4	11.3	4.0	5.0	7.0	7.7	9.7	10.4	11.0	10.3	5.0	8.9	9.7	8.7
		HM in RF	1.7	1.7	3.0	2.0	1.3	1.3	1.3	0.7	2.3	0.3	0.0	1.7	0.7	1.0	3.0	2.0	0.7	0.3	1.7
		M	3.0	3.4	0.7	0.3	0.7	1.7	1.0	0.0	0.0	5.4	5.4	0.7	1.3	2.0	1.7	1.7	2.0	6.0	5.7
		M in RF	0.3	0.3	0.0	0.3	0.0	0.0	0.0	0.0	0.3	0.0	0.0	0.0	0.0	0.0	0.0	0.0	0.0	0.0	0.3
		Lv	1.3	1.4	2.3	0.7	3.3	0.0	0.3	2.0	1.3	0.7	1.0	2.3	2.0	1.7	2.3	1.7	0.3	0.0	0.7
		Lm	1.0	1.4	2.3	1.3	3.0	1.0	1.3	1.3	0.7	1.3	0.0	1.0	2.0	1.0	0.7	0.7	1.4	0.3	0.0
		Lc	0.0	0.0	0.3	0.0	0.7	1.0	0.3	0.3	0.3	1.7	0.3	0.3	1.0	0.3	0.3	0.3	0.3	0.7	1.0
		Ls	0.7	1.4	2.0	1.3	1.0	0.7	0.3	1.0	1.7	0.3	1.3	1.7	2.0	0.3	1.0	0.7	1.4	2.0	0.0

Table 4.4. Petrographic assemblage of the Huab valley fill samples. Ternary diagrams values recalculated to 100 % and framework grains quoted as % of 300 grains. µm = modal grain size in µm. QFL (Garzanti, 2018): total quartz (Q), total feldspar (F) and lithics (L <63 µm). QFRf (Pettijohn *et al*., 1987): quartz, feldspar, and rock fragments (>63 µm). Framework components: monomineralic quartz (Q), composite quartz (Qc), polycrystalline quartz (Qp), quartz in rock fragments (Q in RF), monomineralic K-feldspar (KF), K-feldspar in rock fragments (KF in RF), monomineralic plagioclase (P), plagioclase in rock fragments (P in RF), monomineralic heavy minerals (HM; >2.9 g cm^{-3}), heavy mineral in rock fragments (HM in RF), monomineralic mica (M), mica in rock fragments (M in RF), volcanic lithics (Lv), low-grade metamorphic lithics (Lm), extrabasinal carbonates (Lc), sedimentary lithics (Ls). Intrabasinal carbonate and mud clasts were counted but excluded from recalculation. Samples are listed horizontally in stratigraphic order by site.

Samples have predominantly "very rich" heavy mineral concentrations (10 ≤ HMC < 20) as a volume percentage of the total sample (Garzanti and Ando, 2007). HM assemblages are dominated by pyroxene (33-47 %), epidote (22-34 %) and amphibole (11-19 %), with a lower occurrence of titanite (~6 %), oxides (~3 %; ilmenite, hematite, magnetite), olivine (~2 %), apatite (~1 %), rutile (~1 %), tourmaline (~1 %), garnet (<1 %), anatase (<1 %), and zircon (1-6 %) (Figure 4.8). Within the HM fraction, these samples contain on average 7 % ultradense minerals (>3.80 g cm^{-3}), and 16 % lower density minerals (2.9-3.20 g cm^{-3}). Across the dataset, there is a strong negative correlation between pyroxene and epidote (r^2 = 0.71, p <0.001), and a weaker but still significant positive correlation amongst pyroxene and olivine (r^2 = 0.36, p <0.01) (Table 4.5, Figure 4.10). Coarser grain samples are enriched in oxides, olivine, garnet, zircon and pyroxene, and finer grain samples are depleted in these minerals.

Table 4.5. Heavy mineral assemblage of the Huab valley fill samples. Results quoted as percentage of total grains identified. Apatite (Ap), amphibole (Amp), epidote (Ep), pyroxene (Px), garnet (Grt), olivine (Olv), oxides (Ox), rutile (Rtl), titanite (Ttn), tourmaline (Trm), zircon (Zir), other. Samples are listed in stratigraphic order by site. See Appendix D Table D2 for full heavy mineral assemblage from each grain size measured (30-63 µm, 63-125 µm, 125-250 µm).

Sample	Ap	Amp	Ep	Grt	Px	Olv	Ox	Rtl	Ttn	Trm	Zir	Other
NAM18/1/1	0.3	19.7	28.7	0.6	38.5	2.0	2.0	0.7	4.0	1.1	1.9	0.1
NAM18/1/2	1.7	13.2	31.9	0.5	37.4	1.9	2.7	1.5	7.1	1.3	0.5	0.0
NAM18/1/4	1.2	13.0	27.9	0.4	41.6	2.2	3.3	0.8	6.8	0.7	1.5	0.0
NAM18/1/6	1.3	13.2	24.8	1.4	37.0	2.6	3.2	1.0	7.2	2.0	5.8	0.0
NAM18/1/7	0.9	15.7	24.6	1.0	42.8	3.6	5.7	0.4	3.1	0.5	1.2	0.2
NAM18/1/8	1.8	14.1	34.2	1.0	33.6	0.9	2.7	0.7	8.3	0.8	1.4	0.0
NAM18/1/9	2.3	14.4	32.8	0.5	36.3	0.8	2.8	1.3	6.5	0.6	0.8	0.0
NAM18/1/10	1.4	12.1	33.4	0.6	38.1	2.0	2.3	0.9	5.7	0.5	2.2	0.2
NAM18/1/11	0.5	13.0	23.0	1.1	47.7	3.0	3.8	0.7	4.5	0.2	2.3	0.0
NAM18/1/12	0.8	16.2	22.8	1.1	46.9	1.9	4.5	0.9	2.9	0.9	0.7	0.0
NAM18/2/1	1.8	16.2	33.7	0.5	35.6	0.5	1.8	0.9	6.9	0.6	0.9	0.0
NAM18/2/3	0.9	12.6	25.1	1.3	42.6	2.5	2.6	0.9	6.5	0.6	4.1	0.1
NAM18/2/5	1.6	12.5	29.9	1.0	39.4	2.2	2.5	0.8	7.8	0.8	0.8	0.0
NAM18/2/7	1.0	11.5	33.7	0.7	37.4	1.8	2.4	0.6	7.7	0.5	2.3	0.0
NAM18/2/10	1.0	14.6	33.3	0.8	34.9	1.2	3.8	1.0	5.4	0.7	2.9	0.1
NAM18/2/12	1.5	14.0	26.7	0.4	41.9	1.7	4.5	0.9	5.7	0.7	1.6	0.0
NAM18/7/1	1.7	16.1	29.9	0.5	37.4	1.5	2.3	0.9	7.4	0.7	1.2	0.0
NAM18/7/4	1.4	14.1	29.0	0.3	42.7	1.3	1.6	0.6	7.7	0.4	0.4	0.1
NAM18/7/7	1.0	16.9	30.7	0.5	38.2	1.4	1.8	0.5	7.2	1.1	0.4	0.0

4.4. Interpretation

The sedimentology, composition, and chronology of the Huab valley fill samples is discussed here in terms of: 1) provenance and drainage lithologies; 2) stratigraphic patterns and fluvial processes; and 3) the link between compositions and process changes. The Huab fluvial record will then be considered in the context of existing fluvial archives from the Skeleton Coast in the Discussion.

4.4.1. Provenance: compositions and drainage lithologies

At present, around two thirds of the sand within the terminal tract of the Huab River (1km from the coast) is windblown from the coast (Garzanti *et al*., 2014). The Skeleton Coast valley fill site, however, is far enough inland (~20 km) and separated from the coast by uplands through which

the channel passes to not be significantly influenced by sand contamination from the coast throughout the studied time interval. The petrographic assemblage therefore dominantly reflects sourcing from the Huab Basin. Mafic igneous rock fragments within Huab PT assemblages include lathwork volcanics and plutonic (gabbro) rock fragments. This indicates input from the basalt lavas of the Etendeka Plateau, and the gabbro-dolerite sills within the Huab Basin respectively (Figure 4.2). Clinopyroxene in the HM dataset is likely sourced from both the Etendeka basalts and gabbro sills, yet olivine is only from the gabbro sills (Duncan *et al*., 1989; Garzanti *et al*., 2014; 2021). There is a close association between the occurrence of pyroxene and olivine, and when these heavy minerals increase, gabbro and volcanic fragments increase in the PT dataset. Given these relationships, gabbro sills as a source of olivine are a characteristic component of the Huab's drainage lithology, where records from Namibian rivers show that only the Huab and Ugab river assemblages contain olivine (Garzanti *et al*., 2012; 2014).

Medium-high grade metamorphic rock fragments and low-medium grade lithic fragments indicate sourcing from the metamorphic lithologies in the Huab catchment: the Kamanjab Inlier and the Eastern and Northern Zones of the Damara Orogen. A positive trend in occurrence of metamorphic fragments and garnet HM species suggests that garnet is an indicator of drainage from the metamorphic source rocks in the basin. Garnet often occurs as a common mineral in metamorphic rocks (Garzanti and Andò, 2019), and could be derived from the Huab Metamorphic Complex which comprises a range of metamorphic facies, including garnet-muscovite-quartz-feldspar schists (Kleinhanns *et al*., 2015). The Kamanjab Inlier sheds heavy mineral assemblages rich in epidote (Eitel and Zoller, 1996; Eitel *et al*., 2001) and the Damara Orogen is rich in amphibole-epidote-garnet suites (Garzanti *et al*., 2014). Epidote and amphibole are prevalent in the Huab HM assemblage, yet show no trend with occurrence of metamorphic fragments, indicating that these minerals are also sourced from other lithologies in the basin.

Granite rock fragments are recorded in all PT assemblages. These are likely sourced from the Damara granites or the Fransfontein Granite Suite. Granites commonly source epidote, amphibole, and zircon (Dickinson, 2008), but these minerals are also abundant in other lithologies in the Huab Basin, often as larger crystals than in granites, making it challenging to disentangle the granitic source. The heavy mineral assemblage is likely influenced by differences in the fertility of source lithologies, where some are richer in accessory phases (Chew *et al*., 2020; Dickinson, 2008; Malusà *et al*., 2016). Carbonate lithologies have a low fertility of heavy minerals (Garzanti and Andò, 2007; 2019) and the potential for sand generation is also relatively low compared to other lithologies such as crystalline rocks (Arribas and Tortosa, 2003; Caracciolo, 2020), especially in arid climates with limited tectonic forcing (Mack, 1981). Whilst dolomite and limestone source regions are found within the Otavi group within the Damara Supergroup (Prave, 1996) (Figure 4.2), carbonate lithics comprise the smallest contribution to the rock fragment assemblages from the Huab valley fill. Sandstones and shales are found within the Huab Basin as part of the Karoo Supergroup, and are indicated in the presence of sedimentary rock fragments and fine grained lithics in the PT assemblage.

4.4.2. Stratigraphy: fluvial processes

Environmental reconstruction from four stratigraphic sections indicates changes in fluvial depositional environments of the Huab River (Figure 4.5). By interpreting chronological changes in lithofacies occurrence from each site, these records also indicate lateral migration of the fluvial system over time.

In the early Holocene, deposition is recorded on the north-western side of the valley between 12.10 ± 1.11 ka and 9.83 ± 1.62 ka. Ephemeral deposition dominated during this period, with fine grained sediment deposited in proximal overbank settings (Figure 4.5 P1). Throughout the mid Holocene, deposition is preserved most extensively on the south-eastern side of the fill. Particularly, ~2m of

sediment dates to between 7.10 ± 1.08 ka and 5.53 ± 0.73 ka, and is associated with channel infills (Figure 4.5 P3). A clearly defined erosional-bounded channel lag marks the former position of a channel flowing perpendicular to the present-day exposure (similar to Brook *et al.*, 2006). This mid Holocene sequence indicates a period of more permanent river flow and persistent within-channel sedimentation. Corresponding depositional units are not recorded in the north-western sections, suggesting a lateral shift of the main channel position relative to today, or that evidence of deposition has been shredded (Jerolmack and Paola, 2010).

A sedimentary unit in section NAM18/9 dates to 7.81 ± 0.86 ka and is overlain by debris flow deposits indicative of progradation of valley slope fans. Individual clasts within the debris flow are dark coloured angular basalt pebbles. Given the geological contributions discussed above, this likely represents flow from the Etendeka lavas north of the valley. Similarly, fluvial conglomerates are recorded above early Holocene deposits at NAM18/1. Stratigraphic similarities suggest that this unit pre-dates the overlaying mid Holocene channel succession discussed above (Figure 4.5 P2). These conglomerate and breccia beds indicate a period of higher rainfall than the present-day, with increased river flow in the main channel and sediment discharge from the Etendeka locally.

After 4 ka, continuous channel infill deposition with an upward increasing abundance of floodplain deposits is recorded at site NAM18/2 from until to 1.35 ± 0.16 ka (Figure 4.5 P4). This likely reflects higher frequency lateral migration of the Huab River, and sporadic interbedded breccia and sheetflood deposits indicate occasional local sediment input. Similar deposition is also recorded at other sites located in the middle to south-eastern side of the fill, particularly between 1.82 ± 0.32 ka and 1.38 ± 0.13 ka. As with the mid Holocene, sites in the north-west lack sediment from this stratigraphic interval, indicating that sedimentation of the Huab River mostly occurred to the south-east.

Within the last 1 ka, close correspondence between the north-western sites suggests similar deposition of channel deposits. Sedimentary units on the other side of the fill indicate deposition within the alluvial plain region surrounding the main channel. At the constriction at the western edge of the fill, floodplain depositional settings also dominated during the last 1 ka. The upper most units of the studied sites across the fill date to between 0.52 ± 0.13 ka and 0.32 ± 0.03 ka (Figure 4.5 P5). These units record highly variable flow regimes, where unconfined sheetflood beds are interbedded with floodplain associations, indicating flow conditions similar to the present-day.

4.4.3. Combining provenance and process interpretation

By linking compositional data with stratigraphy and chronology, we interpret the propagation of environmental signals through an assessment of drainage dynamics, changes to river flow, and response to climate perturbations. Sediment transfer processes are often discontinuous, and the 'sediment cascade' theory (Burt and Allison, 2010) can be used to understand these processes as pulses from temporary sediment stores (Allen, 2017, Caracciolo *et al*., 2020). Efficiency of particle sorting determines the resulting grain size distribution and compositional assemblages, and can result in inter-sample variability even when provenance remains constant (Caracciolo *et al*., 2012; 2020). Here, sample compositions display a statistically significant grain size control (Figure 4.11). Two main compositional assembalges can be distinguished in the PT and HM biplots as a function of grain size: 1) samples indicating more humid climate conditions in the early to mid Holocene; and 2) those indicating arid conditions in the late Holocene.

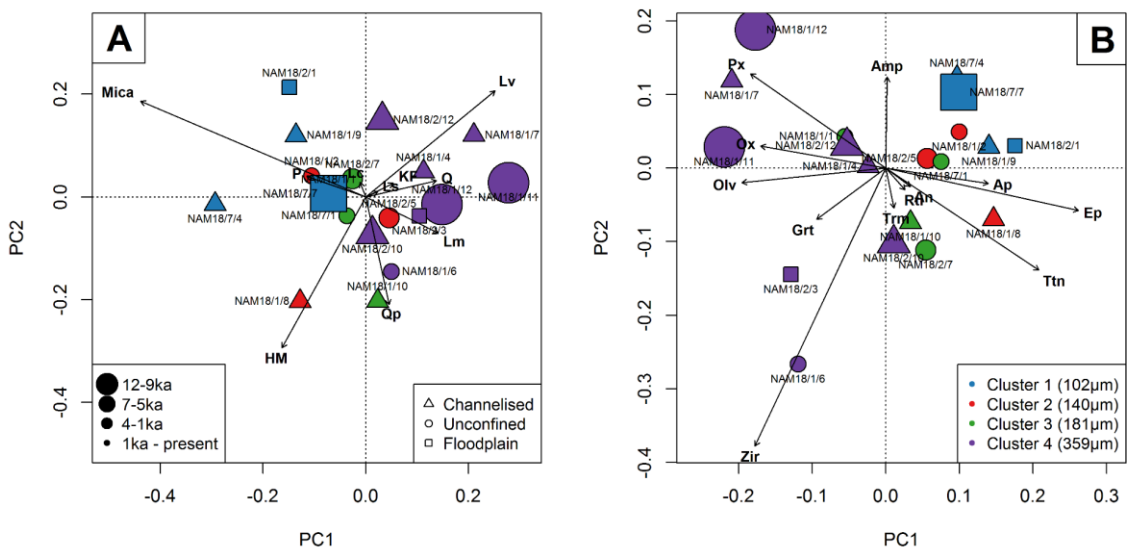

Figure 4.11. Compositional biplots of petrographic and heavy mineral assemblages. Biplots enable a consideration of multivariate observations (points) and variables (rays) (Gabriel, 1971). The length of the ray is proportional to variability of the species, and the angle between rays details correlation between different species: 0˚, 90˚ and 180˚ correspond to correlation, no correlation and inverse correlation respectively. Symbols are coloured by the grain size cluster that the sample belongs to. Average modal grain size: cluster 1 (blue) 102 µm, cluster 2 (red) 140 µm, cluster 3 (green) 181 µm, cluster 4 (purple) 359 µm. The shape of the symbol reflects the lithofacies association, and size of symbol reflects the age group (defined by the lithofacies and chronological analysis) where larger symbols are indicative of older samples. **A)** Petrographic compositional biplot following Dickinson. Quartz (Q), polycrystalline quartz (Qp), K-felspar (KF), Plagioclase (P), heavy minerals (HM), metamorphic lithics (Lm), carbonate lithics (Lc), sedimentary lithics (Ls), volcanic lithics (Lv). **B)** Heavy mineral compositional biplot. Amphibole (Amp), anatase (An), apatite (Ap), epidote (Ep), garnet (Grt), olivine (Olv), oxides (Ox), pyroxene (Px), rutile (Rtl), tourmaline (Trm), titanite (Ttn), zircon (Zir). Grain size is statistically significant in explaining variability of both HM and datasets ($p < 0.01$). Two associations are identified in this plot: 1) those in the purple (largest grain size cluster) in the positive axis of PC1 in plot A and negative axis of PC1 in plot B, and 2) those in the red, blue and orange (smallest grain size clusters) in the opposite axis to the first association. Within the oldest age group (12-9 ka), a distinct difference in grain size can be seen for NAM18/7/7, and can be in part explained by the lithofacies where this sample is from a floodplain deposit, whereas the other samples of this age are unconfined flash flood deposits with coarser grain sizes.

The first assemblage is characterised by the occurrence of lithic and rock fragments, particularly dense minerals, and corresponds to the coarsest grain size cluster (Figure 4.11). This assemblage is indicative of higher sediment transfer due to higher water discharge. Selective transport processes typically preferentially deposit the coarsest grain sizes in upstream temporary sediment stores (Burt and Allison, 2010; Paola *et al*., 1992; Toro-escobar *et al*.,1997), but during more humid periods, the coarse grains are re-mobilised and moved downstream (Allen, 2017). The occurrence of volcanic, sedimentary, and metamorphic fragments in particular indicates activation of sediment stores across the catchment. Several of these units were deposited under a channelised fluvial regime. The oldest samples NAM18/1/11-12 and NAM18/2/10-12 are all found within this group, and Figure 4.12 shows larger and more poorly sorted grain size assemblages in the early to mid Holocene compared to the late Holocene. Poor grain-size sorting is typical of more channelised deposits (Henares *et al*., 2020), where flow is confined and turbulence increases. The HM assemblage shows an enrichment of high density species (e.g. garnet, zircon, oxides), indicating that minerals were less sorted in relation to their size and density, as compared to tractive currents (Malusà *et al*., 2016). Through steep rises in peak discharge, processes of scour and fill result in mobilisation and re-deposition of floodplain and within-channel deposits (Henares *et al*., 2020). Together, these findings indicate that conditions in the early to mid Holocene were more humid than today, with an increased efficiency of the hydrological regime. Sheetflood deposits here also indicate that events of rapid increases in precipitation occurred, which led to high discharge events and high supply of sediment from the surrounding catchment regions (Henares *et al*., 2020). The presence of olivine (a mineral that is susceptible to weathering in humid climates; Macias & Chesworth, 1992) in all samples here indicates that whilst river flow occurred under a climate more humid than today, the climate shift likely occurred on a scale from hyper-arid to arid.

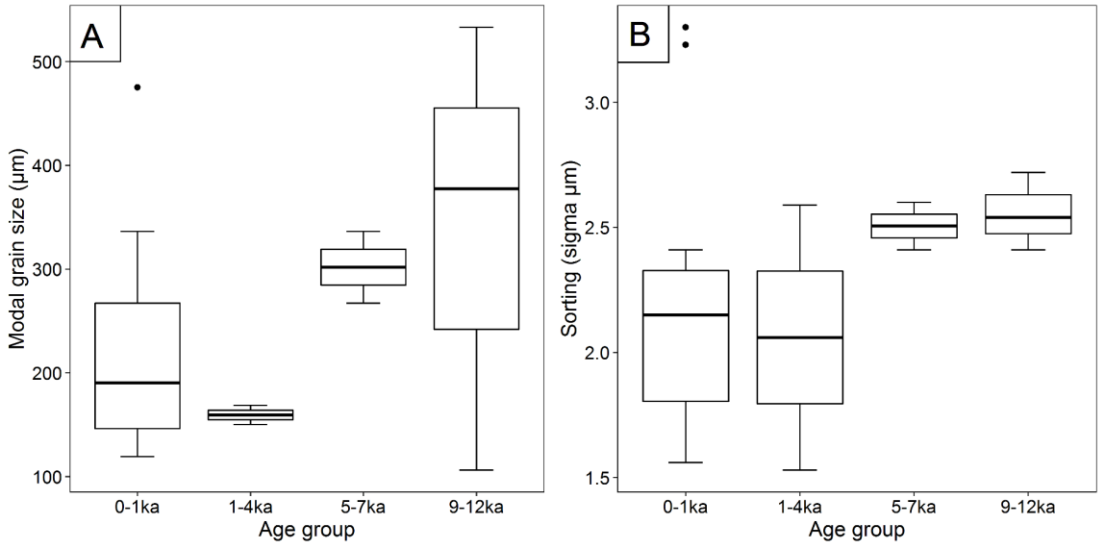

Figure 4.12. Box and Whisker plots of **A)** modal grain size (µm) by age group, and **B)** sorting (σ µm) by age group, where higher sorting values reflect more poorly sorted distributions. Moderately well sorted: 1.41-1.62 σ µm, moderately sorted: 1.62-2.00 σ µm, poorly sorted: 2.00-4.00 σ µm. Age groups were determined through analysis of lithofacies and luminescence chronology in Section 4.2.: 0-1 ka, 1-4 ka, 5-7 ka, 9-12 ka. This figure includes data from only the subset of samples analysed for petrography and heavy minerals to enable direct comparison with Figure 4.11, but the trend is consistent if the full dataset is used. The large spread in modal grain size for age group 9-12 ka is influenced by the fine grain size of the floodplain deposit NAM18/7/7 discussed in Figure 4.11.

Conversely, the second compositional assemblage displays a strong affinity to monomineralic grains, is enriched in lower density HM polymorphs (e.g. amphibole, epidote), and has a smaller average grain size (Figure 4.11). These samples were deposited predominantly within the last 4 ka. These samples indicate more limited sediment transport through the sediment cascade during the late Holocene, where coarser sediments were retained in upstream sediment stores during drier periods with less persistent fluvial activity. Several of these units have unconfined lithofacies associations and the grain size distribution is more moderately sorted than during the early to mid Holocene (Figure 4.12). Here, the HM data suggests that with a narrower grain size range, there was greater consistency in the density of minerals deposited. In unconfined streams, fluvial energy

is dispersed, and traction load transport commonly sorts minerals in relation to their grain size, shape, and density (Komar, 2007; Malusà *et al*., 2016; Schuiling *et al*., 1985).

Chemical weathering rates in dryland Namibia are slow (Garzanti *et al.*, 2021; Viles, 2011), and so changes in sediment composition are more likely to have resulted from physical processes. Increased collisions and more efficient abrasion from geomorphic processes would have resulted in more effective partitioning of sand particles (Cleary and Conolly, 1972; Fontana *et al*., 2003; Harrell and Blatt, 1978). It is also possible that an increase in monocrystalline grains could be a signal from local aeolian input or local aeolian reworking under a more arid climate (Bullard *et al*., 2004; Refaat and Hamdan, 2015). Aeolian-fluvial interactions are greater in a hyper-arid climates, where periods of low precipitation and more ephemeral intermittent flow allow for aeolian processes to transport and deposit sediment across dry surfaces (Henares *et al*., 2020; Liu and Coulthard, 2015; Muhs *et al*., 2000; Xu *et al*., 2006). Chronology from the base of a nebkha dune on the fill surface indicates concurrent fluvial and aeolian deposition within the last 1 ka. Together, compositional data indicates lower precipitation across the catchment within a more arid climate in the late Holocene, with increased rates of mechanical weathering and reduced efficiency of the hydrological regime.

4.5. Discussion

The Huab sedimentary record details fluvial deposition within the Holocene and compositional analysis suggests a climate control. This study is the first analysis of compositional data to reconstruct propagation of environment signals on Quaternary timescales in Namibia, so direct comparison to other published studies is not possible. Despite this, we can consider the Huab record in the context of other studies that directly infer processes of palaeoflow change; principally those with analysis of lithofacies associations and quantitative palaeohydrological assessments

(sites detailed in Figure 4.1). The full implications for palaeoclimate will be assessed in Walsh *et al*. (in review).

Compositional analysis suggests that humid conditions during the early Holocene resulted in higher water discharge and activation of sediment stores across the catchment. Unconfined stream associations indicate periodic episodes of higher discharge along an ephemeral river as a result of a events of rapid increases in precipitation. Across the Skeleton Coast, unconfined lithofacies associations are also noted in deposits along the Khumib (Srivastava *et al*., 2004) and Hoarusib rivers (Srivastava *et al*., 2005). From 14.2 to 8.1 ka, deposits in the Khumib reflect flashy high energy floods with steep rising hydrographs (Srivastava *et al*., 2004). Similar conditions are interpreted for the Kuiseb, where sediment removal and terrace formation is thought to have occurred through intense flash floods during a climate transition from humid to arid after 15 ka (Srivastava *et al*., 2006). At this time (12.8 to 10.5 ka), the Tsondab River extended 6 km west beyond its contemporary end point in the Namib desert, indicating increased moisture availability than today (Stone *et al*., 2010). Compositional analysis from the Huab sediments suggests that the Huab ephemeral flood events transported coarser grains from sediment stores across the Huab catchment, indicative of higher sediment transport. We interpret this period as being a more competent system and slightly more humid than today, but still arid and within a flash flood, ephemeral regime.

In the mid Holocene (7-5 ka), textural and compositional analysis attests to continued transfer of coarse grains through the sediment cascade, and sedimentological analysis suggests the Huab River flowed within a more channelised confined fluvial system. Together, this indicates a period in which the climate was more humid (but not wet enough for notably enhanced chemical weathering) and conducive to sustained river flow. Between 9-4 ka deposition in the inter-dune areas at the distal end of the Tsauchab River suggests that the Tsauchab was able to penetrate further into the Namib

Desert through higher flow in a well-developed channel under wetter conditions (Brook *et al*., 2006). At this time, rapid deposition is recorded in the Kuiseb in a floodplain environment (9.8-6.3 ka: Bourke *et al*., 2003; ~6 ka: Srivastava *et al*., 2006), following a climate transition from an arid to humid. Incision of the Khumib deposits at 8.1 ka is used to infer a period of enhanced precipitation and greater fluvial capacity (Srivastava *et al*., 2004). At other points in longer late Quaternary records (e.g. at ~44-40 ka and ~29-20 ka in the Hoarusib, Srivastava *et al*., 2005; and 27.7 ka and 20.8-15.6 ka in the Khumib, Srivastava *et al*., 2004), channelised deposits represent a record of seasonal floods in a fluvial system with cohesive river banks. These systems had smoothly rising hydrographs as a result of more sustained rainfall with higher vegetation cover in the catchment (Srivastava *et al*., 2004; 2005). The coarse grained nature of Huab deposits dating to 7 to 5 ka suggest that such sustained fluvial conditions enabled effective transfer of coarser grains from upstream sediment stores.

Dating to the late Holocene, the occurrence of unconfined deposits, lateral migration of depositional sites, greater hydraulic sorting and compositional evidence of a mechanical weathering dominated environment suggests that flow occurred within a more arid climate. The stratigraphic record details two periods: continuous channel infill from 3.83 ka to 1.35 ka on the southern side of the fill, and deposition from 1.03 ka to present on the northern edge, in a similar position to today. Aeolian lithofacies in Tsauchab interdune deposits indicate limited fluvial reach from 5.8 to 0.9 ka (Brook *et al*., 2006). Encroachment of dunes and eastward migration of the river terminal point indicates increased aridity and reduced fluvial capacity (Brook *et al*., 2006). Similarly, the Swakop record shows no large floods between 5.1 ka and 1.28 ka. This either indicates reduced flood frequency, or occurrence of small floods below the threshold of signal preservation (Greenbaum *et al*., 2014). From 0.9 to 0.3 ka, however, interdune and channel facies associations of the Tsauchab reflect a wet phase with higher water availability (Brook *et al*., 2006). Quantitative palaeoflood records identified periods of flood occurrence in the Kuiseb and Swakop rivers over

the last 1.28 ka (Greenbaum *et al*., 2014; Grodek *et al*., 2013). These episodes reflect increased flood frequency rather than increased flood magnitude, and are thought to be associated with higher water availability (Grodek *et al*., 2013; Greenbaum *et al*., 2014). Compositional analysis of the Huab samples shows similar assemblages amongst samples dating to the last millennium, attesting to a consistent flood magnitude throughout this period. The upper unit of site NAM18/7 details cycles of fining upwards successions, likely representing a higher frequency of flash flood events, similar to flash floods recorded today.

4.6. Conclusions

This paper presents a systematic study of textural, compositional, and stratigraphic features to reconstruct propagation of environment signals on Quaternary timescales in a Namibian fluvial system. We interpret textural and compositional signals to reflect changes in river discharge, the capacity of the river to transport grains, and role of mechanical weathering, and interpret the lithostratigraphic sedimentary signal to reflect fluvial process response and change in fluvial style.

This study has characterised the Huab HM and PT assemblage and has identified sourcing from all major lithologies in the basin. In the context of sourcing from lithologies across Namibia, the compositional data shows that gabbro, as a source of olivine, is an important signal from the Huab compared to other fluvial systems. Analysis of the main river styles of the Huab River detail deposition as a result of seasonal flow within a well-defined channel, associated floodplains, and unconfined stream associations. Luminescence dating details channelised deposits predominantly between 7 and 5 ka, and periodic occurrence within the last 4 ka. Between 12 and 9 ka and within the last millennium, unconfined facies associations have been interpreted as flashy ephemeral flood regimes.

Sedimentary units rich in rock fragments and coarse grain sizes dating to the early to mid Holocene are indicative of humid climate conditions in the Huab Basin. Higher precipitation than today increased the efficiency of the hydrological regime throughout the drainage basin and increased the capacity to move coarser grains through the sediment cascade. Lithofacies analysis indicates a period in which the climate was conducive to more permanent river flow. In contrast, samples rich in monocrystalline grains and a lower contribution of rock and lithic fragments during the late Holocene are indicative of a greater mechanical weathering under a more arid climate. Lower precipitation rates across the catchment resulted in less activation of the drainage system and a dominance of more unconfined stream facies associations.

To interpret environmental signals from fluvial sediments as records of climate perturbations, it is important to have a developed understanding of palaeoflow changes. Through analysis of multiple sites and use of a detailed analytical approach, we have reached a nuanced interpretation of fluvial system response on late Quaternary timescales. We highlight the importance of linking environmental signals to depositional and compositional features, and of considering the capacity of rivers to transport sediment in producing assemblages recorded in the stratigraphy. This fine scaled analysis of an ephemeral fluvial system presents a useful approach for reconstructing palaeoenvironmental change from complex sedimentary archives in Namibia's Skeleton Coast, and for research across wider dryland environments.

Chapter 5: Paper 2

Chapter 5: A chronological database assessing the palaeoenvironmental record from fluvial sediments in southwestern Africa

Paper 2: Ella Walsh, Sallie Burrough, David Thomas

Manuscript submitted to *Earth-Science Reviews* on 27/1/22 and re-submitted on 16/6/22 following reviewers' comments.

Abstract

Fluvial sediments preserve evidence of past hydroclimatic regimes and are important but potentially under-utilised indicators of palaeoenvironmental change in drylands. This paper presents a new chronological database of 603 ages from late Quaternary fluvial sediments at 70 sites in southern Africa's western dryland regions. This synthesis assesses the spatial and temporal trends in both the palaeoenvironmental record and the supporting data that underpins these interpretations. We find that topographic and climatic characteristics of river catchments influence the nature of fluvial archive formation and preservation. In particular, channel confinement, legacies of research, and sampling strategies in specific river basins control the sedimentary context and length of documented record available for palaeoenvironmental reconstruction. The age range of dated deposits, and the associated magnitude of chronological uncertainties, influence the temporal range of climate and fluvial variability that can be resolved. Where calendar year uncertainties are small enough, predominantly dating to the last millennium, individual flood *events* and *episodes* within flash flood deposits can be linked to synoptic climate patterns, yet when uncertainties are larger, interpretations are restricted to understanding *phases* of flow regimes.

This paper collates a scattered literature to detail the current state of southwestern Africa's fluvial record and highlights opportunities for future research. We consider controls on fluvial archive interpretation that are pertinent to wider dryland contexts and argue that fluvial records provide useful information for inclusion in regional palaeoenvironmental syntheses. Following a filtering process, quality-assessed chronologies are compiled to establish the combined fluvial history of 22 rivers to consider the response of fluvial systems to hydroclimatic drivers. At the Last Glacial Maximum (24-18 ka), records detail a regionally consistent signal of intermittent to perennial flow in currently ephemeral systems under relatively humid conditions. The mid Holocene (8-4ka) is also characterised by the occurrence of sustained river flow and higher discharge events than present, but with greater spatial variability. Sedimentary archives display evidence of both intermittent flow and extreme flood events within ephemeral regimes, and two rivers, the Hoanib and Molopo, are characterised by reduced fluvial activity. Within the last millennium, flash flood regimes within an arid to hyper-arid climate were established with coherence in the timing of flood frequency variations recorded between catchments.

5.1. Introduction

Drylands can support extensive fluvial systems (Jacobson *et al*., 1995; Nanson *et al*., 2002; Tooth, 2000; Tooth and Nanson, 2011; Tooth, 2013). While some are perennial, such as the Orange River in South Africa, the flow of many dryland rivers today is intermittent or ephemeral (Messager *et al*., 2021). Fluvial sedimentary archives attest to the response of rivers to past hydroclimatic regimes (Bull, 1991; Reid, 1994): in drylands these may display evidence of greater fluvial activity or even perennial flow in rivers that are currently ephemeral. Water is a powerful erosive agent (Wainwright and Bracken, 2011) and plays a key role in shaping the geomorphological landscape (Grenfell and Grenfell, 2021; Reid and Frostick, 1997; Tooth and Nanson, 2011; Tooth, 2013). Processes of sediment transfer propagate signals of hydrological response to climate conditions

(Tofelde *et al*., 2021) and these signals are ultimately recorded in sediment stores (Allen, 2017; Caracciolo, 2020; Romans *et al*., 2016).

Geomorphological records are extensive across drylands and are important for understanding late Quaternary terrestrial environmental response to climate dynamics (Fitzsimmons *et al*., 2013; Nanson *et al*., 1995; Stone, 2021; Thomas, 2013; Thomas and Burrough, 2012; Woor *et al*., 2022). Sedimentary landform archives, or *geoproxies* (cf. Thomas, 2013), are relied on for assessing paleoenvironmental conditions in locations that have few alternative long-term palaeoproxy records. Low levels of precipitation and poor organic preservation have often limited the formation and preservation of high-resolution geochemical or botanical proxies (Chase and Meadows, 2007; Thomas, 2013). In the relatively dry western and central parts of southern Africa, lake and speleothem records are commonly discontinuous (e.g. Brook *et al*., 1999; Hipondoka *et al*., 2014) or located in regions fed by large catchments draining the tropics (e.g. palaeolake Makgadikgadi; Burrough *et al*., 2009), and elemental and dendrochronological records are scarce (Humphries, 2021). Evidence of terrestrial environmental response to palaeoclimate change is also preserved in marine (e.g. Farmer *et al*., 2005) and hyrax midden (Chase *et al*., 2012) archives, yet the potential to extrapolate findings to southern Africa is limited by respective challenges of integrating large, often unknown, areas of the terrestrial system into interpretations of marine sediments (Scott *et al*., 2012), or the restricted distribution of suitable midden sites (Humphries, 2021).

Spanning important latitudinal and longitudinal gradients, data generated from southern African fluvial deposits are now substantial (Dollar, 1998; Grenfell and Grenfell, 2021; Stone and Thomas, 2013; Tooth, 2016). The potential for these archives to address questions of past hydroclimates is particularly important for western and central southern Africa. The dryland centre and west of the subcontinent encompasses the desert areas of the Namib (Goudie and Viles, 2015) and Kalahari (Shaw and Goudie, 2002; Thomas and Shaw, 1991) and has a long-standing history of focus within

palaeoclimate and palaeoenvironmental literature (e.g. Burrough and Thomas, 2013; Chase *et al*., 2019; Collins *et al.*, 2014; Heine, 1982; Stone, 2021; Thomas and Shaw, 2002; van Zinderen Bakker, 1984). The palaeoclimate history, however, has been difficult to interpret and controversies exist regarding the relative importance of temperate and tropical climate systems on Quaternary timescales and the nature and magnitude of precipitation changes (Chase *et al*., 2019; Chase and Meadows, 2007; Gasse *et al*., 2008; Singarayer and Burrough, 2015). Fluvial systems commence within or flow through these desert regions and provide evidence for assessing temporal and spatial patterns of palaeoenvironmental change, such as changes in seasonality and demarcating past extents of summer and winter-dominated rainfall zones (e.g. Lyons *et al*., 2014).

Topographically, southern Africa's setting has generated a diversity of fluvial styles (Tooth, 2016), from high gradient rivers draining Namibia's coast-parallel Escarpment zone towards the sea (Jacobson *et al*., 1995), to internally draining endoreic rivers in the Kalahari basin (McCarthy and Ellery, 1998). To assess both the combined fluvial history and the controls on sedimentary archive formation and preservation, a synthesis of records is required. Robust reconstruction of palaeoenvironmental change from sedimentary archives is dependent on both the accuracy and precision of chronology and the proxies used to reach palaeoenvironmental interpretations. With a large chronological dataset, data quality assessments can be performed to obtain a subset of the most robust ages (Small *et al*., 2017; Woor *et al*., 2022). A quality-assured chronology allows for an assessment of the timing of 'real' geomorphological change, reducing potential heterogeneity introduced through chronological uncertainty, and enabling correlation with other proxy records. A regional analysis also enables an assessment of the spatial trends in the sources of evidence used and the impact this has on the type of information that can be retrieved from fluvial deposits. Databases now exist for other geomorphological features in southern Africa, including dunes (Lancaster *et al*., 2016; Thomas and Burrough, 2016) and lakes (De Cort *et al*., 2021), but not yet for fluvial archives.

The initial aims of this paper are to create a new chronological database of late Quaternary fluvial records from the relatively dry western and central regions of southern Africa, hereafter referred to as southwestern Africa (south of 17˚S and west of 26˚E; Figure 5.1) and to use this database to reconstruct the nature and amplitude of hydrological change during the late Quaternary. This compilation encompasses records from 22 rivers (70 sites, 603 ages) spanning from 132 ka to present. This paper then sets out to: i) establish a river typology in terms of dimensions, climatic setting, and hydrological parameters; ii) assess the nature and controls on documented fluvial histories; and iii) evaluate the palaeoenvironmental evidence using an assessment of data quality, particularly in relation to chronological methodology.

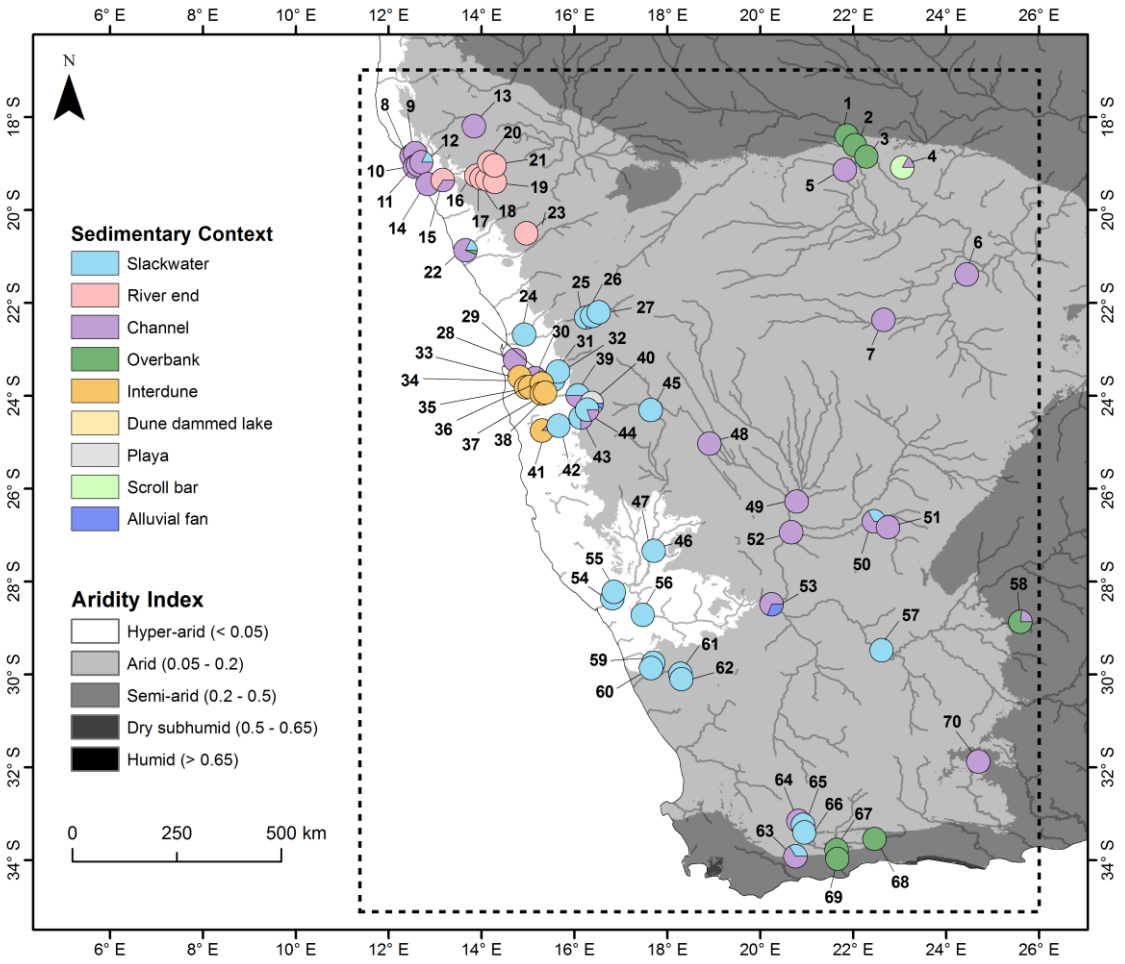

Figure 5.1. All sites in the fluvial chronological database coloured by sedimentary context. Black dotted box demarcates the boundary used in this study to define southwestern Africa and to determine inclusion of records. Contemporary aridity index (AI; Trabucco and Zomer, 2022) is defined by mean annual precipitation over mean annual evapotranspiration (P/PET) (UNEP, 1992). Drylands are where AI <0.65. Site numbers refer to Appendix E Table E1.

5.1.1. Dryland rivers and fluvial palaeoenvironmental archives

Intermittent and ephemeral rivers comprise ~60 % of global rivers by length (Messager *et al*., 2021). In drylands, rivers that periodically cease to flow are prevalent. In hot and dry to extremely hot and arid environments (following the bioclimate map of Metzger *et al*., 2013), 62 to 98 % of river network lengths are prone to flow cessation (Messager *et al*., 2021). There is increasing recognition that river systems exist across a continuum of hydrological conditions (Knighton and Nanson, 1997; Tooth and Nanson, 2011) and a range of fluvial types occur as a response (Larkin *et al*., 2020), yet

the fate of non-perennial rivers has commonly been overlooked (Acuna *et al*., 2014; Messager *et al*., 2021; Sullivan *et al*., 2020) and the dynamics of hydrological activity in dryland ephemeral rivers are poorly understood (Reid and Frostick, 2011).

Drylands host both exogenous perennial fluvial systems sourced in humid regions and non-perennial endogenous intermittent and ephemeral rivers fed by rainfall within the dryland itself and/or by variable groundwater contributions (Busch *et al*., 2020; Tooth and Nanson, 2011). Ephemeral hydrological activity in particular is characterised by flashy discharge with steep rising hydrographs (Busch *et al*., 2020; Reid and Frostick, 1987). Intense runoff events are short lived and interrupt extended periods of relative channel stability where river flow is limited (Tooth and Nanson, 2011). Rainfall in drylands is frequently associated with spatially discrete convective cells (Diskin and Lane, 1972; Sharon, 1974). Reaching high rainfall intensities, the infiltration and storage capacities of typically thin, poorly developed, or near-absent soils can rapidly be overwhelmed (Liu *et al*., 2004; Mavimbela and van Rensburg, 2017), and surface runoff occurs predominantly through Hortonian overland flow (Tooth, 2000). Overland flow is further amplified through the development of surface crusts (Belnap, 2006). Intermittent river flow typically occurs on timescales longer than individual rainfall events and flow can be sustained by connection to groundwater (Busch *et al*., 2020). Together with variable transmission losses (Lange, 2005) and variable surface vegetation cover (Reid and Frostick, 2011), dryland river flow has the potential to erode and mobilise substantial amounts of sediment as bedload (Alnedeij and Diplas, 2005; Rust and Nanson, 1989) and as suspended load (Jacobson *et al*., 2000; Reid and Frostick, 1987).

In response to climate perturbations, fluvial systems experience geomorphological change and evidence is recorded in sedimentary archives (Macklin *et al*., 2012) on scales of individual *events* to multiyear *episodes* to multidecadal- to centennial-scale *phases* (Toonen *et al*., 2017). Across drylands globally, a range of fluvial sedimentary contexts have been studied as records of

Quaternary palaeoenvironmental change. These include the formation of slackwater deposits (SWDs) from extreme floods (e.g. Greenbaum *et al.*, 2000; Haberlah, *et al.*, 2010; Kale *et al*., 2000), overbank floodplain deposits (e.g. Damm and Hagedorn, 2010; Williams *et al.*, 2006), and interdune playa environments formed by settling in still water settings (e.g. Brook *et al.*, 2006; Kocurek *et al*., 2020; Stanistreet and Stollhofen, 2002). In fluvial deposits, environmental signals can be derived from changes in sediment volume, character, and composition (Tofelde *et al*., 2021). First, this can include analysis of terrace height and distribution (e.g. Stokes *et al*., 2017), flow frequency (Benito *et al*., 2020), and meander dimensions (e.g. Hesse *et al*., 2018; Tooth *et al*., 2022). Second, sediment character can include the analysis of textural (e.g. Stone *et al.*, 2010) and architectural facies elements (e.g. Miall, 2006; Srivastava *et al*., 2006). Third, analysis of sediment composition can assess mineralogical changes, such as for provenance analysis (e.g. Ramisch *et al*., 2017; Walsh *et al*., 2022), or components reflective of environmental conditions (e.g. Faust *et al*., 2004; Nash *et al*., 2006). Reconstructing fluvial regimes and associated climatic change from sedimentology and geomorphology, however, can be challenging for several reasons. Information passes through a set of filtering processes from climatic signal to interpretation of geomorphological archives (see Bailey and Thomas, 2014). Partial preservation of fluvial records can occur where environmental signals are shredded by processes of sediment transport (Jerolmack and Paola, 2010), yet Macklin *et al*. (2012; 2022) argue that important palaeoenvironmental information can still be retrieved from these records.

5.1.2. Regional setting

This research focuses on the driest regions of southern Africa, principally the landmass south of approximately 17˚S (Humphries, 2021; Knight and Fitchett, 2021; Stone, 2021; Thomas, 2019) and to the west of 26˚E (Figure 5.1). Within this study area, the Namib Desert occupies the coastal plain of Namibia spanning to ~32°S at the Olifants River (Western Cape, South Africa) and the Kalahari

encompasses the continental interior covered by Kalahari Group sediments spanning to ~29°S at the Orange River (Stone, 2021).

Southern Africa's climate is broadly characterised by a north-east to west rainfall gradient from humid to hyper-arid. The east coast receives precipitation from the warm Indian Ocean (Crétat *et al*., 2012; Wang and Ding, 2008), diminishing in influence with increasing distance westwards. Aridity in the west is further enhanced by the South Atlantic Anticyclone and stabilisation of airmasses above the cold surface waters associated with the Benguela current, which blocks incursions of moisture (Nicholson, 2000; Reason, 2017; Tyson and Preston-Whyte, 2000). Across the majority of southern Africa, the seasonal cycle of rainfall maxima mirrors the migration of low-level convergence of the tropical rainbelt (Nicholson, 2018). At the southern edge of the rainbelt, precipitation is governed by the Congo Air Boundary (CAB) (Howard and Washington, 2019; Taljaard, 1972; Torrance, 1979). During the austral summer, localised convective systems bring incursions of rainfall to the southwestern coast of southern Africa as a result of intensification of the Angola Low (Hermes and Reason, 2009). When coupled with mid-latitude waves, tropical-temperate troughs bring additional seasonal rainfall (Hart *et al*., 2010; Macron *et al*., 2014). Mid-latitude circumpolar westerlies bring rainfall in the winter months to the southwestern Cape of South Africa (Reason *et al*., 2002) and contribute to year-round rainfall along the southern coast.

The geological setting of southern Africa primarily comprises the Congo, Kaapvaal, Zimbabwe Cratons, and the Damara Belt (Jacobs *et al*., 2008; Miller, 2008). Since the break-up of Gondwana, uplift and river incision has resulted in the delineation of bedrock confined river courses in southern Africa (Tooth and Nanson, 2011). Trending north-south throughout Namibia and the west coast in South Africa, the Great Escarpment demarcates the central elevated interior of the continent and the low relief regions at the coast. These coast-parallel ranges host many fluvial systems draining upland areas (Jacobson *et al*., 1995). In the interior of southern Africa, the Kalahari Group

sediments represent infilling of the central basin since the Cretaceous (Garzanti *et al*., 2022; Haddon and McCarthy, 2005; Schulter, 2008). The Okavango Delta drains into the interior depression associated with the East African Rift system (McCarthy and Ellery, 1998). Today, southern Africa hosts large scale perennial exogenous rivers, such as the Orange and Okavango, but is dominated by non-perennial intermittent rivers and ephemeral streams (De Wit and Stankiewicz, 2006; Messager *et al*., 2021).

5.2. The Database

5.2.1. Data selection

To be included in the database, fluvial studies had to meet the following set of criteria: 1) the source publication is peer-reviewed; 2) chronological data are presented (radiocarbon or luminescence ages); 3) sites fall within southwestern Africa, as defined by Figure 5.1 (longitude and latitude data available or estimated from published maps); and 4) dated material was deposited via fluvial processes. Palaeosols developed on fluvial deposits are included if dating provides an estimate of original sediment deposition of the host material, not the age of palaeosol development. For any site where ages are included in several papers (for example in a review following original publication), the original publication was treated as the reference point. This was considered appropriate in order to acknowledge the primary work and to follow the intention and interpretation of the research underpinning the source publications. The full database is presented in the Appendix F.

5.2.2. Database structure and content

The database contains information on: i) publication details; ii) site and river details (including location, sedimentary context); iii) sample details; iv) chronology (chronologies and meta-data); v)

interpretation (fluvial, climate, and independent proxies used); and vi) data quality assessments (Figure 5.2). Details of these categories are provided below and in the Appendix E.

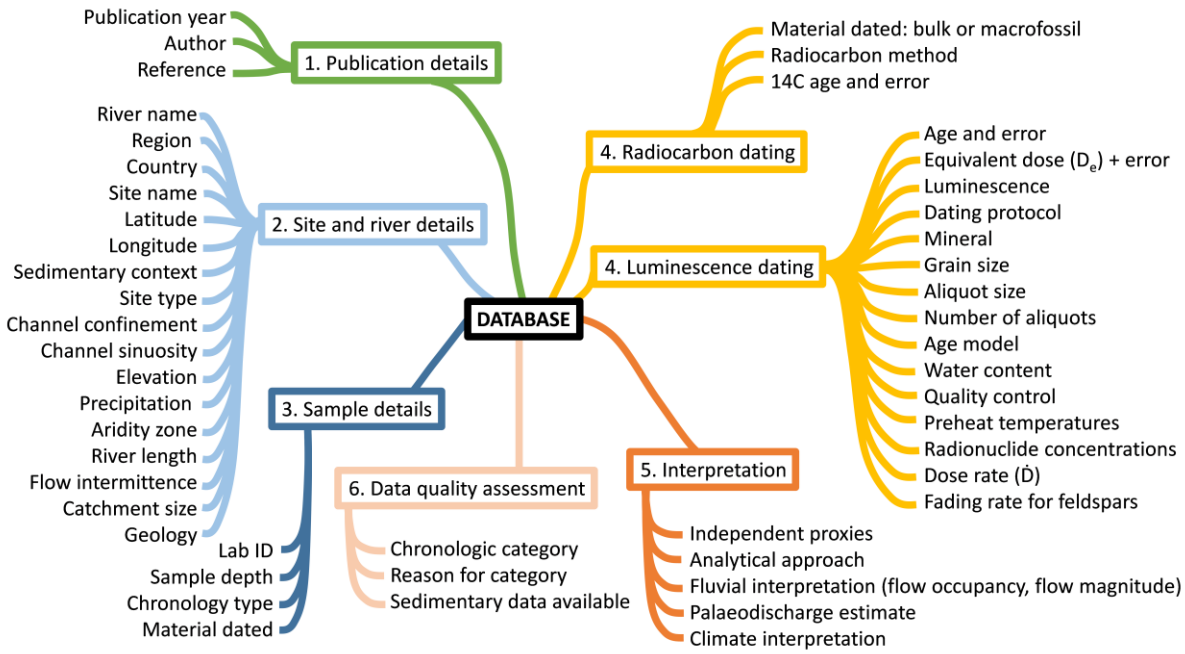

Figure 5.2. Content of the Quaternary chronological fluvial database. The structure of this database follows reporting standards from Khider *et al*. (2019) (PaCTS 1.0: A Crowdsourced Reporting Standard for Paleoclimate Data).

5.2.2.1. Regions

The river systems of southwestern Africa were divided into four regions based on catchment characteristics and the classification of river types by Tooth and Nanson (2011) and Tooth (2016) (Figure 5.3A): 1) **Namib**, the rivers flowing towards the Atlantic Ocean from the coast-parallel Great Escarpment in Namibia and north-western South Africa; 2) **Northern Kalahari**, the rivers within the Okavango Basin draining internally to the Kalahari; 3) **Orange**, the rivers associated with the Orange catchment; and 4) **Eastern Cape**, the rivers flowing from the Great Escarpment to the south coast of South Africa.

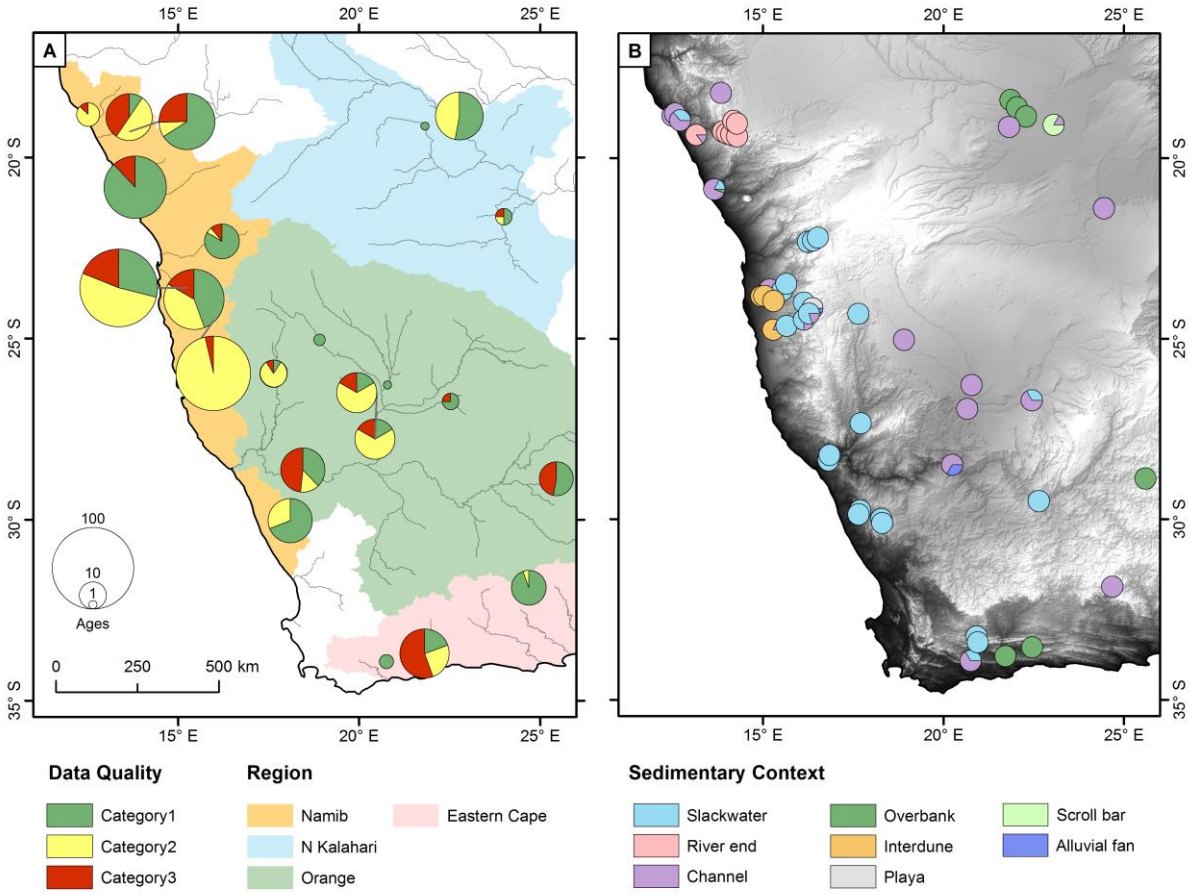

Figure 5.3. Spatial distribution of fluvial sites in the database. **A)** Data quality grouped by river catchment. Pie charts show percentage of ages in Category 1 (most robust), Category 2, Category 3 (least robust), with the size of each chart proportional to the number of ages from each river. **B)** Sedimentary context by site of all records that have passed the data quality filtering (note that no ages from the sedimentary context 'dune dammed lake' passed these criteria).

To interrogate the fluvial and climatic context of these regions, the database has been populated with information on the characteristics of sites and river catchments. This includes data on elevation (ALOS Global Digital Surface Model AW3D30; JAXA), rainfall (WorldClim 2.0; Fick and Hijmans, 2017), aridity index (Trabucco and Zomer, 2022), probability of contemporary flow intermittence (Messager *et al*., 2021), and underlying geology (Garzanti *et al*., 2022). Through investigation of site context using Google Earth, rivers styles at sites were classified according to setting (confined, partly confined, unconfined) and river style (straight, sinuous, meandering; through calculation of reach scale channel sinuosity; straight: sinuosity index < 1.05, sinuous: 1.05-

1.5, meandering: > 1.5) following Fryirs *et al*. (2016), Grenfell *et al*. (2019), and Grenfell and Grenfell (2021) (see Appendix E for further detail on this classification). River catchments were mapped using the HydroSHEDS dataset (Lehner and Grill, 2013) and catchment size, relief, gradient, channel length, average channel sinuosity, and drainage density were calculated for each river catchment.

5.2.2.2. Sedimentary context

Interpretation of palaeoenvironmental change from fluvial geoproxies requires detailed description of the context under which sediments were deposited. Here, sedimentary contexts were differentiated into categories (Table 5.1).

Table 5.1. Key characteristics of the sedimentary contexts recorded in the chronological database. Within a standardised framework, this classification aimed to follow the wording used in original source publications as closely as possible.

Sedimentary context	Description and key characteristics
Slackwater (SWD)	Unconsolidated sands and silts that accumulate rapidly from suspension during major palaeofloods (e.g. Cloete *et al*., 2018; Greenbaum *et al*., 2014). SWDs are commonly found in backflooded tributaries in confined bedrock reaches (Baker, 1987; Heine and Völkel, 2009; Kochel and Baker, 1982). The height of these deposits reflect the peak stage of a flood event and can be used to estimate palaeodischarge (Baker, 2008; Benito *et al*., 2020; Frances, 2004; Jarrett and England, 2002).
Channel	Within-channel sediment aggradation in valley fills can preserve evidence of confined channel infill facies and unconfined sheet flood deposits (e.g. Srivastava *et al*., 2004; Walsh *et al*., 2022). Incision can form fluvial terraces marking previous higher-elevation channel aggradation (e.g. Ramisch *et al*., 2017; Völkel *et al*., 2021). Channel networks that are currently inactive can preserve the location of past hydrological flow as palaeochannel infills (e.g. Tooth *et al*., 2022).
Scroll bar	Depositional point bar ridge features associated with channel margins. Scroll bars are indicative of lateral meander migration (e.g. Tooth *et al*., 2022).
Overbank	Deposition from suspension load in the overbank floodplain area (e.g. Damm and Hagedorn, 2010; Nash *et al*., 1997, 2006; Srivastava *et al*., 2006). Overbank deposits accrete vertically and can display laminated to massive clay silt facies (Grenfell and Grenfell, 2021). Floodplain deposits can be modified by processes of pedogenesis and bioturbation (Tooth *et al*., 2013) and can form stacked palaeosol sequences (e.g. Lyons *et al*., 2014).
Alluvial fan	Deposition when channel confinement and flow velocity is reduced (Blair and McPherson, 1994; Harvey, 2011). Fan deposits can be dissected by subsequent channel processes, forming relict fans (e.g. Ramisch *et al*., 2017).

River-end	Endoreic deposits in upland river reaches indicative of periods of flow incompetence and former termination of rivers upstream of contemporary end points (e.g. Eitel and Zoller, 1996; Eitel *et al*., 2005, 2006; Rust, 1999). River-end deposits can be associated with short distance fluvial transport of fine-grained dust or loess (e.g. Brunotte *et al*., 2009; Eitel *et al*., 2001).
Interdune and playa	Endoreic water-lain sediments deposited within a sand sea at ancient terminal points of adjacent rivers (Feder *et al*., 2018; Krapf *et al*., 2003; Teller *et al*., 1990). Lacustrine mudstones form through deposition during low or still water phases of ponding and can contain diatoms and ostracods (Teller and Lancaster, 1986; Teller *et al*., 1990). Interdunes are a form of playa deposit, where playas can also be found upstream in water courses and are not restricted to the dune areas (e.g. Völkel *et al*., 2021).
Dune-dammed lake	Lacustrine-like sediments deposited when a river course is blocked by aeolian sand dunes (Goudie, 1972; Marker, 1977; Rust and Weinecke, 1974; Scholz, 1972; Vogel and Visser, 1981).

5.2.2.3. Fluvial interpretation

To aid clarification and comparability between interpretations, reporting of the nature of past river flow has been differentiated into detail on flow occupancy and on flow magnitude (Table 5.2). When describing flow occupancy, a wide range of terms have been used within the fluvial literature (e.g. epithets 'arid', 'discontinuous', 'episodic', and 'seasonal' are used for rivers that cease to flow for some period of time, Busch *et al*., 2020). To account for this, we follow Busch *et al*. (2020) in the use of terms 'intermittent' and 'ephemeral' for non-perennial rivers. This distinction maps onto the flow occupancy scale from Tooth and Nanson (2011) and is used by Messager *et al*. (2021) to define the prevalence of non-perennial river systems globally. Categories of flow magnitude were reached through assessment of the terminology used within southern African literature (Table 5.2).

Table 5.2. Description of categories used to classify fluvial interpretation. Data are reported on flow occupancy and flow magnitude.

Fluvial interpretation		Description
Flow occupancy	Perennial	Year-round river flow. Precipitation regime sufficient to sustain continuous flow and connectivity within the drainage basin (Tooth and Nanson, 2011)
	Intermittent	Seasonal river flow with variable cycles of cessation. Persistent flow occurs through multi-peak floods (e.g. Bordy *et al*., 2018; Srivastava *et al*. 2004), commonly lasting longer than an individual storm events (Busch *et al*., 2020; Messager *et al*., 2021). Drainage networks are better connected than ephemeral systems (Tooth and Nanson, 2011), commonly with links to groundwater (Busch *et al*., 2020)
	Ephemeral	Sub-seasonal duration river flow. Floods commonly occur in response to spatially variable convective rainfall (Busch *et al*., 2020; Messager *et al*., 2021; Tooth and Nanson, 2011) and have lower predictability than intermittent rivers (Datry *et al*., 2017). Drainage networks are poorly connected (Tooth and Nanson, 2011), commonly without links to groundwater (Busch *et al*., 2020)
Flow magnitude	Extreme flood	Extraordinary high magnitude floods (Baker, 1987; e.g. Greenbaum *et al*., 2014; Zawada *et al*., 2000)
	High energy flow	Enhanced river flow, where the stream has a high competence (e.g. Brook *et al*., 2006) and has the capacity to carry a high sediment load (e.g. Srivastava *et al*., 2006; Walsh *et al*., 2022)
	Low energy flow	Periods of steady or declining river energy with smooth rising hydrographs (e.g. Srivastava *et al*., 2004), ponding through still water phases (e.g. Teller *et al*., 1990), or low capacity of a flow to transport sediment (e.g. Walsh *et al*., 2022)

5.2.2.4. Chronologies

Geochronological control of fluvial change in southern Africa has been established through luminescence (e.g. Srivastava *et al*., 2006; Tooth *et al*., 2022; Walsh *et al*., 2022), radiocarbon (e.g. Hurkamp *et al*., 2011; Nash *et al*., 2006; Vogel, 1989), uranium-thorium (e.g. Selby *et al*., 1979), palaeomagnetism (e.g. Brink *et al*., 2012), and cosmogenic nuclide burial dating (e.g. Erlanger *et al*., 2012; Matmon *et al*., 2015). The latter two have been used mainly to study fluvial processes pre-dating the late Quaternary and have not been included in this database. Assessment of chronological data quality (Section 5.2.3) has focused on luminescence and radiocarbon chronologies, as these are the most widely used, and the scarcity of uranium-thorium ages make it difficult to make a holistic assessment.

A range of calibration curves have been used for radiocarbon chronologies within the publications included in the database. Here, radiocarbon ages were individually recalibrated using standardised curves (SHCal20, Hogg *et al*., 2020; Bomb13SH12, Hua *et al*., 2013) in OxCal v 4.4.4. (Bronk Ramsey, 2021), to enable comparison between geochronologies (Bronk Ramsey *et al*., 2010). Details of ages as originally published are included in the database alongside the standardised chronological information (quoted to 2 sigma, 95.4 %).

5.2.3. Data quality

Age-controlled fluvial archives from southwestern Africa have been obtained through publications spanning the last 40 years. Within this time, dating protocols and methodological approaches have been developed and adapted. Accurate reconstruction of palaeoenvironmental change from large datasets therefore requires an assessment of data quality to obtain a robust record of regional change. First, there are several established sources of uncertainty in geochronological methodologies (see Small *et al*., 2017). Through assessment of these uncertainties, it is possible to make judgments on whether anomalies and data conflicts are a relic of dating error, or if they detail real palaeoenvironmental and geomorphological heterogeneity. Second, it is then critical to assess whether there is sufficient supporting information for palaeoenvironmental interpretation. Here, entries in the database were considered in terms of the approaches and lines of evidence used to interrogate environmental response of rivers to past climates. Only records that constituted robust chronologies and palaeoenvironmental information generated through independent proxies were considered for analysis of the Quaternary fluvial record.

A systematic classification approach for assessment of chronological data quality requires technique-specific standards in order to assess both luminescence and radiocarbon dating methodologies. To do this, a set of criteria were adapted from the schemes of Lancaster *et al.* (2016) (INQUA Dunes Atlas chronologic database) and Small *et al*. (2017) (BRITICE-CHRONO).

Following Khider *et al*. (2019)'s crowdsourced standards on metadata reporting, we recognise that caution needs to be taken when applying contemporary data reporting standards to previous research that was not subject to the same exacting standards as present, so we differentiate between criteria that are essential and those that are recommended. Table 5.3 details the classification of ages from Category 1 to Category 3, using criteria based on established uncertainties in luminescence and radiocarbon dating. For all ages, the first set of criteria distinguishes between samples that are supported by other geochronology, and those that are not. The presence of other geochronology at a site enables a consideration of stratigraphic consistency and multiple corroborating geochronological methods at a site indicate a robust chronology of deposition. Reporting of sample depth is important here, as stratigraphic relationships between samples cannot be assessed without it.

Table 5.3. Chronological data quality criteria. Each age is classified from Category 3 (least robust) to Category 1 (most robust) based on their stratigraphic context and technique specific criteria. An age needs to have met all requirements in the Category 1 list to be classified as such. If any aspects are not met, it is placed in the category below. If the integrity of an age is questioned within the original publication, it is placed in Category 3. These reasons can include (but are not exclusive to) contamination of modern carbon (e.g. Hv-9485 in Heine, 1990), radioactive disequilibrium (e.g. HDS-1223 in Eitel *et al*., 2006), and re-deposition of fossil wood (e.g. HAM-3635 in Damm and Hagedorn, 2010). If multiple ages are presented for a single sample (e.g. HS-1; Srivastava *et al*., 2006; which is dated through multiple aliquot sizes and age models), the age used for further interpretation in the paper is included in the database.

	Criteria	Category 3	Category 2	Category 1
All ages	Stratigraphic context is well documented. Data on sample depth are available or stratigraphic relationships between ages can be inferred	x	✓	✓
	Other geochronology is available from the site. This can be in the form of multiple dating methods (e.g. radiocarbon and luminescence) at the same depth or multiple ages available from the site	x	✓	✓
	Ages are stratigraphically-consistent (within 2 σ) with other available geochronology	x	x	✓

Luminescence	Laboratory/sample number, luminescence age and error, and mineral dated are reported	x	✓	✓
	Equivalent dose (D_e) and dose rate ($\dot{D}$) are reported	x	✓	✓
	Dating protocol and corrections* applied are reported	x	✓	✓
	Age model and grain size dated are reported	x	x	✓
	Age obtained through the sensitivity normalised single-aliquot regenerative dose protocol (SAR)	x	✓	✓
	Quality control** has been performed (e.g. dose recovery)	x	x	✓
	Potential for partial bleaching is interrogated. Small aliquots or single grain measurements undertaken for Category 1	x	✓	✓
	Feldspar ages are accompanied by assessment of anomalous fading	x	✓	✓
Radiocarbon	Laboratory/sample number, conventional ^{14}C age and error, and material dated are reported	x	✓	✓
	Age is obtained from a macrofossil or microfossil samples	x	x	✓
	Age is obtained from a bulk sample	✓	✓	x
	Potential for reservoir or hard water effects have been addressed	x	✓	✓

**Corrections in luminescence dating include the reporting of water content, aliquot size, grain size, mineral dated, depth for calculation of cosmic dose rates, and rates of anomalous fading in feldspars.*

***An assessment of the extent to which the SAR cycle can recover a known dose.*

Category 1 represents the most reliable ages with the highest levels of data reporting. These ages are produced through robust methods and are supported by other stratigraphically-consistent geochronology. Category 2 represents ages that are produced through robust methods and have stratigraphic context, but where the level of data reporting is not high enough to fully assess the quality of the age. Other geochronological data are available from the site, but ages are not stratigraphically consistent. In some cases, these ages can have less certain accuracy, such as where luminescence dose recoveries have not been reported, or bulk samples rather than macrofossils have been used for radiocarbon dating. Category 3 represents ages with the lowest data quality and the lowest level of data reporting. These ages commonly lack stratigraphic context or supporting ages from a site. Ages in this category often use outdated methods, or the author has stated concern about the age.

For luminescence dating, the key differentiating factors include the use of a sensitivity-normalised dating protocol, the reporting of key dating parameters, and the use of quality control such as dose recovery experiments. The SAR protocol (Murray and Wintle, 2000) includes an assessment of sensitivity change that was not incorporated in previous protocols such as the multiple aliquot additive dose (MAAD) approach (Jain *et al*., 2003; Wintle and Murray, 2006). SAR ages are more precise (Duller, 2004; Hilgers *et al*., 2001; Wintle and Murray, 2006) and it is possible to measure a larger number of D_es per sample, improving the accuracy of ages. The luminescence signals in feldspars can fade anomalously (Lamothe and Auclair, 1999; Wintle, 1973). The post-IR IRSL protocol helps to minimise this fading (Thomsen *et al*., 2008), but assessments of the fading rate are required (Roberts, 2012) for feldspar ages to be Category 2 or above. Age model and grain size can influence the age obtained (Arnold *et al*., 2009; Timar-Gabor *et al*., 2017), yet these parameters are not used as a rejection criteria as the choice is often site and context specific. Partial bleaching is common in dating fluvial deposits, particularly in dryland regions where suspended load can be high (Ditlefsen, 1992; Olley *et al*., 2004). If partial bleaching is identified, small aliquots or single grain measurements are required for an age to be Category 1. These adjustments enable the bleached component of the signal to be isolated (Colarossi *et al*., 2020; Duller, 2008b).

For radiocarbon dating, the distinction between Category 1 and 2 ages is defined by the use of macrofossil rather than bulk samples. Bulk samples, such as organic or calcareous sediment, can combine multiple organisms, can date the formation of a unit over a period of time, and can incorporate dissolved land-derived 'old carbon' (Strunk *et al*., 2020). This has the potential to present the mean of several depositional events or yield ages exceeding the timing of deposition of interest. Age estimates from macrofossils, such as shells or wood, on the other hand are more precise as they are obtained from individual organisms with discrete timings of death (Rey *et al*., 2019; Strunk *et al*., 2020). To be Category 2 or above, the ^{14}C date and error must be reported, as this information is required for recalibration. ^{13}C values are variably reported across publications

and are not used as a criterion in this data quality assessment. Finally, if studies identify the potential for hard water effects but do not account for them, ages were not classified above Category 3, as these effects can result in the production of anomalously old ages (Deevey *et al.*, 1954; Wright, 2017).

5.3. Current status of the database

Quaternary fluvial data from southwestern Africa are derived from 44 sources (as at 1/4/2022). Chronologies have been established for 70 sites across 22 rivers (Figure 5.1, Appendix E Table E1). These rivers are located across four regions (Figure 5.3) that span a range of hydrological, topographic, and climatic contexts (Table 5.4). The Namib region is the most intensely studied (41 sites), followed by Orange (14 sites), Eastern Cape (8 sites), and Northern Kalahari (7 sites). Contemporary mean annual precipitation in these fluvial catchments range from 10 mm yr^{-1} (Kuiseb River at the coast) to 1,426 mm yr^{-1} (headwaters of the Okavango River). Along the main channels of these rivers, two of the studied rivers have a probability of intermittence of less than 0.5 (Orange, Okavango; where 0 is perennial and 1 is non-perennial; Messager *et al.*, 2021), and all other studied rivers of >0.7. Average channel gradients range from 0.34 (Okavango) to 7.8 km m^{-1} (Khumib) and the river styles are predominantly sinuous to meandering, with average sinuosity of the main channels ranging from 1.22 (Huab) to 1.91 (Orange).

Table 5.4. Characteristics of southwestern Africa's rivers that have been studied for records of palaeoenvironmental change. Catchment size, river length, and drainage density (total length of channels by catchment size) are calculated from the HydroSHEDS dataset (Lehner and Grill, 2013). Probability of intermittence is calculated for the main channel of each river and represents the probability that a river will cease to flow for at least one day a year (0: perennial, 1: non-perennial; Messager *et al.* 2021). Catchment relief represents the difference between highest and lowest point in the catchment and mean channel gradient was calculated from the difference in elevation from the start and end of the main channel divided by the length of the main channel. Average channel sinuosity was calculated by dividing the main channel length by the straight distance between start and end (where straight: <1.05, sinuous: 1.05-1.5, and meandering: >1.5). Precipitation data are from the WorldClim 2.0 dataset (Fick and Hijmans, 2017). Mean catchment aridity index was calculated from the Trabucco and Zomer (2022) dataset, and aridity zones are described following the UNEP (1992) definition.

River catchment	Region	Catchment size (km^2)	Probability of intermittence	Mean catchment relief (m)	Length of main channel (km)	Mean channel gradient (km m^{-1})	Drainage density (km km^{-2})	Average channel sinuosity	Mean precipitation (mm yr^{-1})	Mean catchment aridity index and range of aridity zones encompassed
Okavango	N Kalahari	280,157	0.44	1,406	1,275	0.34	0.081	1.32	351-1426	0.32 (humid to arid)
Okwa	N Kalahari	136,357	0.96	719	612	0.39	0.087	1.83	295-441	0.13 (Arid)
Xaudum	N Kalahari	130,516	0.91	849	763	0.49	0.103	1.37	317-553	0.16 (Arid)
Khumib	Namib	2,315	0.90	1,444	124	7.76	0.074	1.26	29-216	0.05 (arid to hyper-arid)
Hoarusib	Namib	15,314	0.88	1,966	254	4.49	0.072	1.29	25-409	0.10 (arid to hyper-arid)
Hoanib	Namib	16,072	0.91	1,869	263	4.67	0.076	1.38	22-393	0.09 (arid to hyper-arid)
Huab	Namib	16,853	0.93	1,648	289	4.15	0.074	1.22	21-336	0.08 (arid to hyper-arid)
Swakop	Namib	29,535	0.95	2,462	416	3.88	0.073	1.28	13-453	0.10 (arid to hyper-arid)
Kuiseb	Namib	16,879	0.95	2,351	387	4.52	0.083	1.59	10-384	0.06 (arid to hyper-arid)
Tsondab	Namib	6,680	0.94	1,737	148	5.24	0.088	1.25	13-240	0.05 (arid to hyper-arid)
Tsauchab	Namib	6,343	0.94	1,546	144	5.11	0.082	1.27	28-232	0.04 (arid to hyper-arid)
Buffels	Namib	10,171	0.89	1,576	234	4.33	0.068	1.58	69-259	0.09 (arid to hyper-arid)
Fish	Orange	87,006	0.94	2,153	869	1.84	0.081	1.68	34-299	0.06 (arid to hyper-arid)
Auob	Orange	58,781	0.94	1,609	707	1.38	0.132	1.27	180-453	0.10 (arid)
Nossob	Orange	159,793	0.97	1,641	924	0.97	0.119	1.46	180-453	0.11 (arid)
Molopo	Orange	360,759	0.84	2,039	1,185	0.88	0.101	1.76	123-630	0.12 (semi-arid to arid)
Kuruman	Orange	40,007	0.94	1,009	414	1.45	0.080	1.31	205-479	0.14 (semi-arid to arid)
Orange	Orange	978,189	0.41	3,479	2,288	1.15	0.084	1.91	31-1061	0.16 (humid to hyper-arid)
Modder	Orange	35,784	0.98	1,260	412	1.13	0.405	1.47	354-714	0.22 (semi-arid to arid)
Huis	Eastern Cape	15,651	0.72	2,243	310	1.88	0.067	1.76	282-875	0.27 (arid to semi-arid)
Gourits	Eastern Cape	45,037	0.86	2,315	373	3.57	0.074	1.48	150-554	0.15 (arid to semi-arid)
Wilgerbosch	Eastern Cape	21,362	0.93	2,493	423	3.43	0.079	1.74	277-591	0.19 (arid to semi-arid)

Chronology from 603 ages from 44 publications met the initial selection criteria to be included in this database (Section 5.2.1). These ages comprise 55 % optically stimulated luminescence, 43 % radiocarbon, and 1 % thermoluminescence ages. The single-aliquot regenerative dose protocol (SAR; Murray and Wintle, 2000; Wintle and Murray, 2006) was used for 92 % of luminescence ages. 490 ages met the criteria for chronological data quality (Section 5.2.3) and of these, 424 ages (70.3 % of total ages) were accompanied by independent proxies for palaeoenvironmental interpretation and were considered for further analysis. In the chronological data quality filtering, 249 ages (41 %) were classified as Category 1, 241 ages (40 %) as Category 2, and 113 ages (19 %) as Category 3. The percentage of filtered ages varied by region (Table 5.5, Figure 5.3A), with the highest acceptance rate recorded in the Northern Kalahari and lowest in the Eastern Cape. Within Category 3, 24 ages were excluded because the integrity of the age was questioned within the original publication, 75 ages due to a lack of stratigraphic context or availability of supporting geochronology from the site, and 20 ages because the method of luminescence dating is outdated (e.g. MAAD). The proportion of Category 1 ages increases with publication year (from 13 % between 1980 and 1990, to 54 % between 2010 and 2022; Figure 5.4).

Table 5.5. Results of data quality assessment by region. Number of ages in Category 3 (lowest data quality) to Category 1 (highest data quality), and number of ages that passed the chronology filtering but were not accompanied by independent proxies to inform palaeoenvironmental interpretation. Filtered ages are those that passed both methodological and chronological filtering, and are the ages used in further analysis. Regions are defined by major basin, ordered in the table by total number of ages available by basin: Namib (26 papers), Orange (11 papers), Eastern Cape (5 papers), Northern Kalahari (4 papers).

Region	Chronology			Methods for interpretation		Total ages	% Filtered	Max. age of filtered (ka)
	Category 1	Category 2	Category 3	Category 1 + 2 without independent proxies	Category 3 without independent proxies			
Namib	170	185	64	51	36	419	72.6	132.3 ± 15.0
Orange	31	29	28	0	3	88	68.2	43.5 ± 3.2
E Cape	27	10	20	15	0	57	38.6	17.0 ± 2.5
N Kalahari	21	17	1	0	0	39	97.4	17.8 ± 0.4
Total	**249**	**241**	**113**	**66**	**39**	**603**	**70.3 %**	-

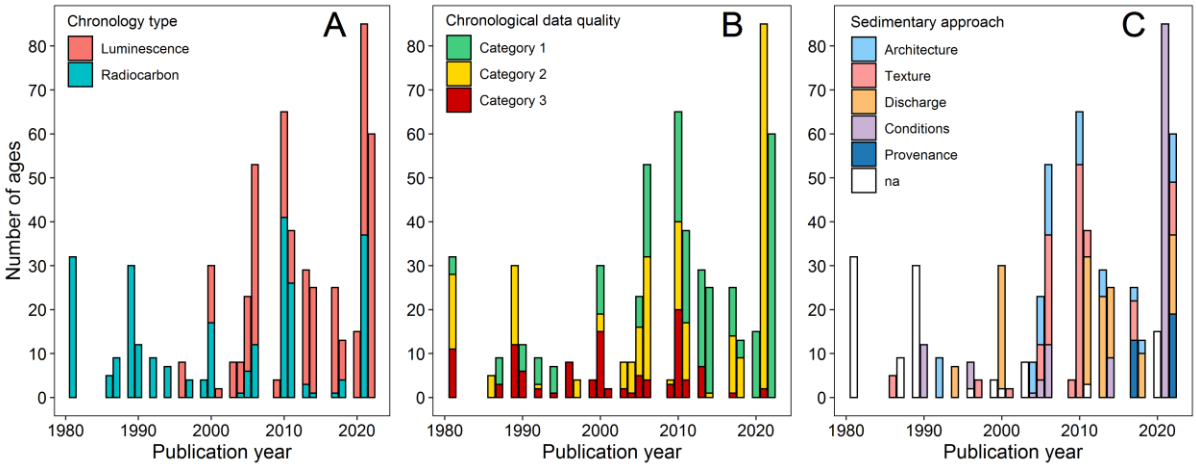

Figure 5.4. Histograms of the number of ages by publication year for all data within the database. Ages classified as Category 1 and Category 2 (B) and with supporting methods (C) were accepted through the data quality filtering process and included in further analysis. **A)** Chronology type: luminescence and radiocarbon. **B)** Results of data quality assessment coloured by category of age: Category 1 to Category 3. **C)** Assessment of approaches used alongside chronology to interpret palaeoenvironmental change. The distribution of the number of ages by publication year can be influenced by several factors, such as intensity of sampling at a site yielding numerous ages in a single publication, and gaps between research and publication timings, but this visualisation is useful for assessing the status of research and providing an overview of the progression of data quality and approaches used.

Around 45 % of the ages in the filtered dataset fall within the last 1 ka, with a steady decay in the number of ages in older millennia (Figure 5.5). As is typical of most chronological data, precision generally decreases with increasing age. Within the filtered dataset, 139 ages have an error of less than 100 years, 196 ages between 100 and 1,000 years, and 77 ages greater than 1,000 years. Site 43 in the Tsauchab River valley (24.47˚S, 16.14˚E) has the largest number of ages, with 39 luminescence and 21 radiocarbon ages (from Völkel *et al.*, 2021). Site 22, the Skeleton Coast valley fill Huab River (20.87˚S, 13.65˚E) has 50 luminescence ages (Thomas *et al*., 2017; Walsh *et al*., 2022). Four sites have >15 ages: site 4 (Okavango), site 30 (Kuiseb), site 43 (Tsauchab), and site 31 (Kuiseb). All other sites have fewer than 15 ages, with 22 sites having three or fewer ages.

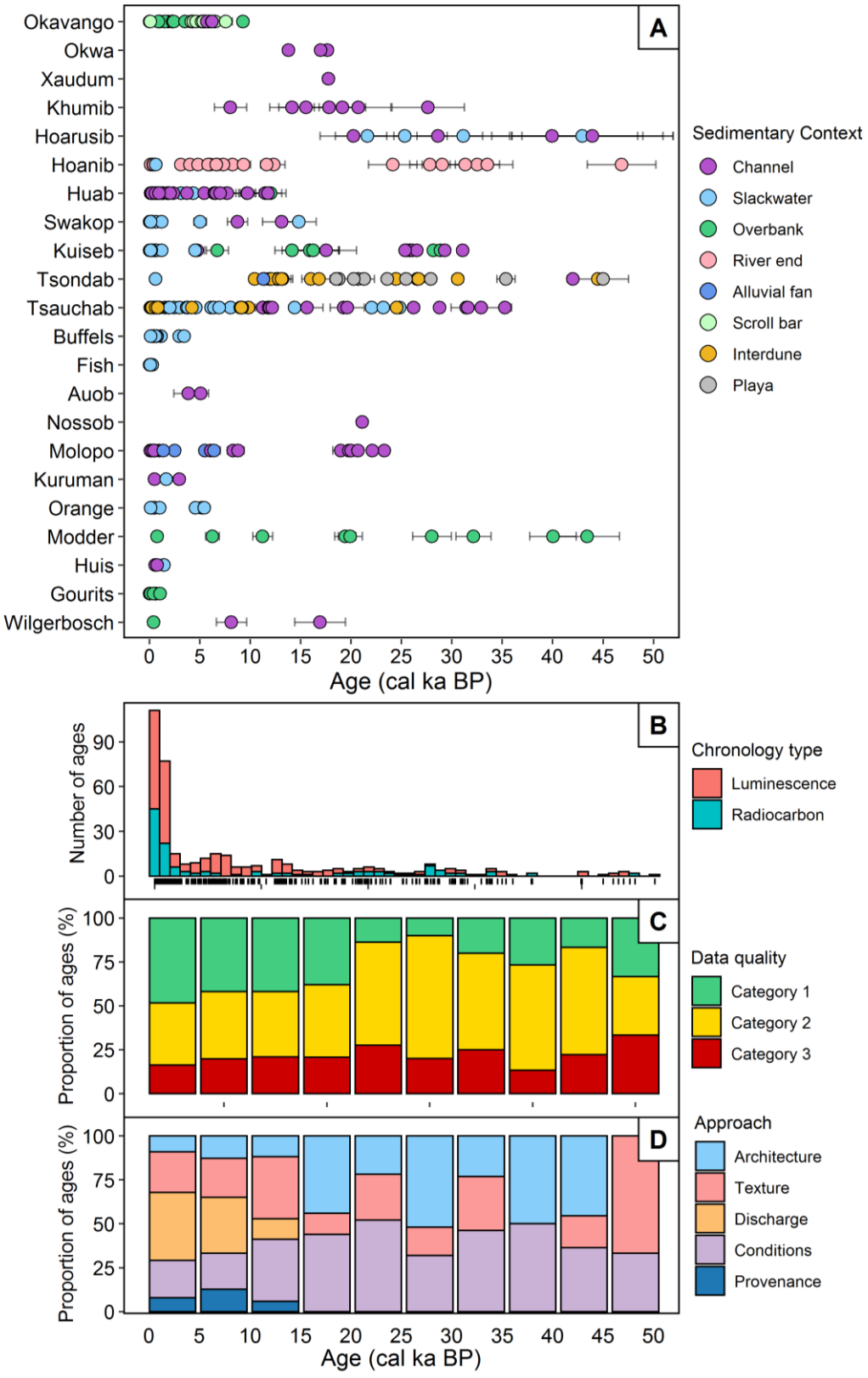

Figure 5.5. Temporal distribution of ages, sedimentary contexts, chronology types, data quality, and analytical approaches applied to southwestern Africa's fluvial deposits. These plots show the results for the last 50 ka that have passed the quality assurance criteria. The full dataset extends to

132 ka, but only 20 ages from 5 sites cover the period 50 ka-132 ka, limiting the potential for comparison of results. **A)** Ages by river, colours represent sedimentary context. **B)** Distribution of ages binned in 1 ka intervals and coloured by chronology type: luminescence and radiocarbon. Vertical lines beneath the plot detail the occurrence of ages within the bins. **C)** Relationship between chronological data quality category and the age of deposit. **D)** Relationship between sedimentary analytical approach and age of deposit. 5 ka intervals have been used for plots C) and D) to reduce the bias of certain time steps with limited ages.

Records from SWDs and channel deposits (Table 5.1) make up the majority of this dataset, comprising 34 % and 32 % of sites respectively (Table 5.6). Overbank (12 %), river end (10 %) and interdune deposits (7 %) are also common. The investigation of different sedimentary contexts varies by region (Figures 5.1 and 5.3B, Table 5.6). Over half of the sites are from unconfined river settings (57 %), with confined and partly confined settings comprising 25 % and 18 % respectively. To interpret changes in sediment deposition and infer the fluvial response to past hydroclimates, the most commonly used data are: stratigraphic, grain size, and sediment colour, closely followed by hydraulic discharge estimates, instrumental data, topographic, XRD, and carbonate content (Table 5.7). These proxies methods have been used to reconstruct palaeoenvironmental change through five key approaches: analysis of sediment architecture (main approach used alongside 78 ages), texture (128 ages), discharge (131 ages), sediment composition to infer prevailing environmental conditions (129 ages), and provenance (32 ages), yet 105 ages are not accompanied by independent proxies (considering the full suite of unfiltered ages). Despite this, 66 of the ages with no accompanying proxies still reach interpretations about climate. These ages were removed through the filtering process and were not used in further analysis. The dominance of each approach used varies by publication year (Figure 5.4C) and age of deposit (Figure 5.5D).

A range of fluvial dynamics have been recorded in evidence dating to the late Quaternary. In terms of flow magnitude, these range from low energy flow representing steady or declining river energy (e.g. Hoanib River, Eitel *et al.*, 2005), to extreme floods of flashy discharge (e.g. Swakop,

Greenbaum *et al.*, 2014). In terms of flow occupancy, studies have interpreted the occurrence of ephemeral (220 ages), intermittent (123 ages) and perennial (21 ages) river flow. Deposition of fluvial sediments are interpreted to record evidence of wet climates (221 ages), and evidence of drier climates than present (81 ages).

Table 5.6. Summary of the number of sites in the full database by sedimentary context and river setting. Data are grouped by region and the river settings that these sites are found in. Some sites contain multiple sedimentary contexts.

		Sedimentary Context									**River Setting**		
		Alluvial fan	Channel	Dune-dammed lake	Interdune	Overbank	Playa	River end	Scroll bar	SWD	Confined	Partially confined	Unconfined
Region	N Kalahari	0	4	0	0	3	0	0	1	0	0	0	7
	Namib	1	16	1	7	2	1	9	0	19	5	11	25
	Orange	1	7	0	0	2	0	0	0	7	7	1	8
	E Cape	0	4	0	0	4	0	0	0	3	6	1	1
Setting	Confined	0	3	0	0	4	0	0	0	13	-	-	-
	Partly confined	1	7	1	0	1	0	3	0	10	-	-	-
	Unconfined	1	21	0	7	6	1	6	1	6	-	-	-

Table 5.7. Summary of the sources of evidence used to reconstruct palaeoenvironmental change. This summary groups the use of methods by river to detail the full suite of approaches across a range of papers and sites for each river. Site numbers refer to Figure 5.1 and Appendix E Table E1.

	Method												
River	**Stratigraphy**	**Sedimentary facies**	**Grain size**	**Carbonate/ organic content**	**Soil characteristics**	**XRD, XRF, mineralogy, heavy minerals**	**DRS, mineral magnetism**	**Stable isotopes**	**Palaeontology Palynology**	**Hydraulic palaeodischarge estimates**	**Topography**	**Instrumental/ Documentary**	**Sites**
Okavango	x		x	x				x	x	x			1- 4
Xaudum	x		x						x				5
Okwa	x		x						x				6-7
Khumib	x	x	x										8-9
Hoarusib	x	x	x	x	x	x							10-13
Hoanib	x		x	x		x							14-21
Huab	x	x	x	x	x	x							22-23
Swakop	x									x	x	x	24-27
Kuiseb	x	x	x		x	x				x	x	x	28-32
Tsondab	x		x	x	x	x		x	x				33-40
Tsauchab		x	x	x	x								41-44
Fish	x	x		x	x				x	x	x	x	45-47
Auob			x		x	x			x				48
Nossob			x		x	x			x				49
Kuruman	x		x						x				50-51
Molopo	x		x	x	x	x			x				52-53
Orange	x					x				x	x	x	54-57
Modder	x		x		x		x		x				58
Buffels	x									x		x	59-62
Huis		x				x					x		63
Gourits	x		x	x						x		x	64-69
Wilgerbosch	x	x	x				x				x		70

5.4. Discussion

Analyses of the database will be discussed here in terms of: i) the typology of rivers studied; ii) the nature and controls on the preserved fluvial record; iii) the sources of evidence and approaches used for palaeoenvironmental interpretation; and iv) the spatial and temporal trends in the regional quality-assessed Quaternary fluvial record.

5.4.1. River typology

Data on the topographical, hydrological, and climatological setting of river catchments (Table 5.4) detail a suite of river typologies that have been studied for evidence of palaeoenvironmental change across southwestern Africa. Ocean-draining moderate gradient rivers from coast-parallel high elevation ranges are located in coastal Namibia, the westward draining rivers in the South African portion of the Namib, and the southward draining rivers of the Eastern Cape, South Africa (Figure 5.3). The Namib rivers have the highest average channel gradients (>3.6 km m^{-1}), the smallest catchments (<30,000 km^2), are currently ephemeral (flow intermittence 0.88-0.95, Messager *et al*., 2021), and all drain from arid to hyper-arid climate zones. The Eastern Cape rivers of the Huis, Gourits and Wilgerbosch have lower gradients (1.9 to 3.6 km m^{-1}), encompass larger catchment sizes (e.g. Gourits River: 45,000 km^2), have lower probabilities of intermittence (e.g. Huis River: 0.7), and all drain from arid to semi-arid zones.

In the northern Kalahari, the Okavango, Okwa, and Xaudum drain internally towards the interior of southern Africa. These rivers all terminate at an elevation of ~850 m a.s.l. and are characterised by low average channel gradients of <0.5 km m^{-1}. The Okwa and Xaudum are located within the arid climate zone (Figure 5.1), have calculated probabilities of flow intermittence of >0.9 (Messager *et al*., 2021), and have not flowed historically (Shaw *et al.*, 1992; Nash, 2022). The Okavango has its headwaters in the humid tropics and the main channel possesses perennial river flow with

probability of flow intermittence of 0.44. The Orange catchment encompasses a range of climatic contexts spanning from humid to hyper-arid regimes, and a suite of river types are recorded. In the Namibian and southern Kalahari portions of the Orange basin, the Fish and Molopo Rivers flow predominantly through arid climate zones towards the Orange River and have probabilities of intermittence of >0.84 and gradients of >0.8 km m^{-1}. Parts of these rivers are deeply incised into bedrock, with a dominant meandering river style (Table 5.4). The main channel of the Orange has a moderate gradient (1.1 km m^{-1}) and is perennial (probability of flow intermittence: 0.41), but the catchment encompasses a range of intermittence with an average probability of flow intermittence of 0.89.

5.4.2. Controls on the preserved fluvial record

5.4.2.1. Controls on the nature of sedimentary contexts

Regional variability in the diversity of documented sedimentary contexts (Figure 5.1, Table 5.6) can in part be explained by the characteristics of the river typologies. Interdune deposits have only been studied in the Namib region (Table 5.6) under the hyper-arid zone (Figure 5.1; Table 5.4). In coastal Namibia, dunefields dominate the landscape in the Namib Desert and Skeleton Coast and can restrict adjacent rivers from terminating at the sea (Stanistreet and Stollhofen, 2002). At the eastern edge of the Namib Desert, channel facies are preserved (Brook *et al*., 2006), yet further into the dunefield, interdune facies dominate (Stone *et al*., 2010). Within the dunefield, evidence is preserved of times where rivers were able to pass through interdunal depressions and deposition occurred under still water ponding (Stanistreet and Stollhofen, 2002; Teller and Lancaster, 1986).

Scroll bars have been studied in the Northern Kalahari (Tooth *et al*., 2022), where relict fluvial features in the Okavango Delta are preserved through peat organic overburden after channel abandonment. Exhumation through peat fires (Ellery *et al*., 1989) has unveiled scroll bars that are evidence of lateral meander migration (Tooth *et al*., 2022). Slackwater deposits (SWD) have been

studied extensively in the Orange, Eastern Cape, Namib, and yet have not been studied in the Northern Kalahari, where records are available instead from channel, overbank, and scroll bar sequences (Table 5.6). The low gradient endoreic nature and lack of bedrock gorges of the rivers of the Northern Kalahari makes these systems distinct from the fluvial systems of the Fish and Molopo within the Orange region that do contain SWDs (Table 5.5; Shaw *et al*., 1992). Whilst sporadic flooding occurs in Namibia and the southern Kalahari (e.g. Kuruman River) in response to high precipitation events, surface flow in dry mekgacha of the Northern Kalahari, (e.g. Okwa and Xaudum) is rare and short lived in response to high-intensity events (Mazor *et al*., 1977; Shaw *et al*., 1992). The chaotic nature of channel switching in the Northern Kalahari means that, whilst slackwater conditions occur, the palaeoenvironmental information preserved is more limited than other settings and SWDs have not been studied.

Channel confinement has a strong control on reach-scale river character and behaviour in fluvial systems and is important for explaining the distribution of documented sedimentary contexts in southwestern Africa (following findings by Fryirs *et al*., 2016; Keen-Zerbert *et al*., 2013). The number of sites from confined, partly confined, or unconfined settings differs between regions and corresponding differences are recorded in the suite of sedimentary contexts studied (Table 5.6). All confinement settings have been studied in the Namib, whereas the sites in the Northern Kalahari are all unconfined. SWDs are predominantly found along confined reaches in rivers of both large and small catchment sizes (e.g. Kuiseb, Grodek *et al*., 2013; Orange, Zawada *et al*., 2000). Confined bedrock reaches favour the accumulation of suspended silt and sand from exceptional floods (Baker, 1987; Cloete *et al*., 2018). In these settings, preservation of sediment deposition from sub-bankfull channel aggradation is limited (Toonen *et al*., 2017) and channel migration is restricted where laterally confined channels lack a substantial alluvial bed (Fryirs *et al*., 2016; Tooth and Nanson, 2000). In contrast, channel, overbank, and scroll bar sedimentary contexts are more predominantly located in partly confined or unconfined reaches (Table 5.6). Unconfined alluvial

rivers possess erodible banks and rivers have a wider range of lateral variability (Fryirs *et al*., 2016; Grenfell and Grenfell, 2021), so can host aggradational sites, and preserve abandoned channels where non-equilibrium conditions prevail (Tooth and Nanson, 2000). All interdune and playa deposits are found in unconfined settings where ponding of sediment and drainage in lacustrine settings is possible (e.g. Völkel *et al*., 2021).

The tendency towards formation of specific deposit types is also dependent on palaeohydrological conditions at deposition and the river's sedimentary response to climatic drivers (Figure 5.6). SWDs have predominantly been interpreted as records of extreme floods or high energy flow as a response to high precipitation events within ephemeral flow regimes (e.g. Cloete *et al*., 2018; Greenbaum *et al*., 2014). River end deposits are consistently interpreted in this database as representing low energy flow during periods of low precipitation, resulting in termination of the river further upstream within a dry or semi-arid climate of an ephemeral flow regime (Eitel *et al*., 2005; 2006). When located beyond the contemporary end point of rivers, interdune deposits are indicative of increased rainfall and increased competence of a river to overcome transmission losses and penetrate into the dunefield (Brook *et al*., 2006; Stone *et al*., 2010). These deposits then attest to low energy flow and settling of water, and the presence of diatoms and ostracods indicate calm, ponded environments (Teller *et al*., 1990). Channel and overbank deposits have a broader range of characteristics and therefore encompass a range of fluvial processes: from different flow occupancy under ephemeral to perennial regimes and flow magnitudes of extreme floods to low energy flow (e.g. Eitel *et al*., 2005; Hurkamp *et al*., 2011; Ramisch *et al*., 2017; Srivastava *et al*., 2005; Tooth *et al*., 2022; Walsh *et al*., 2022).

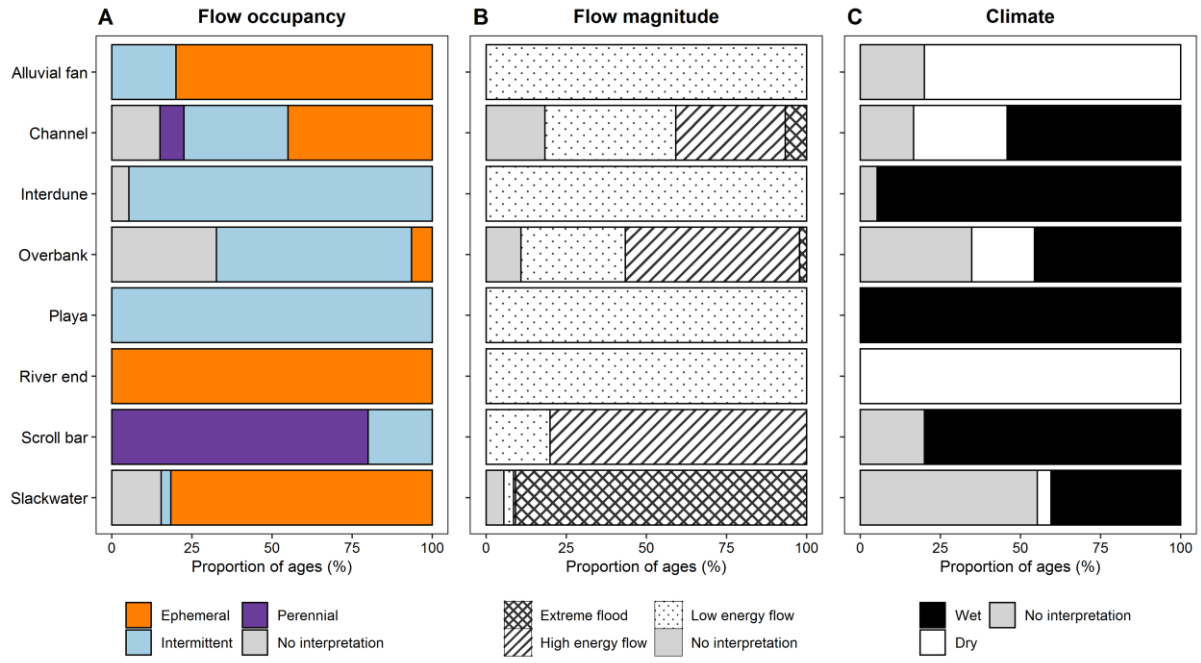

Figure 5.6. Association between sedimentary context and fluvial interpretation (flow occupancy, **A,** and magnitude, **B**) and climate interpretations, **C**. Data includes records that have passed the data quality assessment. Bars are coloured by percentage of ages relating to each interpretation

5.4.2.2. Controls on length of fluvial record

By region, the longest fluvial histories are preserved at sites in the Namib (Table 5.5; Figure 5.7). Here, the record from Narabeb, Tsondab River (site 34; Stone *et al*., 2010), extends to 132 ka, yet the majority of sites from all other regions have maximum ages of <25 ka. The geomorphological setting plays a role in controlling sediment production and preservation, and channel confinement in particular is found to be a control on the length of the fluvial history preserved (Figure 5.7; following findings by Harden *et al*., 2010). Across the regions studied, the longest chronologies are established from unconfined river settings, in contrast to confined settings where 85 % of filtered ages date to the last millennium. Sedimentary archives along bedrock controlled reaches have a lower preservation potential as sediment is removed by subsequent floods (Fryirs and Brierley, 2012; Lewin and Macklin, 2003) and tend to only be preserved in sheltered backflooded tributaries (Grodek *et al*., 2013). As a result, long-term sediment preservation in sedimentary contexts such as SWDs is limited (Figures 5.5A and 5.7). In unconfined settings, the ability of rivers to adjust their

width and meander position in response to hydroclimatic changes (Grenfell and Grenfell, 2021) results in a combination of aggradation and incision rather than removal of sediment. Whilst incision within this process can result in sediment recycling (Grenfell and Grenfell, 2021), and overbank sedimentation can be self-limiting (Lewin and Macklin, 2003), wide valleys have the potential to possess long sedimentary records particularly in abandoned channels and elevated alluvial terraces (Lewin and Macklin, 2003; Tooth *et al*., 2013). In the case of interdune deposits at the distal end of the Tsondab and Tsauchab Rivers in Namibia (sites 33 to 38, and 41), aggradational environments exist where deposition occurred in still water conditions where subsequent floods accumulate rather than erode and remobilise sediment downstream, therefore enabling the potential to preserve a long history of fluvial sedimentation.

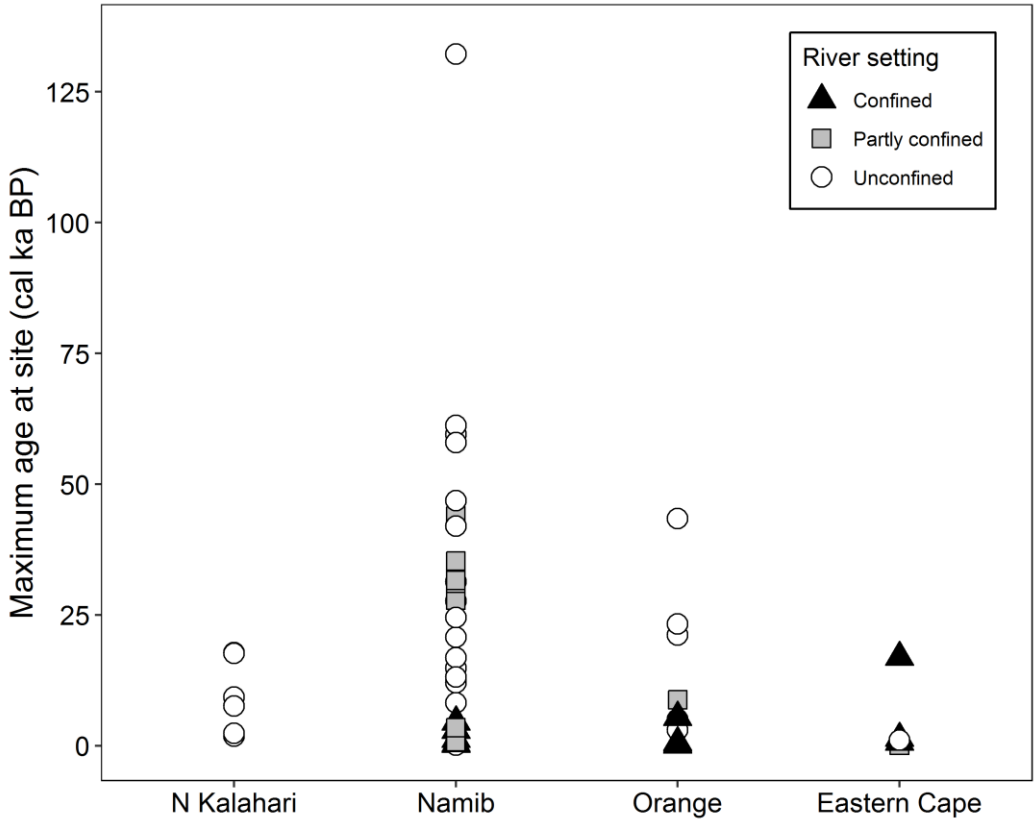

Figure 5.7. Maximum age at each site by region and by river setting. River setting is defined on a scale from confined to unconfined following Fryirs *et al*. (2016).

River sinuosity and resulting style (e.g. straight, meandering) can influence the characteristics of sedimentary deposits (Tooth *et al*., 2013). Analysis of sinuosity at the reach scale, however, indicates that for the southwestern African Quaternary fluvial dataset there is no relationship between channel sinuosity and length of documented chronology ($r^2 = 0$, $p = 0.94$).

The temporal extent of documented fluvial histories within this database also reflects the choice of units sampled and the aims of scientific studies. Within the filtered dataset, ~45 % of ages fall within the last millennium (Figure 5.5B) and whilst the length of the chronologies established shows a relationship with confinement of the channel (Figure 5.7), there is variability in the distribution of chronology lengths between confinement categories and between regions. First, the majority of ages (86 %) within this database were obtained from samples collected from natural exposures. Whilst this section type has numerous advantages (e.g. enabling the identification of clear stratigraphic boundaries), exposures often do not uncover the full extent of fluvial deposition and where exposures do not exist, major periods of deposition are not studied (Eitel *et al*., 2006). Second, the Namib has the longest established history of late Quaternary fluvial sedimentation and is the region that has received the largest research focus, in terms of the number of sites, distribution of sedimentary contexts (Table 5.6), and number of ages used to establish chronologies (Table 5.5). A greater number of dated units is likely to pick up a more complete suite of depositional units. And third, the skew in the distribution of ages could also be driven by the aims of studies to reconstruct specific aspects of late Quaternary change. Several papers (e.g. Zawada *et al*., 2000; Cloete *et al*., 2018) produce chronologies from SWDs of recent floods that map on to the documented timing of historical events.

5.4.2.3. Drivers of geomorphic change

Whilst deposition of fluvial sediment has commonly been linked to changes in hydroclimate, geomorphic change can also occur as a response to a suite of allogenic and autogenic processes (Fryirs and Brierley, 2012; Grenfell and Grenfell, 2021; Tooth *et al*., 2004, 2013). In the case of the fluvial records within this database, 132 filtered ages (31 % of the full dataset) are reported without interpretation of the palaeoclimate context under which sediments were deposited (Figure 5.6C). Non-climatic drivers have been drawn on to explain fluvial sedimentation in three rivers in the Eastern Cape region in particular. These include the role of wildfires on extreme floods in the Huis River (Bordy *et al*., 2018, site 63, Figure 5.1), fluvial channel connectivity in the Wilgerbosch River (Oldknow and Hooke, 2017, site 70), and anthropogenic land use in the Gourits River (Damm and Hagedorn, 2010, sites 67 to 69). At Erfkroon on the Modder River, Orange catchment (Lyons *et al*., 2014; site 58) a luminescence chronology details almost continuous sedimentation throughout the last 44 ka regardless of changes in prevailing climate. Here, it is the magnetic parameters of palaeosols developed contemporaneously that reflect changes in climate, rather than the rate of fluvial sedimentation. Of the filtered ages without climate interpretation, 110 ages are accompanied by interpretations of flow dynamics, where studies focus on investigation of the timing of fluvial sedimentation rather than the nature of drivers of this change (e.g. Thomas *et al*., 2017).

5.4.3. Sources of evidence

The ability to reconstruct palaeoenvironmental change requires both a robust chronology and a suite of independent proxies for interpretation of depositional contexts. Here, we look at the spatial (Figure 5.3, Table 5.5) and temporal (Figures 5.4 and 5.5) distribution of the quality of chronological data and use of sedimentary approaches. From this, we create a framework that considers both the data required to reach specific interpretations and the spatial and temporal scales that these interpretations can be applied.

5.4.3.1. Chronological data quality

De Cort *et al*. (2021) note that the collation of palaeoenvironmental data is susceptible to the "synthesis dilemma", where a trade-off exists between: i) selecting a small number of high-quality records at the expense of reducing the temporal and spatial coverage of the synthesis; and ii) including as much data as possible whilst accepting that the dataset may include more 'noise' in the form of lower quality data. Following the chronological data quality assessment (Table 5.3), the number of filtered ages by chronology in this database remains substantial (490 ages, 81 % of all ages). The proportion of filtered ages has increased with publication year (Figure 5.4B), which is indicative of advances in dating methods and data reporting over time. Older publications (e.g. published between 1980 and 1990) had: i) a higher use of luminescence dating protocols that are less precise (e.g. use of MAAD and SAAD in Eitel and Zoller, 1996; Zawada *et al.*, 2000); ii) more limited data reporting (e.g. limited quotation of stratigraphic context in Vogel and Visser, 1981); and iii) incorporate a larger number of sites that have few ages reported. Approximately 45 % of sites studied between 1980 and 1990 have three or less ages, compared to only 26 % of sites studied since 2010. The former derives from a period of infancy in radiocarbon applications when a focus was placed on capturing a dataset that was spatially broad, rather than targeting specific palaeoenvironmental questions through detailed assessments of individual sites. The age of the deposit is not a determinant of data quality (Figure 5.5C), meaning that older deposits have as equal a chance of having high quality chronological control as younger deposits.

5.4.3.2. Sedimentary approaches

Different sources of evidence have the ability to tell us about different aspects of an environmental response to climate perturbations (Tofelde *et al*., 2021). A suite of sedimentary approaches have been used within the southern African dryland fluvial literature (Table 5.6), including analysis of: i) textural (e.g. grain size; Thomas *et al*., 2017) and architectural elements (e.g. stratigraphic and lithofacies analysis; Srivastava *et al*., 2006; Walsh *et al*., 2022) to indicate of the nature of river flow;

ii) the topographic setting of deposits and meander dimensions to reconstruct palaeodischarge (e.g. Benito *et al*., 2011; Greenbaum *et al*., 2014; Tooth *et al*., 2022); iii) sediment composition to consider provenance (e.g. petrographic datasets to infer source regions; Ramisch *et al*., 2017; Walsh *et al*., 2022); and iv) analysis of sediment content such as characteristics of soil formation, palaeoecology, and palaeontology (e.g. Lyons *et al*., 2014; Nash *et al*., 2006) to assess environmental conditions. The majority of publications without any sedimentary detail are those published in the 1980s, where research was more exploratory with a focus on generating radiocarbon chronologies. Over the last four decades, there has been an increase in the assessment of sediment composition, particularly through the analysis of pedogenic characteristics (e.g. Völkel *et al*., 2021). Analysis of sediment provenance, however, remains a particular research gap in this literature, where it has only formed the main approach of two studies here to date (Ramisch *et al*., 2017; Walsh *et al*., 2022). Provenance analyses in Namibia and across the wider Kalahari (Garzanti *et al*., 2012, 2014, 2022) provide extensive datasets on the mineralogical signatures of many of the rivers considered in the database and could be used as a resource for research on palaeochange to draw on.

Regional differences emerge in the use of specific proxies (Table 5.7). Analyses of palaeodischarge have been performed at sites along seven rivers within the database (Table 5.7). This work shows that palaeodischarge data can be obtained from different types of rivers in different settings, e.g. the confined reaches of rivers in the Orange, Namib, and Eastern Cape regions and the low gradient alluvial rivers and palaeochannels in the Okavango in Northern Kalahari (Table 5.4). For each of these types, a set of conditions need to be met. Estimates from SWDs assume that the topography of bedrock channels has remained stable over time (Benito *et al*., 2020, e.g. Cloete *et al.*, 2018), and estimates from meander dimensions of palaeochannels assume that channel width increases with discharge (based on hydraulic geometry relationships; Tooth *et al*., 2022). Palaeontology and palynology proxies have also only been used in specific environments, such as Okavango Delta

(Nash *et al*., 2006; Shaw *et al*., 1992), the interdune region at the distal end of the Tsondab (Teller and Lancaster, 1986), and in the Huns (Stengel and Leser, 2004), Molopo (Heine, 1990), and Modder rivers (Churchill *et al*., 2000). The majority of these settings include ponding and still water deposition, enabling the preservation of organisms within the fluvial sediments.

5.4.3.3. Establishing interpretations of palaeoenvironmental change

Figure 5.8 links the methodological approaches within this dataset to the type of information gained and considers interpretations in the context of the scale of chronological uncertainties and availability of corroborating records. These factors have an influence on the choice of appropriate proxy analyses to answer specific questions about fluvial change (Figure 5.8A), the temporal range of climate variability that can be discerned (Figure 5.8B), and the implications for reconstructing local or regional scale change (Figure 5.8C). Fluvial systems in southwestern Africa are being studied in increasing detail (e.g. 144 ages published in 2021-2022, Völkel *et al*., 2021; Tooth *et al*., 2022; Walsh *et al*., 2022), and this framework highlights the need for consideration of the data required to reach robust and justifiable conclusions on defined spatial and temporal scales.

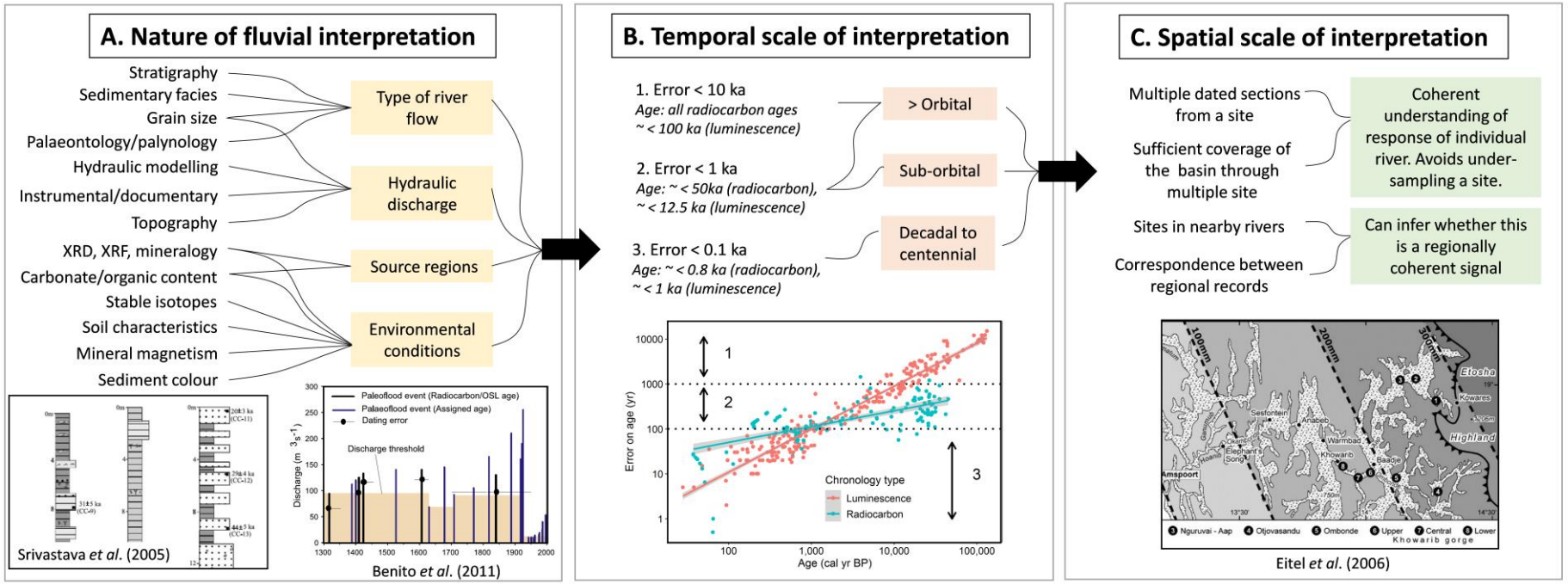

Figure 5.8. Framework for considering the data required for interpretation of dryland fluvial sedimentary records. **A)** Link between independent proxies and the nature of fluvial interpretation that can be reached. Examples: Lithofacies analysis of Hoarusib River sediments (Srivastava *et al*., 2005), palaeoflood discharge estimates, Buffels River (Benito *et al.* 2011). **B)** Link between the scale of chronological uncertainties and the scale of climate variability that can be discerned. Scales of uncertainty are highlighted on this plot as numbers 1 to 3 (reflecting errors <10 ka to < 1ka). **C)** Spatial scale of interpretation: linking the number of sites in both a river basin and across nearby catchments with the ability to interpret regional palaeoenvironmental change. Example: high coverage of sites across the Hoanib River catchment (Eitel *et al*., 2006).

Chronologies with the smallest absolute uncertainties (<100 years: 33 % of the filtered dataset) can be used to establish the timing of river flow on the scale of individual *events* to multi-year *episodes* (cf. Toonen *et al*., 2017). Where there is overlap with instrumental or historical data (e.g. Cloete *et al*., 2018), this temporal resolution enables links to be made between magnitudes of documented floods and climate events (cf. Baker, 2008; Woodward *et al*., 2010). In the southwestern African dataset, these ages predominantly date to the last 1,000 years (Figure 5.8B). When the scale of uncertainty increases (e.g. in the range of 100 to 1,000 years; 46 % of ages), the ability to distinguish individual flood events decreases, and the sedimentary record can be more confidently interpreted in terms of *phases* of river flow (Toonen *et al*., 2017) as a record of millennial scale climate change (Macklin *et al*., 2012). Due to the largest number of ages falling in the Holocene (Figure 5.8B; where the majority of radiocarbon ages have uncertainties of <1,000 years), and where there are cases of overlapping chronologies (e.g. in the headwaters of the Hoanib, Eitel *et al*., 2006; and BüllsPort playa, Völkel *et al*., 2021), investigations at this temporal scale are able to identify periods of distinct fluvial regimes.

The oldest portion of this fluvial dataset (particularly luminescence ages >12.5 ka) have absolute uncertainties of >1,000 years (18 % of ages). Here, statistical errors impact the ability to distinguish between distinct geomorphological events and have the effect of filtering to only the lower frequency events (Bailey and Thomas, 2014). At this scale, it is possible to link fluvial interpretations to marine isotope stages and sub-stages (Macklin *et al*., 2012), but when errors are larger (>10,000 years; 1 % of the filtered dataset), the timing of fluvial change are increasingly difficult to pinpoint. The absolute increase in errors associated with older ages is a universally recognised problem for dated sediments (e.g. Burrough *et al*., 2007; Fitzsimmons *et al*., 2013; Macklin *et al*., 2012) and is important to recognise when considering the temporal scales of change possible to resolve with the achievable temporal resolution offered by the dating precision. Where uncertainties are small enough, individual flood *events* within flash flood deposits have been linked to high precipitation

climate events (e.g. Greenbaum *et al*., 2014; Grodek *et al*., 2013), yet when errors are larger, multidecadal- to centennial-scale *phases* of flash floods can be identified and these conditions are commonly interpreted as episodes of high ephemeral discharge within the context of an otherwise arid climate (e.g. Srivastava *et al*., 2004). The scale of analysis therefore has an influence on the palaeoenvironmental interpretation as wet or dry (e.g. the difference between identification of a wet event or a dry period) and needs to be taken into account when interpreting the combined regional Quaternary record.

Given the limited sampling of river deposits in southwestern Africa to date, Figure 5.8 also details considerations for reaching conclusions about local versus regional scales of change. Dryland geomorphological archives are commonly discontinuous with variable preservation of depositional events. Amongst a number of filtering processes from the climate signal to interpretation (see Allen, 2017; Bailey and Thomas, 2014; Jerolmack and Paola, 2010; Kemp, 2012; Macklin *et al*., 2012), processes of cut and fill can result in sediment recycling and removal of sedimentary units (Grenfell and Grenfell, 2021; Lewin and Macklin, 2003). Investigation of a sufficient number of sections and sites within a fluvial basin is therefore important to increase the stratigraphic completeness and avoid aliasing the record through under-sampling (Toonen *et al*., 2017). If correlations and trends emerge between records across a region, it is possible to start interpreting regional controls on fluvial change. This requirement for nearby sites helps avoid over-interpreting regional change from site specific records, and acknowledges potential limitations of using findings based on spatially and temporally limited ranges of dates.

Following this regional compilation of fluvial records, we suggest that there are important sites within southwestern Africa that could benefit from being revisited and investigated more intensively than to date. First, this could include a focus on establishing additional chronologies from a larger suite of sections at studied sites. The number of ages used to establish chronologies

across southern Africa's fluvial systems is highly variable (Figure 5.3A), and whilst several sites have been studied intensively (e.g. the Homeb Silts, Kuiseb River), around 38 % of the sites in the full dataset have three or fewer ages (Appendix E Table E1). Second, early thermoluminescence work, such as in the Namib region on alluvially-reworked loess in the headwaters of the Hoanib and Huab Rivers (Eitel and Zoller, 1996; Eitel *et al*., 2001) and the Orange on SWDs (Zawada *et al*., 2000), highlights potentially important sites that could benefit from being revisited with the application of newer luminescence protocols. Third, 20 % of the ages within the database were not included in further analysis because they were not accompanied by independent proxies for palaeoenvironmental interpretation. The use of robust analytical methods has increased in recent decades, and approaches such as analysis of sediment provenance and architectural elements could be used to revisit these sites.

5.4.4. The Quaternary fluvial record

With appropriate dating control and acknowledgement of the complexities associated with the analyses of proxies and scale of chronological uncertainties, the Quaternary history of southwestern Africa's rivers is interrogated here (Figure 5.9). We discuss the fluvial history preserved in quality-assessed record (Figure 5.9A, C) at three key timesteps: the Last Glacial Maximum (LGM, 24-18 ka BP; following the conservative EPILOG definition; Chase and Meadows, 2007; Clark and Mix, 2002; Mix *et al*., 2001), the mid Holocene (MH, 8-4 ka BP), and the last millennium (1 ka BP-present). These timesteps were chosen based on the availability of fluvial data and for the relevance to existing regional syntheses of palaeodata (e.g. Burrough and Thomas, 2013; Chase and Meadows, 2007; Gasse *et al*., 2008) and palaeoclimate modelling simulations (Engelbrecht *et al*., 2019; Kageyama *et al*., 2021; Taylor *et al*., 2012). Interpretation of the nature of palaeoclimate change from the fluvial archives are discussed here (Figure 5.9B) and the drivers of this change are assessed in further detail in the context of palaeoclimate model outputs in Walsh *et al*. (in review).

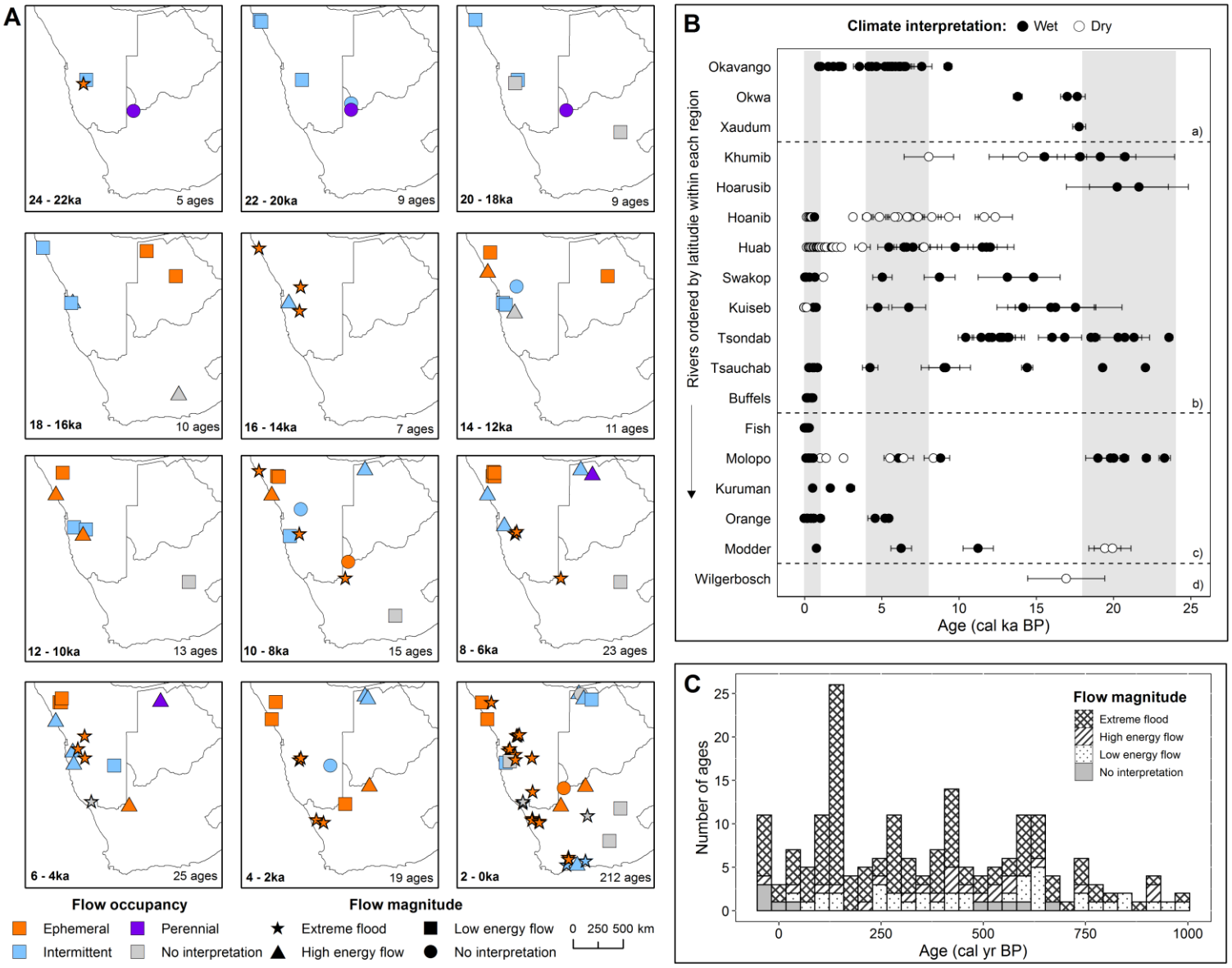
A
24 - 22ka
5 ages
22 - 20ka
9 ages
20 - 18ka
9 ages
18 - 16ka
10 ages
16 - 14ka
7 ages
14 - 12ka
11 ages
12 - 10ka
13 ages
10 - 8ka
15 ages
8 - 6ka
23 ages
6 - 4ka
25 ages
4 - 2ka
19 ages
2 - 0ka
212 ages
Flow occupancy
Ephemeral
Intermittent
Perennial
No interpretation
Flow magnitude
Extreme flood
High energy flow
Low energy flow
No interpretation
0 250 500 km
B
Climate interpretation: Wet Dry
Rivers ordered by latitudie within each region
Okavango
Okwa
Xaudum
Khumib
Hoarusib
Hoanib
Huab
Swakop
Kuiseb
Tsondab
Tsauchab
Buffels
Fish
Molopo
Kuruman
Orange
Modder
Wilgerbosch
a)
b)
c)
d)
0
5
10
15
20
25
Age (cal ka BP)
C
Flow magnitude
Extreme flood
High energy flow
Low energy flow
No interpretation
Number of ages
0
5
10
15
20
25
0
250
500
750
1000
Age (cal yr BP)

Figure 5.9. Southwestern Africa's late Quaternary fluvial and climate conditions inferred from the fluvial records with chronologies (n.b. changes without chronology have not been possible to include). **A)** Fluvial interpretation from quality assessed records for the last 24 ka at 2 ka timeslices. The data presented here (<24 ka) make up 82 % of the filtered dataset. The number of ages dating to each timeslice are recorded in the corner of each map. **B)** Climate interpretations of fluvial deposits (quoted as wetter or drier relative to contemporary conditions). Only records that reach climate interpretations are included. Rivers ordered in the y axis by latitude and region (a: Northern Kalahari, b: Namib, c: Orange, d: Eastern Cape). Grey boxes represent time periods discussed in the text: Last Glacial Maximum (LGM; 24-18 ka BP), mid Holocene (8-4 ka BP), and the last millennium (1 ka-present). **C)** Frequency distribution of ages within the last millennium, coloured by fluvial interpretation (na = no interpretation).

5.4.4.1. The Last Glacial Maximum (LGM; 24-18 ka BP)

The timing of river flow within the LGM is established through 23 ages from seven sites along seven rivers. Sedimentary deposits within currently ephemeral Namibian rivers detail evidence of regionally wetter climatic conditions at the LGM in the Khumib, Hoarusib, Tsondab and Tsauchab catchments (Figure 5.9B). Higher rainfall levels increased the flow occupancy in the Hoarusib River, with deposits providing evidence for intermittent low energy flow (Figure 5.9A; at 21.7 ± 3.2 ka to 20.3 ± 3.3 ka; Srivastava *et al*., 2005; site 12, Figure 5.1). Lithofacies analysis indicates a river system characterised by more continuous flow than today with cohesive river banks (Srivastava *et al*., 2005). A climate with long periods of rainfall during this period is also inferred from evidence of persistent, low energy, slowly charging floods along the Khumib River (20.8 ± 3.2 ka to 19.2 ± 2.3 ka; Srivastava *et al*., 2004; site 9). Playa sediments within the Tsondab catchment also provide a record of fluvial response to wetter conditions than present at the LGM (Völkel *et al*., 2021; site 40). Geochemical analysis of soil characteristics of radiocarbon dated sediment from the BüllsPort Playa (23.6 ± 0.2 cal ka BP to 18.5 ± 0.2 cal ka BP) indicate continuous deposition and sustained water availability in the system (Völkel *et al*., 2021). Sedimentary sequences along the Tsauchab River also attest to a wet LGM (Völkel *et al*., 2021; site 43), in the form of channel aggradation under low energy flow (19.7 ± 1.7 ka) and SWDs from extreme floods (22.1 ± 0.1 cal ka BP).

Records from channel deposits along the Molopo and Nossob Rivers detail evidence of perennial and intermittent flow respectively under wet conditions (Figure 5.9A, B; Heine, 1990; Hurkamp *et al*., 2011; sites 49 and 52). Macrofossil freshwater mollusc and ostrich egg shell radiocarbon ages place fluvial deposition in the Molopo from 23.3 ± 0.7 cal ka BP to 18.9 ± 0.8 cal ka BP (Heine, 1990; Hurkamp *et al*., 2011). Analysis of sediment texture indicates persistent flow of the Molopo alongside evidence of lunette dune cessation. However, across the wider Orange River basin, in the contemporary semi-arid region (Figure 5.1), a mineral magnetism record from an alluvial-palaeosol sequence in the Modder River shows evidence of cold and dry conditions at the LGM (Lyons *et al*., 2014; site 58). The magnetism parameters of sedimentary units within a vertically aggrading overbank sedimentary deposit date to 20.0 ± 1.2 ka and 19.5 ± 1.0 ka and reflect prevailing rainfall levels of around 100-200 mm yr^{-1} (much lower than contemporary levels of 400-500 mm yr^{-1}) (Lyons *et al*., 2014).

5.4.4.2. The mid Holocene (MH; 8-4 ka BP)

At 18 sites along ten rivers, evidence of fluvial deposition at the MH is established through 48 ages. Records from eight rivers within the Namib, Northern Kalahari, and Orange regions (Figure 5.3) indicate conditions of enhanced river flow under a climate wetter than present at the MH (Figure 5.9A and 5.9B). Reduced river flow under dry climate conditions is recorded in the northern Namib throughout the MH and a transition from wet to dry conditions occurred within this period in the southern Kalahari portion of the Orange region.

Stratigraphic, textural, and compositional analysis of channel and overbank sedimentary contexts within the Huab River Skeleton Coast valley fill provide evidence of more humid conditions than present at the MH, where Huab River flow occurred as a more channelised and confined fluvial system from 7.1 ± 1.1 ka to 5.5 ± 0.7 ka (Walsh *et al*., 2022; site 22). The climate setting was conducive to more sustained intermittent, compared to contemporary ephemeral, river flow that

enabled transport of coarse sediment fractions throughout the fluvial system. This record corroborates findings from the Homeb Silts in the Kuiseb River (site 30), reflecting a period of sediment mobilisation under a wet climate at the MH (6.8 ± 1.1 ka; Srivastava *et al*., 2006). Along the Swakop and Kuiseb in Namibia's present-day hyper-arid to arid zone (Figure 5.1), sedimentary deposits further this interpretation of seasonal rains coincident with high energy flow (Greenbaum *et al*., 2014; Grodek *et al*., 2013; sites 25 and 32). From 9 to 7 ka, deposition of interdune sediments indicate an extension of the Tsauchab River beyond its current end point during wetter climate conditions (Brook *et al*., 2006). Evidence is preserved as both channel deposits indicating river flow past the Tsauchab vlei and interdune deposition indicating ponding and low energy flow to enable settling of sediment.

Wet conditions during the MH are recorded in sedimentary deposits in the Okavango Delta, Northern Kalahari (Figure 5.3). In the Xugana region, evidence of enhanced fluvial activity is preserved in scroll bars of abandoned channel meanders and a sinuous palaeochannel from 7.7 ± 0.6 ka to 4.2 ± 0.2 ka (Tooth *et al*., 2022; site 4). Palaeodischarge estimates of 350-450 $m^3 s^{-1}$ are up to nine times greater than contemporary discharge (at the equivalent point in the delta) and suggest a fluvial response to a period of higher rainfall than present (Tooth *et al*., 2022). Enhanced Okavango channel flow under wetter conditions is also dated to 6.1 ± 0.2 cal ka BP in a record of sedimentology and palynology from the panhandle region (Nash *et al*., 2006; site 2). Within the Orange River system, SWDs from high discharge floods (12930-14660 $m^3 s^{-1}$; site 55) indicate a period of hydroclimatic stability with increased rainfall and warmer temperatures (Zawada *et al*., 2000). Along the Modder River (site 58), an increase in hematite content within palaeosols developed in an overbank sedimentary unit indicates a rise in temperature at the site and a period of seasonally and annually higher rainfall (Lyons *et al*., 2014).

In the north of the Namib region and in the southern Kalahari portion of the Orange region (Figure 5.3), evidence of reduced fluvial activity in response to conditions drier than present is preserved (Figure 5.9A). River-end deposits within the Hoanib catchment (7.4 ± 0.4 ka to 4.1 ± 0.3 ka; Eitel *et al*., 2006; sites 17-21) are interpreted as records of low energy flow where the river terminated further upstream than its contemporary end point. These deposits reflect a period of sporadic rainfall and ephemeral river flow within a climate more arid than today. Along the Molopo River, southern Kalahari, a transition from flash flood archives within channel deposits to low energy aggradation of fan deposits is recorded (Ramisch *et al*., 2017; site 53). These fan units were deposited due to decreasing flood intensity at 6.5 ± 0.6 ka and 5.6 ± 0.4 ka as a response to a more arid climate. Provenance analysis of these sediments indicate that the Molopo River was endoreic and connection between the Kalahari drainage and Orange River was limited during the Holocene.

5.4.4.3. The last millennium (1 ka BP to present)

Records from the last millennium, with smaller absolute uncertainties on ages and records overlapping with historical and instrumental datasets, have enabled a consideration of changes in flood frequency, in some cases at an annual resolution (e.g. Zawada *et al.*, 2000). Here ages are quoted with the units 'yr' rather than 'ka' as above. 188 ages from 33 sites along 16 rivers date to the last millennium. The frequency distribution of ages within this period highlights the dominance of records of extreme floods and high energy flow (75 % of filtered ages dating to the last millennium; Figure 5.9C), predominantly reconstructed from SWDs.

Quantitative discharge estimates from flash flood sequences have been calculated for 61 palaeoflood events within this period. In the Swakop River, three intervals of differing flood frequencies are recorded (Greenbaum *et al*., 2014; sites 25-27). These show an increase from i) one extraordinary flood every 180 years between 1,280 and 740 yr BP, ii) one large flood every 80 years from 740 to 200 yr BP, to iii) one large flood every 7 years in the last 200 years. These intervals of

changing flood frequencies are also preserved in the Kuiseb SWD record (Grodek *et al*., 2013; sites 31 and 32), but here with evidence of a large flood every 30-40 years, and periodic increases to flood frequencies of up to 7 floods in 20 years. In the Buffels River, warmer climate conditions resulted in a decreased flood frequency from 525 to 350 yr BP, and a colder wetter period resulted in higher flood occurrence from 350 to 150 yr BP (Benito *et al*., 2011; sites 59-62). SWDs along the Tsauchab (Völkel *et al*., 2021; site 43) and Tsondab (Völkel *et al*., 2021; site 39) correspond in timing to interdune deposits at Sossus Vlei, Tsauchab (Brook *et al*., 2006, site 41). From 0.9 to 0.3 ka, interdune and channel deposits within the Namib Desert indicate increased capacity of the Tsauchab River as a result of higher water availability in the system (Brook *et al*., 2006).

Flash flood records within SWDs have also been dated at sites within the Orange and Eastern Cape regions (Figure 5.3), attesting to occurrence of high discharge events. In the Fish River, palaeodischarge estimates exceed historical records and indicate the occurrence of at least 12 large floods in the last 350 years (Cloete *et al*., 2018; sites 45-46). A regime of high energy ephemeral flow is also recorded in the Molopo River from 600 to 100 yr (Ramisch *et al*., 2017; site 53), and as extreme floods with high discharge in the Bloeddrift and Xobies regions of the Orange River (Zawada *et al*., 2000; sites 54, 55, 57), and Huis River (Bordy *et al*., 2018, site 63). Together, these records indicate evidence of an ephemeral systems with extreme discharge within the last 1 ka years, where decadal scale flood frequencies have been linked to synoptic climate patterns.

Chronologies have also been established from deposits of lower energy flow within the last millennium, indicative of arid conditions in the Namib and Northern Kalahari, and wetter conditions in the headwaters of the Orange. In the Namib, sedimentology of the Amspoort Silts in the Hoanib River indicates that their formation since 550 yr BP occurred as a result of decreasing runoff and aridification (Eitel *et al*., 2005; site 15). Analysis of Huab River sediments indicates an ephemeral flow regime with a lower capacity to transport sediment under lower precipitation than the MH

(Walsh *et al*., 2022; site 22). This diminished fluvial activity is also recorded in the Xugana region of the Okavango at 180 to 200 yr (Tooth *et al*., 2022; site 4), with evidence of smaller channels with lower discharges. This is corroborated by the sedimentological and palynological record indicating a transition at 1 ka towards arid conditions similar to today in the Okavango (Nash *et al.*, 2006).

5.5. Conclusion

This paper presents an integrated assessment of late Quaternary palaeoenvironmental data from fluvial sedimentary archives in the relatively western and central regions of southern Africa. We present a new chronological database of ages, approaches, and interpretations of fluvial and climate conditions from 20 rivers. This analysis highlights the range of river types that have been studied: from moderate gradient ephemeral systems draining from the Great Escarpment in the Namib region, to low gradient endoreic rivers of the Northern Kalahari, and perennial river flow within the Orange River catchment. These systems are differentiated by catchment characteristics such as channel gradient, flow intermittence, and the precipitation regimes encompassed. Interrogation of the sedimentary contexts studied in these regions gives insights into the controls on sediment production and preservation. In particular, this analysis finds that reach-scale channel confinement has a strong control on both the type and length of fluvial histories preserved, supporting earlier investigations on channel confinement in other regions.

Whilst the number of studied fluvial archives is now substantial, the palaeoenvironmental histories they preserve are often complex. By filtering published research to ensure the integrity of their chronological underpinning, we are better able to distinguish between real heterogeneity in the environmental signal and that introduced through chronological uncertainty. We further argue that, as sedimentary archives in rivers can preserve a range of fluvial conditions, independent proxies such as information on the sedimentary context is required to confidently interpret late Quaternary environmental conditions. Here, we present a framework that identifies the types of

data needed to reach interpretations of the nature of fluvial change and the spatial and temporal scales that these interpretations can be applied to. We find that a particular focus has been placed on assessments on the textural and architectural elements of sedimentary units and palaeodischarge estimates, yet analysis of sediment composition in terms of provenance is limited to date.

From this framework, we identify the importance of considering the magnitude of chronological uncertainties in determining the temporal range of climate variability that can be discerned, particularly in terms of distinguishing between *events*, *episodes*, and *phases*. The Quaternary fluvial record has therefore been interrogated at three timesteps with increasing resolution as absolute uncertainties decrease in younger deposits. At the LGM, fluvial deposits preserve evidence of a fluvial response to predominantly wetter climate conditions, where currently ephemeral systems show evidence of intermittent and perennial flow in channelised systems, sustained water availability across the catchments, and ponding in playa environments. This signal is consistent across all studied rivers except the Modder River, located to the east of the study area, in which conditions drier than present prevailed. During the mid Holocene, evidence of seasonally intermittent flow is detailed in the Namibian ephemeral systems, enhanced palaeodischarge in the Northern Kalahari, extreme flood events in the Orange River, and a wetter climate than present at the Modder River site. Whilst these wet conditions represent a spatially extensive signal, records from the northern Namib and southern Kalahari detail reduced fluvial capacity and aggradation of fan deposits under an arid climate. In the last millennium, an ephemeral flow regime is established in the majority of studied systems. Higher resolution chronologies have enabled detailed assessments of flood frequency changes and identification of intervals of increased incursions of rainfall events with consistent timing, particularly amongst rivers in the Namib region.

This research highlights both the complexity and utility of southwestern Africa's fluvial archives and encourages the inclusion of quality-assessed fluvial records in regional palaeoenvironmental syntheses. Mapping of the coverage of sites across the study area highlights priorities for future study. This could include a focus on sites where few ages have so far been used to establish chronologies and sites that would benefit from being revisited in the light of updated chronological protocols and robust independent approaches for palaeoenvironmental interpretation.

Chapter 6: Paper 3

Chapter 6: Model-archive comparison of mid Holocene and Last Glacial Maximum climates in central southwestern Africa

Paper 3: Ella Walsh, David Thomas, Sallie Burrough

Manuscript submitted to *Quaternary Science Reviews* on 18/4/22. In review.

Abstract

Proposed drivers of past climate change in central southwestern Africa carry with them a suite of predictions with respect to the temporal and spatial pattern of precipitation variability during the late Quaternary. Poor coverage of palaeoclimate archives has so far made it challenging to assess these patterns predicted by models. The spatial distribution of new geoproxy records of palaeoenvironmental change and palaeoclimate archives provide data for investigating these patterns of precipitation change. We analyse a compilation of robust palaeoclimate and palaeoenvironmental archive data in the context of palaeomodel simulations of mid Holocene (6 ka) and Last Glacial Maximum (21 ka) climates to investigate the spatial behaviour of climate systems at key timesteps. The analysis supports different dynamics of the tropical rainbelt over land and ocean, responding to thermodynamic and interhemispheric temperature gradient controls respectively. Advection of the ocean signal over the western region of the subcontinent explains a difference between coastal and inland precipitation patterns. Empirical palaeodata and model simulations suggest that the coastal hydroclimate is also modulated by ocean-atmosphere feedbacks, with the wider subcontinent influenced by the role of westerly-derived rainfall and interaction between temperate and tropical systems. This analysis highlights the spatial coverage of available proxy data and suggests recommendations for future priorities in data collection to better resolve regional palaeoclimate variability.

6.1. Introduction

Considerable debate surrounds the timing, magnitude, and forcing factors of significant precipitation changes recorded in southern African Quaternary archives (Chase, 2021; Stone, 2021). An increasingly rich suite of palaeoclimate and palaeoenvironmental proxies is providing vital data on environmental responses to atmospheric changes, but these may add complexities and contradictions within the pool of available data. Usefully, multi-model ensemble simulations within the Palaeoclimate Modelling Intercomparison Project (PMIP) present simulations of key time periods of different orbital and ice sheet forcing. The Last Glacial Maximum (LGM, 21 ka) and mid Holocene (MH, 6 ka) present important time periods for which hypotheses of past climate forcing can be tested against models and a robust set of palaeodata.

Located at the interface between temperate and tropical climate systems, southern African palaeorecords preserve evidence of both high and low latitude forcing. An intensification of the tropical monsoon during periods such as the African Humid Period (AHP; ~14.8-5.5 ka) is now well established in the North African literature (Adeleye *et al*., 2021; deMenocal *et al*., 2000; Lézine *et al*., 2011; Patricola and Cook, 2007; Pausata *et al*., 2020; Tierney *et al*., 2017). The southern African climatic and environmental responses to insolation change, however, are less-well established (Burrough and Thomas, 2013). In comparison to the longitudinally-broad landmass of north Africa, southern Africa is more oceanic, influenced by both the Indian and Atlantic Oceans, with a resulting complexity in the nature of southern African climate and environmental systems (Peel *et al*., 2007). Contradictory palaeorecords of climate change have stimulated lively discussion on the regional climate drivers (e.g. Collins *et al*., 2014; Chase *et al*., 2019). Emerging hypotheses suggest that western and eastern regions of the subcontinent were influenced by multiple drivers, resulting in palaeoclimate signals that were not homogenous across the sub-continent (Burrough and Thomas, 2013; Chase *et al*., 2019; Chase, 2021; Govin *et al*., 2014; Stone, 2014; Stone, 2021). Model simulations indicate differences in the tropical rainbelt response over land and ocean on

Quaternary timescales (Jiang *et al*., 2015; Singarayer *et al*., 2017), and identify the importance of atmosphere-ocean feedbacks on climate systems in southwestern Africa (He *et al*., 2013). Records of palaeoclimate change within central southwestern Africa offer the opportunity to elucidate the spatial patterning of precipitation change between coastal and inland terrestrial regions to test prevailing hypotheses of palaeoclimate drivers.

Alongside marine core evidence of terrestrially derived sediment and leaf waxes (e.g. Collins *et al*., 2014; Stuut *et al*., 2002) and sea surface temperature (SST) and upwelling reconstructions (e.g. Farmer *et al*., 2005; Kirst *et al*., 1999), central southwestern Africa provides data from high-resolution continuous records and quality-assessed geomorphic archives. From terrestrial sources, these data include a suite of geochemical records (e.g. Belz *et al*., 2020; Chase *et al*., 2019; Railsback *et al*., 2016; Schüller *et al*., 2018), pollen assemblages (Gil-Romera *et al*., 2007; Scott *et al*., 2018), and detailed sedimentology from fluvial systems (e.g. Ramisch *et al*., 2017; Völkel *et al*., 2021; Walsh *et al*., 2022). Syntheses of robust geomorphic records are now available for continental aeolian dunes (Thomas and Bailey, 2017; Thomas and Burrough, 2016), lake status histories (De Cort *et al*., 2021), and fluvial archives (Walsh *et al*., in review). Following the compilation of large datasets, filtering for data quality, and interrogation of the controls on sediment deposition in these different environments, the timing and nature of terrestrial response to climate change can be established.

Through comparison of palaeoproxy records and model simulations, model performance can be evaluated prior to instrumental climate observations (Braconnot *et al*., 2012) and hypotheses of drivers of past climates can be tested (e.g. Jiang *et al*., 2015a, b). The utility of model-data comparison has been demonstrated globally (e.g. Bartlein *et al*., 2011; Braconnot *et al*., 2012) and regionally (e.g. Otto-Bliesner *et al*., 2009; Smith *et al*., 2022). Assessments are now available for North Africa (e.g. Joussaume *et al*., 1999; Otto-Bliesner *et al*., 2014), eastern Africa (e.g. Barker and

Gasse, 2003; Chevalier *et al*., 2017; Otto-Bliesner *et al*., 2014), regions affected by tropical rainbelt migration (e.g. Jiang *et al*., 2015; Pinot *et al*., 1999; Singarayer and Burrough, 2015; Singarayer *et al*., 2017), and the winter rainfall region in southern Africa (Engelbrecht *et al*., 2019). Model-data comparisons for the western region of southern Africa have focused on temporal dimensions of change (e.g. Singarayer and Burrough, 2015) or on a subset of sites (e.g. Chase *et al*., 2019), making the spatial pattern of rainbelt response difficult to assess. The rich record from palaeoclimate and palaeoenvironmental archives from central southwestern Africa now provides sufficient spatial coverage for model-data comparison across the region.

In this paper, we address how central southwestern African climate (defined as 17-30˚S and west of 21˚E) responded to past forcing during the mid Holocene (MH; 6 ka) and the Last Glacial Maximum (LGM; 21 ka). Using a compilation of robust empirical palaeoclimate and palaeoenvironmental archives and multi-model ensemble PMIP simulations, we assess: i) the magnitude and seasonality of precipitation anomalies at the mid Holocene and Last Glacial Maximum relative to present; ii) prevailing hypotheses of precipitation drivers in central southwestern Africa that are supported by the current dataset; iii) the extent of model-palaeodata agreement at these timesteps; and iv) future priorities for data collection to better resolve regional differences in palaeoclimate change.

6.1.1. Background

6.1.1.1. Climate setting

The climate of central southwestern Africa is influenced by several atmospheric circulation systems and ocean currents (Figure 6.1). The primary driver of interannual rainfall variability in southern Africa is the position of the tropical rainbelt. Over land, the rainbelt migrates latitudinally, tracking insolation and bringing rainfall to southern Africa in the austral summer months (Figure 6.1A). To the east of the subcontinent, the warm Agulhas ocean current promotes incursion of moisture from

the Indian Ocean to the southern African interior (Crétat *et al*., 2012; Gimeno *et al*., 2010; Rouault *et al*., 2002). Over the west of the subcontinent, summer rainfall maxima are associated with tropical moisture advection, transport in the tropical easterlies, and low pressure associated with the Angolan Low (Crétat *et al*., 2019; Hermes and Reason, 2009). Where moist tropical northwesterly flow from the Atlantic meets the subtropical south easterlies from the Indian Ocean, flow converges at the Congo Air Boundary (CAB; Hachigonta and Reason, 2006; Howard and Washington, 2019; van Heerden and Taljaard, 1998). Whilst direct transport from the Atlantic Ocean reaches only the most northern region (~15˚S, Crétat *et al*., 2019; Rouault *et al*., 2003), when coupled with mid-latitude westerly waves, tropical-temperate troughs (TTTs) bring substantial rainfall to southern Africa (Engelbrecht *et al*., 2015; Hart *et al*., 2010, 2013; Macron *et al*., 2014; Reason, 2017; Taljaard, 1996). When subtropical convergence zones are displaced further south, TTT cloud bands extend across southern Africa to the Indian Ocean (Todd *et al*., 2004). During austral winter, storm tracks associated with the westerlies migrate equatorward (Figure 6.1B). Precipitation extremes in southern Africa are also driven by ENSO cycles, where extreme wet seasons occur as a result of increased convergence in a lower tropospheric cyclone during La Niña (Hoell and Cheng, 2018; Hoell *et al*., 2021).

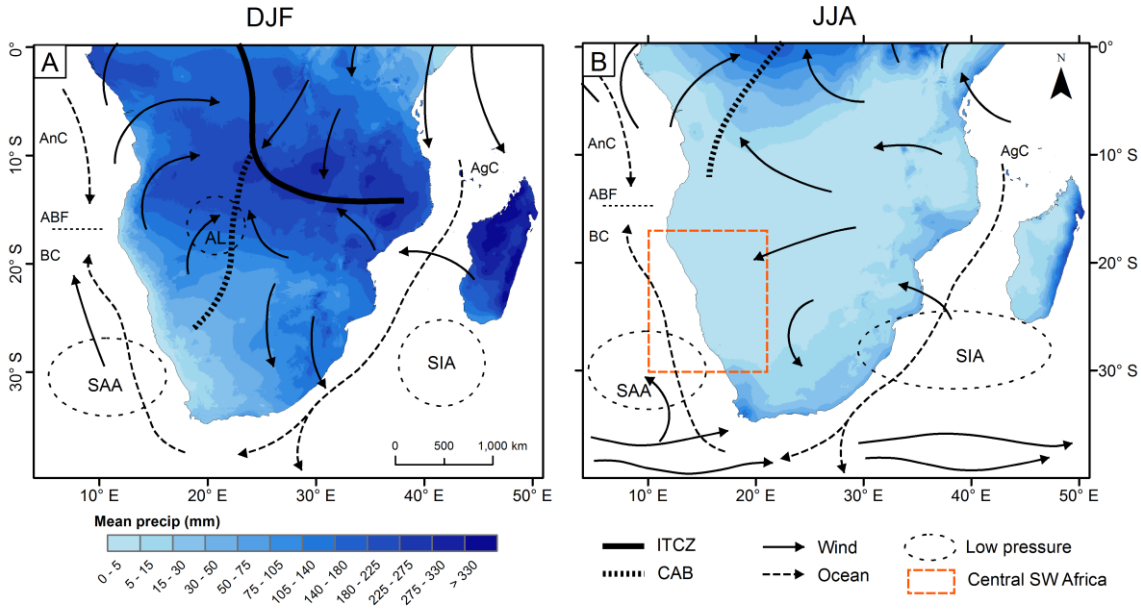

Figure 6.1. Seasonal variability in contemporary synoptic circulation patterns over southern Africa. Shading details seasonal mean precipitation from the WorldClim 2.0 dataset (Fick and Hijmans, 2017), for **A**) December, January, February (DJF; austral summer), and **B**) June, July, August (JJA; austral winter). Solid arrows indicate wind direction following Nicholson (2000). Average positions of the Intertropical Convergence Zone (ITCZ) and Congo Air Boundary (CAB) are marked by the solid black and dotted lines. Ocean currents of the Agulhas (AgC), Angola (AnC), and Benguela (BC) are detailed as dotted lines. SAA: South Atlantic Anticyclone, SIA: South Indian Anticyclone. The orange box demarcates the definition of central southwestern Africa used in this paper (17 to 30˚S, 10 to 21˚E). Note that the rainfall scale is not linear.

The distribution of rainfall across southern Africa is also influenced by distance from the moisture sources and the role of topography and upwelling. Diminishing with increased distance, rainfall from the Indian Ocean does not commonly reach the western coast of southern Africa. Moisture transport is further affected by the topography of the Great Escarpment which enhances local precipitation as a function of orographic effects and reduces the amount of rainfall that reaches the west. Along the coast of southwestern Africa, cold SSTs associated with upwelling of the Benguela current are associated with the development of the South Atlantic Anticyclone (SAA). High pressure in this region suppresses convection (Nicholson and Entekhabi, 1987; Tyson, 1986)

and limits the potential for incursion of moisture to the western-most portion of the subcontinent (Nicholson, 2000, 2012; Tyson and Preston-Whyte, 2000).

6.1.1.2. Hypotheses of palaeoclimate change

On multi-millennial timescales, the relative importance of elements of these climate systems has significantly influenced, and altered, environmental conditions in southwestern Africa. Quaternary records from the region have historically been interpreted in the context of distinct winter and summer rainfall zones and studies have considered changes in the latitudinal extent of these through time (e.g. Chase and Meadows, 2007; Cockroft *et al*., 1987; van Zinderen Bakker, 1967). Analysis of contemporary climate dynamics, however, shows that interactions between tracking lows associated with circumpolar westerlies and tropical air bring convective frontal rainfall to the wider subcontinent beyond the Cape Region that is directly influenced by westerly derived rainfall (Harrison, 1984; Hart *et al*., 2010; Macron *et al*., 2014; Todd and Washington, 1998). Contemporary climatological work demonstrates the complexity of drivers of rainfall both in terms of spatial origins and temporal contributions that are frequently not addressed when considering changes on palaeoclimate timescales. Unpicking this level of detail from Quaternary records is difficult, but inferences can be made on the primary drivers.

Several hypotheses have been developed from a long history of research to explain spatial patterns of southern Africa's palaeoenvironmental responses to climate changes. Advances in modelling, the availability of high-resolution archives, and greater coverage of proxy records, both spatially and temporally, have enabled some of these hypotheses to be tested and refined. With an awareness that hypotheses of Quaternary dynamics are commonly oversimplified and do not incorporate the full suite of climate complexity, we discuss here the prevailing ideas about the drivers of observed patterns of palaeoclimate change in central southwestern Africa. These include: 1) insolation driven latitudinal shifts of the tropical rainbelt resulting in hemispheric asymmetry of

wet phases (Partridge *et al*., 1997); 2) expansion and contraction of the tropical rainbelt resulting in hemispheric symmetry of wet phases (Collins *et al*., 2011); 3) differing controls on the tropical rainbelt over the ocean versus the land resulting in spatially contrasting patterns of symmetry/asymmetry with the northern hemisphere (Singarayer and Burrough, 2015; Singarayer *et al*., 2017); 4) the role of ocean-atmosphere feedbacks in response to high- and low-latitude forcing (Chase *et al*., 2019; He *et al*., 2013); and 5) the extension of the latitudinal reach of westerly frontal rainfall (Chase and Meadows, 2007; Engelbrecht *et al*., 2019).

1) Hemispheric asymmetry of wet phases

Following Partridge *et al*. (1997), a prevailing hypothesis of southern African climate variability over millennial timescales invoked insolation forcing as a key driver of hemispherically antiphased wet and dry periods across Africa. Meridional migration of the tropical rainbelt occurs on millennial timescales following changes to the Earth's orbital configuration (Clement *et al*., 2004; deMenocal *et al*., 2000; Kutzbach *et al*., 2008) and in response to ice sheet configuration at high latitudes (Gasse *et al*., 2008; Schefuß *et al*., 2005; Tjallingii *et al*., 2008). Following orbital precessional variability, the tropical rainbelt is modulated at its extremes through changes in seasonality. The magnitude of the seasonal cycle of heating occurs in opposite directions in each hemisphere, e.g. where seasonality is amplified in the northern hemisphere (warmer summers, cooler winters), it is dampened in the southern hemisphere (cooler summers, warmer winters). The antiphased response to insolation is simulated in models as a shifting latitudinal maximum extent of the tropical rainbelt following the geography of maximum heating (Braconnot *et al*., 2007; Kutzbach *et al*., 2008, Singarayer and Burrough, 2015). At its simplest, this hypothesis predicts that during the mid Holocene, when northern hemisphere summer insolation was high and humid conditions were prevalent in North Africa, corresponding dry conditions would dominate in southern hemisphere Africa. At the LGM, ice sheet forcing is also thought to produce an asymmetric response in the rainbelt. Due to the greater landmass of the high latitude northern hemisphere, a greater extent

of ice sheets developed compared to the more oceanic southern hemisphere, resulting in a southerly displacement of the tropical rainbelt (Braconnot *et al*., 2007; Broccoli *et al*., 2006; Kang *et al*., 2008), which would manifest as homogenous conditions wetter than present in the palaeodata.

2) Hemispheric symmetry of wet phases

Some marine and terrestrial evidence of palaeoenvironmental change indicate that southern Africa responded in phase, *contra* Partridge *et al*. (1997), with North Africa (Chase *et al*., 2010; Collins *et al*., 2011; Stager *et al*., 2011). These data have encouraged researchers to consider additional mechanisms beyond direct insolation forcing. Collins *et al*. (2011) use empirical evidence from a suite of eight marine cores spanning latitudes ~20˚N to ~20˚S to argue that rather than migrating latitudinally, the seasonal oscillation of the tropical rainbelt increased and decreased, resulting in hemispheric symmetry in changes to wet season length and intensity. This argument was similarly supported by the analysis of hyrax middens (Chase *et al*. 2009, 2010), which suggested a progressive aridification during the Holocene, in-phase with the demise of the North African Humid Period. This suggests a homogenous area of positive precipitation anomalies at the mid Holocene across central southwestern Africa as the rainbelt 'expanded', and a homogenous area of drying at the LGM as the rainbelt 'contracted'.

3) Differing controls on the tropical rainbelt over the ocean (and coastal regions) compared to land

Subsequently, analysis of model simulations shows differences in rainbelt variability over the ocean and land (Singarayer and Burrough, 2015; Singarayer *et al*., 2017). This analysis indicates that maximum heating over land in the summer months has a strong thermodynamic control on the average position of the rainbelt over terrestrial regions, yet over the ocean, the influence of interhemispheric temperature gradients in the winter months exerts a control in the opposite direction, leading to greater rainfall even when insolation in southern Africa is low (Singarayer and

Burrough, 2015; Singarayer *et al*., 2017). This model-driven hypothesis infers that moisture is advected over the southwestern terrestrial region of Africa when the ITCZ is further south over the ocean in boreal winter (Singarayer and Burrough, 2015; Singarayer *et al*., 2017). This suggests that archives in the coastal zone might show a pattern of palaeoenvironmental change that mimics the expansion and contraction of the tropical rainbelt rather than the asynchronous behaviour predicted in more continental areas.

4) Role of ocean-atmosphere feedbacks

Empirical evidence from hyrax middens (Chase *et al*., 2019) and simulations from climate models (He *et al*., 2013) indicate a remote control of high-latitude insolation forcing on the strength of the South Atlantic Anticyclone (SAA) and direct low-latitude insolation forcing on land-sea temperature contrasts. These relationships are drawn on to argue that the hydroclimate of the Namib Desert on orbital timescales is moderated by the role of ocean-atmosphere feedbacks in response to both high- and low-latitude forcing (Chase *et al*., 2019). When boreal summer insolation minima coincide with austral summer insolation maxima, for example during the LGM, a strong interhemispheric temperature gradient exists, strengthening the SAA and Benguela upwelling. This decreases the potential for the incursion of moisture-bearing convection and increases aridity over the coastal terrestrial region. In the context of globally cooler temperatures (following boreal summer insolation minima), high austral summer insolation also has the direct effect of heating up the land, increasing atmospheric pressure, and increasing the pressure gradient between land and sea, further enhancing ocean upwelling. As a result, records from the Namib Desert are expected to show a negative trend between humidity and both upwelling and austral summer insolation, resulting in dry conditions in the Namib at the LGM.

5) Extension of the latitudinal reach of westerly frontal rainfall

During periods of global cooling, ice extent increases at the poles and polar amplification enhances the temperature gradient between the poles and the equator (Masson-Delmotte *et al*., 2006, 2013). This results in an equatorward expansion of westerly waves and increases the occurrence of frontal rainfall within the associated storm track (Engelbrecht *et al*., 2019). Under present conditions, whilst the direct influence of westerly frontal rainfall is usually limited to the Cape Region of South Africa (Reason *et al*., 2002), wintertime storms tracking with more northerly paths are not unusual, and the interaction between westerly transient eddies and tropical systems is important for bringing rainfall to wider regions of the subcontinent. These TTTs are thought to also be important on Quaternary timescales (Chase *et al*., 2017). Following this, there is increasing recognition that temperate systems can influence the distribution of rainfall throughout the year, and that winter rainfall may be important in regions that were still predominantly controlled by summer rainfall, even at Quaternary timescales (Engelbrecht *et al*., 2019). This suggests that archives of glacial climates might show evidence of decreased seasonality and increased rainfall in winter months, even if not located within a region defined by the winter rainfall zone (WRZ; >66 % rainfall falls in either winter or summer; Chase and Meadows, 2007).

6.2. Methods

This paper compares simulations from palaeoclimate models with a compilation of palaeorecords from central southwestern Africa (17-30°S and west of 21°E; Figure 6.1) to test hypotheses of late Quaternary palaeoclimate change. This region comprises the entirety of Namibia, the western portion of Botswana, and northwestern South Africa.

6.2.1. Palaeoclimate models

This study uses data from the third generation of the Palaeoclimate Modelling Intercomparison Project (PMIP3; Braconnot *et al*., 2011, 2012), following analysis by Singarayer and Burrough (2015), Chevalier *et al*. (2017), and Engelbrecht *et al*. (2019) on southern African palaeoclimates. At the time of analysis, PMIP4 data was not fully available. As part of the Coupled Model Intercomparison Project (CMIP5), models within these experiments are run under defined boundary conditions for comparability of model outputs (Harrison *et al*., 2015; Taylor *et al*., 2012). Here, we focus on the mid Holocene (6 ka; MH) and the Last Glacial Maximum (21 ka; LGM) as these are key timesteps targeted by PMIP and they present end-members to assess how models deal with forcing factors. The MH simulation tests the influence of changes in insolation forcing and atmospheric greenhouse gasses. The LGM simulation tests the influence of atmospheric greenhouse gas concentrations, sea level, and ice sheet changes (Abe-Ouchi *et al*., 2015). Data on monthly climatologies of precipitation flux were accessed and precipitation anomalies were calculated through subtraction of pre-industrial values (0 ka; PI) from the MH and LGM. Precipitation anomalies are focused on in this analysis as the primary aim is to assess rainfall patterns. Palaeomodel data was obtained for all three timesteps (MH, LGM, PI) from eight models within PMIP3 (Table 6.1).

Table 6.1. Paleoclimate Modelling Intercomparison Project (PMIP3) models used in palaeo model-data comparison. Data accessed from https://esgf-node.llnl.gov/projects/cmip5/. Resolution: atmospheric resolution. Model type AO: atmosphere-ocean model, AOC: coupled atmosphere-ocean-carbon model. Models included in this analysis have data for Pre-Industrial (PI), the mid Holocene (MH) and the Last Glacial Maximum (LGM) experiments. Five other models present simulations for MH and PI, but not for LGM, and so were not included: bcc-csm1-1 (Wu *et al*., 2013), CSIRO-Mk3-6-0 (Rotstayn *et al*., 2010), FGOALS-s2 (Bao *et al*., 2013), HadGEM2-CC (Collins *et al*., 2011), HadGEM2-ES (Collins *et al*., 2011)).

Model	Modelling centre	Type	Resolution	Reference
CCSM4	National Centre for Atmospheric Research (NCAR), USA	AO	288 x 192 x L26	Gent *et al*. (2011)
CNRM-CM5	Centre National de Recherches Météorologique (CNRM) & Centre Européen de Recherche et de Formation Avancées en Calcul Scientifique (CERFACS), France	AO	256 x 128 x L31	Voldoire *et al*. (2013)
FGOALS-g2	Institute of Atmospheric Physics, Chinese Academy of Sciences (LASG-IAP)	AO	128 x 60 x L26	Li *et al*. (2013)
GISS-E2-R	NASA Goddard Institute for Space Studies (GISS), USA	AO	144 x 90 x L40	Schmidt *et al*. (2014)
IPSL-CM5A-LR	Institut Pierre Simon Laplace (IPSL), France	AOC	96 x 96 x L39	Dufresne *et al*. (2013)
MIROC-ESM	Japan Agency for Marine-Earth Science and Technology, Atmosphere and Ocean Research Institute, National Institute for Environmental Studies, University of Tokyo	AOC	128 x 64 x L80	Watanabe *et al*., (2011)
MPI-ESM-P	Max Planck Institute for Meteorologie (MPI), Germany	AO	192 x 96 x L47	Jungclaus *et al*., (2006)
MRI-CGCM3	Meteorological Research Institute (MRI), Japan	AO	320 x 160 x L48	Yukimoto *et al*., (2011)

To assess precipitation anomalies at the MH and LGM, this study investigates changes in rainfall extent in both the contemporary rainy and dry seasons. Central southwestern Africa has a single wet season in the austral summer (Nicholson, 2000; 2018), which is demonstrated in the seasonal pattern of contemporary (WorldClim 2.0; Fick and Hijmans, 2017) and modelled preindustrial rainfall (Figure 6.2A). Central southwestern Africa is currently highly seasonal, but emerging palaeoenvironmental data from fluvial systems (e.g. Walsh *et al*., 2022), indicate evidence of an

extended rainfall season at times during the late Quaternary. The hypotheses of palaeoclimate change discussed in Section 6.1.1.2 consider controls on rainfall systems in specific seasons and identify potential changes in seasonality. For this reason, this study therefore interrogates both the summer (December, January, February; DJF) and winter (June, July, August; JJA) precipitation anomalies for the MH and LGM.

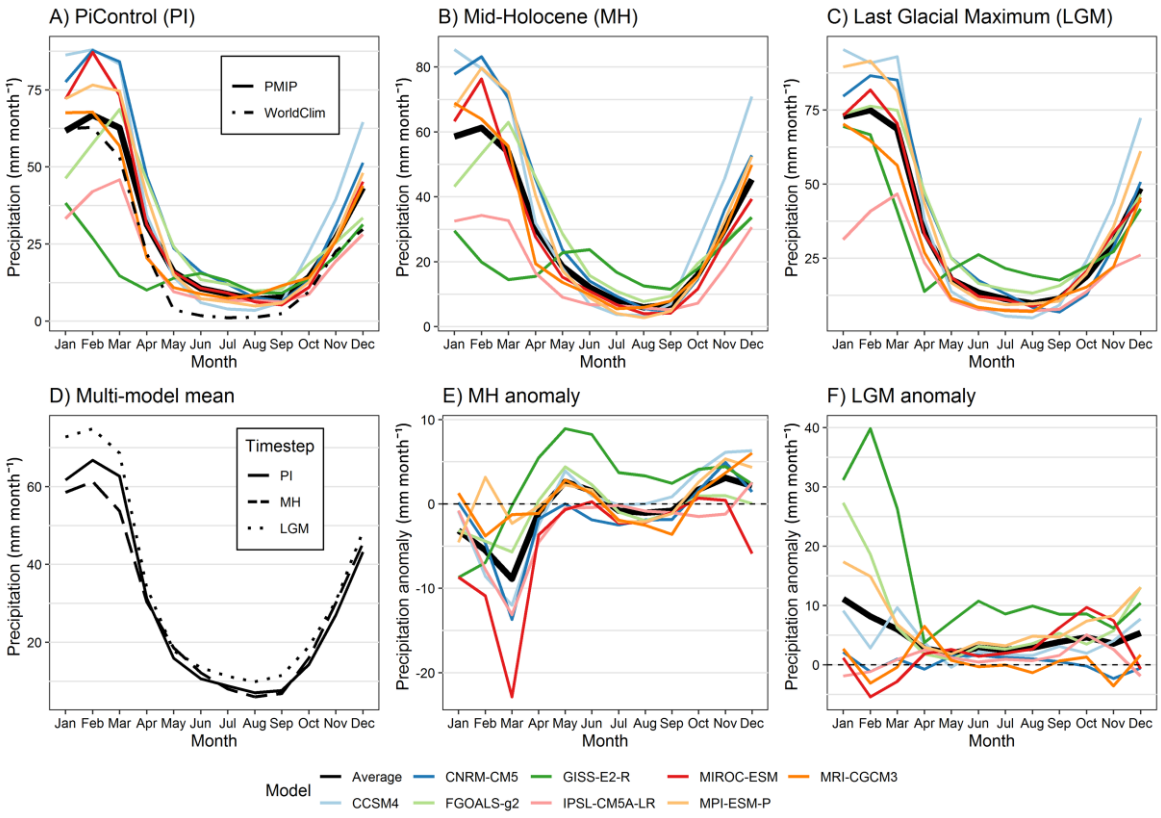

Figure 6.2. PMIP simulations of the annual cycle of precipitation (mm month^{-1}) averaged over central southwestern Africa (defined by box in Figure 6.1) for: **A)** the pre-industrial period (PI); **B)** the mid Holocene (MH); and **C)** the Last Glacial Maximum (LGM). Precipitation anomalies are calculated through subtraction of the PiControl from **E)** MH and **F)** LGM. The bold black line represents the average of the models. **D)** Multi-model mean timeseries of precipitation at the PI, MH and LGM. Modern precipitation values over land within the region of interest (WorldClim 2.0; Fick and Hijmans, 2017) are included in **A)** as a dotted black line.

6.2.2. Palaeorecords

Palaeorecords from central southwestern Africa have been compiled for model-data comparison (Figure 6.3, Table 6.2). For inclusion, palaeorecords must: i) incorporate data within the time periods of interest (MH or LGM); ii) reflect palaeoclimate change within central southwestern Africa; and iii) be supported by sufficient information for clear palaeoclimate interpretation. This analysis incorporates both continuous and discontinuous archives of palaeoclimate change. New ways of constructing and analysing geomorphic datasets (geoproxies) are making it possible to include and have confidence in the interpretations reached (e.g. Bailey and Thomas, 2014; De Cort *et al*., 2021; Thomas, 2013; Thomas and Bailey, 2017; Thomas and Burrough, 2012; Walsh *et al*., in review).

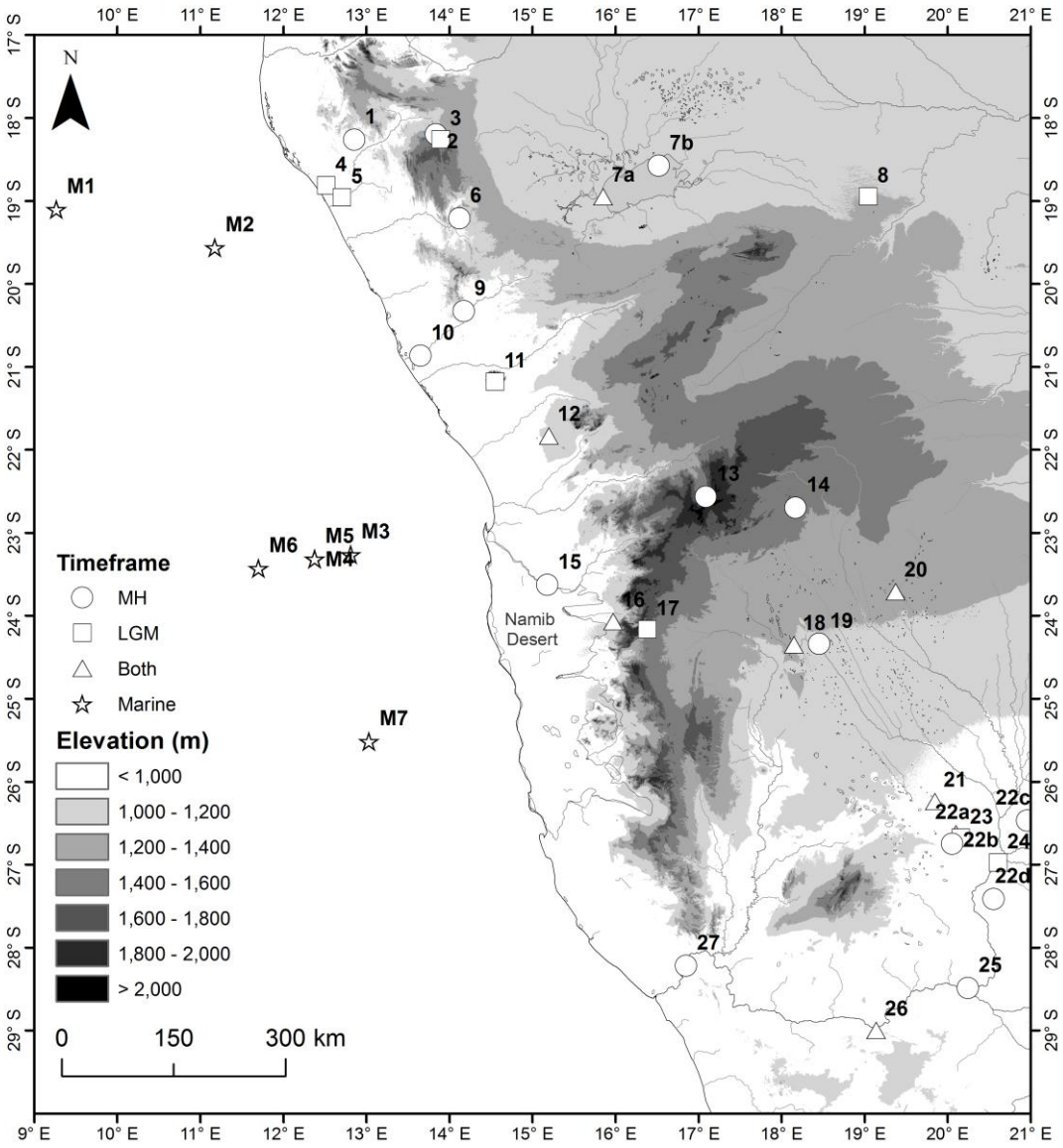

Figure 6.3. Location of archive sites used for model-data comparison within central southwestern Africa. All records have chronology within mid Holocene (MH; defined as 5-7 ka) or the Last Glacial Maximum (LGM; defined as 20-22 ka), as indicated by symbol shape. Records from sites 7 (Etosha) and 21 (southern Kalahari linear dunes) are comprised of multiple sites that were integrated for analysis. All marine cores records (demarcated with a star) cover both the MH and LGM. See Table 6.2 for details of these records, and the text for justification of the filtering criteria applied for inclusion of records. Underlying map shows the topography from the 30m ALOS Global Digital Surface Model (©JAXA).

Table 6.2. Palaeorecords used for model-data comparison (locations in Figure 6.3). See text for justification of the filtering criteria applied for inclusion of records. Sites are broadly listed by latitude, with the first indicating the most northerly site.

no.	Site name	Location	Archive type	Proxy	Timeframe (ka)	Timestep	Reference
1	Okandjombo	18.26S, 12.85E	Midden	Pollen	5.9-0.2	MH	Gil-Romera *et al*. (2007)
2	Opuwo basin	18.19S, 13.83E	Loess	Sedimentology	59.6-2.37	MH	Brunotte *et al*. (2009)
3	Orumana Cave	18.26S, 13.90E	Stalagmite	Stable isotopes	47.3-1	LGM	Railsback *et al*. (2016)
4	Khumib River	18.81S, 12.51E	Fluvial	Sedimentology	27.7-8.1	LGM	Srivastava *et al*. (2004)
5	Hoarusib Clay Castles	18.96S, 12.70E	Fluvial	Sedimentology	17.6-4.8	LGM	Srivastava *et al*. (2005)
6	Hoanib Headwaters	19.21S, 14.12E	Fluvial	Sedimentology	61.3-0.7	MH	Eitel *et al*. (2006)
7a	Etosha (Okondeka and Logan's Island)	18.95S, 15.85E	Beach ridge	Stratigraphy	70.4-0.3	Both	Brook *et al*. (2007), Buch and Zoller, (1992), Hipondoka *et al*. (2014)
7b	Etosha (Poacher's Point)	18.58S, 16.52E	Stromatolites	Sedimentology	33.1-2.6	MH	Brook *et al*. (2011, 2013)
8	N Kalahari linear dunes	18.95, 19.04E	Dune	Stratigraphy	57-21	LGM	Thomas *et al*. (2000)
9	Huab (Vrede)	20.33S, 14.17E	Midden	Pollen	7-0.9	MH	Gil-Romera *et al*. (2006)
10	Huab River (Skeleton C)	20.87S, 13.65E	Fluvial	Sedimentology	12-4	MH	Walsh *et al*., 2022
11	Daures (Brandberg)	21.18S, 14.55	Midden	Pollen	47.5-2.9	LGM	Scott *et al*. (2004, 2018)
12	Spitzkoppe	21.83S, 15.20E	Midden	Stable isotopes	32.6-0	Both	Chase *et al*. (2009, 2019)
13	Windhoek	22.57S, 17.08E	Spring	Pollen	6-1.6	MH	Scott *et al*. (1991)
14	Arnhem Cave	22.7S, 18.17E	Guano	Pollen	10.7-1.5	MH	Marais *et al*. (2015)
15	Kuiseb River Homeb	23.63S, 15.18E	Fluvial	Sedimentology	43-20.3	MH	Srivastava *et al*. (2006)
16	Zizou	24.07S, 15.97E	Midden	Stable isotopes	50.2-0	Both	Chase *et al*. (2019)
17	Tsonsdab River BüllsPort	24.17S, 16.38E	Fluvial	Sedimentology	58-0.2	LGM	Volkel *et al*. (2021)
18	W Kalahari linear dunes	25.70S, 19.43E	Dune	Stratigraphy	186-1.6	Both	Stone and Thomas (2008)
19	Stampriet	24.34S, 18.45E	Aquifer	Isotopes, noble gas	37-2	MH	Stute and Talma (1998)
20	Omongwa Pan	23.71S, 19.37E	Salt pan	Sedimentology, Geochemistry	42.4-0.4	Both	Schüller *et al*. (2018), Belz *et al*. (2020)
21	Branddam East Pan	26.24S, 19.84E	Pan	Sedimentology, Geochemistry	31.5-1.4	Both	Schüller *et al*. (2018)
22	S Kalahari linear dunes	27.06S, 20.56E	Dune	Stratigraphy	77-0.15	Both	Bateman *et al*. (2003), Telfer (2011), Telfer and Thomas (2007)
23	Witpan	26.68S, 20.16E	Pan	Sedimentology, Geochemistry	32-1.7	LGM	Telfer *et al*. (2009)
24	Molopo	26.98S, 20.61E	Fluvial	Sedimentology	23.3-1.1	LGM	Heine (1990), Hurkamp *et al*. (2011)
25	Lower Molopo	28.49S, 20.24E	Fluvial	Sedimentology	25-0.2	MH	Ramisch *et al*. (2017)
26	Pella	29.00S, 19.14E	Midden	Stable isotopes, Pollen	50.2-0	Both	Chase *et al*. (2019), Lim *et al*. (2016)
27	Orange River	28.22S, 16.85E	Fluvial	Hydraulic modelling	5.4-0	MH	Zawada *et al*. (2000)
M1	MD96-2094	19.10S, 9.27E	Marine	Grain size	321-4	Both	Stuut *et al*. (2002)
M2	GeoB 1706	19.56S, 11.18E	Marine	Foraminifera	151-0	Both	Little *et al*. (1997)
M3	GeoB 1712	23.26S, 12.81E	Marine	Alkenone SST	151-6.7	Both	Kirst *et al*. (1999)
M4	MD08-3167	23.32S, 12.38E	Marine	Leaf-wax n-alkanes	140-0	Both	Collins *et al*. (2013, 2014)
M5	GeoB 1711	23.32S, 12.38E	Marine	Alkenone SST, Foraminifera	135-0	Both	Kirst *et al*. (1999), Little *et al*. (1997)
M6	GeoB 1710	23.43S, 11.70E	Marine	Alkenone SST	245-0	Both	Kirst *et al*. (1999)
M7	ODP 1084B	25.51S, 13.03E	Marine	Foraminifera	22.1-1.1	Both	Farmer *et al*. (2005)

For model-data comparison, the periods of 5-7 ka and 20-22 ka were chosen to define the MH and LGM respectively. These time windows of ± 1 ka are comparable to protocols used by Bartlein *et al*. (2011) and Chevalier *et al*. (2017). Whilst some studies used wider intervals to include a greater number of records or to define the full extent of the period (e.g. 26.5-19 ka – DiNezio and Tierney (2013) or 23-19 ka – Engelbrecht *et al*. (2019)), our narrower approach aims to identify the snapshot that is comparable to model simulations. For inclusion in this analysis, a record must have chronology (within 2 σ error) within either of these periods of interest. Radiocarbon ages have been recalibrated using SHCal20 (Hogg *et al*., 2020) in OxCal v 4.4.4. (Bronk Ramsey, 2021), where necessary. Several papers interpret palaeoclimate change from hiatuses or interpret changes at the MH or LGM but do not have data that falls directly within the period of interest. If interpretations do not have a corresponding chronology, however, we were not able to establish a coherent timeline for when these changes happened, so these archives were not included.

Records must reflect palaeoclimate change within the region defined as central southwestern Africa. This criterion is particularly important for determining inclusion of marine records for analysis, where marine archives can integrate the terrestrial signal from large, often uncertain, source regions (Scott *et al*., 2004). Whilst grain size and leaf wax isotope records from cores MD96-2094 and MD08-3167 (Collins *et al*., 2014; Stuut *et al*., 2002) reflect palaeoclimate change in the Namib and Kalahari deserts of southwestern Africa, the source regions for marine pollen records from GeoB 1023 and GeoB 1711 (Shi *et al*., 1998, 2001) are debated. These pollen records have been used to infer expansions of vegetation zones during the late Quaternary, yet comparison with pollen records in the corresponding terrestrial region shows limited evidence for these changes (Scott *et al*., 2004). Bias in pollen distribution from source regions is likely to be higher when upwelling is strong and a number of additional source regions such as the Angolan highlands cannot be ruled out (Scott *et al*., 2004). The source regions for marine pollen records are often large (Dupont *et al*., 2007) and can integrate a wide variety of environments (Scott *et al*., 2004, 2012,

2018). This is important to consider in southern Africa where there is increasing evidence to suggest that at times, different regions experienced very different environmental conditions. For this reason, this analysis considers only terrestrial pollen records (e.g. Gil-Romera *et al*., 2006, 2007; Lim *et al*., 2016; Scott *et al*., 1991, 2004, 2018) to be indicative of local palaeoclimate signatures.

Finally, to have confidence in the combined regional record of palaeoclimate change, we require the climate interpretation from each record to be associated with robust data. This includes both quality of chronology and availability of supporting information for interpretation. Through assessment of these uncertainties, it is possible to reduce anomalies that are a relic of dating error and isolate key spatial and temporal trends in palaeoenvironmental change (Woor *et al*., 2022). Table 6.3 details how each data type is assessed using comparable, yet archive-specific, criteria developed from the literature.

Table 6.3. Data evaluation considerations by archive type based on assessments in published syntheses. See Table 6.2 for examples of each archive type within central southwestern Africa.

Type	Data evaluation
Aeolian	Georeferenced aeolian dune records from southern Africa are available within the INQUA dunes atlas (Lancaster *et al*., 2016; Thomas and Burrough, 2016). Using this data, Thomas and Bailey (2017) produced an assessment of accumulation intensity (based on dune accumulation rate variability, ARV; Bailey and Thomas, 2014) in Kalahari linear dunes. Rather than using luminescence ages as proxies of palaeoenvironmental change, this method takes into account the stratigraphic context and quantifies dune accumulation. For inclusion, there had to be: i) multiple ages from a site; ii) errors associated with age published; and iii) sample depth recorded. Chronologies from additional aeolian features had to be supported by independent proxies for clarity of palaeoclimate interpretation. This is the case for the loess deposits in the Opuwo basin (Brunotte et al., 2009), but the climate context of deposition was not clearly stated in the records of geomorphic activity described in the Namib dunes (Bristow *et al*., 2007; Bubenzer *et al*., 2007). Archives with complicated and unclear drivers of sediment deposition have not been included. For example, sand ramps are highly influenced by accommodation space and sediment supply, and reflect local environmental conditions, making the palaeoenvironmental context difficult to discern (Bateman *et al*., 2012; Rowell *et al*., 2017).

Lacustrine	Lacustrine records were compiled and assessed by De Cort *et al*. (2021). These chronologic records had to reflect changes in lake level as a response to climate drivers. For shorelines and stromatolites, this required data on elevation (e.g. Brook *et al*., 2013; Hipondoka *et al*., 2014). For the Kalahari pan records, whilst four pans have chronology, geochemical data for reconstruction of hydrological changes were only available from two (Omongwa and Branddam East; Belz *et al*., 2020; Schüller *et al*., 2018).
Fluvial	All fluvial records had to pass the filtering process defined by Walsh *et al*. (in review). This quality control required ages to: i) be accompanied by location data (e.g. GPS coordinates of longitude and latitude); ii) have defined stratigraphic context and supporting geochronology; iii) be produced through robust chronological approaches; and iv) be supported by sufficient additional analytical approaches for interpretation (e.g. lithofacies, Srivastava *et al*., 2006; geochemistry, Ramisch *et al*., 2017).
Hyrax midden	Hyrax midden chronologies had to be supported by sufficient information for palaeoclimate interpretation. This includes the study of pollen (e.g. Gil-Romera *et al*., 2007; Lim *et al*., 2016; Scott *et al*., 2018) and stable isotopes (e.g. Chase *et al*., 2019). Many of the chronologies were continuous, with a high temporal resolution established through age-depth models (e.g. Chase *et al*., 2009, 2010, 2019). In cases where hyrax midden formation was discontinuous, radiocarbon ages had to meet the criteria established in existing literature that considers data quality (e.g. Small *et al*., 2017; Woor *et al*., 2022).
Marine	Marine sediment cores can record changes in both ocean dynamics (e.g. SSTs, upwelling rates; Farmer *et al*., 2005; Little *et al*., 1997) and the nature of palaeoenvironmental change on land (e.g. pollen and terrigenous sediment; Shi *et al*., 2001; Stuut *et al*., 2002). If recording terrestrial environmental change, there must be sufficient confidence that the source region lies within central southwestern Africa. Chronology in marine cores is commonly established through radiocarbon dating and event matching of oxygen isotope analysis of benthic foraminifera. This use of multiple chronometers and correspondence between marine cores gives confidence in the age-depth models established, so filtering has not been applied to marine core chronologies.
Speleothem, spring, aquifer, tufa	For inclusion, the climate context of speleothem formation had to be clear (e.g. Railsback *et al*., 2016). Records from spring deposits and aquifers were included if they were supported by information sufficient for climate interpretation, e.g. noble gases (e.g. Stute and Talma, 1998) and pollen (Scott *et al*., 1991). Tufa deposits exist in the Naukluft mountains (Viles *et al*., 2007), but ^{234}U-^{230}Th dating has proved problematic (Stone *et al*., 2010).
Archaeolog-ical	Several archaeological sites are located in central southwestern Africa (e.g. Dewar and Stewart, 2012; McCall *et al*., 2011; Vogelsang *et al*., 2010), but were not included if palaeoclimate interpretation was not clear.

6.3. Results

Archives from 34 sites pass the filtering criteria for comparison with eight PMIP3 palaeoclimate model simulations. This data set comprises 19 terrestrial records for the MH and 16 for the LGM (Figures 6.4, 6.5). Marine core records span both periods, two of which detail terrestrial environmental change and six record changes in the intensity of Benguela current upwelling (Figure 6.6). PMIP3 simulations of pre-industrial rainfall are consistent with contemporary rainfall seasonality, both in terms of timing and magnitude (Figure 6.2A), justifying its use for calculation of precipitation anomalies compared to present.

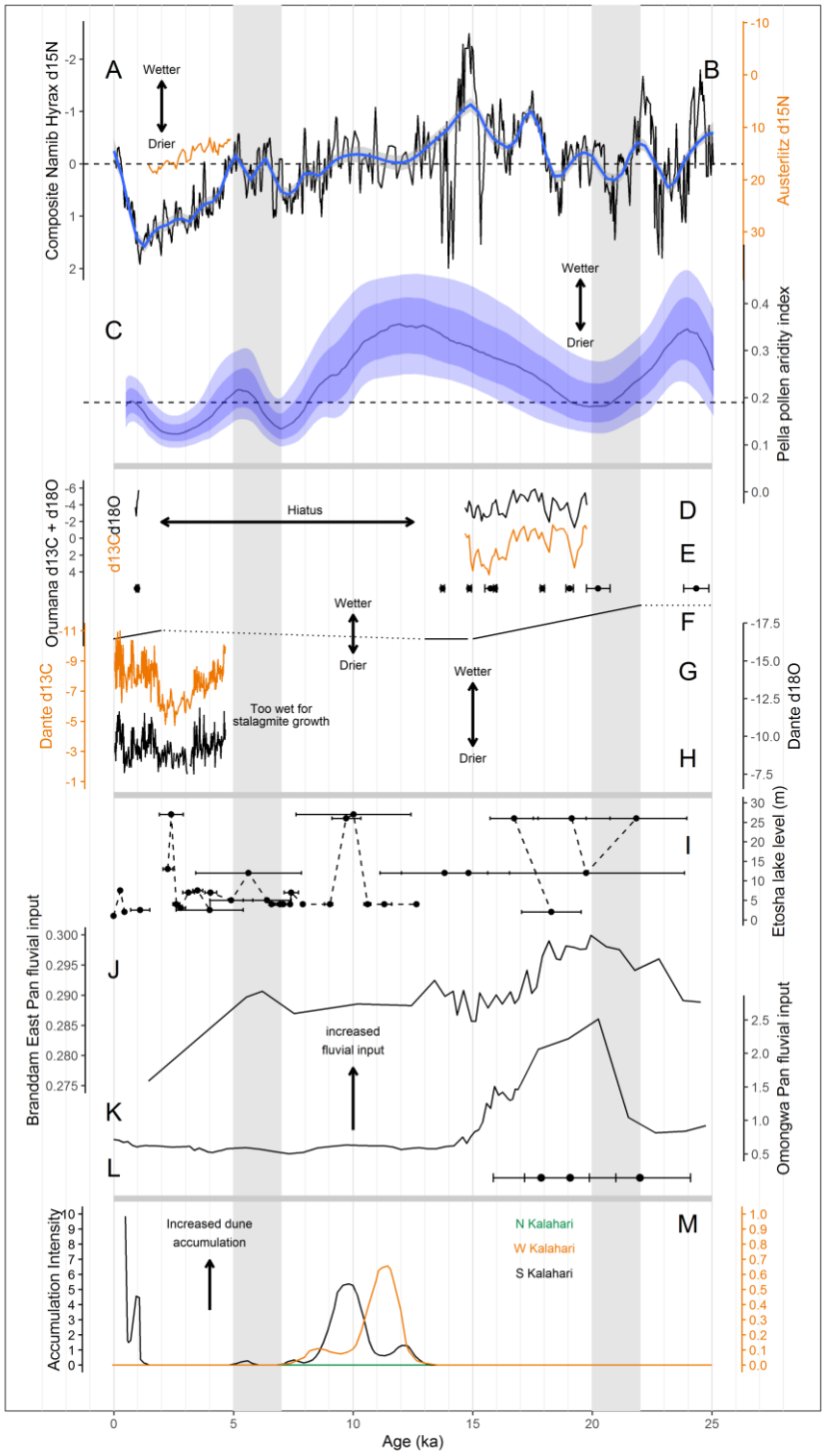

Figure 6.4. Terrestrial records of palaeoclimate and environmental change arranged by proxy type and by latitude. Hydroclimate data are orientated so that increases in y-axis values represent increases in precipitation. Grey bars indicate the timesteps considered for data-model comparisons: Mid Holocene (5-7 ka) and LGM (20-22 ka). Dotted lines on plots A and C indicate contemporary values. **A)** Composite hyrax midden $\delta^{15}N$ record from Spitzkoppe, Zizou and Pella sites (Chase *et al.*, 2019). Data has been normalised, so negative $\delta^{15}N$ values indicate higher environmental water availability. **B)** $\delta^{15}N$ record from the Austerlitz hyrax midden (Chase *et al.*,

2010). **C)** Pollen aridity index from Pella rock hyrax midden (Lim *et al*., 2016). **D)** Orumana stalagmite Orum-1 $\delta^{18}O$ and **E)** $\delta^{13}C$ record, **F)** Uranium-Thorium (U-Th corrected for $^{230}Th_{initial}$) ages indicating stalagmite growth and environmental inferences showing a shift in carbon isotopes from C4 (wetter climate conditions) to C3 (drier climate conditions) vegetation (Railsback *et al*., 2016). **G)** Dante Cave $\delta^{13}C$ and **H)** $\delta^{18}O$ records, both (Sletten *et al*., 2013). **I)** Etosha lake levels compiled by De Cort *et al*. (2021), including data from Buch and Zoller (1992), Brook *et al*. (2007, 2011, 2013), Hipondoka *et al*. (2014). Geochemical records of fluvial input into **J)** Branddam East Pan, and **K)** Omongwa Pan, Kalahari (Schüller *et al*., 2018), where higher K/Al ratios are indicative of increased fluvial inputs. **L)** Luminescence ages from pan floor sediments of Witpan, Kalahari (Telfer *et al*., 2009). **M)** Linear dune accumulation rates (AI) from the northern, western, and southern Kalahari (Thomas and Bailey, 2017). Fluvial data are presented in Figure 6.5.

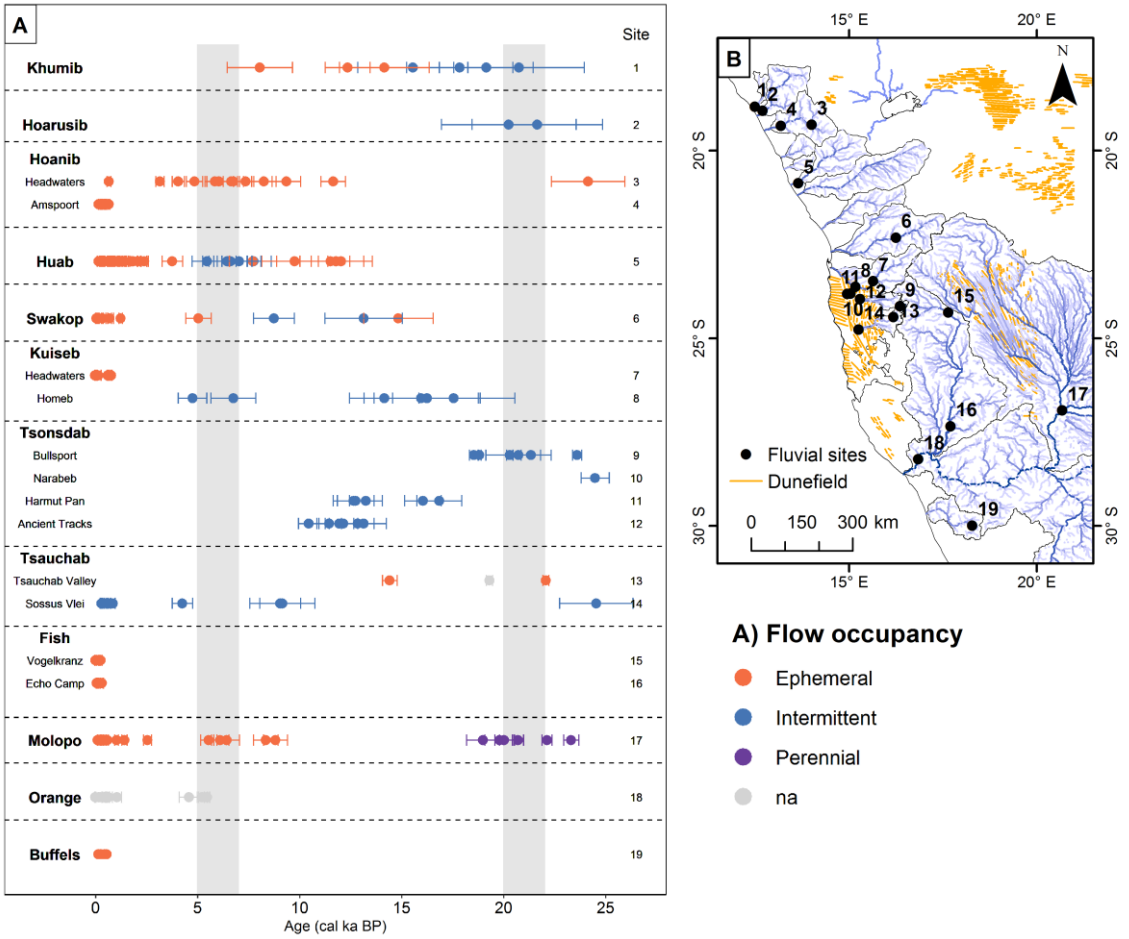

Figure 6.5. A) Sedimentary archive depositional ages from fluvial sites in central southwestern Africa, coloured by interpretation of flow occupancy (ephemeral to perennial), organised by river and by latitude. Site numbers in A) correspond site to locations in B). Data included according to criteria in Table 6.3 (Walsh *et al*., in review). This required chronologies to pass a set of quality criteria, and for each record to be accompanied by sufficient data for climate interpretation. The results here detail the interpretation of river flow duration for all ages that are also accompanied by interpretation of climate (na = no interpretation of flow duration). Grey bars indicate the timesteps considered for data-model comparisons: Mid Holocene (5-7 ka) and LGM (20-22 ka). Data are available from the Khumib (Srivastava *et al*., 2004), Hoarusib (Srivastava *et al*., 2005), Hoanib (Eitel *et al*., 2005, 2006), Huab (Walsh *et al*., 2022), Swakop (Greenbaum *et al*., 2014), Kuiseb (Grodek *et al*., 2013; Srivastava *et al*., 2006), Tsondab (Stone *et al*., 2010; Teller and Lancaster, 1986; Völkel *et al*., 2021), Tsauchab (Brook *et al*., 2006), Fish (Cloete *et al*., 2018), Molopo (Heine, 1990; Hurkamp *et al*., 2011; Ramisch *et al*., 2017), Orange (Zawada *et al*., 2000), and Buffels (Benito *et al*., 2011).

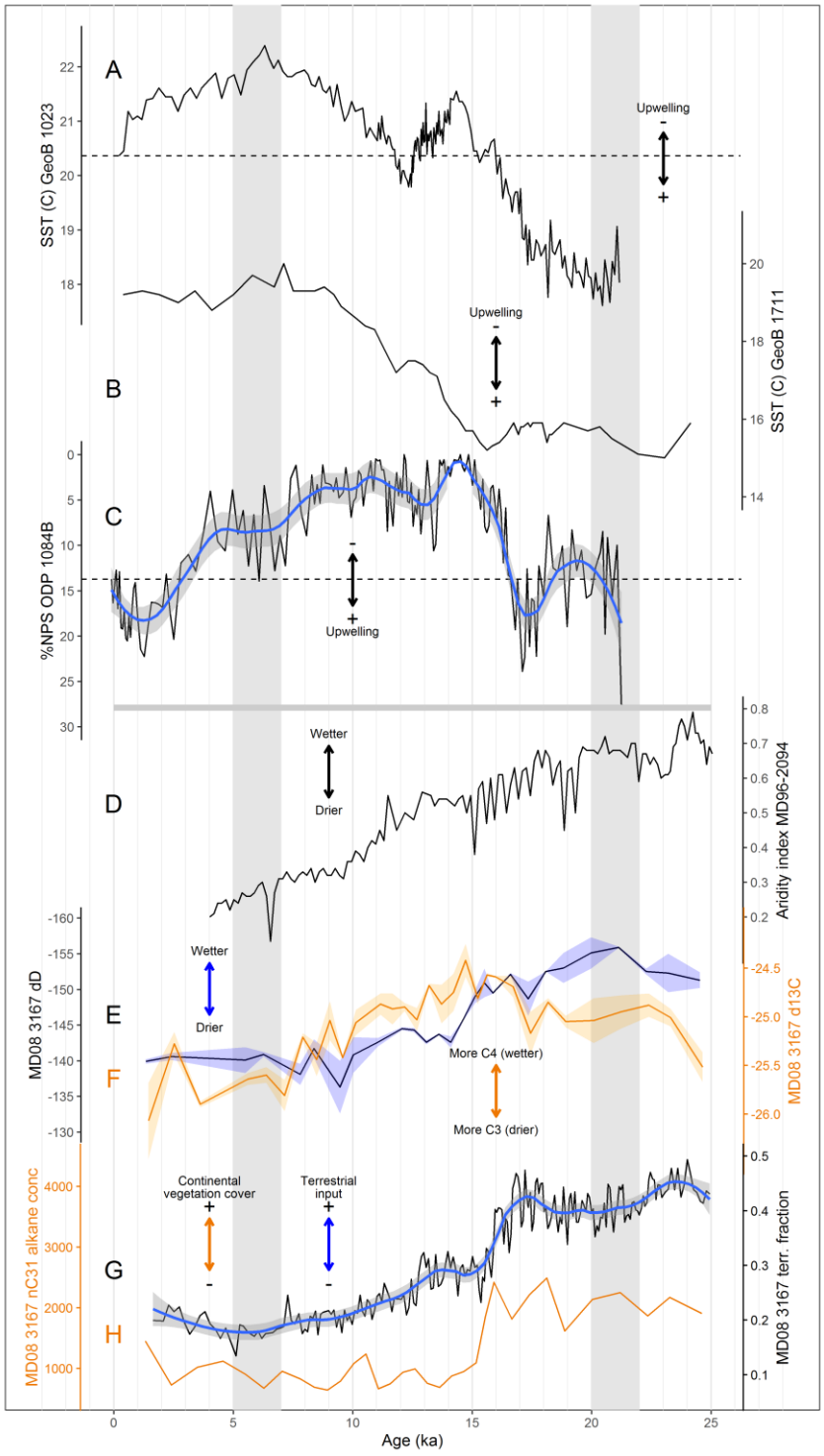

Figure 6.6. Marine records of Benguela current upwelling and terrestrial environmental change. Records are orientated so that increases in y-axis values represent increases in precipitation over land, or decreases in oceanic Benguela upwelling. Records are organised by type and then by latitude. Grey bars indicate the timesteps considered for data-model comparisons: Mid Holocene (5-7 ka) and LGM (20-22 ka). **A)** Sea surface temperature (SST) record from core GeoB 1023 (Kim *et al*., 2002), where colder SSTs are indicative of increased Benguela upwelling. **B)** Alkenone-based

SST record from core GeoB 1711 (Kirst *et al*., 1999). **C)** % NPS from core ODP 1084B (Farmer *et al*., 2005) where higher contributions from n pachyderma are indicative of increased Benguela upwelling. **D)** Aridity index calculated from core MD08-2094 (Stuut *et al*., 2002). **E)** δD, **F)** δ13C, **G)** n-C31 alkane (‰ VSMOW) record, and **H)** Terrigenous fraction from MD08 3167 (Collins *et al*., 2014).

6.3.1. Mid Holocene (MH)

The ensemble of model simulations for the MH shows predominantly negative precipitation anomalies over southern Africa and positive precipitation anomalies over northern Africa (Figure 6.7). Over central southwestern Africa, modelled rainfall anomalies range from -57 to 26.6 mm $year^{-1}$, with an average of -10.4 mm $year^{-1}$ (Table 6.4). This spatially averaged value encompasses differences in rainfall over the ocean and land (with extremes of -76.2 and 84.7 mm $year^{-1}$ recorded across space). Where the majority of models detail positive anomalies over the ocean, drier conditions are simulated over inland areas (Figure 6.8). The extent of these land-ocean differences, however, varies between models, where some simulate particularly dry (MIROC-ESM, IPSL-CM5A-LR) or wet (GISS-E2-R) conditions over land, or particularly dry (FGOALS-g2) or wet (MPI-ESM-P) conditions over the ocean and coastal region. This pattern is latitudinally limited and starts to break down further south. All marine records show decreased Benguela upwelling relative to present at the MH (Farmer *et al*., 2005; Kirst *et al*., 1999; Little *et al*., 1997; Figure 6.6).

Table 6.4. PMIP precipitation anomaly results averaged over central southwestern Africa, with minimum and maximum precipitation values recorded across the region quoted in brackets. Comparison between mid Holocene (MH) with the LGM for the austral summer (December, January, February; DJF) and austral winter (June, July, August; JJA). DJF and JJA values are quoted as mm month^{-1} anomalies and annual values are quoted as mm year^{-1}. Mean row: multi-model ensemble mean.

	Mid Holocene			**LGM**		
Model	**DJF** (mm month^{-1})	**JJA** (mm month^{-1})	**Annual** (mm year^{-1})	**DJF** (mm month^{-1})	**JJA** (mm month^{-1})	**Annual** (mm year^{-1})
CCSM4	-1.3 (-20.8 to 34.7)	0.3 (-1.3 to 1.4)	-2.9 (-57.7 to 101.8)	6.4 (-6.7 to 29.7)	1.8 (-0.1 to 5.4)	46.7 (-14.9 to 166.6)
CNRM-CM5	-1.1 (-11.9 to 22.6)	-2.1 (-6.9 to 0.1)	-20.3 (-41.6 to 11.7)	0.1 (-9.8 to 12.5)	1.3 (-2.0 to 13.5)	3.4 (-43.6 to 166.6)
FGOALS-g2	-2.6 (-12.5 to 0.7)	-0.2 (-1.9 to 4.0)	-8.4 (-42.1 to 19.1)	19.7 (-30.4 to 118.3)	3.1 (-5.0 to 14.1)	92.5 (-180.8 to 166.6)
GISS-E2-R	-4.5 (-32.5 to 6.5)	5.1 (1.1 to 18.5)	26.6 (-53.9 to 106.1)	27.6 (-1.0 to 111.4)	9.8 (2.6 to 27.6)	173.2 (7.6 to 166.6)
IPSL-CM5A-LR	-2.2 (-14.6 to 4.9)	-0.5 (-1.4 to 0.1)	-29.9 (-112.3 to 13.1)	-1.7 (-21.5 to 10.5)	0.7 (-3.3 to 3.6)	10.7 (-159.1 to 166.6)
MIROC-ESM	-8.6 (-49.7 to 19.0)	-1.4 (-5.6 to 0.5)	-57.0 (-192.9 to 11.7)	-1.8 (-37.3 to 21.5)	2.0 (-13.1 to 8.5)	25.4 (-97.5 to 166.6)
MPI-ESM-P	1.1 (-19.6 to 73.8)	-0.8 (-4.2 to 0.3)	7.1 (-80.9 to 177.0)	15.1 (-9.0 to 49.3)	3.9 (-5.7 to 12.1)	89.4 (-35.9 to 166.6)
MRI-CGCM3	1.0 (-14.6 to 39.5)	-1.1 (-3.9 to 0.4)	1.7 (-28.4 to 143.3)	0.3 (-38.1 to 15.8)	-0.6 (-3.3 to 1.8)	4.2 (-106.0 to 166.6)
Mean	**-2.3 (-22.0 to 25.2)**	**-0.1 (-3.0 to 3.1)**	**-10.4 (-76.2 to 84.7)**	**8.2 (-19.2 to 46.1)**	**2.7 (-3.7 to 10.8)**	**55.7 (-78.8 to 249.2)**

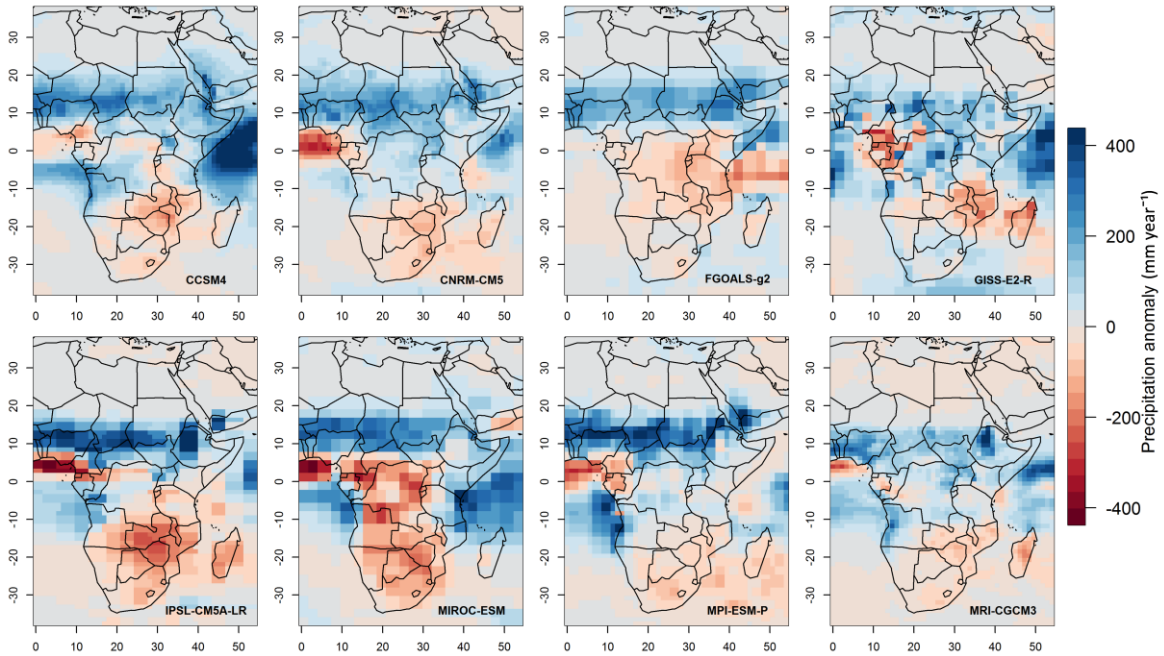

Figure 6.7. Mid Holocene PMIP annual precipitation anomalies (mm year^{-1}) over Africa relative to the pre-industrial period (red: drier than present, blue: wetter than present).

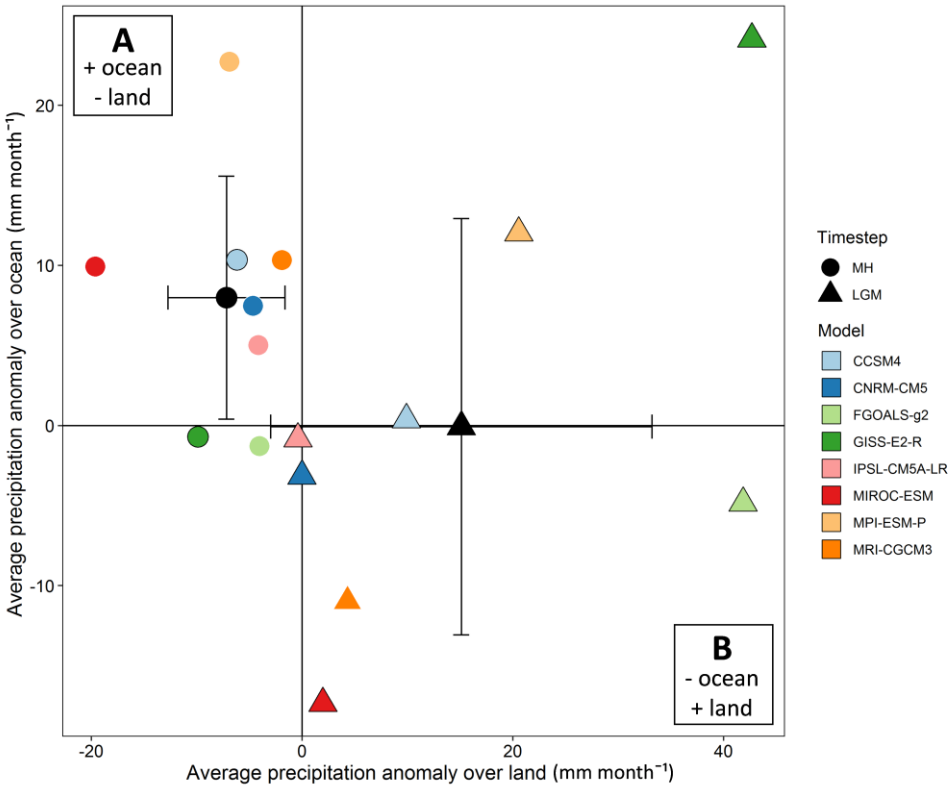

Figure 6.8. The extent of summer (DJF) precipitation anomalies over ocean (9-15˚E, 14-27˚S) and over land (15-21˚E, 17-30˚S) for each model at each time step (circles: MH, triangles: LGM). The points are outlined if precipitation anomalies for winter (JJA) are positive. **A)** Quadrant of models

that simulate positive precipitation anomalies over the ocean and negative anomalies over land. **B)** Quadrant of models that simulate negative precipitation anomalies over the ocean and positive anomalies over land.

6.3.1.1. Negative precipitation anomalies

The largest negative precipitation anomalies over central southwestern Africa are simulated for the austral summer (Figures 6.2, 6.9), with a mean of -2.3 mm month^{-1} across the whole region (Table 6.4), with models simulating ~ -22 mm month^{-1} at locations inland (Figure 6.8, Table 6.4). This simulation is supported by some records from archives located predominantly inland from the coast (Figure 6.9; Belz *et al*., 2020; Brunotte *et al*., 2009; Eitel *et al*., 2006; Ramisch *et al*., 2017; Schüller *et al*., 2018). The Hoanib River record suggests that low-energy runoff and limited ephemeral river flow resulted in sediment deposition in the upper catchment of the river (Eitel *et al*., 2006). These fine-grained units are indicative of weak summer monsoonal rain where oscillating runoff occurred within a climate more arid than today. Preservation of loess units dating to the MH is a signal of arid conditions in the Opuwo basin with limited fluvial activity (Brunotte *et al*., 2009). Aggradation of alluvial fan deposits in the Molopo basin also attest to limited sediment mobilization, decreased flood intensity, and decreased storm intensity (Ramisch *et al*., 2017). Limited fluvial input to Omongwa Pan at the MH suggests that the climate was drier than present (Belz *et al*., 2020; Schüller *et al*., 2018).

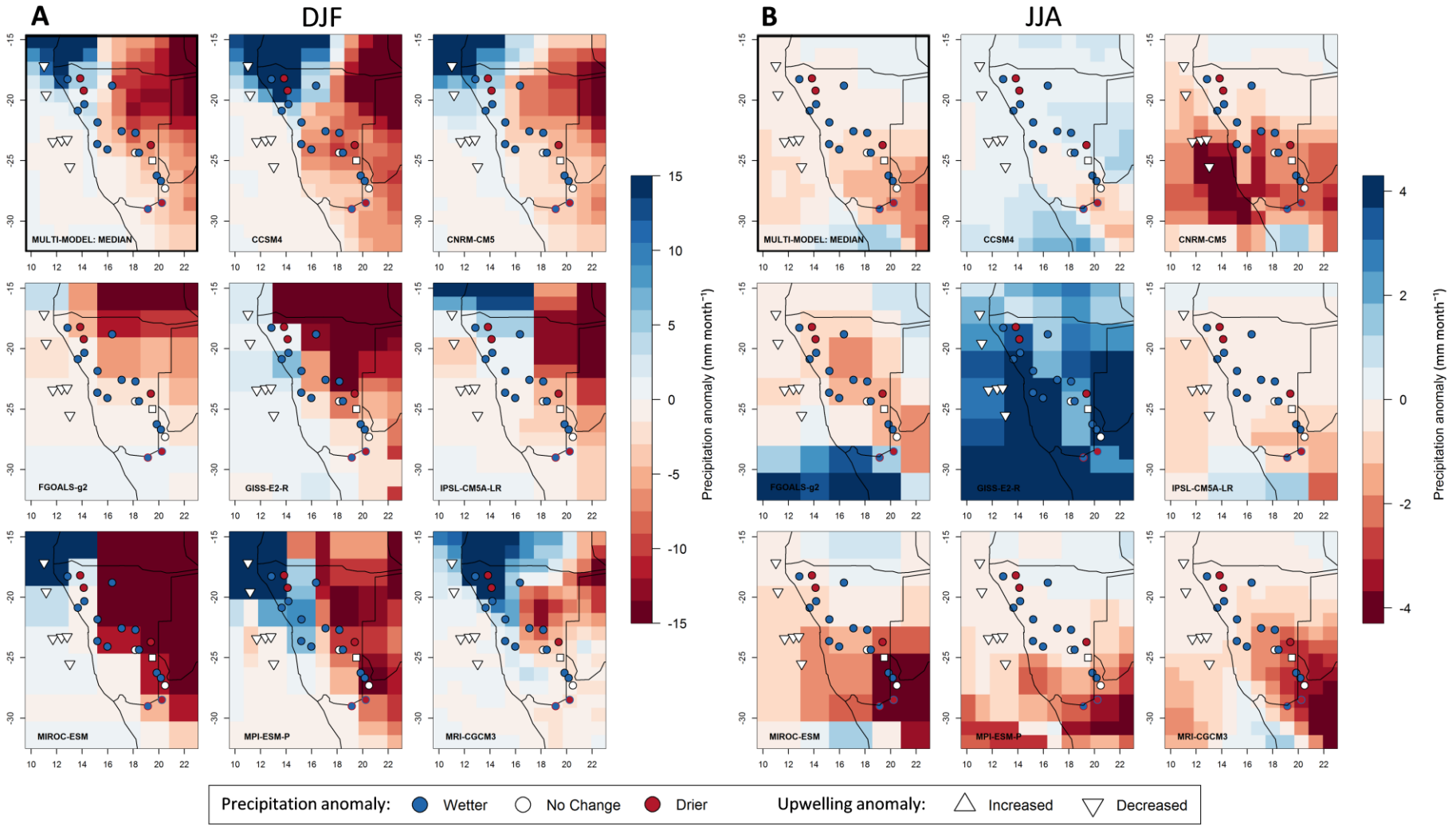
A
DJF
B
JJA
MULTI-MODEL: MEDIAN
CCSM4
CNRM-CM5
FGOALS-g2
GISS-E2-R
IPSL-CM5A-LR
MIROC-ESM
MPI-ESM-P
MRI-CGCM3
Precipitation anomaly (mm month⁻¹)
15
10
5
0
-5
-10
-15
4
2
0
-2
-4
Precipitation anomaly:
Wetter
No Change
Drier
Upwelling anomaly:
Increased
Decreased

Figure 6.9. Model-data comparison for the mid Holocene (palaeodata: 5-7 ka, models: 6 ka) detailing the spatial pattern of precipitation anomalies across central southwestern Africa. **A)** Austral summer (DJF), and **B)** austral winter (JJA) precipitation anomalies relative to the pre-industrial period (mm month^{-1}). The median has been used as the measure of central tendency to account for extreme values in the distribution that skew the mean. Archive sites (from Table 6.2) are coloured by the palaeoclimate conditions relative to present (red: wetter than present, blue: drier than present, white = no change). Points are outlined with black if these represent the conditions throughout the period of interest, or outlined with blue or red to indicate a transition. Circles: terrestrial record, triangles: marine record of upwelling, and squares: marine core records of terrestrial environmental change in the Kalahari/Namib.

6.3.1.2. Positive precipitation anomalies

Over the Atlantic, PMIP models consistently simulate positive precipitation anomalies south of the tropics in the austral summer as far as 30˚S (CNRM-CM5) (Figure 6.8) and simulate advection of this precipitation over the adjacent continental region in the western portion of southwestern Africa as far as 18˚E (MRI-CGCM3) (Figures 6.7, 6.9). In this region, geochemical and geomorphic records support the models through evidence of predominantly wetter conditions than present. Marine records of terrestrial dynamics detail no change relative to present, but this could reflect an averaging effect of the spatial variability in the terrestrial signal. Encompassing the Namib and Kalahari, the source regions for the sedimentary and leaf wax records from cores MD96-2094 (Stuut et al., 2002) and MD08-3167 (Collins *et al*., 2014) cover regions of both positive and negative precipitation anomalies inferred for the western and north-eastern regions of the study area (Figure 6.9).

Pollen records indicate an increased abundance of Poaceae in most hyrax midden records, with increases also recorded in the abundance of Cyperaceae at Vrede (Huab) (Gil-Romera *et al*., 2006) and Windhoek (Scott *et al*., 1991), Aizoaceae type and Dombeya and Euclea elements at Brandberg (Scott *et al*., 2004), and Asteraceae at Pella (Lim *et al*., 2016). The occurrence of these pollen

species, particularly with a dominance of grasses in the pollen assemblages, are interpreted in the primary sources to indicate increased moisture availability at the MH. The diatomaceous nature of the Windhoek deposits also indicates water logging at the site (Scott *et al*., 1991). The aridity index calculations from pollen assemblages at Pella details a wet event at 6 ka (Lim *et al*., 2016). This is also recorded in the leaf wax n-alkane records from Spitzkoppe, Zizou and Pella hyrax middens (Chase *et al*., 2010; 2019), and as the occurrence of excess air in the Stampriet aquifer as evidence of a transition to wetter conditions (Stute and Talma, 1998). Geochemical records from the Kalahari pans indicate an incursion of Atlantic moisture to central southwestern Africa at the MH which resulted in wetter conditions with increased fluvial input to the pan.

Together with the pollen records, landform archives (geoproxies) indicate that the climate was both wetter and the rainy season was longer at the MH than present. Textural and compositional analysis of the Huab River valley fill deposits suggest that flow occurred under a climate more humid and less seasonal than today. The climate was conducive to more sustained channelised river flow, in contrast to its current highly ephemeral nature (Walsh *et al*., 2022). Deposition of floodplain sediments occurred at this time in the Kuiseb River which also attest to these conditions (Srivastava et al., 2006). In the catchment of the Huab River, the dominance of grass in the Vrede hyrax midden pollen sequence likely indicates increased moisture availability as a result of an increased frequency of rainfall events (Gil-Romera *et al*., 2006). Dates from beach ridges bounding Etosha have been interpreted as reflecting the presence of a palaeolake here at this time (Brook *et al*., 2007, Hipondoka *et al*., 2014). Inactivity of aeolian dunes in the southern Kalahari also suggests that widespread aridity in the southern Kalahari did not occur, and could support a hypothesis of an extended rainy season and increased dune vegetation to inhibit activation of sediment (Thomas and Bailey, 2017). Whilst still exhibiting a summer rainfall-dominated regime (Figure 6.2B), the models do show support for decreased seasonal extremes at the MH. Precipitation anomalies are less negative in the winter than the summer (average of -0.1 compared to -2.3 mm month^{-1}), and

the annual simulation of rainfall shows positive precipitation anomalies in May-June and October-November (Figure 6.2).

6.3.2. Last Glacial Maximum (LGM)

The ensemble of model simulations for the LGM detail predominantly positive precipitation anomalies over southern Africa and negative anomalies over northern and tropical Africa in most models (Figure 6.10). On average, the precipitation anomaly over central southwestern Africa is 55.7 mm year^{-1}, ranging from 3.4 mm year^{-1} to 173.2 mm year^{-1} (encompassing spatial variability of -78.8 to 249.2 mm year^{-1} in the model mean). Negative precipitation anomalies are simulated over the tropical ocean to the west of southwestern Africa in 5 out of 8 of the models, with all models simulating positive precipitation anomalies over the land (Figure 6.8). The extent of terrestrial anomalies is variable, from a strong positive trend (GISS-E2-R), to only a slight increase annually (CNRM-CM5). All marine records attest to increased Benguela upwelling relative to present at the LGM (Farmer *et al*., 2005; Kirst *et al*., 1999; Little *et al*., 1997; Figure 6.6).

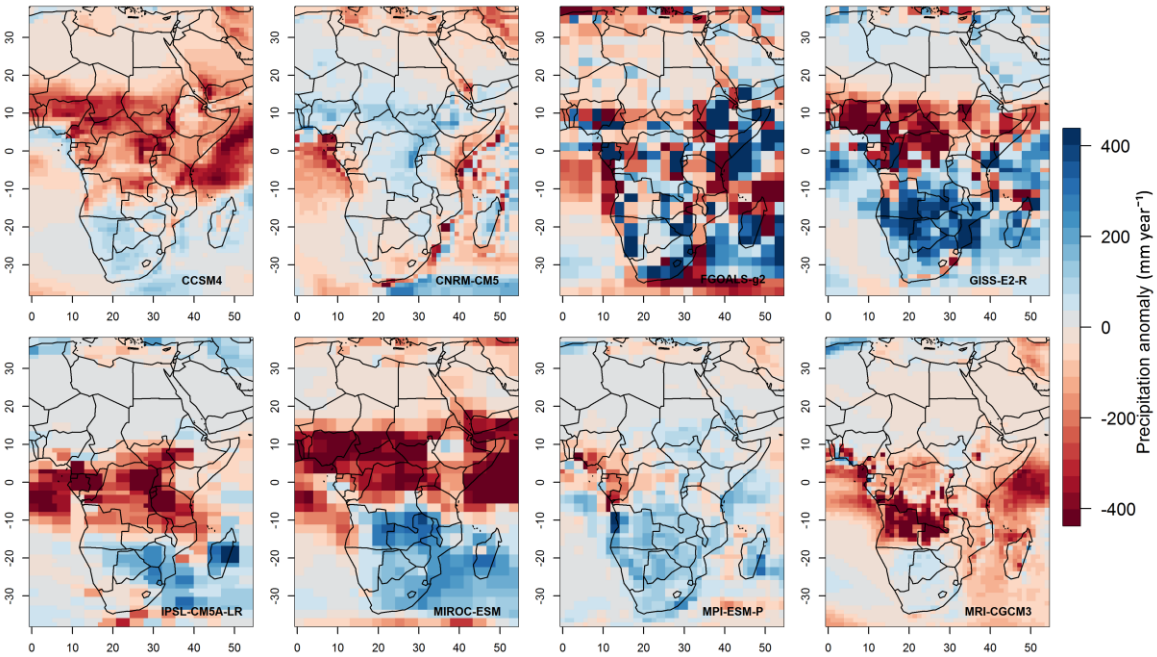

Figure 6.10. Last Glacial Maximum PMIP annual precipitation anomalies (mm year^{-1}) over Africa relative to the pre-industrial period (red: drier than present, blue: wetter than present).

6.3.2.1. Positive precipitation anomalies

The multi-model ensemble simulates positive rainfall anomalies over central southwestern Africa in the austral summer (Figure 6.2, Table 6.4; anomaly of on average 8.2 mm $month^{-1}$ across space), with particularly strong positive anomalies over land of ~46 mm $month^{-1}$ in the model mean, and >100 mm $month^{-1}$ in specific models (Figure 6.11, Table 6.4). Terrestrial records also indicate predominantly wetter conditions across much of central southwestern Africa at the LGM. Geochemical records from speleothem (Railsback *et al*., 2016), lacustrine settings (Belz *et al*., 2020), and pollen records from hyrax middens (Scott *et al*., 2004, 2018) indicate that conditions were cooler and more humid than present. Particularly, an increase in Artemisia, Stoebe type, and Oleaceae pollen species that are not currently dominant were recorded at Brandberg (Scott *et al*., 2018). Stoebe type reflect the occurrence of dwarf-shrubland, and Artemisia and Olea suggest the prevalence of moist conditions (Scott *et al*., 2004). At Orumana Cave, stalagmite Orum-1 records a dominance of C4 grasses over C3 vegetation at the LGM (Railsback *et al*., 2016). These vegetation records are supported by marine core evidence of higher $\delta^{13}C$ in MD08-3167 at the LGM, indicative of C4 vegetation (Collins *et al*., 2014). Higher n-alkane concentrations at the LGM could also represent greater coverage of vegetation across central southwestern Africa (Collins *et al*., 2014). With a corresponding depletion in δD, this record suggests increased tropical summer rainfall. Collins *et al*. (2014) propose that the leaf waxes analysed from the marine core incorporate sediments sourced from the eastern Kalahari Desert, which is supported by the geochemical record from the Omongwa Pan, Kalahari. The leaf-wax biomarker $\delta^{2}H$ is low at the LGM and is interpreted to exclude an influence of Atlantic derived rainfall and indicate sourcing from tropical regions (Belz *et al*., 2020).

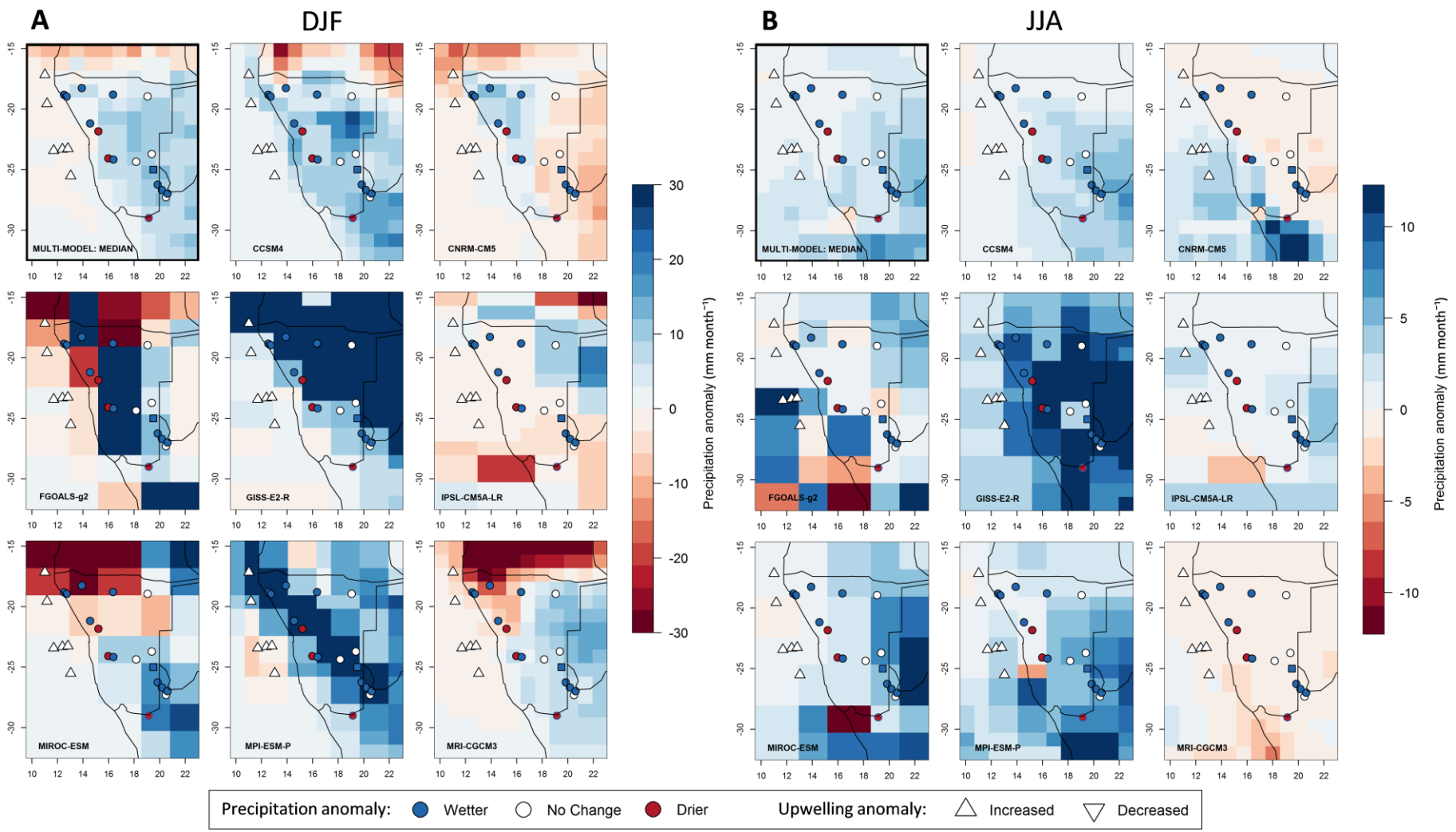
A
DJF
B
JJA
MULTI-MODEL: MEDIAN
CCSM4
CNRM-CM5
FGOALS-g2
GISS-E2-R
IPSL-CM5A-LR
MIROC-ESM
MPI-ESM-P
MRI-CGCM3
Precipitation anomaly (mm month⁻¹)
30
20
10
0
-10
-20
-30
10
5
0
-5
-10
Precipitation anomaly:
Wetter
No Change
Drier
Upwelling anomaly:
Increased
Decreased

Figure 6.11. Model-data comparison for the Last Glacial Maximum (palaeodata: 20-22 ka, models: 21 ka) detailing the spatial pattern of precipitation anomalies across central southwestern Africa. **A)** Austral summer (DJF), and **B)** austral winter (JJA) precipitation anomalies relative to the pre-industrial period (mm month^{-1}). The median has been used as the measure of central tendency to account for extreme values in the distribution that skew the mean. Archive sites (from Table 6.2) are coloured by the palaeoclimate conditions relative to present (red: wetter than present, blue: drier than present, white = no change). Points are outlined with black if these represent the conditions throughout the period of interest, or outlined with blue or red to indicate a transition. Circles: terrestrial record, triangles: marine record of upwelling, and squares: marine core records of terrestrial change in the Kalahari/Namib.

Geoproxy records across central southwestern Africa also detail a wetter climate than present at the LGM through evidence of increased fluvial activity, lake and pan filling, and limited dune accumulation. Intermittent river flow within a more channelised system and limited occurrence of flash floods is recorded along the Khumib and Hoarusib (Srivastava *et al*., 2004, 2005), ponding at BüllsPort playa along the Tsondab River (Völkel *et al*., 2021), and evidence of more persistent or perennial river flow in the Molopo (Heine, 1990; Hurkamp *et al*., 2011). Correspondence between the geochemical and geomorphic archives is observable between Hoarusib fluvial record and stalagmite Orum-1 located in the Hoarusib catchment. In the Kalahari, chronologies detail pan filling at Witpan (Telfer *et al*., 2009) and Branddam East Pan (Schüller *et al*., 2018). The marine grain size record of terrestrial change support these findings, indicating increased fluvial activity (Stuut *et al*., 2002) and terrestrial input (Collins *et al*., 2014).

Dune sites across the northern, southern and western Kalahari yield luminescence ages dating to this period (Stone and Thomas, 2008; Telfer and Thomas, 2007; Thomas *et al*., 2000), but assessment of the stratigraphic context shows that dune accumulation was not significant at the LGM (Thomas and Bailey, 2017). Northern Kalahari dunes are predominantly located in downwind regions of fluvial systems, where dune building occurs in periods following fluvial activity and input

of sediment. In southern and western Kalahari, the timing of dune accumulation in the early Holocene coincides with precipitation minima from the MD08-3167 marine δD record (δD maxima) (Thomas and Bailey, 2017). The LGM, in contrast, is a period of δD minima (Collins *et al*., 2014), indicating higher precipitation and a lack of significant accumulation at the LGM indicates that widespread aridity did not prevail in these dunefields. These dune records therefore support the fluvial and pan accumulation records of increased rainfall at the LGM.

6.3.2.2. Extended rainfall season

As well as a total increase in precipitation, both the models (all except MRI-CGCM3) and several palaeorecords indicate a decrease in seasonality (Figures 6.2, 6.8, 6.11). Whilst the largest increase in precipitation is recorded during the austral summer (average 8.2 mm month^{-1} across space; Table 6.4), models simulate an increase of 2.7 mm month^{-1} in the winter (with up to 10.8 mm month^{-1} inland in the multi-model mean; Table 6.4). During the summer, positive precipitation anomalies are predominantly confined to continental regions, but in the austral winter, an increase in precipitation across the whole region is simulated (Figure 6.11).

Evidence of more persistent channelised flow of intermittent and perennial rivers (Figure 6.5) and ponding in playa and pan environments are indicative of more sustained year-round rainfall at the LGM. In comparison to the MH, where Molopo river flow did not reach the Orange river (Ramisch *et al*., 2017), the flow was more sustained and perennial at the LGM (Heine, 1990; Hurkamp *et al*., 2011). In the Kalahari, the sedimentological record from Branddam East Pan indicates increased fluvial input at the LGM under increased Atlantic sourced rainfall (Schüller *et al*., 2018). By contrast, Omongwa pan, located further north, details very little Atlantic sourced rainfall (Belz *et al*., 2020), and the MD08-3167 marine core record of Indian Ocean-derived rainfall likely reflects the Kalahari region further north-east of this influence (Collins *et al*., 2014). The contemporary winter rainfall zone is characterised by fynbos elements, yet distinctive pollen types of Ericaceae and

Restionaceae are near-absent from hyrax midden records (Lim *et al*., 2016; Scott *et al*., 2004, 2018). Whilst the PMIP model ensemble simulates an increase in rainfall during winter months, the temporal rainfall distribution remains dominated by summer rainfall (Figure 6.2C).

6.3.2.3. Negative precipitation anomalies

In several PMIP models, negative precipitation anomalies are simulated over the Atlantic Ocean and the adjacent continental region as far as 20˚S (Figures 6.8, 6.11). This signal is identified in model simulations for austral summer rather than winter, indicating a decrease in summer tropical precipitation. This signal is supported by hyrax middens records in the west of southwestern Africa, where negative precipitation anomalies are recorded at Spitzkoppe, Zizou and Pella (Chase *et al*., 2019; Lim *et al*., 2016). Other records in close proximity to these middens, but further inland, show wetter conditions at the LGM (e.g. BüllsPort playa is close to the Zizou hyrax midden), suggesting that the signal of negative precipitation anomalies is relatively confined to the Namib Desert.

6.4. Discussion

Using this compilation of robust palaeoclimate and palaeoenvironmental archive records and multi-model ensemble PMIP simulations, the findings are discussed here in terms of: i) the hypotheses of precipitation change in central southwestern Africa that are supported by the current dataset; ii) the contributions of models and archive data and extent of model-data agreement; and iii) suggested recommendations for future priorities for data collection to better resolve regional differences in palaeoclimate response.

6.4.1. Spatial pattern of precipitation response

One of the key differentiators between the hypotheses of central southwestern African palaeoclimate change (outlined in Section 6.1.1) is the consistency in direction of precipitation

anomalies across the study region. Hypotheses of hemispheric asynchronicity (Partridge *et al*., 1997) and synchronicity (Collins *et al*., 2011) are based on the occurrence of homogenous areas of precipitation increase or decrease at key timesteps. The spatial pattern of precipitation response in the palaeodata and model simulations, however, indicates differing sensitivities to palaeoclimate drivers over space (following Singarayer and Burrough, 2015), with key differences noted between the coastal and inland regions (Figure 6.12). At its most general interpretation, this suggests that patterns of hemispheric synchronicity are restricted to the coastal region and greater evidence for hemispheric asynchronicity is found further inland. The palaeodata and models examined in this study principally support the hypothesis of differing response of the tropical rainbelt over the land and ocean/coastal zone (Singarayer and Burrough, 2015; Singarayer *et al*., 2017), where the precipitation response is modulated by ocean-atmosphere feedbacks in the coastal region (Chase *et al*., 2019) and the role of westerly derived rainfall (Engelbrecht *et al*., 2019).

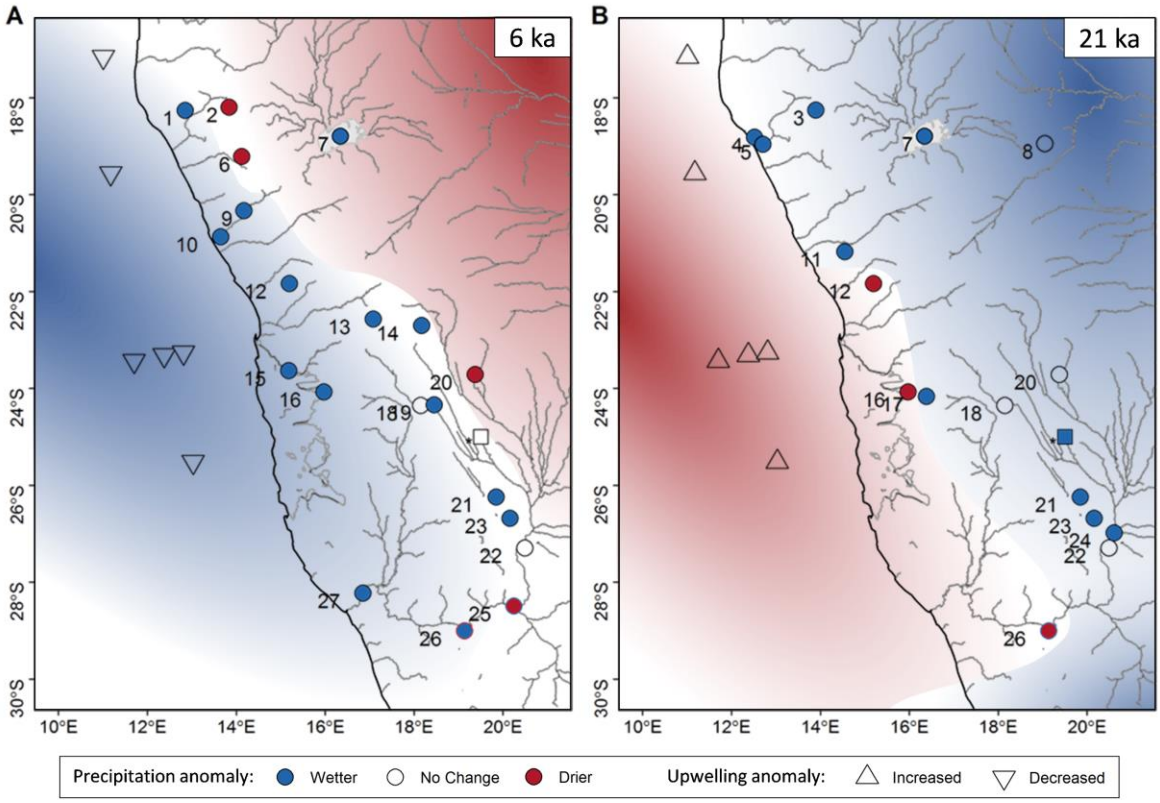

Figure 6.12. Interpretation of the distribution of climate anomalies based on available palaeodata and the PMIP3 model simulations. **A)** Mid Holocene (6 ka), **B)** Last Glacial Maximum (21 ka). Terrestrial archive precipitation anomalies are demonstrated by circles (site numbers relate to Table 6.2) coloured by change relative to present, and marine records of Benguela upwelling are detailed by triangles. Palaeoclimate interpretations from marine records of grain size and leaf wax alkanes from marine cores MD96-2094 (Stuut et al., 2002) and MD08-3167 (Collins *et al.*, 2014) are indicative of change over the Namib and Kalahari Deserts, represented here by a square.

6.4.2. Differing controls on the tropical rainbelt over ocean and land

6.4.2.1. Mid Holocene

At the MH, fluvial, lacustrine, pollen, and geochemical records from the west of the study region indicate sustained wetter conditions compared to the present. The majority of PMIP models also consistently simulate positive precipitation anomalies over the ocean and coastal region during austral summer (Figure 6.8). These conditions are in-phase with positive precipitation anomalies in the North African Humid Period, and reflect changes in the dynamics of the ITCZ over the ocean to insolation (Singarayer and Burrough, 2015; Singarayer *et al.*, 2017). At the MH, the southern

hemisphere was warmer during boreal winter than the northern hemisphere, which increased the extent of latitudinal migration of the ITCZ where it tracked further south during boreal winter (austral summer) to scavenge heat (Broccoli *et al*., 2006). Evidence of fluvial input to Branddam East Pan in the Kalahari (Schüller *et al*., 2018) indicates that associated positive precipitation anomalies penetrated into the southern African subcontinent to at least ~20˚E (up to 18˚E in the models), inferring that a large proportion of the western terrestrial signal during the MH can be explained by the dynamics of the ITCZ over the ocean and advection of moisture over land.

Further inland, key palaeorecord evidence of conditions drier than present (e.g. Hoanib River, Eitel *et al*., 2006; Omongwa pan, Belz *et al*., 2020) supports the hypothesis that the response of the tropical rainbelt over land occurred in the opposite direction to that observed over the ocean. Over a large proportion of terrestrial central southwestern Africa, all PMIP models simulate year-round conditions that are drier than present, particularly in the austral summer (Figures 6.7, 6.8, 6.9). Evidence from southwestern Africa corresponds with several records from central southern Africa that indicate periods of aridity during the African Humid Period (Burrough and Thomas, 2013). In the context of simulated precipitation across Africa (Figure 6.7) and established evidence of wetter conditions in the northern hemisphere at this time (e.g. deMenocal *et al*., 2000; Lézine *et al*., 2011; Pausata *et al*., 2020), this suggests that the maximum latitudinal extent of tropical rainbelt during the MH was further north, resulting in an asymmetric pattern of rainfall anomalies over land. This follows the proposition that the tropical rainbelt responds to the thermodynamic control of insolation on heating in summer months, at the MH tracking to the northern hemisphere when boreal summer insolation was high (Singarayer and Burrough, 2015; Singarayer *et al*., 2017).

Within the inland region where a dominant trend of drying is inferred from both some empirical records and the models (Figure 6.12), lake shorelines and stromatolites at Etosha indicate conditions wetter than present at the MH with lake filling between 4 m and 12 m (Brook *et al*.,

2007, Brook *et al*., 2011; Hipondoka *et al*., 2014). At the MH, evidence further east in the subcontinental interior indicates that the Okavango-Makgadikgadi system was also active at this time (Burrough *et al*., 2007, 2009; Cordova *et al*., 2017; Tooth *et al*., 2022). High lake levels within a predominantly arid context are recorded at palaeolake Makgadikgadi (Burrough *et al*., 2009) and correspond to evidence of lake filling at Etosha. As both systems catchments extend north to the wet tropics, it can be hypothesised that distal-end responses were fed by rainfall associated with a strengthened Congo Air Boundary as a result of enhanced Atlantic monsoonal rainfall (Cordova *et al*., 2017). ^{14}C chronologies demonstrate peatland accumulation under humid conditions in the Angolan highlands at 6-7 ka (Lourenco *et al*., 2022; a record that is outside the defined study region of this paper), further indicating that the source region of these lakes was wet.

6.4.2.2. Last Glacial Maximum

At the LGM, archive and model data detail a hemispherically asymmetric response of the tropical rainbelt over the continent. Palaeorecords of conditions wetter than present are widespread in southern Africa, and models are coherent in simulating conditions on average wetter than present over land during austral summer (Figure 6.8). The latitudinal response of the tropical rainbelt at the LGM is consistent with extratropical forcing through the establishment of large ice-sheets and a decrease in greenhouse gases and temperature (Arbuszewski *et al*., 2013; McGee *et al*., 2014). Colder conditions at the LGM are supported by evidence from pollen assemblages (e.g. Scott *et al*., 2004, 2018) and noble gases in Stampriet aquifer (Stute and Talma, 1998). Ice-sheet forcing at the LGM was hemispherically asymmetric, where the continental land mass is larger in the northern hemisphere, leading to greater cooling in the northern hemisphere compared to southern. This caused a southerly displacement of the tropical rainbelt towards the warmer hemisphere (Broccoli *et al*., 2006; Kang *et al*., 2008), resulting in an overall trend of negative precipitation anomalies in the northern hemisphere and positive anomalies in the southern hemisphere (Figure 6.10). Geochemical records from pan and marine cores indicate sustained tropical sourcing of rainfall to

the eastern Kalahari (Collins *et al*., 2014; Belz *et al*., 2020) at the LGM, which is consistent with a southerly shift of the tropical rainbelt (Jiang *et al*., 2015b).

An opposite response of the ITCZ over the ocean is also inferred at the LGM. A compilation of geochemical data and a pollen aridity index from hyrax midden records in the Namib Desert (Spitzkoppe, Zizou, Pella; Chase *et al*., 2019; Lim *et al*., 2016) indicate conditions drier than present at the LGM. Following the mechanism described for the MH, but in the opposite direction, the maximum latitudinal extent of the tropical rainbelt migration reduced at the LGM. During boreal winter, the tropical rainbelt tracked further north following the interhemispheric temperature gradient. There is less consistency amongst models on the direction of change over the ocean compared to the MH (Figure 6.8) and palaeorecord evidence suggests that advection of this oceanic signal was not wide-reaching and tropical rainfall sources remained important.

6.4.3. Role of ocean-atmosphere feedbacks

Evidence also suggests that the central southwestern African precipitation response was modulated by the role of ocean-atmosphere feedbacks. The theory presented by He *et al*. (2013) and Chase *et al*. (2019) postulates that the Namib Desert hydroclimate inversely followed austral summer insolation, oceanic upwelling, and the strength of the SAA. These controls modulate the difference in hydroclimate response of the coastal region compared to inland that are described above. This control enhanced incursions of rainfall across a large proportion of the study region at the MH, yet the corresponding drying trend at the LGM was limited to only the coastal region.

At the MH, marine core records indicate increased southeast Atlantic SSTs and reduced upwelling of the cold Benguela current (Farmer *et al*., 2005; Kirst *et al*., 1999; Little *et al*., 1997; Figure 6.6). Reduced summer interhemispheric temperature gradient (following boreal summer insolation maxima and austral summer insolation minima), would have reduced the extent of atmospheric

subsidence in this region and enabled incursion of moisture bearing systems to the western part of southern Africa. This would have amplified the effect of the extended oscillation of the ITCZ over the ocean following winter insolation (described above) and together these dynamics could explain the positive precipitation anomalies recorded in the palaeoclimate and palaeoenvironmental archives. The palaeodata indicate that the wetter than present signal extends to the southern Kalahari (Figure 6.12), beyond the influence inferred by Chase *et al*. (2019) from the Namib Desert sites.

At the LGM, the strength of the SAA and intensity of Benguela upwelling increased (Farmer *et al*., 2005; Kirst *et al*., 1999; Little *et al*., 1997; Figure 6.6). This can be explained both by remote controls of strong interhemispheric temperature gradient and direct response of land-sea temperature contrast where austral summer insolation was high within the context of globally cool temperatures following boreal summer insolation minima. Enhanced atmospheric subsidence would have blocked moisture-bearing systems and had the effect of decreasing precipitation in the region. This link between ocean-atmosphere interactions and precipitation response is found to hold true for the hyrax midden sites in the Namib Desert (Chase *et al*., 2019), but interrogation of additional sites across central southwestern Africa at the LGM, however, indicate that widespread aridity did not prevail as a result. This supports the contention from Lancaster (2002) that even during relatively wet times, the Namib Desert remained well within conditions of a semi-arid climate. This could in part explain the difference in response noted between the records from Collins *et al*. (2014) and Chase *et al*. (2019), where the former could reflect wetter conditions inland, whereas the latter reflects conditions closer to coast.

6.4.4. Extension of the latitudinal reach of westerly frontal rainfall

Evidence of perennial river flow (e.g. Molopo River; Heine, 1990; Hurkamp *et al*., 2011), pan filling (e.g. Branddam East, Kalahari; Schüller *et al*., 2018), and PMIP simulations of increased rainfall year

round at the LGM (Figures 6.2, 6.11) support the hypothesis of an increased contribution of rainfall from westerly frontal systems to year round rainfall (Engelbrecht *et al*., 2019). The equator-to-pole temperature gradient increased as a result of an expansion of continental ice sheets at the poles during the LGM, resulting in an equatorward displacement of the extent of the westerlies transporting Atlantic moisture (Engelbrecht *et al*., 2019; Kohfeld *et al*., 2013; Perren *et al*., 2020). To distinguish this from an influence of an tropical rainbelt that migrates south in winter, the latitudinal positions of sites can be considered. Singarayer *et al*. (2017) simulate a maximum southerly latitude of the ITCZ of ~22.5˚S at the LGM, yet sites including the Molopo and Branddam East Pan are located further south at 26.9˚S and 26.2˚S respectively. At these sites, the rainfall is likely to have been sourced from the westerlies rather than the tropical rainbelt. Through comparison of two pan sequences within the Kalahari (Figure 6.12), the northerly limit of the extent of westerly-derived rainfall is suggested. The sedimentological record from Branddam East Pan indicates increased fluvial input at the LGM under increased winter rainfall (Schüller *et al*., 2018), yet the Omongwa pan record details very little Atlantic sourced rainfall (Belz *et al*., 2020). The MD08-3167 marine core record details sustained Indian Ocean-derived rainfall during this time, and therefore likely reflects the Kalahari region farther north-east of the westerly influence (Collins *et al*., 2014).

Whilst the area affected by winter rainfall likely increased, pollen records and model simulations do not indicate that the Namibian palaeoclimate was dominated by winter rainfall at the LGM, and do not suggest an expansion of the Winter Rainfall Zone to this region (WRZ, where >66 % of rainfall occurs within the winter months; Chase and Meadows, 2007). An expansion of the WRZ would be accompanied by evidence of fynbos elements, yet distinctive pollen types of Ericaceae and Restionaceae are near-absent from hyrax midden records (Lim *et al*., 2016; Scott *et al*., 2004, 2018), or records from southern Africa's interior (Cordova *et al*., 2017). Alongside an increase in the latitudinal extent of winter rainfall, an extended role of the westerlies would also have increased

the occurrence of summer-time frontal rainfall through interactions with tropical systems. The ensemble of PMIP models simulate rainfall in both summer and winter seasons, and the temporal pattern of rainfall is still dominated by summer rainfall (Figure 6.2C). Given the importance of these interactions and occurrence of tropical temperate troughs (TTTs) in contemporary contexts (Hart *et al*., 2010, 2013; Reason, 2017), it is likely that TTTs were also important on Quaternary timescales (as suggested by Chase *et al*., 2017), and complexity exists beyond the definition of winter and summer rainfall zones that is difficult to unpick from interpretations from existing palaeorecords. Supporting model simulations of an increase in both winter and summer rainfall (Engelbrecht *et al*., 2019), the palaeodata provide evidence of less seasonal rainfall regimes across several central southwestern African sites (Figure 6.12).

6.4.5. Assessing data contributions

6.4.5.1. Palaeoclimate models

Following analysis of the ensemble of model simulations in the context of the palaeodata, we identify the importance of simulation of anomalies over the ocean, over the land, and the distribution of rainfall between seasons. Through evaluating the scale of these anomalies at the MH and LGM (Figure 6.8) and the spatial patterns across central southwestern Africa (Figures 6.9, 6.11) we can assess the variability in model simulations and can consider where models over or underestimate precipitation anomalies based on the palaeoproxy data available.

For the MH, a high degree of convergence in model outcomes is indicative of a clear pattern of negative austral summer precipitation anomalies over the ocean and negative anomalies over land (Figure 6.8). Whilst these east-west trends are consistent with the general pattern of empirical palaeorecord interpretations, the spatial extent of observed precipitation anomalies (Figure 6.9) suggests that the models under-estimate the extent of terrestrial advection of the tropical rainbelt over the western portion of central southwestern Africa. The palaeodata indicate that the wetter-

than-present signal extends to the southern Kalahari to ~20˚E (Branddam East Pan; Schüller *et al*., 2018), yet the model with the greatest incursion of rainfall in austral summer (MRI-CGCM3) reaches only 18˚E (Figure 6.9), and several models do not simulate advection of the positive anomalies over land (e.g. FGOALS-g2, MIROC-ESM). In northern Africa, analysis of the northward shift of the tropical rainbelt suggests that compared to the palaeodata, the models underestimate the magnitude of precipitation increase (Bartlein *et al*., 2011; Braconnot *et al*., 2012; Harrison *et al*., 2015; Perez-Sanz *et al*., 2014). Where there is support for the hypothesis of extended latitudinal migration of the ITCZ over the ocean, this underestimation of tropical rainbelt intensity in the northern hemisphere could hold true for the oceans in the southern hemisphere. The corroboration between inland palaeorecords and models of negative precipitation anomalies indicates that terrestrial aridity is a robust response. This trend is also supported by model-data comparison in south-eastern Africa (Chevalier *et al*., 2017).

For the LGM, there is good correspondence between the model ensemble and the palaeodata in the simulation of terrestrial anomalies. The majority of models simulate wetter conditions than present in summer and winter (Figure 6.8). There is variability amongst the extent of this simulation, and we suggest that anomalies of greater magnitude in both seasons best explain the palaeodata. Figure 6.8 shows a much wider range in the extent of precipitation anomalies over the ocean, however, with an opposite trend recorded between some models (e.g. MPI-ESM-P, GISS-E2-R). In contrast to the MH where consistent positive precipitation anomalies over the ocean match consistent positive precipitation trends observed in palaeorecords along the west coast, reduced convergence in the pattern of modelled ocean anomalies at the LGM is matched by a less consistent signal in the palaeodata. Only the Namib Desert appears to have been influenced by this drying trend, and the influence of advection of the ocean signal eastwards inland was more limited in extent than for the MH. For this terrestrial west coast drying trend to occur, and in the context

of records of oceanic upwelling, we have greater confidence in the models that simulate negative precipitation over the ocean but without extended advection of this signal over land.

6.4.5.2. Palaeorecords

Alongside model variability, there are also several factors that influence the ability of palaeodata to usefully test model simulations. Here, we discuss the importance of incorporating a range of archive types, the utility of geoproxies in this analysis, the importance of data quality assessments for complex and discontinuous records, and the role of chronological uncertainty for comparison with models.

Archives preserve evidence of palaeoclimate changes in complex ways that are frequently challenging to unpick. Responses to climate include geomorphic change (e.g. type of river flow recorded in formation of sedimentary sequences), changes in the extent and distribution of biomes (e.g. recorded as pollen changes), and changes to the source of precipitation (e.g. hydrogen isotopes), and these can be recorded with different time lags (Stone, 2014). Whilst model simulations cover the full spatial range of interest, terrestrial proxies commonly provide site-specific details that require careful interpretation. Through interrogation of a range of these archive types, in particular with incorporation of geomorphic archives that are widespread across the dryland region (Thomas and Burrough, 2012; Thomas, 2013), the spatial coverage of sites across the region of interest can be increased. Where there is close correspondence in the timing and direction of precipitation anomalies between different archive types (e.g. the Orumana speleothem and Hoarusib River fluvial sedimentary archives; Railsback *et al*., 2016; Srivastava *et al*., 2005), we can have greater confidence in the conclusions reached. These examples of consistency between traditionally used archives and discontinuous geomorphic records that are commonly excluded from this type of analysis demonstrate the utility of geoproxy records for future syntheses.

On late Quaternary timescales, identifying the extent of changes in seasonality is critical to differentiating climate controls. We find that evidence of seasonality is predominantly preserved in pollen and fluvial sedimentary records in central southwestern Africa. Literature on conditions in which specific pollen types prevail (e.g. Chevalier *et al*., 2021) can be used to determine the quantity and frequency of rains (e.g. Gil-Romera *et al*., 2006). In the context of recent records from fluvial archives using detailed sedimentological analyses (e.g. Ramisch *et al*., 2017; Walsh *et al*., 2022), qualitative assessments of the seasonality of the climate have been possible. It is possible to differentiate between ephemeral river flow as a result of intense isolated storms interspersed with a long dry season (e.g. the lower Molopo at the MH, Ramisch *et al*., 2017) and more continuous or perennial flow as a result of more sustained rainfall across a greater proportion of the year (e.g. the Molopo at the LGM, Hurkamp *et al*., 2011).

Whilst continuous long-term records are best for comparison with model simulations, discontinuous data can be informative for testing specific model outcomes. For palaeo model-data comparison, this study has filtered records to obtain data of the highest quality. Our analysis specifically tests the palaeodata with model outcomes at two key timesteps, so clarity of timing and certainty in the climate context is critical. The requirement for there to be data available in the period of interest (5-7 ka, 20-22 ka) helped to deal with the complexity of how hiatuses are interpreted between datasets. Whilst interpretations of hiatuses are commonly indicative of palaeoclimate change that fits with the hypotheses presented in Figure 6.12 (e.g. Chase *et al*. (2010) infer wetter conditions at the MH preceding the onset of record formation) it is difficult to pinpoint chronology of these periods, and this can add complexity where the timing of change is uncertain. We therefore argue that whilst the dataset size decreased following the filtering process, we have greater confidence in the interpretations from the incorporated archives.

An important consideration for this type of analysis is whether the precision and the scale of analysis in the palaeodata are high enough to sufficiently test these models. PMIP analyses are snapshots of climatologies run under constant conditions, yet the palaeorecords we compare against incorporate a suite of temporal and spatial complexities. This is particularly evident in records that indicate periods of transition rather than consistent climate regimes at periods of interest (6 ka and 21 ka). Of note is the Pella hyrax midden that records a transition from arid to humid at ~6 ka (Lim *et al*., 2016), and the Molopo River sediments which detail a shift from humid to arid at this time (Ramisch *et al*., 2017). When considered in the context of North African literature, there is debate with increasing recognition that the African Humid Period ended through a time transgressive transition (i.e. it ended at different times at different latitudes) rather than an abrupt continent-wide termination (Dallmeyer *et al*., 2020; Shanahan *et al*., 2015). Such transitions were also likely gradual in southern Africa. Analysis of contemporary climate systems in southern Africa also demonstrates the complexity of interactions and dynamics that Quaternary studies are interested in. The scale at which we can examine change on Quaternary timescales is not commensurate with the scale at which they are studied in contemporary climatology, however. There is recognition that extreme events, such as a heavy rainfall within a dominantly dry season as a result of TTTs, can do a lot of geomorphological work, and these complexities must be considered when interpreting geoproxy records, such as fluvial records, where possible.

6.4.6. Recommendations

Through a compilation of model simulations and palaeodata, Figure 6.12 presents a hypothesis for future research to test. This figure also highlights the spatial coverage of available proxy data and enables recommendations to be made for determining locations of future data collection. In particular, there is a gap in the availability of records from the north-eastern portion of southwestern Africa, where archives east of Etosha with chronology dating to the MH or LGM are limited. This region is important for providing sufficient palaeodata to adequately test the model

simulations of conditions drier than present over the terrestrial region during the MH. Confirmation of the hypothesis of a latitudinal shift of the tropical rainbelt over land is currently limited by the small dataset from this region.

There is a need for the production of long, high-quality datasets from central southwestern Africa, including records that quantify precipitation changes (e.g. commensurate with the pollen records incorporated in analysis of eastern African palaeoclimates; Chevalier *et al*., 2017), and geoproxy records with robust independent proxies for interpretation of palaeoenvironmental conditions (e.g. fluvial archives; Walsh *et al*., in review). The findings from application of novel approaches to fluvial deposits suggest that more nuanced data on flow regimes can be established (Tooth *et al*., 2022; Walsh *et al*., 2022). Analyses of isotopes within leaf waxes (e.g. Belz *et al*., 2020; Collins *et al*., 2013, 2014) and hyrax middens (e.g. Chase *et al*., 2019) are increasing the sensitivity by which we can understand past precipitation changes. New records must therefore be accompanied by reliable chronologies and detailed interrogation of the climate setting. Alongside the production of records from additional sites, it may also be appropriate to reinterpret, revisit, or resample existing sample locations in the light of recent research.

6.5. Conclusions

This paper compiles a robust set of palaeoclimate and palaeoenvironmental archive data and a suite of palaeomodel simulations from central southwestern Africa to assess the direction and seasonality of precipitation anomalies at the mid Holocene and the Last Glacial Maximum. Data from empirical palaeorecords provides sufficient spatial coverage for model-data comparison at these two timesteps to test theories of palaeoclimate change.

Empirical palaeodata and models detail a spatial pattern of precipitation anomalies across central southwestern Africa at the MH and LGM that can be explained by west-east differences in moisture

supply. The data support the theory presented by Singarayer and Burrough (2015) and Singarayer *et al*. (2017) of divergence in the response of the ocean and land on Quaternary timescales and enables the spatial extent of response to be mapped. We also suggest amplification of this pattern through ocean-atmosphere feedbacks (as suggested by Chase *et al*., 2019) and winter rainfall (as found by Engelbrecht *et al*., 2019). Across central southwestern Africa, the data together support hypotheses of: i) a latitudinal shift in the seasonal extremes of the tropical rainbelt over land as a thermodynamic response to insolation; ii) an extension and reduction of the seasonal oscillation of the ITCZ over the ocean as a response to interhemispheric temperature gradients; iii) modulation of the coastal hydroclimate through the role of ocean-atmosphere interactions; and iv) an additional role of changes in seasonality as a result of an increased northerly extent of the westerlies at the LGM. Advection of moisture over the southwestern terrestrial region when the ITCZ is further south over the ocean explains positive precipitation anomalies in the coastal region when inland regions were dry at the MH following low insolation. The role of upwelling and high pressure to the west of the continent enhance this, and explain negative precipitation anomalies in the Namib Desert when inland regions were wet at the LGM following a southerly shift of the tropical rainbelt and northerly influence of westerly derived rainfall. Model-data comparisons show predominantly robust simulations of dynamics that explain the palaeodata at both timesteps. At the MH, however, we suggest that the models underestimate the extent of oscillation of the tropical rainbelt, and therefore underestimate the extent to which moisture is advected over land.

This analysis uses a robust dataset obtained through a set of inclusion criteria to enable confidence in the environmental response recorded. Through this assessment of the current state of palaeodata from the region, we identify gaps in the availability of records and highlight northeastern Namibia as a priority for future research where archives with chronologies dating to the MH and LGM are currently limited. We demonstrate the utility of using discontinuous geomorphic records that are often excluded from this form of analysis and identify the need for

palaeoproxies that enable a quantification of precipitation response. With a larger and more robust dataset, the potential for model-data comparison in greater detail would be improved and the key trends identified in this analysis could be tested further.

Chapter 7:

Conclusions

7.1. Introduction

This thesis sought to ***assess the hydroclimatic history preserved in the depositional record of southwestern Africa's dryland rivers to address how the palaeoclimate responded to past forcing***. In doing so, the research in the published and submitted papers has focused on three primary research objectives:

1. To establish the timing and nature of depositional regimes of the Huab River valley fill archive, Skeleton Coast, Namibia, using a high-resolution luminescence chronology and a systematic assessment of stratigraphic, compositional, and sedimentological changes;
2. To construct a database of chronologies established from dryland fluvial contexts to critically evaluate how sediments have been used as palaeoenvironmental archives in southwestern Africa;
3. To test hypotheses of the spatial patterning of late Quaternary precipitation change using quality-assessed data from empirical palaeoarchives and palaeoclimate model simulations.

This chapter draws together the key findings of the thesis to address the research objectives, with reference to a new fluvial palaeoenvironmental record from the Huab River (Chapter 4), the analysis of a chronological database of southwestern African fluvial records (Chapter 5), and empirical-model data comparison to interpret these records in the context of prevailing hypotheses of palaeoclimate change (Chapter 6). The final section of this chapter discusses the prospects for the study of dryland fluvial Quaternary archives, in southwestern Africa and beyond.

7.2. Depositional regimes of the Huab River

To address the first objective of this thesis, **to establish the timing and nature of depositional regimes of the Huab River valley fill archive, Skeleton Coast, Namibia,** Chapter 4 presents a new

fluvial record combining a high-resolution luminescence chronology with integrated stratigraphic, compositional, and sedimentological analysis.

7.2.1. Timing of sediment deposition

The timing of sediment deposition in the Skeleton Coast valley fill was established through 42 ages from nine sites. This record spans the period from 11.58 ± 0.95 ka to 0.2 ± 0.05 ka and thus establishes the timing of fluvial deposition during nearly the entire Holocene. This chronology contains ages commensurate with the timing of sedimentation across several other Namibian fluvial systems and has ages within the mid Holocene time period used for model data comparison in Chapter 6 (5-7 ka). Together, this offers the opportunity for interpretation of the Huab record in the context of palaeoenvironmental and palaeoclimate archives across the region. In the context of the existing chronology from the Huab Skeleton Coast site(Thomas *et al.*, 2017), the new detailed chronology increases both the resolution of dated sedimentary units, and the length of documented fluvial history (through dating additional deeper sections with longer preserved histories).

Taken together, ages from a suite of sections present a detailed history of sediment deposition and preservation, yet variability in the age profiles between individual sections exists (Figure 7.1). Some sections preserve a more complete history of sedimentation and others only record certain phases (e.g. sedimentation from 7 to 5 ka is recorded particularly at site NAM18/2, but not widely at other sites). This confirms the ground penetrating radar (GPR) analysis (Section 3.2.1) which indicates spatial variability in the lateral continuity of stratigraphic sections. This attests to a key challenge of studying fluvial geomorphic systems, where environmental signals can be variably recorded across space or can be removed through subsequent fluvial processes (e.g. discussed by Jerolmack and Paola, 2010; Bailey and Thomas, 2014; Lewin and Macklin 2003). Together, these data detail the importance of studying multiple sections across a valley fill and highlight that caution in

extrapolating the findings to basin-wide or region-wide scale should be applied when investigating individual sites. With a larger number of ages, it is expected that a more complete history of fluvial deposition can be captured (e.g. Figure 7.1), yet it is not clear, as many studies allude to, what a sufficient number actually is.

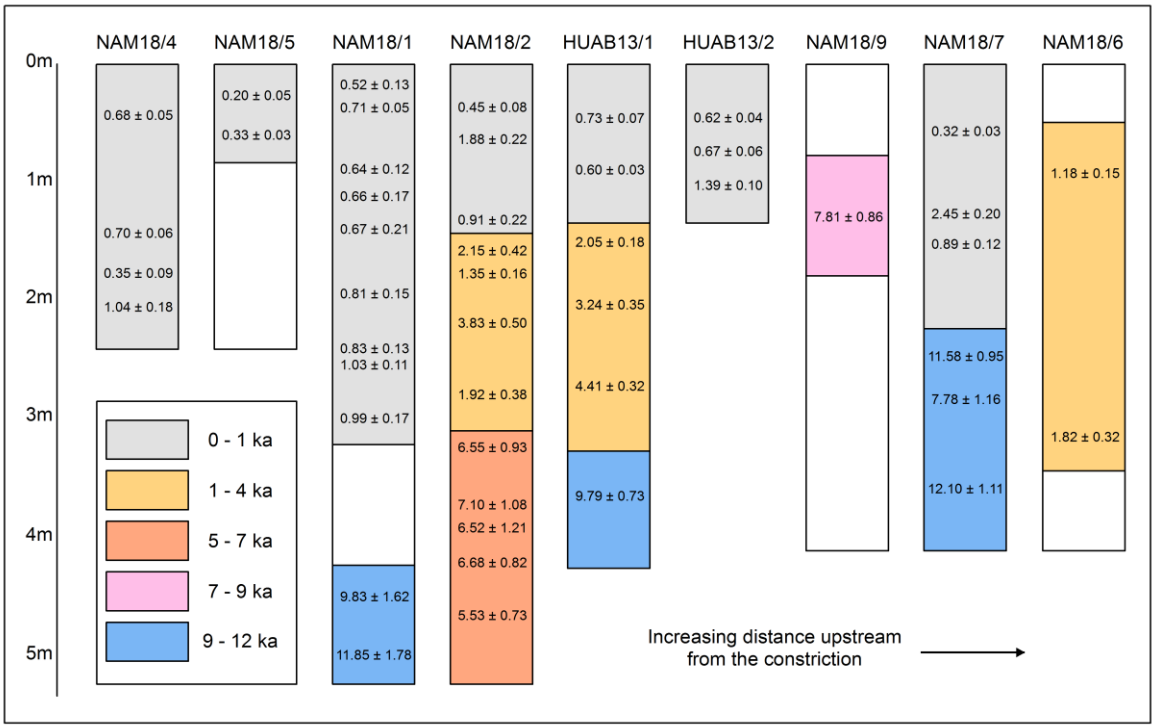

Figure 7.1. Correspondence between chronologies established for the main Huab Skeleton Coast valley fill stratigraphic sections. Boundaries between chronological units are defined from the results of lithofacies analysis in Chapter 4 and have been applied to the main stratigraphic sections produced in this thesis (NAM18) and the two sections from Thomas *et al*. (2017) (HUAB13). Sections are organised by increasing distance upstream from the constriction. Some fluvial depositional events would not be identified if only one section was studied.

In the case of the Huab valley fill, observations during fieldwork suggest a role of aeolian processes and fluvial incision in controlling the variable history of sediment preservation. First, the presence of dunes across the surface of the fill and within the channel indicate reworking of fluvially derived sediment into aeolian dunes, which might remove sediment at certain sites, and protect fluvial units from reworking at others (e.g. at site NAM18/8 deposition is preserved below a nebkha dune). Second, aeolian processes can have a noteworthy role in the removal and redeposition of sediment

as dust, especially where remote sensing has identified the Namibian ephemeral fluvial systems and Huab valley fill in particular as sources of atmospheric dust (Eckardt and Kuring, 2005; Vickery *et al*., 2013; Dansie *et al*., 2017). Third, protection of fluvial sedimentary units below resistant layers of alluvial slope inputs is recorded at site NAM18/9 where an upper unit of sediment is dated to 7.8 ka at the same depth to which majority of other sites date to ~ 0.5 ka (Figure 7.1). Fluvial-aeolian interactions are common in some dryland fluvial settings (Liu and Coulthard, 2015, 2017) and need to be taken into account when considering the stratigraphic completeness of a fluvial record and the interpretation of hiatuses in fluvial sections.

7.2.2. Nature of sediment deposition

To reconstruct the Holocene hydrological regimes of the Huab River, Chapter 4 used a multi-method approach incorporating lithofacies analysis, heavy mineral and petrographic assemblages, and grain size analysis. This investigation of sedimentology and stratigraphy enabled a consideration of both the capacity of the river to transport grains throughout the catchment and the fluvial conditions under which these grains were deposited in the valley fill.

Analyses of the main river styles from lithofacies associations detail deposition as a result of unconfined stream associations, more sustained flow within a well-defined channel, and overbank deposition in associated floodplains. A fine-scaled analysis of textural parameters identified a strong grain size control on the compositional assemblage. When combined with the luminescence chronology of the timing of deposition, these data were used to differentiate between units deposited at times of different climate regimes. Sedimentary units containing coarse grain sizes and petrographic assemblages rich in rock and lithic fragments dating to the early to mid Holocene are indicative of humid climate conditions in the Huab. Deposition dating from 12 to 9 ka exhibits evidence of a flash flood regime, suggesting the dominance of ephemeral river flow, but sedimentology suggests that this flow occurred within a climate less arid than today. From 7 to 5

ka, the prevailing channelised stratigraphy is indicative of a climate conducive to more sustained river flow, where flow occupancy was more intermittent than ephemeral. Higher precipitation than today increased the efficiency of the hydrological regime throughout the drainage basin and increased the capacity to move coarser grains through the sediment cascade.

Within the last 4 ka, samples with finer grain sizes and petrographic assemblages rich in monocrystalline grains (rather than rock and lithic fragments) are indicative of less activation of the drainage system, greater hydraulic sorting within sheet flood events, and the potential for greater mechanical breakdown of polycrystalline grains under a more arid climate. Lower average precipitation rates across the catchment are inferred from a dominance of more unconfined stream facies associations. Within the last millennium, in particular, this lithofacies is interpreted to reflect ephemeral river flow similar to today. This record corresponds to key hydrological changes recorded in other Namibian fluvial archives considered in Chapter 5 and contributes to an understanding of fluvial response in a regional palaeoclimate context (Chapter 6; discussed in Section 7.4).

7.3. Fluvial sediments as palaeoenvironmental records in southwestern Africa

To address the second objective of this thesis, **to evaluate how sediments in dryland fluvial contexts have been used as palaeoenvironmental records in southwestern Africa**, Chapter 5 presents the creation and analysis of a chronological fluvial database. The aim of this analysis was to synthesise dated fluvial records from the western desert regions of southern Africa, to filter out the least robust components of the dataset, and to analyse the combined fluvial history contained within the remaining data. This research contributes to: i) evaluating the status of Quaternary fluvial research in the region; ii) determining the potential controls on fluvial sediment archive

formation, preservation, and interpretation; and iii) interrogating the Quaternary fluvial history preserved, providing a dataset from which the climate implications could be considered in subsequent research.

7.3.1. Status of fluvial research in southwestern Africa

The database includes 603 ages from 44 publications, from 70 sites along 22 rivers. This analysis highlights the diversity of river settings that have been studied in southwestern Africa, both across river systems differentiated by catchment characteristics and at the reach scale in terms of channel confinement. A suite of sedimentary contexts have been studied, with the largest proportion of sites displaying evidence of channel (34 % sites) or slackwater (32 % sites) deposition, and a smaller proportion from overbank, interdune, and river end settings. Within the literature from this region, a particular focus has been placed on reconstructing the palaeoenvironmental history of Namibian rivers (41 sites, 26 papers), and the widest range of sedimentary contexts have been studied in this region. Following the data-quality assessment, a substantial dataset of 424 ages (70.3 % of the full dataset) was available. Across southwestern Africa, sites encompass important latitudinal and longitudinal gradients, providing a dataset for interrogation of spatial patterns of past climates. Evidence from sedimentary archives has been used to detail the fluvial responses to hydroclimate drivers, with evidence for both sustained river flow and reduced flow capacity (incorporating changes in flow occupancy and flow magnitude), characterising times of both wetter and drier climates.

7.3.2. Controls on records obtained

Analysis of the setting from which palaeoenvironmental records have been produced has been undertaken through characterisation of river typologies and consideration of the site-scale controls on archive formation and preservation. Distinct assemblages of documented sedimentary contexts attest to topographic and climatic controls. Analysis in Chapter 5 finds that channel confinement is

a strong control on both the nature and the length of the fluvial history preserved (following findings by Fryirs and Brierley, 2012; Fryirs *et al*., 2016; Grenfell and Grenfell, 2021 Lewin and Macklin, 2003; Keen-Zerbert *et al*., 2013), likely through an influence on the balance between aggradation and incision on Quaternary timescales. The longest fluvial histories by site are predominantly found in unconfined river reaches and are particularly located in the Namib region where the study of such reaches has been extensive. Sampling approaches, research aims, and legacies of research, such as a long history of interest on specific deposits (e.g. Homeb Silts, Kuiseb River, Namibia) has also influenced both the number of ages and the length of histories produced as a wider suite of sedimentary sections have been studied.

Alongside controls on archive formation, the methodologies employed to investigate and interpret fluvial sedimentary deposits influence the record obtained. The use of specific methods and independent proxies has varied across the study region and in part is determined by the type of deposit, the nature of the system studied, and the climate context for preservation. Across the dataset, a particular focus has been placed on assessments of sediment texture and architecture to determine the nature of past river flow, yet a focus on sediment composition in terms of provenance has been limited so far.

Following the compilation of this large dataset, a key aim of Chapter 5 was to undertake a data quality filtering process to obtain records accompanied by rigorous chronologies and sufficient analytical detail to allow for robust interpretation of palaeoenvironmental change. Chapter 5 uses this data to present a framework linking the types of data available to possible interpretations of the nature of fluvial change and the spatial and temporal scales that these interpretations can be applied to. Of particular importance here is the recognition that several pioneering studies interpreted fluvial change based on chronologies alone. Given the range of fluvial responses recorded in the database, independent proxies for deciphering the nature of this change are

critical. By excluding ages without this data from regional analyses, we hope to reduce artificial complexity in the dataset, and provide a dataset that is justifiably indicative of palaeoenvironmental change.

The magnitude of chronological uncertainties influences the scale at which fluvial variability can be resolved. Here, the potential to resolve individual *events*, multiyear *episodes*, or multidecadal- to centennial-scale *phases* of river flow (following Toonen *et al*., 2017) is given particular attention. Where uncertainties are small, individual flood *events* or *episodes* can be resolved, and assessments of flood magnitude can be combined with documentary or instrumental data to perform flood frequency analyses. When errors are larger, *phases* of fluvial conditions can be identified and a different type and scale of information is recorded by fluvial deposits. The recognition of this influence places limits on the questions we can ask of the available data. Recognising the precisional limitations of the chronological data is thus critical for ensuring that interpretations reached are robust.

7.3.3. Quaternary history recorded

Quality-assessed chronologies were compiled to establish the Quaternary history of southwestern Africa's rivers. The full suite of fluvial change is detailed in Figure 5.9 and discussed in detail in Chapter 5 at three key timesteps. The climate dynamics responsible for precipitation variability are discussed in Chapter 6 and below in Section 7.4.1.

During the Last Glacial Maximum (24-18 ka BP; LGM) the majority of fluvial deposits detail evidence of more persistent flow of currently ephemeral systems as a response to humid conditions relative to present. Assessment of these records in the context of flow occupancy indicate evidence of sedimentation under intermittent to perennial river flow (e.g. Hurkamp *et al*., 2011). Sustained water availability across catchments at the LGM is recorded in sedimentary archives as flow in

channelised systems, ponding in playa environments, and backfilling of tributaries. This fluvial signal is coherent across the Namib and Southern Kalahari regions, and the only documented record suggesting drier conditions at this time is in the Modder River, further east in South Africa within the wider Orange region.

During the mid Holocene (8-4 ka BP; MH), sedimentological evidence from eight river systems suggests the occurrence of sustained river flow and higher discharge events than today, but the combined fluvial record details greater regional and temporal variability than during the LGM. Conditions wetter than present are inferred from evidence of channelised systems with more intermittent (rather than ephemeral) river flow in the Namib region, evidence of fluvial deposition beyond current end points in the Namib Desert, enhanced fluvial activity inferred from palaeodischarge estimates of palaeochannels in the northern Kalahari, and high discharge in flood deposits in the Orange River. Fluvial deposition indicative of conditions drier than present is dated to the mid Holocene further north in the Khumib River, and inland in the Molopo River as aggradation of fan deposits detailing decreasing flow occurrence.

The largest proportion of ages fall in the last millennium and are predominantly obtained from slackwater flash flood deposits. These records indicate the establishment of an arid to hyper-arid climate and fluvial deposits attest to an ephemeral flow regime and occurrence of extreme flood events linked to the passage of convective systems. Quantitative discharge estimates and flood frequency analysis enable analysis of individual flood events. Comparison of flood records from the Namib region details correspondence in the timing of flood frequency variations between catchments.

7.4. Model-data comparison of southwestern African Quaternary climate

The third research objective of this thesis was **to test hypotheses of the spatial patterning of late Quaternary precipitation change using quality-assessed data from empirical palaeoarchives and palaeoclimate model simulations**. Throughout the history of research on southern African palaeoclimates, several hypotheses have been proposed, refined, and tested as new data has emerged. Model-data comparisons of southwestern African climate so far have predominantly considered the temporal evolution of palaeoclimate change through a focus on long-term, high-resolution archives (e.g. Chase *et al.* 2019; Singarayer and Burrough 2015). With the availability of quality-assessed datasets of geomorphological change, such as from rivers (Chapter 5), dunes (Thomas and Bailey, 2017), and lakes (De Cort *et al*., 2021), the spatial patterning of change can now be considered. Chapter 6 compiled a robust set of palaeodata and analysed palaeoclimate model outputs (from the Palaeoclimate Modelling Intercomparison Project; PMIP3) to test prevailing hypotheses of palaeoclimate change at the mid Holocene (MH) and Last Glacial Maximum (LGM). This analysis found evidence to support several hypotheses that propose differing controls over space. In the context of other palaeoenvironmental and palaeoclimate archives and palaeoclimate models, the utility of fluvial archives has been considered.

7.4.1. Which hypotheses are supported by the available evidence?

Spatial variability in both empirical palaeodata and modelled precipitation anomalies indicate a divergence in palaeoclimate signal between the coastal and inland parts of southwestern Africa. This patterning shows support for the hypothesis of differing controls on the tropical rainbelt over the ocean and land, and advection of the ocean signal to the coastal region (Singarayer and Burrough, 2015; Singarayer *et al*., 2017). Over land, the tropical rainbelt responds to thermodynamic controls and exhibits a latitudinal shift in seasonal extremes following insolation.

This has the effect of producing a hemispherically asymmetric precipitation response over land, explaining negative and positive precipitation anomalies in the palaeodata at the MH and LGM respectively. Over the ocean, the dynamic response of the ITCZ follows interhemispheric temperature gradients and the extension and reduction of the seasonal oscillation is controlled by heating in the winter months. Advection of this signal over the western coastal region of southern Africa produces a precipitation response in the opposite direction to inland terrestrial records, with signals in-phase with the northern hemisphere.

The tropical rainbelt response does not occur in isolation and data in Chapter 6 finds evidence to support modulation of this signal through ocean-atmosphere interactions. Following the hypothesis presented by Chase *et al*. (2019), the hydroclimate response of the coastal Namib region is found to vary in the opposite direction to Benguela upwelling (following remote controls of high latitude insolation) and local insolation. At the MH, Benguela upwelling and local insolation relative to the northern hemisphere reduced atmospheric pressure and enabled incursions of moisture to the region. Whilst Chase *et al*. (2019) focus on sites from the Namib Desert, the data presented in Chapter 6 suggests that positive precipitation anomalies extended further into the subcontinent. This likely incorporates a combination of ocean-atmosphere interactions and advection of moisture from response of the ITCZ over the ocean at the MH (Singarayer and Burrough, 2015). At the LGM, the ocean-atmosphere response holds true in the opposite direction, where Benguela upwelling and atmospheric subsidence was high, yet the coastal signal appears to be isolated to the Namib Desert, and only the hyrax midden sites studied by Chase *et al*. (2019) show this relationship.

The palaeomodel and proxy data also support the increased importance of circumpolar westerlies in the delivery of moisture in the winter months and throughout the year through tropical temperate troughs. The signal manifests as a decrease in seasonality across the region in the models and evidence of more persistent river flow and pan filling in the palaeodata, incorporating

sites that are located further south than an extent that could reflect tropical rainbelt change. At the LGM, the expansion of ice at the poles enhanced the equator-to-pole temperature gradient and increased the equatorward extent of circumpolar westerlies (Engelbrecht *et al*., 2019). Palaeoclimate interpretations have often greatly oversimplified atmospheric components associated with winter and summer derived rainfall, and this analysis supports ideas of interactions between temperate and tropical systems, bringing rainfall further inland in the winter (beyond the Winter Rainfall Zone) and in the summer months (following Engelbrecht *et al*., 2019).

7.4.2. Utility of fluvial archives

This analysis demonstrates the importance of having a wide latitudinal and longitudinal coverage of sites to interrogate the spatial patterning of precipitation response. This is particularly important for understanding controls on climate variability in southwestern Africa where differences emerge between the coastal and inland region that are difficult to differentiate from archives such as marine cores that can integrate signals from a wide source region. Here, through the inclusion of geoproxies, and in particular through the inclusion of fluvial records, an improved spatial coverage has been possible.

The compilation of palaeoproxy records and interrogation in the context of palaeoclimate model simulations enables an assessment of the consistency of interpretations from fluvial sediments amongst regional records. Challenges in reaching hydrological interpretations, both in the resolution by which we can date events and in the emergence of contradictory records and interpretations within the literature, has commonly resulted in fluvial archives being excluded from regional palaeoclimate syntheses. Analysis in Chapter 6, however, finds that when filtered for chronological data quality and the availability of supporting independent proxies (Chapter 5), fluvial records detail palaeoclimate changes coherent with spatial patterns of precipitation response across southwestern Africa.

Key examples of close correspondence in the timing and direction of precipitation anomalies between fluvial archives and other palaeoproxy records include: i) channelised river flow in the Hoarusib River (Srivastava *et al*., 2005) and conditions wetter than present inferred from the Orumana speleothem at the LGM (Railsback *et al*., 2016); ii) channelised river flow in the Huab River (Chapter 4) and wetter conditions inferred from the Vrede pollen hyrax midden record within the Huab catchment at the MH (Gil-Romera *et al*., 2006); and iii) perennial river flow in the Molopo River (Heine, 1990; Hurkamp *et al*., 2011) and pan filling through fluvial input at Branddam East Pan at the LGM (Schüller *et al*., 2018). The spatial pattern of fluvial response can be used to verify palaeoclimate model simulations. Whilst the Hoanib and Molopo records of conditions drier than present at the MH (Eitel *et al*., 2005; Ramisch *et al*., 2017) appear at odds with the dominant wetting signal found in the majority of fluvial records (Chapter 5) and palaeoproxy archives (Chapter 6), the location of these archives to the north and east appear to be indicative of a terrestrial response to the tropical rainbelt further inland. Together, these examples and an overall synthesis of palaeoproxy records have resulted in greater confidence in the conclusions that can be drawn from fluvial deposits.

7.5. Future research

This final section builds on the findings presented in this thesis to discuss future priorities for the study of fluvial sedimentary deposits as palaeoenvironmental archives. These recommendations include: i) further investigation of sedimentary archives in the Skeleton Coast, Namibia; ii) priorities for the study of southwestern African fluvial archives; and iii) implications for constructing fluvial databases of dryland Quaternary data in other regions.

7.5.1. Fluvial records from the Skeleton Coast, Namibia

Fluvial archives have been studied along the Khumib, Hoarusib, Hoanib, and Huab rivers within the Skeleton Coast region and have provided key records for corroborating spatial patterns of past

hydroclimates simulated in palaeoclimate models. Within this region, however, there is potential to re-analyse a number of these sites that were previously dated with outdated luminescence protocols. This is particularly the case for studies that identify extensive fluvially re-worked loess deposits in the headwaters of these rivers. In particular, deposits in the headwaters of the Huab have been dated by Eitel and Zoller (1996) and Eitel *et al*. (2001), but ages were either produced using outdated protocols or presented without sufficient description of stratigraphic context, so did not pass the data quality filtering criteria in Chapter 5. The chronology established from these deposits indicates deposition between 30 and 8 ka (Eitel and Zoller, 1996; Eitel *et al*., 2001), with the authors' interpretation being that fluvial incision occurred after ~ 8 ka under a climate wetter than today. This corresponds well with palaeoclimate model simulations (Chapter 6), and in particular to the Skeleton Coast valley fill record of wetter conditions from 7-5 ka (Chapter 4). Data did not pass the data quality filtering, however, and the key environmental findings from these sites are based on hiatuses within sedimentary units and could not be incorporated in the palaeoclimate model-data comparison.

The new record presented in Chapter 4 has enhanced our understanding of depositional regimes of the Huab River within this region, yet observations during fieldwork and findings from GPR data indicate that there is a more extensive record to be studied. Within the Skeleton Coast valley fill, two aspects could be explored: i) obtaining a longer record at natural exposures through digging deeper pits in the fill; and ii) coring at sites across the valley fill beyond the natural exposure. These were beyond the scope of this PhD as it was not possible to revisit the site, but these sampling approaches have the potential to reveal a longer and more complete history of sediment preservation. Evidence from nearby rivers (e.g. Khumib, Srivastava *et al*., 2004; Hoarusib, Srivastava *et al*., 2005) and the headwaters of the Huab (Eitel and Zoller, 1996; Eitel *et al*., 2001) indicate a fluvial response to climates of the LGM and prior, a record of which might be preserved in the deeper Skeleton Coast fill units.

The extensive sedimentary deposit studied in the Huab and the suite of sedimentary archives across the Skeleton Coast could also provide a setting to interrogate the number of samples that is sufficient to capture a hydroclimate history. Chronologies established from these settings could be combined with a modelling approach, similar to Bailey and Thomas (2014) for dated dune stratigraphies, to quantify how many samples is enough. This could inform future guidance on determining which sedimentary sections are worth re-visiting (e.g. in the context of considerations discussed in further detail below, Section 7.5.2). The Skeleton Coast hosts sedimentary archives in river settings ranging from confined to unconfined, and given the control that setting has on the nature and length of preserved record, analysis of these contexts would enable a consideration of the extent to which extensively dated stratigraphies are required in different settings.

7.5.2. Fluvial records from southwestern Africa

Findings from both the fluvial database (Chapter 5) and palaeoclimate model-data comparison (Chapter 6) indicate regions in which future study of fluvial sedimentary archives is important. A focus could be placed on rivers that do not yet have published records from fluvial sites (Figure 7.2A), or rivers in which fluvial deposits have been identified and studied, but that have few ages (Figure 7.2B), have poor chronological data quality (Figure 7.2C), or are without independent proxies for fluvial interpretation (Figure 7.2D). Given these opportunities, findings from Chapter 6 could be used to refine this choice of sites to key regions of debate. Through a compilation of model simulations and palaeodata, Figure 6.12 in Chapter 6 presents a hypothesis for future research to test and details the spatial coverage of both fluvial archives and other types of proxy data.

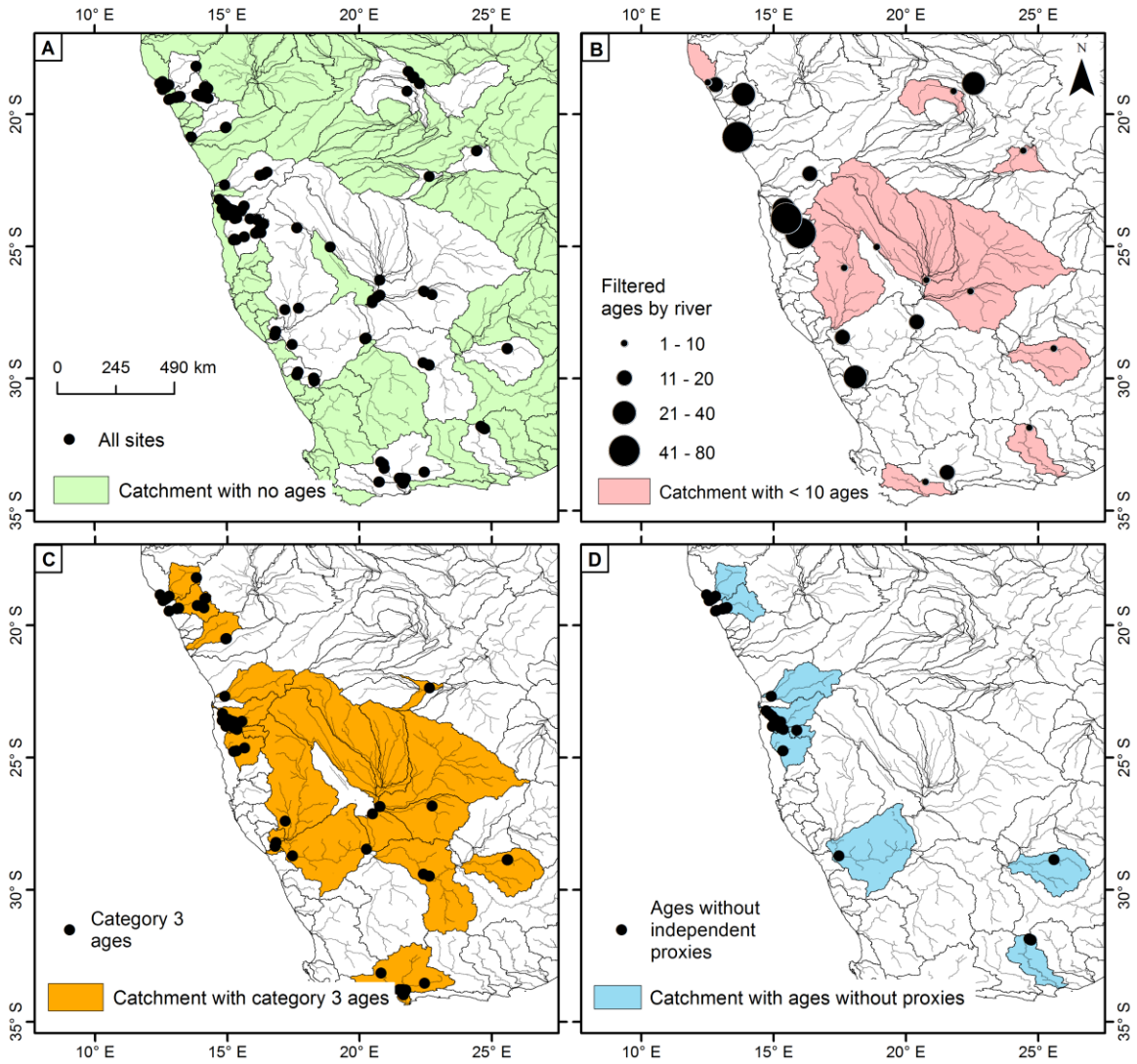

Figure 7.2. Location of sites, river courses, and river catchments within southwestern Africa, and possibilities for future foci of research. **A)** Location of all sites, catchments highlighted if they do not contain sites included in the database. **B)** Number of filtered ages by river, catchments highlighted if fewer than 10 ages are available for reconstruction of palaeoenvironmental change. **C)** Location of sites and catchments that contain ages that did not pass the chronological data quality filtering. **D)** Location of sites and catchments that contain ages were not supported by sedimentary approaches for interpretation of fluvial change. Maps B, C, and D reflect sites in which reconnaissance of sediment deposits has been undertaken and indicates that the deposits are dateable using luminescence or radiocarbon dating, and so there is potential to produce a fluvial record.

Combining the findings from Chapters 5 and 6, fluvial catchments in three key regions are identified, each with differing priorities for further study. First, northeastern Namibia is identified as a region for new fluvial sites to be studied (Figure 7.2A). Palaeoclimate model-data comparison indicates that new records from this region (both fluvial and other palaeoproxy) that span the MH and LGM are important for resolving the spatial patterning of palaeoclimate change to adequately test model simulations. Studies could investigate rivers within the Kavango, Oshikoto, Otjozondjupa, and Omaheke regions of Namibia. Dry river valleys (or megkacha) in similar systems have been studied by Shaw *et al.* (1992) and Nash *et al.* (1997, 2006), but not extensively across northeastern Namibia.

Second, river catchments in the southern Kalahari and Namibia, including the Molopo, Fish, and parts of the Orange, are also located in a region that is important for demarcating the extent of influence of the tropical rainbelt and westerly derived rainfall. These rivers host numerous sites (e.g. those studied by Heine *et al*., 1990; Shaw *et al.*, 1992; Stengel and Leser, 2004; Zawada *et al*., 2000), yet several ages were removed through chronological data quality filtering (Figure 7.2C). These category 3 ages were predominantly obtained through outdated dating protocols or had limited stratigraphic context, and so present important archives to revisit with improved dating control. Initial ages and analysis of mineralogy from sedimentary deposits along the Huns River and Fish River basin, in Appendix B begins to address this. And third, whilst Namibian ephemeral fluvial systems have been studied in the greatest detail, this is the region that hosts the greatest number of ages that are not accompanied by independent proxies for interpretation of palaeoenvironmental conditions (Figure 7.2D). These sites could be revisited with advanced methodologies to produce a more complete record (e.g. following Völkel *et al*., 2021).

The new record from the Huab River (Chapter 4) details the opportunity and importance of using robust methods to interpret palaeoflow changes. A key outcome of the data-model comparison for

southwestern Africa is that whilst it is now possible to test hypotheses of palaeoclimate change through inclusion of discontinuous geoproxy records in regional assessments, there remains a requirement for long high-quality datasets (e.g. similar to the record from the Modder site, Lyons *et al*., 2014) to further understand mechanisms of hydroclimate change. New records must be accompanied by reliable chronologies and detailed interrogation of the climate setting (e.g. following Tooth *et al*., 2022; Walsh *et al*., 2022). The link between archives of sediment deposition and the climate conditions responsible for fluvial response has typically been difficult to pin down, yet is further complicated when analyses of sedimentary contexts are limited. Figure 5.8 in Chapter 5 considers the links between methods used and proxies analysed and possible interpretations that can be reached, and this could be used as a framework in the decision-making process for establishing robust methods relevant to the aims of new research. Given these considerations and those in Figure 7.2, it may therefore be appropriate to revisit, resample, and reinterpret existing fluvial sites in the light of recent research, both in terms of the methods available and in the context of the potential to reconstruct a suite of scales of palaeoclimate change.

7.5.3. Database of fluvial archives in other dryland regions

Database approaches have been employed to study geomorphological features such as dunes (Lancaster *et al*., 2016) and lakes (De Cort *et al*., 2021) globally and regionally. Whilst the study of fluvial archives beyond southwestern Africa was beyond the scope of this thesis, the database approach could be used to interrogate the controls and fluvial histories preserved in other dryland settings. Chapter 5 presents a database framework that would enable consistency in data reporting and facilitate analysis of factors that influence the interpretation reached. Variability exists both within and between drylands (Tooth and Nanson, 2011) and an analysis of fluvial chronologies through a database approach would enable these differences to be better understood. Regions to focus on could include the eastern portion of southern Africa (e.g. incorporating literature: Grenfell *et al*., 2010; Keen-Zerbert *et al.*, 2013; Tooth *et al*., 2014) and a focus on the extensive fluvial

literature in the drylands of Australia (e.g. Cohen *et al*., 2010; Hesse *et al*., 2018; Mueller *et al*., 2018), Mediterranean (e.g. Benito et al., 2003, 2010), or USA (e.g. Hereford, 2002; Rittenour *et al*., 2003; Scherler *et al*., 2016). Sufficient records exist from these regions to allow for detailed investigations within each region, and a wider global comparison. This thesis highlights both the complexity and utility of southwestern Africa's fluvial archives as records of palaeoenvironmental change, and encourages the study of Quaternary fluvial archives in other dryland settings. Finding a way to make databases dynamic, such as has been done for the palaeoflood records compiled by the Flood Working Group of PAGES (Past Global Changes), would enable data to be continually added so that the database remains up to date.

References

Abe-Ouchi, A., Saito, F., Kageyama, M., Braconnot, P., Harrison, S.P., Lambeck, K., Otto-Bliesner, B.L., Peltier, W.R., Tarasov, L., Peterschmitt, J.Y. and Takahashi, K. 2015. Ice-sheet configuration in the CMIP5/PMIP3 Last Glacial Maximum experiments. *Geoscientific Model Development*, 8 (11): 3621–3637, https://doi.org/10.5194/gmd-8-3621-2015.

Adeleye, M.A., Connor, S.E. and Haberle, S.G. 2021. A quantitative synthesis of Holocene vegetation change in Nigeria (Western Africa). *The Holocene*, 31 (11–12): 1681–1689, https://doi.org/10.1177/09596836211033198.

Aitken, M.J. 1985. *Thermoluminescence Dating*. London, Academic Press Inc.

Aitken, M.J. 1998. *An Introduction to Optical Dating*. Oxford University Press.

Allen, P.A. 2017. *Sediment Routing Systems: the Fate of Sediment from Source to Sink*. Cambridge: Cambridge University Press.

Allen, P.A. 2008. From landscapes into geological history. *Nature*, 451 (7176): 274–276, https://doi.org/10.1038/nature06586.

Alnedeij, J. and Diplas, P. 2005. Bedload sediment transport in ephemeral and perennial gravel bed streams. *Transactions of the American Geophysical Union*, 86: 429–434, https://doi.org/https://doi.org/10.1029/2005EO440002.

Andò, S. 2020. Gravimetric separation of heavy minerals in sediments and rocks. *Minerals*, 10 (3), https://doi.org/10.3390/min10030273.

Ando, S. and Garzanti, E. 2014. Raman spectroscopy in heavy-mineral studies. *Geological Society, London, Special Publications*, 386: 395–412, https://doi.org/http://dx.doi.org/10.1144/SP386.2.

Annan, A.P. 2009. Chapter 1 - Electromagnetic principles of ground penetrating radar. In Jol, H. (Ed), Ground Penetrating Radar Theory and Applications, pp. 3–40. Elsevier, https://doi.org/https://doi.org/10.1016/B978-0-444-53348-7.00001-6.

Arbuszewski, J.A., Demenocal, P.B., Cléroux, C., Bradtmiller, L. and Mix, A. 2013. Meridional shifts of the Atlantic intertropical convergence zone since the Last Glacial Maximum. *Nature Geoscience*, 6 (11): 959–962, https://doi.org/10.1038/ngeo1961.

Arnold, L.J., Demuro, M. and Ruiz, M.N. 2012. Empirical insights into multi-grain averaging effects from “pseudo” single-grain OSL measurements. *Radiation Measurements*, 47 (9): 652–658, https://doi.org/10.1016/j.radmeas.2012.02.005.

Arnold, L.J., Roberts, R.G., Galbraith, R.F. and Delong, S.B. 2009. Quaternary Geochronology A revised burial dose estimation procedure for optical dating of young and modern-age sediments. *Quaternary Geochronology*, 4 (4): 306–325, https://doi.org/10.1016/j.quageo.2009.02.017.

Arribas, J. and Tortosa, A. 2003. Detrital modes in sedimenticlastic sands from low-order streams in the

Iberian Range, Spain: The potential for sand generation by different sedimentary rocks. *Sedimentary Geology*, 3–4: 275–303, https://doi.org/10.1016/S0037-0738(02)00332-9.

Asselman, N.E.M. and Middelkoop, H. 1995. Floodplain sedimentation: quantities, patterns and processes. *Earth Surface Processes and Landforms*, 20 (6): 481–499, https://doi.org/10.1002/esp.3290200602.

Bailey, R.M. 2001. Towards a general kinetic model for optically and thermally stimulated luminescence of quartz. *Radiation Measurements*, 33 (1): 17–45, https://doi.org/10.1016/S1350-4487(00)00100-1.

Bailey, R.M. and Thomas, D.S.G. 2014. A quantitative approach to understanding dated dune stratigraphies. *Earth Surface Processes and Landforms*, 39 (5): 614–631, https://doi.org/10.1002/esp.3471.

Baker, G.S., Jordan, T.E. and Pardy, J. 2007. An introduction to ground penetrating radar (GPR). *The Geological Society of America Special Paper*, 432: 1–18, https://doi.org/10.1130/2007.2432(01)..

Baker, V.R. 1987. Paleoflood hydrology and extraordinary flood events. *Journal of Hydrology*, 96 (1–4): 79–99, https://doi.org/10.1016/0022-1694(87)90145-4.

Baker, V.R. 2008. Paleoflood hydrology: origin, progress, prospects. *Geomorphology*, 101 (1–2): 1–13, https://doi.org/10.1016/j.geomorph.2008.05.016.

Bao, Q., Lin, P., Zhou, T., Liu, Y., Yu, Y., Wu, G., He, B., He, J., Li, L., Li, J., Li, Y., Liu, H., Qiao, F., Song, Z., Wang, B., Wang, J., Wang, P., Wang, X., Wang, Z., Wu, B., Wu, T., Xu, Y., Yu, H., Zhao, W., Zheng, W. and Zhou, L. 2013. The Flexible Global Ocean-Atmosphere-Land system model, Spectral Version 2: FGOALS-s2. *Advances in Atmospheric Sciences*, 30 (3): 561–576, https://doi.org/10.1007/s00376-012-2113-9.

Barker, P. and Gasse, F. 2003. New evidence for a reduced water balance in East Africa during the Last Glacial Maximum: Implication for model-data comparison. *Quaternary Science Reviews*, 22 (8–9): 823–837, https://doi.org/10.1016/S0277-3791(03)00010-6.

Bartlein, P.J., Harrison, S.P., Brewer, S., Connor, S., Davis, B.A.S., Gajewski, K., Guiot, J., Harrison-Prentice, T.I., Henderson, A., Peyron, O., Prentice, I.C., Scholze, M., Seppä, H., Shuman, B., Sugita, S., Thompson, R.S., Viau, A.E., Williams, J. and Wu, H. 2011. Pollen-based continental climate reconstructions at 6 and 21 ka: A global synthesis. *Climate Dynamics*, 37 (3): 775–802, https://doi.org/10.1007/s00382-010-0904-1.

Bateman, M.D., Bryant, R.G., Foster, I.D.L., Livingstone, I. and Parsons, A.J. 2012. On the formation of sand ramps: A case study from the Mojave Desert. *Geomorphology*, 161–162: 93–109, https://doi.org/10.1016/j.geomorph.2012.04.004.

Bateman, M.D., Frederick, C.D., Jaiswal, M.K. and Singhvi, A.K. 2003. Investigations into the potential

effects of pedoturbation on luminescence dating. *Quaternary Science Reviews*, 22 (10–13): 1169–1176, https://doi.org/10.1016/S0277-3791(03)00019-2.

Bateman, M.D., Thomas, D.S.G. and Singhvi, A.K. 2003. Extending the aridity record of the Southwest Kalahari: Current problems and future perspectives. *Quaternary International*, 111 (1): 37–49, https://doi.org/10.1016/S1040-6182(03)00013-2.

Bell, W.T. 1979. Thermoluminescence dating: Radiation dose-rate data 2: 243–245.

Belnap, J. 2006. The potential roles of biological soil crusts in dryland hydrological cycles. *Hydrological Processes*, 20: 3159–3178, https://doi.org/10.1002/hyp.6325.

Belz, L., Schüller, I., Wehrmann, A., Köster, J. and Wilkes, H. 2020. The leaf wax biomarker record of a Namibian salt pan reveals enhanced summer rainfall during the Last Glacial-Interglacial Transition. *Palaeogeography, Palaeoclimatology, Palaeoecology*, 543: 109561, https://doi.org/10.1016/j.palaeo.2019.109561.

Bengtsson, L. and Enell, M. 1986. Chemical analysis. In Berglund, B. (Ed), Handbook of Holocene Palaeoecology and Palaeohydrology, pp. 423–445. Wiley, Chichester.

Benito, G., Botero, B.A., Thorndycraft, V.R., Rico, M., Sánchez-Moya, Y., Sopeña, A., MacHado, M.J. and Dahan, O. 2010. Rainfall-runoff modelling and palaeoflood hydrology applied to reconstruct centennial scale records of flooding and aquifer recharge in ungauged ephemeral rivers. *Hydrology and Earth System Sciences*, 15 (4): 1185–1196, https://doi.org/10.5194/hess-15-1185-2011.

Benito, G., Harden, T. and O'Connor, J. 2020. Quantitative Paleoflood Hydrology. In Reference Module in Earth Systems and Environmental Sciences.

Benito, G., Sánchez-Moya, Y. and Sopena, A. 2003. Sedimentology of high-stage flood deposits of the Tagus River, Central Spain. *Sedimentary Geology*, 157 (1–2): 107–132, https://doi.org/10.1016/S0037-0738(02)00196-3.

Benito, G., Thorndycraft, V.R., Rico, M.T., Sánchez-Moya, Y., Sopeña, A., Botero, B.A., Machado, M.J., Davis, M. and Pérez-González, A. 2011. Hydrological response of a dryland ephemeral river to southern African climatic variability during the last millennium. *Quaternary Research*, 75 (3): 471–482, https://doi.org/10.1016/j.yqres.2011.01.004.

Berger, G.W. 1990. Effectivenes of Natural Zeroing of the Thermoluminescence in Sediments. *Journal of Geophysical Research*, 95: 12375–12397.

Berman, S., Boyko, V., Clancy, V., Lam, J., Maxwell, P., McLaren, J., Methven, B., Brophy, C., Sturgeon, R., Willie, S. and Yang, L. 1997. HISS-1: Marine Sediment Reference Material for Trace Metals and other Constituents. https://doi.org/10.4224/crm.1997.hiss-1.

Blair, T. and McPherson, J. 1994. Alluvial fan processes and forms. In Abrahams, A. and Parsons, A. (Eds), Geomorphology of Desert Environments, pp. 354–402. Chapman and Hall, London.

Blott, S.J. and Pye, K. 2001. Gradistat: A grain size distribution and statistics package for the analysis of unconsolidated sediments. *Earth Surface Processes and Landforms*, 26 (11): 1237–1248, https://doi.org/10.1002/esp.261.

Bordy, E.M., Bowen, D.A., Moore, J., Garnett, M.H. and Tsikos, H. 2018. A Holocene "Frozen Accident": Sediments of Extreme Paleofloods and Fires in the Bedrock-Confined Upper Huis River, Western Cape, South Africa. *Journal of Sedimentary Research*, 88 (6): 696–716, https://doi.org/10.2110/jsr.2018.29.

Bourke, M.C., Child, A. and Stokes, S. 2003. Optical age estimates for hyper-arid fluvial deposits at Homeb, Namibia. *Quaternary Science Reviews*, 22 (10–13): 1099–1103, https://doi.org/10.1016/S0277-3791(03)00085-4.

Bowman, S. 2019. *Principles of Alluvial Fan Morphology*. Springer, Dordrecht.

Braconnot, P., Harrison, S., Otto-Bliesner, B., Abe-Ouchi, A., Jungclaus, J. and Peterschmitt, J.Y. 2011. The Paleoclimate Modeling Intercomparison Project contribution to CMIP5. *CLIVAR Exchanges No. 56*, 16 (2): 15–19.

Braconnot, P., Harrison, S.P., Kageyama, M., Bartlein, P.J., Masson-Delmotte, V., Abe-Ouchi, A., Otto-Bliesner, B. and Zhao, Y. 2012. Evaluation of climate models using palaeoclimatic data. *Nature Climate Change*, 2 (6): 417–424, https://doi.org/10.1038/nclimate1456.

Braconnot, P., Otto-Bliesner, B., Harrison, S., Joussaume, S., Peterchmitt, J.Y., Abe-Ouchi, A., Crucifix, M., Driesschaert, E., Fichefet, T., Hewitt, C.D., Kageyama, M., Kitoh, A., Laîné, A., Loutre, M.F., Marti, O., Merkel, U., Ramstein, G., Valdes, P., Weber, S.L., Yu, Y. and Zhao, Y. 2007. Results of PMIP2 coupled simulations of the Mid-Holocene and last glacial maximum - Part 1: Experiments and large-scale features. *Climate of the Past*, 3 (2): 261–277, https://doi.org/10.5194/cp-3-261-2007.

Bridgland, D.R. and Westaway, R. 2014. *Quaternary fluvial archives and landscape evolution: A global synthesis*. *Proceedings of the Geologists' Association* 5–6: 600–629, https://doi.org/10.1016/j.pgeola.2014.10.009.

Brink, J.S., Herries, A.I.R., Moggi-Cecchi, J., Gowlett, J.A.J., Bousman, C.B., Hancox, J.P., Grün, R., Eisenmann, V., Adams, J.W. and Rossouw, L. 2012. First hominine remains from a ~1.0 million year old bone bed at Cornelia-Uitzoek, Free State Province, South Africa. *Journal of Human Evolution*, 63 (3): 527–535, https://doi.org/10.1016/j.jhevol.2012.06.004.

Bristow, C.S., Balley, S.D. and Lancaster, N. 2000. *The sedimentary structure of linear sand dunes*. *Nature*, 6791: 56–59, 2000, https://doi.org/10.1038/35017536.

Bristow, C.S., Duller, G.A.T. and Lancaster, N. 2007. Age and dynamics of linear dunes in the Namib Desert. *Geology*, 35 (6): 555–558, https://doi.org/10.1130/G23369A.1.

Bristow, C.S. and Jol, H.M. 2003. An introduction to ground penetrating radar in sediments. *Ground*

Penetrating Radar in Sediments, 2432 (1): 211, https://doi.org/10.1130/2007.2432(01)..

Bristow, C.S., Lancaster, N. and Duller, G.A.T. 2005. Combining ground penetrating radar surveys and optical dating to determine dune migration in Namibia. *Journal of the Geological Society*, 162 (2): 315–321, https://doi.org/10.1144/0016-764903-120.

Broccoli, A.J., Dahl, K.A. and Stouffer, R.J. 2006. Response of the ITCZ to Northern Hemisphere cooling. *Geophysical Research Letters*, 33 (1): 1–4, https://doi.org/10.1029/2005GL024546.

Bronk Ramsey, C. 2021. OxCal. v 4.4.4. *Https://c14.arch.ox.ac.uk/oxcal.html*.

Bronk Ramsey, C., Dee, M., Lee, S., Nakagawa, T. and Staff, R. 2010. Developments in the calibration and modelling of radiocarbon dates. *Radiocarbon*, 52 (3): 953–961.

Brook, G.A., Cherkinsky, A., Railsback, L.B., Marais, E. and Hipondoka, M.H.T. 2013. ^{14}C dating of organic residue and carbonate from stromatolites in ages and evidence of > 8m deep lake during the late Pleistocene. *Radiocarbon*, 55 (2): 1156–1163, https://doi.org/10.2458/azu_js_rc.55.16401.

Brook, G.A., Marais, E. and Cowart, J.B. 1999. Evidence of wetter and drier conditions in Namibia from tufas and submerged cave speleothems. *Cimbebasia*, 15: 29–39.

Brook, G.A., Marais, E., Srivastava, P. and Jordan, T. 2007. Timing of lake-level changes in Etosha Pan, Namibia, since the middle Holocene from OSL ages of relict shorelines in the Okondeka region. *Quaternary International*, 175 (1): 29–40, https://doi.org/10.1016/j.quaint.2007.05.020.

Brook, G.A., Railsback, L.B. and Marais, E. 2011. Reassessment of carbonate ages by dating both carbonate and organic material from an Etosha Pan (Namibia) stromatolite: Evidence of humid phases during the last 20ka. *Quaternary International*, 229 (1–2): 24–37, https://doi.org/10.1016/j.quaint.2010.05.009.

Brook, G.A., Srivastava, P. and Marais, E. 2006. Characteristics and OSL minimum ages of relict fluvial deposits near Sossus Vlei, Tsauchab River, Namibia, and a regional climate record for the last 30 ka. *Journal of Quaternary Science*, 21 (4): 347–362, https://doi.org/10.1002/jqs.977.

Brunotte, E., Maurer, B., Fischer, P., Lomax, J. and Sander, H. 2009. A sequence of fluvial and aeolian deposits (desert loess) and palaeosoils covering the last 60 ka in the Opuwo basin (Kaokoland/Kunene Region, Namibia) based on luminescence dating. *Quaternary International*, 196 (1–2): 71–85, https://doi.org/10.1016/j.quaint.2008.06.008.

Bubenzer, O., Bodecker, O. and Besler, H. 2007. A transcontinental comparison between the southern Namib Erg (Namibia) and the southern Great Sand Sea (Egypt). *Zentralblatt für Geologie und Paläontologie Teil*, *1* 1 (4): 7–23.

Buch, M. and Zoller, L. 1992. Pedostratigraphy and thermoluminescence-chronology of the western margin- (lunette-) dunes of Etosha Pan/Northern Namibia. *Würzburger Geographische Arbeiten*, 84: 361–384.

Bull, L. and Kirkby, M. 2002. Dryland River Characteristics and Concepts. In Bull, L. and Kirkby, M. (Eds), Dryland Rivers: Hydrology and Geomorphology of Semi-Arid Channels, Chichester: Wiley.

Bull, L.J., Kirkby, M.J., Shannon, J. and Hooke, J.M. 1999. The impact of rainstorms on floods in ephemeral channels in southeast Spain. *Catena* 38 (3): 191–209, https://doi.org/10.1016/S0341-8162(99)00071-5.

Bull, W. 1991. *Geomorphic Responses to Climatic Change*. Oxford University Press, New York.

Bullard, J.E., McTainsh, G.H. and Pudmenzky, C. 2004. Aeolian abrasion and modes of fine particle production from natural red dune sands: An experimental study. *Sedimentology*, 51 (5): 1103–1125, https://doi.org/10.1111/j.1365-3091.2004.00662.x.

Burger, A., Clifford, T. and Miller, R. 1976. Zircon U-Pb ages of the Franzfontein granitic suite, northern South West Africa. *Precambrian Research*, 3: 415–31.

Burow, C. 2020. calc_AliquotSize(): Estimate the amount of grains on an aliquot. Function version 0.31. In Kreutzer, S., Burow, C., Dietze, M., Fuchs, M.C., Schmidt, C., Fischer, M., Friedrich, J., Riedesel, S., Autzen, M. and Mittelstrass, D. (Eds), Luminescence: Comprehensive Luminescence Dating Data Analysis. R package version 0.9.10. https://CRAN.R-project.org/package=Luminescence.

Burrough, S.L. and Thomas, D.S.G. 2013. Central southern Africa at the time of the African Humid Period: A new analysis of Holocene palaeoenvironmental and palaeoclimate data. *Quaternary Science Reviews*, 80: 29–46, https://doi.org/10.1016/j.quascirev.2013.08.001.

Burrough, S.L., Thomas, D.S.G., Shaw, P.A. and Bailey, R.M. 2007. Multiphase Quaternary highstands at Lake Ngami, Kalahari, northern Botswana. *Palaeogeography, Palaeoclimatology, Palaeoecology*, 3–4: 280–299, https://doi.org/10.1016/j.palaeo.2007.06.010.

Burrough, S.L., Thomas, D.S.G. and Singarayer, J.S. 2009. Late Quaternary hydrological dynamics in the Middle Kalahari: Forcing and feedbacks. *Earth-Science Reviews*, 96 (4): 313–326, https://doi.org/10.1016/j.earscirev.2009.07.001.

Burt, T. and Allison, R. 2010. Sediment cascades. In Burt, T. and Allison, R. (Eds), Sediment Cascades in the Environment: An Integrated Approach, pp. 1–15. John Wiley & Sons.

Busch, M.H., Costigan, K.H., Fritz, K.M., Datry, T., Krabbenhoft, C.A., Hammond, J.C., Zimmer, M., Olden, J.D., Rocha, M.P., Godsey, S., Allen, G.H. and Blaszczak, J.R. 2020. Defining Non-Perennial Rivers and Streams. *Water*, 1–19.

Buylaert, J.P., Vandenberghe, D., Murray, A.S., Huot, S., De Corte, F. and Van den Haute, P. 2007. Luminescence dating of old (>70 ka) Chinese loess: A comparison of single-aliquot OSL and IRSL techniques. *Quaternary Geochronology*, 2 (1–4): 9–14, https://doi.org/10.1016/j.quageo.2006.05.028.

Caracciolo, L. 2020. Sediment generation and sediment routing systems from a quantitative provenance

analysis perspective: Review, application and future development. *Earth-Science Reviews*, 209: 103226, https://doi.org/10.1016/j.earscirev.2020.103226.

Caracciolo, L., Chew, D. and Andò, S. 2020. Sediment Generation and Sediment Routing Systems. *Earth-Science Reviews*, 207: 103221, https://doi.org/10.1016/j.earscirev.2020.103221.

Caracciolo, L., Von Eynatten, H., Tolosana-Delgado, R., Critelli, S., Manetti, P. and Marchev, P. 2012. Petrological, geochemical, and statistical analysis of eocene-oligocene sandstones of the western Thrace basin, Greece and Bulgaria. *Journal of Sedimentary Research*, 82 (7): 482–498, https://doi.org/10.2110/jsr.2012.31.

Cassidy, N. 2009. Chapter 2 - Electrical and Magnetic Properties of Rocks, Soils and Fluids. In Jol, H. (Ed), Ground Penetrating Radar Theory and Applications, pp. 41–72. Elsevier, https://doi.org/https://doi.org/10.1016/B978-0-444-53348-7.00002-8..

Chase, B.M. 2021. Orbital forcing in southern Africa: Towards a conceptual model for predicting deep time environmental change from an incomplete proxy record. *Quaternary Science Reviews*, 265: 107050, https://doi.org/10.1016/j.quascirev.2021.107050.

Chase, B.M., Boom, A., Carr, A.S., Carré, M., Chevalier, M., Meadows, M.E., Pedro, J.B., Stager, J.C. and Reimer, P.J. 2015. Evolving southwest African response to abrupt deglacial North Atlantic climate change events. *Quaternary Science Reviews*, 121: 132–136, https://doi.org/10.1016/j.quascirev.2015.05.023.

Chase, B.M., Chevalier, M., Boom, A. and Carr, A.S. 2017. The dynamic relationship between temperate and tropical circulation systems across South Africa since the last glacial maximum. *Quaternary Science Reviews*, 174: 54–62, https://doi.org/10.1016/j.quascirev.2017.08.011.

Chase, B.M. and Meadows, M.E. 2007. Late Quaternary dynamics of southern Africa's winter rainfall zone. *Earth-Science Reviews*, 84 (3–4): 103–138, https://doi.org/10.1016/j.earscirev.2007.06.002.

Chase, B.M., Meadows, M.E., Carr, A.S. and Reimer, P.J. 2010. Evidence for progressive Holocene aridification in southern Africa recorded in Namibian hyrax middens: Implications for African Monsoon dynamics and the "'African Humid Period.'" *Quaternary Research*, 74 (1): 36–45, https://doi.org/10.1016/j.yqres.2010.04.006.

Chase, B.M., Meadows, M.E., Scott, L., Thomas, D.S.G., Marais, E., Sealy, J. and Reimer, P.J. 2009. A record of rapid Holocene climate change preserved in hyrax middens from southwestern Africa. *Geology*, 37 (8): 703–706, https://doi.org/10.1130/G30053A.1.

Chase, B.M., Niedermeyer, E.M., Boom, A., Carr, A.S., Chevalier, M., He, F., Meadows, M., Ogle, N. and Reimer, P.J. 2019. Orbital controls on Namib Desert hydroclimate over the past 50,000 years 47: 867–871, https://doi.org/https:// doi .org /10 .1130 /G46334.1.

Chase, B.M., Scott, L., Meadows, M.E., Gil-Romera, G., Boom, A., Carr, A.S., Reimer, P.J., Truc, L.,

Valsecchi, V. and Quick, L.J. 2012. Rock hyrax middens: A palaeoenvironmental archive for southern African drylands. *Quaternary Science Reviews*, 56: 107–125, https://doi.org/10.1016/j.quascirev.2012.08.018.

Chevalier, M., Brewer, S. and Chase, B.M. 2017. Qualitative assessment of PMIP3 rainfall simulations across the eastern African monsoon domains during the mid-Holocene and the Last Glacial Maximum. *Quaternary Science Reviews*, 156: 107–120, https://doi.org/10.1016/j.quascirev.2016.11.028.

Chevalier, M., Chase, B., Quick, L. and Scott, L. 2021. An atlas of southern African pollen types and their climatic affinities. In Quaternary Vegetation Dynamics, pp. 239–258. CRC Press, doi: 10.1201/9781003162766-15.

Chevalier, M. and Chase, B.M. 2015. Southeast African records reveal a coherent shift from high- to low-latitude forcing mechanisms along the east African margin across last glacial-interglacial transition. *Quaternary Science Reviews*, 125: 117–130, https://doi.org/10.1016/j.quascirev.2015.07.009.

Chew, D., O'Sullivan, G., Caracciolo, L., Mark, C. and Tyrrell, S. 2020. Sourcing the sand: Accessory mineral fertility, analytical and other biases in detrital U-Pb provenance analysis. *Earth-Science Reviews*, 202: 103093, https://doi.org/10.1016/j.earscirev.2020.103093.

Churchill, S.E., Brink, J.S., Berger, L.R., Hutchison, R.A., Rossouw, L., Stynder, D., Hancox, P.J., Brandt, D., Woodborne, S., Loock, J.C., Scott, L. and Ungar, P. 2000. Erfkroon: A new Florisian fossil locality from fluvial contexts in the western Free State, South Africa. *South African Journal of Science*, 96 (4): 161–163.

Clark, P.U. and Mix, A.C. 2002. Ice sheets and sea level of the Last Glacial Maximum. *Quaternary Science Reviews*, 21 (1–3): 1–7, https://doi.org/10.1016/S0277-3791(01)00118-4.

Cleary, W.J. and Conolly, J.R. 1972. Embayed quartz grains in soils and their significance. *Journal of Sedimentary Research*, 42 (4): 899–904, https://doi.org/10.1306/74d7266c-2b21-11d7-8648000102c1865d.

Clement, A.C., Hall, A. and Broccoli, A.J. 2004. The importance of precessional signals in the tropical climate. *Climate Dynamics*, 22 (4): 327–341, https://doi.org/10.1007/s00382-003-0375-8.

Clifford, T.N., Rooke, J.M. and Allsopp, H.L. 1969. Petrochemistry and age of the Franzfontein granitic rocks of northern South-West Africa. *Geochimica et Cosmochimica Acta*, 33 (8): 973–986, https://doi.org/10.1016/0016-7037(69)90107-0.

Cloete, G., Benito, G., Grodek, T., Porat, N. and Enzel, Y. 2018. Analyses of the magnitude and frequency of a 400-year flood record in the Fish River Basin, Namibia. *Geomorphology*, 320: 1–17, https://doi.org/10.1016/j.geomorph.2018.07.025.

Cockroft, M., Wilkinson, M. and Tyson, D. 1987. The application fo a present-day climatic model to the

late Quaternary of southern Africa. *Climate Change*, 10: 161–181.

Cohen, T.J., Nanson, G.C., Larsen, J.R., Jones, B.G., Price, D.M., Coleman, M. and Pietsch, T.J. 2010. Late Quaternary aeolian and fluvial interactions on the Cooper Creek Fan and the association between linear and source-bordering dunes, Strzelecki Desert, Australia. *Quaternary Science Reviews*, 29 (3–4): 455–471, https://doi.org/10.1016/j.quascirev.2009.09.024.

Colarossi, D., Duller, G.A.T., Roberts, H.M., Tooth, S. and Botha, G.A. 2020. A comparison of multiple luminescence chronometers at Voordrag, South Africa. *Quaternary Geochronology*, 60: 101094, https://doi.org/10.1016/j.quageo.2020.101094.

Collins, J.A., Schefuß, E., Govin, A., Mulitza, S. and Tiedemann, R. 2014. Insolation and glacial-interglacial control on southwestern African hydroclimate over the past 140000 years. *Earth and Planetary Science Letters*, 398: 1–10, https://doi.org/10.1016/j.epsl.2014.04.034.

Collins, J.A., Schefuß, E., Heslop, D., Mulitza, S., Prange, M., Zabel, M., Tjallingii, R., Dokken, T.M., Huang, E., MacKensen, A., Schulz, M., Tian, J., Zarriess, M. and Wefer, G. 2011. Interhemispheric symmetry of the tropical African rainbelt over the past 23,000 years. *Nature Geoscience*, 4 (1): 42–45, https://doi.org/10.1038/ngeo1039.

Collins, J.A., Schefuß, E., Mulitza, S., Prange, M., Werner, M., Tharammal, T., Paul, A. and Wefer, G. 2013. Estimating the hydrogen isotopic composition of past precipitation using leaf-waxes from western Africa. *Quaternary Science Reviews*, 65: 88–101, https://doi.org/10.1016/j.quascirev.2013.01.007.

Collins, W.J., Bellouin, N., Doutriaux-Boucher, M., Gedney, N., Halloran, P., Hinton, T., Hughes, J., Jones, C.D., Joshi, M., Liddicoat, S., Martin, G., O'Connor, F., Rae, J., Senior, C., Sitch, S., Totterdell, I., Wiltshire, A. and Woodward, S. 2011. Development and evaluation of an Earth-System model - HadGEM2. *Geoscientific Model Development*, 4 (4): 1051–1075, https://doi.org/10.5194/gmd-4-1051-2011.

Cook, B.I., Smerdon, J.E., Seager, R. and Coats, S. 2014. Global warming and 21st century drying. *Climate Dynamics*, 43 (9–10): 2607–2627, https://doi.org/10.1007/s00382-014-2075-y.

Cook, C., Reason, C.J.C. and Hewitson, B.C. 2004. Wet and dry spells within particularly wet and dry summers in the South African summer rainfall region. *Climate Research*, 26 (1): 17–31, https://doi.org/10.3354/cr026017.

Cordova, C.E., Scott, L., Chase, B.M. and Chevalier, M. 2017. Late Pleistocene-Holocene vegetation and climate change in the Middle Kalahari, Lake Ngami, Botswana. *Quaternary Science Reviews*, 171: 199–215, https://doi.org/10.1016/j.quascirev.2017.06.036.

De Cort, G., Chevalier, M., Burrough, S.L., Chen, C.Y. and Harrison, S.P. 2021. An uncertainty-focused database approach to extract spatiotemporal trends from qualitative and discontinuous lake-status histories. *Quaternary Science Reviews*, 258: 106870,

https://doi.org/10.1016/j.quascirev.2021.106870.

Costa, A.C., Bronstert, A. and De Araújo, J.C. 2012. A channel transmission losses model for different dryland rivers. *Hydrology and Earth System Sciences*, 16 (4): 1111–1135, https://doi.org/10.5194/hess-16-1111-2012.

Coulthard, T.J., Lewin, J. and Macklin, M.G. 2005. Modelling differential catchment response to environmental change. *Geomorphology*, 69 (1–4): 222–241, https://doi.org/10.1016/j.geomorph.2005.01.008.

Coulthard, T.J., Lewin, J. and Macklin, M.G. 2008. Non-stationarity of basin scale sediment delivery in response to climate change. In Habersack, H., Piegay, H. and Rinaldi, M. (Eds), Gravel-bed rivers VI: from process understanding to river restoration, pp. 315–331. Amsterdam, The Netherlands: Elsevier.

Coward, M.P. 1981. The junction between Pan African mobile belts in Namibia: Its structural history. *Tectonophysics*, 76 (1–2): 59–73, https://doi.org/10.1016/0040-1951(81)90253-5.

Craigie, N.S. 2018. *Principles of elemental chemostratigraphy*. Cham: Springer International Publishing.

Crétat, J., Pohl, B., Dieppois, B., Berthou, S. and Pergaud, J. 2019. The Angola Low: relationship with southern African rainfall and ENSO. *Climate Dynamics*, 52 (3–4): 1783–1803, https://doi.org/10.1007/s00382-018-4222-3.

Crétat, J., Richard, Y., Pohl, B., Rouault, M., Reason, C. and Fauchereau, N. 2012. Recurrent daily rainfall patterns over South Africa and associated dynamics during the core of the austral summer. *International Journal of Climatology*, 32 (2): 261–273, https://doi.org/10.1002/joc.2266.

Cunningham, A.C. and Wallinga, J. 2012. Realizing the potential of fluvial archives using robust OSL chronologies. *Quaternary Geochronology*, 12: 98–106, https://doi.org/10.1016/j.quageo.2012.05.007.

D'Odorico, P., Bhattachan, A., Davis, K.F., Ravi, S. and Runyan, C.W. 2013. Global desertification: Drivers and feedbacks. *Advances in Water Resources*, 51: 326–344, https://doi.org/10.1016/j.advwatres.2012.01.013.

Dahan, O., Tatarsky, B., Enzel, Y., Kulls, C., Seely, M. and Benito, G. 2008. Dynamics of flood water infiltration and ground water recharge in hyperarid desert. *Ground Water*, 46 (3): 450–461, https://doi.org/10.1111/j.1745-6584.2007.00414.x.

Dallmeyer, A., Claussen, M., Lorenz, S. and Shanahan, T. 2020. The end of the African humid period as seen by a transient comprehensive Earth system model simulation of the last 8000 years. *Climate of the Past Discussions*, 16: 117–140, https://doi.org/10.5194/cp-2019-86.

Damm, B. and Hagedorn, J. 2010. Holocene floodplain formation in the southern Cape region, South Africa. *Geomorphology*, 122 (3–4): 213–222, https://doi.org/10.1016/j.geomorph.2009.06.025.

Daniels, J.M. 2003. Floodplain aggradation and pedogenesis in a semiarid environment. *Geomorphology*, 56 (3–4): 225–242, https://doi.org/10.1016/S0169-555X(03)00153-3.

Dansie, A.P., Thomas, D.S.G., Wiggs, G.F.S. and Munkittrick, K.R. 2018. Spatial variability of ocean fertilizing nutrients in the dust-emitting ephemeral river catchments of Namibia. *Earth Surface Processes and Landforms*, 43 (3): 563–578, https://doi.org/10.1002/esp.4207.

Dansie, A.P., Wiggs, G.F.S., Thomas, D.S.G. and Washington, R. 2017. Measurements of windblown dust characteristics and ocean fertilization potential: The ephemeral river valleys of Namibia. *Aeolian Research*, 29: 30–41, https://doi.org/10.1016/j.aeolia.2017.08.002.

Das, A., Joseph, J., Solanki, T., Makwana, N., Chauhan, G. and Thakkar, M.G. 2020. Reconstructing Late Quaternary Palaeo-environmental change from the dryland fluvial landscape of the Southern Kachchh Mainland, western India: Insights from new OSL and sedimentological datasets. *Geological Journal*, 55 (10): 7041–7056, https://doi.org/10.1002/gj.3861.

Das, A., Prizomwala, S.P., Makwana, N. and Thakkar, M.G. 2017. Late Pleistocene-Holocene climate and sea level changes inferred based on the tidal terrace sequence, Kachchh, Western India. *Palaeogeography, Palaeoclimatology, Palaeoecology*, 473: 82–93, https://doi.org/10.1016/j.palaeo.2017.02.026.

Datry, T., Singer, G., Sauquet, E., Capdevilla, J., von Schiller, D., Subbington, R., Magrand, C., Paril, P., Milisa, M., Acuna, V., Alves, M., Augeard, B., Brunke, M., Cid, N. and Csabai. Z. 2017. Science and management of intermittent rivers and ephemeral streams (SMIRES). *Research Ideas Outcomes*, 3: 21774, https://doi.org/10.3897/rio.3.e21774.

Dean, D.J. and Topping, D.J. 2019. Geomorphic change and biogeomorphic feedbacks in a dryland river: The Little Colorado River, Arizona, USA. *Bulletin of the Geological Society of America*, 131 (11–12): 1920–1942, https://doi.org/10.1130/B35047.1.

Dean, W.E. 1974. Determination of carbonate and organic matter in calcareous sediments and sedimentary rocks by loss on ignition: Comparison with other methods. *Journal of Sedimentary Petrology*, 44: 242–248.

Deevey, E., Gross, M., Hutchinson, G. and Kraybill, H. 1954. The natural C14 contents of materials from hard-water lakes. *Proceedings of the National Academy of Sciences of the United States of America*, 40 (5): 285–288.

DeMenocal, P., Ortiz, J., Guilderson, T., Adkins, J., Sarnthein, M., Baker, L. and Yarusinsky, M. 2000. Abrupt onset and termination of the African Humid Period: Rapid climate responses to gradual insolation forcing. *Quaternary Science Reviews*, 19 (1–5): 347–361, https://doi.org/10.1016/S0277-3791(99)00081-5.

Dewar, G. and Stewart, B.A. 2012. Preliminary results of excavations at Spitzkloof Rockshelter,

Richtersveld, South Africa. *Quaternary International*, 270: 30–39, https://doi.org/10.1016/j.quaint.2011.04.046.

Dickinson, W.R. 1985. Interpreting provenance relations from detrital modes of sand-stones. In Zuffa, G.G. (Ed), Provenance of Arenites, pp. 333–361. Reidel, Dordrecht, NATO ASI Series 148.

Dickinson, W.R. 2008. Impact of differential zircon fertility of granitoid basement rocks in North America on age populations of detrital zircons and implications for granite petrogenesis. *Earth and Planetary Science Letters*, 275 (1–2): 80–92, https://doi.org/10.1016/j.epsl.2008.08.003.

DiNezio, P.N. and Tierney, J.E. 2013. The effect of sea level on glacial Indo-Pacific climate. *Nature Geoscience*, 6 (6): 485–491, https://doi.org/10.1038/ngeo1823.

Diskin, M.H. and Lane, L.J. 1972. A basinwide stochastic model for ephemeral stream runoff in south-eastern arizona. *Hydrological Sciences Bulletin*, 17 (1): 61–76, https://doi.org/https://doi.org/10.1080/02626667209493803.

Ditlefsen, C. 1992. Bleaching of K-feldspars in turbid water suspensions: A comparison of photo- and thermoluminescence signals. *Quaternary Science Reviews*, 11 (1–2): 33–38, https://doi.org/10.1016/0277-3791(92)90039-B.

Dollar, E.S. 1998. Palaeofluvial geomorphology in southern Africa: A review. *Progress in Physical Geography*, 22: 325–349.

Donselaar, M.E. and Overeem, I. 2008. Connectivity of fluvial point-bar deposit: An example from the Miocene Huesca fluvial fan, Ebro Basin, Spain. *American Association of Petroleum Geologists Bulletin*, 92 (9): 1109–1129, https://doi.org/10.1306/04180807079.

Draut, A.E. 2012. Effects of river regulation on aeolian landscapes, Colorado River, southwestern USA. *Journal of Geophysical Research: Earth Surface*, 117 (2): 1–22, https://doi.org/10.1029/2011JF002329.

Dufresne, J.L., Foujols, M.A., Denvil, S., Caubel, A., Marti, O., Aumont, O., Balkanski, Y., Bekki, S., Bellenger, H., Benshila, R., Bony, S., Bopp, L., Braconnot, P., Brockmann, P., Cadule, P., Cheruy, F., Codron, F., Cozic, A., Cugnet, D., de Noblet, N., Duvel, J.P., Ethé, C., Fairhead, L., Fichefet, T., Flavoni, S., Friedlingstein, P., Grandpeix, J.Y., Guez, L., Guilyardi, E., Hauglustaine, D., Hourdin, F., Idelkadi, A., Ghattas, J., Joussaume, S., Kageyama, M., Krinner, G., Labetoulle, S., Lahellec, A., Lefebvre, M.P., Lefevre, F., Levy, C., Li, Z.X., Lloyd, J., Lott, F., Madec, G., Mancip, M., Marchand, M., Masson, S., Meurdesoif, Y., Mignot, J., Musat, I., Parouty, S., Polcher, J., Rio, C., Schulz, M., Swingedouw, D., Szopa, S., Talandier, C., Terray, P., Viovy, N. and Vuichard, N. 2013. *Climate change projections using the IPSL-CM5 Earth System Model: From CMIP3 to CMIP5*. Climate Dynamics, 40 9–10, https://doi.org/10.1007/s00382-012-1636-1.

Duller, G.A.T. 2003. Distinguishing quartz and feldspar in single grain luminescence measurements.

Radiation Measurements, 37 (2): 161–165, https://doi.org/10.1016/S1350-4487(02)00170-1.

Duller, G.A.T. 2004. Luminescence dating of Quaternary sediments: Recent advances. *Journal of Quaternary Science*, 19 (2): 183–192, https://doi.org/10.1002/jqs.809.

Duller, G.A.T. 2008a. Luminescence Dating: guidelines on using luminescence dating in archaeology. English Heritage.

Duller, G.A.T. 2008b. Single-grain optical dating of Quaternary sediments: Why aliquot size matters in luminescence dating. *Boreas*, 37 (4): 589–612, https://doi.org/10.1111/j.1502-3885.2008.00051.x.

Duller, G.A.T. 2015. The Analyst software package for luminescence data: overview and recent improvements. *Ancient TL*, 33 (1): 35–42.

Duncan, A.R., Newton, S.R., van den Berg, C. and Reid, D.L. 1989. Geochemistry and petrology of dolerite sills in the Huab River Valley, Damaraland, north-western Namibia. *Communications of the Geological Survey of Namibia*, 5: 5–17.

Durcan, J.A., King, G.E. and Duller, G.A.T. 2015. DRAC: Dose Rate and Age Calculator for trapped charge dating. *Quaternary Geochronology*, 28: 54–61, https://doi.org/10.1016/j.quageo.2015.03.012.

Durcan, J.A., Thomas, D.S.G., Gupta, S., Pawar, V., Singh, R.N. and Petrie, C.A. 2019. Holocene landscape dynamics in the Ghaggar-Hakra palaeochannel region at the northern edge of the Thar Desert, northwest India. *Quaternary International*, 501: 317–327, https://doi.org/10.1016/j.quaint.2017.10.012.

Eckardt, F.D. and Kuring, N. 2005. SeaWiFS identifies dust sources in the Namib Desert. *International Journal of Remote Sensing*, 26 (19): 4159–4167, https://doi.org/10.1080/01431160500113112.

Eitel, B., Dieter Blümel, W., Hüser, K. and Mauz, B. 2001. Dust and loessic alluvial deposits in Northwestern Namibia (Damaraland, Kaokoveld): Sedimentology and palaeoclimatic evidence based on luminescence data. *Quaternary International*, 76–77: 57–65, https://doi.org/10.1016/S1040-6182(00)00089-6.

Eitel, B., Kadereit, A., Blümel, W.D., Hüser, K. and Kromer, B. 2005. The Amspoort Silts, northern Namib desert (Namibia): Formation, age and palaeoclimatic evidence of river-end deposits. *Geomorphology*, 64 (3–4): 299–314, https://doi.org/10.1016/j.geomorph.2004.07.006.

Eitel, B., Kadereit, A., Blümel, W.D., Hüser, K., Lomax, J. and Hilgers, A. 2006. Environmental changes at the eastern Namib Desert margin before and after the Last Glacial Maximum: New evidence from fluvial deposits in the upper Hoanib River catchment, northwestern Namibia. *Palaeogeography, Palaeoclimatology, Palaeoecology*, 234 (2–4): 201–222, https://doi.org/10.1016/j.palaeo.2005.10.015.

Eitel, B. and Zoller, L. 1996. Soils and sediments in the basin of Dieprivier-Uitskot (Khorixas District, Namibia): Age, geomorphic and sedimentological investigation, paleoclimatic interpretation.

Palaeoecology of Africa and the surrounding islands, 24: 159–173.

Ellery, W.N., Ellery, K., McCarthy, T.S., Cairncross, B. and Oelofse, R. 1989. A peat fire in the Okavango Delta, Botswana, and its importance as an ecosystem process. *African Journal of Ecology*, 27: 7–21.

Engelbrecht, C.J., Landman, W.A., Engelbrecht, F.A. and Malherbe, J. 2015. A synoptic decomposition of rainfall over the Cape south coast of South Africa. *Climate Dynamics*, 44 (9–10): 2589–2607, https://doi.org/10.1007/s00382-014-2230-5.

Engelbrecht, F.A., Marean, C.W., Cowling, R.M., Engelbrecht, C.J., Neumann, F.H., Scott, L., Nkoana, R., O'Neal, D., Fisher, E., Shook, E., Franklin, J., Thatcher, M., McGregor, J.L., Van der Merwe, J., Dedekind, Z. and Difford, M. 2019. Downscaling Last Glacial Maximum climate over southern Africa. *Quaternary Science Reviews*, 226: 105879, https://doi.org/10.1016/j.quascirev.2019.105879.

Enzel, Y. and Wells, S.G. 1997. Extracting Holocene paleohydrology and paleoclimatology information from modern extreme flood events: An example from southern California. *Geomorphology*, 19 (3–4): 203–226, https://doi.org/10.1016/s0169-555x(97)00015-9.

Erlanger, E.D., Granger, D.E. and Gibbon, R.J. 2012. Rock uplift rates in South Africa from isochron burial dating of fluvial and marine terraces. *Geology*, 40 (11): 1019–1022, https://doi.org/10.1130/G33172.1.

van der Esch, S., ten Brink, B., Stehfest, E., Bakkenes, M., Sewell, A. and Bouwman, A. 2017. Exploring Future Changes in Land Use and Land Condition and the Impacts on Food, Water, Climate Change and Biodiversity: Scenarios for the UNCCD Global Land Outlook.

Ewart, A., Marsh, J.S., Milner, S.C., Duncan, A.R., Kamber, B.S. and Armstrong, R.A. 2004. Petrology and geochemistry of early cretaceous bimodal continental flood volcanism of the NW Etendeka, Namibia. part 1: Introduction, mafic lavas and re-evaluation of mantle source components. *Journal of Petrology*, 45 (1): 59–105, https://doi.org/10.1093/petrology/egg083.

Farmer, E.C., deMenocal, P.B. and Marchitto, T.M. 2005. Holocene and deglacial ocean temperature variability in the Benguela upwelling region: Implications for low-latitude atmospheric circulation. *Paleoceanography*, 20 (2): 1–16, https://doi.org/10.1029/2004PA001049.

Faust, D., Zielhofer, C., Baena Escudero, R. and Diaz Del Olmo, F. 2004. *High-resolution fluvial record of late Holocene geomorphic change in northern Tunisia: Climatic or human impact? Quaternary Science Reviews*, 16–17: 1757–1775, https://doi.org/10.1016/j.quascirev.2004.02.007.

Feder, A., Zimmermann, R., Stollhofen, H., Caracciolo, L., Garzanti, E. and Andreani, L. 2018. Fluvial-aeolian sedimentary facies, sossusvlei, namib desert. *Journal of Maps*, 14 (2): 630–643, https://doi.org/10.1080/17445647.2018.1526719.

Fick, S.E. and Hijmans, R.J. 2017. WorldClim 2: new 1-km spatial resolution climate surfaces for global

land areas. *International Journal of Climatology*, 37 (12): 4302–4315, https://doi.org/10.1002/joc.5086.

Fitzsimmons, K.E., Cohen, T.J., Hesse, P.P., Jansen, J., Nanson, G.C., May, J.H., Barrows, T.T., Haberlah, D., Hilgers, A., Kelly, T., Larsen, J., Lomax, J. and Treble, P. 2013. Late Quaternary palaeoenvironmental change in the Australian drylands. *Quaternary Science Reviews*, 74: 78–96, https://doi.org/10.1016/j.quascirev.2012.09.007.

Folk, R.L. and Ward, W.C. 1957. Brazos river bar: A study in the significance of grain size parameters. *Journal of Sedimentary Petrology*, 27: 3–26.

Fontana, D., Parea, G.C., Bertacchini, M., Bessi, P., Valloni, R. and Basu, A. 2003. Sand production by chemical and mechanical weathering of well lithified siliciclastic turbidites of the Northern Apennines (Italy). *Quantitative provenance studies in Italy. Mem. Descr. Carta Geol. Ital*, 61: 51–60.

Forbes, M., Jankowski, N., Cohen, T., Hopf, F., Mueller, D., Bird, M., Haberle, S. and Jacobs, Z. 2020. Palaeochannels of Australia's Riverine Plain - Reconstructing past vegetation environments across the Late Pleistocene and Holocene. *Palaeogeography, Palaeoclimatology, Palaeoecology*, 545: 109533, https://doi.org/10.1016/j.palaeo.2019.109533.

Frances, F. 2004. Flood frequency analysis using systematic and non-systematic information. In Benito, G. and Thorndycraft, V. (Eds), Systematic, palaeoflood and historical data for the improvement of flood risk estimation, pp. 55–70. CSIC, Madrid.

Fraser, G.S. and Suttner, L. 1986. *Alluvial Fans and Fan Deltas: A Guide To Exploration for Oil and Gas*. Prentice Hall, Boston, MA.

Frets, D.C. 1969. Geology and structure of the Huab- Welwitschia area. *SW Africa Bulletin of the Precambrian Research Unit, University of Cape Town*, 5 (235).

Frezzotti, M.L., Tecce, F. and Casagli, A. 2012. Raman spectroscopy for fluid inclusion analysis. *Journal of Geochemical Exploration*, 112: 1–20, https://doi.org/10.1016/j.gexplo.2011.09.009.

Fryirs, K.A. and Brierley, G.J. 2012. *Geomorphic Analysis of River Systems: An approach to Reading the Landscape*. John Wiley & Sons Ldt., Chichester.

Fryirs, K.A., Wheaton, J.M. and Brierley, G.J. 2016. An approach for measuring confinement and assessing the influence of valley setting on river forms and processes. *Earth Surface Processes and Landforms*, 41 (5): 701–710, https://doi.org/10.1002/esp.3893.

Gabriel, K.R. 1971. The biplot graphic display of matrices with application to principal component analysis. *Biometrika*, 58 (3): 453–467.

Galbraith, R.F., Roberts, R.G., Laslett, G.M., Yoshida, H., Olley, J.M., Galbraith, R.F., Olley, J.M., Yoshida, H. and Laslett, G.M. 1999. Optical dating of single and multiple grains of quartz from Jinmium rock shelter, Northern Australia: Part I, Experimetal design and statistical models. *Archaeometry*, 41 (2):

339–364, https://doi.org/10.1111/j.1475-4754.1999.tb00987.x.

Galloway, W.E. and Hobday, D.K. 2012. *Terrigenous clastic depositional systems: applications to petroleum, coal, and uranium exploration*. Springer Science and Business Media.

Gary, M., McAffee, R. and Wolf, C.L. 1974. *Glossary of Geology*. American Geology Institute, Washington DC..

Garzanti, E. 2018. Petrographic classification of sand and sandstone. *Earth-Science Reviews*, 192: 545–563, https://doi.org/10.1016/j.earscirev.2018.12.014.

Garzanti, E. and Andò, S. 2007. Chapter 20 Heavy Mineral Concentration in Modern Sands: Implications for Provenance Interpretation. *Developments in Sedimentology*, 58 (7): 517–545, https://doi.org/10.1016/S0070-4571(07)58020-9.

Garzanti, E. and Andò, S. 2019. Heavy minerals for junior woodchucks. *Minerals*, 9 (3): 1–25, https://doi.org/10.3390/min9030148.

Garzanti, E., Andò, S. and Vezzoli, G. 2008. Settling equivalence of detrital minerals and grain-size dependence of sediment composition. *Earth and Planetary Science Letters*, 1–2: 138–151, 2008, https://doi.org/10.1016/j.epsl.2008.06.020.

Garzanti, E., Andò, S. and Vezzoli, G. 2009. Grain-size dependence of sediment composition and environmental bias in provenance studies. *Earth and Planetary Science Letters*, 277 (3–4): 422–432, https://doi.org/10.1016/j.epsl.2008.11.007.

Garzanti, E., Andò, S., Vezzoli, G., Lustrino, M., Boni, M. and Vermeesch, P. 2012. Petrology of the Namib Sand Sea: Long-distance transport and compositional variability in the wind-displaced Orange Delta. *Earth-Science Reviews*, 112(3–4): 173–189, https://doi.org/10.1016/j.earscirev.2012.02.008.

Garzanti, E., Dinis, P., Vermeesch, P., Andò, S., Hahn, A., Huvi, J., Limonta, M., Padoan, M., Resentini, A., Rittner, M. and Vezzoli, G. 2018. Sedimentary processes controlling ultralong cells of littoral transport: Placer formation and termination of the Orange sand highway in southern Angola. *Sedimentology*, 65 (2): 431–460, https://doi.org/10.1111/sed.12387.

Garzanti, E., Dinis, P., Vezzoli, G. and Borromeo, L. 2021. Sand and mud generation from continental flood basalts in contrasting landscapes and climatic conditions (Paraná–Etendeka conjugate igneous provinces, Uruguay and Namibia). *Sedimentology*, 68: 3447–3475, https://doi.org/10.1111/sed.12905.

Garzanti, E., Pastore, G., Stone, A., Vainer, S., Vermeesch, P. and Resentini, A. 2022. Provenance of Kalahari Sand: Paleoweathering and recycling in a linked fluvial-aeolian system. *Earth-Science Reviews*, 224: 103867.

Garzanti, E., Vermeesch, P., Andò, S., Lustrino, M., Padoan, M. and Vezzoli, G. 2014. Ultra-long distance littoral transport of Orange sand and provenance of the Skeleton Coast Erg (Namibia). *Marine*

Geology, 357: 25–36, https://doi.org/10.1016/j.margeo.2014.07.005.

Garzanti, E. and Vezzoli, G. 2003. A classification of metamorphic grains in sands based on their composition and grade. *Journal of Sedimentary Research*, 73 (5): 830–837, https://doi.org/10.1306/012203730830.

Gasse, F., Chalié, F., Vincens, A., Williams, M.A.J. and Williamson, D. 2008. Climatic patterns in equatorial and southern Africa from 30,000 to 10,000 years ago reconstructed from terrestrial and near-shore proxy data. *Quaternary Science Reviews*, 27 (25–26): 2316–2340, https://doi.org/10.1016/j.quascirev.2008.08.027.

Gent, P.R., Danabasoglu, G., Donner, L.J., Holland, M.M., Hunke, E.C., Jayne, S.R., Lawrence, D.M., Neale, R.B., Rasch, P.J., Vertenstein, M., Worley, P.H., Yang, Z.L. and Zhang, M. 2011. The community climate system model version 4. *Journal of Climate*, 24 (19): 4973–4991, https://doi.org/10.1175/2011JCLI4083.1.

Gibbon, R.J.; Granger, D.E.; Kuman, K. and Partridge, T.C. 2009. Early Acheulean technology in the Rietputs Formation, South Africa, dated with cosmogenic nuclides. *Journal of Human Evolution*, 56(2): 152–160, https://doi.org/10.1016/j.jhevol.2008.09.006.

Gil-Romera, G., Scott, L., Marais, E. and Brook, G.A. 2006. Middle- to late-Holocene moisture changes in the desert of northwest Namibia derived from fossil hyrax dung pollen. *Holocene*, 16 (8): 1073–1084, https://doi.org/10.1177/0959683606069397.

Gil-Romera, G., Scott, L., Marais, E. and Brook, G.A. 2007. Late Holocene environmental change in the northwestern Namib Desert margin: New fossil pollen evidence from hyrax middens. *Palaeogeography, Palaeoclimatology, Palaeoecology*, 249 (1–2): 1–17, https://doi.org/10.1016/j.palaeo.2007.01.002.

Gimeno, L., Drumond, A., Nieto, R., Trigo, R.M. and Stohl, A. 2010. On the origin of continental precipitation. *Geophysical Research Letters*, 37 (13): 1–7, https://doi.org/10.1029/2010GL043712.

Goscombe, B., Foster, D.A., Gray, D., Wade, B., Marsellos, A. and Titus, J. 2017. Deformation correlations, stress field switches and evolution of an orogenic intersection: The Pan-African Kaoko-Damara orogenic junction, Namibia. *Geoscience Frontiers*, 8 (6): 1187–1232, https://doi.org/10.1016/j.gsf.2017.05.001.

Goudie, A. and Viles, H. 2015. *Landscapes and landforms of Namibia*. Dordrecht: Springer.

Goudie, A.S. 1972. Climate, weathering, crust formation, dunes and fluvial features of the central Namib Desert near Gobabeb, South West Africa. *Madoqua*, 11: 15–31.

Govin, A., Varma, V. and Prange, M. 2014. Astronomically forced variations in western African rainfall (21°N–20°S) during the Last Interglacial period. *Geophysical Research Letters*, 41: 2117–2125, doi:10.1002/2013GL058999.

Gray, D.R., Foster, D.A., Meert, J.G., Goscombe, B.D., Armstrong, R., Trouw, R.A.J. and Passchier, C.W. 2008. A Damara orogen perspective on the assembly of southwestern Gondwana. *Geological Society Special Publication*, 294: 257–278, https://doi.org/10.1144/SP294.14.

Greber, N.D., Davies, J.H.F.L., Gaynor, S.P., Jourdan, F., Bertrand, H. and Schaltegger, U. 2020. New high precision U-Pb ages and Hf isotope data from the Karoo large igneous province, implications for pulsed magmatism and early Toarcian environmental perturbations. *Results in Geochemistry*, 1: 100005, https://doi.org/10.1016/j.ringeo.2020.100005.

Greenbaum, N., Schick, A.P. and Baker, V.R. 2000. *The palaeoflood record of a hyperarid catchment, Nahal Zin, Negev Desert, Israel*. *Earth Surface Processes and Landforms*, 9: 951–971, https://doi.org/10.1002/1096-9837(200008)25:9<951::AID-ESP110>3.0.CO,2-8.

Greenbaum, N., Schwartz, U., Benito, G., Porat, N., Cloete, G.C. and Enzel, Y. 2014. Paleohydrology of extraordinary floods along the Swakop River at the margin of the Namib Desert and their paleoclimate implications. *Quaternary Science Reviews*, 103: 153–169, https://doi.org/10.1016/j.quascirev.2014.08.021.

Grenfell, S. and Grenfell, M. 2021. Characterising the late Quaternary facies stratigraphy of floodplains in south africa. *South African Journal of Geology*, 124 (4): 963–976, https://doi.org/10.25131/sajg.124.0056.

Grenfell, S., Ellery, W., Grenfell, M., Lisa, R. and Flugel, T. 2010. Sedimentary facies and geomorphic evolution of a blocked-valley lake: Lake Futululu, northern Kwazulu-Natal, South Africa. *Sedimentology*, 57: 1159–1174, https://doi.org/10.1111/j.1365-3091.2009.01141.x.

Grenfell, S., Grenfell, M., Ellery, W., Job, N. and Walters, D. 2019. A genetic geomorphic classification system for Southern African palustrine wetlands: Global implications for the management of wetlands in drylands. *Frontiers in Environmental Science*, 7, https://doi.org/10.3389/fenvs.2019.00174.

Grodek, T., Benito, G., Botero, B.A., Jacoby, Y., Porat, N., Haviv, I., Cloete, G. and Enzel, Y. 2013. The last millennium largest floods in the hyperarid Kuiseb River basin, Namib Desert. *Journal of Quaternary Science*, 28 (3): 258–270, https://doi.org/10.1002/jqs.2618.

Guérin, G. 2013. Luminescence Dating, Dose Rates. In Rink, W.J. and Thompson, J. (Eds), Encyclopedia of scientific dating methods, pp. 1–6. Springer Netherlands, Dordrecht, https://doi.org/10.1007/978-94-007-6326-5_33-1.

Guérin, G., Mercier, N. and Adamiec, G. 2011. Dose-rate conversion factors: Update Dose-rate conversion factors.

Guyez, A., Bonnet, S., Reimann, T., Carretier, S. and Wallinga, J. 2022. Illuminating past river incision, sediment source and pathways using luminescence signals of individual feldspar grains (Rangitikei

River, New Zealand). *Earth Surface Processes and Landforms*, https://doi.org/10.1002/esp.5357.

Haberlah, D., Williams, M., Halverson, G., McTainsh, G., Hill, S., Hrstka, T., Jaime, P., Butcher, A. and Glasby, P. 2010. Loess and floods: High-resolution multi-proxy data of Last Glacial Maximum (LGM) slackwater deposition in the Flinders Ranges, semi-arid South Australia. *Quaternary Science Reviews*, 29 (19–20): 2673–2693, https://doi.org/10.1016/j.quascirev.2010.04.014.

Hachigonta, S. and Reason, C.J.C. 2006. Interannual variability in dry and wet spell characteristics over Zambia. *Handbook of Environmental Chemistry, Volume 5: Water Pollution*, 32 (1): 49–62, https://doi.org/10.3354/cr032049.

Haddon, I.G. and McCarthy, T.S. 2005. The Mesozoic-Cenozoic interior sag basins of Central Africa: The Late-Cretaceous-Cenozoic Kalahari and Okavango basins. *Journal of African Earth Sciences*, 43 (1–3): 316–333, https://doi.org/10.1016/j.jafrearsci.2005.07.008.

Hall, K. 2004. Glaciation in southern Africa. *Developments in Quaternary Science*, 2(PART C): 337–338, https://doi.org/10.1016/S1571-0866(04)80139-8.

Hanson, R.E. 2003. Proterozoic geochronology and tectonic evolution of southern Africa. In Yoshida, M., Windley, B.F. and Dasgupta, S. (Eds), Proterozoic East Gondwana: Supercontinent Assembly and Breakup, 206: 427–463. Geological Society, London, Special Publications.

Harden, T., Macklin, M.G. and Baker, V.R. 2010. Holocene flood histories in south-western USA. *Earth Surface Processes and Landforms*, 35: 707–716, https://doi.org/DOI: 10.1002/esp.1983.

Harrell, K. and Blatt, H. 1978. Polycrystallinity: effect on the durability of detrital quartz. *Journal of Sedimentary Research*, 48 (1): 25–30, https://doi.org/10.1306/212f73e7-2b24-11d7-8648000102c1865d.

Harrison, M.S.J. 1984. A generalized classification of South African summer rain-bearing synoptic systems. *Journal of Climatology*, 4 (5): 547–560, https://doi.org/10.1002/joc.3370040510.

Harrison, S.P., Bartlein, P.J., Izumi, K., Li, G., Annan, J., Hargreaves, J., Braconnot, P. and Kageyama, M. 2015. Evaluation of CMIP5 palaeo-simulations to improve climate projections. *Nature Climate Change*, 5 (8): 735–743, https://doi.org/10.1038/nclimate2649.

Hart, N.C.G., Reason, C.J.C. and Fauchereau, N. 2010. Tropical-extratropical interactions over southern Africa: Three cases of heavy summer season rainfall. *Monthly Weather Review*, 138 (7): 2608–2623, https://doi.org/10.1175/2010MWR3070.1.

Hart, N.C.G., Reason, C.J.C. and Fauchereau, N. 2013. Cloud bands over southern Africa: Seasonality, contribution to rainfall variability and modulation by the MJO. *Climate Dynamics*, 41 (5–6): 1199–1212, https://doi.org/10.1007/s00382-012-1589-4.

Hartley, A.J., Weissmann, G.S., Nichols, G.J. and Warwick, G.L. 2010. Large distributive fluvial systems: Characteristics, distribution, and controls on development. *Journal of Sedimentary Research*, 80

(2): 167–183, https://doi.org/10.2110/jsr.2010.016.

Harvey, A. 2011. Dryland alluvial fans. In Thomas, D.S.G. (Ed), Arid Zone Geomorphology: Process, from and change in Drylands, pp. 333–371. Wiley-Blackwell, New York.

He, F., Shakun, J.D., Clark, P.U., Carlson, A.E., Liu, Z., Otto-Bliesner, B.L. and Kutzbach, J.E. 2013. Northern Hemisphere forcing of Southern Hemisphere climate during the last deglaciation. *Nature*, 494 (7435): 81–85, https://doi.org/10.1038/nature11822.

Heer, A., Adamiec, G. and Moska, P. 2012. How many grains are there on a single aliquot? *Ancient TL*, 30 (1): 9–11.

van Heerden, J. and Taljaard, J.J. 1998. Africa and Surrounding Waters. In Karoly, D.J. and Vincent, D.G. (Eds), *Meteorology of the Southern Hemisphere*, pp. 141–174. Boston, MA: American Meteorological Society, https://doi.org/10.1007/978-1-935704-10-2_6.

Heine, K. 1982. The main stages of the Late Quaternary evolution of the Kalahari region, southern Africa. *Palaeoecology of Africa*, 15: 53–76.

Heine, K. 1990. Some observations concerning the age of the dunes in the western Kalahari and palaeoclimatic implications. *Palaeoecology of Africa*, 19: 305–315.

Heine, K. 1992. On the ages of humid Late Quaternary phases in southern African arid areas (Namibia, Botswana). *Palaeoecology of Africa and the surrounding islands*, 23: 149–164.

Heine, K. and Heine, J.T. 2002. A paleohydrologic reinterpretation of the Homeb Silts, Kuiseb River, central Namib Desert (Namibia) and paleoclimatic implications. *Catena*, 48 (1–2): 107–130, https://doi.org/10.1016/S0341-8162(02)00012-7.

Heine, K. and Völkel, J. 2009. Desert flash flood series - Slackwater deposits and floodouts in Namibia: their significance for palaeoclimatic reconstructions. *Zbl. Geol. Paläont. Teil I*, 287–308.

Heine, K. and Völkel, J. 2011. Extreme floods around AD 1700 in the northern Namib desert, Namibia, and in the orange river catchment, South Africa - were they forced by a decrease of solar irradiance during the little ice age? *Geographia Polonica*, SUPPL. 1: 61–80, https://doi.org/10.7163/GPol.2011.1.4.

Heiri, O., Lotter, A.F. and Lemcke, G. 2001. Loss on ignition as a method for estimating organic and carbonate content in sediments: reproducibility and comparability of results. *Journal of Paleolimnology*, 25: 101–110.

Henares, S., Donselaar, M.E. and Caracciolo, L. 2020. Depositional controls on sediment properties in dryland rivers: Influence on near-surface diagenesis. *Earth-Science Reviews*, 208, https://doi.org/10.1016/j.earscirev.2020.103297.

Hereford, R. 2002. Valley-fill alluviation during the Little Ice Age (ca. A.D. 1400-1880), Paria River basin and southern Colorado Plateau, United States. *Bulletin of the Geological Society of America*, 114

(12): 1550–1563, https://doi.org/10.1130/0016-7606(2002)114<1550:VFADTL>2.0.CO,2.

Hermes, J.C. and Reason, C.J.C. 2005. Ocean model diagnosis of interannual coevolving SST variability in the South Indian and South Atlantic Oceans. *Journal of Climate*, 18 (15): 2864–2882, https://doi.org/10.1175/JCLI3422.1.

Hermes, J.C. and Reason, C.J.C. 2009. Variability in sea-surface temperature and winds in the tropical south-east Atlantic Ocean and regional rainfall relationships. *International Journal of Climatology*, 29: 11–21.

Hesse, P.P., Williams, R., Ralph, T.J., Fryirs, K.A., Larkin, Z.T., Westaway, K.E. and Farebrother, W. 2018. Palaeohydrology of lowland rivers in the Murray-Darling Basin, Australia. *Quaternary Science Reviews*, 200: 85–105, https://doi.org/10.1016/j.quascirev.2018.09.035.

Hilgers, A., Murray, A.S., Schlaak, N. and Radtke, U. 2001. Comparison of quartz OSL protocols using Lateglacial and Holocene dune sands from Brandenburg, Germany. *Quaternary Science Reviews*, 20 (5–9): 731–736, https://doi.org/10.1016/S0277-3791(00)00050-0.

Hipondoka, M.H.T., Mauz, B., Kempf, J., Packman, S., Chiverrell, R.C. and Bloemendal, J. 2014. Chronology of sand ridges and the Late Quaternary evolution of the Etosha Pan, Namibia. *Geomorphology*, 204: 553–563, https://doi.org/10.1016/j.geomorph.2013.08.034.

Hoell, A. and Cheng, L. 2018. Austral summer Southern Africa precipitation extremes forced by the El Niño-Southern oscillation and the subtropical Indian Ocean dipole. *Climate Dynamics*, 50 (9–10): 3219–3236, https://doi.org/10.1007/s00382-017-3801-z.

Hoell, A., Gaughan, A.E., Magadzire, T. and Harrison, L. 2021. The modulation of daily southern Africa precipitation by el Niño-Southern oscillation across the summertime wet season. *Journal of Climate*, 34 (3): 1115–1134, https://doi.org/10.1175/JCLI-D-20-0379.1.

Hogg, A.G., Heaton, T.J., Hua, Q., Palmer, J.G., Turney, C.S.M., Southon, J., Bayliss, A., Blackwell, P.G., Boswijk, G., Bronk Ramsey, C., Pearson, C., Petchey, F., Reimer, P., Reimer, R. and Wacker, L. 2020. SHCal20 Southern Hemisphere Calibration, 0-55,000 Years cal BP. *Radiocarbon*, 62 (4): 759–778, https://doi.org/10.1017/RDC.2020.59.

von Holdt, J.R. and Eckardt, F.D. 2018. Dust activity and surface sediment characteristics of the dustiest river in southern Africa: the Kuiseb River, Central Namib. *South African Geographical Journal*, 100 (1): 104–121, https://doi.org/10.1080/03736245.2017.1339627.

Hooke, J.M. and Mant, J.M. 2000. Geomorphological impacts of a flood event on ephemeral channels in SE Spain. *Geomorphology*, 34: 163–180, https://doi.org/10.1016/S0169-555X(00)00005-2.

Howard, E. and Washington, R. 2019. Drylines in southern Africa: Rediscovering the Congo air boundary. *Journal of Climate*, 32 (23): 8223–8242, https://doi.org/10.1175/JCLI-D-19-0437.1.

Hua, Q., Barbetti, M. and Rakowski, A.Z. 2013. Atmospheric radiocarbon for the period 1950–2010.

Radiocarbon, 55 (4): 2059–2072, https://doi.org/10.2458/azu_js_rc.v55i2.16177.

Humphries, M.S. 2021. Elemental proxy evidence for late Quaternary palaeoenvironmental change in southern african sedimentary records: Interpretation and applications. *South African Journal of Geology*, 124 (4): 1033–1046, https://doi.org/10.25131/sajg.124.0046.

Hurkamp, K., Volkel, J., Heine, K., Bens, O., Leopold, M. and Winkelbauer, J. 2011. Late Quaternary environmental changes from aeolian and fluvial geoarchives in the southwestern Kalahari, South Africa: Implications for past African climate dynamics. *South African Journal of Geology*, 114 (3–4): 459–474, https://doi.org/10.2113/gssajg.114.3-4.459.

Ingersoll, R., Bullard, T., Ford, R., Grimm, J., Pickle, J. and Sares, S. 1984. The effect of grain size on detrital modes: a test of the Gazzi-Dickinson point-counting method. *Journal of Sedimentary Petrology*, 54 (1): 103–116.

IPCC. 2021. Climate Change 2021: The physical science basis. Contribution of working group I to the sixth assessment report of the Intergovernmental Panel on Climate Change.

Jacobs, J., Pisarevsky, S., Thomas, R.J. and Becker, T. 2008. The Kalahari Craton during the assembly and dispersal of Rodinia 160: 142–158, https://doi.org/10.1016/j.precamres.2007.04.022.

Jacobs, Z., Roberts, R.G., Galbraith, R.F., Deacon, H.J., Grün, R., Mackay, A., Mitchell, P., Vogelsang, R. and Wadley, L. 2008. Ages for the Middle Stone Age of southern Africa: Implications for human behavior and dispersal. *Science*, 322 (5902): 733–735, https://doi.org/10.1126/science.1162219.

Jacobson, P., Jacobson, K. and Seely, M. 1995. Ephemeral rivers and their catchments: sustaining people and development in western Namibia.pp. 1–160. Desert Research Foundation of Namibia, Windhoek, 1995, papers2://publication/uuid/30B5939B-4F7C-4BA3-9BCB-F78F57AE1BB3.

Jacobson, P.J., Jacobson, K.M., Angermeier, P.L. and Cherry, D.O.N.S. 2000. Variation in material transport and water chemistry along a large ephemeral river in the Namib Desert. *Freshwater Biology*, 44: 481-491.

Jain, M., Murray, A.S. and Botter-jensen, L. 2004. Optically stimulated luminescence dating: how significant is incomplete light exposure in fluvial environments? *Quaternaire*, 15 (1–2): 143–157.

Jain, M., Murray, A.S. and Botter-Jensen, L. 2003. Characterisation of blue-light stimulated luminescence components in di erent quartz samples: implications for dose measurement. *Radiation Measurements*, 37: 441–449, https://doi.org/10.1016/S1350-4487(03)00052-0.

Jarrett, R. and England, J. 2002. Reliability of paleostage indicators for paleoflood studies. In House, P., Webb, R., Baker, V. and Levish, D. (Eds), Ancient floods, modern hazards: Principles and applications of paleoflood hydrology. Water Science and Application, pp. 91–109. American Geophysical Union: Washington.

JAXA. 2021. 30m ALOS Global Digital Surface Model, Japanese Aerospace Exploration Agency (JAXA)

Earth Observation Research Centre. *Https://www.eorc.jaxa.jp/ ALOS/en/aw3d30/index.htm*.

Jerolmack, D.J. and Paola, C. 2010. Shredding of environmental signals by sediment transport 37: 1–5, https://doi.org/10.1029/2010GL044638.

Jerram, D., Mountney, N., Holzfo, F. and Stollhofen, H. 1999. Internal stratigraphic relationships in the Etendeka Group in the Huab Basin , NW Namibia : understanding the onset of ¯ ood volcanism 28.

Jerram, D.A., Mountney, N., Howell, J. and Stollhofen, H. 2000. The Fossilised Desert : recent developments in our understanding of the Lower Cretaceous deposits in the Huab Basin , NW Namibia 12: 303–313.

Jiang, D., Tian, Z. and Lang, X. 2015. Mid-Holocene global monsoon area and precipitation from PMIP simulations. *Climate Dynamics*, 44 (9–10): 2493–2512, https://doi.org/10.1007/s00382-014-2175-8.

Jiang, D., Tian, Z., Lang, X., Kageyama, M. and Ramstein, G. 2015. The concept of global monsoon applied to the last glacial maximum: A multi-model analysis. *Quaternary Science Reviews*, 126: 126–139, https://doi.org/10.1016/j.quascirev.2015.08.033.

Jiménez Cisneros, B.E., Oki, T., Arnell, N.W., Benito, G., Cogley, J.G., Döll, P., Jiang, T., Mwakalila, S.S., Kundzewicz, Z. and Nishijima, A. 2014. *Freshwater resources*. *Climate Change 2014 Impacts, Adaptation and Vulnerability: Part A: Global and Sectoral Aspects*, 229–270, 2014, https://doi.org/10.1017/CBO9781107415379.008.

Joussaume, S., Taylor, K.E., Braconnot, P., Mitchell, J.F.B., Kutzbach, J.E., Harrison, S.P., Prentice, I.C., Broccoli, A.J., Abe-Ouchi, A., Bartlein, P.J., Bonfils, C., Dong, B., Guiot, J., Herterich, K., Hewitt, C.D., Jolly, D., Kim, J.W., Kislov, A., Kitoh, A., Loutre, M.F., Masson, V., McAvaney, B., McFarlane, N., De Noblet, N., Peltier, W.R., Peterschmitt, J.Y., Pollard, D., Rind, D., Royer, J.F., Schlesinger, M.E., Syktus, J., Thompson, S., Valdes, P., Vettoretti, G., Webb, R.S. and Wyputta, U. 1999. Monsoon changes for 6000 years ago: Results of 18 simulations from the Paleoclimate Modeling Intercomparison Project (PMIP). *Geophysical Research Letters*, 26(7): 859–862, https://doi.org/10.1029/1999GL900126.

Jung, S. and Mezger, K. 2003. Petrology of basement-dominated terranes : I . Regional metamorphic T – t path from U – Pb monazite and Sm – Nd garnet geochronology (Central Damara orogen , Namibia) 198: 223–247, https://doi.org/10.1016/S0009-2541(03)00037-8.

Jungclaus, J.H., Keenlyside, N., Botzet, M., Haak, H., Luo, J.J., Latif, M., Marotzke, J., Mikolajewicz, U. and Roeckner, E. 2006. Ocean circulation and tropical variability in the coupled model ECHAM5/MPI-OM. *Journal of Climate*, 19: 3952–3972.

Kageyama, M., Harrison, S.P., Kapsch, M.L., Lofverstrom, M., Lora, J.M., Mikolajewicz, U., Sherriff-Tadano, S., Vadsaria, T., Abe-Ouchi, A., Bouttes, N., Chandan, D., Gregoire, L.J., Ivanovic, R.F.,

Izumi, K., Legrande, A.N., Lhardy, F., Lohmann, G., Morozova, P.A., Ohgaito, R., Paul, A., Richard Peltier, W., Poulsen, C.J., Quiquet, A., Roche, D.M., Shi, X., Tierney, J.E., Valdes, P.J., Volodin, E. and Zhu, J. 2021. The PMIP4 Last Glacial Maximum experiments: Preliminary results and comparison with the PMIP3 simulations. *Climate of the Past*, 17 (3): 1065–1089, https://doi.org/10.5194/cp-17-1065-2021.

Kale, V.S., Singhvi, A.K., Mishra, P.K. and Banerjee, D. 2000. Sedimentary records and luminescence chronology of Late Holocene palaeofloods in the Luni River, Thar Desert, northwest India. *Catena*, 40 (4): 337–358, https://doi.org/10.1016/S0341-8162(00)00091-6.

Kang, S.M., Held, I.M., Frierson, D.M.W. and Zhao, M. 2008. The response of the ITCZ to extratropical thermal forcing: Idealized slab-ocean experiments with a GCM. *Journal of Climate*, 21 (14): 3521–3532, https://doi.org/10.1175/2007JCLI2146.1.

Keen-Zebert, A., Tooth, S., Rodnight, H., Duller, G.A.T., Roberts, H.M. and Grenfell, M. 2013. Late Quaternary floodplain reworking and the preservation of alluvial sedimentary archives in unconfined and confined river valleys in the eastern interior of South Africa. *Geomorphology*, 185: 54–66, https://doi.org/10.1016/j.geomorph.2012.12.004.

Kemp, D.B. 2012. Stochastic and deterministic controls on stratigraphic completeness and fidelity. *International Journal of Earth Sciences*, 101 (8): 2225–2238, https://doi.org/10.1007/s00531-012-0784-1.

Khider, D., Emile-Geay, J., McKay, N.P., Gil, Y., Garijo, D., Ratnakar, V., Alonso-Garcia, M., Bertrand, S., Bothe, O., Brewer, P., Bunn, A., Chevalier, M., Comas-Bru, L., Csank, A., Dassié, E., DeLong, K., Felis, T., Francus, P., Frappier, A., Gray, W., Goring, S., Jonkers, L., Kahle, M., Kaufman, D., Kehrwald, N.M., Martrat, B., McGregor, H., Richey, J., Schmittner, A., Scroxton, N., Sutherland, E., Thirumalai, K., Allen, K., Arnaud, F., Axford, Y., Barrows, T., Bazin, L., Pilaar Birch, S.E., Bradley, E., Bregy, J., Capron, E., Cartapanis, O., Chiang, H.W., Cobb, K.M., Debret, M., Dommain, R., Du, J., Dyez, K., Emerick, S., Erb, M.P., Falster, G., Finsinger, W., Fortier, D., Gauthier, N., George, S., Grimm, E., Hertzberg, J., Hibbert, F., Hillman, A., Hobbs, W., Huber, M., Hughes, A.L.C., Jaccard, S., Ruan, J., Kienast, M., Konecky, B., Le Roux, G., Lyubchich, V., Novello, V.F., Olaka, L., Partin, J.W., Pearce, C., Phipps, S.J., Pignol, C., Piotrowska, N., Poli, M.S., Prokopenko, A., Schwanck, F., Stepanek, C., Swann, G.E.A., Telford, R., Thomas, E., Thomas, Z., Truebe, S., von Gunten, L., Waite, A., Weitzel, N., Wilhelm, B., Williams, J., Williams, J.J., Winstrup, M., Zhao, N. and Zhou, Y. 2019. PaCTS 1.0: A Crowdsourced Reporting Standard for Paleoclimate Data. *Paleoceanography and Paleoclimatology*, 34 (10): 1570–1596, https://doi.org/10.1029/2019PA003632.

Kim, J.H., Schneider, R.R., Müller, P.J. and Wefer, G. 2002. Interhemispheric comparison of deglacial sea-surface temperature patterns in Atlantic eastern boundary currents. *Earth and Planetary Science*

Letters, 194 (3–4): 383–393, https://doi.org/10.1016/S0012-821X(01)00545-3.

Kinabo, B.D., Atekwana, E.A., Hogan, J.P., Modisi, M.P., Wheaton, D.D. and Kampunzu, A.B. 2007. Early structural development of the Okavango rift zone, NW Botswana. *Journal of African Earth Sciences*, 48 (2–3): 125–136, https://doi.org/10.1016/j.jafrearsci.2007.02.005.

Kirst, G.J., Schneider, R.R., Müller, P.J., Von Storch, I. and Wefer, G. 1999. Late Quaternary temperature variability in the Benguela Current System derived from Alkenones. *Quaternary Research*, 52 (1): 92–103, https://doi.org/10.1006/qres.1999.2040.

Kleinhanns, I.C., Fullgraf, T., Wilsky, F., Nolte, N., Fliegel, D., Klemd, R. and Hansen, B.T. 2015. U-Pb zircon ages and (isotope) geochemical signatures of the Kamanjab Inlier (NW Namibia): Constraints on palaeoproterozoic crustal evolution along the southern Congo craton. *Geological Society Special Publication*, 389 (1): 165–195, https://doi.org/10.1144/SP389.1.

Knight, J. and Fitchett, J.M. 2021. A proposed chronostratigraphic framework for the late Quaternary of southern Africa. *South African Journal of Geology*, 124 (4): 843–862, https://doi.org/10.25131/sajg.124.0030.

Knighton, A.D. and Nanson, G.C. 1997. Distinctiveness, diversity and uniqueness in arid zone river systems. In Thomas, D.S.G. (Ed), Arid Zone Geomorphology: Process, Form and Change in Drylands, pp. 185–203. Wiley, Chichester.

Knighton, D. and Nanson, G. 1994. Flow transmission along an arid zone anastomising river, Cooper Creek, Australia. *Hydrological Processes*, 8: 137–154.

Kochel, C R, Baker, V.R. 1982. Hydrology. *American Association for the Advancement of Science*, 215 (35054531): 353–361.

Kocurek, G., Westerman, R., Hern, C., Tatum, D., Rajapara, H.M. and Singhvi, A.K. 2020. Aeolian dune accommodation space for Holocene Wadi Channel Avulsion Strata, Wahiba Dune Field, Oman. *Sedimentary Geology*, 399: 105612, https://doi.org/10.1016/j.sedgeo.2020.105612.

Kohfeld, K.E., Graham, R.M., de Boer, A.M., Sime, L.C., Wolff, E.W., Le Quéré, C. and Bopp, L. 2013. Southern Hemisphere westerly wind changes during the Last Glacial Maximum: Paleo-data synthesis. *Quaternary Science Reviews*, 68: 76–95, https://doi.org/10.1016/j.quascirev.2013.01.017.

Komar, P. and Wang, C. 1984. Processes of selective grain transport and the formation of placers on beaches. *The Journal of Geology*, 92 (6): 637–635.

Komar, P.D. 2007. The Entrainment, Transport and Sorting of Heavy Minerals by Waves and Currents. In Mange, M.A. and Wright, D.T. (Eds), Developments in Sedimentology, pp. 3–48.

Kondolf, G.M. and Piegay, H. 2016. *Tools in fluvial geomorphology*. Second edition. Chichester, West Sussex: Wiley Blackwell.

Koutroulis, A.G. 2019. Dryland changes under different levels of global warming. *Science of the Total Environment*, 655: 482–511, https://doi.org/10.1016/j.scitotenv.2018.11.215.

Krapf, C.B.E., Stollhofen, H. and Stanistreet, I.G. 2003. Contrasting styles of ephemeral river systems and their interaction with dunes of the Skeleton Coast erg (Namibia). *Quaternary International*, 104: 41–52, https://doi.org/10.1016/S1040-6182(02)00134-9.

Kreutzer, S., Burow, C., Dietze, M., Fuchs, M., Schmidt, C., Fischer, M., Friedrich, J., Mercier, N., Smedley, R., Christophe, C., Zink, A., Durcan, J., King, G., Philippe, A., Guerin, G. and Riedesel, S. 2020. Comprehensive luminescence dating data analysis, version 0.9.10. https://cran.r-project.org/web/packages/Luminescence/index.html.

Kreutzer, S., Schmidt, C., Fuchs, M.C., Dietze, M., Fischer, M. and Fuchs, M. 2012. Introducing an R package for luminescence dating analysis. *Ancient TL*, 30 (1): 1–8.

Kröpelin, S., Verschuren, D., Lézine, A.M., Eggermont, H., Cocquyt, C., Francus, P., Cazet, J.-P., Fagot, M. and Rumes, B. 2008. Climate-Driven Ecosystem Succession in the Sahara: The Past 6000 years. *Science*, 320 (5877): 765–768, https://doi.org/DOI: 10.1126/science.1154913.

Kundzewicz, Z.W., Kanae, S., Seneviratne, S.I., Handmer, J., Nicholls, N., Peduzzi, P., Mechler, R., Bouwer, L.M., Arnell, N., Mach, K., Muir-Wood, R., Brakenridge, G.R., Kron, W., Benito, G., Honda, Y., Takahashi, K. and Sherstyukov, B. 2014. Flood risk and climate change: global and regional perspectives. *Hydrological Sciences Journal*, 59 (1): 1–28, https://doi.org/10.1080/02626667.2013.857411.

Kutzbach, J.E., Liu, X., Liu, Z. and Chen, G. 2008. Simulation of the evolutionary response of global summer monsoons to orbital forcing over the past 280,000 years. *Climate Dynamics*, 30 (6): 567–579, https://doi.org/10.1007/s00382-007-0308-z.

Lafuente, B., Downs, R.T., Yang, Y.H. and Stone, N. 2016. The power of databases: the RRUFF project. In Armbruster, T. and Danisi, R.M. (Eds), Highlights in Mineralogical Crystallography, pp. 1–30. W. De Gruyter, Berlin, Germany.

Lamothe, M. and Auclair, M. 1999. A solution to anomalous fading and age shortfalls in optical dating of feldspar minerals. *Earth and Planetary Science Letters*, 171 (3): 319–323, https://doi.org/10.1016/S0012-821X(99)00180-6.

Lancaster, N. 2002. How dry was dry? Late Pleistocene palaeoclimates in the Namib Desert. *Quaternary Science Reviews*, 21 (7): 769–782, https://doi.org/10.1016/S0277-3791(01)00126-3.

Lancaster, N., Wolfe, S., Thomas, D.S.G., Bristow, C., Bubenzer, O., Burrough, S., Duller, G., Halfen, A., Hesse, P., Roskin, J., Singhvi, A., Tsoar, H., Tripaldi, A., Yang, X. and Zárate, M. 2016. The INQUA Dunes Atlas chronologic database. *Quaternary International*, 410: 3–10, https://doi.org/10.1016/j.quaint.2015.10.044.

Lange, J. 2005. Dynamics of transmission losses in a large arid stream channel. *Journal of Hydrology*, 1–4: 112–126, https://doi.org/10.1016/j.jhydrol.2004.09.016.

Larkin, Z.T., Ralph, T.J., Tooth, S., Fryirs, K.A. and Carthey, A.J.R. 2020. Identifying threshold responses of Australian dryland rivers to future hydroclimatic change. *Scientific Reports*, 10 (1): 1–15, https://doi.org/10.1038/s41598-020-63622-3.

Lehmann, J., Saalmann, K., Naydenov, K. V., Milani, L., Belyanin, G.A., Zwingmann, H., Charlesworth, G. and Kinnaird, J.A. 2016. Structural and geochronological constraints on the Pan-African tectonic evolution of the northern Damara Belt, Namibia. *Tectonics*, 35 (1): 103–135, https://doi.org/10.1002/2015TC003899.

Lehner, B. and Grill, G. 2013. Global river hydrography and network routing: Baseline data and new approaches to study the world's large river systems. *Hydrological Processes*, 27 (15): 2171–2186, https://doi.org/10.1002/hyp.9740.

Leopold, M., Volkel, J. and Heine, K. 2006. A ground-penetrating radar survey of late Holocene fluvial sediments in NW Namibian river valleys: characterization and comparison. *Journal of the Geological Society*, 163 (6): 923–936, https://doi.org/10.1144/0016-76492005-092.

Lewin, J. and Macklin, M.G. 2003. Preservation potential for late Quaternary river alluvium. *Journal of Quaternary Science*, 18 (2): 107–120, https://doi.org/10.1002/jqs.738.

Lézine, A.M., Hély, C., Grenier, C., Braconnot, P. and Krinner, G. 2011. Sahara and Sahel vulnerability to climate changes, lessons from Holocene hydrological data. *Quaternary Science Reviews*, 30 (21–22): 3001–3012, https://doi.org/10.1016/j.quascirev.2011.07.006.

Li, L., Lin, P., Yu, Y., Wang, B., Zhou, T., Liu, L., Liu, J., Bao, Q., Xu, S., Huang, W., Xia, K., Pu, Y., Dong, L., Shen, S., Liu, Y., Hu, N., Liu, M., Sun, W., Shi, X., Zheng, W., Wu, B., Song, M., Liu, H., Zhang, X., Wu, G., Xue, W., Huang, X., Yang, G., Song, Z. and Qiao, F. 2013. The Flexible Global Ocean-Atmosphere-Land System Model, Grid-Point Version 2: FGOALS-g2. *Flexible Global Ocean-Atmosphere-Land System Model: A Modeling Tool for the Climate Change Research Community* 30 (3): 39–43, https://doi.org/10.1007/978-3-642-41801-3_6.

Lian, X., Piao, S., Chen, A., Huntingford, C., Fu, B., Li, L.Z.X., Huang, J., Sheffield, J., Berg, A.M., Keenan, T.F., McVicar, T.R., Wada, Y., Wang, X., Wang, T., Yang, Y. and Roderick, M.L. 2021. Multifaceted characteristics of dryland aridity changes in a warming world. *Nature Reviews Earth and Environment*, 2 (4): 232–250, https://doi.org/10.1038/s43017-021-00144-0.

Lim, S., Chase, B.M., Chevalier, M. and Reimer, P.J. 2016. 50,000 years of vegetation and climate change in the southern Namib Desert, Pella, South Africa. *Palaeogeography, Palaeoclimatology, Palaeoecology*, 451: 197–209, https://doi.org/10.1016/j.palaeo.2016.03.001.

Little, M.G., Schneider, R.R., Kroon, D., Price, B., Bickert, T. and Wefer, G. 1997. Rapid

palaeoceanographic changes in the Benguela Upwelling System for the last 160,000 years as indicated by abundances of planktonic foraminifera. *Palaeogeography, Palaeoclimatology, Palaeoecology*, 130 (1–4): 135–161, https://doi.org/10.1016/S0031-0182(96)00136-8.

Liu, B. and Coulthard, T.J. 2015. Mapping the interactions between rivers and sand dunes: Implications for fluvial and aeolian geomorphology. *Geomorphology*, 231: 246–257, https://doi.org/10.1016/j.geomorph.2014.12.011.

Liu, B. and Coulthard, T.J. 2017. Modelling the interaction of aeolian and fluvial processes with a combined cellular model of sand dunes and river systems. *Computers and Geosciences*, 106: 1–9, https://doi.org/10.1016/j.cageo.2017.05.003.

Liu, Q.Q., Chen, L., Li, J.C. and Singh, V.P. 2004. Two-dimensional kinematic wave model of overland-flow. *Journal of Hydrology*, 1–2: 28–41, https://doi.org/10.1016/j.jhydrol.2003.12.023.

Lourenco, M., Fitchett, J.M. and Woodborne, S. 2022. Angolan highlands peatlands: Extent, age and growth dynamics. *Science of the Total Environment*, 810: 152315, https://doi.org/10.1016/j.scitotenv.2021.152315.

Lowick, S.E., Preusser, F. and Wintle, A.G. 2010. Investigating quartz optically stimulated luminescence dose-response curves at high doses. *Radiation Measurements*, 45 (9): 975–984, https://doi.org/10.1016/j.radmeas.2010.07.010.

Lünsdorf, N.K., Kalies, J., Ahlers, P. and Eynatten, H. Von. 2019. Semi-automated heavy-mineral analysis by raman spectroscopy. *Minerals*, 9: 385–417, https://doi.org/doi:10.3390/min9070385.

Lyons, R., Tooth, S. and Duller, G.A.T. 2014. Late Quaternary climatic changes revealed by luminescence dating, mineral magnetism and diffuse reflectance spectroscopy of river terrace palaeosols: A new form of geoproxy data for the southern African interior. *Quaternary Science Reviews*, 95: 43–59, https://doi.org/10.1016/j.quascirev.2014.04.021.

Macias, F. and Chesworth, W. 1992. Chapter 12 - Weathering in humid regions, with emphasis on igneous rocks and their metamorphic equivalents. In Martini, I.P. and Chesworth, W. (Eds), Developments in Earth Surface Processes, pp. 283–306. Elsevier, https://doi.org/10.1016/B978-0-444-89198-3.50017-9..

Mack, G. 1981. Composition of modern stream sand in a humid climate derived from a low-grade metamorphic and sedimentary foreland fold-thrust belt of North Georgia. *Journal of Sedimentary Petrology*, 51 (4): 1247–1258.

Macklin, M.G. and Lewin, J. 2003. River sediments, great floods and centennial-scale Holocene climate change. *Journal of Quaternary Science*, 18 (2): 101–105, https://doi.org/10.1002/jqs.751.

Macklin, M.G., Booth, J., Brewer, P.A., Tooth, S. and Duller, G.A.T. 2022. How have Cretan rivers responded to late Holocene uplift? A multi-millennial, multi-catchment field experiment to

evaluate the applicability of Schumm and Parker's (1973) complex response model. *Earth Surface Processes and Landforms*, 47 (9): 2178–2197, https://doi.org/https://doi.org/10.1002/esp.5370.

Macklin, M.G., Lewin, J. and Woodward, J.C. 2012. The fluvial record of climate change. *Philosophical Transactions of the Royal Society A: Mathematical, Physical and Engineering Sciences*, 370 (1966): 2143–2172, https://doi.org/10.1098/rsta.2011.0608.

Macron, C., Pohl, B., Richard, Y. and Bessafi, M. 2014. How do tropical temperate troughs form and develop over Southern Africa? *Journal of Climate*, 27 (4): 1633–1647, https://doi.org/10.1175/JCLI-D-13-00175.1.

Malusà, M.G., Carter, A., Limoncelli, M., Villa, I.M. and Garzanti, E. 2013. Bias in detrital zircon geochronology and thermochronometry. *Chemical Geology*, 359: 90–107, https://doi.org/10.1016/j.chemgeo.2013.09.016.

Malusà, M.G., Resentini, A. and Garzanti, E. 2016. Hydraulic sorting and mineral fertility bias in detrital geochronology. *Gondwana Research*, 31: 1–19, https://doi.org/10.1016/j.gr.2015.09.002.

Marais, E., Scott, L., Gil-Romera, G. and Carrión, J.S. 2015. The potential of palynology in fossil bat-dung from Arnhem Cave, Namibia. *Transactions of the Royal Society of South Africa*, 70 (2): 109–115, https://doi.org/10.1080/0035919X.2014.999734.

Marker, M.E. 1977. Aspects of the geomorphology of the Kuiseb River, South West Africa. *Madoqua*, 10 (3): 199–206.

Marker, M.E. and Muller, D. 1978. Relict vlei silts of the middle Kuiseb River valley, South West Africa. *Madoqua*, 11 (2): 151–162.

Marsaglia, K.M. and Ingersoll, R. V. 1992. Compositional trends in arc-related, deep-marine sand and sandstone: a reassessment of magmatic-arc provenance. *Geological Society of America Bulletin*, 104 (12): 1637–1649, https://doi.org/10.1130/0016-7606(1992)104<1637:CTIARD>2.3.CO,2.

Marsh, J.S., Erlank, A.J. and Duncan, A.R. 1991. Preliminary geochemical data for dolerite dykes and sills of the southern part of the Etendeka Igneous Province. *Communications of the Geological Survey Namibia*, 7: 71–73.

Marsh, J.S., Ewart, A., Milner, S.C., Duncan, A.R. and Miller, R.M.G. 2001. The Etendeka Igneous Province: Magma types and their stratigraphic distribution with implications for the evolution of the Paraná-Etendeka flood basalt province. *Bulletin of Volcanology*, 62 (6–7): 464–486, https://doi.org/10.1007/s004450000115.

Martin, H. 1953. Notes on the Dwyka succession and on some pre-Dwyka valleys in South West Africa. *Transactions of the geological society of South Africa*, 56: 37–41.

Maslin, M.A. and Christensen, B. 2007. Tectonics, orbital forcing, global climate change, and human evolution in Africa: introduction to the African paleoclimate special volume. *Journal of Human*

Evolution, 53 (5): 443–464, https://doi.org/10.1016/j.jhevol.2007.06.005.

Masson-Delmotte, V., Kageyama, M., Braconnot, P., Charbit, S., Krinner, G., Ritz, C., Guilyardi, E., Jouzel, J., Abe-Ouchi, A., Crucifix, M., Gladstone, R.M., Hewitt, C.D., Kitoh, A., LeGrande, A.N., Marti, O., Merkel, U., Motoi, T., Ohgaito, R., Otto-Bliesner, B., Peltier, W.R., Ross, I., Valdes, P.J., Vettoretti, G., Weber, S.L., Wolk, F. and Yu, Y. 2006. Past and future polar amplification of climate change: Climate model intercomparisons and ice-core constraints. *Climate Dynamics*, 26 (5): 513–529, https://doi.org/10.1007/s00382-005-0081-9.

Masson-Delmotte, V., Schulz, M., Abe-Ouchi, A., Beer, J., Ganopolski, A., Gonzalez Rouco, J.F., Jansen, E., Lambeck, K., Luterbacher, J., Naish, T., Osborn, T., OttoBliesner, B., Quinn, T., Ramesh, R., Rojas, M., Shao, X. and Timmermann, A. 2013. Information from paleoclimate archives. In Climate Change 2013: The Physical Science Basis. Contribution of Working Group I to the Fifth Assessment Report of the Intergovernmental Panel on Climate Change, Cambridge University Press, Cambridge, United Kingdom and New York, NY, USA.

Mather, A.E., Stokes, M. and Whitfield, E. 2017. River terraces and alluvial fans: The case for an integrated Quaternary fluvial archive. *Quaternary Science Reviews*, 166: 74–90, https://doi.org/10.1016/j.quascirev.2016.09.022.

Matmon, A., Hidy, A.J., Vainer, S., Crouvi, O., Fink, D., Erel, Y., Horwitz, L.K. and Chazan, M. 2015. New chronology for the southern Kalahari Group sediments with implications for sediment-cycle dynamics and early hominin occupation. *Quaternary Research*, 84 (1): 118–132, https://doi.org/10.1016/j.yqres.2015.04.009.

Mavimbela, S.S.W. and van Rensburg, L.D. 2017. Characterizing infiltration and internal drainage of South African dryland soils. *Earth Surface Processes and Landforms*, 42 (3): 414–425, https://doi.org/10.1002/esp.3991.

Mayaud, J.R., Bailey, R.M. and Wiggs, G.F.S. 2017. A coupled vegetation/sediment transport model for dryland environments. *Journal of Geophysical Research: Earth Surface*, 122 (4): 875–900, https://doi.org/10.1002/2016JF004096.

Mazor, E., Verhagen, B.T., Sellschop, J.P.F., Jones, M.T., Robins, N.E., Hutton, L. and Jennings, C.M.H. 1977. Northern Kalahari groundwaters: hydrologic, isotopic and chemical studies at Orapa, Botswana. *Journal of Hydrology*, 34: 203–234.

McCall, G.S., Marks, T.P., Thomas, J.T., Eller, M., Horn, S.W.I., Horowitz, R. a., Kettler, K. and Taylor-Perryman, R. 2011. Erb tanks: A Middle and Later Stone Age rockshelter in the Central Namib Desert, Western Namibia. *PaleoAnthropology*, 398–421, https://doi.org/10.4207/PA.2011.ART67.

McCarthy, T.S. and Ellery, W.N. 1998. The Okavango Delta. *Transactions of the Royal Society of South Africa*, 53(2): 157–182, https://doi.org/10.1080/00359199809520384.

Mccarthy, T.S., Ellery, W.N. and Stanistreet, I.G. 1992. Avulsion mechanisms on the Okavango fan, Botswana: the control of a fluvial system by vegetation. *Sedimentology*, 39: 779–795.

Mccarthy, T.S., Stanistreet, I.G. and Cairncross, B. 1991. The sedimentary dynamics of active fluvial channels on the Okavango fan, Botswana. *Sedimentology*, 38: 471–487.

Mccarthy, T.S. and Tooth, S. 2004. Incised meanders along the mixed bedrock-alluvial Orange River, Northern Cape Province, South Africa. *Zeitschrift für Geomorphologie Supplementary Issues*, 48 (3): 273–292.

McGee, D., Donohoe, A., Marshall, J. and Ferreira, D. 2014. Changes in ITCZ location and cross-equatorial heat transport at the Last Glacial Maximum, Heinrich Stadial 1, and the mid-Holocene. *Earth and Planetary Science Letters*, 390: 69–79, https://doi.org/10.1016/j.epsl.2013.12.043.

Medialdea, A., Thomsen, K.J., Murray, A.S. and Benito, G. 2014. Reliability of equivalent-dose determination and age-models in the OSL dating of historical and modern palaeoflood sediments. *Quaternary Geochronology*, 22: 11–24, https://doi.org/10.1016/j.quageo.2014.01.004.

Mejdahl, V. 1979. Thermoluminescence dating: Beta-dose 1: 61–72.

Mendelsohn, J., Jarvis, A., Roberts, C. and Robsertson, T. 2002. *Atlas of Namibia: A portrait of the land and its people*. David Philip Publishers, Cape Town, South Africa.

Merifield, P.M. 1987. Mapping desert alluvial deposits from satellite imagery. In Berkofsky, L. and Wurtele, M.G. (Eds), Progress in Desert Research, pp. 198–216. Rowman and Littlefield, New Jersey.

Messager, M.L., Lehner, B., Cockburn, C., Lamouroux, N., Pella, H., Snelder, T., Tockner, K., Trautmann, T., Watt, C. and Datry, T. 2021. Global prevalence of non-perennial rivers and streams. *Nature*, 594 (7863): 391–397, https://doi.org/10.1038/s41586-021-03565-5.

Metzger, M.J., Bunce, R.G.H., Jongman, R.H.G., Sayre, R., Trabucco, A. and Zomer, R. 2013. A high-resolution bioclimate map of the world: A unifying framework for global biodiversity research and monitoring. *Global Ecology and Biogeography*, 22 (5): 630–638, https://doi.org/10.1111/geb.12022.

Mhopjeni, K. 2006. Mineralisation in the northern part of the Khoabendus Group, NW Namibia. University of Stellenbosch, Cape Town, South Africa.

Miall, A.D. 1978. Lithofacies types and vertical profile models in braided river deposits: a summary. *Fluvial Sedimentology*, 5: 597–600.

Miall, A.D. 1985. Architectural-element analysis: A new method of facies analysis applied to fluvial deposits. *Earth-Science Reviews*, 22: 261–308, https://doi.org/10.1016/0012-8252(85)90001-7.

Miall, A.D. 2006. *Geology of Fluvial deposits, Sedimentary facies, Basin Analysis, and Pertoleum Geology 4th corrected printing*.

Miall, A.D. 2014. *Fluvial depositional systems*. Cham: Springer International Publishing.

Middleton, N.J. and Thomas, D.S.G. 1997. *World Atlast of Desertification*. 2nd editio. UNE/Edward

Arnold, London.

Milan, D.J., Tooth, S. and Heritage, G.L. 2020. Topographic, hydraulic, and vegetative controls on bar and island development in mixed bedrock-alluvial, multichanneled, dryland Rivers. *Water Resources Research*, 56 (5): 1–23, https://doi.org/10.1029/2019WR026101.

Millennium Ecosystem Assessment, M. 2005. Ecosystems and human well-being: wetlands and water. World Resources Institute: Washington, DC.

Miller, R. 1983. The Pan-African Damara Orogen of S. W. Africa, Namibia. *Special Publication of the Geological Society of South Africa*, 11: 431–515.

Miller, R. 2008. *The Geology of Namibia*. Ministry of Mines and Energy, Windhoek.

Milly, P.C.D. and Dunne, K.A. 2020. Colorado River flow dwindles as warming-driven loss of reflective snow energizes evaporation. *Science*, 367 (6483): 1252–1255, https://doi.org/10.1126/science.aax0194.

Milly, P.C.D., Wetherald, R.T., Dunne, K.A. and Delworth, T.L. 2002. Increasing risk of great floods in a changing climate. *Nature*, 415 (6871): 514–517, https://doi.org/10.1038/415514a.

Mirzabaev, A., Wu, J., Evans, J., García-Oliva, F., Hussein, I.A.., Iqbal, M.H., Kimutai, J., Knowles, T., Meza, F. and Nedjraoui, D. 2019. Desertification. In Shukla, P.R., Skea, J., Calvo Buendia, E., Masson-Delmotte, V., Pörtner, H.., Roberts, D.. and Zhai, P. (Eds), Climate Change and Land: an IPCC special report on climate change, desertification, land degradation, sustainable land management, food security, and greenhouse gas fluxes in terrestrial ecosystems.

Mix, A.C., Bard, E. and Schneider, R. 2001. Environmental processes of the ice age: Land, oceans, glaciers (EPILOG). *Quaternary Science Reviews*, 20 (4): 627–657, https://doi.org/10.1016/S0277-3791(00)00145-1.

Miyamoto, S. 2010. Late Pleistocene sedimentary environment of the “Homeb Silts” deposits , along the middle Kuiseb River in the Namib Desert, Namibia. *African Study Monographs Suppl* 40: 51–66.

Modisi, M.P., Atekwana, E.A., Kampunzu, A.B. and Ngwisanyi, T.H. 2000. Rift kinematics during the incipient stages of continental extension: Evidence the nascent Okavango rift basin, Northwest Botswana. *Geology*, 28 (10): 939–942, https://doi.org/10.1130/0091-7613(2000)28<939:RKDTIS>2.0.CO,2.

Morin, E., Grodek, T., Dahan, O., Benito, G., Kulls, C., Jacoby, Y., Langenhove, G. Van, Seely, M. and Enzel, Y. 2009. Flood routing and alluvial aquifer recharge along the ephemeral arid Kuiseb River, Namibia. *Journal of Hydrology*, 368 (1–4): 262–275, https://doi.org/10.1016/j.jhydrol.2009.02.015.

Mueller, D., Jacobs, Z., Cohen, T.J., Price, D.M., Reinfelds, I. V. and Shulmeister, J. 2018. Revisiting an arid LGM using fluvial archives: a luminescence chronology for palaeochannels of the Murrumbidgee River, south-eastern Australia. *Journal of Quaternary Science*, 33 (7): 777–793,

https://doi.org/10.1002/jqs.3059.

Muhs, D.R., Swinehart, J.B., Loope, D.B., Been, J., Mahan, S.A. and Bush, C.A. 2000. Geochemical evidence for an eolian sand dam across the North and South Platte rivers in Nebraska. *Quaternary Research*, 53 (2): 214–222, https://doi.org/10.1006/qres.1999.2104.

Mujere, N., Masocha, M., Makurira, H. and Mazvimavi, D. 2021. Dynamics and scales of transmission losses in dryland river systems: a meta-analysis. *Australian Journal of Water Resources*, 1–15, https://doi.org/10.1080/13241583.2021.1996680.

Murray, A., Arnold, L., Buylaert, J.-P., Guérin, G., Qin, J., Singhvi, A., Smedley, R. and Thomsen, K. 2021. Optically stimulated luminescence dating using quartz. *Nature Reviews Methods Primers*, 1: 1–72.

Murray, A., Buylaert, J.P. and Thiel, C. 2015. A luminescence dating intercomparison based on a Danish beach-ridge sand. *Radiation Measurements*, 81: 32–38, https://doi.org/10.1016/j.radmeas.2015.02.012.

Murray, A.S. 1996. Developments in optically stimulated luminescence and photo-transferred thermoluminescence dating of young sediments: Application to a 2000-year sequence of flood deposits. *Geochimica et Cosmochimica Acta*, 60 (4): 565–576, https://doi.org/10.1016/0016-7037(95)00418-1.

Murray, A.S. and Wintle, A.G. 2000. Luminescence dating of quartz using an improved single-aliquot regenerative-dose protocol. *Radiation Measurements*, 1: 57–73, 2000, https://doi.org/10.1016/S1350-4487(99)00253-X.

Muvangua, E. 2006. Petrology and geochemistry of the Khoabendus Group and the Fransfontein Suite in the Kamanjab Area, northwestern Namibia. University of Stellenbosch.

Nanson, G., Tooth, S. and Knighton, A. 2002. A global perspective on dryland rivers: perceptions, misconceptions and distinctions. In Bull, L. and Kirkby, M. (Eds), Dryland Rivers: Hydrology and Geomorphology of Semi-Arid Channels, pp. 17–54. Wiley, Chichester.

Nanson, G.C., Chen, X.Y. and Price, D.M. 1995. Aeolian and fluvial evidence of changing climate and wind patterns during the past 100 ka in the western Simpson Desert, Australia. *Palaeogeography, Palaeoclimatology, Palaeoecology*, 1: 87–102, https://doi.org/10.1016/0031-0182(95)00064-S.

Nash, D.J., Meadows, M.E., Baxter, A.J., Shaw, P.A. and Gieske, A. 1997. Late Holocene sedimentation rates and geomorphological significance of the Ncamasere Valley, Okavango Delta, Botswana. *South African Geographical Journal*, 79(2): 93–100, https://doi.org/10.1080/03736245.1997.9713629.

Nash, D.J., Meadows, M.E. and Gulliver, V.L. 2006. Holocene environmental change in the Okavango Panhandle, northwest Botswana. *Quaternary Science Reviews*, 25 (11–12): 1302–1322, https://doi.org/10.1016/j.quascirev.2005.11.004.

Nathan, R.P., Thomas, P.J., Jain, M., Murray, A.S. and Rhodes, E.J. 2003. Environmental dose rate heterogeneity of beta radiation and its implications for luminescence dating: Monte Carlo modelling and experimental validation. *Radiation Measurements*, 37 (4–5): 305–313, https://doi.org/10.1016/S1350-4487(03)00008-8.

Niang, I., Ruppel, O.C., Abdrabo, M.A., Essel, A., Lennard, C., Padgham, J. and Urquhart, P. 2014. Africa. In Barros, V.R., Field, C.B., Dokken, D. j., Mastrandrea, M.D., Mach, K.J., Bilir, T.E., Chatterjee, M., Ebi, K.L., Estrada, Y.O., Genova, R.C. and Girma, B. (Eds), Climate Change 2014: Impacts, Adaptation, and Vulnerability. Part B: Regional Aspects. Contribution of Working Group II to the Fifth Assessment Report of the Intergovernmental Panel on Climate Change, pp. 1199–1265. Cambridge University Press, Cambridge.

Nicholson, S. 2018. The ITCZ and the seasonal cycle over equatorial Africa. *Bulletin of the American Meteorological Society*, 99 (2): 337–348, https://doi.org/10.1175/BAMS-D-16-0287.1.

Nicholson, S. and Entekhabi, D. 1987. Rainfall variability in equatorial and southern Africa: Relationships with sea surfacetemperatures along the southwestern coast of Africa. *Journal of Climate and Applied Meteorology*, 26: 561–578, https://www.jstor.org/stable/26183107.

Nicholson, S.E. 2000. The nature of rainfall variability over Africa on time scales of decades to millenia. *Global and Planetary Change*, 26 (1–3): 137–158, https://doi.org/10.1016/S0921-8181(00)00040-0.

Nicholson, S.E. 2009. A revised picture of the structure of the “monsoon” and land ITCZ over West Africa. *Climate Dynamics*, 32 (7–8): 1155–1171, https://doi.org/10.1007/s00382-008-0514-3.

Nicholson, S.E., Klotter, D. and Dezfuli, A.K. 2012. Spatial reconstruction of semi-quantitative precipitation fields over Africa during the nineteenth century from documentary evidence and gauge data. *Quaternary Research (United States)*, 78 (1): 13–23, https://doi.org/10.1016/j.yqres.2012.03..

Oksanen, J., Blanchet, F.G., Friendly, M., Kindt, R., Legendre, P., McGlinn, D., Minchin, P., O’Hara, R., Simpson, G., Solymos, P., Stevens, H., Szoecs, E. and Wagner, H. 2020. Package ‘vegan’, Community Ecology Package. https://cran.r-project.org/web/packages/vegan/vegan.pdf.

Oldknow, C.J., Carr, A.S., Hooke, J.M. and Shen, Z. 2020. The suitability of a low temperature post-IR IRSL signal for dating alluvial and colluvial “cut and fill” sequences in the Great Karoo, South Africa. *Quaternary Geochronology*, 58, https://doi.org/10.1016/j.quageo.2020.101064.

Oldknow, C.J. and Hooke, J.M. 2017. Alluvial terrace development and changing landscape connectivity in the Great Karoo, South Africa. Insights from the Wilgerbosch River catchment, Sneeuberg. *Geomorphology*, 288: 12–38, https://doi.org/10.1016/j.geomorph.2017.03.009.

Olley, J.M., Pietsch, T. and Roberts, R.G. 2004. Optical dating of Holocene sediments from a variety of geomorphic settings using single grains of quartz. *Geomorphology*, 60 (3–4): 337–358,

https://doi.org/10.1016/j.geomorph.2003.09.020.

Otto-Bliesner, B.L., Russell, J.M., Clark, P.U., Liu, Z., Overpeck, J.T., Konecky, B., Demenocal, P., Nicholson, S.E., He, F. and Lu, Z. 2014. Coherent changes of southeastern equatorial and northern African rainfall during the last deglaciation. *Science*, 346 (6214): 1223–1227, https://doi.org/10.1126/science.1259531.

Otto-Bliesner, B.L., Schneider, R., Brady, E.C., Kucera, M., Abe-Ouchi, A., Bard, E., Braconnot, P., Crucifix, M., Hewitt, C.D., Kageyama, M., Marti, O., Paul, A., Rosell-Melé, A., Waelbroeck, C., Weber, S.L., Weinelt, M. and Yu, Y. 2009. A comparison of PMIP2 model simulations and the MARGO proxy reconstruction for tropical sea surface temperatures at last glacial maximum. *Climate Dynamics*, 32 (6): 799–815, https://doi.org/10.1007/s00382-008-0509-0.

Paola, C., Hellert, P.L. and Angevinet, C.L. 1992. The large-scale dynamics of grain-size variation in alluvial basins, 1: Theory. *Basin Research*, 4: 73–90.

Paola, C., Straub, K., Mohrig, D. and Reinhardt, L. 2009. The "unreasonable effectiveness" of stratigraphic and geomorphic experiments. *Earth-Science Reviews*, 97 (1–4): 1–43, https://doi.org/10.1016/j.earscirev.2009.05.003.

Partridge, T.C., Demenocal, P.B., Lorentz, S.A., Paiker, M.J. and Vogel, J.C. 1997. Orbital forcing of climate over South Africa: A 200,000-year rainfall record from the Pretoria Saltpan. *Quaternary Science Reviews*, 16 (10): 1125–1133, https://doi.org/10.1016/S0277-3791(97)00005-X.

Patricola, C.M. and Cook, K.H. 2007. Dynamics of the West African monsoon under mid-Holocene precessional forcing: Regional climate model simulations. *Journal of Climate*, 20 (4): 694–716, https://doi.org/10.1175/JCLI4013.1.

Pausata, F.S.R., Gaetani, M., Messori, G., Berg, A., Maia de Souza, D., Sage, R.F. and deMenocal, P.B. 2020. The Greening of the Sahara: Past Changes and Future Implications. *One Earth*, 2 (3): 235–250, https://doi.org/10.1016/j.oneear.2020.03.002.

Peate, D.W. 1997. The Paraná-Etendeka province. *Geophysical Monograph Series*, 217–245, https://doi.org/10.1029/GM100p0217.

Peel, M.C., Finlayson, B.L. and McMahon, T.A. 2007. Updated world map of the Koppen-Geiger climate classification. *Hydrology and Earth System Sciences*, 11: 1633–1644.

Perez-Sanz, A., Li, G., González-Sampériz, P. and Harrison, S.P. 2014. Evaluation of modern and mid-Holocene seasonal precipitation of the Mediterranean and northern Africa in the CMIP5 simulations. *Climate of the Past*, 10 (2): 551–568, https://doi.org/10.5194/cp-10-551-2014.

Perren, B.B., Hodgson, D.A., Roberts, S.J., Sime, L., Van Nieuwenhuyze, W., Verleyen, E. and Vyverman, W. 2020. Southward migration of the Southern Hemisphere westerly winds corresponds with warming climate over centennial timescales. *Communications Earth & Environment*, 1 (1): 1–8,

https://doi.org/10.1038/s43247-020-00059-6.

Pettijohn, F., Potter, P.E. and Siever, R. 1987. Petrography of common sands and sandstones. In Sand and Sandstone, pp. 139–213. Springer, New York, https://doi.org/10.1007/978-1-4615-9974-6_6.

Phillips, J. 1995. Self-organization and landscape evolution. *Progress in Physical Geography*, 19 (3): 309–321.

Phillips, J.D. 2009. Changes, perturbations, and responses in geomorphic systems. *Progress in Physical Geography*, 33 (1): 17–30, https://doi.org/10.1177/0309133309103889.

Pierce, D. 2019. Interface to Unidata netCDF (Version 4 or Earlier) Format Data Files. http://cirrus.ucsd.edu/~pierce/ncdf.

Pinot, S., Ramstein, G., Harrison, S.P., Prentice, I.C., Guiot, J., Stute, M. and Joussaume, S. 1999. Tropical paleoclimates at the Last Glacial Maximum: Comparison of Paleoclimate Modeling Intercomparison Project (PMIP) simulations and paleodata. *Climate Dynamics*, 15 (11): 857–874, https://doi.org/10.1007/s003820050318.

Prave, A. 1996. Tale of three cratons: Tectonostratigraphic anatomy of the Damara orogen in northwestern Namibia and the assembly of Gondwana. *Geology*, 24: 1115–1118.

Preusser, F., Chithambo, M.L., Götte, T., Martini, M., Ramseyer, K., Sendezera, E.J., Susino, G.J. and Wintle, A.G. 2009. Quartz as a natural luminescence dosimeter. *Earth-Science Reviews*, 97 (1–4): 184–214, https://doi.org/10.1016/j.earscirev.2009.09.006.

Preusser, F., Degering, D., Fuchs, M., Hilgers, A., Kadereit, A., Klasen, N., Krbetschek, M., Richter, D. and Spencer, J.Q.G. 2008. Luminescence dating: basics, methods and applications. *Quaternary Science Journal*, 57 (1-2): 95–149, https://doi.org/10.3285/eg.57.1-2.5.

Preusser, F. and Kasper, H. 2001. Comparison of dose rate determination using high-resolution gamma spectrometry and inductively coupled plasma-mass spectrometry. *Ancient TL*, 1: 19–23, 2001.

Pryor, W.A. and Hester, N.C. 1969. X-ray diffraction analysis of heavy minerals. *Journal of Sedimentary Petrology*, 39: 1384–1389.

Railsback, L.B., Brook, G.A., Liang, F., Marais, E., Cheng, H. and Edwards, R.L. 2016. A multi-proxy stalagmite record from northwestern Namibia of regional drying with increasing global-scale warmth over the last 47kyr: The interplay of a globally shifting ITCZ with regional currents, winds, and rainfall. *Palaeogeography, Palaeoclimatology, Palaeoecology*, 461: 109–121, https://doi.org/10.1016/j.palaeo.2016.08.014.

Ramisch, A., Bens, O., Buylaert, J.P., Eden, M., Heine, K., Hürkamp, K., Schwindt, D. and Völkel, J. 2017. Fluvial landscape development in the southwestern Kalahari during the Holocene – Chronology and provenance of fluvial deposits in the Molopo Canyon. *Geomorphology*, 281: 94–107, https://doi.org/10.1016/j.geomorph.2016.12.021.

Reason, C.J.C. 2017. *Climate of Southern Africa*. https://oxfordre.com/view/10.1093/acrefore/9780190228620.001.0001/acrefore-9780190228620-e-513.

Reason, C.J.C., Landman, W. and Tennant, W. 2006. Seasonal to decadal prediction of southern African climate and its links with variability of the Atlantic ocean. *Bulletin of the American Meteorological Society*, 87 (7): 941–955, https://doi.org/10.1175/BAMS-87-7-941.

Reason, C.J.C., Rouault, M., Melice, J.L. and Jagadheesha, D. 2002. Interannual winter rainfall variability in SW South Africa and large scale ocean-atmosphere interactions. *Meteorology and Atmospheric Physics*, 80 (1–4): 19–29, https://doi.org/10.1007/s007030200011.

Refaat, A.A. and Hamdan, M.A. 2015. Mineralogy and grain morphology of the aeolian dune sand of Toshka area, southeastern Western Desert, Egypt. *Aeolian Research*, 243–254, https://doi.org/10.1016/j.aeolia.2015.04.006.

Reid, I. 1994. River landforms and sediments: Evidence of climatic change. In Abrahams, A. and Parsons, A. (Eds), Geomorphology of Desert Environments, pp. 571–592. Springer, Dordrecht.

Reid, I. 2009. River landforms and sediments: Evidence of climatic change. In Parsons, A. and Abrahams, A. (Eds), Geomorphology of Desert Environments, pp. 695–721.

Reid, I. and Frostick, L.E. 1987. Flow dynamics and suspended sediment properties in arid zone flash floods. *Hydrological Processes*, 1 (3): 239–253, https://doi.org/10.1002/hyp.3360010303.

Reid, I. and Frostick, L.E. 1997. Channel form, flows and sediments in deserts. In Thomas, D.S.G. (Ed), Arid Zone Geomorphology: Process, Form and Change in Drylands, pp. 205–229. Wiley, Chichester.

Reid, I. and Frostick, L.E. 2011. Channel form, flows and sediments of endogenous ephemeral rivers in deserts. In Thomas, D.S.G. (Ed), Arid Zone Geomorphology: Process, Form and Change in Drylands, pp. 301–332. Chichester: Wiley-Blackwell.

Renne, P.R., Glen, J.M., Milner, S.C. and Duncan, A.R. 1996. Age of Etendeka flood volcanism and associated intrusions in southwestern Africa. *Geology*, 24 (7): 659–662, https://doi.org/10.1130/0091-7613(1996)024<0659:AOEFVA>2.3.CO,2.

Resentini, A., Goren, L., Castelltort, S. and Garzanti, E. 2017. Partitioning sediment flux by provenance and tracing erosion patterns in Taiwan. *Journal of Geophysical Research: Earth Surface*, 122 (7): 1430–1454, https://doi.org/10.1002/2016JF004026.

Rey, F., Gobet, E., Szidat, S., Lotter, A., Gilli, A., Hafner, A. and Tinner, W. 2019. Radiocarbon wiggle matching on laminated sediments delivers high-precision chronologies 61 (1): 265–285, https://doi.org/10.1017/RDC.2018.47.

Rhodes, E. and Schwenninger, J. 2007. Dose rates and radioisotope concentrations in the concrete calibration blocks at Oxford. *Ancient TL*, 25 (1): 5–8.

Rhodes, E.J. 2011. Optically stimulated luminescence dating of sediments over the past 200,000 years, https://doi.org/10.1146/annurev-earth-040610-133425.

Rifkin, R.F., Prinsloo, L.C., Dayet, L., Haaland, M.M., Henshilwood, C.S., Diz, E.L., Moyo, S., Vogelsang, R. and Kambombo, F. 2016. Characterising pigments on 30000-year-old portable art from Apollo 11 Cave, Karas Region, southern Namibia. *Journal of Archaeological Science: Reports*, 5: 336–347, https://doi.org/10.1016/j.jasrep.2015.11.028.

Rittenour, T.M. 2008. Luminescence dating of fluvial deposits: Applications to geomorphic, palaeoseismic and archaeological research. *Boreas*, 37 (4): 613–635, https://doi.org/10.1111/j.1502-3885.2008.00056.x.

Rittenour, T.M., Goble, R.J. and Blum, M.D. 2003. *An optical age chronology of Late Pleistocene fluvial deposits in the northern lower Mississippi valley*. *Quaternary Science Reviews*, 10–13: 1105–1110, https://doi.org/10.1016/S0277-3791(03)00041-6.

Roberts, H.M. 2012. Testing Post-IR IRSL protocols for minimising fading in feldspars, using Alaskan loess with independent chronological control. *Radiation Measurements*, 47 (9): 716–724, https://doi.org/10.1016/j.radmeas.2012.03.022.

Roberts, R.G., Galbraith, R.F., Olley, J.M., Yoshida, H. and Laslett, G.M. 1999. Optical dating of single and multiple grains of quartz from Jinmium rock shelter, northern Australia: Part II, results and implications. *Archaeometry*, 41 (2): 365–395, https://doi.org/10.1111/j.1475-4754.1999.tb00988.x.

Rodell, M., Famiglietti, J.S., Wiese, D.N., Reager, J.T., Beaudoing, H.K., Landerer, F.W. and Lo, M.H. 2018. Emerging trends in global freshwater availability. *Nature*, 557 (7707): 651–659, https://doi.org/10.1038/s41586-018-0123-1.

Romans, B.W., Castelltort, S., Covault, J.A., Fildani, A. and Walsh, J.P. 2016. Environmental signal propagation in sedimentary systems across timescales. *Earth-Science Reviews*, 153: 7–29, https://doi.org/10.1016/j.earscirev.2015.07.012.

Rotstayn, L.D., Collier, M.A., Dix, M.R., Feng, Y., Gordon, H.B., O'Farrell, S.P., Smith, I.N. and Syktus, J. 2010. Improved simulation of Australian climate and ENSO-related rainfall variability in a global climate model with an interactive aerosol treatment. *International Journal of Climatology*, 30 (7): 1067–1088, https://doi.org/10.1002/joc.1952.

Rouault, M., Florenchie, P., Fauchereau, N. and Reason, C.J.C. 2003. South East tropical Atlantic warm events and southern African rainfall. *Geophysical Research Letters*, 30 (5): 1–4, https://doi.org/10.1029/2002GL014840.

Rouault, M., White, S.A., Reason, C.J.C., Lutjeharms, J.R.E. and Jobard, I. 2002. Ocean-atmosphere interaction in the Agulhas Current region and a South African extreme weather event. *Weather and Forecasting*, 17 (4): 655–669, https://doi.org/10.1175/1520-

0434(2002)017<0655:OAIITA>2.0.CO,2.

Rowell, A. 2016. Sand ramps as late Quaternary palaeoenvironmental archives: analysis from Southern Africa [PhD thesis]. University of Oxford.

Rowell, A., Thomas, D.S.G., Bailey, R., Stone, A., Garzanti, E. and Padoan, M. 2017. Controls on sand ramp formation in southern Namibia. *Earth Surface Processes and Landforms*, https://doi.org/10.1002/esp.4159.

Rubey, W. 1933. The size-distribution of heavy minerals within a water-laid sandstone. *Journal of Sedimentary Petrology*, 3 (1): 3–29.

Rust, B. and Nanson, G. 1989. Bedload transport of mud as pedogenic aggregates in modern and ancient rivers. *Sedimentology*, 36: 291–306.

Rust, U. 1999. River-end deposits along the Hoanib River, northern Namib: archives of Late Holocene climatic variation on a subregional scale. *South African Journal of Science*, 95: 205–208.

Rust, U. and Weinecke, F. 1974. Studies on Gramadulla Formation in the middle part of the Kuiseb River. *Madoqua*, 3: 5–15.

Saylor, B., Grotzinger, J. and Germs, G. 1995. Sequence stratigraphy and sedimentology of the Neoproterozoic Kuibis and Swarzrand Subgroups (Nama Group), southwestern Namibia. *Precambrian Research*, 73: 153–171.

Schefuß, E., Schouten, S. and Schneider, R.R. 2005. Climatic controls on central African hydrology during the past 20,000 years. *Nature*, 437 (7061): 1003–1006, https://doi.org/10.1038/nature03945.

Scherler, D., Lamb, M.P., Rhodes, E.J. and Avouac, J.P. 2016. Climate-change versus landslide origin of fill terraces in a rapidly eroding bedrock landscape: San Gabriel River, California. *Bulletin of the Geological Society of America*, 128 (7): 1228–1248, https://doi.org/10.1130/B31356.1.

Schewe, J., Heinke, J., Gerten, D., Haddeland, I., Arnell, N.W., Clark, D.B., Dankers, R., Eisner, S., Fekete, B.M., Colón-González, F.J., Gosling, S.N., Kim, H., Liu, X., Masaki, Y., Portmann, F.T., Satoh, Y., Stacke, T., Tang, Q., Wada, Y., Wisser, D., Albrecht, T., Frieler, K., Piontek, F., Warszawski, L. and Kabat, P. 2014. Multimodel assessment of water scarcity under climate change. *Proceedings of the National Academy of Sciences of the United States of America*, 111 (9): 3245–3250, https://doi.org/10.1073/pnas.1222460110.

Schmidt, G.A., Kelley, M., Nazarenko, L., Ruedy, R., Russell, G.L., Aleinov, I., Bauer, M., Bauer, S.E., Bhat, M.K., Bleck, R., Canuto, V., Chen, Y., Cheng, Y., Clune, T.L., Genio, A. Del, Fainchtein, R. De, Faluvegi, G., Hansen, J.E., Healy, R.J., Kiang, N.Y., Koch, D., Lacis, A.A., Legrande, A.N., Lerner, J., Lo, K.K., Matthews, E.E., Menon, S., Miller, R.L., Oinas, V. and Oloso, A.O. 2014. Configuration and assessment of the GISS ModelE2 contributions to the CMIP5 archive. *Journal of Advances in Modeling Earth Systems*, 6: 141–184, https://doi.org/10.1002/2013MS000265.Received.

Scholz, H. 1972. The soils of the central Namib desert with special consideration of the soils in the vicinity of Gobabeb. *Madoqua*, 1972 (1): 33–51, https://journals.co.za/content/madoqua/2/1/AJA10115498_45#abstract_content%0Ahttps://hdl.handle.net/10520/AJA10115498_45.

Schuiling, R.D., De Meijer, R.J., Riezebos, H.J. and Scholten, M.J. 1985. Grain size distribution of different minerals in a sediment as a function of their specific density. *Geologie en Mijnbouw*, 64: 199–203.

Schüller, I., Belz, L., Wilkes, H. and Wehrmann, A. 2018. Late Quaternary shift in southern African rainfall zones: Sedimentary and geochemical data from Kalahari pans. *Zeitschrift fur Geomorphologie*, 61 (4): 339–362, https://doi.org/10.1127/zfg/2018/0556.

Schulter, T. 2008. *Geological Atlas of Africa*. Springer, Heidelberg.

Schumm, S.A. 1977. *The fluvial system*. New York, NY: Wiley-Interscience.

Scott, L., Cooremans, B., De Wet, J.S. and Vogel, J.C. 1991. Holocene environmental changes in Namibia inferred from pollen analysis of swamp and lake deposits. *Holocene*, 1 (1): 8–13, https://doi.org/10.1177/095968369100100103.

Scott, L., Gil Romera, G., Marais, E. and Brook, G.A. 2018. Pollen in fossil hyrax dung from Marine Isotope Stages 2 and 3 reveals past environments in Namibia. *Quaternary International*, 464: 260–272, https://doi.org/10.1016/j.quaint.2017.06.054.

Scott, L., Marais, E. and Brook, G.A. 2004. Fossil hyrax dung and evidence of Late Pleistocene and Holocene vegetation types in the Namib Desert. *Journal of Quaternary Science*, 19(8): 829–832, https://doi.org/10.1002/jqs.870.

Scott, L., Neumann, F.H., Brook, G.A., Bousman, C.B., Norström, E. and Metwally, A.A. 2012. Terrestrial fossil-pollen evidence of climate change during the last 26 thousand years in Southern Africa. *Quaternary Science Reviews*, 32: 100–118, https://doi.org/10.1016/j.quascirev.2011.11.010.

Selby, M.J., Hendy, C.H. and Seely, M.K. 1979. The late Quaternary lake in the central Namib Desert, southern Africa, and some implications. *Palaeogeography, Palaeoclimatology, Palaeoecology*, 26: 37–41.

Seth, B., Kröner, A., Mezger, K., Nemchin, A.A., Pidgeon, R.T. and Okrusch, M. 1998. Archaean to Neoproterozoic magmatic events in the Kaoko belt of NW Namibia and their geodynamic significance. *Precambrian Research*, 92 (4): 341–363, https://doi.org/10.1016/S0301-9268(98)00086-2.

Shanahan, T.M., Mckay, N.P., Hughen, K.A., Overpeck, J.T., Otto-Bliesner, B., Heil, C.W., King, J., Scholz, C.A. and Peck, J. 2015. The time-transgressive termination of the African humid period. *Nature Geoscience*, 8 (2): 140–144, https://doi.org/10.1038/ngeo2329.

Sharon, D. 1974. The spatial pattern of convective rainfall in Sukumaland, Tanzani - A statistical analysis.

Archiv für Meteorologie, Geophysik und Bioklimatologie Serie B, 22 (3): 201–218, https://doi.org/10.1007/BF02243468.

Shaw, A. and Goudie, A. 2002. Geomorphological evidence for the extension of the mega-kalahari into south-central angola. *South African Geographical Journal*, 84 (2): 182–194, https://doi.org/10.1080/03736245.2002.9713769.

Shaw, P.A., Thomas, D.S.G. and Nash, D.J. 1992. Late Quaternary fluvial activity in the dry valleys (mekgacha) of the Middle and Southern Kalahari, southern Africa. *Journal of Quaternary Science*, 7 (4): 273–281, https://doi.org/10.1002/jqs.3390070402.

Shi, N., Dupont, L.M., Beug, H.J. and Schneider, R. 1998. Vegetation and climate changes during the last 21 000 years in S.W. Africa based on a marine pollen record. *Vegetation History and Archaeobotany*, 7 (3): 127–140, https://doi.org/10.1007/BF01374001.

Shi, N., Schneider, R., Beug, H.J. and Dupont, L.M. 2001. Southeast trade wind variations during the last 135 kyr: Evidence from pollen spectra in eastern South Atlantic sediments. *Earth and Planetary Science Letters*, 187 (3–4): 311–321, https://doi.org/10.1016/S0012-821X(01)00267-9.

Singarayer, J.S. and Burrough, S.L. 2015. Interhemispheric dynamics of the African rainbelt during the late Quaternary. *Quaternary Science Reviews*, 124: 48–67, https://doi.org/10.1016/j.quascirev.2015.06.021.

Singarayer, J.S., Valdes, P.J. and Roberts, W.H.G. 2017. Ocean dominated expansion and contraction of the late Quaternary tropical rainbelt. *Scientific Reports*, 7 (1): 1–9, https://doi.org/10.1038/s41598-017-09816-8.

Sletten, H.R., Railsback, L.B., Liang, F., Brook, G.A., Marais, E., Hardt, B.F., Cheng, H. and Edwards, R.L. 2013. A petrographic and geochemical record of climate change over the last 4600years from a northern Namibia stalagmite, with evidence of abruptly wetter climate at the beginning of southern Africa's Iron Age. *Palaeogeography, Palaeoclimatology, Palaeoecology*, 376: 149–162, https://doi.org/10.1016/j.palaeo.2013.02.030.

Small, D., Clark, C.D., Chiverrell, R.C., Smedley, R.K., Bateman, M.D., Duller, G.A.T., Ely, J.C., Fabel, D., Medialdea, A. and Moreton, S.G. 2017. Devising quality assurance procedures for assessment of legacy geochronological data relating to deglaciation of the last British-Irish Ice Sheet. *Earth-Science Reviews*, 164: 232–250, https://doi.org/10.1016/j.earscirev.2016.11.007.

Smedley, R. and Skirrow, G.K. 2019. Luminescence dating in fluvial sediments: overcoming the challenge of partial bleaching. *Geography of the Physical Environment*, https://doi.org/10.1007/978-3-030-23315-0_8.

Smedley, R.K., Buylaert, J.P. and Újvári, G. 2019. Comparing the accuracy and precision of luminescence ages for partially-bleached sediments using single grains of K-feldspar and quartz. *Quaternary*

Geochronology, 53: 101007, https://doi.org/10.1016/j.quageo.2019.101007.

Smith, R.J., Singarayer, J.S. and Mayle, F.E. 2022. Response of Amazonian forests to mid-Holocene drought: A model-data comparison. *Global Change Biology*, 28 (1): 201–226, https://doi.org/10.1111/gcb.15929.

Smith, R.M.H., Mason, T.R. and Ward, J.D. 1993. Flash-flood sediments and ichnofacies of the Late Pleistocene Homeb Silts, Kuiseb River, Namibia. *Sedimentary Geology*, 85 (1–4): 579–599, https://doi.org/10.1016/0037-0738(93)90103-C.

Sneh, A. 1983. Desert stream sequences in the Sinai Peninsula. *Journal of Sedimentary Research*, 53 (4): 1271–1279.

Srivastava, P., Brook, G.A. and Marais, E. 2004. A record of fluvial aggradation in the northern Namib Desert margin during the Late Pleistocene–Holocene. *Zeitschrift für Geomorphologie, Supplementary Issues*, 133: 1–18.

Srivastava, P., Brook, G.A. and Marais, E. 2005. Depositional environment and luminescence chronology of the Hoarusib River Clay Castles sediments, northern Namib Desert, Namibia. *Catena*, 59 (2): 187–204, https://doi.org/10.1016/j.catena.2004.06.003.

Srivastava, P., Brook, G.A., Marais, E., Morthekai, P. and Singhvi, A.K. 2006. Depositional environment and OSL chronology of the Homeb silt deposits, Kuiseb River, Namibia. *Quaternary Research*, 65 (3): 478–491, https://doi.org/10.1016/j.yqres.2006.01.010.

Stager, J.C., Ryves, D.B., Chase, B.M. and Pausata, F.S.R. 2011. Catastrophic drought in the Afro-Asian monsoon region during Heinrich Event 1. *Science*, 331 (6022): 1299–1302, https://doi.org/10.1126/science.1198322.

Stanistreet, I.G. and McCarthy, T.S. 1993. The Okavango Fan and the classification of subaerial fan systems. *Sedimentary Geology*, 85 (1–4): 115–133.

Stanistreet, I.G. and Stollhofen, H. 1999. Onshore equivalents of the main Kudu gas reservoir in Namibia. *Geological Society Special Publication*, 153: 345–365, https://doi.org/10.1144/GSL.SP.1999.153.01.21.

Stanistreet, I.G. and Stollhofen, H. 2002. Hoanib River flood deposits of Namib Desert interdunes as analoques for thin permeability barrier mudstone layers in aeolianite reservoirs. *Sedimentology*, 49 (4): 719–736, https://doi.org/10.1046/j.1365-3091.2002.00458.x.

Stengel, I. and Leser, H. 2004. Late Quaternary valley-fill terraces and palaeoenvironments of the Huns River, Southern Namibia. *Die Erde*, 135: 129–149.

Stokes, M., Mather, A.E., Belfoul, M., Faik, F., Bouzid, S., Geach, M.R., Cunha, P.P., Boulton, S.J. and Thiel, C. 2017. Controls on dryland mountain landscape development along the NW Saharan desert margin: Insights from Quaternary river terrace sequences (Dadès River, south-central High Atlas,

Morocco). *Quaternary Science Reviews*, 166: 363–379, https://doi.org/10.1016/j.quascirev.2017.04.017.

Stollhofen, H. and Stanistreet, I.G. 1994. Interaction between bimodal volcanism, fluvial sedimentation and basin development in the Permo-Carboniferous Saar-Nahe Basin (south-west Germany). *Basin Research*, 6 (4): 245–267, https://doi.org/10.1111/j.1365-2117.1994.tb00088.x.

Stone, A. 2021. Dryland dunes and other dryland environmental archives as proxies for late Quaternary stratigraphy and environmental and climate change in southern Africa. *South African Journal of Geology*, 124 (4): 927–962, https://doi.org/10.25131/sajg.124.0055.

Stone, A.E.C. 2014. Last Glacial Maximum conditions in southern Africa: Are we any closer to understanding the climate of this time period? *Progress in Physical Geography*, 38 (5): 519–542, https://doi.org/10.1177/0309133314528943.

Stone, A.E.C. and Bailey, R.M. 2012. The effect of single grain luminescence characteristics on single aliquot equivalent dose estimates. *Quaternary Geochronology*, 11: 68–78, https://doi.org/10.1016/j.quageo.2012.03.014.

Stone, A.E.C. and Thomas, D.S.G. 2008. Linear dune accumulation chronologies from the southwest Kalahari, Namibia: challenges of reconstructing late Quaternary palaeoenvironments from aeolian landforms. *Quaternary Science Reviews*, 27 (17–18): 1667–1681, https://doi.org/10.1016/j.quascirev.2008.06.008.

Stone, A.E.C. and Thomas, D.S.G. 2013. Casting new light on late Quaternary environmental and palaeohydrological change in the Namib Desert: A review of the application of optically stimulated luminescence in the region. *Journal of Arid Environments*, 93: 40–58, https://doi.org/10.1016/j.jaridenv.2012.01.009.

Stone, A.E.C., Thomas, D.S.G. and Viles, H.A. 2010. Late Quaternary palaeohydrological changes in the northern Namib Sand Sea: New chronologies using OSL dating of interdigitated aeolian and water-lain interdune deposits. *Palaeogeography, Palaeoclimatology, Palaeoecology*, 288 (1–4): 35–53, https://doi.org/10.1016/j.palaeo.2010.01.032.

Stone, A.E.C., Viles, H.A., Thomas, L. and Van Calsteren, P. 2010. Can ^{234}U-^{230}Th dating be used to date large semi-arid tufas? Challenges from a study in the Naukluft Mountains, Namibia. *Journal of Quaternary Science*, 25 (8): 1360–1372, https://doi.org/10.1002/jqs.1435.

Strunk, A., Olsen, J., Sanei, H., Rudra, A. and Larsen, N.K. 2020. Improving the reliability of bulk sediment radiocarbon dating. *Quaternary Science Reviews*, 242: 106442, https://doi.org/10.1016/j.quascirev.2020.106442.

Stute, M. and Talma, A.S. 1998. Glacial temperatures and moisture transport regimes reconstructed from noble gases and d18O, Stampriet aquifer, Namibia. Isotope techniques in the study of

environmental change. *Proceedings of a Symposium Vienna*, 307–318.

Stuut, J.B.W., Prins, M.A., Schneider, R.R., Weltje, G.J., Fred Jansen, J.H. and Postma, G. 2002. A 300-kyr record of aridity and wind strength in southwestern Africa: Inferences from grain-size distributions of sediments on Walvis Ridge, SE Atlantic. *Marine Geology*, 180 (1–4): 221–233, https://doi.org/10.1016/S0025-3227(01)00215-8.

Svensen, H., Corfu, F., Polteau, S., Hammer, Ø. and Planke, S. 2012. Rapid magma emplacement in the Karoo Large Igneous Province. *Earth and Planetary Science Letters*, 325–326: 1–9, https://doi.org/10.1016/j.epsl.2012.01.015.

Taljaard, J. 1996. Atmospheric circulation systems, synoptic climatology and weather phenomena of South Africa. Part 6: Rainfall in South Africa. In South African Weather Bureau. Technical Paper 32.

Taljaard, J.J. 1972. Synoptic meteorology of the Southern Hemisphre. *American Meteorological Society*, 139–213.

Tankard, A.J. and Rogers, J. 1978. Late Cenozoic palaeoenvironments on the west coast of southern Africa. *Journal of Biogeography*, 5 (4): 319, https://doi.org/10.2307/3038026.

Taylor, K.E., Stouffer, R.J. and Meehl, G.A. 2012. An overview of CMIP5 and the experiment design. *Bulletin of the American Meteorological Society*, 93 (4): 485–498, https://doi.org/10.1175/BAMS-D-11-00094.1.

Telfer, M.W. 2011. Growth by extension, and reworking, of a south-western Kalahari linear dune. *Earth Surface Processes and Landforms*, 36 (8): 1125–1135, https://doi.org/10.1002/esp.2140.

Telfer, M.W. and Thomas, D.S.G. 2007. Late Quaternary linear dune accumulation and chronostratigraphy of the southwestern Kalahari: implications for aeolian palaeoclimatic reconstructions and predictions of future dynamics. *Quaternary Science Reviews*, 26 (19–21): 2617–2630, https://doi.org/10.1016/j.quascirev.2007.07.006.

Telfer, M.W., Thomas, D.S.G., Parker, A.G., Walkington, H. and Finch, A.A. 2009. Optically Stimulated Luminescence (OSL) dating and palaeoenvironmental studies of pan (playa) sediment from Witpan, South Africa. *Palaeogeography, Palaeoclimatology, Palaeoecology*, 273 (1–2): 50–60, https://doi.org/10.1016/j.palaeo.2008.11.012.

Teller, J.T. and Lancaster, N. 1986. Lacustrine sediments at Narabeb in the central Namib desert, Namibia. *Palaeogeography, Palaeoclimatology, Palaeoecology*, 56: 177–195.

Teller, J.T., Rutter, N. and Lancaster, N. 1990. Sedimentology and paleohydrology of Late Quaternary lake deposits in the northern Namib Sand Sea, Namibia. *Quaternary Science Reviews*, 9 (4): 343–364, https://doi.org/10.1016/0277-3791(90)90027-8.

Thomas, D.S.G. 2011. Arid environments: their nature and extent. In Thomas, D.S.G. (Ed), Arid Zone Geomorphology: Process, Form and Change in Drylands, pp. 3–16. Chichester: Wiley-Blackwell.

Thomas, D.S.G. 2013. Reconstructing paleoenvironments and palaeoclimates in drylands: What can landform analysis contribute? *Earth Surface Processes and Landforms*, 38 (1): 3–16, https://doi.org/10.1002/esp.3190.

Thomas, D.S.G. 2019. Quaternary Climate Variation in Southern Africa. *Oxford Research Encyclopedia of Climate Science*, https://doi.org/10.1093/acrefore/9780190228620.013.527.

Thomas, D.S.G. and Bailey, R.M. 2017. Is there evidence for global-scale forcing of Southern Hemisphere Quaternary desert dune accumulation? A quantitative method for testing hypotheses of dune system development. *Earth Surface Processes and Landforms*, 42 (14): 2280–2294, https://doi.org/10.1002/esp.4183.

Thomas, D.S.G. and Burrough, S.L. 2012. Interpreting geoproxies of late Quaternary climate change in African drylands: Implications for understanding environmental change and early human behaviour. *Quaternary International*, 253: 5–17, https://doi.org/10.1016/j.quaint.2010.11.001.

Thomas, D.S.G. and Burrough, S.L. 2016. Luminescence-based dune chronologies in southern Africa: Analysis and interpretation of dune database records across the subcontinent. *Quaternary International*, 410: 30–45, https://doi.org/10.1016/j.quaint.2013.09.008.

Thomas, D.S.G., Durcan, J.A., Dansie, A. and Wiggs, G.F.S. 2017. Holocene fluvial valley fill sources of atmospheric mineral dust in the Skeleton Coast, Namibia. *Earth Surface Processes and Landforms*, 42 (12): 1884–1894, https://doi.org/10.1002/esp.4151.

Thomas, D.S.G., O'Connor, P.W., Bateman, M.D., Shaw, P.A., Stokes, S. and Nash, D.J. 2000. Dune activity as a record of late Quaternary aridity in the Northern Kalahari: New evidence from northern Namibia interpreted in the context of regional arid and humid chronologies. *Palaeogeography, Palaeoclimatology, Palaeoecology*, 156 (3–4): 243–259, https://doi.org/10.1016/S0031-0182(99)00143-1.

Thomas, D.S.G. and Shaw, P.A. 1991. *The Kalahari environment*. Cambridge University Press, Cambridge.

Thomas, D.S.G. and Shaw, P.A. 2002. Late Quaternary environmental change in central southern Africa: New data, synthesis, issues and prospects. *Quaternary Science Reviews*, 21 (7): 783–797, https://doi.org/10.1016/S0277-3791(01)00127-5.

Thomsen, K.J., Murray, A. and Jain, M. 2012. The dose dependency of the over-dispersion of quartz OSL single grain dose distributions. *Radiation Measurements*, 47 (9): 732–739, https://doi.org/10.1016/j.radmeas.2012.02.015.

Thomsen, K.J., Murray, A.S., Bøtter-Jensen, L. and Kinahan, J. 2007. Determination of burial dose in incompletely bleached fluvial samples using single grains of quartz. *Radiation Measurements*, 42 (3): 370–379, https://doi.org/10.1016/j.radmeas.2007.01.041.

Thomsen, K.J., Murray, A.S., Jain, M. and Bøtter-Jensen, L. 2008. Laboratory fading rates of various

luminescence signals from feldspar-rich sediment extracts. *Radiation Measurements*, 43 (9–10): 1474–1486, https://doi.org/10.1016/j.radmeas.2008.06.002.

Tierney, J.E., Pausata, F.S.R. and De Menocal, P.B. 2017. Rainfall regimes of the green Sahara. *Science Advances*, 3 (1): 1–10, https://doi.org/10.1126/sciadv.1601503.

Timar-Gabor, A., Buylaert, J., Guralnik, B., Tranda, O., Hao, Q. and Wintle, A.G. 2017. On the importance of grain size in luminescence dating using quartz. 106: 464–471, https://doi.org/10.1016/j.radmeas.2017.01.009.

Tjallingii, R., Claussen, M., Stuut, J.B.W., Fohlmeister, J., Jahn, A., Bickert, T., Lamy, F. and Röhl, U. 2008. Coherent high- and low-latitude control of the northwest African hydrological balance. *Nature Geoscience*, 1 (10): 670–675, https://doi.org/10.1038/ngeo289.

Todd, M. and Washington, R. 1998. Extreme daily rainfall in southern African and Southwest Indian Ocean tropical-temperate links. *Southern African Journal of Science*, 94: 64–70.

Todd, M.C., Washington, R. and Palmer, P.I. 2004. Water vapour transport associated with tropical-temperate trough systems over southern Africa and the southwest Indian Ocean. *International Journal of Climatology*, 24 (5): 555–568, https://doi.org/10.1002/joc.1023.

Tofelde, S., Bernhardt, A., Guerit, L. and Romans, B.W. 2021. Times associated with source-to-sink propagation of environmental signals during landscape transience. *Frontiers in Earth Science*, 9: 1–26, https://doi.org/10.3389/feart.2021.628315.

Toonen, W.H.J., Foulds, S.A., Macklin, M.G. and Lewin, J. 2017. Events, episodes, and phases: Signal from noise in flood-sediment archives. *Geology*, 45 (4): 331–334, https://doi.org/10.1130/G38540.1.

Tooth, S. 2000a. Process, form and change in dryland rivers: A review of recent research. *Earth Science Reviews*, 51(1–4): 67–107, https://doi.org/10.1016/S0012-8252(00)00014-3.

Tooth, S. 2000b. Downstream changes in dryland river channels: The Northern Plains of arid central Australia. *Geomorphology*, 34 (1–2): 33–54, https://doi.org/10.1016/S0169-555X(99)00130-0.

Tooth, S. 2013. Dryland fluvial environments: assessing distinctiveness and diversity from a global perspective. In Schroder, J. and Wohl, E. (Eds), *Treatise on Geomorphology*, pp. 612–644. Academic Press, San Diego, CA, https://doi.org/10.1016/j..

Tooth, S. 2016. Changes in fluvial systems during the Quaternary. *Quaternary Environmental Change in Southern Africa: Physical and Human Dimensions*, 170–187, https://doi.org/10.1017/CBO9781107295483.011.

Tooth, S., Brandt, D., Hancox, P.J. and McCarthy, T.S. 2004. Geological controls on alluvial river behaviour: A comparative study of three rivers on the South African Highveld. *Journal of African Earth Sciences*, 38 (1): 79–97, https://doi.org/10.1016/j.jafrearsci.2003.08.003.

Tooth, S., Hancox, P.J., Brandt, D., McCarthy, T.S., Jacobs, Z. and Woodborne, S. 2013. Controls on the

genesis, sedimentary architecture, and preservation potential of dryland alluvial successions in stable continental interiors: insights from the incising Modder River, South Africa. *Journal of Sedimentary Research*, 83 (7): 541–561, https://doi.org/10.2110/jsr.2013.46.

Tooth, S.,McCarthy, T.S., Rodnight, H., Keen-Zebert, A., Rowberry, M. and Brandt, D. 2014. Late Holocene development of a major fluvial discontinuity in floodplain wetlands of the Blood River, eastern South Africa. *Geomorphology*, 205: 128–141, https://doi.org/10.1016/j.geomorph.2011.12.045.

Tooth, S., McCarthy, T.S., Duller, G.A.T., Assine, M.L., Wolski, P. and Coetzee, G. 2022. Significantly enhanced mid Holocene fluvial activity in a globally important, arid-zone wetland: The Okavango Delta, Botswana. *Earth Surface Processes and Landforms*, 1–18, https://doi.org/10.1002/esp.5289.

Tooth, S. and Nanson, G. 2000. Equilibrium and nonequilibrium conditions in dryland rivers. *Physical Geography*, 21 (3): 183–211.

Tooth, S. and Nanson, G.C. 2011. Distinctiveness and diversity of arid zone river systems. In Thomas, D.S.G. (Ed), Arid Zone Geomorphology: Process, Form and Change in Drylands, pp. 269–300. Chichester: Wiley-Blackwell.

Toro-escobar, C.M., Parker, G. and Paola, C. 1997. Transfer function for the deposition of poorly sorted gravel in response to streambed aggradation. *Journal of Hydraulic Research/De Recherches Hydrauliques*, 35 (4): 563–566, https://doi.org/10.1080/00221689709498411.

Torrance, J.D. 1979. Upper windflow patterns in relation to rainfall in south-east central Africa. *Weather*, 34 (3): 106–115, https://doi.org/10.1002/j.1477-8696.1979.tb03418.x.

Trabucco, A. and Zomer, R. 2022. Global Aridity Index and Potential Evapotranspiration (ET0) Climate Database v3. figshare. Dataset. https://doi.org/https://doi.org/10.6084/m9.figshare.7504448.v4.

Trampush, S.M., Hajek, E.A., Straub, K.M. and Chamberlin, E.P. 2017. Identifying autogenic sedimentation in fluvial-deltaic stratigraphy: Evaluating the effect of outcrop-quality data on the compensation statistic. *Journal of Geophysical Research: Earth Surface*, 122 (1): 91–113, https://doi.org/10.1002/2016JF004067.

Trisos, C., Adelekan, I., Ayanlade, A., Efitre, J. and Gemeda, A. 2021. Chapter 9: Africa. In IPCC WGII Sixth Assessment Report.

Tucker, G.E., Arnold, L., Bras, R.L., Flores, H., Istanbulluoglu, E. and Sólyom, P. 2006. Headwater channel dynamics in semiarid rangelands, Colorado high plains, USA. *Bulletin of the Geological Society of America*, 118 (7–8): 959–974, https://doi.org/10.1130/B25928.1.

Tyson, P. 1986. *Climatic change and variability in southern Africa*. Oxford University Press.

Tyson, P.D. and Preston-Whyte, R.A. 2000. *The Weather and Climate of Southern Africa*. Second Edi. Oxford University Press.

Ukkola, A.M., Prentice, I.C., Keenan, T.F., Van Dijk, A.I.J.M., Viney, N.R., Myneni, R.B. and Bi, J. 2016. Reduced streamflow in water-stressed climates consistent with CO_2 effects on vegetation. *Nature Climate Change*, 6 (1): 75–78, https://doi.org/10.1038/nclimate2831.

UNEP. 1992. *World Atlas of Desertification*. Edward Arnold: London.

Vainer, S., Matmon, A., Erel, Y., Hidy, A.J., Crouvi, O., De Wit, M., Geller, Y., Aumaître, G., Bourlès, D.L. and Keddadouche, K. 2021. Landscape responses to intraplate deformation in the Kalahari constrained by sediment provenance and chronology in the Okavango Basin. *Basin Research*, 33 (2): 1170–1193, https://doi.org/10.1111/bre.12509.

Vickery, K.J., Eckardt, F.D. and Bryant, R.G. 2013. A sub-basin scale dust plume source frequency inventory for southern Africa, 2005-2008. *Geophysical Research Letters*, 40 (19): 5274–5279, https://doi.org/10.1002/grl.50968.

Viles, H. 2011. Weathering systems. In Thomas, D.S.G. (Ed), Arid Zone Geomorphology: Process, Form and Change in Drylands, pp. 85–101. Chichester: Wiley-Blackwell.

Viles, H.A., Taylor, M.P., Nicoll, K. and Neumann, S. 2007. Facies evidence of hydroclimatic regime shifts in tufa depositional sequences from the arid Naukluft Mountains, Namibia. *Sedimentary Geology*, 195 (1–2): 39–53, https://doi.org/10.1016/j.sedgeo.2006.07.007.

Viseras, C., Henares, S., Yeste, L.M. and Garcia-Garcia, F. 2018. Reconstructing the architecture of ancient meander belts by compiling outcrop and subsurface data: A Triassic example. *Fluvial Meanders and their Sedimentary Products in the Rock Record*, 419–444.

Vogel, J.C. 1989. Evidence of past climate change in the Namib Desert. *Elsevier Science Publishers B.V*, 70: 355–366, https://ac.els-cdn.com/0031018289901132/1-s2.0-0031018289901132-main.pdf?_tid=3b76079a-f384-46b4-b390-0b6245b18b51&acdnat=1521418979_5c3de5af6d9248e71e65b3df6f50e08b.

Vogel, J.C. and Rust, U. 1987. Environmental changes in the Kaokoland Namib Desert during the present millennium. *Madoqua*, 15: 5–16.

Vogel, J.C. and Visser, E. 1981. Pretoria radiocarbon dates II. *Radiocarbon* 23(1): 43–80.

Vogelsang, R., Richter, J., Jacobs, Z., Eichhorn, B., Linseele, V. and Roberts, R.G. 2010. New excavations of Middle Stone Age deposits at Apollo 11 rockshelter, Namibia: Stratigraphy, archaeology, chronology and past environments. *Journal of African Archaeology*, 8 (2): 185–218, https://doi.org/10.3213/1612-1651-10170.

Voldoire, A., Sanchez-Gomez, E., Salas y Mélia, D., Decharme, B., Cassou, C., Sénési, S., Valcke, S., Beau, I., Alias, A., Chevallier, M., Déqué, M., Deshayes, J., Douville, H., Fernandez, E., Madec, G., Maisonnave, E., Moine, M.P., Planton, S., Saint-Martin, D., Szopa, S., Tyteca, S., Alkama, R., Belamari, S., Braun, A., Coquart, L. and Chauvin, F. 2013. The CNRM-CM5.1 global climate model:

Description and basic evaluation. *Climate Dynamics*, 40 (9–10): 2091–2121, https://doi.org/10.1007/s00382-011-1259-y.

Völkel, J., Bens, O., Eden, M., Krauß, L., Murray, A.S. and Heine, K. 2021. Fluvial sediments and playa deposits of the Naukluft mts. Foreland and Tsauchab Valley, Namibia – new insights from key sections in the late Quaternary landscape and climate change in Southern Africa. *Zeitschrift fur Geomorphologie*, 62 (4): 313–350, https://doi.org/10.1127/zfg/2021/0705.

Vörösmarty, C.J., Douglas, E.M., Green, P.A. and Revenga, C. 2005. Geospatial indicators of emerging water stress: An application to Africa. *Ambio*, 34 (3): 230–236, https://doi.org/10.1579/0044-7447-34.3.230.

Wainwright, J. and Bracken, L. 2011. Runoff generation, overland flow and erosion on hillslopes. In Thomas, D.S.G. (Ed), Arid Zone Geomorphology: Process, Form and Change in Drylands, pp. 237–267. Wiley-Blackwell.

Wallinga, J. 2002. Optically stimulated luminescence dating of fluvial deposits: a review. *Boreas*, 31: 303–322.

Walsh, E., Caracciolo, L., Ravidà, D., Burrough, S. and Thomas, D.S.G. 2022. Holocene fluvial depositional regimes of the Huab River, Skeleton Coast, Namibia. *Earth Surface Processes and Landforms*, 1–25, https://doi.org/10.1002/esp.5349.

Walsh, E., Burrough, S. and Thomas, D.S.G. In Review. A chronological database assessing the palaeo-environmental record from fluvial sediments in southwestern Africa. *Earth-Science Reviews.*

Walsh, E., Thomas, D.S.G., Burrough, S. In Review. Model – archive comparison of mid-Holocene and Last Glacial Maximum climates in central southwestern Africa. *Quaternary Science Reviews.*

Wang, B. and Ding, Q. 2008. Global monsoon: Dominant mode of annual variation in the tropics. *Dynamics of Atmospheres and Oceans*, 44 (3–4): 165–183, https://doi.org/10.1016/j.dynatmoce.2007.05.002.

Wang, L., D'Odorico, P., Evans, J.P., Eldridge, D.J., McCabe, M.F., Caylor, K.K. and King, E.G. 2012. Dryland ecohydrology and climate change: Critical issues and technical advances. *Hydrology and Earth System Sciences*, 16 (8): 2585–2603, https://doi.org/10.5194/hess-16-2585-2012.

Watanabe, S., Hajima, T., Sudo, K., Nagashima, T., Takemura, T., Okajima, H., Nozawa, T., Kawase, H., Abe, M., Yokohata, T., Ise, T., Sato, H., Kato, E., Takata, K., Emori, S. and Kawamiya, M. 2011. MIROC-ESM 2010: Model description and basic results of CMIP5-20c3m experiments. *Geoscientific Model Development*, 4 (4): 845–872, https://doi.org/10.5194/gmd-4-845-2011.

Van De Wiel, M.J. and Coulthard, T.J. 2010. Self-organized criticality in river basins: Challenging sedimentary records of environmental change. *Geology*, 38 (1): 87–90, https://doi.org/10.1130/G30490.1.

Williams, M.A.J., Pal, J.N., Jaiswal, M. and Singhvi, A.K. 2006. River response to Quaternary climatic fluctuations: evidence from the Son and Belan valleys, north-central India. *Quaternary Science Reviews*, 25 (19–20): 2619–2631, https://doi.org/10.1016/j.quascirev.2005.07.018.

Wintle, A.G. 1973. Anomalous fading of thermoluminescence in mineral samples. *Nature*, 245: 143–144.

Wintle, A.G. and Murray, A.S. 2006. A review of quartz optically stimulated luminescence characteristics and their relevance in single-aliquot regeneration dating protocols. *Radiation Measurements*, 4: 369–391, https://doi.org/10.1016/j.radmeas.2005.11.001.

De Wit, M. and Stankiewicz, J. 2006. Changes in surface water supply across Africa with predicted climate change. *Science*, 311 (5769): 1917–1921, https://doi.org/10.1126/science.1119929.

Woillez, M.N., Levavasseur, G., Daniau, A.L., Kageyama, M., Urrego, D.H., Sánchez-Goñi, M.F. and Hanquiez, V. 2014. Impact of precession on the climate, vegetation and fire activity in southern Africa during MIS4. *Climate of the Past*, 10 (3): 1165–1182, https://doi.org/10.5194/cp-10-1165-2014.

Woodward, J.C., Tooth, S., Brewer, P.A. and Macklin, M.G. 2010. The 4th International Palaeoflood Workshop and trends in palaeoflood science. *Global and Planetary Change*, 1–4, https://doi.org/10.1016/j.gloplacha.2009.11.002.

Woodward, J.C., Williams, M.A.J., Garzanti, E., Macklin, M.G. and Marriner, N. 2015. From source to sink: Exploring the Quaternary history of the Nile. *Quaternary Science Reviews*, 130: 3–8, https://doi.org/10.1016/j.quascirev.2015.10.022.

Woor, S., Buckland, C., Parton, A. and Thomas, D.S.G. 2022. Assessing the robustness of geochronological records from the Arabian Peninsula: A new synthesis of the last 20ka. *Global and Planetary Change*, https://doi.org/10.1016/j.gloplacha.2022.103748.

Wright, D.K. 2017. Accuracy vs. precision: Understanding potential errors from radiocarbon dating on African landscapes. *African Archaeological Review*, 34 (3): 303–319, https://doi.org/10.1007/s10437-017-9257-z.

Wu, T., Li, W., Ji, J., Xin, X., Li, L., Wang, Z., Zhang, Y., Li, J., Zhang, F., Wei, M., Shi, X., Wu, F., Zhang, L., Chu, M., Jie, W., Liu, Y., Wang, F., Liu, X., Li, Q., Dong, M., Liang, X., Gao, Y. and Zhang, J. 2013. Global carbon budgets simulated by the Beijing Climate Center Climate System Model for the last century. *Journal of Geophysical Research Atmospheres*, 118 (10): 4326–4347, https://doi.org/10.1002/jgrd.50320.

Xie, J., Coulthard, T.J. and McLelland, S.J. 2022. Modelling the impact of seismic triggered landslide location on basin sediment yield, dynamics and connectivity. *Geomorphology*, 398: 108029, https://doi.org/10.1016/j.geomorph.2021.108029.

Xu, J., Yang, J. and Yan, Y. 2006. Erosion and sediment yields as influenced by coupled eolian and fluvial

processes: The Yellow River, China. *Geomorphology*, 1–2: 1–15, https://doi.org/10.1016/j.geomorph.2005.03.012.

Yamagata, K. and Mizuno, K. 2005. Landform development along the middle course of hte Kuiseb river in the Namib desert, Namibia. *African Study Monographs*, 30 (15–25).

Yukimoto, S., Yoshimura, H., Hosaka, M., Sakami, T., Tsujino, H., Hirabara, M., Tanaka, T.Y., Deushi, M., Obata, A., Nakano, H., Adachi, Y., Shindo, E., Yabu, S., Ose, T. and Kitoh, A. 2011. Meteorological Research Institute Earth System Model Version 1 (MRI-ESM1): Model Description. *Meteorological Research Institute*, 64: 88.

Zawada, P.K. 1994. Palaeoflood hydrology of the Buffels River, Laingsburg, South Africa: was the 1981 flood the largest? *South African Journal of Geology*, 97 (1): 21–32.

Zawada, P.K., Hattingh, J., Van Bladeren, D. 2000. Paleoflood hydrological analysis of selected South African rivers. *Memoir of the Council for Geoscience, South Africa*, 87: 173.

Zimmer, M.A., Kaiser, K.E., Blaszczak, J.R., Zipper, S.C., Hammond, J.C., Fritz, K.M., Costigan, K.H., Hosen, J., Godsey, S.E., Allen, G.H., Kampf, S., Burrows, R.M., Krabbenhoft, C.A., Dodds, W., Hale, R., Olden, J.D., Shanafield, M., DelVecchia, A.G., Ward, A.S., Mims, M.C., Datry, T., Bogan, M.T., Boersma, K.S., Busch, M.H., Jones, C.N., Burgin, A.J. and Allen, D.C. 2020. Zero or not? Causes and consequences of zero-flow stream gage readings. *Wiley Interdisciplinary Reviews: Water*, 1–25, https://doi.org/10.1002/wat2.1436.

van Zinderen Bakker, E.M. 1967. Upper Pleistocene and Holocene stratigraphy and ecology on the basis of vegetation changes in sub-Saharan Africa. In Bishop, W. and Clark, J. (Eds), Background to Evolution in Africa, pp. 125–147. University of Chicago Press.

van Zinderen Bakker, E.M. 1976. The evolution of Late Quaternary palaeoclimates of southern Africa. *Palaeoecology of Africa*, 9: 160–202.

Zuffa, G. 1985. Optical analyses of arenites: influence of methodology on compositional results. In Zuffa, G. (Ed), Provenance of Arenites, pp. 165–189. D. Reidel Publishing Company.

Appendices

Appendix A – Author contributions

The majority of the research conducted for this thesis was my own (EW), however, a small proportion was contributed by the co-authors of the three papers. Author contributions for each of these papers are detailed below.

Paper 1 (Chapter 4)

Sampling in the Huab River, Namibia, in September 2018 was conducted by EW and David Thomas (DT) with the assistance of Baoli Liu (BL). Laboratory sample preparation for luminescence dating was conducted by EW after guidance from Sallie Burrough (SB). Laboratory analysis for ICP-MS and grain size analysis were undertaken by EW. Heavy mineral separation, analysis of mineralogy using Raman laser spectroscopy, and analysis of petrographic thin sections using optical microscopy were conducted by EW after guidance from Luca Caracciolo (LC). Domenico Ravidà (DR) assisted with construction of the stratigraphic log following discussion with EW and using photos and field sketches of detailed sections produced by EW and DT. Interpretation of the stratigraphic log was undertaken by EW and DR. All authors contributed to discussions on interpretation of results. The original full draft of the paper was written by EW. The paper was reviewed and edited by LC, DR, SB, and DT.

Paper 2 (Chapter 5)

The construction and analysis of the database was undertaken by EW. SB and DT assisted in the formulation of the database structure. The original full draft of the paper was written by EW and was reviewed and edited by SB and DT.

Paper 3 (Chapter 6)

EW conducted the analysis of palaeoclimate model outputs and the compilation of palaeoproxy data. DT and SB contributed to the planning of this analysis and guided interpretation of the results. The original full draft of the paper was written by EW and was reviewed and edited by DT and SB.

Appendix B – Initial study of the Huns River valley fill, southern Namibia

Appendix B presents initial luminescence ages, compositional analysis of heavy mineral assemblages, and grain size analysis of samples from the Huns River, southern Namibia. Range finder samples were collected during fieldwork in September 2018 and a second field season was planned for May 2020 to collect a more extensive suite of samples to characterise the depositional history of the valley fill deposits. Due to COVID-19, it was not possible to return to the site, so a focus of this thesis was on interpretation of the Huab River archive (Chapter 4) in the context of regional records (Chapters 5 and 6), and the Huns results have not been fully interpreted. Unpublished ages from samples collected by Eugene Marais and George Brook in 2011 are also available from the deposits and the results from both investigations are presented here.

1. Setting

The Huns River is a tributary of the Fish River, southern Namibia (Figure B1, Figure B2). Exposed valley fill sediments at a site within this system were investigated by Stengel and Leser (2004). This site is located in close proximity to Apollo 11 cave, a key site of archaeological importance (Rifkin *et al.* 2016; Vogelsang *et al.* 2010), meaning that the palaeoenvironmental interpretations from these deposits have potential implications for understanding the conditions that sustained human occupation in the region. Currently, the climate at this site is dominated by rainfall during the austral summer, yet results from existing analysis of stratigraphy, carbonate content, vegetation associations and grain size indicate evidence of past climate conditions quite different to those that prevail today (Stengel and Leser, 2004). Stengel and Leser (2004) interpret sedimentary deposits as evidence of an increased contribution from westerly derived rainfall in the winter months, and of decreased seasonality and development of a wetland environment that sustained vegetation.

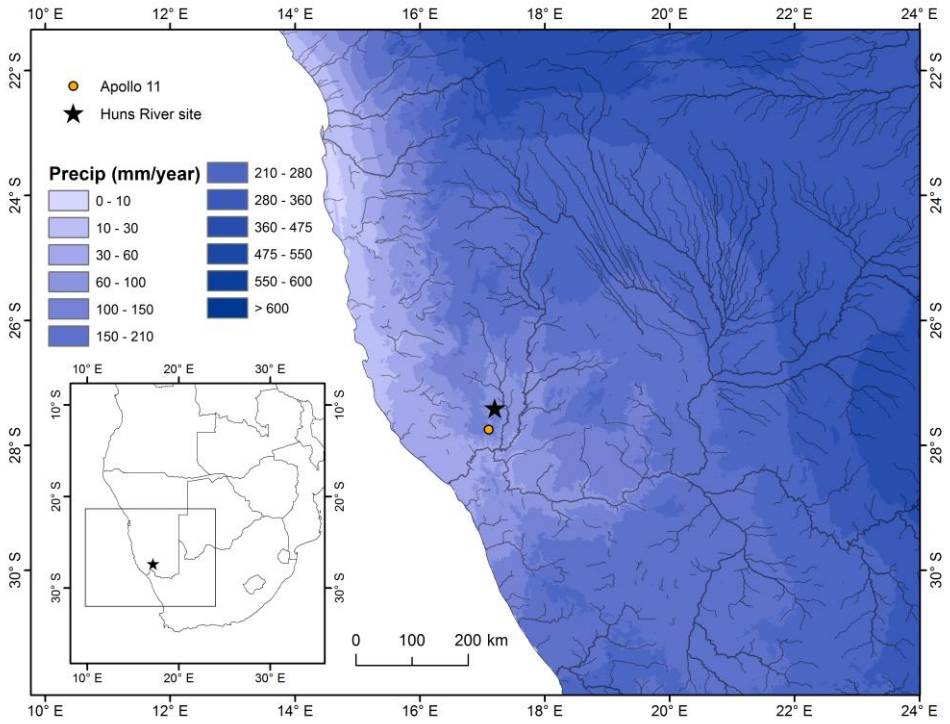

Figure B1. Climate setting of southern Namibia and western South Africa (Mendelsohn *et al*., 2002, data sourced from Project E1 – Atlas of Namibia). Location of Huns valley fill and Apollo 11 site described in the text.

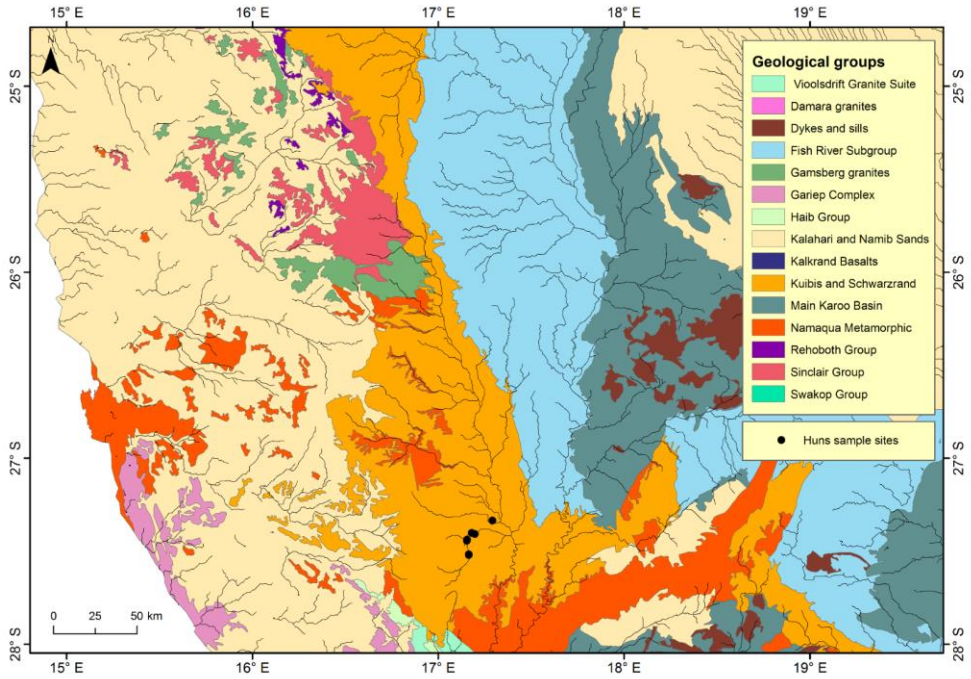

Figure B2. Geological setting of southern Namibia (Mendelsohn *et al*., 2002, data sourced from Project E1 – Atlas of Namibia). Huns valley fill sampling sites detailed in black.

To date, published chronological control for these deposits is provided by only one radiocarbon age (Stengel and Leser, 2004): 30.9 ± 0.5 cal ka BP (uncal ^{14}C age: 26.9 ± 0.3 ka BP). This dates fluvial deposition to the last glacial period, coincident with Late Middle Stone Age (MSA) sequences in Apollo 11 Cave dated to ~ 30 ka BP (Jacobs *et al.*, 2008; Vogelsang *et al.*, 2010). Extensive sediment deposition is preserved across the valley, yet from Stengel and Leser's age alone it is not possible to determine whether the entirety of valley fill sediments were deposited during this period, or whether this site contains a longer history of fluvial activity.

The objectives of this study are to i) reconstruct the timing of sediment deposition in the Huns valley fill at multiple sections, ii) analyse the grain size distributions to characterise the depositional conditions, and iii) analyse the heavy mineral assemblage to interrogate potential source regions.

2. Methods

2.1. Sample site collection

Eight samples were collected during fieldwork in 2018 (Walsh and Thomas; NAM18) and chronological data are available from a further ten samples collected during fieldwork in 2011 (Marais and Brook; HUNS11). Sites of sample collection include the section studied by Stengel and Leser (2004), sedimentary units preserved upstream, and sedimentary units along the adjacent Konkeip tributary (Figures B3 and B4, Table B1). The following description of methodological approaches focuses on the NAM18 samples and a brief description of the methods used for the HUNS11 is provided.

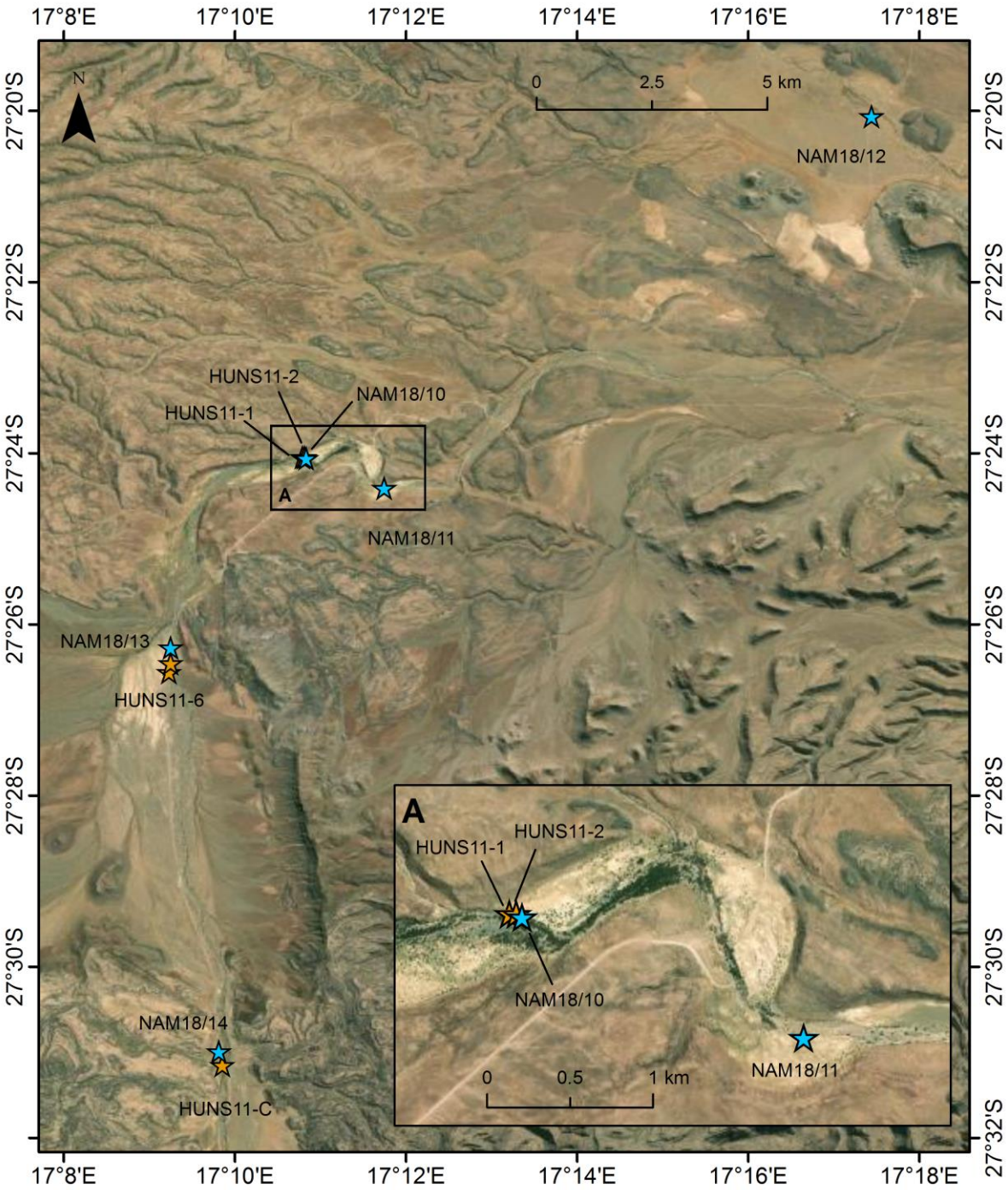

Figure B3. Location of sample collection sites, Huns River, southern Namibia, collected during two field seasons (blue: Walsh and Thomas, 2018; orange: Brook and Marais, 2011).

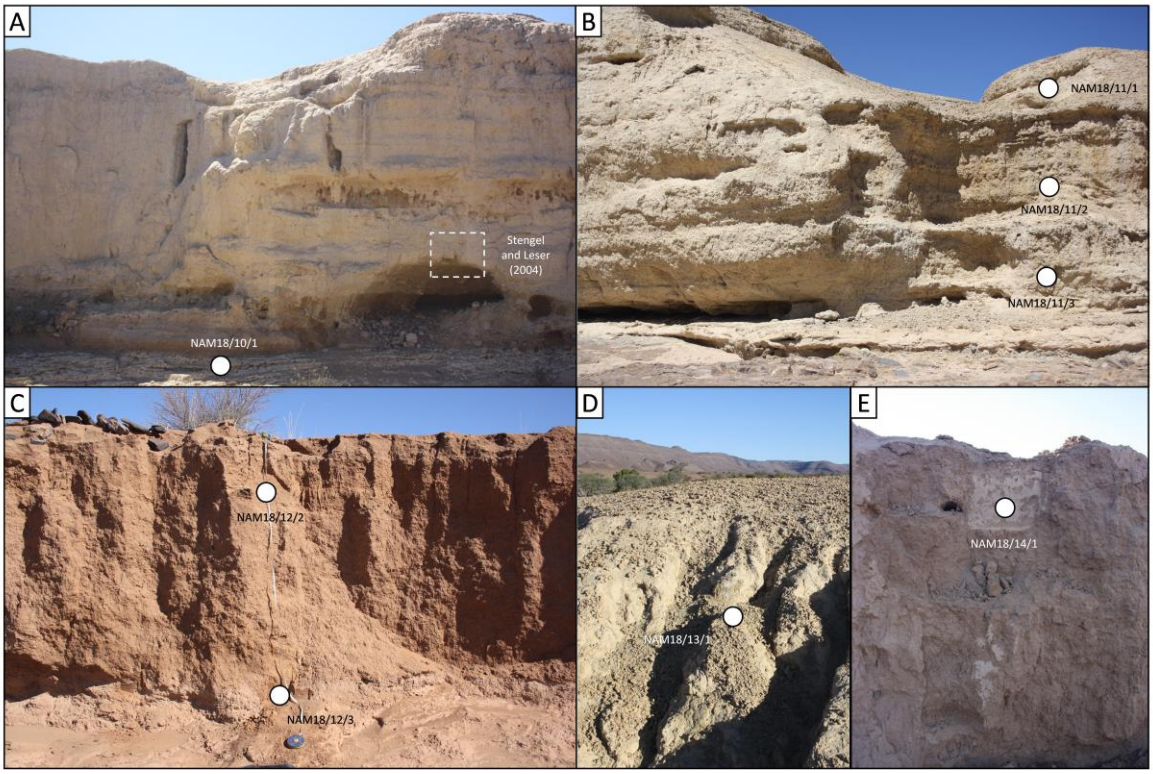

Figure B4. Huns River sediments. **A)** NAM18/10: section studied by Stengel and Leser (2004). **B)** NAM18/11 **C)** NAM18/12 in the Konkeip River. **D)** NAM18/13. **E)** NAM18/14.

Table B1. Sample site details.

Sample ID	Depth (m)	Elevation (m a.s.l.)	Latitude	Longitude
NAM18/10/1	15	880	-27.401	17.181
NAM18/11/1	2	859	-27.407	17.196
NAM18/11/2	5.5	859	-27.407	17.196
NAM18/11/3	8	859	-27.407	17.196
NAM18/13/1	1	912	-27.438	17.154
NAM18/14/1	1	966	-27.517	17.164
NAM18/12/2	1.1	771	-27.334	17.291
NAM18/12/3	2.4	771	-27.334	17.291
HUNS11-1-1	6.0	878	-27.401	17.180
HUNS11-1-2	2.5	878	-27.401	17.180
HUNS11-1-3	0.5	878	-27.401	17.180
HUNS11-1-4	0.5	878	-27.401	17.180
HUNS11-2-1	1.47	878	-27.401	17.180
HUNS11-2-2	2.7	878	-27.401	17.180
HUNS11-2-3	2.5	878	-27.401	17.180
HUNS11-6-1	0.5	917	-27.443	17.154
HUNS11-6-2	1.3	893	-27.441	17.154
HUNS11-C-1	0.5	969	-27.519	17.164

2.2. Luminescence dating

The NAM18 samples were collected using opaque black tubes and were prepared under subdued orange light (600nm) in the Oxford Luminescence Dating laboratory (OLDLab). The quartz fraction

of these samples was obtained through standard preparation process, following the protocols described in detail in Chapter 3 (Section 3.3) and Chapter 4 (Section 4.2.2). Samples were sieved to 4-11 µm, 63-90 µm, 90-125 µm, and 125-180 µm to test the role of grain size on the age obtained. Coarse grained sample preparation followed the preparation of the Huab samples, and fine grained samples were prepared through sequential settling (following Stoke's Law) and treatment in 35 % fluorosilicic acid (H_2SiF_6) for two weeks. Coarse grained discs were prepared as small aliquots (2 mm) and fine grained discs were prepared by pipetting around 0.5 mm of 4-11 µm quartz onto 9.8 mm aluminium discs. The ages calculated by Brook and Marais (HUNS11) were obtained from the 125-180 µm fraction through consistent laboratory protocols to those used on the samples collected in 2018.

2.3. Grain size, loss on ignition, heavy minerals

Grain size analyses were performed in a Malvern Mastersizer Hydro 2000MU and water, organic, and carbonate contents were estimated through sequential loss on ignition at 105˚C, 550˚C and 950˚C (LOI; Heiri *et al.* 2001). To investigate the composition of the Huns valley fill deposits, four samples from three key stratigraphic sections were selected for heavy mineral (HM) analysis. HM fractions were obtained and prepared following the methods described in Chapter 4 (Section 4.2.4), analyses were undertaken using Raman laser spectroscopy, and heavy minerals were identified from the RRUFF database (Lafuente *et al.*, 2016) using the automated TrueMatch software (WITec) and manual verification.

3. Results

3.1. Chronology

Results from preheat and dose recovery tests (Figure B5) show that all samples recovered a dose well using a preheat of 220˚C for 10 s and a cut heat of 180˚C for 10 s. Luminescence dating of a selection of grain size fractions shows that there is consistency in the D_e estimations reached from each grain size (Figure B6). There is greater variability in the D_e estimates from larger grain sizes, which is to be expected as fewer grains are considered and variability between grains is resolved (Duller, 2008). Following this analysis, the grain size fraction of 63 to 90 µm was used as it best reflected the fine grained nature of these samples, whilst not averaging out variability (as is common in the 4 to 11 µm fraction), and provided a narrow grain size window.

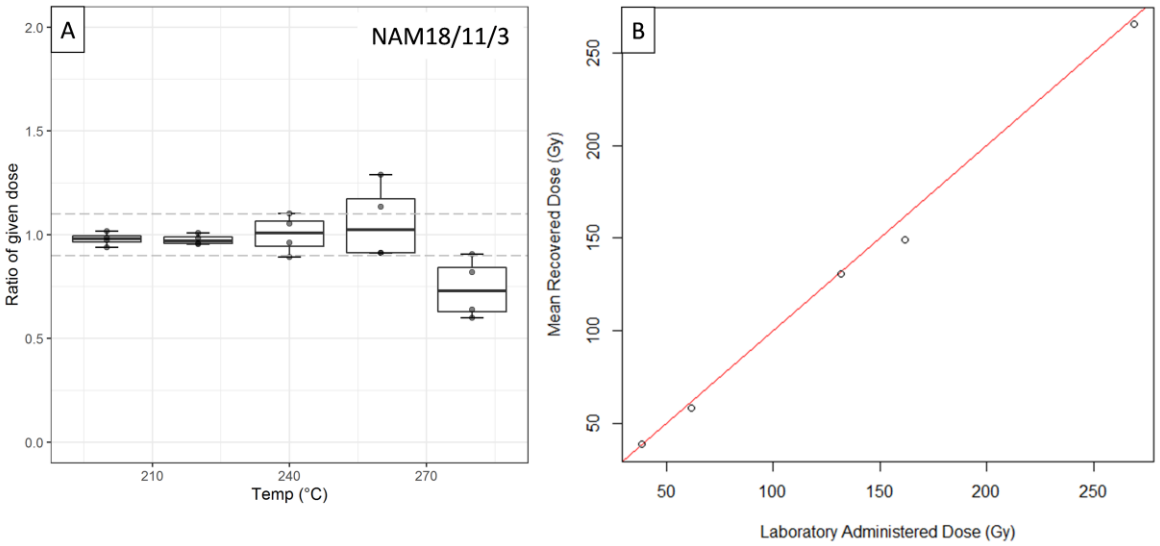

Figure B5. Tests of the applicability of the SAR protocol for dating Huns River valley fill sediments. **A)** Preheat plateau test results for sample NAM18/11/3. Aliquots were bleached twice with blue LEDs for 100 s at 20˚C, followed by a 10,000 s pause to remove the trapped charge. **B)** Dose recovery test results using a preheat of 200˚C. Dotted line indicates unity, where the laboratory administered dose and recovered dose are equal. Laboratory administered doses were chosen based on range finder ages for each sample to reflect natural conditions.

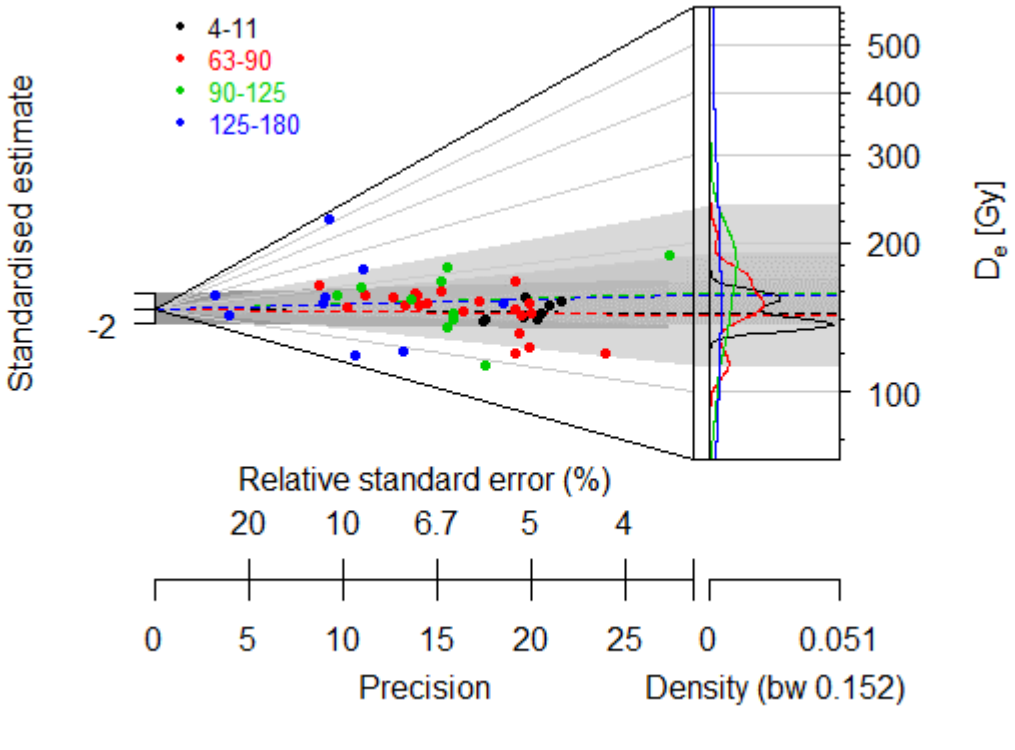

Figure B6. D_e estimation from a selection of grain sizes of sample NAM18/11/3 (4-11 µm, 63-90 µm, 90-125 µm, 125-180 µm).

Depositional ages range from 146.13 ± 12.16 ka (HUNS11-1-1) to 15.2 ± 1.0 ka (NAM18/14/1), with differences in the extent of fluvial histories preserved in different sections. The oldest deposition (HUNS11-1-1) is preserved in hard conglomeratic material at the base of the Stengel and Leser (2004) site. Sample NAM18/10/1, dating to 112.2 ± 8.3 ka is also from this unit. Ages from site NAM18/11 range from 60.1 ± 3.8 ka to 38.9 ± 4.0 ka. Upstream, incorporating sites NAM18/13, NAM18/14 and HUNS11-6, chronologies are younger and preserve a record from 15.2 ± 1.0 ka to 25.93 ± 2.48 ka. Konkeip ages (NAM18/12) span from 27.8 ± 5.7 ka to 57.4 ± 8.4 ka. These ages are relatively old given the semi-confined setting of the sites.

Table B2. Results of luminescence dating. n: number of accepted discs used for age calculation. Dose rates and D_e results for NAM18/ samples, and ages from all samples. 63 to 90 µm fraction was used for NAM18 samples and 125 to 180 µm was used for HUNS11 samples.

Sample	n	Beta dose rate	Gamma dose rate	Cosmic dose rate	Env Dose rate	D_e	Age (ka)
NAM18/							
10/1	21	1.7 ± 0.1	1.0 ± 0.1	0.1 ± 0	2.7 ± 0.2	307.5 ± 14.8	**112.2 ± 8.3**
11/1	14	2.1 ± 0.2	1.2 ± 0.1	0.2 ± 0	3.4 ± 0.2	153.9 ± 11.6	**44.5 ± 4.1**
11/2	22	1.9 ± 0.2	1.1 ± 0.1	0.1 ± 0	3.1 ± 0.2	123.3 ± 10.9	**38.9 ± 4.0**
11/3	21	1.5 ± 0.1	0.9 ± 0.1	0.1 ± 0	2.4 ± 0.1	148.2 ± 5.3	**60.1 ± 3.8**
13/1	21	2.2 ± 0.2	1.2 ± 0.1	0.2 ± 0	3.6 ± 0.2	81.3 ± 3.4	**22.8 ± 1.6**
14/1	20	1.8 ± 0.2	1.0 ± 0.1	0.2 ± 0	3.0 ± 0.2	46.6 ± 1.8	**15.2 ± 1.0**
12/2	15	1.7 ± 0.1	1.0 ± 0.1	0.2 ± 0	2.8 ± 0.2	78.9 ± 15.9	**27.8 ± 5.7**
12/3	22	1.7 ± 0.1	1.0 ± 0.1	0.2 ± 0	2.9 ± 0.2	166.4 ± 22.8	**57.4 ± 8.4**
HUNS11-							
1-1	-	-	-	-	-	-	**146.13 ± 12.16**
1-2	-	-	-	-	-	-	**32.20 ± 2.56**
1-3	-	-	-	-	-	-	**26.99 ± 2.15**
1-4	-	-	-	-	-	-	**26.89 ± 2.87**
2-1	-	-	-	-	-	-	**25.36± 2.55**
2-2	-	-	-	-	-	-	**23.59 ± 1.99**
2-3	-	-	-	-	-	-	**22.89 ± 2.33**
6-1	-	-	-	-	-	-	**25.93 ± 2.48**
6-2	-	-	-	-	-	-	**21.91 ± 1.70**

3.2. Heavy mineral assemblages

The HM assemblages are dominated by epidote (22-28 %), titanite (10-18%) and garnet (7-14%), with a lower occurrence of amphibole (~6%), anatase (~6%), rutile (~8%), tourmaline (~4%), and oxides (~3%) (Table B3). Samples from NAM18/11 are differentiated from NAM18/13 and NAM18/14 particularly in relation to the prevalence of pyroxene (Figure B7). Pyroxene is near

absent in NAM18/11 samples (0-0.4 %), but makes up the largest proportion of heavy minerals in the upstream samples (17-30 %).

Table B3. Heavy mineral assemblage of the Huns valley fill samples. Results are quoted as percentage of total grains identified. Apatite (Ap), amphibole (Amp), anatase (An), epidote (Ep), garnet (Grt), oxides (Ox), pyroxene (Px), rutile (Rtl), titanite (Ttn), tourmaline (Trm), zircon (Zir), other. Samples are listed in stratigraphic order by site.

Sample	Amp	An	Ap	Ep	Grt	Ox	Px	Rtl	Trm	Ttn	Zir	Other
NAM18/11/1	4.0	8.1	9.2	26.7	12.3	2.7	0.4	7.4	3.6	18.4	5.4	1.8
NAM18/11/3	4.4	7.8	5.9	27.9	14.4	3.0	0.0	9.6	5.5	11.1	5.9	4.4
NAM18/13/1	5.3	4.2	6.7	22.3	10.1	1.6	17.0	8.5	3.4	11.7	6.7	2.5
NAM18/14/1	8.7	4.0	0.7	21.5	6.7	3.4	29.5	8.1	5.4	10.1	0.7	1.3

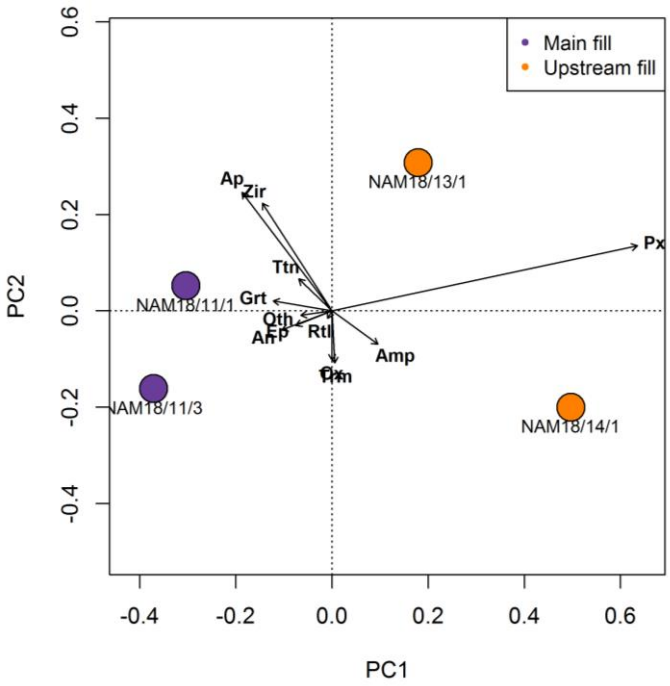

Figure B7. Compositional biplot of heavy mineral assemblages. Biplots enable a consideration of multivariate observations (points) and variables (rays) (Gabriel, 1971). The length of the ray is proportional to variability of the species, and the angle between rays details correlation between different species: 0˚, 90˚ and 180˚ correspond to correlation, no correlation and inverse correlation respectively. Apatite (Ap), amphibole (Amp), anatase (An), epidote (Ep), garnet (Grt), olivine (Olv), oxides (Ox), pyroxene (Px), rutile (Rtl), titanite (Ttn), tourmaline (Trm), zircon (Zir), other (oth).

3.3. Grain size and loss on ignition

Sediment grain size distributions are predominantly unimodal very fine to medium sand (Figure B8; Table B3). Samples are poorly sorted with predominantly unimodal grain size distributions (apart from NAM18/11/3 and NAM18/12/3 which are bimodal), and have modal grain sizes ranging from 27 to 238 µm. The Huns samples are differentiated from the Konkeip samples (NAM18/12) by grain

size. Huns samples are composed of medium to very coarse silt (4-63 µm: 59.8 %), whereas the Konkeip are composed of fine to very coarse sand (125 µm-2 mm: 64.9 %). Samples comprise ~1.5 % water, ~ 4 % organic content, and ~ 11 % carbonate (estimated from loss on ignition analysis).

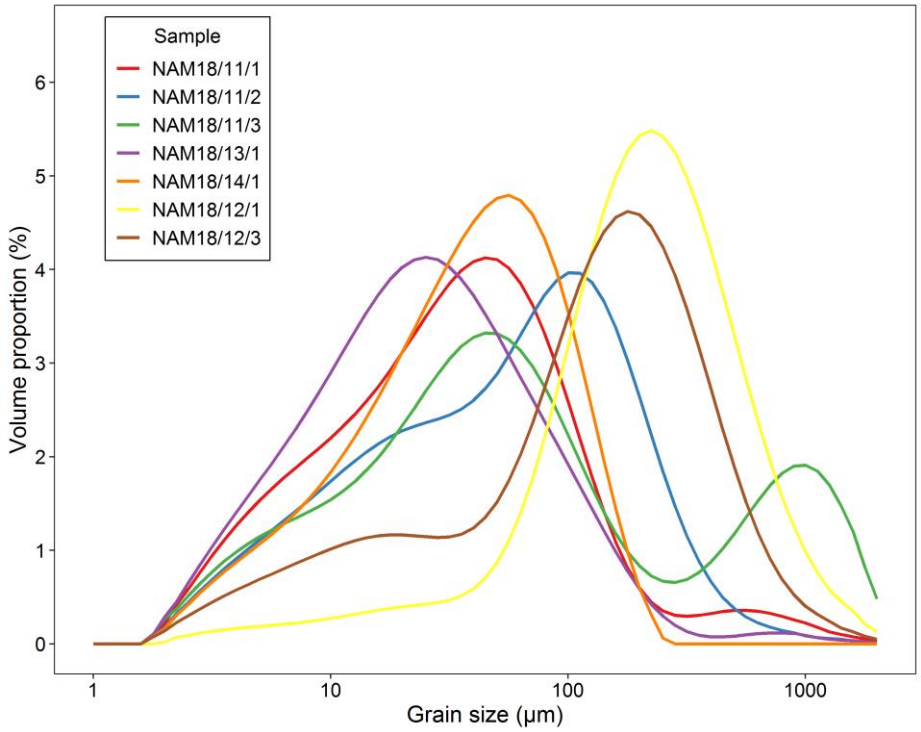

Figure B8. Grain size distributions by volume coloured by sample. Samples include three key groups: Huns main valley fill (NAM18/11), upstream valley fill (NAM18/13, NAM18/14), and a sedimentary unit in the Konkeip (NAM18/12).

Table B3. Results of grain size analysis (% contribution) and loss on ignition (water, organic, and carbonate content %).

Sample (NAM-)	% very coarse to medium sand (2 mm-250 µm)	% fine sand (250 µm-125 µm)	% very fine sand (125 µm-63 µm)	% very coarse to coarse silt (63 µm-16 µm)	% medium silt (16 µm-4 µm)	% very fine silt (4 µm-2 µm)	% clay (< 2 µm)	105˚C LOI (water content)	550˚C LOI (organic content)	950˚C LOI (carbonate content)
18/11/1	4.65	6.14	18.53	40.67	24.61	5.30	0.10	1.116	3.978	11.770
18/11/2	8.14	18.79	22.35	27.81	18.92	3.90	0.09	1.116	5.179	11.826
18/11/3	23.55	6.80	15.51	31.95	17.66	4.43	0.10	0.920	5.537	18.268
18/13/1	1.81	5.42	13.58	41.80	31.41	5.90	0.09	0.963	4.771	13.933
18/14/1	0.06	7.80	24.23	43.92	20.18	3.73	0.08	1.102	5.582	14.211
18/12/1	44.97	29.99	14.93	6.30	3.06	0.75	0.00	1.941	1.288	3.214
18/12/3	28.04	26.77	17.58	13.91	11.05	2.57	0.07	3.023	1.935	4.250

4. Discussion

These initial results from the Huns valley fill sediments indicate that there is variability amongst the samples collected, particularly in the span of ages calculated and differences in the heavy mineral and grain size distributions obtained.

This analysis finds that a number of units date to ~ 25 to 30 ka, corroborating the Stengel and Leser (2004) age, yet the distribution of ages show that the valley fill contains evidence of multiple periods of deposition. Within the main fill, the sampled units provide chronologies broadly dating to three periods: 145 to 112 ka, 60 to 40 ka, and 30 to 15 ka. Extensive sedimentation and consistency in chronologies obtained from certain units (e.g. HUNS11-2 and similarity between NAM18/13 and HUNS11-6) suggest periods of significant fluvial deposition. This dataset provides a chronology more extensive than was previously available, with increased confidence in the timing of river flow where there are supporting stratigraphically consistent ages. If Stengel and Leser's (2004) interpretation of the nature of river flow as a result increased westerly derived rainfall under a climate less seasonal than today can be verified, the record from 21 to 25 ka (NAM18/13, HUNS11-2, HUNS11-6) shows support for the findings in Chapter 6 at the LGM. Further data on the stratigraphic setting and depositional contexts are required to reach robust conclusions, however.

The grain size data suggests the occurrence of differences in the depositional regimes recorded in the sedimentary units. For example, within section NAM18/11, whilst samples from both the top (NAM18/11/1) and base (NAM18/11/3) of the section are dominated by a fine grained component (modal grain size of ~ 47 µm), NAM18/11/3 also incorporates a coarse fraction and the two samples have different mean grain sizes (mean grain sizes of 31 and 75 µm respectively). At present, grain size data is not available for the HUNS11 samples, but if possible to obtain, this would help to tie together depositional units and interrogate differences across the full dataset. The difference in grain size distribution between the Huns and Konkeip samples mirrors observable differences in the characteristics of these sedimentary units (Figure B4, e.g. colour and stratigraphic structures). These differences could reflect catchment scale differences in sediment supply, and should be considered in further detail.

The heavy mineral data also identify differences in either the depositional regime or differences in source region of the units deposited in the main valley fill (NAM18/11) and the upstream fills (NAM18/13, NAM18/14). The HM assemblages are distinct (Figure B7), with particular importance noted in the contribution of pyroxene and amphibole, but further data from additional samples

and data on the geological setting are needed to understand the significance of these differences. The geological map in Figure B2 shows that the source of the river lies within the Kuibis and Schwarzrand groups, which are subgroups of the Nama Group (Saylor *et al.*, 1995). To gain further information on the provenance of these sediments, detailed geological data from potential source regions are required. This could include geological maps similar to those used in Chapter 4 (Figure 4.2). To distinguish these samples, data on the petrographic assemblage is also required. Thin sections for petrography have been prepared and Raman laser analysis for petrography has been performed following the methods described in Section 4.2.4, but the microscopy step has not yet been undertaken and the data have not been analysed. Given the potential utility of geochemistry for distinguishing between underlying geologies in the Huab catchment (Section 3.4.3.2; Figure 3.15), it would also be useful to interrogate the geochemical signature of the Huns valley fill samples.

Appendix C – Supplementary material for Chapter 3 (Methods)

Appendix C presents supplementary data and plots for analysis described in Chapter 3 (Methods).

Table C1. Ground Penetrating Radar (GPR) measurement conditions.

Profile no.	Coordinates of start point	Coordinates of end point	MHz	Set time window (ns)	Radar velocity	Sampling interval	Rx-Tx offset (m)	Step size (m)	Length (m)	Stack-ing	Orientation relative to channel
00	20.865˚S, 13.649˚E	20.865˚S, 13.649˚E	100	200-300	0.06-0.15	0.8	1	0.25	50	64	Perpendicular
01	20.865˚S, 13.649˚E	20.865˚S, 13.649˚E	200	100-200	0.06-0.15	0.4	0.5	0.1	50	64	Perpendicular
02	20.866˚S, 13.647˚E	20.866˚S, 13.647˚E	200	100-200	0.06-0.15	0.4	0.5	0.1	6.5	64	Perpendicular
03	20.866˚S, 13.647˚E	20.866˚S, 13.647˚E	200	100-200	0.06-0.15	0.4	0.5	0.1	4	64	CMP
04	20.866˚S, 13.647˚E	20.866˚S, 13.648˚E	200	100-200	0.06-0.15	0.4	0.5	0.1	10	64	Parallel in channel
05	20.868˚S, 13.651˚E	20.868˚S, 13.651˚E	200	100-200	0.06-0.15	0.4	0.5	0.1	10	64	Parallel
06	20.868˚S, 13.651˚E	20.868˚S, 13.651˚E	200	100-200	0.06-0.15	0.4	0.5	0.1	5	64	CMP
07	20.868˚S, 13.651˚E	20.868˚S, 13.651˚E	200	100-200	0.06-0.15	0.4	0.5	0.1	20	64	Perpendicular
08	20.871˚S, 13.635˚E	20.872˚S, 13.635˚E	100	200-300	0.06-0.15	0.8	1	0.25	40	64	Perpendicular
09	20.871˚S, 13.635˚E	20.872˚S, 13.635˚E	100	200-300	0.06-0.15	0.8	1	0.25	19	32	Perpendicular
10	20.871˚S, 13.635˚E	20.872˚S, 13.635˚E	100	200-300	0.06-0.15	0.8	1	0.25	19	8	Perpendicular
11	20.867˚S, 13.652˚E	20.867˚S, 13.652˚E	100	200-300	0.06-0.15	0.8	1	0.20	12	32	Parallel
12	20.867˚S, 13.652˚E	20.867˚S, 13.652˚E	100	200-300	0.06-0.15	0.8	1	0.20	30	32	Perpendicular
13	20.867˚S, 13.652˚E	20.867˚S, 13.652˚E	100	200-300	0.06-0.15	0.8	1	0.2	19	32	CMP
14	20.867˚S, 13.641˚E	20.866˚S, 13.641˚E	100	200-300	0.06-0.15	0.8	1	0.2	20	32	Top of sand dune
15	20.866˚S, 13.641˚E	20.866˚S, 13.641˚E	100	200-300	0.06-0.15	0.8	1	0.2	20	32	Across sand dune
16	20.866˚S, 13.641˚E	20.866˚S, 13.642˚E	100	200-300	0.06-0.15	0.8	1	0.2	20	32	Sand dune/fluvial

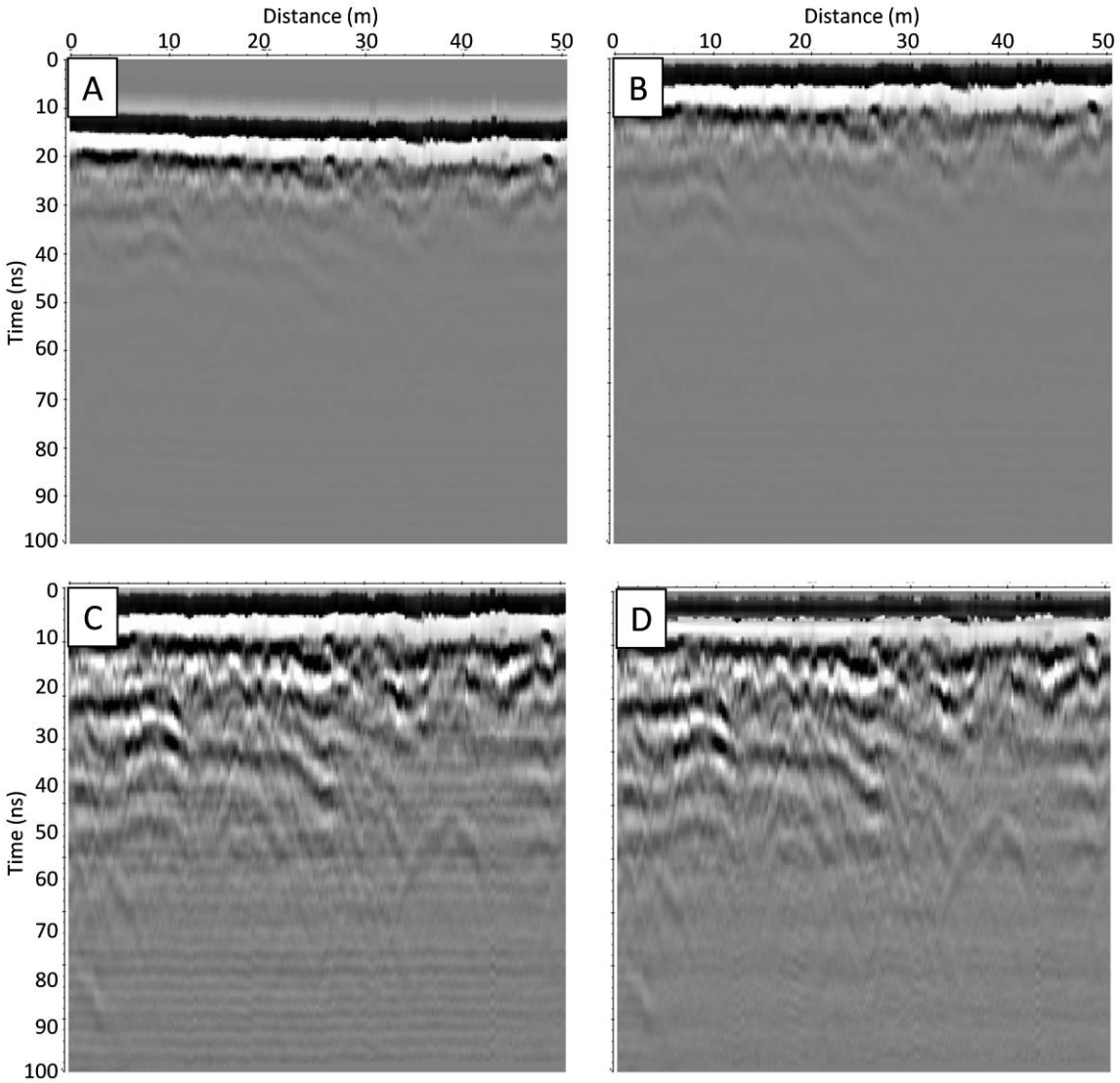

Figure C1. Example of the data processing steps applied to GPR transect line 01 in the ReflexW software. **A)** dewow (subtract-mean 1D filter), **B)** static correction time-zero, **C)** gain, **D)** f-k filtering.

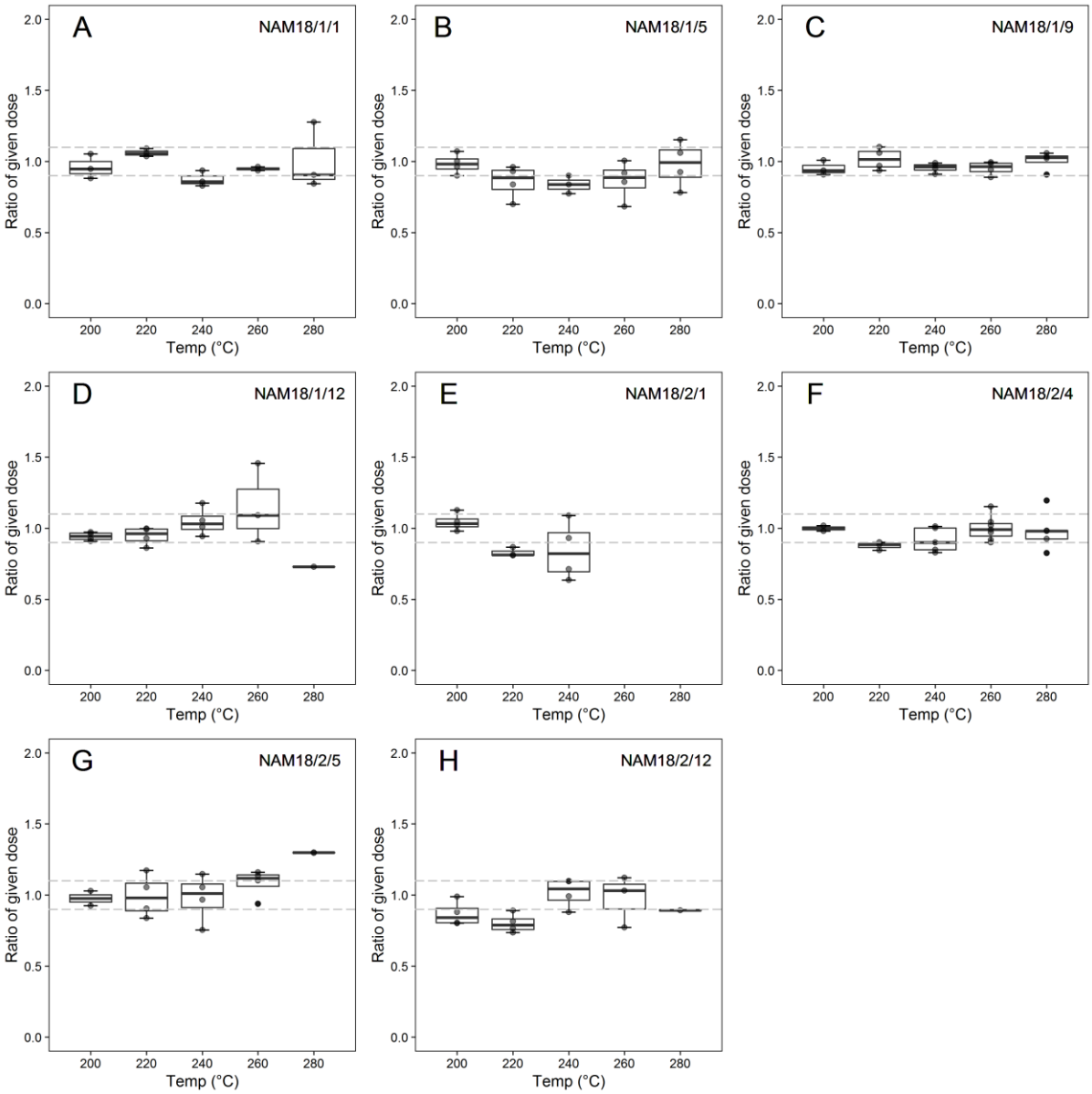

Figure C2. All preheat results. Aliquots were bleached twice with blue LEDs for 100 s at 20˚C, followed by a 10,000 s pause to remove trapped charge. Aliquots were irradiated with a known dose (chosen based on range finder ages for each sample to reflect natural conditions) and analysed following the SAR protocol using different preheats. Preheat temperatures were set to 200˚C, 220˚C, 240˚C, 260˚C, and 280˚C for 10s, each with a cut heat of 180˚C for 10 s. Results include accepted aliquots plotted as the ratio between given and recovered dose. All samples recovered a dose well using a preheat of 200˚C for 10 s and a cut heat of 180˚C for 10 s.

Table C2. Dose recovery results. MG: multigrain, SG: single grain. [a]Number of aliquots that passed all rejection criteria; [b]Given dose chosen to be close to the burial D_e of the sample; [c]Recovered dose calculated as the averaged of all aliquots of each sample; [d]Ratio between given and recovered dose using the mean recovered dose; [e]Recovered dose calculated using the central age model (Galbraith *et al.*, 1999); [f]Overdispersion calculated from the central age model: overdispersion is a measure of the variability of D_e beyond what would be expected from incomplete bleaching or heterogeneity in dose rate; [g]Ratio between given and recovered dose using the CAM recovered dose. Ratios d) and g) show that the majority of D_es are within 10 % of unity.

Sample (NAM18/)	n[a]	Given dose (Gy)[b]	Mean recovered dose ± 1σ (Gy)[c]	Ratio[d]	Recovered dose (CAM) (Gy)[e]	Over-dispersion (OD)[f]	Ratio[g]
1/1 (MG)	11	2.43	2.20 ± 0.31	0.91 ± 0.13	2.18 ± 0.10	11 ± 3	0.90 ± 0.04
1/2 (MG)	18	1.94	2.17 ± 0.77	1.12 ± 0.39	2.04 ± 0.12	21 ± 4	1.05 ± 0.06
1/4 (MG)	8	3.97	4.21 ± 1.11	1.06 ± 0.28	4.10 ± 0.34	23 ± 6	1.03 ± 0.09
1/5 (MG)	14	6.53	5.85 ± 0.97	0.90 ± 0.15	5.78 ± 0.27	16 ± 3	0.89 ± 0.04
1/6 (MG)	10	4.98	4.79 ± 0.45	0.96 ± 0.09	4.85 ± 0.08	2 ± 3	0.97 ± 0.02
1/8 (MG)	10	5.16	5.04 ± 0.76	0.98 ± 0.15	4.98 ± 0.23	13 ± 4	0.96 ± 0.04
1/9 (MG)	9	4.80	4.58 ± 0.49	0.96 ± 0.10	4.56 ± 0.16	8 ± 2	0.95 ± 0.03
1/12 (MG)	19	22.56	21.43 ± 1.69	0.95 ± 0.07	21.76 ± 0.44	0 ± ∞	0.96 ± 0.02
2/1 (MG)	21	2.38	2.18 ± 0.20	0.91 ± 0.08	2.16 ± 0.05	8 ± 2	0.91 ± 0.02
2/3 (MG)	11	9.97	9.08 ± 0.66	0.91 ± 0.07	9.07 ± 0.20	6 ± 2	0.91 ± 0.02
2/4 (MG)	11	16.18	14.25 ± 1.95	0.88 ± 0.12	14.12 ± 0.60	13 ± 3	0.87 ± 0.04
2/5 (MG)	24	4.83	4.46 ± 0.79	0.92 ± 0.16	4.42 ± 0.16	14 ± 2	0.91 ± 0.03
2/7 (MG)	10	8.98	8.44 ± 0.98	0.94 ± 0.11	8.37 ± 0.29	10 ± 3	0.93 ± 0.03
2/10 (MG)	8	19.59	22.04 ± 7.08	1.12 ± 0.36	20.98 ± 2.30	29 ± 8	1.07 ± 2.12
3/1 (MG)	8	13.79	13.44 ± 1.15	0.97 ± 0.08	13.29 ± 0.35	3 ± 4	0.96 ± 0.03
3/2 (MG)	12	5.94	5.84 ± 0.48	0.98 ± 0.08	5.83 ± 0.14	8 ± 2	0.98 ± 0.02
4/1 (MG)	10	2.99	3.42 ± 1.46	1.14 ± 0.49	3.23 ± 0.31	30 ± 7	1.08 ± 0.10
4/3 (MG)	12	3.96	3.88 ± 0.28	0.98 ± 0.07	3.87 ± 0.08	7 ± 2	0.98 ± 0.02
4/5 (MG)	10	6.21	6.32 ± 1.35	1.02 ± 0.22	6.21 ± 0.36	18 ± 4	1.00 ± 0.06
6/1 (MG)	18	6.00	5.55 ± 0.75	0.92 ± 0.12	5.50 ± 0.17	12 ± 2	0.92 ± 0.03
6/2 (MG)	4	16.16	14.70 ± 0.73	0.91 ± 0.05	14.51 ± 0.57	0 ± ∞	0.90 ± 0.04
7/1 (MG)	7	2.55	2.28 ± 0.35	0.89 ± 0.14	2.23 ± 0.13	1 ± 9	0.88 ± 0.05
7/4 (MG)	11	9.97	8.71 ± 0.86	0.87 ± 0.09	8.57 ± 0.26	8 ± 2	0.86 ± 0.03
7/7 (MG)	11	54.97	51.82 ± 2.74	0.94 ± 0.05	52.26 ± 0.96	3 ± 3	0.95 ± 0.02
8/1 (MG)	8	1.95	2.52 ± 1.23	1.29 ± 0.63	2.33 ± 0.30	36 ± 9	1.19 ± 0.15
8/2 (MG)	7	6.25	5.21 ± 2.21	0.83 ± 0.35	5.45 ± 0.48	0 ± 0	0.87 ± 0.08
1/12 (SG)	38	24.34	24.68 ± 13.51	1.01 ± 0.55	22.40 ± 1.54	31 ± 6	0.92 ± 0.06
2/1 (SG)	16	2.66	2.97 ± 2.11	1.12 ± 0.79	2.62 ± 0.38	49 ± 11	0.99 ± 0.04
2/5 (SG)	26	5.17	5.52 ± 2.55	1.07 ± 0.49	5.14 ± 0.44	34 ± 7	0.99 ± 0.09
2/10 (SG)	16	18.99	20.92 ± 5.99	1.10 ± 0.32	21.21 ± 1.64	22 ± 8	1.12 ± 1.19

Table C3. Results of analysis of ICP-MS repeats. Total errors are calculated by propagating in quadrature. This analysis aimed to assess the uncertainty associated with analytical errors (tested through repeat measurements of the same digested sample in the ICP-MS machine), incomplete digestion of the sample (tested through repeat digestion of a homogenised sample), and heterogeneity in the dose rate within a sample (tested through analysis of multiple subsamples of the same sample).

Type of error	Uranium 238 (ppm)	Thorium 232 (ppm)	Potassium 40 (%)
Analytical	2.08	2.61	1.27
Digestion	2.68	2.98	4.85
Subsample	2.46	10.92	3.51
Total	**4.18 %**	**11.61 %**	**6.11 %**

Table C4. Peak energy of radionuclides recorded within gamma spectra and energy windows used for measurement of each radionuclide.

Isotope	Peak (MeV)	Typical Peak window (MeV)
Potassium-40	1.46	1.38-1.53
Bismuth-214 (U series)	1.76	1.69-1.84
Thallium-208 (Th series)	2.61	2.46-2.76

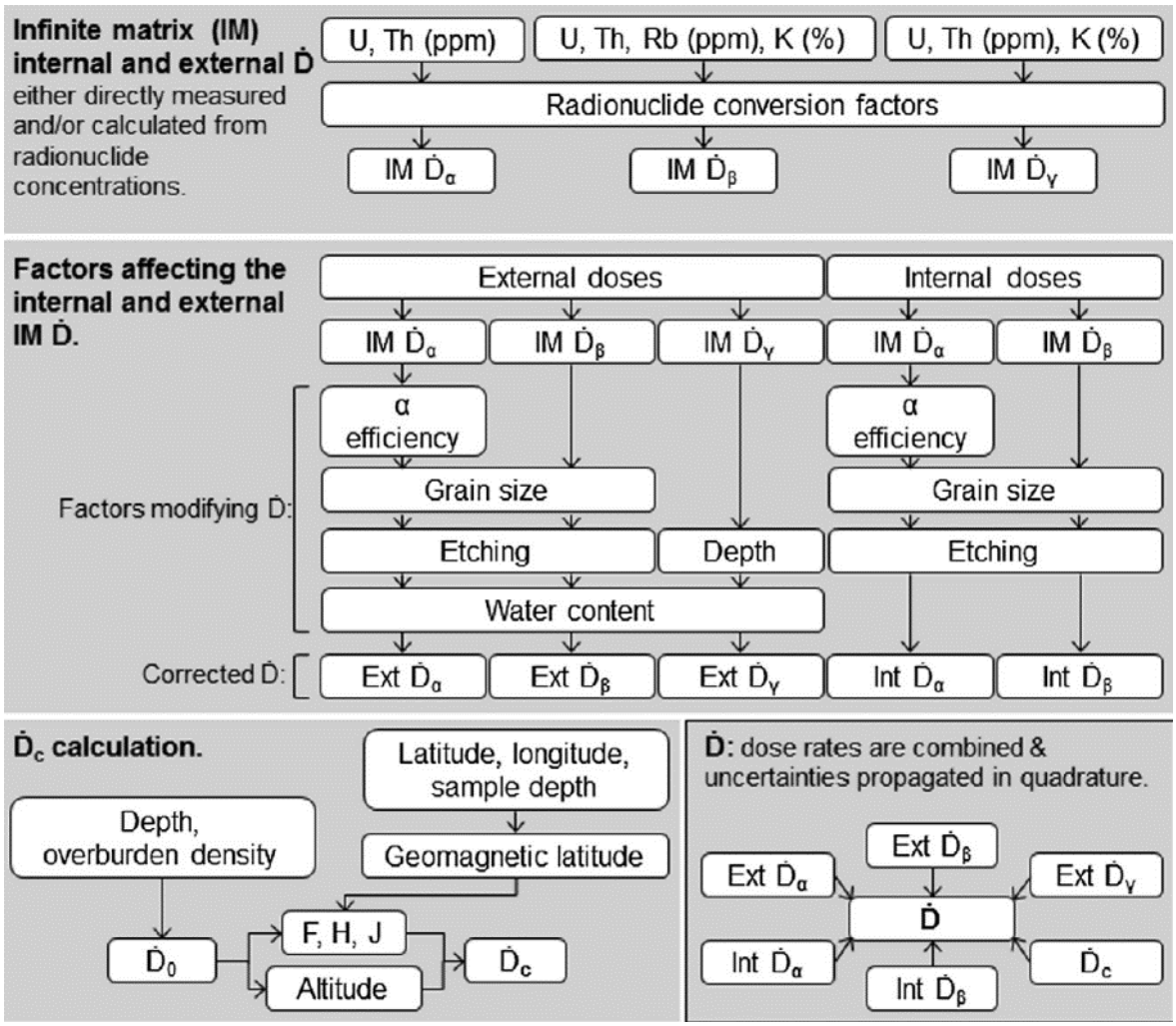

Figure C3. Steps within the Dose Rate and Age Calculator for trapped charge dating (DRAC (v1.2) software; Durcan *et al.*, 2015) for calculation of dose rates.

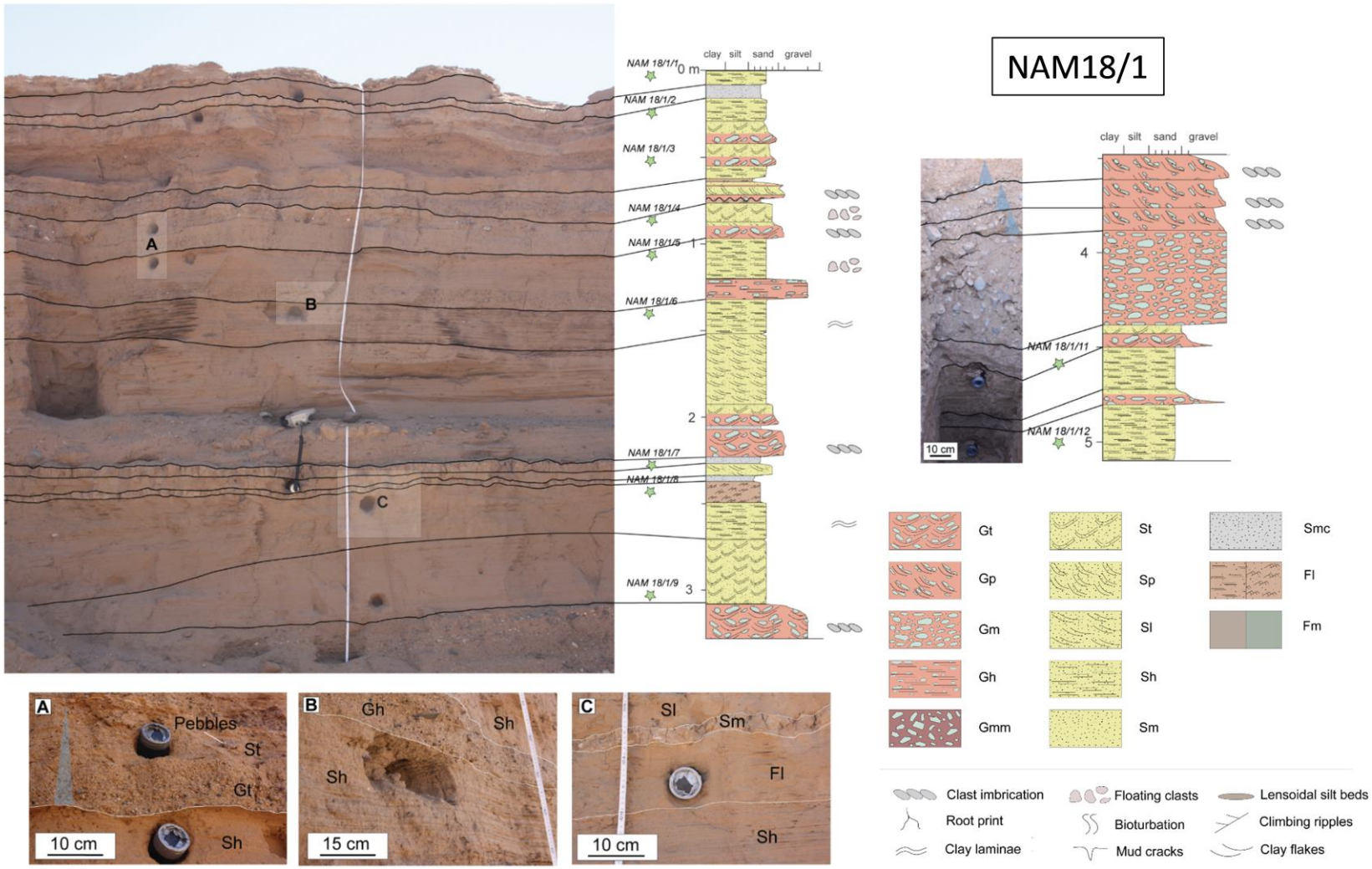

Figure C4. Stratigraphic log of site NAM18/1. Inserts A, B, C, give examples of classification of lithofacies.

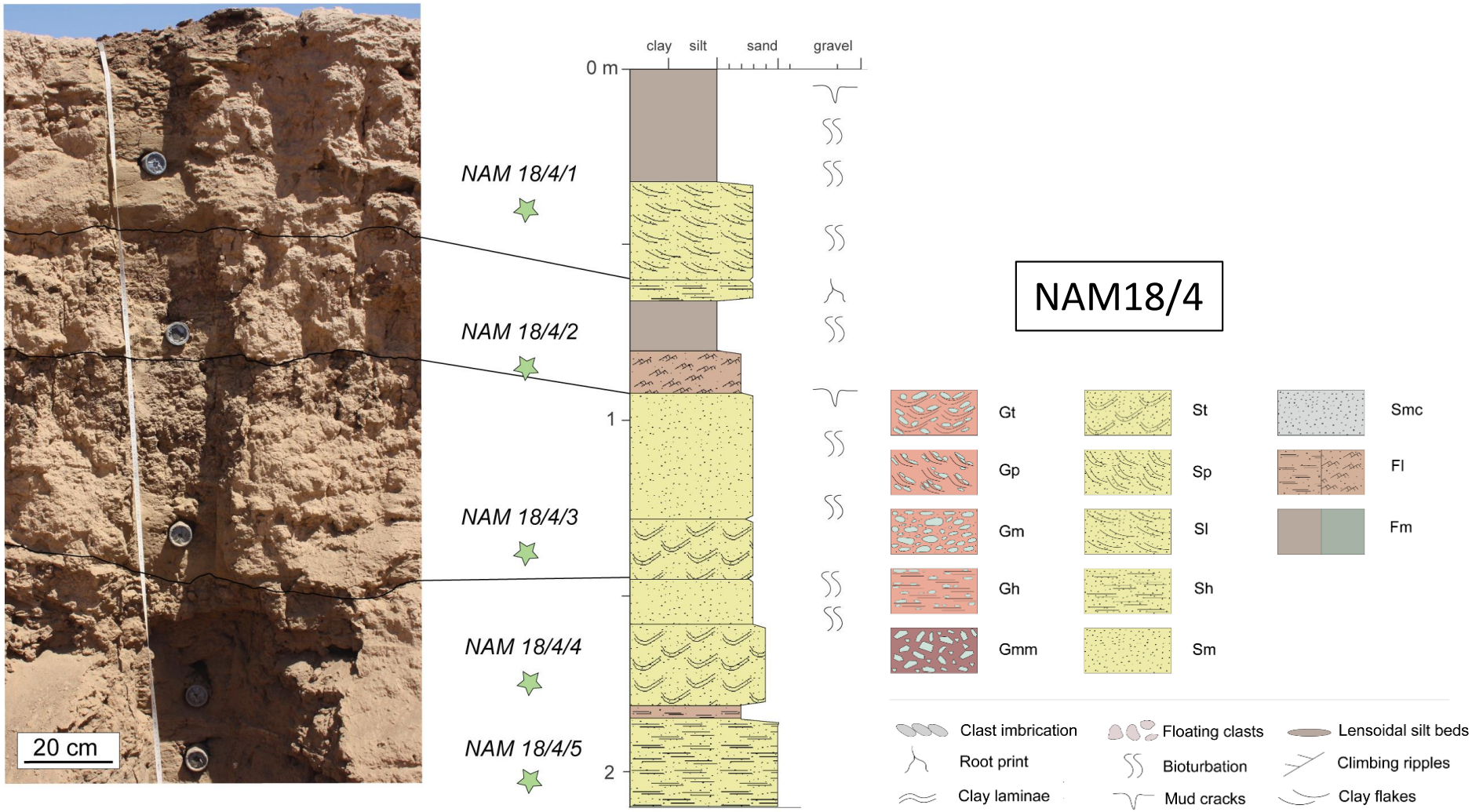

Figure C5. Stratigraphic log of site NAM18/4.

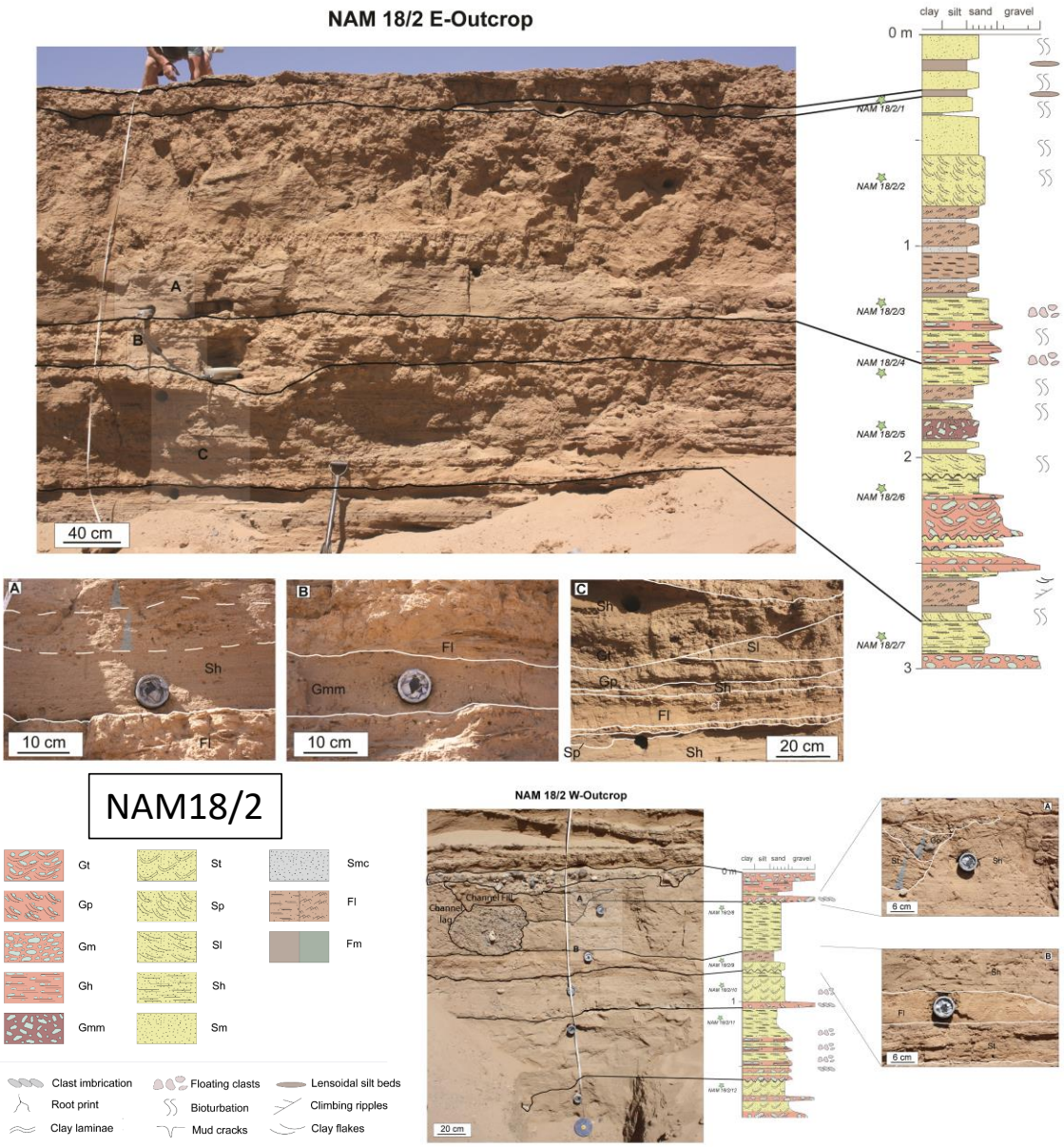

Figure C6. Stratigraphic log of site NAM18/2. Inserts A, B, C, give examples of classification of lithofacies.

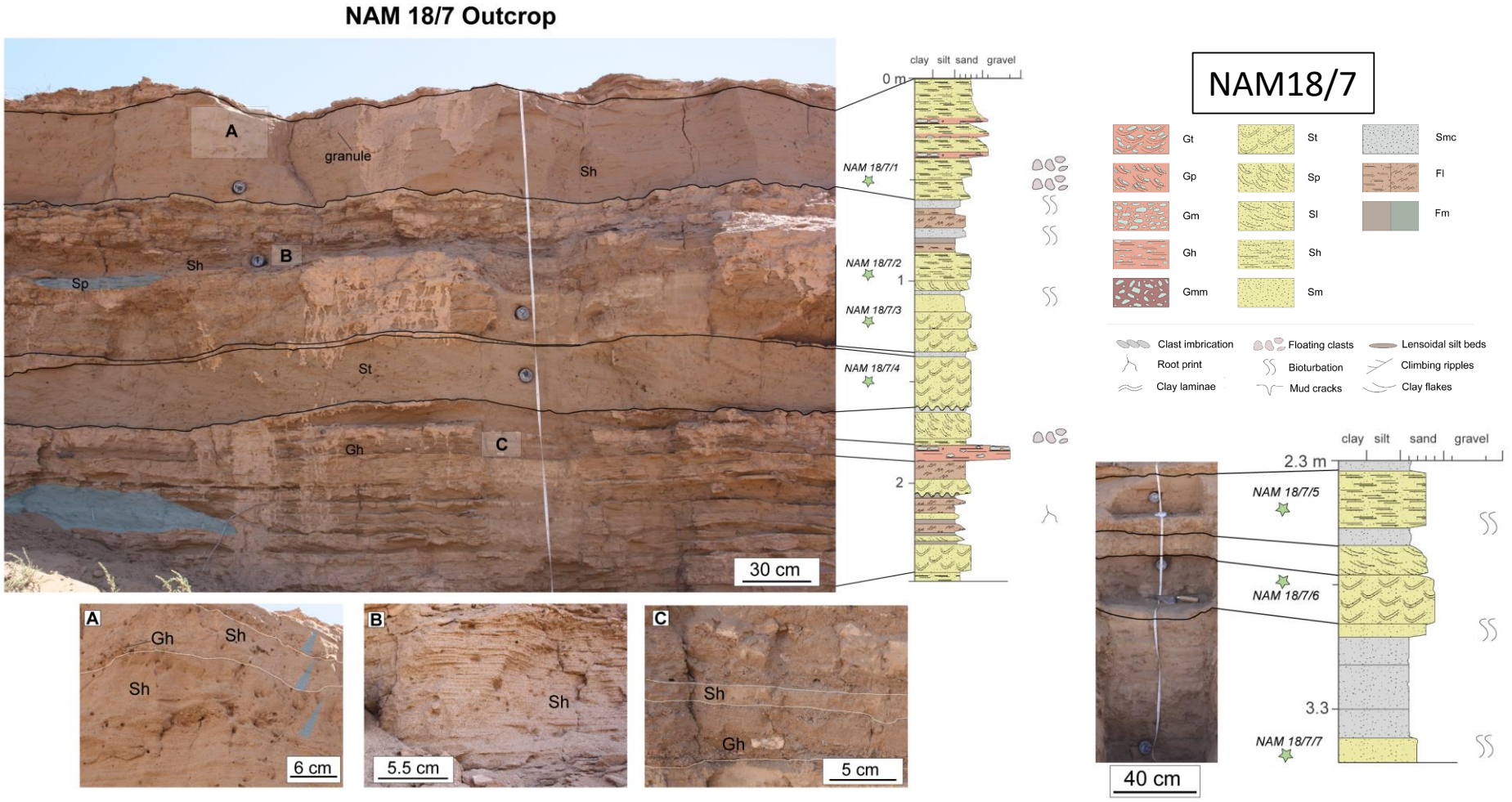

Figure C7. Stratigraphic log of site NAM18/7. Inserts A, B, C, give examples of classification of lithofacies.

Table C5. Results of bulk and clay mineralogy from X-ray diffraction (XRD).

	Bulk mineralogy								Clay mineralogy			
Sample (NAM18/)	**Quartz**	**K-feldspar**	**Plagioclase**	**Pyroxene**	**Amphibole**	**Muscovite**	**Chlorite**	**Clay Subtotal**	**Chlorite**	**Nontronite/ Hectorite**	**Glauconite/ Saponite**	**Muscovite/ Illite**
1/1	29	16	18	0	1	29	7	36	54	3	5	38
1/10	29	34	18	2	1	10	6	16	52	13	6	30
1/12	41	13	6	3	2	26	9	35	52	13	35	0
2/1	29	27	24	3	1	12	3	15	51	0	0	49
2/5	28	31	6	4	1	25	6	31	52	0	0	48
2/12	29	20	5	5	1	32	9	41	48	8	34	10
Average	31	24	13	2.8	1.2	22	6.7	29	51	6	13	29

Table C6. Loss on ignition results. Water content calculated from percentage mass lost after heating to 105˚C for 12 hours. Organic content calculated from subsequent percentage mass lost after heating to 550˚C for 4 hours, and carbonate content calculated from subsequent percentage mass lost after heating to 950˚C for 2 hours.

Sample	Water Content (%)	Organic Content (%)	Carbonate Content (%)
NAM18/1/1	0.48	0.90	0.85
NAM18/1/2	0.77	2.01	1.20
NAM18/1/4	1.72	0.90	0.68
NAM18/1/5	0.70	0.92	0.79
NAM18/1/6	1.26	1.00	0.83
NAM18/1/7	0.42	0.71	0.81
NAM18/1/8	1.24	1.29	1.24
NAM18/1/9	2.90	1.30	1.30
NAM18/1/10	0.62	1.05	0.64
NAM18/1/11	1.02	0.59	0.91
NAM18/1/12	0.39	0.79	0.70
NAM18/2/1	0.75	1.24	1.06
NAM18/2/2	1.73	0.85	1.09
NAM18/2/3	1.20	0.71	1.06
NAM18/2/4	0.63	0.76	1.18
NAM18/2/5	0.87	1.32	0.88
NAM18/2/6	2.75	0.83	1.15
NAM18/2/7	1.46	1.14	0.63
NAM18/2/8	1.59	1.27	0.63
NAM18/2/9	4.19	3.17	1.17
NAM18/2/10	0.61	0.97	0.67
NAM18/2/11	1.90	0.89	0.75
NAM18/2/12	0.37	0.76	0.79
NAM18/4/1	2.32	2.59	1.86
NAM18/4/3	2.67	1.87	1.32
NAM18/4/4	3.34	1.39	0.91
NAM18/4/5	0.50	0.63	0.69
NAM18/7/1	2.69	1.02	1.05
NAM18/7/3	3.28	1.84	1.31
NAM18/7/4	2.46	1.57	1.48
NAM18/7/5	2.00	0.92	0.75
NAM18/7/6	1.03	0.95	0.74
NAM18/7/7	1.25	1.40	1.21

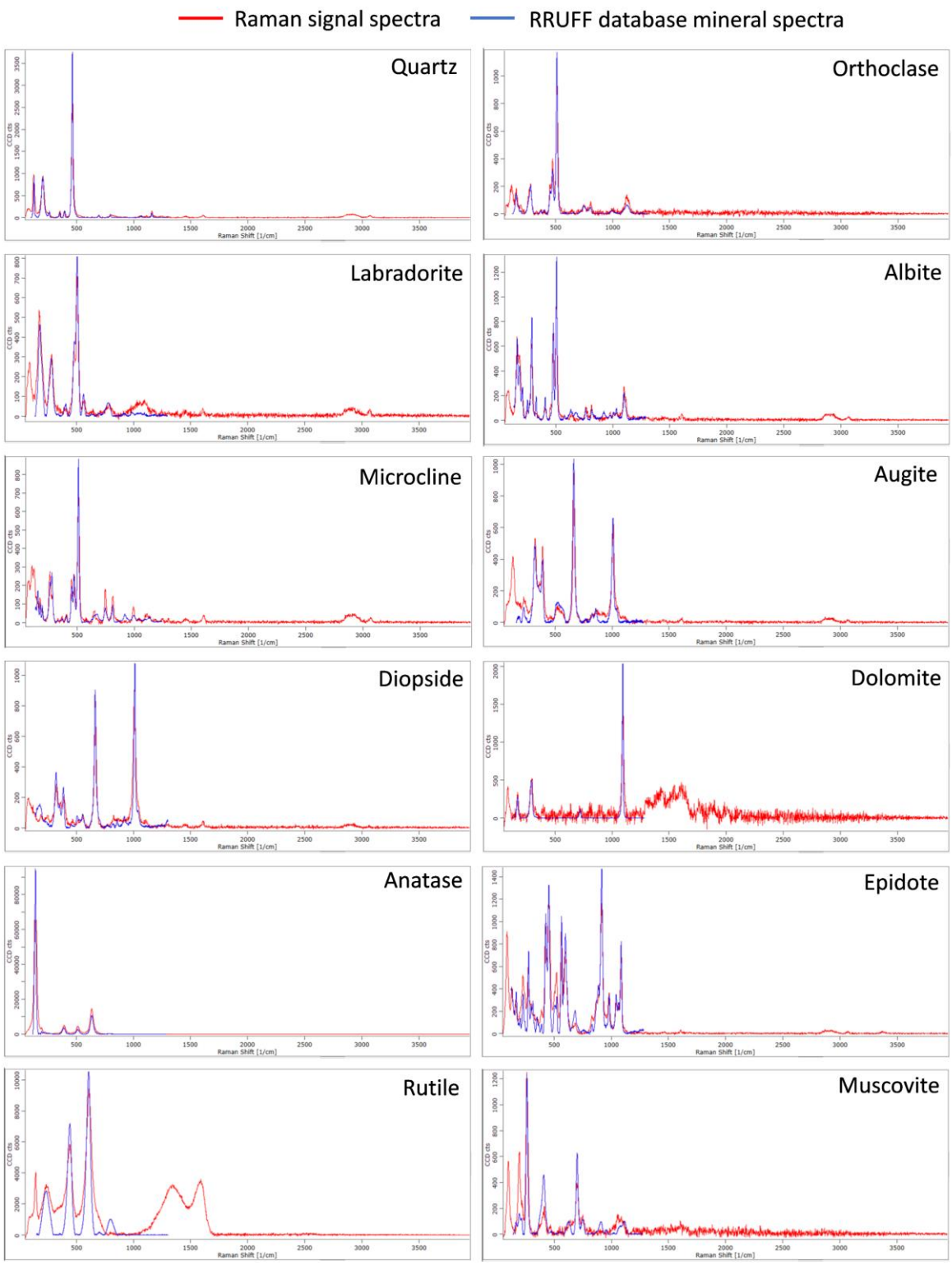

Figure C8. Raman spectra of key minerals identified in petrographic analysis. The red line represents the Raman spectra recorded and the blue line indicates the closest spectra from the reference database in RRUFF using the TrueMatch software. Each mineral has a characteristic spectra, so mineral identification could be undertaken through this approach. Each match was manually verified and manual identification was undertaken where necessary.

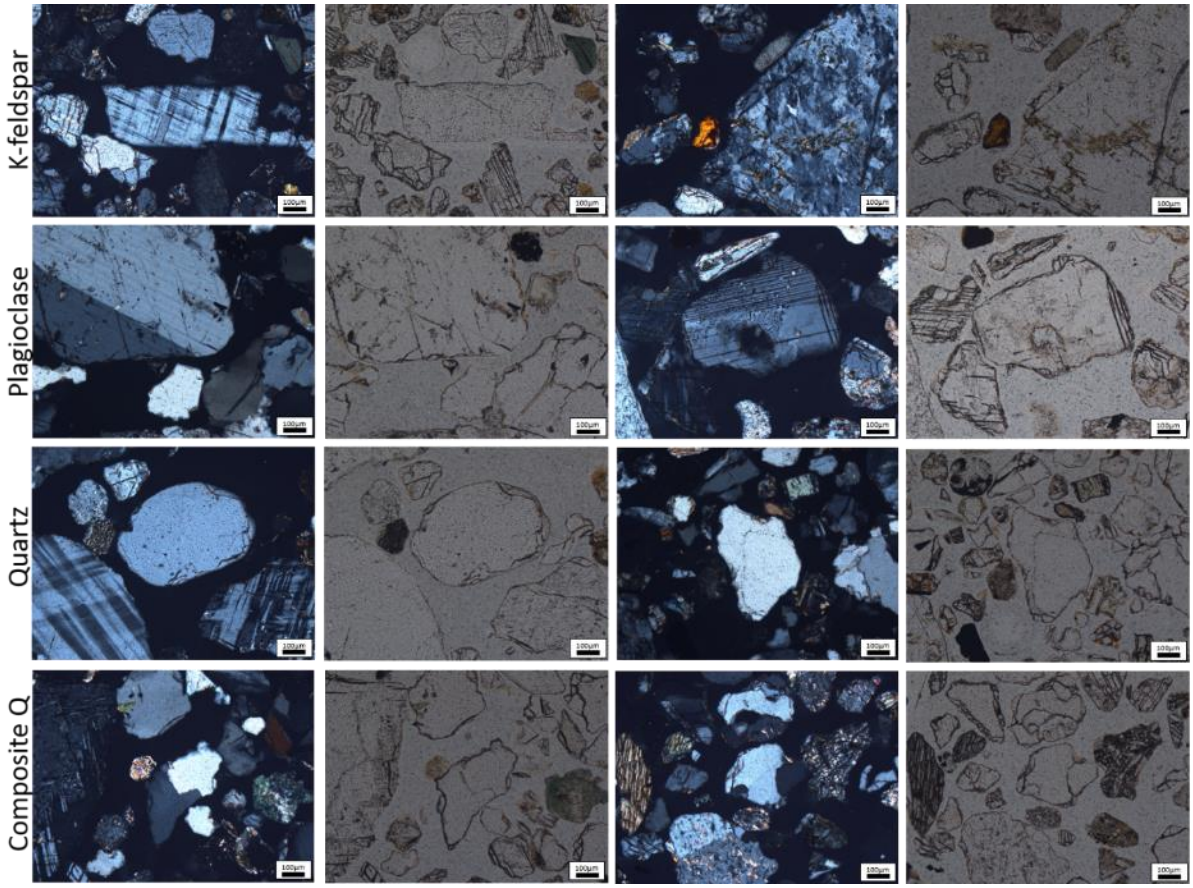

Figure C9. Petrographic images under cross-polarised and plane-polarised light. K-feldspar, plagioclase, quartz, composite quartz. Scale bar = 100 µm for all images.

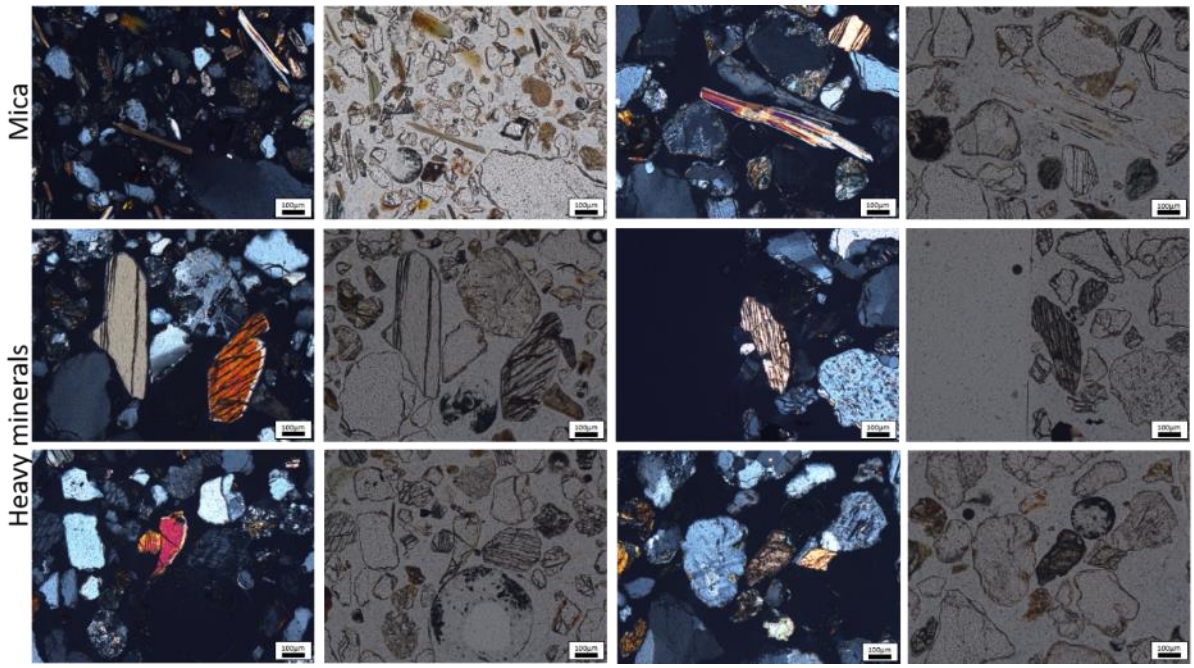

Figure C10. Petrographic images under cross-polarised and plane-polarised light. Mica and heavy minerals. Scale bar = 100 µm for all images.

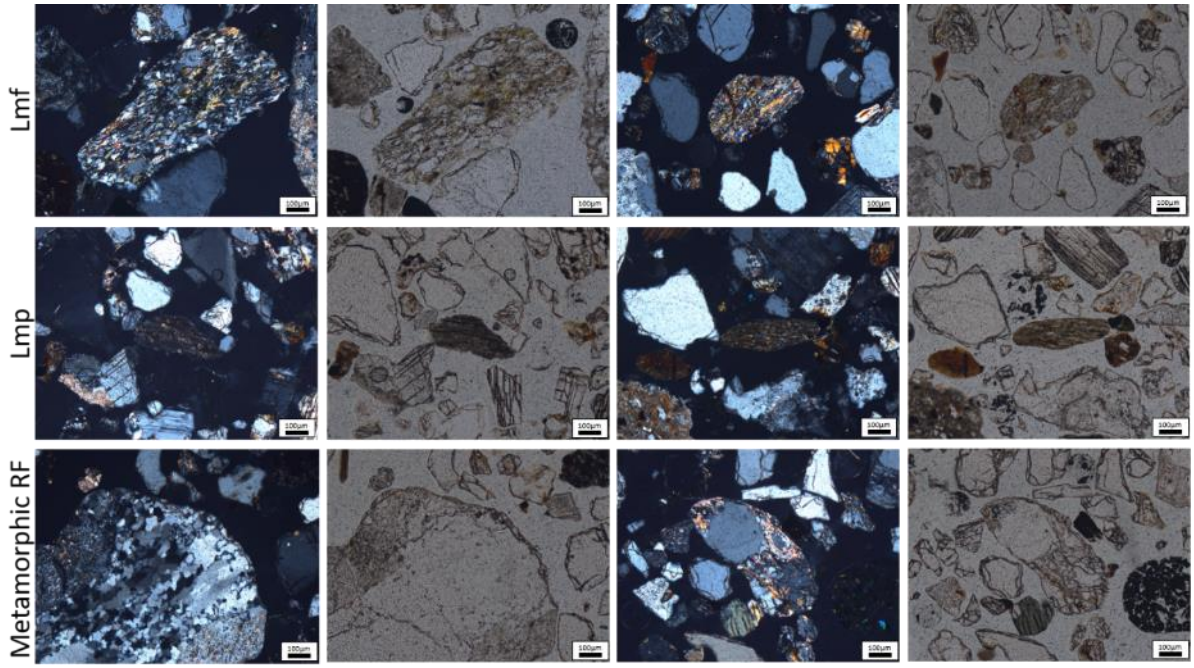

Figure C11. Petrographic images under cross-polarised and plane-polarised light. Metamorphic lithics and rock fragments. Scale bar = 100 µm for all images.

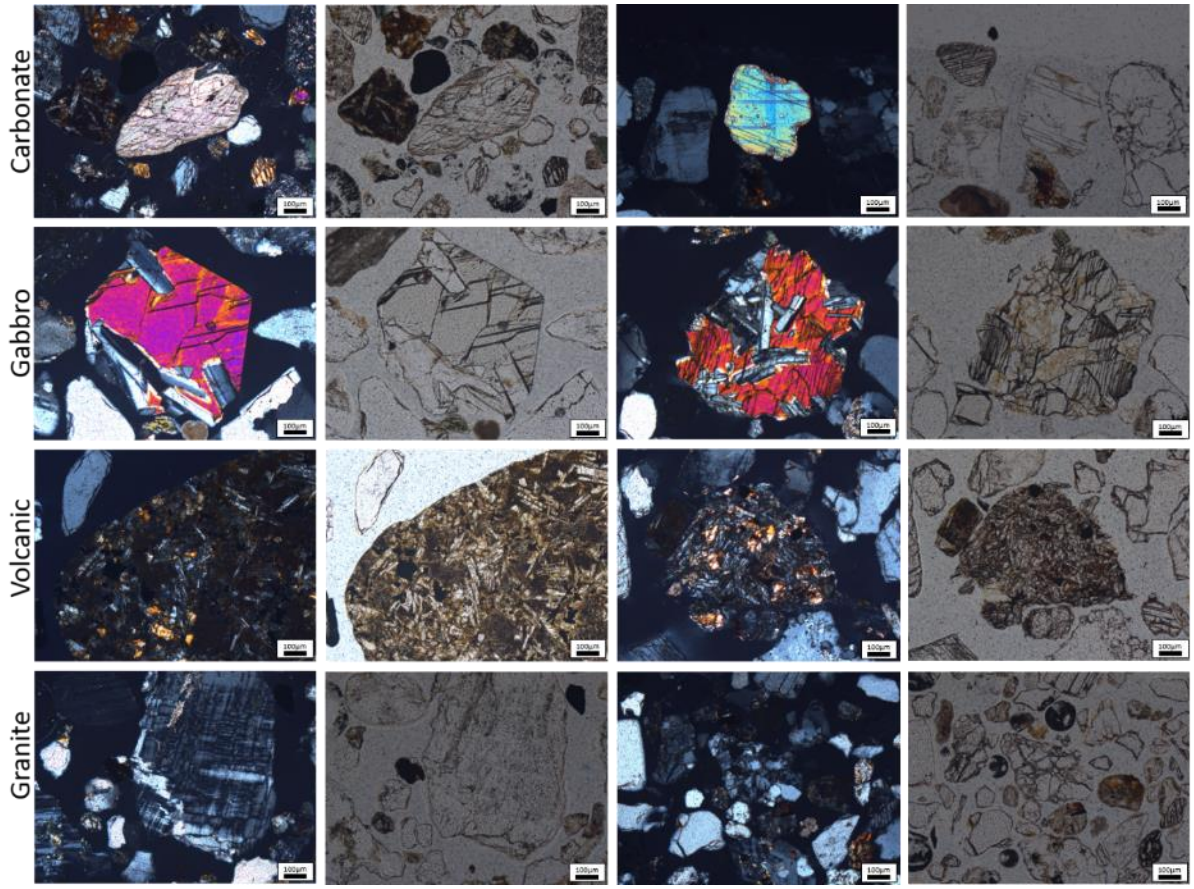

Figure C12. Petrographic images under cross-polarised and plane-polarised light. Rock fragments: carbonate, gabbro, volcanic, and granite. Scale bar = 100 µm for all images.

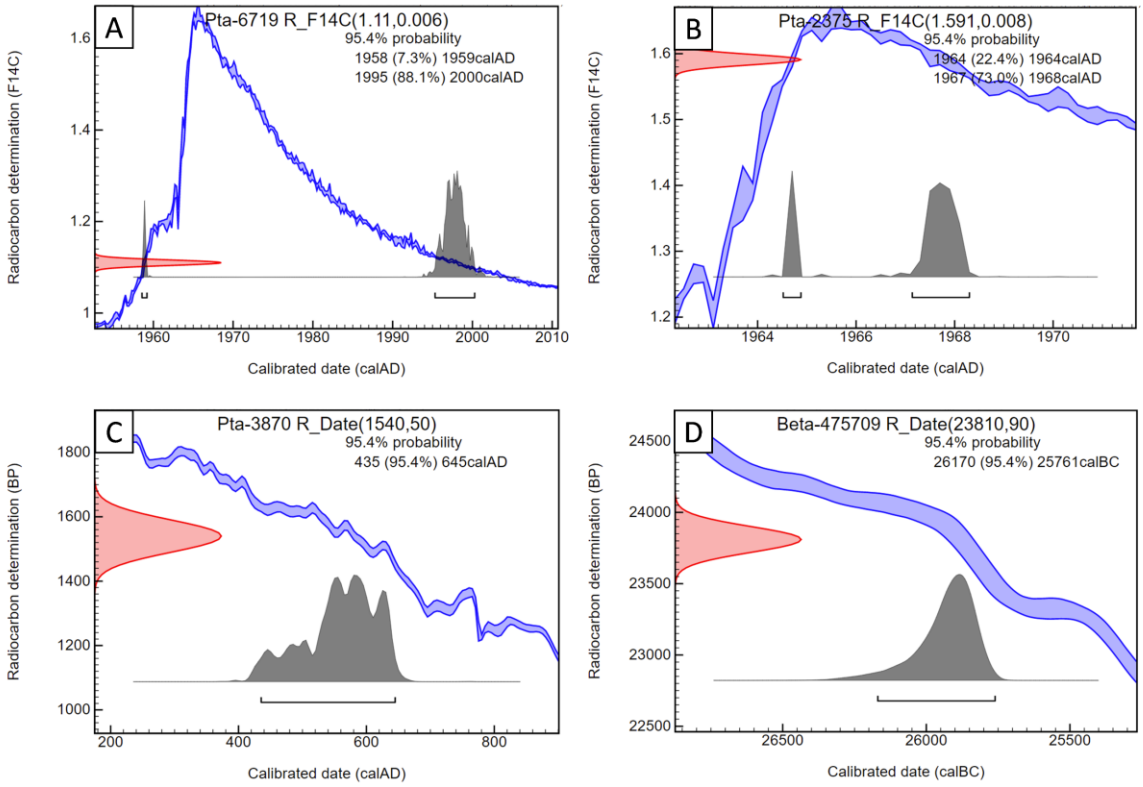

Figure C13. Examples of radiocarbon ages recalibrated in OxCal v4.4.4. (Bronk Ramsey, 2021) Bomb13SH12 (Hua *et al*., 2013; Hogg *et al*., 2020; A and B) and SHCal20 (Hogg *et al*., 2020; C and D). **A)** Pta-6719 (1.11 ± 0.006 %; Nash *et al*., 1997), **B)** Pta-2375 (1.591 ± 0.008 %; Vogel and Visser, 1981), **C)** Pta-3870 (1540 ± 50 yr; Vogel, 1989), **D)** Beta-475709 (23810 ± 90 yr; Völkel *et al*., 2021).

Appendix D – Supplementary material for Chapter 4 (Paper 1)

This appendix includes the Supplementary Material for Chapter 4, Paper 1: *Holocene fluvial depositional regimes of the Huab River, Skeleton Coast, Namibia.*

Calculation of lithological contribution

The contribution of source lithologies to the Huab valley fill was assessed through analysis of the surface area of each geological group within the basin. The watershed upstream of the valley fill was delineated using the ESRI hydrological modelling workflow (ESRI, 2021). This analysis was performed on a 30m digital elevation model (ALOS Global Digital Surface Model; ©JAXA). Geological data was provided by the Atlas of Namibia Project (2002), using data from Mendelsohn *et al.* (2002).

The Huab catchment is made up of 6 key lithological groups. In terms of surface area of the catchment, the Huab drains from the Etendeka Plateau (17 %), the metamorphic components of the Kamanjab Inlier (41 %), the Swakop Group and Otavi Group of the Damara Orogen (21.5 %), the sandstones and dolerite intrusions of the Huab basin (11 %), the granite lithologies of the Fransfontein Granite Suite and Damara granites (9 %), and the Kalahari sands in the headwaters (0.5 %).

Grain size

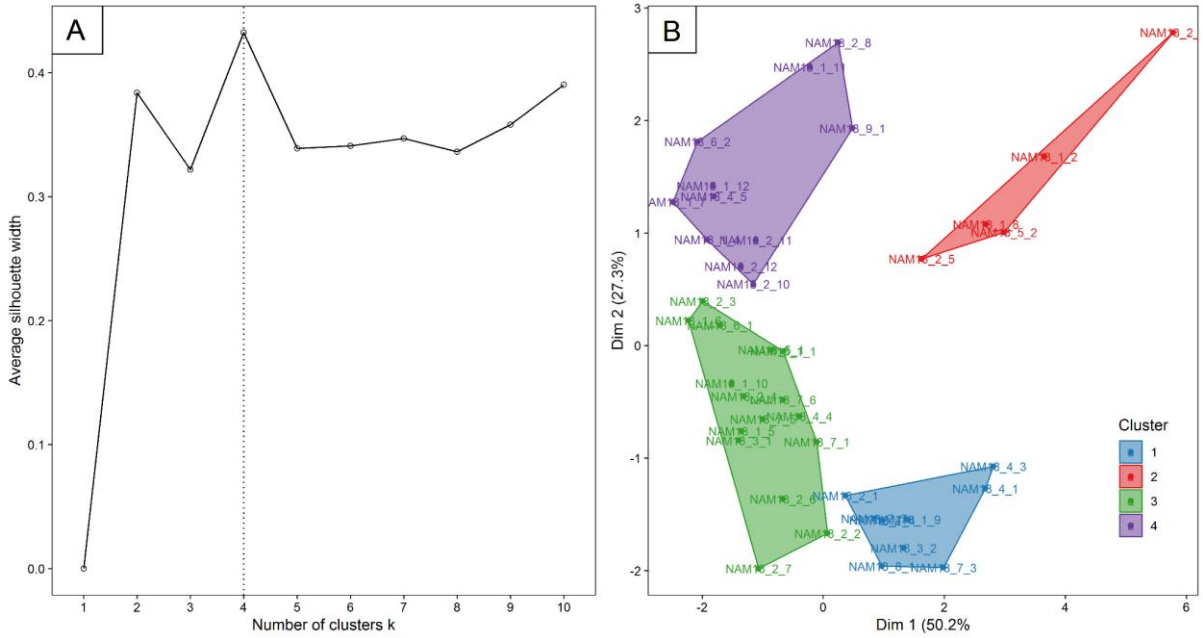

Figure D1. A) Analysis of the optimal number of clusters using the silouhette method in kmeans clustering. This analysis determines how well each sample lies within its cluster, where a high average silhouette width indicates good clustering. The dotted line indicates that 4 clusters is the optimal number of clusters. B) Location of samples amongst clusters.

Table D1. Grain size data used for cluster analysis. % contribution of each grain size range from dry analysis.

Sample (NAM18/)	Depth	% very coarse to medium sand (2 mm-250 µm)	% fine sand (250 µm-125 µm)	% very fine sand (125 µm-63 µm)	% very coarse to coarse silt (63 µm-16 µm)	% medium silt (16 µm-4 µm)	% very fine silt (4 µm-2 µm)	% clay (< 2 µm)
1/1	0.05	34.89	42.23	14	4.18	3.71	0.99	0
1/2	0.25	11.69	33.44	28	12.29	11.69	2.81	0.08
1/4	0.85	66.18	25.16	5.24	1.2	1.74	0.49	0
1/5	1.05	29.17	51.92	16.11	1.03	1.37	0.4	0
1/6	1.35	52.58	42.44	4.42	0	0.25	0.3	0
1/7	1.95	80.28	15.37	2.57	0.81	0.89	0.09	0
1/8	2.3	13.46	39.39	25.33	8.04	11.3	2.42	0.05
1/9	2.45	3.88	34.56	42.06	12.29	6.08	1.13	0
1/10	3	36.44	49.35	10.78	1.3	1.68	0.45	0
1/11	4.6	68.43	16.59	0.53	6.54	6.36	1.52	0.03
1/12	5	76.85	12.42	3.6	4.09	2.58	0.46	0
2/1	0.3	18.13	29.07	27.63	21.48	3.2	0.5	0
2/2	0.7	10.32	44.36	35.35	6.14	3.35	0.48	0
2/3	1.3	52.61	41.38	3.48	0.99	1.05	0.5	0
2/4	1.6	33.41	49.16	13.97	1.19	1.7	0.57	0
2/5	1.85	20.5	39.03	24.35	7.05	7.15	1.87	0.05
2/6	2.15	14.2	56.47	24.36	1.84	2.68	0.45	0
2/7	2.85	12.72	54.5	31.74	1.04	0	0	0
2/8	3.3	59.1	27.07	4.02	2.8	5.02	1.94	0.06
2/9	3.75	6.05	24.71	31.84	16.63	16.45	4.23	0.1
2/10	3.9	51.87	30.67	11.17	2.4	3.04	0.84	0
2/11	4.15	58	25.77	8.5	3.31	3.41	1.01	0
2/12	4.7	58.33	25.22	8.69	4.17	3.01	0.58	0
3/1	1.5	27.86	53.56	15.8	1.11	1.33	0.33	0
3/2	1.5	4.5	28.8	40.14	20.78	5.01	0.78	0
4/1	0.4	4.68	12.02	29.79	44.04	8.2	1.26	0
4/3	1.35	4.14	15.24	33.3	36.73	8.99	1.61	0
4/4	1.8	21	52.6	20.36	1.35	3.55	1.13	0
4/5	1.95	72.03	19.5	3.94	1.54	2.31	0.68	0
5/1	0.25	40.57	35.11	13.49	6.98	3.18	0.66	0
5/2	0.5	11.15	35.04	25.14	15.93	10.33	2.36	0.06
6/1	0.85	46.3	44.01	5.89	1.51	1.76	0.54	0
6/2	3.15	86.24	7.06	1.62	2.28	2.35	0.46	0
7/1	0.5	21.45	41.82	24.11	7.84	4	0.77	0
7/3	1.2	1.75	17.3	39.7	35.16	5.31	0.77	0
7/4	1.5	9.95	29.59	34.44	20.59	4.76	0.68	0
7/5	2.45	31.68	42.41	16.6	6.9	2.01	0.41	0
7/6	2.85	33.85	36.22	22.28	3.71	3.42	0.52	0
7/7	3.65	12.19	28.44	36.4	17.68	4.71	0.57	0
8/1	1.35	5.11	31.03	40.27	19.28	3.71	0.6	0
9/1	1.3	44.91	35.03	11.7	1.76	4.72	1.82	0.06

Heavy mineral assemblage

Table D2. Heavy mineral data from each grain size fraction (30, 63, 125 µm), the proportion that these grain sizes comprise of the heavy mineral fraction of sediment, the number of signals analysed using Raman spectroscopy, and the heavy mineral concentration (HMC; following Garzanti and Andò (2007)). All = the grain sizes averaged together. Ap = Apatite, Amp = amphibole, Ep = epidote, Px = pyroxene, Grt = garnet, Olv = olivine, Ox = oxides, Rtl = rutile, Ttn = titanite, Trm = tourmaline, Zir = zircon. The contribution of each grain size to the bulk HM fraction varies between samples: 30-63 µm (1-45 %), 63-125 µm (14-69 %), 125-250 µm (6-66 %). Across most samples, occurrence of amphibole, olivine, and pyroxene increases with grain size fraction. In contrast, the occurrence of apatite, epidote, titanite, and zircon decreases. The proportion of ultradense minerals are highest in the smallest grain size: ~6.5 % in 30-63 µm, ~2.4 % in 63-125 µm, and ~1.7 % in 125-250 µm, and lower density minerals are highest in the largest grain size: ~7.8 % in 30-63 µm, ~17.0 % in 63-125 µm, and ~24.4 % in 125-250 µm.

Sample (NAM18)	Fraction (µm)	Proportion of HM fraction (%)	Mineral (%)											Signals	HMC
			Ap	Amp	Ep	Grt	Olv	Ox	Pyx	Rtl	Ttn	Trm	Zir		
1/1	**all**	-	**0.3**	**19.7**	**28.7**	**0.6**	**2.0**	**2.0**	**38.5**	**0.7**	**4.0**	**1.1**	**1.9**	**1573**	**14.4**
	30	13.3	0.4	13.0	38.2	0.9	0.7	2.2	33.9	0.4	4.5	0.2	4.9	559	-
	63	61.2	0.2	22.5	27.9	0.5	2.2	2.0	37.3	0.9	4.2	1.4	0.7	567	-
	125	25.5	0.5	23.6	20.0	0.2	3.1	1.9	44.3	0.7	3.4	1.7	0.0	447	-
1/2	**all**	-	**1.7**	**13.2**	**31.9**	**0.5**	**1.9**	**2.7**	**37.4**	**1.5**	**7.1**	**1.3**	**0.5**	**1483**	**12.8**
	30	22.3	2.6	4.6	43.0	0.7	0.5	2.9	35.3	0.4	7.7	0.5	1.3	556	-
	63	61.8	1.7	13.5	32.0	0.8	1.5	1.2	39.8	1.7	6.9	0.2	0.2	542	-
	125	15.9	0.9	21.5	20.6	0.0	3.7	4.0	37.1	2.5	6.5	3.1	0.0	385	-
1/4	**all**	-	**1.2**	**13.0**	**27.9**	**0.4**	**2.2**	**3.3**	**41.6**	**0.8**	**6.8**	**0.7**	**1.5**	**1373**	**12.6**
	30	3.2	1.7	3.7	37.7	0.7	0.4	3.1	38.8	0.9	8.3	0.2	3.1	474	-
	63	29.9	0.8	14.3	30.2	0.2	1.9	2.5	40.1	0.8	7.0	0.4	1.5	514	-
	125	66.9	0.9	20.9	15.7	0.3	4.4	4.4	45.9	0.6	5.2	1.5	0.0	385	-
1/6	**all**	-	**1.3**	**13.2**	**24.8**	**1.4**	**2.6**	**3.2**	**37.0**	**1.0**	**7.2**	**2.0**	**5.8**	**1343**	**12.0**
	30	1.0	2.8	4.2	28.9	2.1	1.0	1.0	33.1	0.7	9.4	1.7	15.0	292	-
	63	35.5	0.8	15.6	29.7	1.6	3.1	4.7	33.8	0.8	6.4	0.6	1.8	517	-
	125	63.6	0.4	19.8	15.7	0.4	3.7	3.9	44.0	1.4	5.8	3.7	0.6	534	-
1/7	**all**	-	**0.9**	**15.7**	**24.6**	**1.0**	**3.6**	**5.7**	**42.8**	**0.4**	**3.1**	**0.5**	**1.2**	**1308**	**19.8**
	30	1.1	1.1	10.5	34.4	0.4	1.1	3.2	43.2	0.0	3.0	0.6	2.1	482	-
	63	21.5	1.5	19.2	25.4	0.4	4.1	4.3	39.4	0.2	3.0	0.4	1.3	495	-
	125	77.4	0.0	17.3	14.1	2.2	5.8	9.6	45.8	1.0	3.2	0.3	0.3	331	-
1/8	**all**	-	**1.8**	**14.1**	**34.2**	**1.0**	**0.9**	**2.7**	**33.6**	**0.7**	**8.3**	**0.8**	**1.4**	**1175**	**13.0**
	30	10.9	3.3	3.8	42.6	1.5	0.8	2.5	31.3	1.0	8.0	1.0	3.8	406	-
	63	69.4	1.6	17.0	31.4	0.8	1.4	3.0	35.4	0.5	7.8	0.5	0.3	394	-
	125	19.7	0.6	21.5	28.8	0.6	0.6	2.6	34.0	0.6	9.0	0.9	0.3	375	-
1/9	**all**	-	**2.3**	**14.4**	**32.8**	**0.5**	**0.8**	**2.8**	**36.3**	**1.3**	**6.5**	**0.6**	**0.8**	**1510**	**11.8**
	30	31.7	3.4	5.1	37.7	1.0	0.5	3.0	36.2	1.3	8.0	0.2	2.3	619	-
	63	61.7	2.1	12.7	33.7	0.4	1.0	1.4	40.2	0.4	5.7	1.0	0.2	512	-
	125	6.5	1.5	25.3	27.1	0.0	0.9	4.0	32.3	2.1	5.8	0.6	0.0	379	-
1/10	**all**	-	**1.4**	**12.1**	**33.4**	**0.6**	**2.0**	**2.3**	**38.1**	**0.9**	**5.7**	**0.5**	**2.2**	**1441**	**12.5**
	30	2.3	1.5	4.4	43.9	0.7	0.7	1.5	33.2	1.3	5.6	0.5	5.8	562	-

	63	40.3	1.7	12.6	34.4	1.0	2.7	2.7	35.4	1.5	6.9	0.0	0.4	502	-
	125	57.5	0.9	19.3	21.8	0.0	2.5	2.8	45.8	0.0	4.7	0.9	0.3	377	-
1/11	**all**	-	**0.5**	**13.0**	**23.0**	**1.1**	**3.0**	**3.8**	**47.7**	**0.7**	**4.5**	**0.2**	**2.3**	**1439**	**13.2**
	30	2.2	0.6	3.8	24.6	1.4	3.4	3.0	52.8	0.6	4.4	0.0	5.4	522	-
	63	23.6	0.8	14.5	26.5	1.3	2.1	4.6	43.2	0.8	4.2	0.2	1.5	496	-
	125	74.2	0.0	20.6	18.0	0.5	3.5	3.8	47.2	0.8	4.8	0.5	0.0	421	-
1/12	**all**	-	**0.8**	**16.2**	**22.8**	**1.1**	**1.9**	**4.5**	**46.9**	**0.9**	**2.9**	**0.9**	**0.7**	**1481**	**20.0**
	30	5.1	1.1	10.1	27.9	1.1	1.1	1.3	51.7	0.7	2.8	0.2	1.3	551	-
	63	29.3	0.8	19.1	25.7	1.0	1.6	2.2	43.4	1.0	3.0	1.2	0.8	538	-
	125	65.7	0.5	19.5	14.7	1.3	2.9	10.0	45.5	1.1	2.9	1.3	0.0	392	-
2/1	**all**	-	**1.8**	**16.2**	**33.7**	**0.5**	**0.5**	**1.8**	**35.6**	**0.9**	**6.9**	**0.6**	**0.9**	**1584**	**12.9**
	30	35.7	2.9	3.6	42.8	0.9	0.5	1.1	36.7	0.5	8.8	0.4	1.8	567	-
	63	46.5	1.2	12.3	33.1	0.6	0.4	3.7	38.0	1.5	7.1	0.4	0.4	519	-
	125	17.8	1.3	32.7	25.3	0.0	0.4	0.7	32.2	0.7	4.9	1.1	0.4	498	-
2/3	**all**	-	**0.9**	**12.6**	**25.1**	**1.3**	**2.5**	**2.6**	**42.6**	**0.9**	**6.5**	**0.6**	**4.1**	**1351**	**11.2**
	30	0.8	1.6	1.9	34.9	2.2	0.9	3.1	36.1	0.9	7.2	0.0	10.9	327	-
	63	36.1	0.0	13.8	24.1	1.1	3.1	3.1	43.2	1.1	7.4	1.3	1.3	577	-
	125	63.1	1.0	22.0	16.2	0.5	3.3	1.5	48.6	0.8	5.1	0.5	0.0	447	-
2/5	**all**	-	**1.6**	**12.5**	**29.9**	**1.0**	**2.2**	**2.5**	**39.4**	**0.8**	**7.8**	**0.8**	**0.8**	**1323**	**13.1**
	30	13.8	2.2	8.9	34.2	1.9	1.9	2.5	34.2	0.9	9.2	0.9	1.9	323	-
	63	61.1	1.7	11.0	33.0	0.0	1.5	2.7	38.8	1.2	8.9	0.8	0.2	507	-
	125	25.2	1.0	17.7	22.5	1.0	3.1	2.4	45.1	0.2	5.3	0.7	0.2	493	-
2/7	**all**	-	**1.0**	**11.5**	**33.7**	**0.7**	**1.8**	**2.4**	**37.4**	**0.6**	**7.7**	**0.5**	**2.3**	**1455**	**12.8**
	30	5.7	1.5	1.5	40.2	1.0	1.0	2.5	36.3	1.2	8.1	0.2	6.1	414	-
	63	67.6	1.3	12.4	34.9	0.4	2.6	2.3	38.6	0.0	6.9	0.0	0.4	565	-
	125	26.7	0.2	20.7	25.9	0.7	1.9	2.4	37.4	0.5	8.0	1.2	0.5	476	-
2/10	**all**	-	**1.0**	**14.6**	**33.3**	**0.8**	**1.2**	**3.8**	**34.9**	**1.0**	**5.4**	**0.7**	**2.9**	**1527**	**10.9**
	30	3.7	0.9	3.3	44.3	0.9	0.4	3.3	32.2	2.0	5.5	0.0	6.8	463	-
	63	41.9	1.4	16.4	32.7	0.6	0.8	5.5	34.1	0.4	5.5	0.6	1.6	540	-
	125	54.4	0.9	24.0	22.9	0.9	2.4	2.6	38.6	0.7	5.0	1.5	0.4	524	-
2/12	**all**	-	**1.5**	**14.0**	**26.7**	**0.4**	**1.7**	**4.5**	**41.9**	**0.9**	**5.7**	**0.7**	**1.6**	**1466**	**16.5**
	30	3.6	3.0	5.6	33.3	0.2	1.5	3.9	40.6	1.1	5.6	0.0	4.3	548	-

	63	32.7	1.2	13.4	28.7	0.4	1.6	2.4	42.3	1.2	6.4	1.8	0.4	556	-
	125	63.6	0.3	23.0	17.9	0.6	1.9	7.2	42.8	0.3	5.0	0.3	0.0	362	-
7/1	**all**	-	**1.7**	**16.1**	**29.9**	**0.5**	**1.5**	**2.3**	**37.4**	**0.9**	**7.4**	**0.7**	**1.2**	**1505**	**14.4**
	30	13.1	2.8	3.5	40.2	0.4	1.5	1.3	35.9	1.5	9.1	0.4	3.0	468	-
	63	61.5	1.3	15.5	30.9	1.0	1.1	3.1	38.2	0.4	7.3	0.6	0.4	557	-
	125	25.4	0.9	29.3	18.4	0.2	1.9	2.6	38.1	0.9	5.7	1.2	0.2	480	-
7/4	**all**	-	**1.4**	**14.1**	**29.0**	**0.3**	**1.3**	**1.6**	**42.7**	**0.6**	**7.7**	**0.4**	**0.4**	**1551**	**8.8**
	30	37.3	2.5	5.3	40.6	0.4	0.4	1.1	38.3	0.7	9.0	1.2	0.2	573	-
	63	51.7	1.4	15.9	26.7	0.5	1.1	1.4	44.4	0.2	7.3	0.0	0.5	485	-
	125	11.0	0.5	21.1	19.8	0.0	2.5	2.5	45.2	0.9	6.8	0.0	0.5	493	-
7/7	**all**	-	**1.0**	**16.9**	**30.7**	**0.5**	**1.4**	**1.8**	**38.2**	**0.5**	**7.2**	**1.1**	**0.4**	**1507**	**11.9**
	30	45.8	1.3	6.6	42.7	0.6	0.2	0.6	34.9	0.8	10.8	0.9	0.6	539	-
	63	41.7	1.2	15.8	29.6	0.2	1.0	1.8	41.3	0.2	6.5	1.8	0.2	529	-
	125	12.4	0.5	28.4	19.8	0.8	3.1	3.1	38.3	0.5	4.2	0.5	0.5	439	-

Appendix E – Supplementary data for Chapter 5 (Paper 2): part 1

This appendix includes the Supplementary Material for Chapter 5, Paper 2: *A chronological fluvial database: assessing the palaeoenvironmental record from rivers in southwestern Africa.* The excel spreadsheet of the database is available electronically as Appendix F.

This document contains the details of sites and a description of the metadata included in the chronological database of southwestern Africa's fluvial archives. The database is included in the Supplementary Material as an excel spreadsheet.

Table E1. Highlights of the database. Ordered by site (see Figure 5.1 in the paper)

No	Site Name	River	Location	Region	Sed. Context	No. OSL ages	No. ^{14}C ages	Reference(s)
1	Gauxa Lagoon	Okavango	18.40˚S, 21.86˚E	N Kalahari	Overbank	0	4	Nash *et al.* (2006)
2	Ncamasere Valley	Okavango	18.60˚S, 22.03˚E	N Kalahari	Overbank	0	9	Nash *et al.* (1997) Nash *et al.* (2006)
3	Tamacha Valley	Okavango	18.85˚S, 22.28˚E	N Kalahari	Overbank	0	3	Nash *et al.* (2006)
4	Xugana	Okavango	19.08˚S, 23.05˚E	N Kalahari	Scroll bar, Channel	18	0	Tooth *et al.* (2022)
5	Xaudum Valley	Xaudum	19.13˚S, 21.82˚E	N Kalahari	Channel	0	1	Shaw *et al.* (1992)
6	Gidikwe Ridge	Okwa	21.39˚S, 24.44˚E	N Kalahari	Channel	0	3	Shaw *et al.* (1992)
7	Okwa valley	Okwa	22.37˚S, 22.65˚E	N Kalahari	Channel	0	1	Shaw *et al.* (1992)
8	Khumib Silts 1	Khumib	18.83˚S, 12.49˚E	Namib	Channel	5	1	Vogel (1989) Srivastava *et al.* (2004)
9	Khumib Silts 2	Khumib	18.77˚S, 12.57˚E	Namib	Channel	2	0	Srivastava *et al.* (2004)
10	Hoarusib River Mouth	Hoarusib	19.07˚S, 12.57˚E	Namib	Channel	0	4	Vogel (1989) Vogel and Rust (1987)
11	Hoarusib Young Terrace	Hoarusib	19.03˚S, 12.63˚E	Namib	Channel	0	1	Vogel (1989)
12	Hoarusib Clay Castles	Hoarusib	18.97˚S, 12.70˚E	Namib	Channel, SWD	11	12	Vogel (1989) Vogel and Rust (1987) Srivastava *et al.* (2005)
13	Opuwo	Hoarusib	18.20˚S, 13.83˚E	Namib	Channel	4	0	Brunotte *et al.* (2009)
14	Hoanib Dune Belt	Hoanib	19.44˚S, 12.84˚E	Namib	Channel	0	3	Vogel (1989) Vogel and Rust (1987)
15	Amspoort Silts	Hoanib	19.35˚S, 13.16˚E	Namib	Channel, River end	6	12	Vogel (1989) Vogel and Rust (1987) Rust (1999) Eitel *et al.* (2005)
16	Lower Khowarib Gorge	Hoanib	19.26˚S, 13.88˚E	Namib	River end	3	0	Eitel *et al.* (2001) Eitel *et al.* (2006)
17	Central Khowarib Gorge	Hoanib	19.31˚S, 14.00˚E	Namib	River end, SWD	7	0	Eitel *et al.* (2006)
18	Ombonde	Hoanib	19.34˚S, 14.12˚E	Namib	River end	4	0	Eitel *et al.* (2006)
19	Otjovasandu	Hoanib	19.40˚S, 14.28˚E	Namib	River end	3	0	Eitel *et al.* (2006)
20	Okawerongo-Nguruvai-Aap	Hoanib	18.98˚S, 14.17˚E	Namib	River end	6	0	Eitel *et al.* (2006)
21	Okawerongo	Hoanib	19.04˚S, 14.28˚E	Namib	River end	3	0	Eitel *et al.* (2006)
22	Huab Skeleton Coast valley fill	Huab	20.87˚S, 13.65˚E	Namib	Channel, Overbank, SWD	51	0	Thomas *et al.* (2017) Walsh *et al.* (2022)
23	Dieprivier	Huab	20.50˚S, 14.96˚E	Namib	River end	7	0	Eitel and Zoller (1996) Eitel *et al.* (2001)
24	Khan	Swakop	22.68˚S, 14.92˚E	Namib	SWD	2	0	Heine and Völkel (2011)
25	Otjimbingwe	Swakop	22.32˚S, 16.25˚E	Namib	Channel, SWD	8	0	Greenbaum *et al.* (2014)
26	Ranches	Swakop	22.28˚S, 16.38˚E	Namib	SWD	2	0	Greenbaum *et al.* (2014)

27	Swakoppoort Dam	Swakop	22.20˚S, 16.52˚E	Namib	SWD	5	1	Greenbaum *et al.* (2014)
28	Rooibank	Kuiseb	23.23˚S, 14.72˚E	Namib	Channel	0	2	Vogel and Visser (1981)
29	Kuiseb valley	Kuiseb	23.39˚S, 14.88˚E	Namib	SWD	0	4	Vogel and Visser (1981)
30	Homeb	Kuiseb	23.62˚S, 15.15˚E	Namib	Channel, Dune-dammed lake, Overbank, SWD	17	44	Vogel and Visser (1981) Vogel (1989) Eitel and Zoller (1996) Bourke *et al.* (2003) Yamagata and Mizuno (2005) Srivastava *et al.* (2006) Miyamoto (2010)
31	K-400	Kuiseb	23.65˚S, 15.54˚E	Namib	SWD	16	1	Grodek *et al.* (2013)
32	K-130	Kuiseb	23.48˚S, 15.64˚E	Namib	SWD	4	2	Grodek *et al.* (2013)
33	West Pan A	Tsondab	23.60˚S, 14.82˚E	Namib	Interdune	0	1	Teller *et al.* (1990)
34	Narabeb	Tsondab	23.82˚S, 14.95˚E	Namib	Interdune	13	7	Vogel and Visser (1981) Teller and Lancaster (1986) Vogel (1989) Stone *et al.* (2010)
35	Harmut Pan	Tsondab	23.81˚S, 15.04˚E	Namib	Interdune	5	0	Stone *et al.* (2010)
36	Salty Pan, Namib IV, Bone Pan	Tsondab	23.74˚S, 15.29˚E	Namib	Interdune	0	3	Teller *et al.* (1990)
37	Ancient Tracks	Tsondab	23.96˚S, 15.29˚E	Namib	Interdune	6	0	Stone *et al.* (2010)
38	Tsondab vlei	Tsondab	23.93˚S, 15.37˚E	Namib	Interdune	0	3	Vogel and Visser (1981)
39	Tsondab Valley	Tsondab	23.99˚S, 16.07˚E	Namib	Channel, SWD	0	4	Vogel (1989) Völkel *et al.* (2021)
40	BüllsPort Playa	Tsondab	24.16˚S, 16.37˚E	Namib	Alluvial fan, Playa	3	9	Völkel *et al.* (2021)
41	Sossus Vlei	Tsauchab	24.75˚S, 15.30˚E	Namib	Channel, Interdune	9	7	Vogel and Visser (1981) Brook *et al.* (2006) Völkel *et al.* (2021)
42	Tsauchab valley a	Tsauchab	24.64˚S, 15.66˚E	Namib	SWD	2	0	Völkel *et al.* (2021)
43	Tsauchab valley b	Tsauchab	24.47˚S, 16.14˚E	Namib	Channel, SWD	39	21	Völkel *et al.* (2021)
44	Tsauchab valley c	Tsauchab	24.30˚S, 16.27˚E	Namib	Channel, SWD	4	1	Völkel *et al.* (2021)
45	Vogelkranz	Fish	24.31˚S, 17.64˚E	Orange	SWD	4	1	Cloete *et al.* (2018)
46	Echo Camp	Fish	27.34˚S, 17.70˚E	Orange	SWD	5	0	Cloete *et al.* (2018)
47	Huns	Fish	27.40˚S, 17.19˚E	Orange	Overbank	0	1	Stengel and Leser (2004)
48	Auob	Auob	25.03˚S, 18.90˚E	Orange	Channel	0	2	Heine (1990)
49	Nossob	Nossob	26.28˚S, 20.78˚E	Orange	Channel	0	1	Heine (1990)
50	Bella Vista + Aansluit	Kuruman	26.71˚S, 22.44˚E	Orange	Channel, SWD	0	3	Shaw *et al.* (1992)
51	Groot Drink	Kuruman	26.83˚S, 22.75˚E	Orange	Channel	0	1	Shaw *et al.* (1992)
52	Molopo confluence	Molopo	26.94˚S, 20.66˚E	Orange	Channel	2	9	Heine (1990) Hurkamp *et al.*, (2011)
53	Molopo canyon	Molopo	28.49˚S, 20.24˚E	Orange	Alluvial fan, Channel	13	0	Ramisch *et al.* (2017)
54	Bloeddrift	Orange	28.36˚S, 16.81˚E	Orange	SWD	3	6	Zawada *et al.* (2000)
55	Xobies	Orange	28.22˚S, 16.85˚E	Orange	SWD	3	8	Zawada *et al.* (2000)
56	Helskloof	Orange	28.72˚S, 17.47˚E	Orange	SWD	1	0	Heine and Völkel (2011)
57	Orange Site 9,14,19	Orange	29.48˚S, 22.61˚E	Orange	SWD	5	3	Zawada *et al.* (2000)
58	Erfkroon	Modder	28.87˚S, 25.60˚E	Orange	Channel, Overbank	17	0	Churchill *et al.* (2000) Tooth *et al.* (2013) Lyons *et al.* (2014)
59	Eselfontein	Buffels	29.76˚S, 17.69˚E	Namib	SWD	0	4	Benito *et al.* (2011)
60	Messelpad	Buffels	29.86˚S, 17.64˚E	Namib	SWD	0	5	Benito *et al.* (2011)
61	Kamassies	Buffels	29.99˚S, 18.28˚E	Namib	SWD	5	9	Benito *et al.* (2011)
62	Rooifontein	Buffels	30.10˚S, 18.30˚E	Namib	SWD	2	4	Benito *et al.* (2011)
63	Huis	Huis	33.92˚S, 20.75˚E	Eastern Cape	Channel, SWD	0	3	Bordy *et al.* (2018)
64	Wilgehout	Gourits	33.16˚S, 20.82˚E	Eastern Cape	Channel	0	1	Zawada (1994)
65	Buffels a	Gourits	33.24˚S, 20.92˚E	Eastern Cape	Channel, SWD	0	3	Zawada (1994)

66	Buffels b	Gourits	33.41˚S, 20.95˚E	Eastern Cape	SWD	0	3	Zawada (1994)
67	Oude Wagendrift, Karre Kamma, Uitspan	Gourits	33.78˚S, 21.64˚E	Eastern Cape	Overbank	0	18	Damm and Hagedorn (2010)
68	Le Roux	Gourits	33.54˚S, 22.46˚E	Eastern Cape	Overbank	0	4	Damm and Hagedorn (2010)
69	Poort-Ottershoek	Gourits	33.98˚S, 21.66˚E	Eastern Cape	Overbank	0	7	Damm and Hagedorn (2010)
70	Wilgerbosch	Wilgerbosch	31.88˚S, 24.69˚E	Eastern Cape	Channel, Overbank	17	1	Oldknow and Hooke (2017) Oldknow *et al.* (2020)

Content of database

1. Publication details

PUBDATE: numeric value; Publication year.

AUTHOR: character entry; e.g. Srivastava *et al*.

REFERENCE: character entry.

PAPERID: numeric value; Unique number ID of the paper.

2. Site and river details

RIVER: character entry; River name (e.g. Hoarusib).

RIVERID: numeric value; Unique number ID of the river.

REGION: character entry; e.g. Namib, N Kalahari, Orange, E Cape.

COUNTRY: character entry; e.g. Namibia.

SITENAME: character entry; e.g. Rooifontein.

SITEID: numeric value; Unique number ID of the site.

LAT: numeric value; Decimal degrees to 3 digits (negative for southern hemisphere).

LONG: numeric value; Decimal degrees to 3 digits (negative for western hemisphere).

PRECISELOC: character entry; Yes: location as coordinates quoted in text, No: best estimate of location made using maps within source publications and Google Earth.

SEDIMENTARY_CONTEXT: character entry; Alluvial Fan, Channel, Dune-dammed Lake, Interdune, Overbank, Playa, River End, Scroll Bar, Slackwater. See Table 5.1 for description of sedimentary contexts.

RIVER_SETTING: character entry; Unconfined, Partly confined, Confined; following Fryirs *et al*., 2016; see Figure E1 for examples at site location.

RIVER_STYLE: character entry; Straight, Sinuous, Meandering. Based on calculation of channel sinuosity index (straight: < 1.05, sinuous: 1.05-1.5, meandering: > 1.5) at site location. NA if site is not located on a contemporary channel.

CHANNEL_SINUOSITY_INDEX: numeric value; Distance measured between two points along a stream divided by the straight distance between two points. Calculated for the river reach (~10 km) at each site.

VALLEY_SINUOSITY_INDEX: numeric value; Distance measured along the centre of a valley between two points divided by the straight distance between two points. Calculated for the river reach (~10 km) at each site.

ELEVATION: numeric value; Elevation at site in meters. Calculated from the digital elevation model ALOS Global Digital Surface Model AW3D30 (JAXA).

INTERMITTENCE_PROB_SITE: numeric value; Probability of intermittence at the site: probability that the river will cease to flow for at least 1 day. Using data from Messager *et al.* (2021). Rivers are classified on a scale from non-perennial (high probability of flow intermittence) to perennial (low probability of flow intermittence).

PRECIP_ANNUAL: numeric value; Average annual precipitation at site. Contemporary total rainfall levels per year (mm $year^{-1}$).

PRECIP_VAR: numeric value; standard deviation of contemporary rainfall levels across a year (mm $year^{-1}$).

ARIDITY_SITE: numeric value; Aridity Index at site, using data from Trabucco and Zomer (2022).

ARIDITY_CAT: character entry; Aridity at site (Hyper arid: < 0.05, Arid: 0.05-0.2, Semi-arid: 0.2-0.5; using data from Trabucco and Zomer (2022) and classification into categories following UNEP (1992).

GEOLOGY: character entry; Geology at site, using geological map presented by Garzanti *et al.* (2022).

ARIDITY _VALUE_CATCHMENT: numeric value; Average aridity value across catchment. Using data from Trabucco and Zomer (2022).

ARIDITY_CAT_CATCHMENT: character entry; Category of average aridity value across catchment (Hyper arid: < 0.05, Arid: 0.05-0.2, Semi-arid: 0.2-0.5; using data from Trabucco and Zomer (2022) and classification into categories following UNEP (1992).

INTERMITTENCE_PROB_CATCHMENT: numeric value; Probability of flow intermittence averaged across all channels in the catchment. Using data from Messager *et al.* (2021).

INTERMITTENCE_MAIN_CHANNEL: numeric value; Probability of flow intermittence of the main channel. Using data from Messager *et al.* (2021).

CATCHMENT_SIZE: numeric value; Size of main catchment in km^2. Calculated from the HydroSHEDS dataset (Lehner and Grill, 2013).

CATCHMENT_RELIEF: numeric value; Difference between highest and lowest point in catchment (m). Calculated using catchment outline from HydroSHEDS dataset (Lehner and Grill, 2013) and the digital elevation model ALOS Global Digital Surface Model AW3D30 (JAXA).

MAIN_RIVER_LENGTH: numeric value; Length of main river within the catchment (km). Calculated using the HydroSHEDS dataset (Lehner and Grill, 2013).

CHANNEL_GRADIENT: numeric value; Mean channel gradient (km m^{-1}) calculated as change in elevation from the start and end of the river by the length of the main channel.

DRAINAGE_DENSITY: numeric value; relationship between total length of channels and catchment size (km km^{-2}).

SINUOSITY_CATCHMENT: numeric value; Main river length divided by straight distance between start and end of the river.

SINUOSITY_CATCHMENT: character entry; Straight, Sinuous, Meandering. Based on calculation of catchment sinuosity index (straight: < 1.05, sinuous: 1.05-1.5, meandering: > 1.5).

3. Sample details

AGEID: numeric value; Unique number ID of the age.

LABID: character entry; Laboratory identification number.

SITETYPE: character entry (Artificial Section (e.g. pit), Core, Natural Section).

SAMPDEPTH: numeric value; Sample depth in metres.

AGETYPE: character entry; Luminescence or Radiocarbon.

MATDATED: character entry; Type of material dated (Bone, Bulk Charred Material Calcareous Sediment, Carbonates, Charcoal, Detrital Organics, Organic Sediment, Ostrich Egg Shell, Plant, Root Cast, Sand, Seed, Shell, Termite Nest, Wood). NA if sample material not reported.

4. Chronology

LUMAGE: numeric value; Luminescence age in years, NA if age is radiocarbon.

LUMERR: numeric value; Uncertainty associated with luminescence age in years; NA if not reported.

DE: numeric value; Luminescence equivalent dose (Gy); NA if age is radiocarbon.

DE_ERR: numeric value; Uncertainty associated with luminescence equivalent dose (Gy).

14CDATE: numeric value; Reported radiocarbon age in years. Not calibrated.

14CDATE_ERR: numeric value; Uncertainty associated with radiocarbon age in years.

RCAGE_CALIB: numeric value; Calibrated radiocarbon age in years BP. All ages recalibrated using SHCal20 (Hogg *et al.*, 2020) and Bomb13SH12 (Hua *et al.*, 2013; Hogg *et al.*, 2020) in OxCal v 4.4.4. (Bronk Ramsey, 2021). NA if age is luminescence.

RCERR_CALIB: numeric value; Uncertainty associated with calibrated radiocarbon age in years.

4.1. Luminescence specific chronologic metadata

LUMTYPE: character entry (TL: Thermoluminescence, OSL: Optically Stimulated Luminescence, IRSL: Infra-red Stimulated Luminescence), NA if no luminescence type stated.

MINERAL: character entry; Mineral dated (Q: Quartz, F: Feldspar, PM: Polymineral), NA if no mineral stated.

MEANGRAIN: character entry; Average of grain size range dated; NA if no grain size range quoted.

MINGRAIN: character entry; Minimum of grain size range dated; NA if no grain size range quoted.

MAXGRAIN: character entry; Maximum of grain size range dated; NA if no grain size range quoted.

PROTOCOL: character entry; Luminescence dating protocol used (MAAD: Multiple aliquot additive and regenerative dose, SAAD: Single aliquot additive and regenerative dose, SAR: single aliquot regenerative dose, OTHER), NA if protocol not stated.

PREHEAT: numeric value; in °C.

CUTHEAT: numeric value; number in °C.

QUALITY_CONTROL: character entry; Has quality control (e.g. preheat plateau or dose recovery) been performed; Yes, No.

AGEMODEL: character entry; Age model used for SAR ages only (mean, MAM: minimum, FMM: finite mixture, CAM: central; OTHER). NA if no age model was quoted.

SCALE: character entry; Scale of analysis (MG: multigrain, SG: single grain, FG: fine grain); NA if not quoted.

ALIQUOTSIZE: numeric value; Aliquot size in mm.

ALIQUOTNUM: numeric value; Number of aliquots accepted, NA if not reported.

ALIQUOTMEASURED: numeric value; Number of aliquots measured, NA if not reported.

WATERCONTENT: numeric value; Measured or assumed water content in %, NA if not reported.

WATERCONTENTERR: numeric value; Uncertainty on measured or assumed water content in %, NA if not reported.

OVERDISPERSION: numeric value; Overdispersion of equivalent doses in %, NA if not reported.

OVERDISPERSIONERR: numeric value; Uncertainty associated with overdispersion of equivalent doses in %, NA if not reported.

K: numeric value; Measured Potassium radionuclide concentration in %, NA if not reported.

KERR: numeric value; Uncertainty associated with measured Potassium radionuclide concentration in %, NA if not reported.

TH: numeric value; Measured Thorium radionuclide concentration in ppm, NA if not reported.

THERR: numeric value; Uncertainty associated with measured Potassium radionuclide concentration in ppm, NA if not reported.

U: numeric value; Measured Uranium radionuclide concentration in ppm, NA if not reported.

UERR: numeric value; Uncertainty associated with measured Potassium radionuclide concentration in ppm, NA if not reported.

BETADOSE: numeric value; Calculated beta dose rate in Gy ka^{-1}, NA if not reported.

BETADOSEERR: numeric value; Uncertainty associated with calculated beta dose rate in in Gy ka^{-1}, NA if not reported.

GAMMADOSE: numeric value; Calculated gamma dose rate in Gy ka^{-1}, NA if not reported.

GAMMADOSEERR: numeric value; Uncertainty associated with calculated gamma dose rate in Gy ka^{-1}, NA if not reported.

COSMIC: numeric value; Calculated cosmic dose rate in Gy ka^{-1}, NA if not reported.

COSMICERR: numeric value; Uncertainty associated with calculated cosmic dose rate in Gy ka^{-1}, NA if not reported.

DOSERATE: numeric value; Calculated environmental dose rate in Gy ka^{-1}, NA if not reported.

DOSERATEERR: numeric value; Uncertainty associated with calculated environmental dose rate in Gy ka^{-1}, NA if not reported.

4.2. Radiocarbon specific chronologic metadata

RCMETHOD: character entry; dating method used (AMS, Counting).

RCAGECALIB1: numerical value; Calibrated age in years AD as quoted in the original publication. Oldest year.

RCAGECALIB2: value; Calibrated age in years AD. Calibrated age in years AD as quoted in the original publication. Youngest year.

CALIB: character entry; Calibration curve used in original publication.

RC_MATERIAL: character entry; material used for radiocarbon dating (Bulk, Macrofossil), NA if material not stated.

5. Interpretation

METHODS: character entry; Methods used to reach palaeoenvironmental interpretation (Amino Acids, Archaeological Artefacts, Documentary, Diffuse Reflectance Spectroscopy, Carbonate

Content, Geochemistry, Grain Size, Heavy Minerals, Instrumental, Micromorphology, Microscopy, Mineral Magnetism, Mineralogy, Organic Content, Palaeodischarge, Palaeontology, PSI (Palaeostage Indicators), Palynology, PH, Provenance, Sediment Colour, Sedimentary Facies, SEM, Soil Characteristics, Stable Isotopes, Stratigraphy, Thin Sections, Topography, Vegetation Associations, XRD, XRF). NA if no method used.

APPPROACH: character entry; Methods grouped into type of information gained (Architecture, Conditions, Discharge, Provenance, Texture). Can list more than one. NA if no approach used.

MAIN_APPROACH: character entry; Main approach used from the list in APPROACH category.

FLOW_OCCUPANCY: character entry; Ephemeral, Intermittent, Perennial. NA if no interpretation flow occupancy is reached. See Table 5.2 for description of flow occupancy scale.

FLOW_MAGNITUDE: character entry; Extreme Flood, High Energy Flow, Low Energy Flow. See Table 5.2 for description of flow magnitude scale. NA if no interpretation of flow magnitude is reached.

RIVER_LENGTH: character entry; Interpretation of change in river length (Extended River Length, Shortened River Length, Short Distance Fluvial Transport). NA if no change in river length reported.

DISCHARGE: numeric value; Estimated discharge of sedimentary unit, in $m^3\ s^{-1}$. Average if range quoted. NA if no discharge estimates available.

CLIMATE: character entry; Interpretation of precipitation relative to present (Wet, Dry). NA if no interpretation reached in precipitation change.

OTHER_DRIVER: character entry; Detail of drivers other than climate responsible for fluvial change. (e.g. Anthropogenic land use, Wildfires). NA if no other driver discussed.

6. Data quality assessment

CHRONOLOGY_CATEGORY: character entry; Chronological filtering category (Category 1: highest quality, Category 2, Category 3: lowest quality).

CHRONOLOGY_CATEGORY_REASON: character entry; Reason for classification of the age into the chronological filtering category (No depth/stratigraphic context; No supporting chronology; Supporting chronology is available, but is not stratigraphically consistent; Stratigraphic context not sufficient to assess supporting chronology; SAR protocol not used; Quality control not reported; De not reported; Dose rate not reported; Age model not reported; Dating protocol not reported; Grain size dated not reported; Partial bleaching identified but single grains not used; Feldspar ages presented with no assessment of anomalous fading; Bulk sample used; Age questioned by author; Met all criteria for Category 1).

SUPPORTING_METHODS: character entry; Are ages supported by sedimentary approaches for interpretation of palaeoenvironmental conditions? (Yes, No).

ACCEPTED: character entry; Does the age meet the chronological data quality criteria and availability of supporting methods (Yes, No).

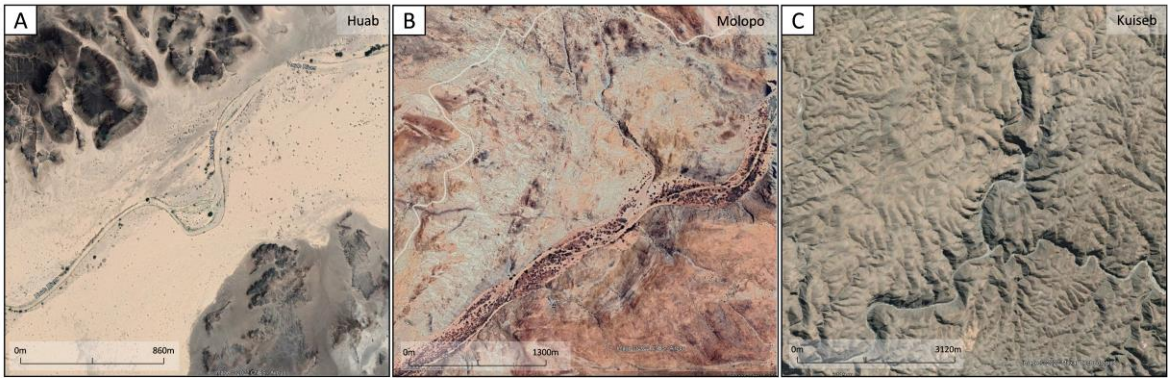

Figure E1. Classification of channel confinement in Google Earth following Fryirs *et al*. (2016). Unconfined (Huab River; site 22), Partially confined (Molopo River; site 53), Confined (Kuiseb River; site 32).

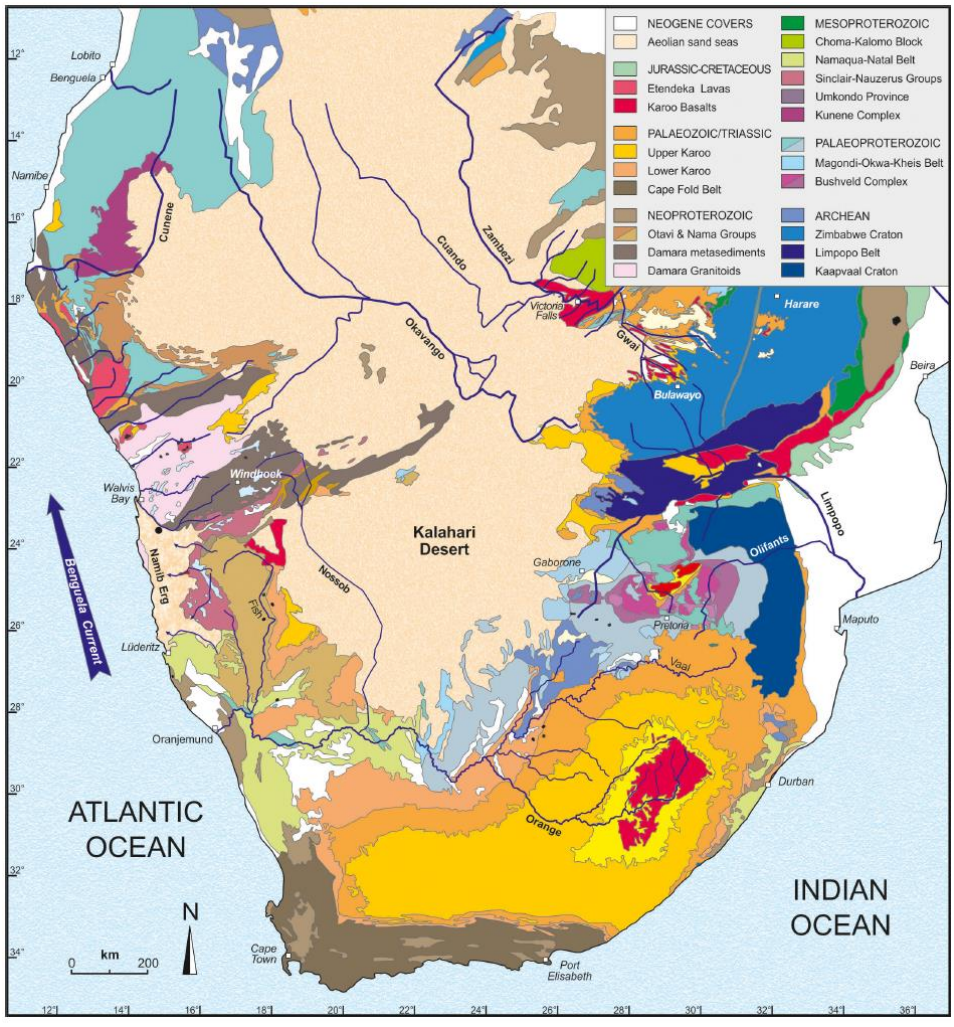

Figure E2. Map of key geological units in southern Africa map from Garzanti *et al*. (2018) and Garzanti *et al.* (2022) adapted from Schulter (2008).

Appendix F – Supplementary data for Chapter 5 (Paper 2): part 2

The Database

The database has been submitted as Appendix F in an electronic form attached to this thesis.